NOTICE

The quality of this microform is heavily dependent upon the quality of the original thesis submitted for microfilming. Every effort has been made to ensure the highest quality of reproduction possible.

If pages are missing, contact the university which granted the degree.

Some pages may have indistinct print especially if the original pages were typed with a poor typewriter ribbon or if the university sent us an inferior photocopy.

Reproduction in full or in part of this microform is governed by the Canadian Copyright Act, R.S.C. 1970, c. C-30, and subsequent amendments.

AVIS

La qualité de cette microforme dépend grandement de la qualité de la thèse soumise au microfilmage. Nous avons tout fait pour assurer une qualité supérieure de reproduction.

S'il manque des pages, veuillez communiquer avec l'université qui a conféré le grade.

La qualité d'impression de certaines pages peut laisser à désirer, surtout si les pages originales ont été dactylographiées à l'aide d'un ruban usé ou si l'université nous a fait parvenir une photocopie de qualité inférieure.

La reproduction, même partielle, de cette microforme est soumise à la Loi canadienne sur le droit d'auteur, SRC 1970, c. C-30, et ses amendements subséquents.

ORIGIN AND IMPLICATION OF CORONA STRUCTURES WITHIN DIABASE DYKES INTRUDING THE ARCHEAN ORTHOGNEISSES OF THE CENTRAL GRENVILLE PROVINCE, EAST OF CHIBOUGAMAU, QUEBEC

by

Catherine Madore

A Thesis
submitted to the School of Graduate Studies and Research
in Partial Fulfillment of the Requirements
for the Degree of Master of Science at
The University of Ottawa

ISBN 0-315-68040-7

UNIVERSITÉ D'OTTAWA
UNIVERSITY OF OTTAWA

ABSTRACT

Geological mapping has defined a distinct group of NNE trending diabase dykes east of the Grenville Front in the Chibougamau area. These dykes are found intruding Archean orthogneisses within a narrow zone, the Parautochthonous terrane, bounded to the northwest by the Grenville Front and to the southeast by the Allochthon Front. The best preserved dykes, exhibiting primary igneous minerals and textures, are located along the Grenville Front, whereas the most metamorphosed dykes (i.e. amphibolites) are located along the Allochthon Front.

The dykes are tholeiitic to weakly alkaline and can be divided into four main groups, based on texture and certain major and trace elements: 1) low-TiO_2 (average TiO_2 1.19 wt%, K_2O 0.45 wt%, P_2O_5 0.13 wt%, Y 18ppm, Zr 92ppm, Yb 1.8ppm), 2) high-TiO_2 (average TiO_2 2.24 wt%, K_2O 0.82 wt%, P_2O_5 0.33 wt%, Y 34ppm, Zr 176ppm, Yb 3.3ppm), 3) high-TiO_2 segregations (average TiO_2 2.63 wt%, K_2O 0.97 wt%, P_2O_5 0.58 wt%, Y 51ppm, Zr 241ppm, Yb 5.1ppm) and 4) high-Al_2O_3 (average Al_2O_3 23.3 wt%, TiO_2 0.27 wt%, K_2O 0.37 wt%, P_2O_5 0.04 wt%, Y 7ppm, Zr 34ppm, Yb 0.8ppm). The low-TiO_2 dykes are similar to N-type MORB and to low-TiO_2 flood basalts, whereas the high-TiO_2 diabase dykes and high-TiO_2 pegmatoidal segregations are similar to high- Fe-Ti, continental flood basalts. Comparison of the dykes with other dyke swarms of the Grenville and Superior Provinces shows that the high-TiO_2 group is most similar to the Grenville dyke swarm. The high-Al_2O_3

group, characterized also by high Mg number and Ni contents, are similar to high-Al_2O_3 basalts; however, they are considered to be cumulate rocks.

Igneous minerals include olivine, augite, plagioclase, magnetite, biotite, and pargasite. Igneous biotite forms single corona layers around primary magnetite and pargasite occurs at olivine-magnetite and olivine-plagioclase contacts. These early formed corona layers are interpreted as products of late- to post-magmatic equilibration with a fluid phase at grain boundaries. The chemical composition of primary (igneous) mineral assemblages are for the most part not pristine because of reaction and recrystallization during the formation of post-magmatic corona structures. The olivine composition is overall uniform and ranges from Fo_{45} to Fo_{60}. Igneous clinopyroxene varies from $En_{40}Wo_{39}Fs_{21}$ to $En_{44}Wo_{39}Fs_{17}$. Plagioclase composition ranges from An_{50} to An_{60}. Primary biotite flakes are uniform in composition with 3.14-3.19 wt% TiO_2, 14.45-15-09 wt% Al_2O_3, 2.87-3.31 wt% Fe_2O_3, 15.87-18.29 wt% FeO, and 11.49-14.38 wt% MgO. Post-magmatic amphiboles are pargasitic in composition with low TiO_2 (0.02-0.18 wt%) and high Al_2O_3 (17.0-21.0 wt%).

The principal metamorphic minerals are enstatite, hornblende, spinel, corundum, garnet, albite, and quartz. The evolution from primary to secondary minerals can be followed through several complex reactions, four of which are:

1) olivine + plagioclase = enstatite + pargasite + Al_2O_3

2) olivine + O_2 = enstatite + magnetite

3) pargasite + plagioclase = garnet + diopside + albite + Al_2O_3

4) augite + plagioclase = pargasite

5) biotite + plagioclase = garnet + pargasite + diopside

Reactions (1), (2), and (5) are spacially and temporaly associated. The orthopyroxene produced by reaction (1) is more magnesian-rich ($En_{61-72}Fs_{27-39}$) than the orthopyroxene associated with magnetite crystals ($En_{38-64}Fs_{36-62}$). Metamorphic clinopyroxene varies from salitic augitic to diopsidic in composition. Metamorphic plagioclase compositions are sodic, ranging from An_{20} to An_{50}. The chemical composition of metamorphic amphibole is defined by high TiO_2 (0.79-1.25 wt%) and low Al_2O_3 (3.0-11.0 wt%) values. Garnet crystals produced during reaction (2) are magnesian-rich ($Fe_{47-55}Mg_{16-22}Ca_{19-32}$) whereas garnet crystals from reaction (4) are iron-rich ($Fe_{68-72}Mg_{7-11}Ca_{16-20}$).

The development of metamorphic assemblages progressively increases from the Grenville Front to the Allochthon Front, where the dykes have been affected by the Grenvillian Orogeny to produce atoll garnet and hornblende.

A tentative P-T path of corona reactions (based on several estimates of pressure and temperature from various geothermometers and geobarometers) across the parautochthonous terrane extends from 600°C to 950°C at 6.0 to 9.0 kbars.

A mes parents,

Odette et Gaston

Le jour où l'on atteint l'objet d'un rêve,
on a bien vécu l'instant d'une rose.
L'on a compris que la vie est trop brève
et que l'on meurt en sachant peu de choses.

Ernest Pallascio-Morin
(La Magie de l'eau, 1978)

ACKNOWLEDGEMENTS

I am grateful to Dr. André Ciesielski of the Geological Survey of Canada (G.S.C) for suggesting and initiating me to the study of diabase dykes in the Chibougamau area. I am extremely thankful to him for logistical support. I wish to acknowledge and thank Dr. Irvine Annesley, Eric Ouellet, and André Ciesielski for their field assistance and exchange of ideas in the field. I would like to thank Dr. Ralph Kretz of the University of Ottawa (U.O.) for the supervision of the project and for providing valuable insights regarding many aspects of the thesis.

Financial support was obtained from the Geological Survey of Canada and the National Sciences and Engineering Research Council. Rocks and minerals were analysed at the Geological Survey of Canada. Special thanks are directed to G.J. Pringle and M. Bonardi of the Geological Survey of Canada for their valuable advice and assistance throughout the duration of the microprobe and scanning electron microprobe work. I am indebted to Karyne Besso for her hospitality during my visits to Ottawa for microprobe work. G. Mrazek (U.O.) prepared some of the thin sections.

I would like to thank Ralph Kretz, Dr. Tony Fowler (U.O.), and André Ciesielski for their discussion and revisions of the early drafts of the thesis. The study has also benefitted from

discussions with Dr. Toby Rivers and Dr. C.F. Mengel of Memorial University, and Dr. Terry Gordon of the University of Calgary.

Thanks go to Christine Payette of the University of Saskatchewan for permission to use the microprobe to determine fluorine (F) and chlorine (Cl) in amphibole, biotite, and apatite crystals.

Finally, I am grateful to Irvine Annesley of the Saskatchewan Research Council for providing working space, computer and laboratory facilities, and most of all for valuable discussion and exchange of ideas on various aspects of the thesis.

TABLE OF CONTENTS

LIST OF FIGURES

LIST OF TABLES

LIST OF APPENDICES

Apppendices

INTRODUCTION

1.1 LOCATION

The study area is located approximatly 40 km southeast of Chibougamau, Quebec (Figure 1). It covers most of the Chibougamau and Riviere Mistassini map areas (32G, 32H) and the southeastern and southwestern corners of the Lac Assimica and Baie Abatouche map areas (32J, 32I). The study area lies within a narrow 60 km wide zone, which separates the Superior Province to the northwest from the Grenville Province to the southeast (see Figure 2). Rivers and Chown (1986) have defined this zone as the "Parautochthonous Terrane".

The area under investigation is accessible from Chibougamau by highway 167, and is located on the Donahue property. Most of the outcrops mapped and sampled by the author are situated along gravel roads. Rock exposures are sporadic and where present are most commonly covered by heavy vegetation. The field season extends from approximately mid-May to early September.

1.2 PREVIOUS INVESTIGATIONS OF STUDY AREA

The first systematic mapping of the Chibougamau area was carried out by the geologists of the Ministère des Mines du Québec (Imbault, 1950; Gilbert, 1951; Grenier, 1952; Deland, 1953; Neale, 1953; and Laurin, 1954). A compilation of this

Figure 1. Location of study area with respect to other dyke swarms in the Superior and Grenville Provinces. Figure modified from Ciesielski (1990)

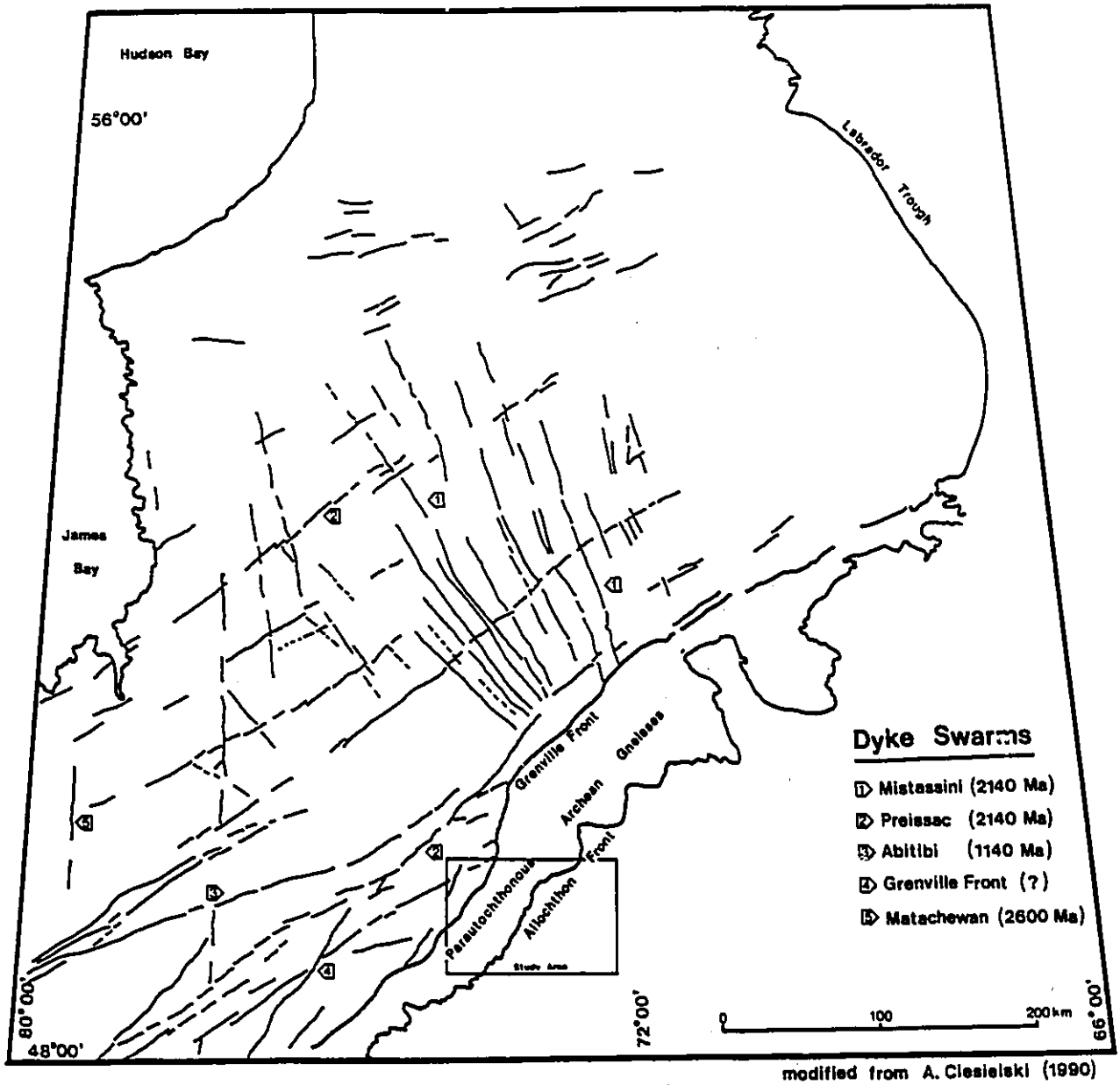

modified from A. Ciesielski (1990)

Figure 2. Litho-tectonic map of the Grenville Front in the Chibougamau area, showing the distribution of the NNE diabase dykes (Proterozoic meta-diabase) within the Parautochthon domain (Ciesielski and Madore, 1989).

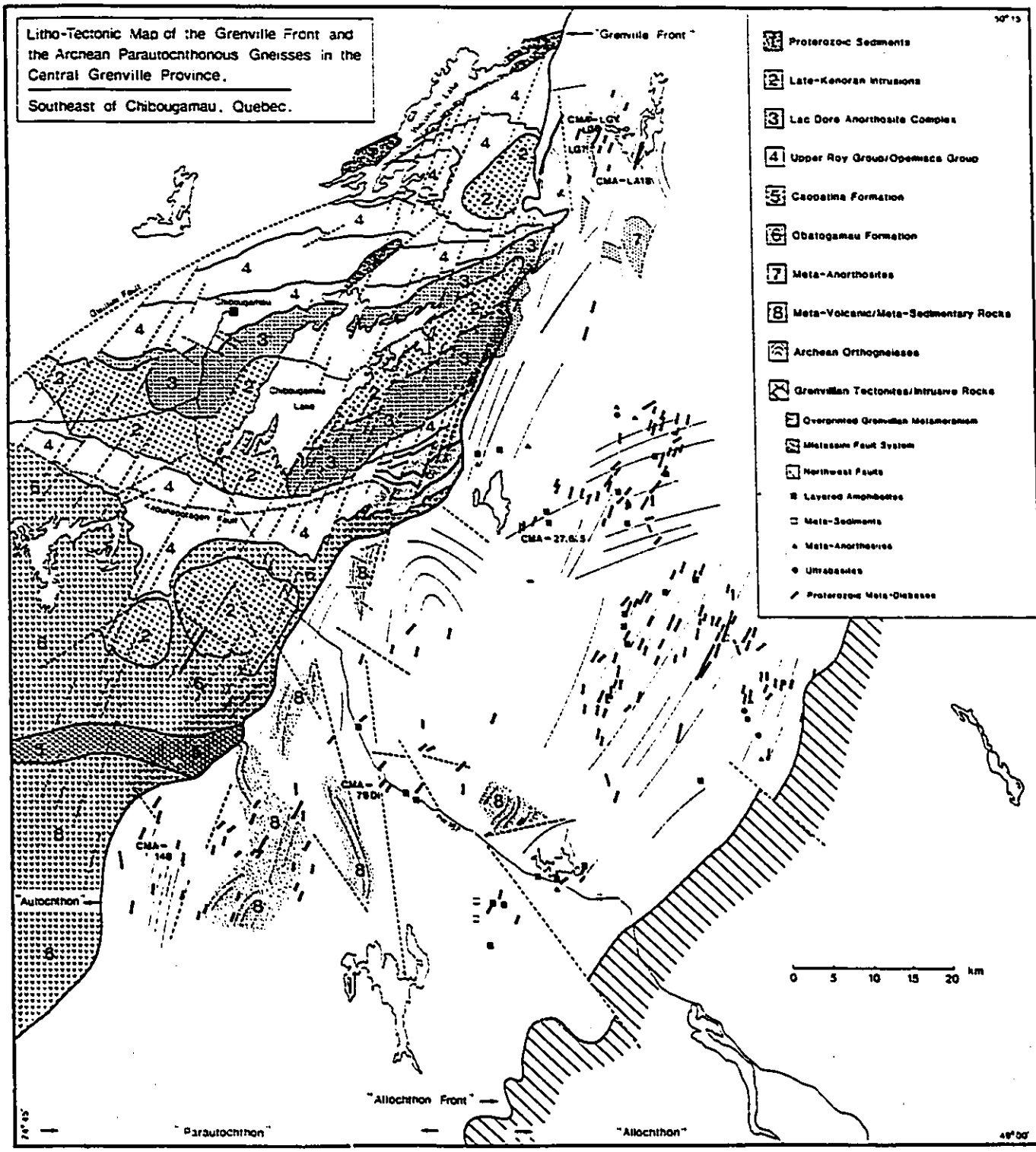

Ciesielski, A and Madore, C. (1989)

mapping was completed by Avrantchev (1979). An area contiguous to the Grenville Front has been investigated recently in detail by Ciesielski and Ouellet (1985), Ciesielski et al. (1986), and Ciesielski (1988).

1.3 PREVIOUS STUDIES OF GABBROIC DYKES IN THE GRENVILLE PROVINCE

Numerous metamorphosed gabbroic dykes and bodies occur in the Grenville Province. They are characterized by a similar chemical affinity of tholeiitic composition. Detailed petrographic descriptions of these mafic intrusions, given by Whitney and McLelland (1973), Grieve and Gittins (1975), Emslie (1983), Grant (1988), Rivers and Mengel (1988), and Kretz et al. (1989), reveal a great similarity in mineralogy and textures (e.g. corona structures). The corona structures seem to be a diagnostic characteristic of most dyke swarms and gabbroic bodies situated in the Grenville Front area. Such corona structures, apparently, have not been observed within the dykes of the Superior Province.

Several gabbroic complexes and diabase dykes from the Grenville Province have been studied in detail and commonly display well developed reaction rims around primary minerals such as olivine, pyroxene, and oxides. From the western Grenville Province, in the Georgian Bay area, several deformed gabbroic masses have been mapped in detail by Grant (1985 and 1988) and Davidson and Grant (1986). These gabbroic bodies commonly display corona reactions about olivine and oxide minerals. The evolution

of those corona structures can be followed through one or more metamorphic events. Deformed fragments of Sudbury dykes are found in the Grenville Front Tectonic Zone with well developed corona structures around olivine (Bethune and Davidson, 1988). Felsic to mafic coronitic metagabbros from the Ottawa region have been described by Kretz et al. (1989) and they display similarities with the metagabbros from the Georgian Bay area. From the eastern Grenville Province, four gabbroic complexes have been studied in detail. These gabbroic complexes are part of the Otish-Seal node, as defined by Fahrig (1987). They are as follows: a) the Otish sills (1800-1900 Ma) with associated northeast trending dykes (1718 Ma, Chown and Archambault, 1987), b) the coronitic Shabogamo Gabbro (1375 Ma) located at the southern end of the Labrador Through, c) the Seal Lake Group (1300 Ma) north of the Grenville Front, and d) the Michael gabbros (1500 Ma) which consist of elongated sheet-like bodies that occur at the eastern end of Labrador (Fahrig, 1987). The Michael gabbros trend southwest from the Grenville Front (Emslie, 1983).

1.4 PREVIOUS STUDIES OF CORONA STRUCTURES

Corona structures were first recognized in mafic and ultramafic rocks by Tornebohm (1877) and Holland (1896). These structures have been observed in troctolites (Huang and Merritt, 1954) and in metagabbros or metadolerites (Sederholm 1916;

Brögger 1934; Buddington 1939, 1952; Shand 1945; Gjelsvik 1952; Poldervaart and Gilkey 1954; Murthy 1958; Bose 1961; and others).

Corona structures are characterized by concentric layers of one or more different minerals about a central crystal. The number of layers ranges from one to five depending on the stage of evolution. The most common corona structure occurs at the junction of olivine and plagioclase grains. This corona type is generally composed of an inner layer of orthopyroxene adjacent to the olivine, followed by an intermediate layer of amphibole - spinel symplectite, and finally an outer layer of garnet. Well developed corona structures are also found around central pyroxene, garnet, and iron oxide minerals.

Five different, possible hypotheses have been proposed for the formation of corona structures, according to Buddington (1939). Three of these hypotheses appeal to a magmatic origin, and differ from each other in explaining corona formation by the order of nucleation, by the interaction of early formed minerals with a residual melt, or by intergranular deuteric alteration. The other two proposed hypotheses for corona formation appeal to a metamorphic origin, either by thermal or regional metamorphism, which would involve the diffusion of components in a solid or semi-solid state. The problem of distinguishing between magmatic and metamorphic corona structures is still controversial. The mechanism(s) responsible for the formation of corona structures is still not well understood and remains conjectural. The formation of corona structures (i.e. hypotheses and mechanisms)

and their tectonic and metamorphic significance will be discussed in detail in Chapter 6 of this study.

1.5 PURPOSE OF THE STUDY

Most mafic dyke swarms are considered to have formed in rift environments related to active intraplates or plate margins (Halls, 1988). However, new evidence suggests that some Precambrian dyke swarms were emplaced during crustal uplift in compressional tectonic environments such as those of continental collisions. Examples of this situation are recorded by the 1250 Ma Sudbury dykes (Davidson and Bethune, 1988) and the Kapuskasing dykes (Halls, 1988). Both of these dyke swarms are thought to have been emplaced during compressional uplift. The narrow and deformed fragments of the Sudbury dykes that are found in the vicinity of the Grenville Front would represent the deeper levels of the Sudbury dykes within the Superior Province that have been brought to the surface. Evidence for petrological and geochemical differences between these dykes of compressional tectonic settings and those of extensional tectonic settings would provide valuable criteria for the classification of Precambrian mafic dykes (Halls, 1988).

The purpose of the present study is to provide further information on Precambrian dykes from a family of diabase dykes in the Chibougamau area, Central Grenville Province; informally named herein as "the NNE diabase dykes". The study examines in

detail the primary (igneous) and secondary (metamorphic) characteristics of this family of diabase dykes. The NNE diabase dykes are characterized by distinct mineral assemblages and corona structures, and therefore, systematic sampling of the dykes across the parautochthonous domain provides good control on analyzing the textural and mineralogical variation that occurs within them. A detailed examination of the dyke minerals, including their chemistry, is an integral part of the present study, and forms the basis of an investigation of the corona structures. The texture and mineralogy associated with each of the corona structure types is indicative of varying P-T conditions. Therefore, the evolution of corona structures may be followed through a series of modelled reactions in P-T space.

In addition, this study discusses the controversial hypotheses surrounding the origin of coronas and gives a brief review of the irreversible thermodynamic models developed by Fisher (1977) and Joesten (1977). Development of a pertinent model for the different types of corona structure displayed in the NNE dykes is another important aspect of this study. P-T conditions are determined separately for each of the corona structure types and their corresponding mineral assemblages, and then they are compared with one another. Corona layers, when modelled using irreversible thermodynamics, are assumed to be part of a closed system, and thus should have recorded the incremental P-T evolution through magma cooling and metamorphism. Therefore, a comparison of the P-T estimate of the mineral

assemblages outside corona structures and the P-T estimate within corona structures should permit verification of this assumption.

Another component of the study is a preliminary investigation of the petrochemistry of the NNE diabase dykes. This entails comparing the geochemistry of the NNE diabase dykes from the parautochthon with some Precambrian dykes of the Superior Province autochthon in the Chibougamau area (i.e. the Abitibi, Preissac, Mistassini swarms, and Otish sills).

The final component of the study discusses the tectonic environment(s) responsible for forming corona structures in mafic intrusions. The mineral assemblages of mafic rocks are quite susceptible to variations in physical conditions, hence they are possible indicators of the pressure(P)-temperature(T) conditions of their tectonic environment (e.g. Rivers and Mengel, 1988). Corona structures from mafic dykes and gabbroic bodies have become increasingly used in this manner as P-T indicators of the uplift history of an area. They provide a means of reconstructing the P-T path of their emplacement and the subsequent tectonometamorphic history of their geological environment (i.e. from the emplacement and cooling of the body to the subsequent metamorphism). This reconstruction is accomplished by studying the mineral assemblages and the mineral reactions responsible for the various types of corona structures found in variably metamorphosed basic and ultrabasic intrusive rocks. It is with this in mind that a study of the NNE coronitic dykes of the parautochthonous domain was carried out. Possibly, the

determination of the P-T conditions of the NNE diabase dykes from the parautochthonous domain may reveal valuable information on the amount of uplift movement that has been recorded by the autochthonous domain during the Grenvillian tectonometamorphic overprinting event.

1.6 METHODS OF INVESTIGATION

The study was carried out as part of a Geological Survey of Canada (G.S.C.) field project. Field support and logistics were provided by a G.S.C. field party under the direction of A. Ciesielski.

Field work was carried out by the author and a field assistant during the first three weeks of June, 1988. Mapping and sampling of the dykes was achieved by traversing the logging roads of the region. Field data were recorded on 1 inch = 1 mile photocopies of aerial photographs and transferred to a 1:250,000 scale map.

Subsequent work in the office involved the study of approximately 65 thin sections, including some from samples collected by A. Ciesielski. Most of the samples were chemically analyzed in order to determine the chemical characteristics of the NNE diabase dykes. Microprobe analyses of constituent minerals were determined from representative coronitic samples in order to characterize the igneous and metamorphic mineral assemblages and to elucidate the post-magmatic evolution of the

NNE diabase dykes. Details of the methods, standards, and detection limits of the whole rock and mineral chemistry analyses are found in Chapters 4 and 5, respectively.

GEOLOGICAL SETTING

2.1 INTRODUCTION:

The study area is shown in Figures 1 and 2. It is situated in the parautochthon (parautochthonous domain) of the Grenville Province in a region 50 km southeast of Chibougamau, Quebec. The parautochthon comprises one of three major components of the Grenville Province as defined by Rivers and Chown (1986) in their new tectonic classification of the eastern Grenville Orogen. The other two major components are the autochthon and the allochthon which lie, respectively, to the northwest and the southeast of the parautochthon. The autochthon consists, for the most part, of lithological units that belong to older structural provinces (e.g. Superior and Churchill). Locally, the autochthon includes mildly deformed cover successions of early to middle Proterozoic age. The parautochthon consists of a diverse package of reworked autochthonous sequences (i.e. highly deformed equivalents of autochthonous sequences found into the Grenville Province). The parautochthonous domain defines a narrow zone of variable width, which is 60 km in the study area. This domain extends from the Labrador Trough to Southeastern Québec, where it narrows out in the Val D'Or area (Rivers and Chown, 1986).

The parautochthonous rocks, characteristically, have a well developed Kenoran fabric locally superimposed by NNE Grenvillian deformation which progessively increases in intensity towards the

allochthon. The allochthon consists of high grade orthogneisses and paragneisses of upper amphibolite to granulite facies, and associated plutonic rocks. The autochthon and the parautochthon are separated by a major litho-tectonic break, the Grenville Front.

In many places, the Grenville Front is defined by an abrupt lithological change from Archean metavolcanic-metasedimentary sequences of the autochthon to Archean gneisses of the parautochthon. However in other localities, the change is not lithological but is structural and/or tectonometamorphic. Similarly, the parautochthon and the allochthon are separated from each other by a major litho-tectonic break, the Allochthon Front as defined by Ciesielski (1988 and pers. comm.).

2.2 REGIONAL GEOLOGY OF THE STUDY AREA:

Three major tectono-lithological domains and two discordances are recognized in the Chibougamau area (Ciesielski, 1988). The three lithological domains are defined respectively as the Superior Province, the reworked orthogneisses (mainly relatively homogeneous grey orthogneisses), and the Grenvillian tectonites, and these correspond respectively to the autochthon, the parautochthon, and the allochthon of Rivers and Chown (1986). The two discordances are namely the Grenville Front (GF) and the Allochthon Front (AF). The Grenville Front extends from Georgian Bay to the Labrador Coast and represents the southern limit of

the Superior Province, whereas the AF marks a lithological boundary between the orthogneisses and the granulites of the Grenville Province (Ciesielski, 1988). Both fronts are remarkably well defined on an aeromagnetic map mainly because of the contrasting low magnetic profile exhibited by the parautochthonous domain (Fig. 3, from Rivers et al., 1989). This low magnetic profile results from the combined effects of a) the low magnetite content of the parautochthonous rocks, b) the presence of mafic intrusive rocks, and c) the occurrence of some high grade metamorphic rocks in association with the orthogneisses (Ciesielski, 1988).

2.2.1 The Autochthon

The autochthon, in the Chibougamau area, comprises two groups of Archean metavolcanic-metasedimentary sequences, the Roy Group and the overlying Opemisca Group. These Archean Groups of the Superior Province are in turn overlain by three Proterozoic meta-sedimentary formations. The intrusive rocks associated with the Archean supracrustal sequences are comprised of the Lac Doré complex, and the Chibougamau, La Dauversière and Frances Lake plutons.

The structures within the rocks of the autochthonous domain reveal two episodes of deformation that are related to the Kenoran Orogeny (circa 2700 Ma, Daigneault and Allard, 1984). The first phase of deformation is associated with local plutonism,

Fig. 3. Bouguer gravity (a) and aeromagnetic (b) anomaly maps of the Grenville Province. Solid line in both maps is the position of the Grenville Front.

whereas the second phase is responsible for the development of east-west trending synforms and antiforms. Three sets of faults transect the Archean supracrustal sequences: 1) the east-west Kapunapotagen faults, which probably result from the second phase of deformation that produced the east-west foliation, 2) the northeast Gwillim fault, and 3) the north-northeast Mistassini faults, which are Proterozoic in age and transect the two earlier fault systems. The latest faults are distributed along the Grenville Front in a zone that penetrates circa 40 km into the autochthon and approximatly 10 km into the parautochthon. The Mistassini faults are believed to have been reactivated during the Grenvillian deformation that has affected the autochthon in the vicinity of the Grenville Front.

The autochthonous domain situated along the Grenville Front has recorded the effects of the Grenville Orogeny. These effects are expressed by the incomplete rotation of the Kenoran east-west foliation towards the north-northeast, the presence of a northeast trending crenulation and southeast plunging lineations, the development of the Mistassini fault system, and the increase in metamorphic grade to amphibolite facies towards the east.

2.2.2 The Grenville Front

The Grenville Front is highly variable in character, depending on its structural and lithological geometry along strike. It can be defined as a lithological boundary, a

geochronological boundary, a fault boundary (e.g. it coincides with major faults such as the Mistassini faults) and/or a tectonic boundary (i.e. a zone characterized by the presence of high strain rocks).

The Grenville Front, in the Chibougamau area, is characterized by a sharp lithological break which separates Archean metavolcanic-metasedimentary sequences and associated syn- to post-tectonic intrusions of the Superior Province from Archean orthogneisses, tectonites and intrusive rocks of the Grenville Province.

In the Grenville Front area, the supracrustal rocks and associated intrusive rocks show evidence of polyphase deformation and metamorphism. The most prevalent deformational and metamorphic event recorded in the rocks is thought to be principally the product of the Grenvillian Orogeny (Rivers and Chown, 1986; among others).

2.2.3 The Parautochthon

In the Chibougamau area, the parautochthonous domain is principally composed of Archean orthogneisses that range in chemical composition from tonalitic to trondhjemitic. The texture of the orthogneisses varies from a fine-grained tonalite to a coarse brecciated diatexitic granodiorite (Ciesielski, 1988). In the vicinity of the Grenville Front, the parautochthon comprises large inclusions of anorthosites and meta-anorthosites bordered

by north-northeast faults. To the southwest of the Grenville Front, large inclusions of amphibolites are present and are related to the supracrustal sequences of the autochthon. In general, the parautochthon orthogneisses include various reworked fragments of volcanic and sedimentary units equivalent to the Archean autochthon. Most of these inclusions have reached the upper amphibolite facies as indicated by their epidote - garnet - clinopyroxene - hornblende assemblages. In most places, the parautochthonous gneisses have retained microstructures of the east-west trending Kenoran Orogeny, but superimposed on the Kenoran structures are the effects of the Grenvillian deformation. These effects are locally expressed by the incomplete rotation of the east-west foliations and associated fold axes into a north-northeast trend, and as well by the strong development of a mineral lineation plunging to the southeast. The parautochthonous rocks have undergone Grenvillian metamorphism of greenschist to middle amphibolite grade.

In summary, the parautochthonous domain within the study area is considered to represent the basement to the autochthonous metavolcanic-metasedimentary sequences of the Superior Province. This parautochthonous domain has been thrusted over the autochthon by the Grenville nappes which did not reach the Grenville Front (Ciesielski and Ouellet, 1985).

2.2.4 Diabase Dyke Swarms

Several swarms of diabase dykes occupy the Superior Province (i.e. the autochthonous domain) in the Chibougamau area. One of these is the east-northeast trending Abitibi swarm (1140 Ma) which consists of ten principal dykes and contains the longest dyke in the world (i.e. the Abitibi Dyke, approximately 600 km in length). This swarm extends from Georgian Bay to the Abitibi Belt (Fahrig, 1987). The other swarms include: 1) the east-northeast trending Preissac swarm (2140 Ma) which extends from the Grenville Front to Hudson Bay and from Lake Superior to the Chibougamau area, 2) the north-northwest Mistassini swarm (2140 Ma), which radiates from Mistassini Lake and extends northeast of Chibougamau up to Hudson Bay, and 3) a family of north-northeast trending (NNE) diabase dykes that are located along the Grenville Front parallel to the Mistassini fault system (Fahrig, 1987). The latter dyke family may belong to the "Otish dykes" of the Otish Mountains, although no dating has been done on this family (Chown and Archambault, 1987). Ciesielski (1988) has suggested that may belong to a different swarm which he informally called the "Grenville Front dyke swarm".

Semi-detail mapping by Ciesielski (1988) revealed the presence of north north-east trending (NNE), coronitic diabase dykes in the parautochthonous domain. Ciesielski (pers. comm., 1988) believes that these dykes may be of the same parentage as those in the autochthonous domain along the Grenville Front. The tectonic implications of the dykes in the parautochthonous domain (Ciesielski, 1988) promoted the initiation of this study.

2.3 GEOLOGY OF THE NNE DIABASE DYKES

A family of NNE diabase dykes intrude grey orthogneisses and subordinate pargagneisses and amphibolites (Fig. 5) of the parautochthonous domain, and crosscut the transposed east-west regional foliation (Fig. 4). This family of dykes is oriented parallel to subparallel to the Grenville Front which forms the boundary between the Superior and Grenville Provinces. The distribution of these dykes within the parautochthonous domain appears to be fairly uniform on the basis of the aeromagnetic pattern defined by the dykes. The dykes do not appear to be continuous over long strike lengths, but instead form en-echelon patterns. Their distribution and extent outside the parautochthonous domain is not known. The average strike of the NNE diabase dykes is approximately 025°. The dykes are dipping vertically to subvertically (> 75° ESE).

NNE diabase dykes occurring in the vicinity of the Allochthon Front are crosscut by granitic pegmatite dykes of Grenvillian age (Ciesielski, 1988) which would give a pre-Grenvilllian age to the NNE diabase dykes (Fig. 6).

Most of the diabase dykes are narrow (less than 10 m, typically 1 m in width) and discontinuous, cropping out over short distances up to several hundred meters in length. A few large dykes are present and they outcrop as prominant ridges up to 30-40 meters in width and one kilometer in length.

Figure 4. Close-up of intrusive contact of metamorphosed NNE diabase dyke with grey tonalitic orthogneiss. The width of the field of view is 1 meter.

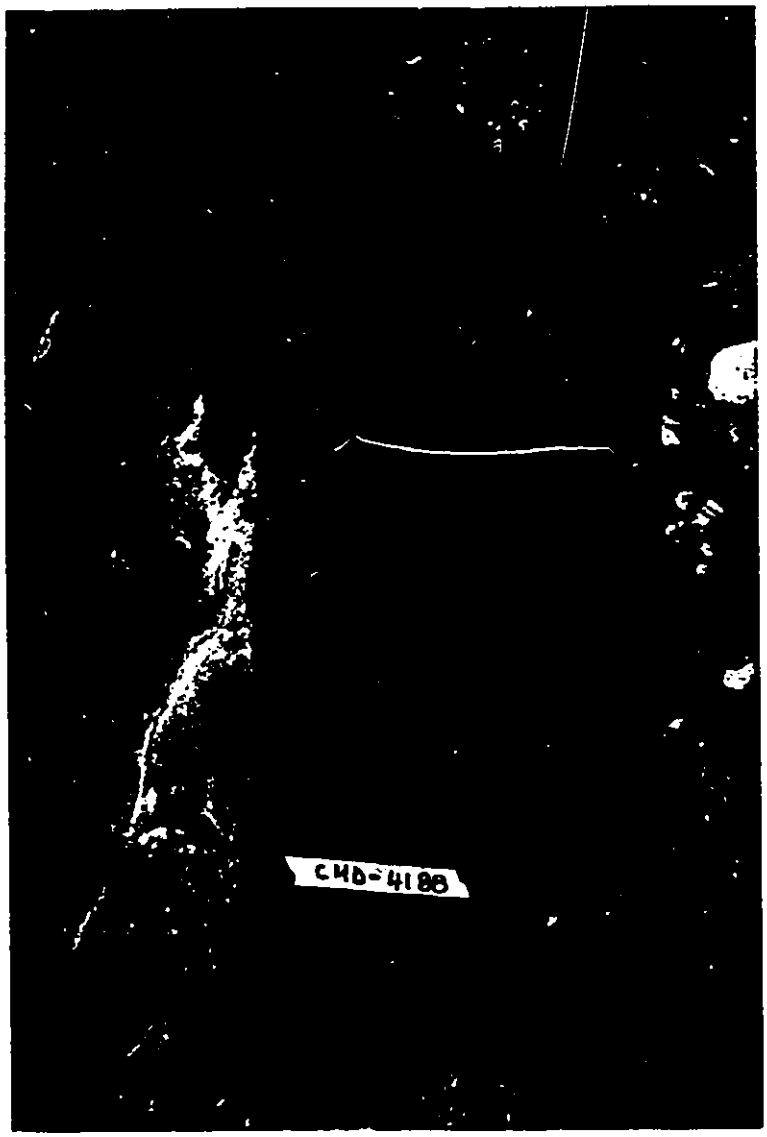

Figure 5. Metamorphosed NNE diabase dyke (on the right) crosscutting amphibolitic bands within the grey orthogneiss. The field of view is 0.5 meter.

Figure 6. Sharp walled granitic pegmatite dyke cutting across metamorphosed NNE diabase dyke near the Allochthon front. The width of the field of view is 1 meter.

The dyke contacts are generally sharp and regular. However in some places, the contacts are irregular and exhibit "flame-like" structures (Fig. 7). These "flame-like" structures are composed of several small penetrative fractures extending into the basement gneisses. These fractures are oriented parallel to subparallel to the margins of the dykes. Angular fragments of gneiss are observed at the boundary of the dykes. The fractures extend over a distance ranging from a few centimeters to a few meters and commonly show evidence of being pulled apart.

Most of the diabase dykes are mildly deformed with a weak foliation having developed along the dyke margins. However, some of the dykes are more strongly deformed, which is indicated by boudinage or pull-apart structures. Metamorphism appears to be contemporaneous with the deformation. Alteration to amphibole generally occurs along fractures, but in other instances, a patchy pattern of amphibole alteration is developed within the dyke interior. In most cases, the foliation developed in the dykes is discordant with the foliation of the host rock (i.e. orthogneisses).

Field observations show that a great number of the NNE diabase dykes crosscut the lit par lit amphibolite units within the grey orthogneisses. The amphibolite units are mostly characterized by internal layering composed of hornblende-rich and garnet porphyroblast-rich layers. When in contact with the country rock amphibolites, the NNE diabase dykes typically contain large garnet porphyroblasts at their margins (Fig. 8).

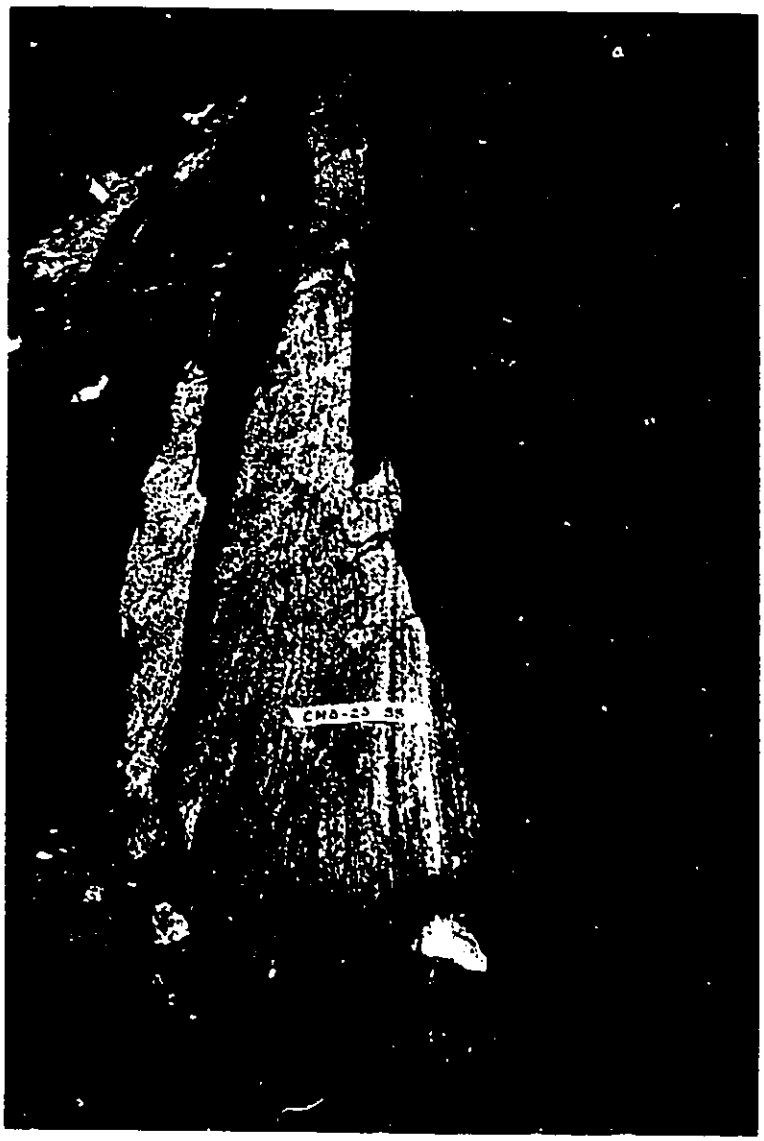

Figure 7. Diabase dykes crosscutting grey orthogneisses and showing "flame-like" structure along the boundary. The field of view is 0.5 meter.

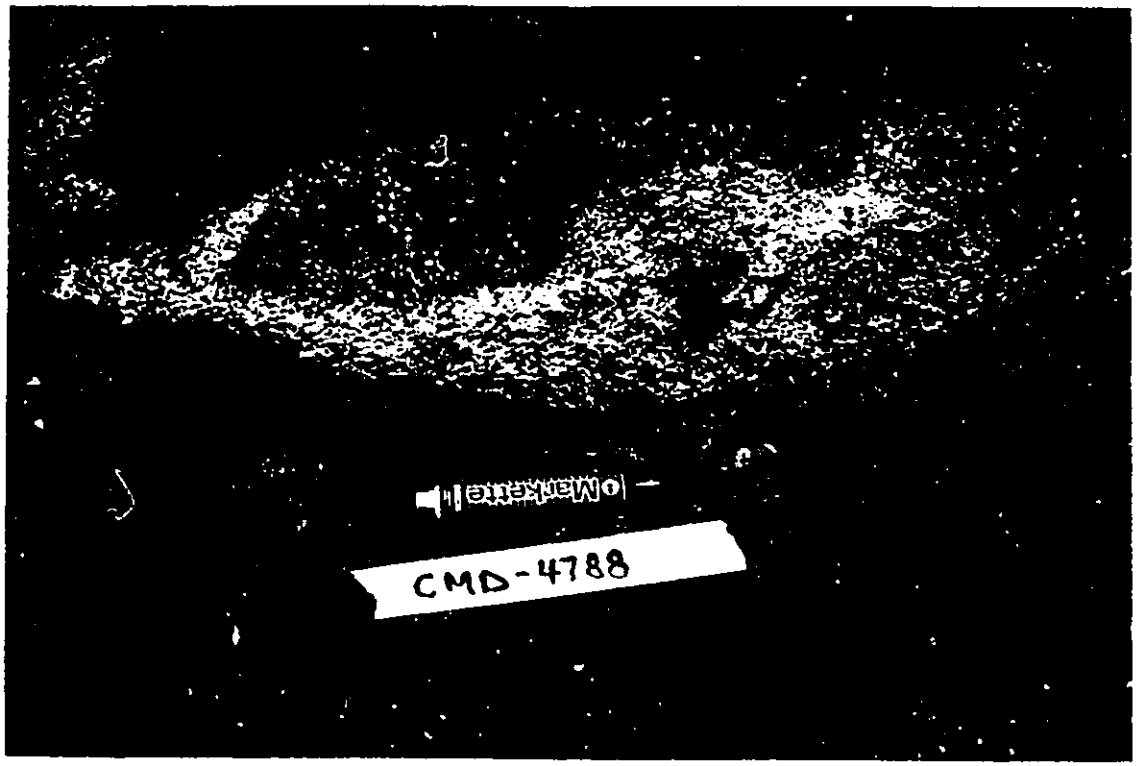

Figure 8. Pods of garnet porphyroblasts occurring at the margin of NNE diabase dyke where in contact with garnet-bearing amphibolite bands. The dyke is situated at the bottom of the photograph.

Also, pods of garnet-rich porphyroblasts occur sporadically in the dyke interiors.

The NNE diabase dykes are commonly a dull black to rusty brown color on weathered surfaces. The texture is generally massive with igneous microstructures well preserved, except at the dyke margins. Their grain size varies from fine-grained to coarse-grained, depending on the thickness of the dyke under consideration. Not uncommon, the dykes show an increase in grain size towards their centers, however, the opposite relationship has also been observed.

Most dykes that are thicker than one meter are mostly composite dykes and their internal boundaries are distinguished by differences in grain size. In most cases, the internal boundaries are irregular and generally parallel to the strike direction of the dyke. In other instances, the dyke interior displays a very irregular texture composed of various zones richer in felsic or mafic phases (Fig. 9). Evidence of a secondary pulse is observed in only one dyke (CMD-16). The secondary pulse is characterized by two small veins (1 to 3 cm thick) and is composed of very fine grains of garnet with minor clinopyroxene and plagioclase. The veins are cutting across a medium-grained host dyke along its strike. The fine-grained pulse exhibits a brownish pink color due to the presence of abundant garnet.

The primary minerals are commonly observed in most of the dykes, however, a few dykes have experienced partial to complete

Figure 9. Irregular shaped mafic mineral cluster found within typical coronitic diabase dykes. The field of view in the photograph is approximatly 0.5 meter.

alteration to amphibole. The best preserved dykes exhibit ophitic to subophitic textures (Fig. 10), and are typically composed of olivine, plagioclase, pyroxene, and oxide minerals, with lesser amounts of biotite, apatite, hornblende, orthopyroxene, garnet, spinel, and corundum.

An increase in metamorphic grade from northeast to southwest is observed in the study area along the Grenville Front, and this is defined by the appearence of hornblende, garnet, spinel and corundum. In general, primary textures and mineralogy are partly obliterated but corona structures are still preserved. According to Ciesielski (personal communication, 1988), an increase in metamorphism has been recorded by the supracrustal amphibolite units, along the Grenville Front. This increase in metamorphism is thought to be the result of a narrowing of the Parautochthon Domain to the southwest, hence, allowing the effects of the Grenville Orogeny to be recorded deeper into the Parautochthon domain and the Superior Province.

The dykes are also characterized by a porphyritic texture consisting of large phenocrysts of plagioclase up to 4 cm long. The phenocrysts are generally oriented parallel to the dyke margin (Fig. 11).

Locally, igneous layering occurs in some large dykes and is defined by alternating mafic-rich and plagioclase-rich bands. The layering is generally parallel to the dyke margin but may also be oblique to the dyke margin (i.e. cross banding, Fig. 12a and 12b). In some cases, the occurrence of flow structure may be

Figure 10. Typical medium- to coarse-grained diabase dyke showing the subophitic to ophitic texture.

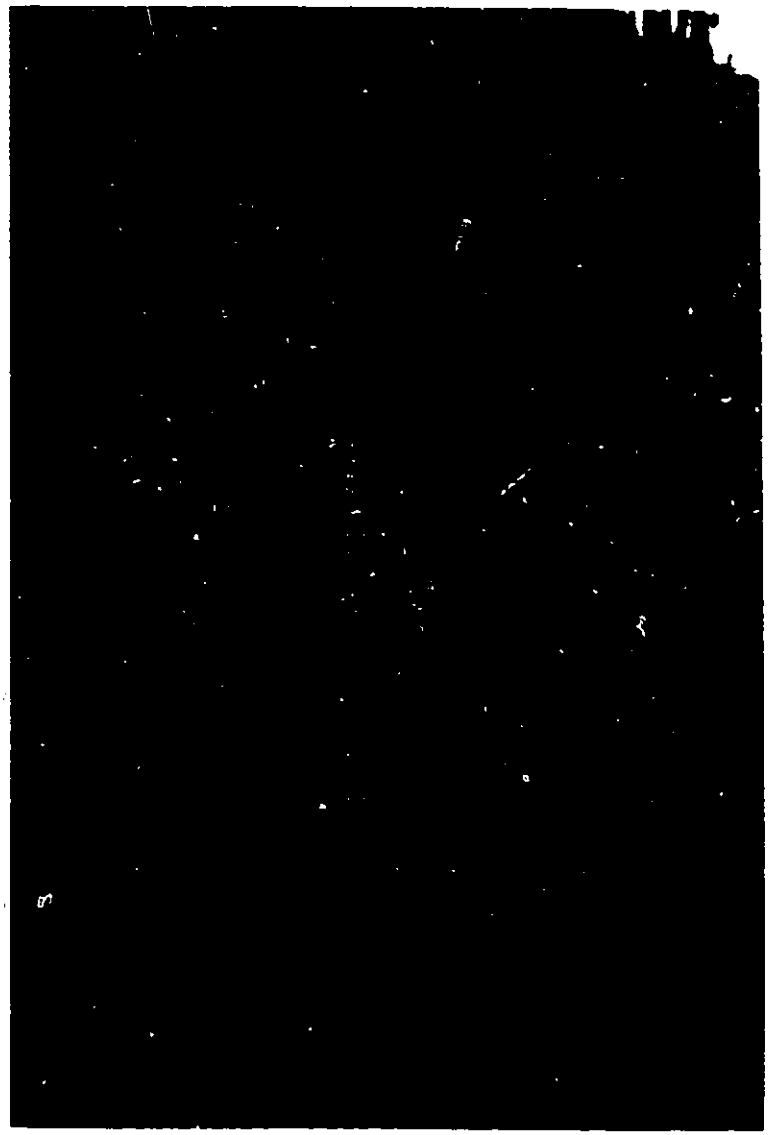

Figure 11. Diabase dyke displaying large phenocrysts (up to 4 cm long) of zoned plagioclase. Field of view from left to right is approximatly 1 meter.

Figure 12a. Isomodal layering displayed within the central portion of a thick (>10 meters) diabase dyke; possibly indicating different magmatic pulses.

Figure 12b. Crosscutting modal layering within a thick (>10 meters) diabase dyke.

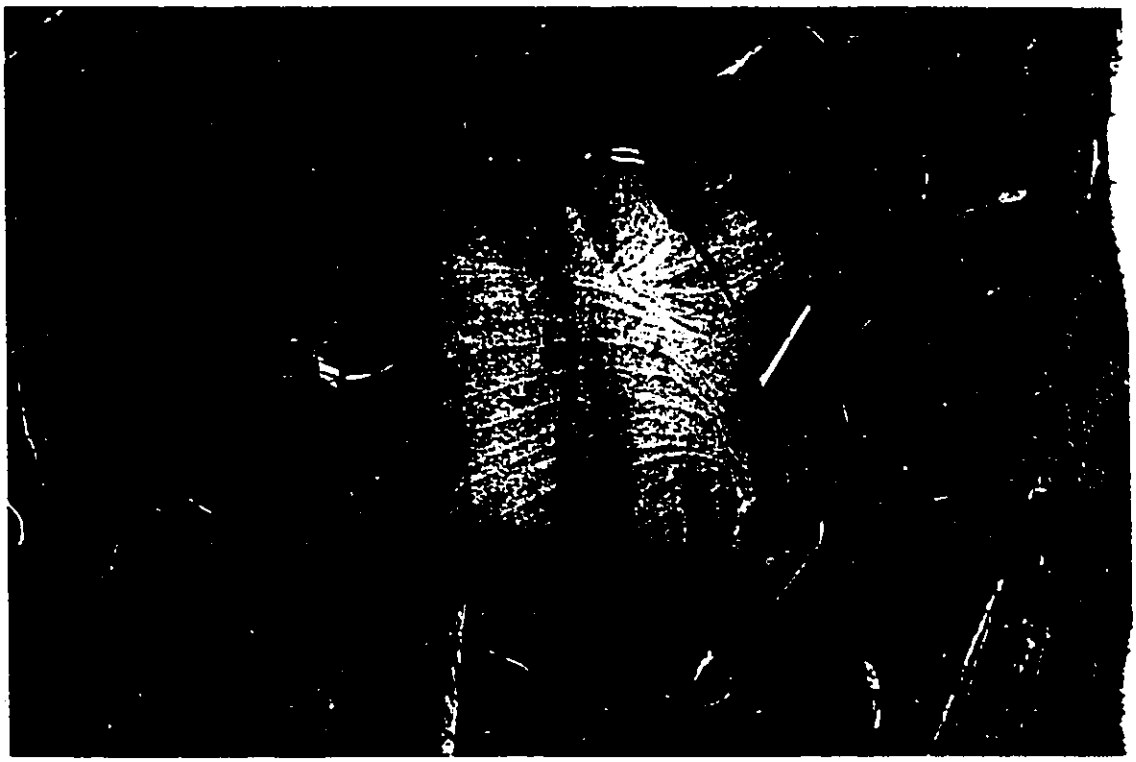

Figure 12a

Figure 12b

confused with the foliation. Within massive dykes, flow-like textures (i.e. possibly shear bands) have developed (Fig. 13). These are defined by the alignment of pyroxene and especially plagioclase phenocrysts. The flow-like structure is generally heterogeneously developed where present, and hence gives a raft-like or agmatitic character to the dykes. The layering displayed by some dykes is caused by mineralogical and textural variations.

Corona structures are observed on the outcrop surface of medium-to coarse-grained dykes. Characteristically, corona structures have developed between primary olivine and plagioclase. The corona structures can be discerned with the naked eye on the outcrop surface of medium- to coarse-grained diabase dykes. These corona structures are highly variable in mineral content, and the number and thickness of corona layers. Some are relatively simple with only a single corona layer present, whereas others are more complex with double or triple layer corona structures present. This change is apparently the result of progressive metamorphism, since the initial double layer corona structure appears to have evolved to a triple layer corona structure by the addition of a metamorphic garnet shell. At more advanced stages of metamorphism, most of the primary mineralogy has recrystallized and the relict corona stuctures are pseudomorphed by circular chains of garnet surrounding a mosaic of recrystallized primary minerals.

Characteristic of the fine- to medium-grained diabase dykes

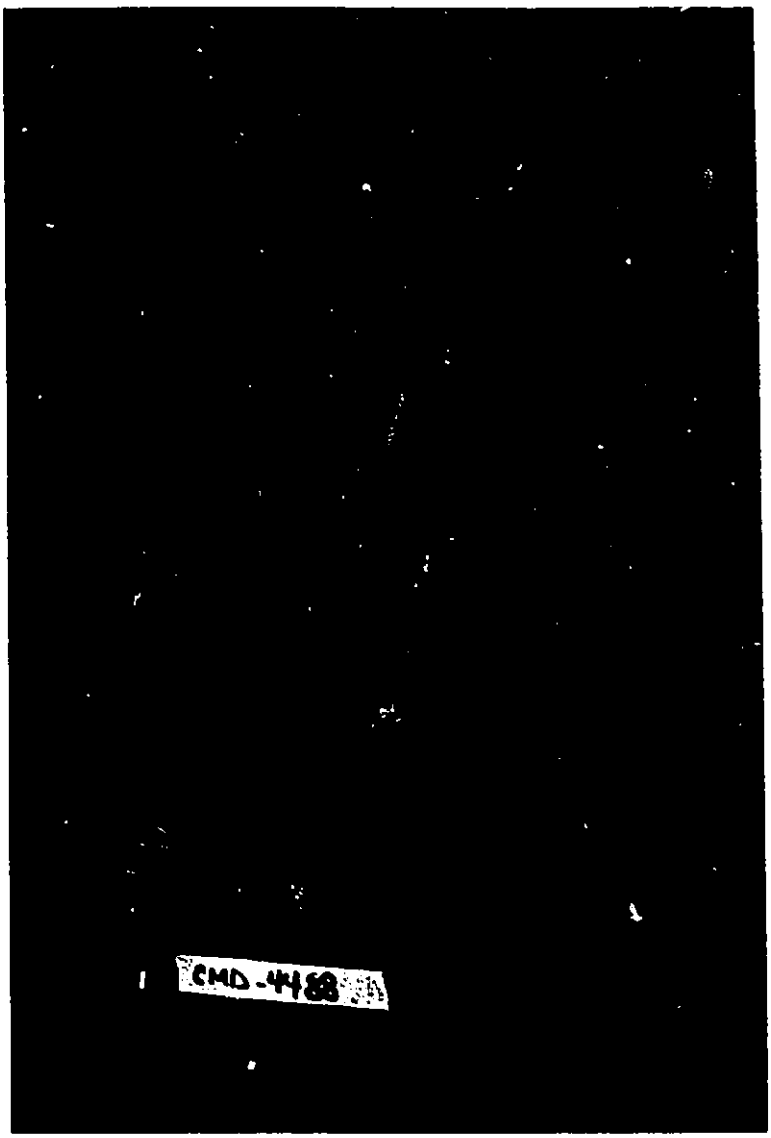

Figure 13. Medium-grained diabase dyke displaying flow-like structure (shear bands) defined by the alignment of pyroxene and plagioclase phenocrysts.

is the presence of coarse-grained (pegmatitic) segregations (Fig. 14) which are variable in shape and consist of the same mineral assemblage as the host dyke, except for the abundance of hornblende and the absence of biotite. They generally occur in the central portion of the dyke, however some "ball-like" segregations have been observed along the margin of one dyke (CMD-49). They are typically composed of hornblende, augite, plagioclase, minor K-feldspar, trace amounts of quartz, and locally contain abundant garnet. The coarse-grained pegmatitic segregations grade sharply into a fine- to medium-grained host dyke.

Figure 14. Felsic mineral segregation within typical coronitic diabase dyke. The segregations have sharp to gradational contacts, irregular shapes, and pegmatitic textures.

DESCRIPTION OF THE NNE DIABASE DYKES

3.1 MINERALOGY AND TEXTURE

The NNE diabase dykes have a variety of mineral assemblages and textures. All of the dykes have been metamorphosed to some degree which in part explains the extreme variety observed in the dykes. They contain between 10 and 90 percent secondary (metamorphic) phases. Despite the alteration and metamorphism, primary (igneous) minerals and textures are commonly well preserved, especially in the least metamorphosed samples which are located near the Grenville Front. Exceptions are those samples collected near the Allochthon Front where the dykes are extensively overprinted by the Grenvillian Orogeny, and those samples from the dyke margins where they are partially to totally recrystallized to well foliated amphibolites. However, in some samples with abundant secondary mineral phases, it is possible to deduce the primary assemblages on the basis of textural criteria.

The location of the dykes sampled in this study is presented in Figure 15 (in backpocket). The distribution of mineral assemblages observed in the NNE diabase dykes with respect to their sample location is given in Figure 16 (in backpocket). Note that different symbols have been assigned to the various mineral phases, and those indicated with small letters are secondary phases. The distribution of mineral assemblages reveals

an increase in metamorphic grade, from lower to upper amphibolite facies, towards the Allochthon Front. The mineral assemblages of the NNE diabase dykes situated along the Allochthon Front are composed mainly of hornblende, plagioclase, garnet, sphene, and calcite. Detailed petrographic descriptions of only those samples probed for mineral compositions are given in Appendix A.

The NNE diabase dykes are commonly massive and relatively fresh (i.e. < 10% altered) with grain sizes ranging from 1 to 10 mm (i.e. medium- to coarse-grained). Most dykes have relict subophitic to ophitic (i.e. diabasic) textures. Some of the dykes are plagioclase-phyric. Well developed igneous layering was observed in several dykes, and is defined by alternating plagioclase-rich and mafic-rich layers. The NNE diabase dykes range in composition from Mg-rich gabbro (olivine bearing) to Fe-rich gabbro (ilmenite and magnetite bearing) with Fe-rich varieties seemingly being more common.

The freshest dykes consist mainly of olivine, randomly oriented plagioclase laths, and augite which partially to completely enclose the olivine and plagioclase crystals. Ti-magnetite, reddish brown biotite, amphibole, and apatite occur in minor amounts in most samples. Mineral assemblages of the NNE diabase dykes are represented in Table 1.

Olivine grains are present in the least altered samples (e.g. CMA-LA18) and one metamorphosed sample (CMA-27.6.5). They constitute less than 5 modal percent of the rock. The olivine grains may be partly or completely enclosed by primary

Table 1. Mineral assemblages of the NNE diabase dykes.

Samples	Ol	Pl	Primary Cpx	Bt P	Bt S	Oxide Mag	Oxide Ilm	Amph Prg	Amph Hbl	Opx	Grt	Di	Idd	Crn	Qtz
CMA-La18	+	+	+	+	-	+	-	+	-	+/-	-	-	+	-	-
CMA-LGY	+	+	+	+	-	+	+	+	-	+	-	-	+	-	-
CMA-M-R01A	+/-	+	+	+	-	+	+	+	+/-	+	+/-	-	+	+/-	+/-
CMA-LG6	+/-	+	+	+	-	+	+	+	+/-	+	+/-	-	+	+/-	+/-
CMA-LG7	+/-	+	+	+	-	+	+	+	+/-	+	+/-	-	+	+/-	+/-
CMA-27.6.5	+/-	+	+	+	-	+	+	+	+/-	+	+/-	-	+	+/-	+/-
CMA-M-015A	+/-	+	+	+	-	+	+	+	+/-	+	+/-	-	+	+/-	+/-
CMA-F-12.3	-	+	+	-	+	+	+	+	+	+	+	+/-	+	+	+
CMA-M-V01	-	+	+	-	+	+	+	+	+	+	+	+/-	+	+	+
CMA-27.6.3	-	+	+	-	+	+	+	+	+	+	+	+/-	+	+	+
CMA-79Di	-	+	+	-	+	+	+	+	+	+	+	+/-	+	+	+
CMA-146	-	+	+/-	-	+	+	+	-	+	-	+	+	-	+	+

Ol = Olivine
Pl = Plagioclase
Cpx = Clinopyroxene
Bt = Biotite
Mag = Magnetite
Ilm = Ilmenite
Prg = Pargasite

Hbl = Hornblende
Opx = Orthopyroxene
Grt = Garnet
Di = Diopside
Idd = Iddingsite
Amp = Amphibole
Crn = Corundum

Qtz = Quartz
P = Primary, igneous
S = Secondary, metamorphic

+ = Present
- = Absent
+/- = Trace

clinopyroxene or may occur as individual grains in contact with plagioclase. They appear as euhedral to rounded phenocrysts and/or megacrysts, ranging in size from 0.5 to 3.0 mm. Smaller olivine phenocrysts with euhedral to anhedral shapes are found occasionally aggregated together (CMA-LA18). The olivine grains are pale yellow color with a weak pleochroism. They are euhedral to anhedral, commonly rounded and fractured, and altered to serpentine on grain margins and along fractures. Further alteration has resulted in the formation of bowlingite (i.e. a mixture of chlorite and goethite), and finally deep red iddingsite (i.e. a mixture of smectite, chlorite, and goethite or hematite) and calcite (e.g. CMD-043, CMA-27.6.3, CMD-025).

Primary clinopyroxene grains comprise approximately 15 to 20 modal percent of the samples. They occur mainly as anhedral to subhedral grains, which range in size from 0.5 mm up to 4.0 mm in length. They are typically found comprising ophitic to subophitic textures, in which they form intergrowths with plagioclase grains. Sometimes, they are partially enclosing olivine and Ti-magnetite grains. They are also found as interstitial phases between plagioclase laths. Clinopyroxene grains observed in the least altered (e.g. CMA-LA18) and the weakly metamorphosed (e.g. CMA-LGY and CMA-LG6 with minor amounts of garnet crystals) samples are light brown to light green in plane light, and they exhibit a pleochroism that varies from pale green or pale brown to dark green or reddish brown. The clinopyroxene grains found in sample CMA-LA18 are characteristically inclusion-free, whereas

those found in samples CMA-LGY and CMA-LG6 contain very fine-grained exsolution blebs of magnetite (note: the mineralogical composition of these exsolutions were determined under reflected light). At more advanced stages of recrystallization, the clinopyroxene grains take on a dark green to dark brown color because they are heavily clouded with fine-grained exsolution crystals of magnetite.

Plagioclase grains make up 25 to 45 modal percent of most samples. They occur either as randomly oriented laths (phenocrysts) up to 3 cm in length or as groundmass laths. The phenocrysts and the groundmass laths have a similar composition. Typically, the plagioclase grains are partly to completely recrystallized but primary compositions can still be found in the least altered samples. Together with augite and olivine they define an ophitic texture in most of the dykes. They show a well defined twinning, commonly albite and Carlsbad twinning which is locally deformed. Normal zoning is characteristic of plagioclase phenocrysts. Sparce inclusions of spinel crystals are found within the plagioclase grains in proximity to the corona structures around olivine. The plagioclase grains occasionally contain inclusions of clinopyroxene within a zoned arrangement in the plagioclase cores (Figs. 17a and 17b). The outer edge of these zoned plagioclase grains is mostly inclusion-free.

Primary (igneous) biotite is a common accessory mineral, constituting 1 to 4 modal percent of the least altered samples. It is usually intimately associated with opaque mineral and

Figure 17a. A plagioclase crystal containing augite grains which were presumably trapped within the plagioclase structure at the time of crystal growth. Plane-polarized light (sample CMA-LGY). The field of view is 3.5 mm across.

Figure 17b. Same photomicrograph under cross-polarized light.

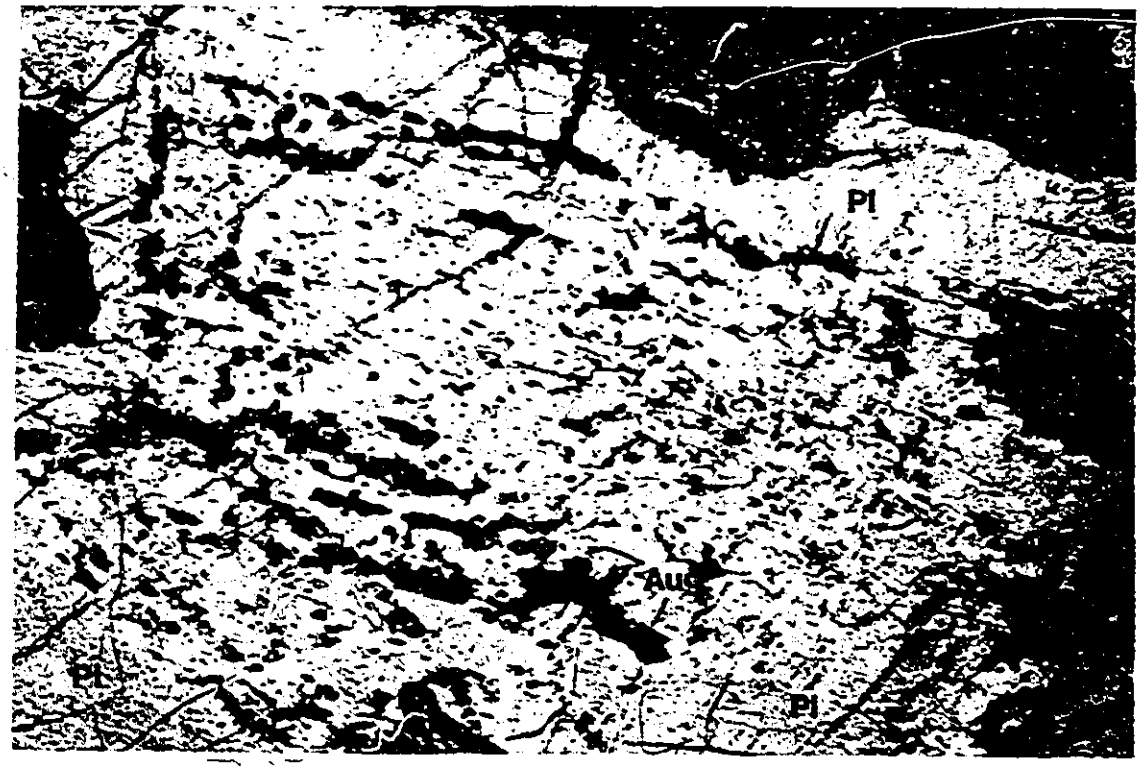

Figure 17a

Figure 17b

apatite grains in the interstices between the major mineral grains. The biotite grains typically exhibit a strong pleochroism from light brown to dark reddish brown. Biotite occurs in three forms: as elongated to stumpy independant flakes, as stumpy to elongated flakes that partially to completely enclose apatite and opaque mineral grains, and as partial to complete reaction rims around opaque mineral grains. There are no compositional differences, on the basis of petrographic and chemical criteria (see Chapter 5 on mineral chemistry), between these different forms of biotite. Hence, the biotite reaction rims are considered to have formed during a late magmatic reaction.

The Ti-magnetite crystals occur as anhedral grains, which vary in size from 0.15 to 4.0 mm in diameter and exhibit ilmenite exsolution lamellae. Trace amounts of sulfide minerals (pyrite, chalcopyrite, pyrrhotite, and pentlandite) are commonly associated with the Ti-magnetite crystals.

Apatite grains are present in all samples. They are usually associated with biotite and opaque mineral grains. They also occur within plagioclase laths as tiny equant or tabular euhedral grains up to 0.5 mm in size, and occasionally along plagioclase grain boundaries.

Zircon grains are rare but where found are most commonly associated with biotite flakes.

Trace amounts of quartz and K-feldspar grains, commonly as interstitial material, are observed in a few samples.

Within the least altered sample (i.e. CMA-LA18), calcic

amphibole occurs as extremely thin rims around olivine and iron oxide. The thickness of the rims does not exceed a few micrometers. These amphibole rims exhibit a pale green color in plane light and show a pleochroism ranging from pale green to yellow green. They are considered to be, in part, igneous in origin. This is alluded to because the corona structures are thin and the igneous grains have, in general, well-preserved grain boundaries. Also, the occurrence and textural features of the calcic amphibole rims around the iron oxides are similar to those of the biotite rims mentioned above. Both the calcic amphibole and biotite rims are associated with interstitial biotite, and appear to have crystallized at the same time. Metamorphic minerals and textures are highly variable in nature and abundance, depending upon the degree of recrystallization of the sample. The textures vary from narrow simple corona layers in the least recrystallized dykes to granoblastic in the completely recrystallized dykes. For all cases of the completely recrystallized dykes, the igneous minerals and textures, as well as the corona structures, have been completely obliterated and replaced by metamorphic mineral assemblages.

The metamorphic minerals which occur in the corona structures include orthopyroxene, diopside, amphibole, plagioclase, spinel, magnetite, ilmenite, and garnet. Corundum plates are found associated with the corona structures but not within the actual corona structure. Other metamorphic minerals, within either coronitic or non-coronitic dykes, include hornblende,

cummingtonite, serpentine (and its alteration products), chlorite, epidote, sphene, leucoxene, quartz, K-feldspar, calcite, and sericite.

A brief description of the metamorphic minerals will be part of the following description of corona structures and the subsequent description of completely recrystallized dykes.

It should be noted here that the metamorphic clinopyroxene grains have been classified into two main textural types:

1) in the first type, magmatic textures are completely preserved and metamorphic clinopyroxene (i.e. salitic augite or diopside/ferrosalite) partially or entirely replaces the primary clinopyroxene.
2) in the second type, magmatic minerals and textures are partially to completely recrystallized and reconstituted to equilibrium metamorphic textures (i.e. granoblastic with triple point grain boundaries) with the crystallization of metamorphic clinopyroxene (i.e. diopside/ferrosalite).

3.2 DESCRIPTION OF CORONA STRUCTURES

Four major corona types and two subtypes are recognized on the basis of mineralogy. The different layers of each corona type are named from the center of the corona structure to the margin that is in contact with plagioclase grains. These types are as follows:

Type 1) an olivine corona structure composed of double or triple layers,

olivine (core) orthopyroxene amphibole plagioclase	olivine (core) orthopyroxene amphibole garnet plagioclase

Type 2) an orthopyroxene-magnetite symplectite-cored corona structure characterized by double or triple layers,

orthopyroxene-magnetite symplectite (core) orthopyroxene amphibole plagioclase	orthopyroxene-magnetite symplectite (core) orthopyroxene amphibole garnet plagioclase

The orthopyroxene - magnetite core occasionally is broken down in the later stages of corona development to a core comprising only orthopyroxene. This subtype is as follows:

orthopyroxene (core)
amphibole
garnet
plagioclase

Type 3) a primary clinopyroxene (augite) corona structure typically composed of double or triple layers,

augite (core)	augite (core)

amphibole	amphibole
Na-plagioclase	Na-plagioclase
	garnet
plagioclase	plagioclase

The breakdown of primary clinopyroxene (augite) results in the formation of granoblastic diopside. This subtype is characterized by a triple layer corona structure,

augite ---> diopside (core)
Na-plagioclase (moat)
amphibole
garnet (with inclusions of diopside)
plagioclase

Type 4) a Ti-magnetite corona structure composed of double or triple layers,

Ti-magnetite (core)	Ti-magnetite (core)
biotite	biotite
amphibole	amphibole
	garnet
plagioclase	plagioclase

The distribution of corona structures with respect to their sample location is shown in Figure 18 (in backpocket). The distribution of corona types in the Parautochthonous Domain does not reveal any particular relationship. Most corona types occur in the central part, whereas pairs of corona structures are characteristic within the vicinity of the Grenville Front.

Progressive increase of metamorphism and alteration in these rocks can be followed through the evolution of the corona structures, as well as by the appearance of new metamorphic and

alteration minerals.

3.2.1 Olivine Corona Structure

Typically, a two layer symmetrical corona structure has developed where olivine is surrounded by plagioclase (Fig. 19a). The inner layer is composed of a thin (10 μm) prismatic to columnar orthopyroxene layer in contact with olivine. The outer layer is composed of columnar grains of light green pargasitic amphibole which forms a sharp contact with the orthopyroxene layer. This outer layer is continuous and is approximately 0.10 mm thick (Note: thickness is dependent on section cut). Little or no reaction rim is observed when olivine is completely enclosed in primary clinopyroxene. An asymmetrical corona structure has developed where olivine and Ti-magnetite are found partly enclosed in clinopyroxene and in direct contact with plagioclase (Figs. 19a and 19b). In some cases, a thin layer of up to a few microns in thickness is observed at the contact between olivine and clinopyroxene.

At a more advanced stage of disequilibrium and reaction, the corona growth around the olivine grains is thick and consists of columnar orthopyroxene and pargasitic amphibole layers.

With further reaction (i.e. approaching equilibrium conditions as indicated by the formation of granoblastic textures), the olivine corona structure is characterized by

Figure 19a. Symmetrical (upper left) and asymmetrical corona structures developed around olivine grains. The symmetrical corona structure is composed of a thin layer of prismatic orthopyroxene in contact with olivine, followed by a outer layer of acicular pargasite.
In the center, a partly enclosed olivine grain within primary augite shows an asymmetrical corona structure where in direct contact with plagioclase. No reaction occurs between olivine and augite (sample CMA-LA18).

Mineral abbreviations:

Ol = olivine	Pl = plagioclase
Id = iddingsite	Aug = augite
Prg = pargasite	Opx = orthopyroxene
Mag = magnetite	Spl = spinel
Crn = corundum	Grt = garnet

Figure 19b. Asymmetrical corona structure developed around Ti-magnetite that is partly enclosed by augite grains. The corona layer consists of acicular pargasite at the contact with plagioclase (sample CMA-LA18).

Note: Figures 19a, 19b, 19c, 19d, 22a, 22b, 24a, 24b, 25a, and 25b were sketched from photographs.

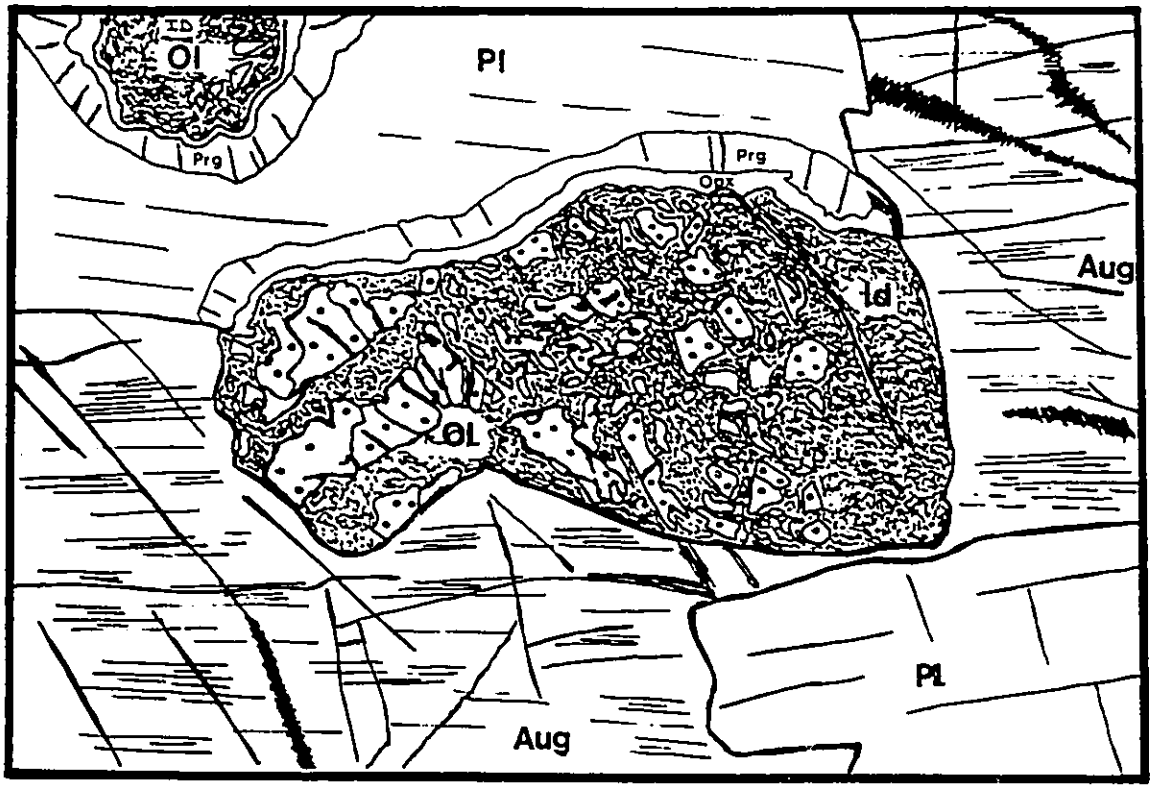

Figure 19a

0.5 mm

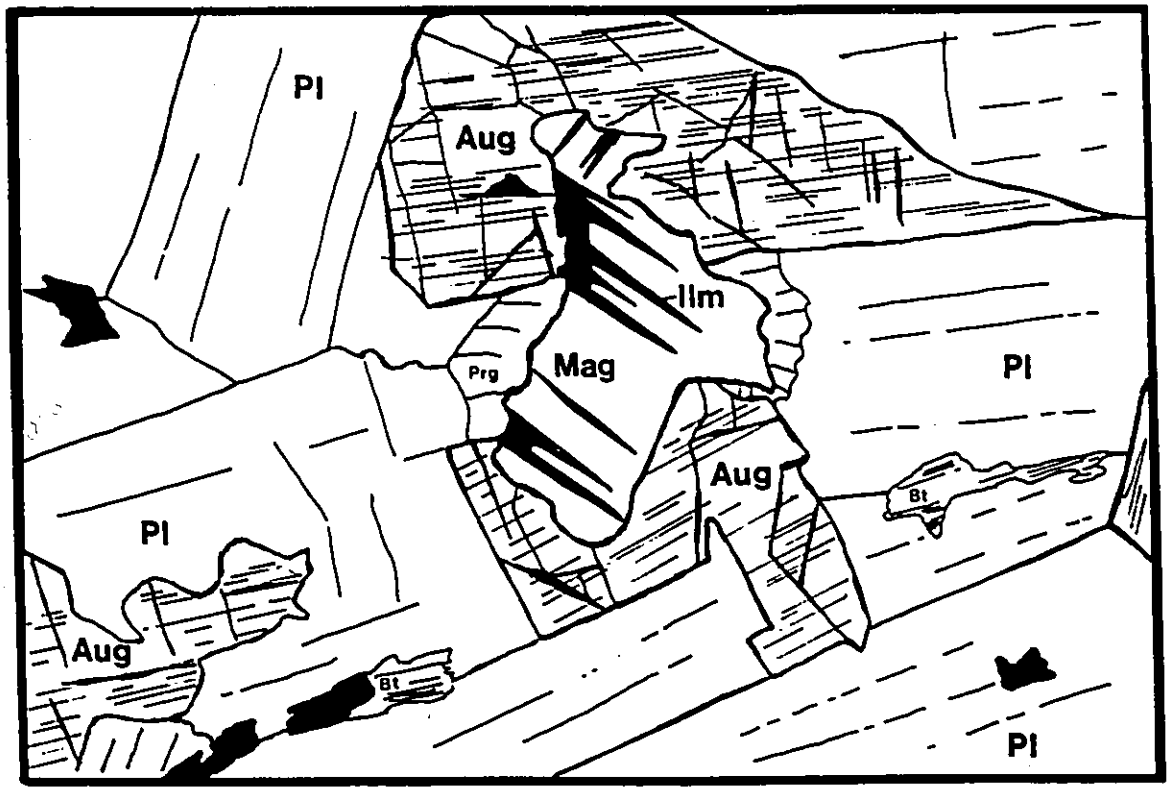

Figure 19b

1.0 mm

idioblastic garnet crystals forming an additional layer around olivine (Figs. 19c and 19d). It is observed in those samples with minor garnet that the anhedral crystals of garnet started nucleating within the amphibole layer at the orthopyroxene/amphibole interface. As these garnet crystals become larger, they completely replace the amphibole layer and show inclusions of the former. The garnet crystals generally form idioblastic terminations in contact with the plagioclase grains. An increase in the abundance of corundum plates occurs with nucleation of garnet. These corundum plates are found within plagioclase grains in proximity to the triple layer corona structure that is developed around olivine.

Also associated with the above mentioned olivine corona structures is the progressive clouding of plagioclase laths. This is responsible for imparting a light brown to dark brown color to the center of grains. The spinel crystals are colorless to pale green. In addition, needles of more sodic plagioclase have exsolved from the primary, more calcic plagioclase laths (Figs. 20a and 20b). Minor amounts of corundum plates are also observed along the (001) and (010) planes. The sodic plagioclase exsolutions exhibit very complex patterns. They are generally randomly oriented within the (001) and (010) planes (Figs. 21a, 21b, and 21c). These exsolutions are visible due to the optical contrast provided by the distribution of the spinel dust around them (Fig. 22b, the composition of the microcrystals of plagioclase, spinel, and corundum were confirmed by SEM traverses

Figure 19c. Olivine corona structure displaying a triple layer consisting of prismatic to acicular orthopyroxene, anhedral garnet, and acicular pargasite, in contact with plagioclase (sample CMA-27.6.5).

Figure 19d. Preserved anhedral fragments of olivine included in primary augite. The olivine shows extensive replacement into orthopyroxene. Primary augite crystals are rimmed by zoned garnet grains. Garnet zoning consists of a inner turbid zone rich in amphibole inclusions, and an outer inclusion-free zone that forms idioblastic termination in contact with plagioclase. The plagioclase laths are partly clouded by tiny inclusions of spinel (sample CMA-27.6.5).

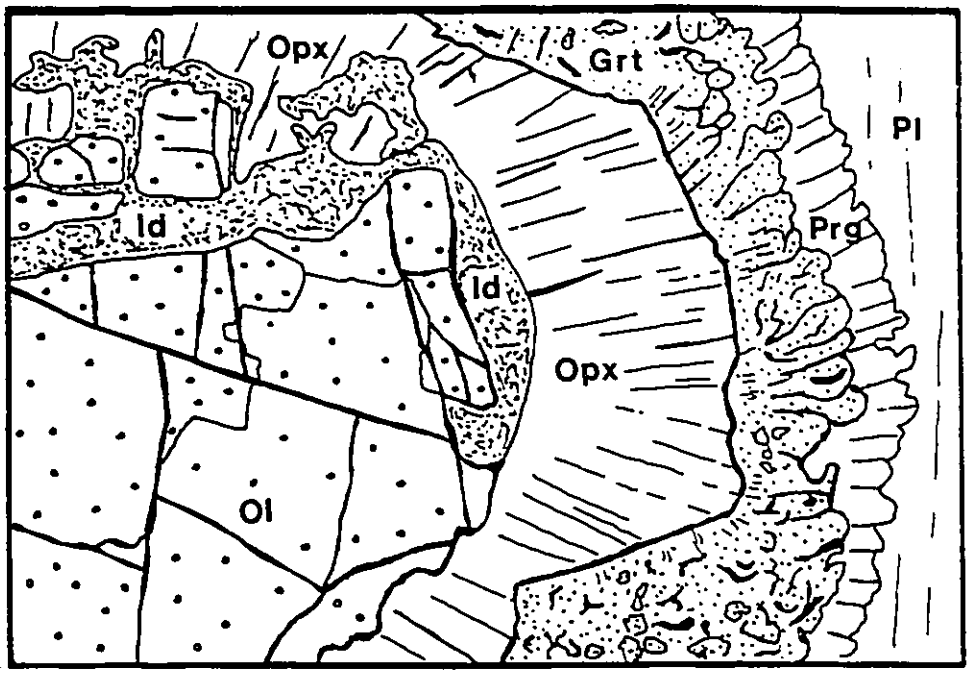

Figure 19c

0.5 mm

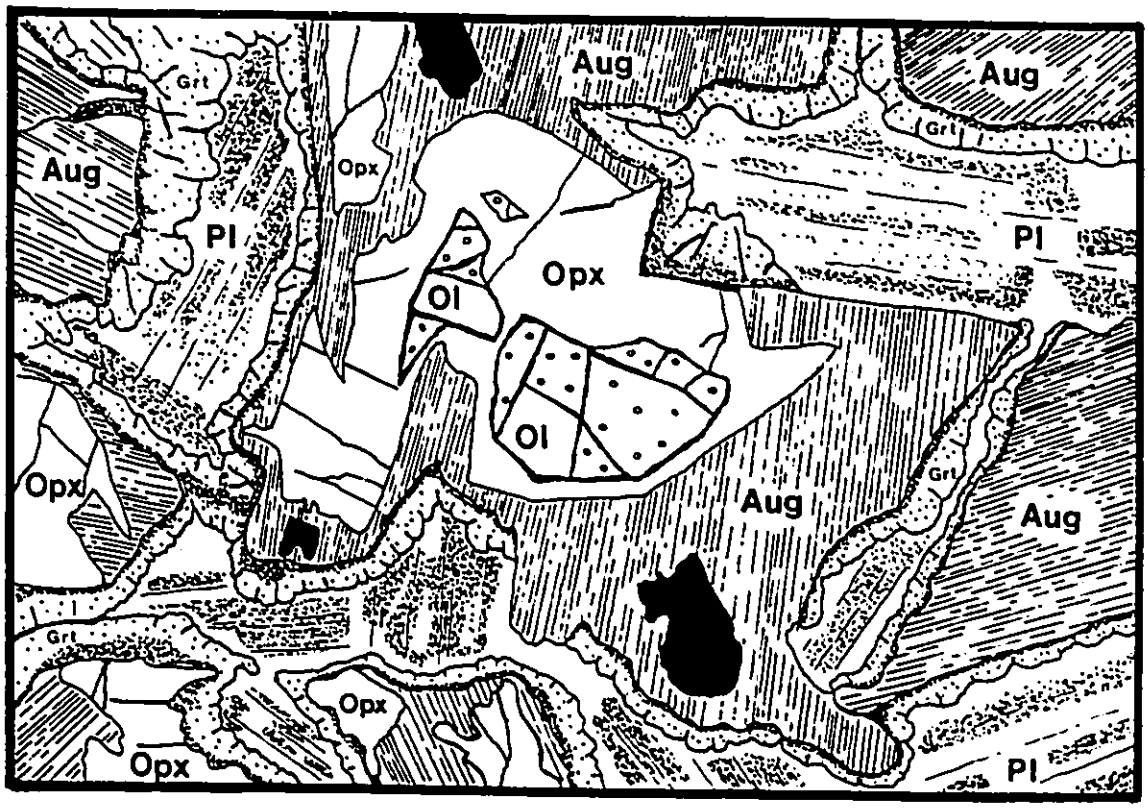

Figure 19d

1.0 mm

Figure 20a. Photomicrograph of randomly oriented microcrystals of more sodic plagioclase within primary calcic plagioclase laths, under plane polarized light. The field of view is 3.5 mm across (sample CMA-79DI).

Figure 20b. Same field of view as above but in cross-polarized light.

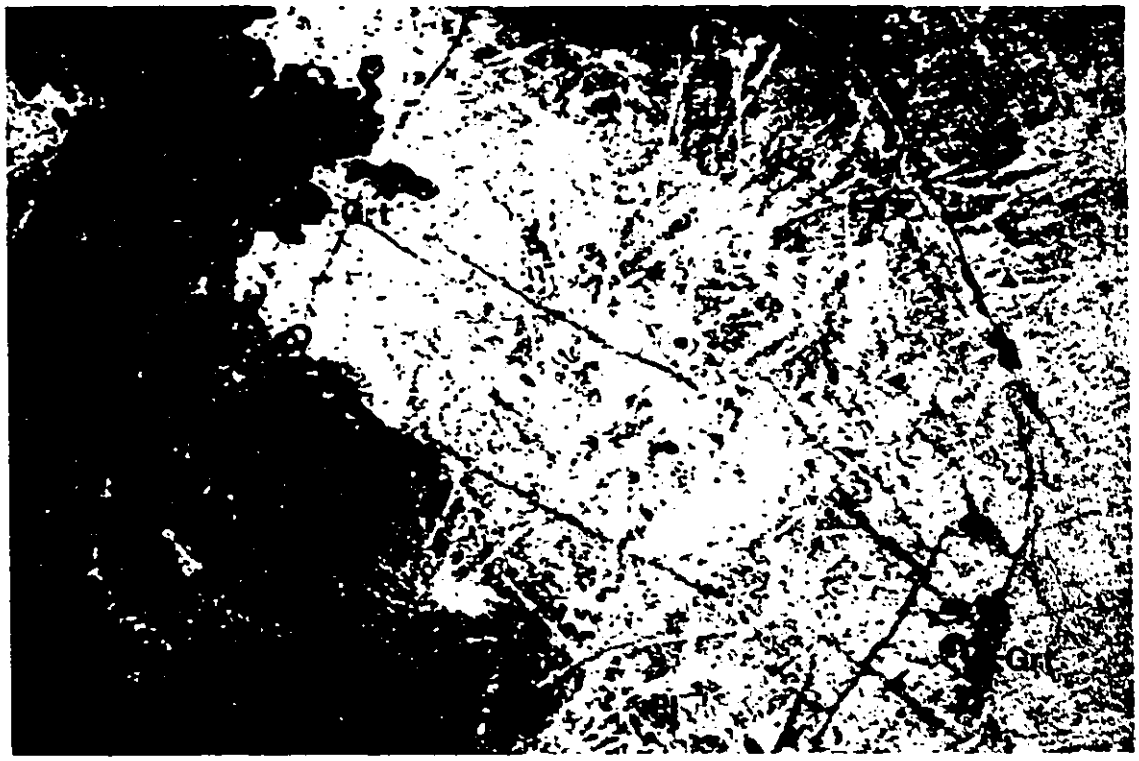

Figure 20a

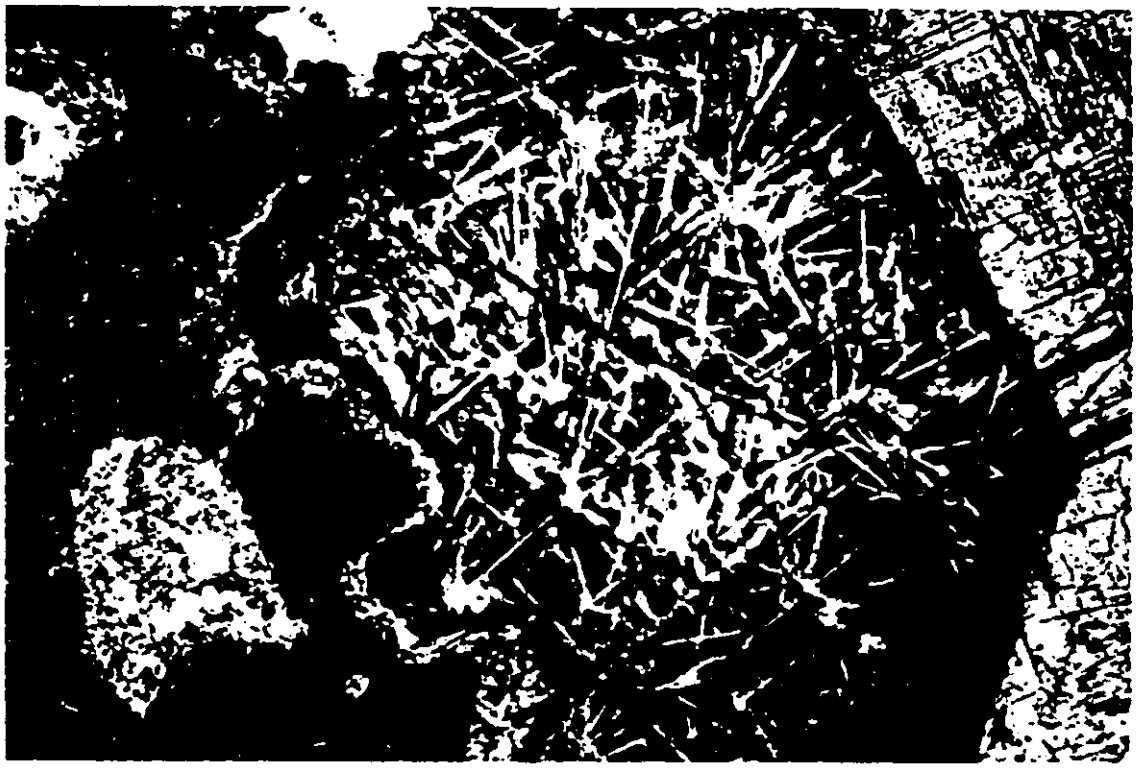

Figure 20b

Sample: CMA-79 Di (B)-86

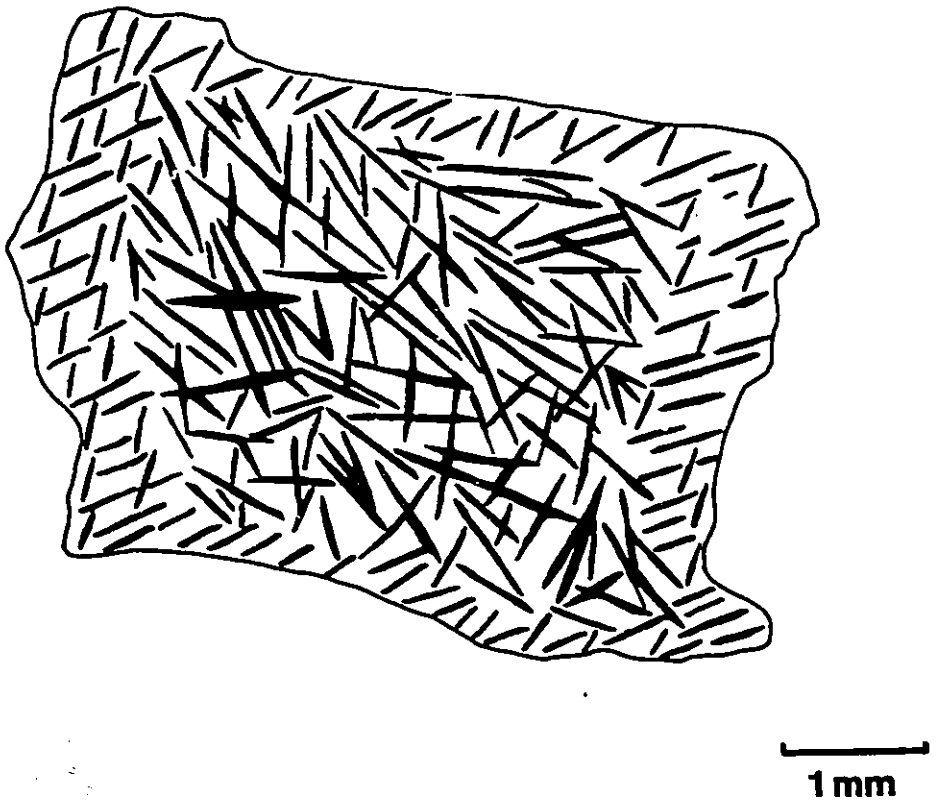

Figure 21a. Plagioclase crystal displaying randomly oriented plagioclase microcrystals.

Sample: CMA-79 Di (B)-86

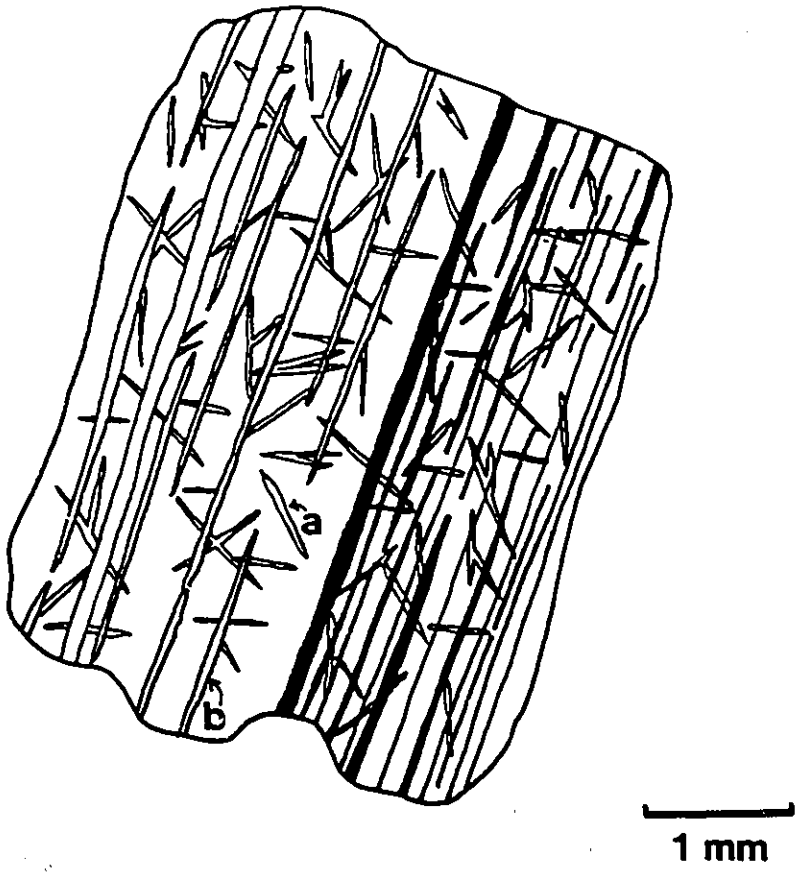

Figure 21b. Plagioclase crystal displaying (a) randomly oriented plagioclase microcrystals and (b) albite and Carlsbad twins.

Sample: B 79 Di - 2 - 86

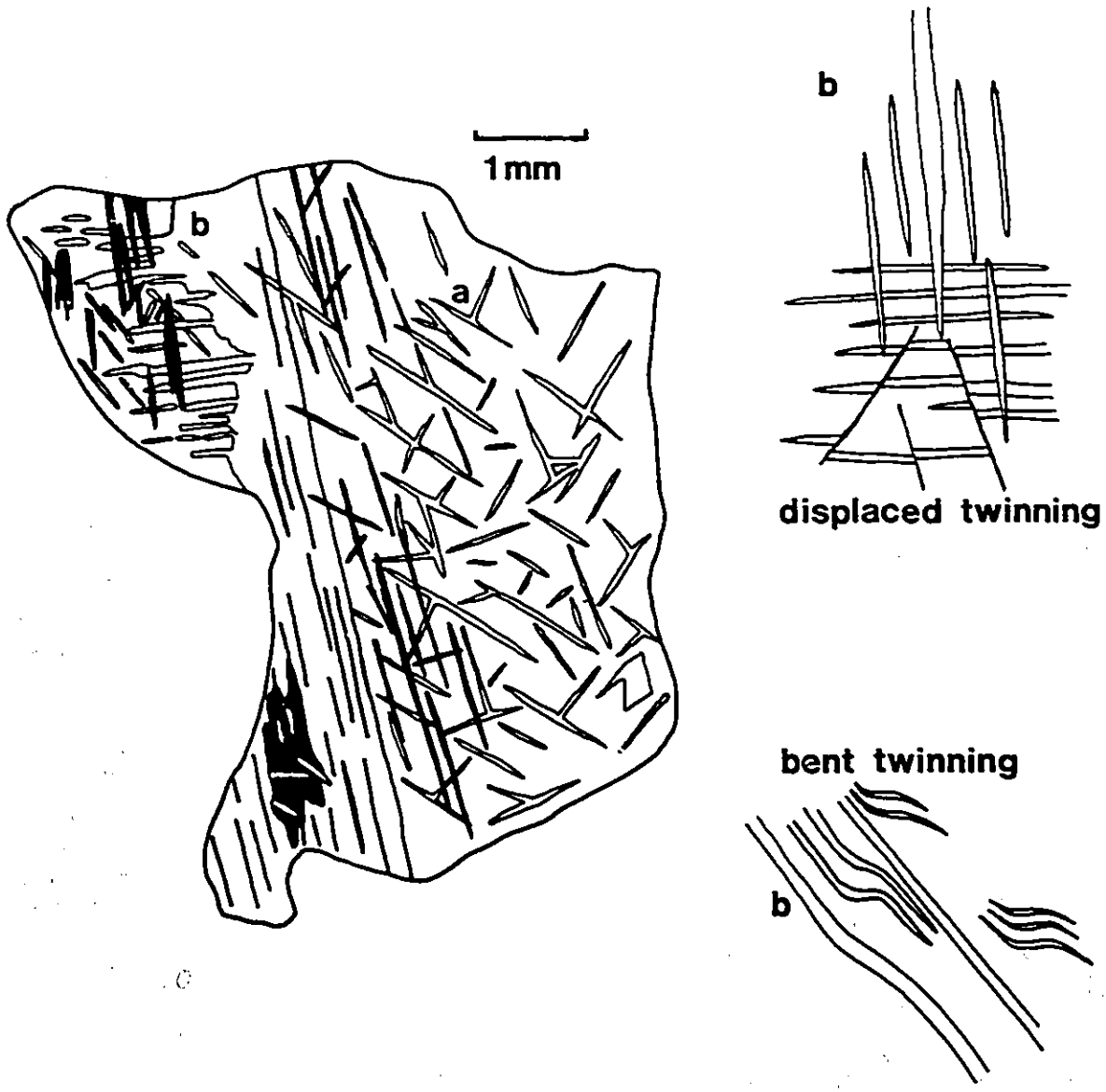

Figure 21c. Randomly oriented microcrystals of plagioclase within a plagioclase grain.
a) plagioclase microcrystals
b) deformed twins

Figure 22a. Orthopyroxene and magnetite symplectite corona structure characterized by a double layer consisting of an inner prismatic orthopyroxene and an outer acicular pargasitic amphibole layers. Ti-magnetite corona structure is also present and exhibits a double corona layer of biotite and acicular pargasite (sample CMA-LG7).

Figure 22b. Primary augite exhibiting a corona structure composed of prismatic pargasitic hornblende and sodic plagioclase. Aggregates of idioblastic garnet grains are present in the plagioclase laths. The plagioclase laths are characterized by abundant inclusions of spinel that are distributed around more sodic plagioclase exsolutions (sample CMA-79Di).

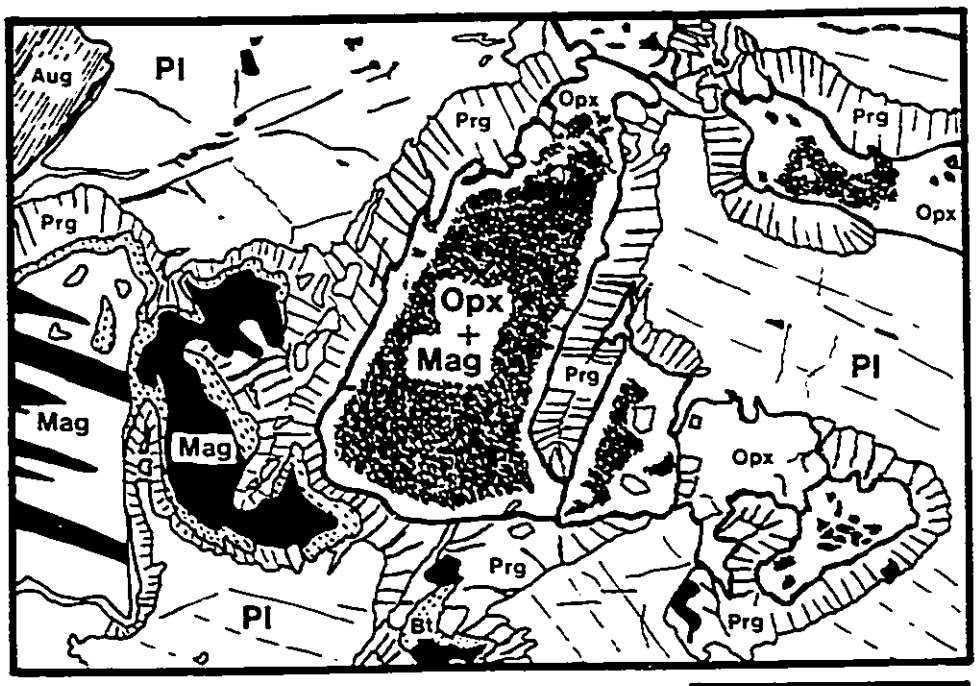

Figure 22a

1.0 mm

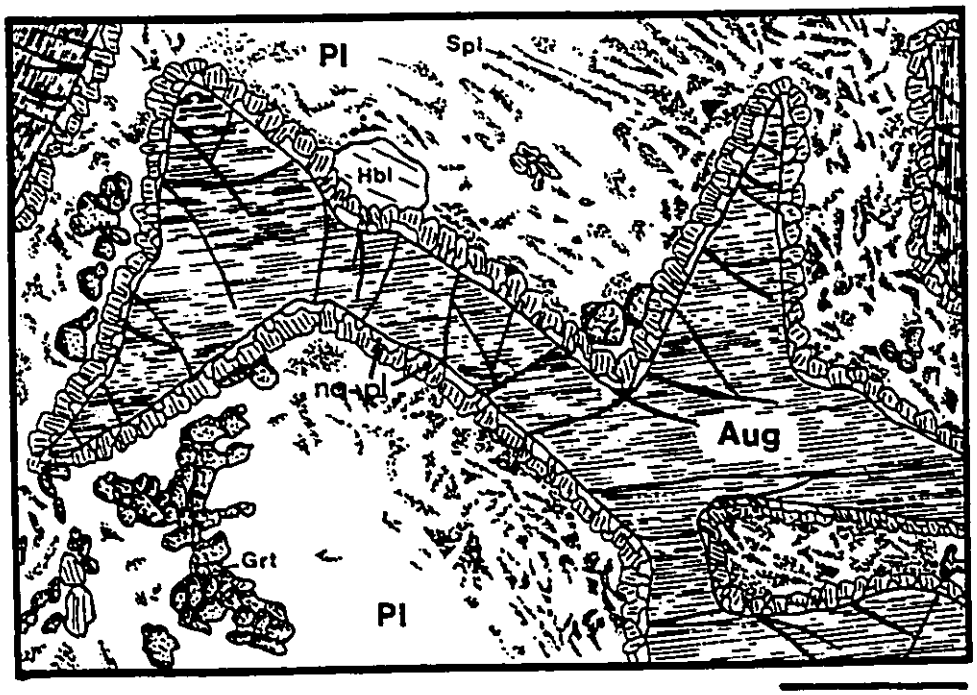

Figure 22b

1.0 mm

across plagioclase crystals). Eventually, with further recrystallization and reaction, there is a decrease in spinel clouding. This decrease is caused by aggregation and annealing of the spinel dust into discrete, coarser grained, dark green spinel crystals. Alteration of the primary plagioclase grains is defined by the formation of more sodic plagioclase at the grain margins and by the presence of fine epidote grains and sericite crystals within the cores. Sericite crystals replace preferentially the corundum plates and they develop at the margin of garnet inclusions. Recrystallization of primary plagioclase grains is initiated at the grain boundaries (i.e. synchronous with granulation) and within the crystals, hence forming collars (term from Barker, 1990) of sodic plagioclase subgrains. Furthermore, primary plagioclase grains, which contain clinopyroxene intergrowths within their cores, show replacement of the inclusions by hornblende and magnetite.

3.2.2 Orthopyroxene - magnetite Symplectite-cored Corona Structure

This corona structure consists of a double corona layer developed around an orthopyroxene - magnetite symplectite core. The corona layers are typically composed of an inner layer of prismatic orthopyroxene (0.10 to 0.20 mm) and an outer layer of acicular pargasitic amphibole (Fig. 22a). According to Goode (1974), the orthopyroxene - magnetite symplectite is

suggestive of a late stage oxidation reaction of olivine. However, in most cases, textural evidence does not support this relationsip (e.g. the presence of trace amounts of iddingsite associated with orthopyroxene and magnetite symplectite). The amount of magnetite present in the symplectite core is variable. Magnetite vermiculite may be so predominant that the core looks similar to that of the Ti-magnetite corona structure. In some cases, the distribution of magnetite vermiculite in orthopyroxene grains may exhibit a zoning pattern (Figs. 23a and 23b).

3.2.3 Clinopyroxene Corona Structure

At a more advanced stage of recrystallization and reaction (i.e. relative to the corona structure development about olivine), primary clinopyroxene grains have developed a double layer corona structure (type 3) composed of a continuous inner layer of pargasitic hornblende and a discontinuous outer layer of sodic plagioclase and pargasitic hornblende crystals (Fig. 22b). This corona structure does not exceed 0.30 mm in thickness. At this time of corona structure development around clinopyroxene, the primary clinopyroxene varies in color from light brown to dark brown or dark green. The patchy exsolution patterns (note: possibly exsolved crystals) of tiny magnetite inclusions within the clinopyroxene grains is the cause of this change in color. With further recrystallization, some elements within the Ti-magnetite inclusions evidently diffuse out of the crystal

Figure 23a. Photomicrograph of orthopyroxene and magnetite symplectite under plane polarized light (1.5 mm across, sample CMA-LGY).

Figure 23b. Same texture as above under reflected light. Vermicular magnetite crystals are distinct (1.5 mm across).

Figure 23a

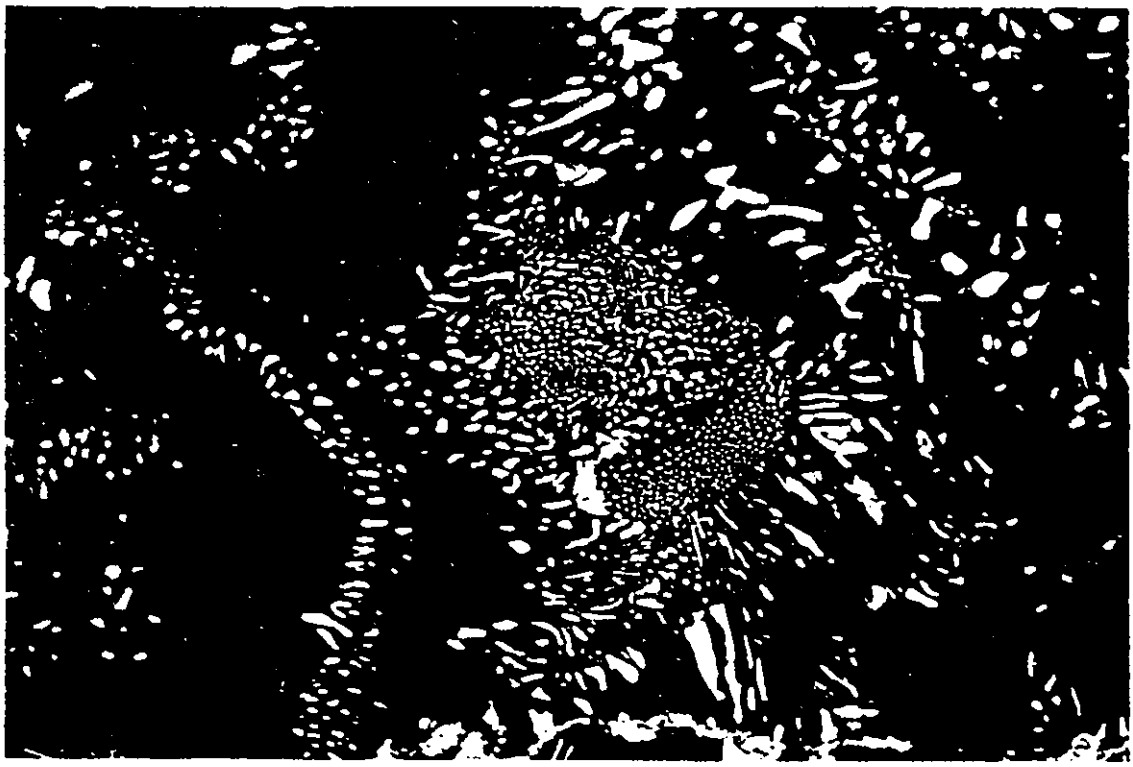

Figure 23b

lattice to produce needles of rutile. At more advanced stages of recrystallization, the augite is replaced by diopsidic pyroxene, most commonly along the grain margins (Fig. 24b). The diopside is recognized by its light green color under plane light and by a different birefringence under cross polarized light. The diopside crystals may form granoblastic aggragates, which are in contact with primary augite or as independent aggregates within plagioclase laths associated with secondary biotite, calcite, sodic plagioclase, and hornblende. Corona structures may be present around the diopside aggregates, consisting of an inner layer or moat of sodic plagioclase, an intermediate granoblastic hornblende layer, and an outer idioblastic garnet layer (Fig. 25b).

Within some thin sections, the primary clinopyroxene does not breakdown into secondary diopside, but instead is directly altered to hornblende (Fig. 24a). This replacement is initiated along grain boundaries and within fractures, and progressively evolves towards the center of respective grains. Small elongated hornblende crystals are found along the cleavage planes. Intensive replacement has generally destroyed the delicate hornblende corona structure. However, in some cases, the prismatic hornblende corona structure has evolved to a columnar hornblende corona layer that surrounds granoblastic hornblende of a different composition. At more advanced stages, the aggregate of small hornblende crystals may be recrystallized into a single large grain of hornblende.

Figure 24a. Extensive replacement of primary augite by hornblende. The relic augite grain is heavily clouded with minute exsolutions of magnetite and minor rutile. Hornblende forms granoblastic aggregates. Small idioblastic garnet crystals are disseminated throughout the sample. Plagioclase laths have recrystallized and show a granoblastic texture. (sample CMA-146)

Figure 24b. Replacement of primary augite by light green diopside. The replacement takes place at the grain boundary and along fractures. Commonly as shown, pyroxene is rimmed by zoned garnet grains.

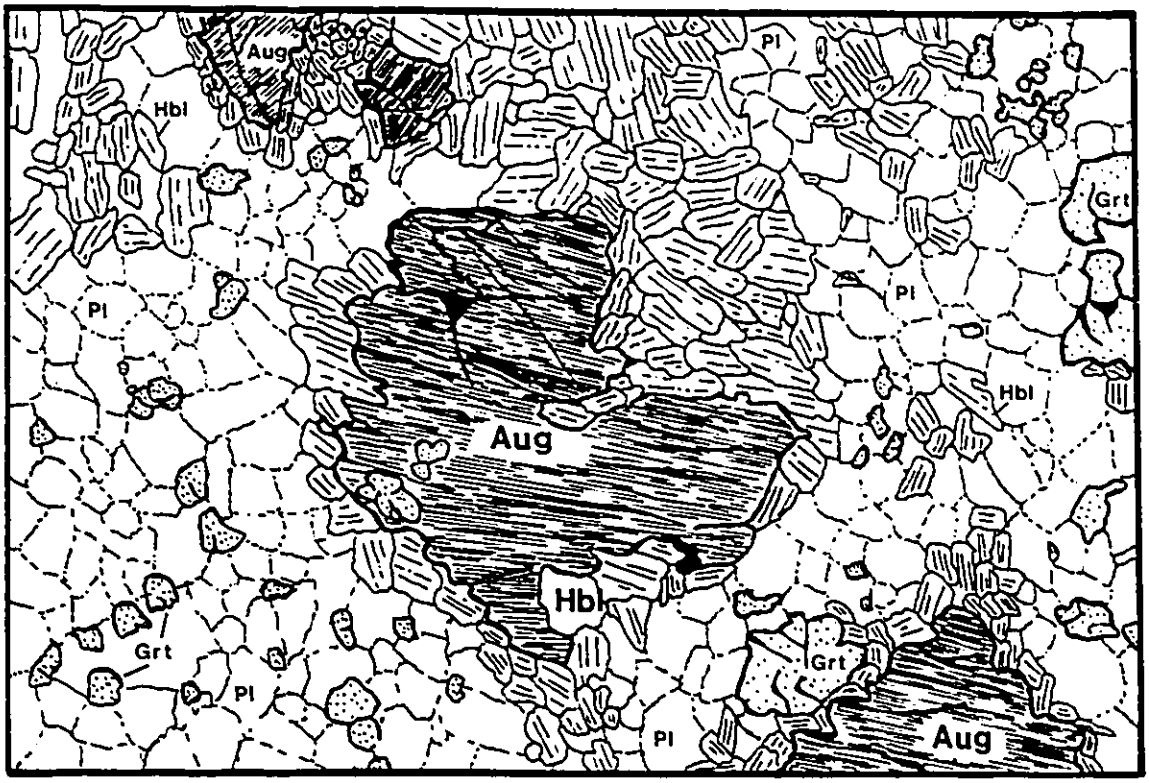

Figure 24a

1.0 mm

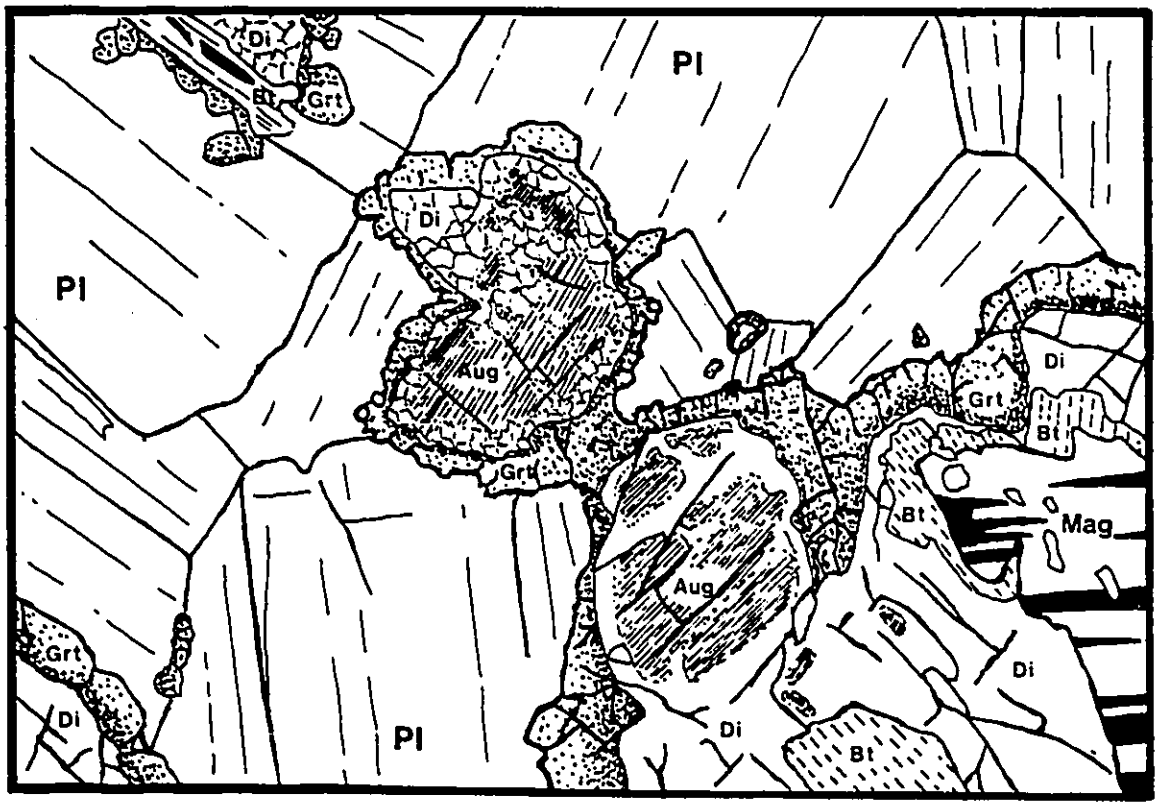

Figure 24b

1.0 mm

Figure 25a. Small aggregate of orthopyroxene surrounded by a double layer corona structure consisting of granoblastic hornblende and zoned garnet grains. This corona structure is thought to represent a more evolved version of the orthopyroxene and magnetite symplectite corona structure. Plagioclase laths are heavily clouded with spinel and corundum inclusions.

Figure 25b. Corona structure developed around an aggregate of fine-grained diopside crystals. The corona structure is composed of an inner moat of sodic plagioclase and an outer layer of garnet crystals. The plagioclase laths contain abundant corundum inclusions.

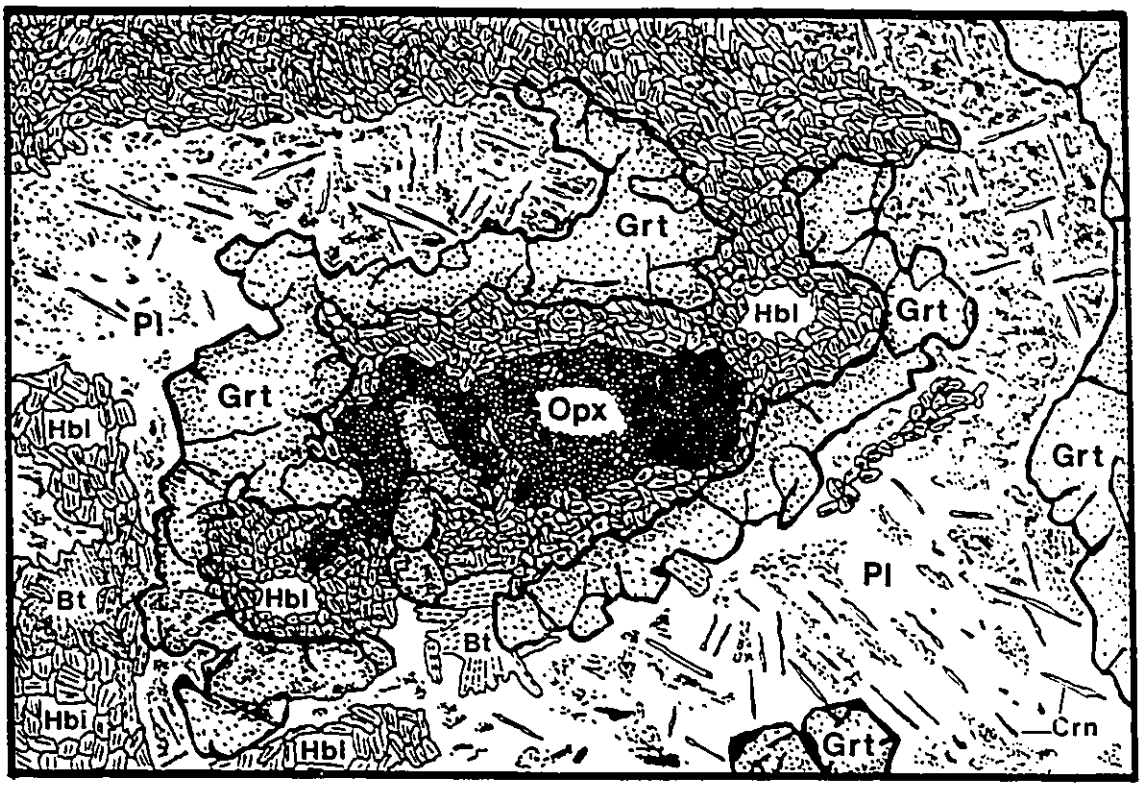

Figure 25a

1.0 mm

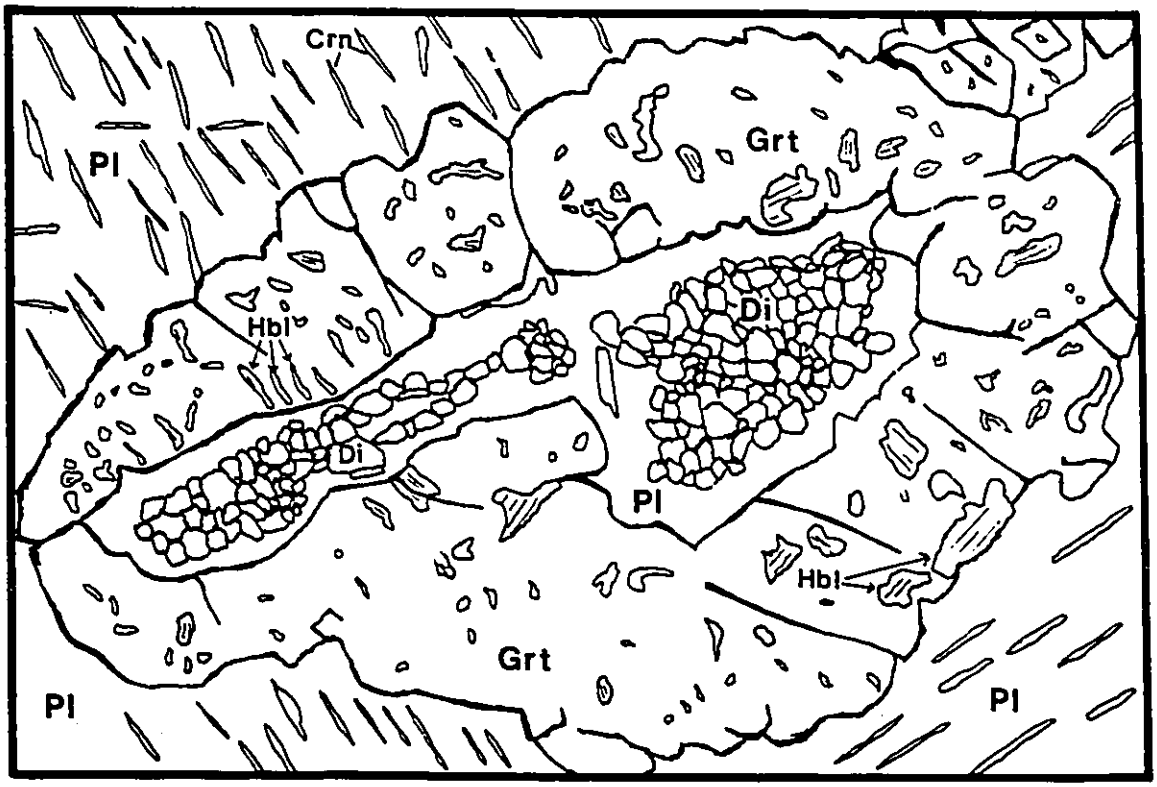

Figure 25b

0.25 mm

3.2.4 Ti-magnetite Corona Structure

Ti-magnetite crystals are surrounded by continuous to discontinuous corona layers consisting of biotite and acicular pargasite (Fig. 19b). Most of the Ti-magnetite crystals have experienced recrystallization and reaction and consist of an aggregate of ilmenite and magnetite grains.

With further recrystallization and reaction, the reddish brown biotite corona layer around the Ti-magnetite core is partially to completely replaced by blue green pargasitic amphibole. The appearance of the orthopyroxene - magnetite symplectite-cored corona structure is observed at this stage.

The layers of garnet crystals that have formed around iron oxide minerals, commonly, have developed with an internal zoning pattern. This zoning pattern is composed of an inner turbid zone in contact with the iron oxide mineral and an outer inclusion-free zone. In some cases, when in contact with primary augite, the outer zone consists of vermicular clinopyroxene. These two zones may be further subdivided according to the nature of the inclusions. For instance, the inner zone may be divided into an inner part consisting of biotite-rich inclusions and an outer part consisting of amphibole-rich inclusions. The outer zone, when occupied by clinopyroxene, grades from fine to coarse vermicular inclusions (Fig 26). The outer, inclusion-free zone generally displays idioblastic terminations in contact with plagioclase grains.

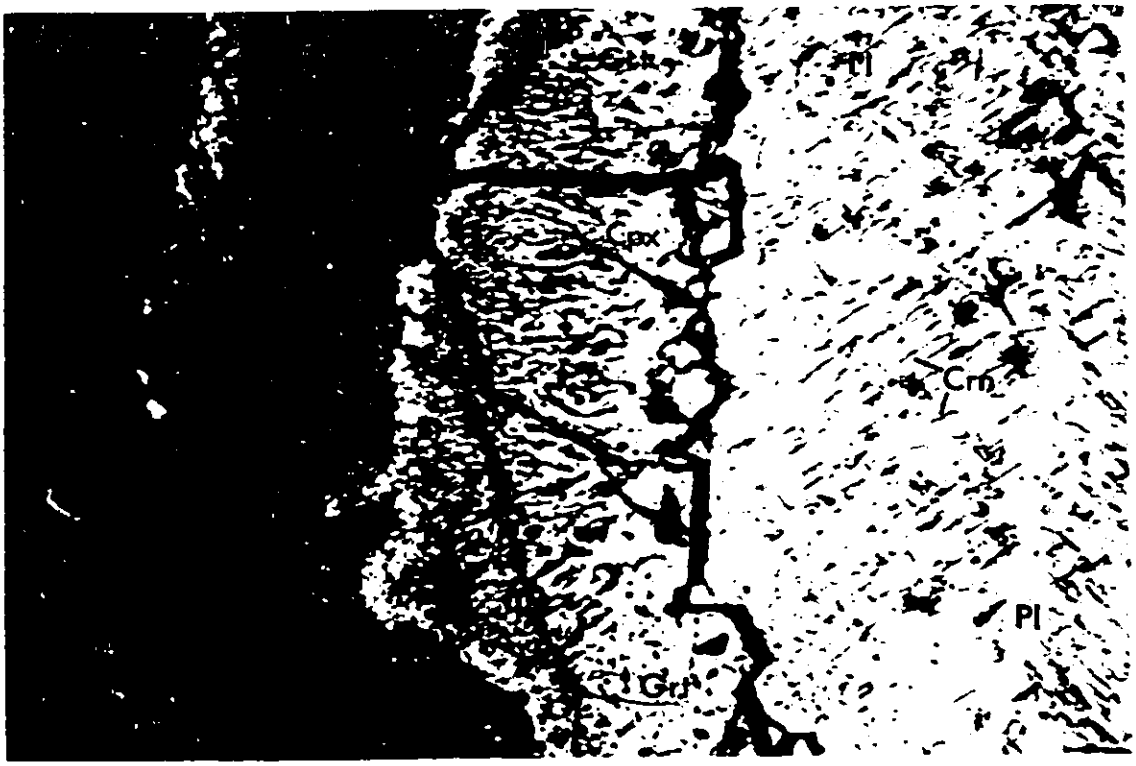

Figure 26. Ti-magnetite grain surrounded by a two layer corona structure. The inner layer is composed of biotite and the outer layer of zoned garnet. The garnitiferous layer is comprised of an inner biotite-rich zone, and an intermediate hornblende-rich zone, and an outer vermicular clinopyroxene-rich zone, under plane polarized light (sample CMD-49). The field of view is 1.5 mm across.

3.2.5 Garnet Atoll (Non-corona) Structure

Subhedral to euhedral garnet crystals typically form an additional layer around primary olivine, orthopyroxene/magnetite symplectite, Ti-magnetite, and primary augite corona structures. Their size does not exceed 0.1 mm in diameter. Garnet generally nucleated within the amphibole layer or at the amphibole/orthopyroxene and amphibole/oxide interfaces. At these interfaces the garnet crystals progressively replace the amphibole layer of the corona structure. At advanced stages of garnet formation (> 2 to 3 modal percent), euhedral garnet crystal are observed forming discontinuous shells around most of the ferromagnesian minerals. They may also form small aggregates within plagioclase laths. The formation of abundant garnet crystals is typically associated with heavily spinel clouded plagioclase laths and the presence of corundum plates. Where discontinuous chains of idioblastic garnet crystals are observed, they are found rimming most rock-forming minerals (i.e. apatite, primary biotite, plagioclase, and augite). They commonly occur around primary clinopyroxene grains and at the margins of plagioclase grains. These garnet crystals differ from those that formed around olivine and iron oxide corona structures. They are generally small (<1 mm), and contain inclusions of corundum when found within plagioclase laths. The spatial and temporal relationship between the garnets around olivine and iron oxide corona structures and the discontinuous chains of garnet around

the clinopyroxene corona structure is not clear. The habit of these chains of garnet suggests that they are different from those found within the corona structures around olivine and iron oxide minerals. In some instances, the garnet crystals are found replacing hornblende within the corona structure that surrounds clinopyroxene, whereas, in most cases the garnet crystals are not found in direct contact with the hornblende of corona structures. At this advanced stage of recrystallization, most primary minerals have been recrystallized and most of the corona structures have been destroyed. Large garnet grains may be found surrounding an aggregate of granoblastic hornblende crystals, which mark the location of an earlier formed corona structure (Fig. 27). Primary plagioclase laths have been recrystallized into a mosaic of sodic plagioclase grains. Garnet chains are often found circling these sodic plagioclase aggregates, which define the original grain boundaries. Despite the intensive recrystallization experienced by some diabase dykes, the original igneous texture is still preserved, which possibly indicates the relative absence of tectonic stresses exerted on these dykes.

The final stage of recrystallization is represented by mineral assemblages composed of hornblende, plagioclase, garnet, and minor amounts of oxide minerals, quartz, calcite, and sphene. The hornblende is coarse-grained and generally zoned. The zoning consists of a central core of poikiloblastic hornblende replacing primary clinopyroxene and an outer zone of massive (inclusion-free) hornblende crystals (Fig. 28). The central core

Figure 27. Metamorphosed corona structures consisting of aggregates of hornblende crystals surrounded by idioblastic garnet grains, under plane polarized light (sample CMA-F-1236, 3.5 mm across).

Figure 28. Metamorphosed diabase dyke composed of hornblende, garnet, biotite, plagioclase, and sphene. The hornblende grains are medium- to coarse-grained, and display well developed cleavages at 120°. Disseminated oxide minerals are replaced by sphene. Plagioclase grains are completely recrystallized into a granoblastic texture. Advanced metamorphism has destroyed all evidence of earlier formed corona structure (sample CMA-F-1236, 3.5 mm across).

Figure 27

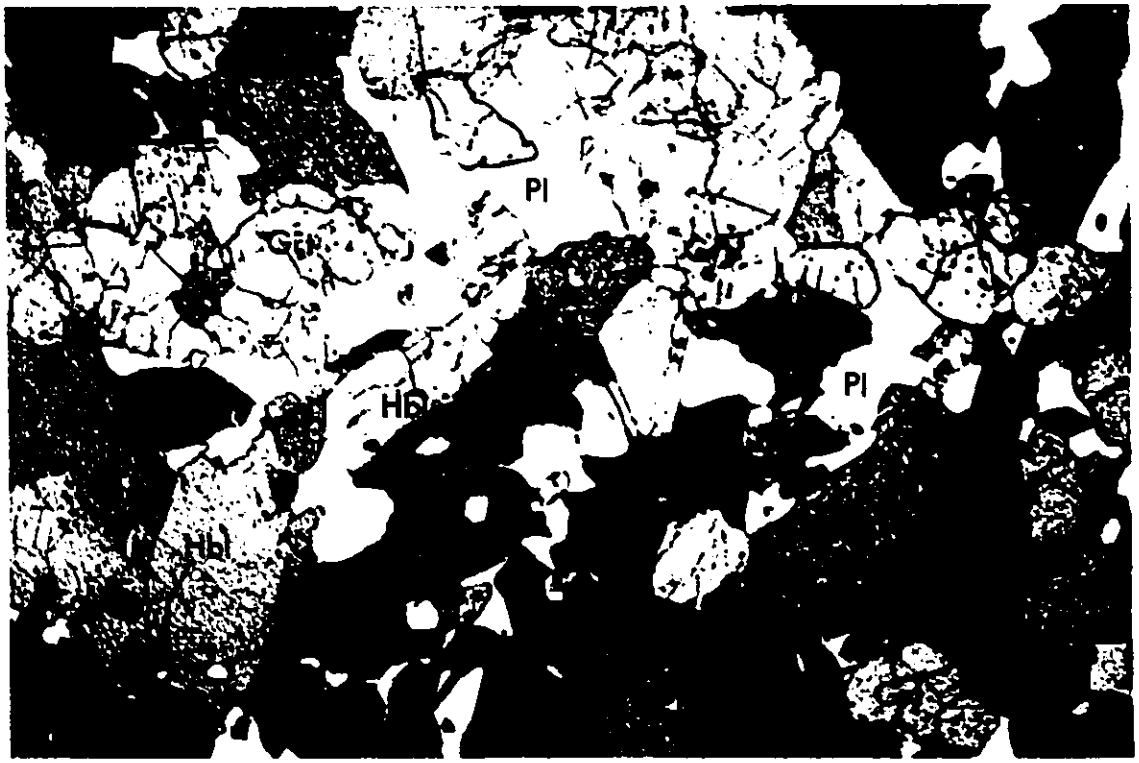

Figure 28

is rich in plagioclase and quartz inclusions. The outer zone may form as a polygonal aggregate or a single crystal. A mosaic of fine-grained plagioclase grains is present between the hornblende grains. Garnet crystals are found associated with the plagioclase aggregate and are generally inclusion-free. The oxide minerals are disseminated within hornblende grains and are replaced by sphene and calcite. The texture may be massive or may show a foliation displayed by the presence of plagioclase-rich layers. At this stage, all evidence of primary mineralogy has been destroyed.

3.3 SUMMARY OF CORONA STRUCTURE DEVELOPMENT

A summary of mineralogical and textural evolution of coronitic diabase dykes is given in Table 2. From Table 2, it is possible to state that the first reactions occurring in the diabase dykes resulted in the formation of double layer corona structures between olivine and plagioclase, as well as single or double layer corona structures between Ti-magnetite and plagioclase. Primary augite, stable during the above reactions, later reacted with plagioclase to produce double layer corona structures of pargasitic hornblende and sodic plagioclase. At this stage, double layer corona structures of orthopyroxene and pargasitic amphibole have formed around orthopyroxene and magnetite symplectite. Subsequent corona reactions involved the formation of garnet at the expense of amphibole and biotite

layers. The later stages of corona reactions, represented by the appearance of diopside and orthopyroxene corona structures, formed by the breakdown of primary augite and the orthopyroxene - magnetite symplectite, respectively. Further reactions resulted in the total destruction of earlier formed corona structures and this involved extensive recrystallization into granoblastic textures.

Table 2. Progressive evolutionary history of mineral and textural variations in coronitic diabase dykes.

least altered	1	2	3	4
OLIVINE	- Primary phase, euhadral, fractured primary alteration to serpentine, bowlingite, iddingsite, and minor magnetite.	- More pervasive alteration to iddingsite and magnetite. - Thicker corona structure of opx and magnetite, in contact with plagioclase.	- Oxidation of olivine to opx and magnetite symplectite. - Thick opx and pargasite corona layers with local	- Relict olivine grains, mostly replaced by opx and magnetite symplectite. - Thick opx, pargasite, and garnet corona stucture is observed.

Table 2. Progressive evolutionary history of mineral and textural variations in coronitic diabase dyke.

least altered 1	2	3	4
OLIVINE - Primary phase, euhadral, fractured primary alteration to serpentine, bowlingite, iddingsite, and minor magnetite. - Thin corona layer composed of orthopyroxene and pargasite in contact with plagioclase.	- More pervasive alteration to iddingsite and magnetite. - Thicker corona structure of opx and magnetite, in contact with plagioclase. - Thin layer of opx form when in contact with primary augite.	- Oxidation of olivine to opx and magnetite symplectite. - Thick opx and pargasite corona layers with local garnet forming in pargasite layer.	- Relict olivine grains, mostly replaced by opx and magnetite symplectite. - Thick opx, pargasite, and garnet corona stucture is observed.
PLAGIOCLASE - Primary, well twinned, and colourless with straight grain boundaries.	- Well twinned, weakly clouded by minute inclusions of spinel which imparts a brown color to the plagioclase.	- Well twinned, dark brown core and clear margins. - Minor inclusion of corundum are present. - Presence of subgrains at the plagioclase margin. - Exsolutions of sodic plagioclase occurs in primary calcic plagioclase.	- Primary, well twinned laths of plagioclase. - Heavily clouded by spinel dust and corundum plates. - Clear sodic plagioclase develop at the grain boundaries, next to corona structures. - Exsolution of sodic plagioclase are present in primary plagioclase.
AUGITE - Primary, brown, subhedral grains without inclusion. - No corona structure present.	- Primary, brown, subhedral grains with no inclusion. - Very thin rim of prismatic amphibole and sodic plagioclase occurs around most grains.	- Primary, dark brown to dark green subhedral grains. - Heavily clouded by minute exsolution of magnetite blebs. - Thin corona layers of prismatic pargasite and sodic plagioclase are present.	- Primary core with patchy recrystallization into light green diopside, mostly at the grain boundary. - Magnetite exsolution migrated out of the augite grains. - Corona structure around augite is observed, composed of hornblende, sodic plagioclase, and garnet.

		- Exsolutions of sodic plagioclase occurs in primary calcic plagioclase.	- Exsolution of sodic plagioclase are present in primary plagioclase.
AUGITE - Primary, brown, subhedral grains without inclusion. - No corona structure present.	- Primary, brown, subhedral grains with no inclusion. - Very thin rim of prismatic amphibole and sodic plagioclase occurs around most grains.	- Primary, dark brown to dark green subhedral grains. - Heavily clouded by minute exsolution of magnetite blebs. - Thin corona layers of prismatic pargasite and sodic plagioclase are present.	- Primary core with patchy recrystallization into light green diopside, mostly at the grain boundary. - Magnetite exsolution migrated out of the augite grains. - Corona structure around augite is observed, composed of hornblende, sodic plagioclase, and garnet.
BIOTITE - Primary reddish brown well formed flakes. - Observed mantling some Ti-magnetite grains and are found between plagioclase laths.	- Evidence of replacement by chlorite along grain boundaries and cleavage planes.	- Chlorite and actinolite pseudomorph after biotite. - Replacement of biotite layer by amphibole layer within Ti-magnetite corona structure. - Garnet are found associated with amphibole corona layer.	- Biotite flakes within plagioclase aggregates are partly recrystallized by chlorite or actinolite/tremolite.
OXIDE MINERALS - Primary anhedral to subhedral Ti-magnetite crystals with ilmenite lamellae. - Rare inclusions of hyrcenite. - Single corona structure is observed, composed of acicular pargasite, in contact with plagioclase.	- Recrystallization of some Ti-magnetite grains into an aggregate of ilmenite and magnetite.	- Primary to secondary aggregates of ilmenite and magnetite. - Typical corona structure composed of biotite, pargasite, and garnet.	- Totally recrystallized with corona layers of amphibole and garnet grains. - Secondary oxide minerals display vermiculite texture within augite and orthopyroxene.

5	6	7
- No primary olivine grains are observed, at this stage. - Orthopyroxene and magnetite symplectite corona structure predominates. It is composed of a triple corona layers of orthopyroxene, pargasite, and garnet.	ORTHOPYROXENE - Occur as granoblastic aggregates with diopside. - Often surrounded by amphibole and garnet corona layers.	HORNBLENDE - Coarse-grained poikiloblastic hornblende with inclusions of quartz and sodic plagioclase.
- Relict primary plagioclase, intensively recrystallized. - Abundant corundum are observed - Idioblastic garnet are formed along plagioclase grain margins.	- Occurs as fine to medium-grained granoblastic aggregates. - Rare amount of corundum are present. - Original outline of primary plagioclase is preserved. - Trace amount of spinel is observed.	PLAGIOCLASE - Completely recrystallized displaying granoblastic texture.
- Rare primary grains, most commonly recrystallized to light green diopside aggregates which develop corona structure composed of sodic plagioclase moat, hornblende, and garnet layers.	- Relict of primary grains, they are mostly recrystallized to granoblastic aggregates of diopside and/or amphibole.	GARNET - Coarse-grained idioblastic crystals associated with the plagioclase.
		MAGNETITE/ILMENITE - Fine disseminated grains altered to sphene and calcite.
- Biotite flakes are entirely recrystallized and are associated with granoblastic	- Coarse-grained secondary flakes occuring within plagioclase laths.	

along plagioclase grain margins.	is preserved. - Trace amount of spinel is observed.	
- Rare primary grains, most commonly recrystallized to light green diopside aggregates which develop corona structure composed of sodic plagioclase moat, hornblende, and garnet layers.	- Relict of primary grains, they are mostly recrystallized to granoblastic aggregates of diopside and/or amphibole.	GARNET - Coarse-grained idioblastic crystals associated with the plagioclase.
		MAGNETITE/ILMENITE - Fine disseminated grains altered to sphene and calcite.
- Biotite flakes are entirely recrystallized and are associated with granoblastic aggregates of diopside and plagioclase.	- Coarse-grained secondary flakes occuring within plagioclase laths.	
- Opaque minerals are completely recrystallized. They form aggregate of ilmenite and magnetite surrounded by double corona layers of amphibole and garnet.	- Recrystallized aggregate of ilmenite and magnetite.	

WHOLE-ROCK CHEMISTRY OF NNE DIABASE DYKES

4.1 ANALYTICAL METHODS

Rock samples were cut to remove all weathered surfaces, and then ground into a fine rock powder (< 80 mesh). To minimize contamination, the crushing dish was cleaned with compressed air and acetone after the processing of each sample. Futhermore, quartz chips were crushed after every fifth sample in order to remove contaminants from the crushing dish.

The powdered samples were submitted for geochemical analyses to the Analytical Services Section of the Central Laboratories and Technical Services Division of the Geological Survey of Canada. The samples were analyzed for major and some trace elements with an automated energy-dispersive X-ray fluorescence instrument (XRF). An estimate of the validity of results for this analytical technique is listed in Table 3.

FeO, H_2O_T, CO_{2T}, and S were determined by rapid chemical methods: FeO by cold acid decomposition and back titration with $K_2Cr_2O_7$, H_2O_T by fusion in a Penfield tube and a Karl Fisher titration. Fe_2O_3 was calculated using the formula: Fe_2O_3 = Fe_2O_3 (XRF) - (1.11134 x FeO (volumetric)).

Analyses of minor and rare earth elements were determined using ion-exchange separation columns (i.e. for REE's and Y) and inductively coupled plasma - atomic emission spectroscopy

Table 3. Estimates of validity of results for the major elements. Abs = absolute analytical error, Rel = relative analytical error, Det = detection limit, and 2S = (abs + rel), which is the confidence limit (i.e. precision) expressed as 2.0 times standard deviation.
For example, if Al_2O_3 is 15.6 wt%, then 2S for this value is ± 0.556 wt% (i.e. ± 0.40 wt% ± [1% of 15.6 wt%] at 95% confidence level).

Wavelength-Dispersive XRF

	Abs (± wt%)	Rel (± %)	Det (wt%)
SiO_2	0.40	1	0.40
TiO_2	0.02	1	0.02
Al_2O_3	0.40	1	0.40
Cr_2O_3	0.02	1	0.02
Fe_2O_3	0.10	1	0.10
FeO	0.20	2	0.20
MnO	0.01	2	0.01
MgO	0.10	1	0.10
CaO	0.10	1	0.10
Na_2O	0.50	1	0.50
K_2O	0.05	1	0.05
H_2O_t	0.10	5	0.10
CO_2	0.05	3	0.05
P_2O_5	0.02	1	0.02
S	0.04	5	0.04

(ICP-AES). Detection limits and precision estimates of this method are presented in Table 4.

4.2 CHEMICAL CHARACTERISTICS OF NNE DIABASE DYKES:

Fifty four samples of NNE dykes were analyzed to determine the composition of the dykes and to examine the relationship of these dykes with other well known diabase dyke swarms of the Chibougamau area. Appendix D1 presents the chemical analyses, CIPW norms, and certain ratios for the NNE dykes from the Parautochthonous Domain. The average analyses of representative groups of the NNE diabase dykes are shown in Table 5, and are presented with other gabbroic dykes and basaltic volcanics of the Grenville and Superior Provinces, and other continental basalt provinces (i.e. for comparison).

4.2.1 Alteration

It is well known that alteration can be a major problem to the interpretation of the geochemistry of rocks, especially those from highly metamorphosed terrains where elements are more likely to be mobile. Therefore, before discussing the overall chemical attributes of the NNE diabase dykes, the problem of alteration (i.e. the degree and nature of alteration processes) must be addressed. To overcome this problem, it is essential to identify the geochemical effects of the alteration processes that have

Table 4. Estimates of validity of results for minor and rare earth elements using ICP analytical technique. Abs = absolute analytical error, Rel = relative analytical error, and note that 2S (the precision) is determined by the same procedure as in Table 3.

Minor Elements by ICP

	Abs (± wt%)	Abs (± ppm)	Rel (± %)
Ba	0.01	-	5
Be	-	0.5	5
Co	0.01	5	5
Cr	0.01	10	5
Cu	0.01	10	5
Ni	0.01	10	5
V	0.01	5	5
Zn	0.01	5	5
Zr	0.01	-	5

Rare Earth Elements by ICP

	Abs (± ppm)	Rel (± %)
La	0.5	5
Ce	0.5	5
Nd	0.5	5
Sm	0.3	5
Eu	0.1	5
Gd	0.2	5
Dy	0.2	5
Yb	0.1	5
Y	1.0	5

Table 5. Comparison of average analysis of representative NNE diabase dykes with other basaltic dykes and mafic volcanic suites.

	1 High-Al2O3 (n=2)	2 Low-TiO2 (n=18)	3 High-TiO2 (n=26)	4 Segreg. (n=6)	5 Grenville (n=15)	6 Grenville (n=3)	7 Grenville (n=26)	8 Sudbury (n=5)	9 Keween (n=6)	10 Keween (n=6)	11 Columbia (n=3)
SiO2	48.80	48.20	47.58	48.58	49.70	48.70	47.17	47.20	47.90	48.89	49.30
TiO2	0.32	1.16	2.22	2.63	1.91	2.20	2.32	2.88	0.92	2.19	1.36
Al2O3	23.35	16.25	15.01	14.07	14.60	13.70	14.29	14.60	17.66	15.72	15.70
Fe2O3	1.45	1.83	2.98	3.53	3.60	3.80	15.28	2.70	4.12	7.12	2.43
FeO	4.65	9.46	11.50	11.72	10.00	10.50	nd	12.90	5.39	5.60	8.19
MnO	0.10	0.18	0.22	0.25	0.22	0.21	0.19	0.21	0.14	0.17	0.19
MgO	4.59	8.11	5.67	4.77	5.89	6.70	6.24	5.70	7.25	5.05	7.29
CaO	12.16	10.24	9.19	8.97	10.50	10.63	9.72	7.69	11.02	8.36	10.49
Na2O	2.55	2.44	2.75	2.48	2.42	2.10	2.77	3.20	2.32	3.19	2.51
K2O	0.37	0.45	0.79	0.83	0.50	0.53	0.88	1.36	0.29	1.03	0.48
P2O5	0.04	0.13	0.33	0.58	0.12	0.16	0.29	0.59	0.09	0.28	0.22
CO2	0.55	0.50	0.31	0.38	nd	0.30	nd	0.10	0.06	0.10	0.05
H2O	0.95	0.80	0.99	0.72	nd	1.10	(0.70)	0.60	2.43	2.33	0.86
Total	99.33	99.25	99.32	99.12	99.46	100.61	99.85	99.73	99.59	100.03	99.07
Ba	159	231	397	500	60	107	395	662	55	207	240
Co	49	82	71	76	132	nd	48	nd	46	44	nd
Cr	28	158	101	105	nd	nd	148	nd	284	133	154
Cu	36	66	65	60	nd	nd	nd	nd	nd	nd	nd
Nb	bl	10	18	24	nd	nd	9	17	nd	nd	nd
Ni	64	136	69	50	nd	nd	49	nd	193	120	77
Rb	7	21	30	33	8	6	16	39	7	31	7
Sc	nd	nd	nd	nd	nd	nd	nd	nd	27	28	37
Sr	293	284	271	261	211	182	289	324	269	283	282
V	72	201	260	277	nd	nd	377	nd	nd	nd	nd
Y	7	17	35	51	29	31	50	50	nd	nd	24
Zn	57	116	157	170	nd	nd	nd	nd	nd	nd	nd
Zr	35	91	172	241	125	108	145	221	82	127	nd
La	4.9	8.3	18	26	nd	nd	nd	nd	6.2	23	10
Ce	10	19	43	62	nd	nd	nd	nd	14	53	23
Nd	6.5	12	28	39	nd	nd	nd	nd	nd	nd	nd
Sm	0.40	2.6	5.8	8.5	nd	nd	nd	nd	2.4	6.9	3.7
Eu	0.60	1.1	2.1	2.9	nd	nd	nd	nd	1.0	2.0	1.3
Gd	1.5	3.4	6.8	9.8	nd	nd	nd	nd	nd	nd	nd
Tb	nd	nd	nd	nd	nd	nd	nd	nd	0.51	1.2	0.73
Dy	1.5	3.5	6.7	9.7	nd	nd	nd	nd	nd	nd	nd
Er	nd	nd	nd	nd	nd	nd	nd	nd	nd	nd	nd
Tm	nd	nd	nd	nd	nd	nd	nd	nd	nd	nd	nd
Yb	0.75	1.7	3.3	5.1	nd	nd	nd	nd	1.6	3.1	2.5
Lu	nd	nd	nd	nd	nd	nd	nd	nd	0.22	0.47	0.37

Table 5 (continued)

	12 Columbia (n=7)	13 Taos (n=6)	14 Parana (n=12)	15 Parana (n=64)	16 Atka (n=18)	17 Ferrar (n=1)	18 N1-MORB	19 N2-MORB	20 E-MORB
SiO2	51.16	50.92	51.91	51.41	49.76	51.94	50.26	50.42	51.18
TiO2	2.74	1.21	0.94	3.50	0.89	0.55	1.10	1.50	1.69
Al2O3	13.75	16.26	15.82	13.56	20.53	21.64	15.80	14.93	16.01
Fe2O3	3.60	2.31	nd	nd	nd	1.71	nd	nd	9.40
FeO	9.65	8.30	9.81	14.09	9.10	4.53	9.40	10.41	nd
MnO	0.22	0.16	0.16	0.19	0.18	0.10	0.17	0.18	0.16
MgO	4.30	7.03	7.39	3.80	3.63	3.12	7.84	7.46	6.90
CaO	8.08	8.96	10.75	8.40	10.11	12.16	12.48	11.49	11.49
Na2O	2.79	3.18	2.18	2.84	3.21	2.42	2.13	2.43	2.74
K2O	1.44	0.66	0.76	1.45	0.70	0.83	0.24	0.20	0.43
P2O5	0.55	0.22	0.15	0.57	0.16	0.09	0.09	0.14	0.15
CO2	0.06	0.09	nd	nd	nd	0.93	nd	nd	nd
H2O	1.10	0.56	nd	nd	nd	0.15	nd	nd	nd
Total	99.44	99.85	99.87	99.81	98.27	100.17	99.51	99.00	100.15
Ba	876	32	272	684	317	185	9	12	86
Co	nd	nd	nd	nd	nd	nd	50	54	nd
Cr	56	176	nd	nd	74	27	341	260	225
Cu	nd	nd	nd	nd	119	49	nd	nd	nd
Nb	nd	8	nd	nd	nd	4	2	4	9
Ni	nd	127	nd	nd	46	39	113	110	132
Rb	32	9	34	45	9	32	2	2	10
Sc	32	24	nd	nd	24	22	40	40	nd
Sr	297	352	236	488	649	206	96	103	155
V	nd	nd	nd	nd	270	129	nd	nd	nd
Y	41	20	18	34	nd	14	25	35	39
Zn	nd	nd	nd	nd	nd	43	78	87	nd
Zr	nd	97	96	272	49	71	63	89	121
La	28	12	14	40	nd	8.2	1.9	2.9	6.9
Ce	63	28	nd	nd	nd	19	6.0	9.3	18
Nd	nd	nd	nd	nd	nd	9.5	5.9	8.7	14
Sm	8.2	3.6	nd	nd	nd	2.4	2.2	3.2	4.6
Eu	2.6	1.2	nd	nd	nd	0.86	0.90	1.2	1.6
Gd	nd	nd	nd	nd	nd	2.5	nd	nd	6
Tb	1.5	0.66	nd	nd	nd	0.44	0.61	0.85	nd
Dy	nd	nd	nd	nd	nd	nd	nd	nd	nd
Er	nd	nd	nd	nd	nd	nd	nd	nd	nd
Tm	nd	nd	nd	nd	nd	nd	nd	nd	nd
Yb	3.9	2.0	nd	nd	nd	1.8	2.6	3.5	3.5
Lu	0.59	0.31	nd	nd	nd	0.27	0.47	0.64	0.46

Table 5a. Source reference for Table 5.

1. High-Al_2O_3 NNE diabase dykes, this study.

2. Low-TiO_2 NNE diabase dykes, this study.

3. High-TiO_2 NNE diabase dykes, this study.

4. High-TiO_2 pegmatitic segregations, this study.

5. Grenville dykes, Otter Lake area, Kretz et al. (1985).

6. Grenville dykes, Georgian Bay, Bethune and Davidson (1988)

7. Grenville dykes, Hastings area, Holm et al. (1986)

8. Sudbury dykes, Georgian Bay, Bethune and Davidson (1988)

9. Low-TiO_2 continental flood basalts, Keweenawan Reference Suite, Basaltic Volcanism Study Project (BVSP, 1981)

10. High-TiO_2 continental flood basalts, Keweenawan Reference Suite, BVSP (1981)

11. Low-TiO_2 continental flood basalts, Columbia River Basalt Reference Suite, BVSP (1981)

12. High-TiO_2 continental flood basalts, Columbia River Basalt Reference Suite, BVSP (1981)

13. Continental Rift Basalts, Taos Plateau Volcanic Field, New Mexico, BVSP (1981)

14. Low-TiO_2 flood basalts, Serra Geral, Brazil, Fodor (1987)

15. High-TiO_2 flood basalts, Serra Geral, Brazil, Fodor (1987)

16. Atka basalts, Aleutian Volcanic Arc, Alaska, Myers et al. (1986)

17. Tholeiitic sills of the Ferrar Group of Portal Peak, Antartica, Hergt et al. (1989)

18. N-MORB sub-types, DSDP/IPOD leg 82, Viereck et al. (1989)

19. N-MORB sub-types, DSDP/IPOD leg 82, Viereck et al. (1989)

20. E-MORB, Wilson (1989)

affected the rocks being studied.

A multitude of approaches have been used to evaluate the extent of secondary (post-magmatic) chemical remobilization. These include:

1) identification and rejection of rocks that are too modified (i.e. chemically altered) on the basis of H_2O and CO_2 analysis, the presence of anomalous minerals in the CIPW norm, the existence of anomalous minerals in the rock, and the position of the chemical data on variation and discrimination diagrams,

2) comparison of altered rocks with equivalent fresh rocks,

3) analysis of relict mineral phases for comparison with whole-rock chemical data (i.e. to test whether the magmatic affinity (e.g. tholeiitic) indicated by mineral phase(s) are consistent or compatible with the determined rock compositions),

4) analysis and comparison of trace element and isotopic abundances,

5) identification of broad chemical trends on Harker-type or similar diagrams, and subsequent confirmation or rejection by use of immobile elements (e.g. Ti, Nb, Y, Zr, etc.),

6) identification of element mobility by means of Pearce element ratio (PER) or molecular proportion ratio (MPR) diagrams (Pearce, 1968).

Many authors have shown that high field strength (i.e. high ionic potential) elements such as Ti, Nb, Y, and Zr are commonly immobile during amphibolite and granulite grades of metamorphism (Smith and Smith, 1976; Pearce and Norry, 1979; among others).

The Ti/Zr ratio of the NNE diabase dykes (Figure 29a) divides the rocks into two distinct groups: 1) a group with relatively high Ti/Zr ratios (i.e. > chondritic values) and 2) a group with relatively low Ti/Zr ratios (i.e < chondritic values). Except for

Figure 29a. Plot of Ti/Zr versus Zr (ppm) for the NNE diabase dykes. Chondrite value from Beswick (1983).

Figure 29b. Plot of Zr/Y versus Zr (ppm) in the NNE diabase dykes. Chondrite value from Beswick (1983).

Fig. 29a

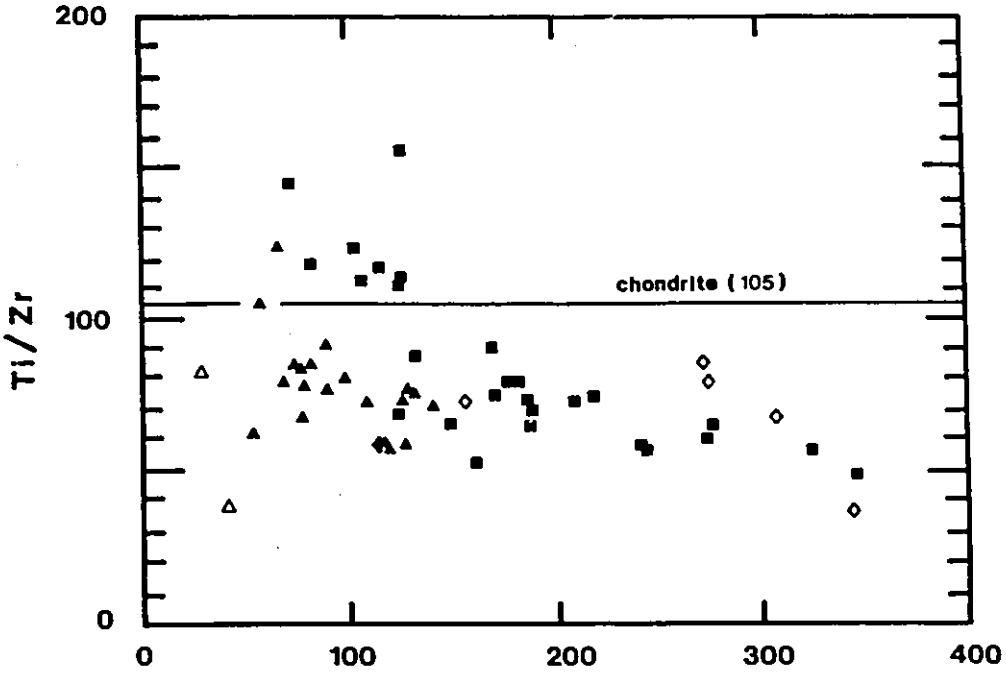

Fig. 29b

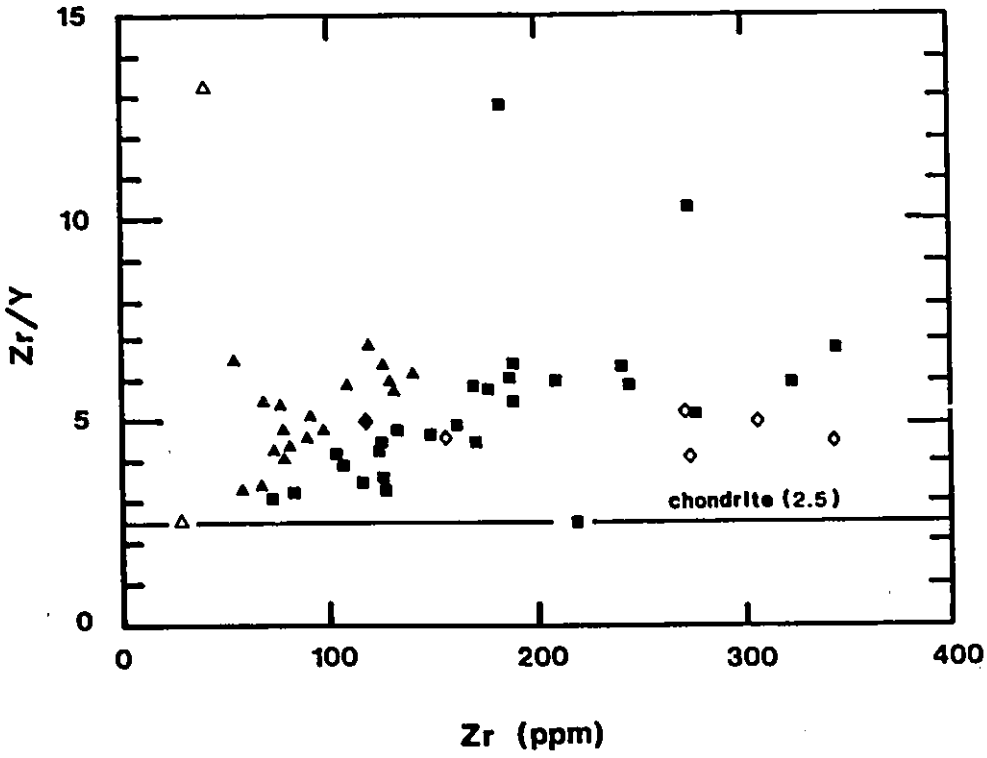

two samples, the high Ti/Zr group shows a systematic trend that is consistent with magmatic differentiation in basic rocks of a comagmatic suite. The low Ti/Zr group also defines a systematic trend with some scatter, but in general the Ti and Zr values have not been appreciably affected by alteration processes (as shown later in the chapter by conserved trace element plots). The petrological implications of the low Ti/Zr group will be discussed later in the chapter. The Zr/Y ratio and the Mg# (100•Mg/(Mg+Fe) - molecular) versus Zr (Figure 29b and Figure 30a) also are good indices for distinguishing igneous processes from alteration processes. Except for a few (approximatly 6 to 8) samples, the consistency of the results on Zr/Y versus Zr and Mg# versus Zr diagrams suggests that these elements have remained essentially unchanged during alteration processes. Alteration processes are considered unlikely to produce such consistent patterns in variation diagrams using immobile elements (and their ratios, Cox et al., 1979, Wilson, 1989). In addition, these elements and ratios show no correlation with the volatile contents of the rocks. However, the effects of closure (i.e. the principle of constant sums) must be kept in mind when using variation diagrams, since closure enhances correlation (Rollinson and Roberts, 1986; Pearce, 1987).

A relatively recent approach for recognizing element mobility in rocks, especially altered mafic and ultramafic metavolcanics, is that of Pearce element ratio (PER) diagrams (e.g. Pearce, 1968; Beswick, 1982; Barnes, 1985; among others). These diagrams,

Figure 30a. Mg# (molecular) versus Zr (ppm) diagram.

Figure 30b. Ni/Zr versus Zr (ppm) diagram. Note the inflection at approximatly 120 ppm Zr.

Fig. 30a

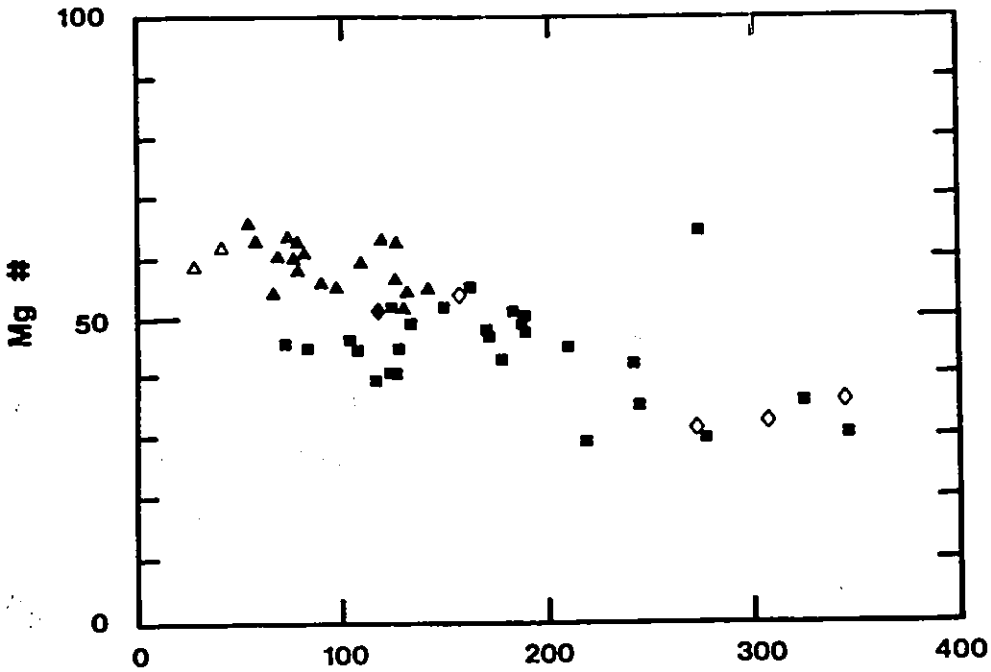

Fig. 30b

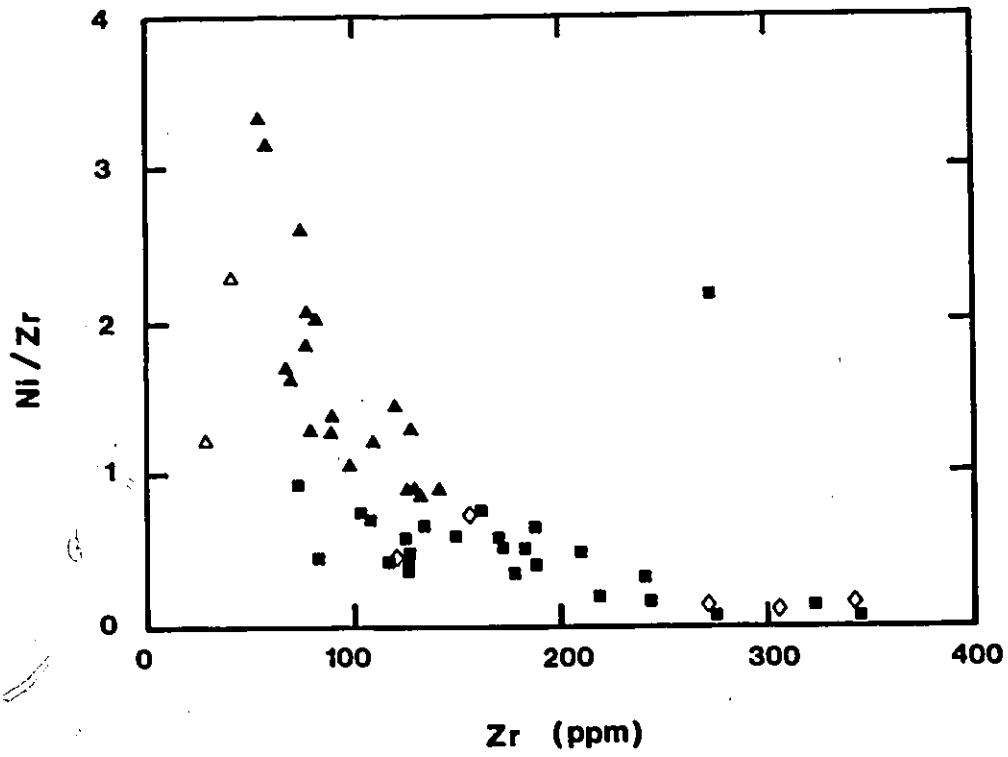

which show variations in ratios of molecular proportions, can differentiate trends produced by primary magmatic processes from those produced by secondary (alteration or metamorphic) processes. A necessary prerequisite for using PER diagrams is the determination of at least one conserved constituent (i.e. an element that has remained constant during the primary and secondary processes that have affected the rocks). Conserved constituents can be determined quite easily by knowing the system under investigation, including the phases and their compositions that comprise the system. For example in the NNE diabase dykes, olivine, plagioclase, clinopyroxene, and Ti-magnetite are the major phases. In this case, several elements, including K, P and Zr, are expected <u>not</u> to have changed in their absolute abundances in the fractionation chamber via igneous processes because the elements are not major constituents of these phases. A means of evaluating the conserved nature of these and other elements is by constructing conserved constituent diagrams. A plot of Ti/Zr versus P/Zr (Figure 31) shows three distinct (tight) clusters that plot on a line with a slope close to ∞. This indicates that either Ti or Zr, most likely Zr, is not conserved for the data set as a whole, but instead is conserved for subgroups of the data set. This suggests that three distinct suites of rocks make up the NNE diabase dyke family (they may or may not be comagmatic to one another). This also applies if Mn (Figures 32 and 33) or K (not shown, also used with caution since K is generally very mobile) is used in place of either P or Zr. The Ti/Zr ratio

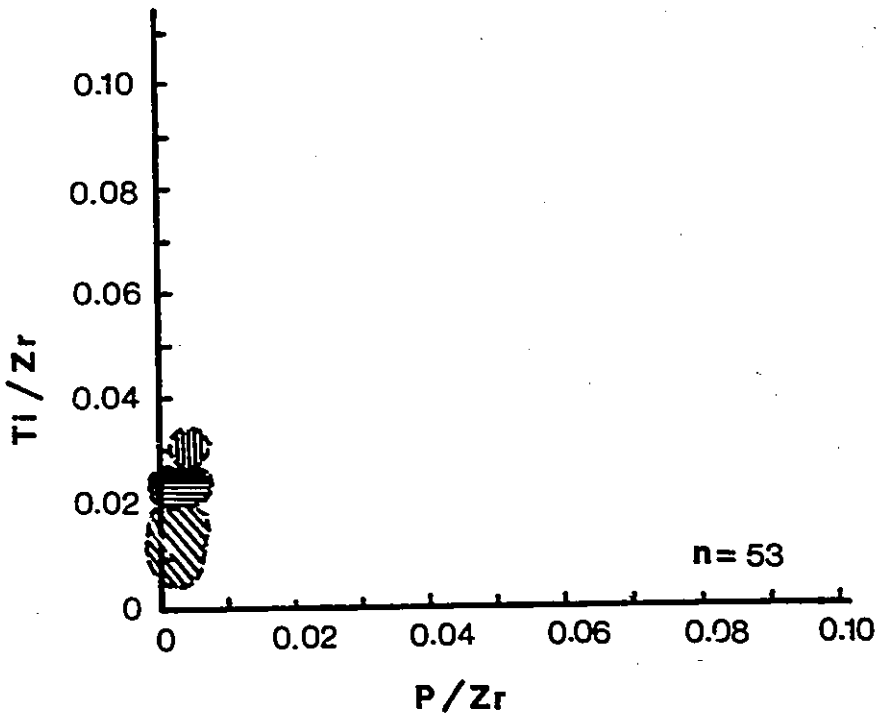

Figure 31. Pearce Element Ratio (PER) diagram of Ti and P normalized to Zr. The field with vertical stripes corresponds to the high aluminum group, the field with horizontal stripes to the high Ti/Zr group, and the field with oblique stripes to the low Ti/Zr group.

Note: Ti and P were calculated, respectively, from the weight percent of TiO_2 and P_2O_5, whereas Zr was calculated from parts per million Zr. This has the effect of the scale being 10 000 times less than actual.

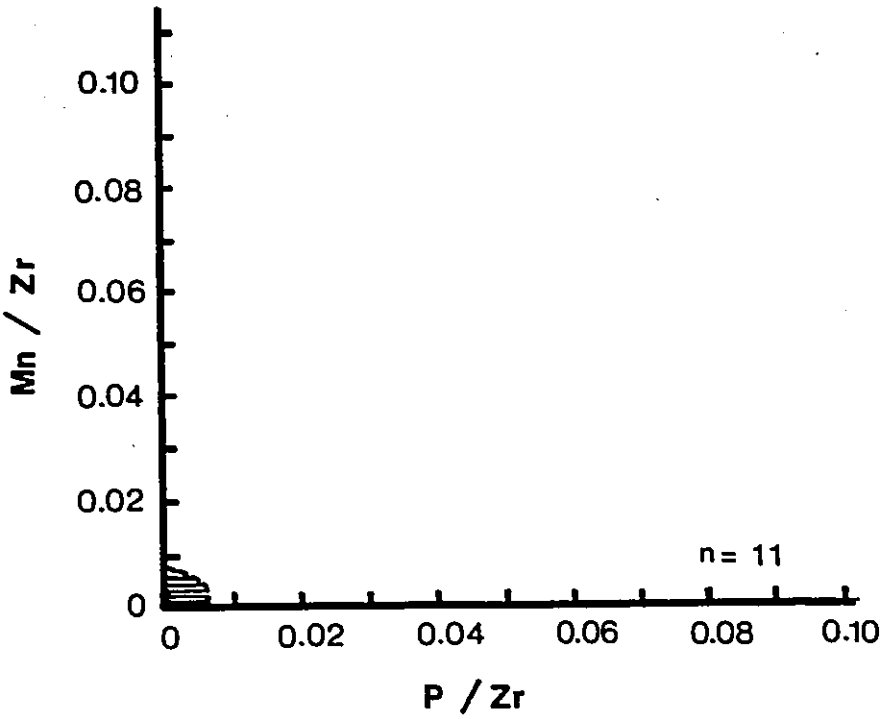

Figure 32. PER diagram of Mn and P normalized to Zr. The data comes from the high-Ti/Zr group. The tight cluster of analyses implies that they are from a comagmatic suite of rocks.

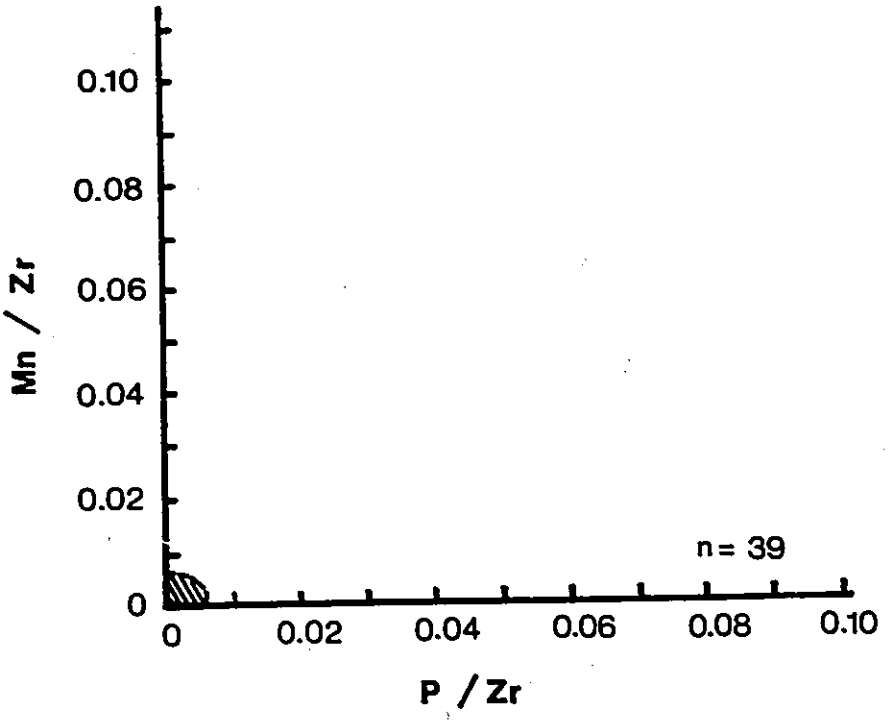

Figure 33. PER diagram of Mn and P normalized to Zr. The data are from the low-Ti/Zr group. Test of ratio of elements that are conserved during fractional crystallization. Tight cluster indicates that the rocks are comagmatic.

appears to set apart the three suites, which are:

1) a high-Al_2O_3 group with high Ti/Zr ratios,

2) a low- to high-TiO_2 group with high Ti/Zr ratios,

3) a low- to high-TiO_2 group with low Ti/Zr ratios.

Hence on this basis, PER diagrams can and will be used to evaluate the causes of chemical diversity within each of the three distinct comagmatic suites.

To summarize, the overall effects of alteration on the chemistry of the NNE diabase dykes appears to be minor, as indicated by the similarity of chemical variation patterns between strongly metamorphosed and weakly to unmetamorphosed dykes. However, in some rocks, SiO_2, Al_2O_3, Fe_2O_3, CaO, Na_2O, K_2O, Ba, and Sr have been mobile to varying degrees during metamorphism. Hence in this study, more weight is placed on the chemical evidence obtained from chemical variation patterns of those elements normally thought to be immobile (i.e. Ti, P, Ni, Zr, Y, Nb, and some REE).

4.2.2 Composition

The NNE diabase dykes show a relatively large degree of compositional variability. For example, TiO_2 varies from 0.26 to 3.78 wt% and MgO from 3.34 to 10.22 wt%. Maximum and minimum values for the other oxides also differ to the same degree. Selected major elements (SiO_2, Al_2O_3, K_2O, P_2O_5, and FeO_T) and trace elements (Cr, Ni, V, Zr, etc.) have been plotted against

MgO and TiO_2 (Appendix D2). On these and other Harker-type diagrams, most of the oxides and elements display relatively well defined distribution patterns, which most likely are indicative of primary magmatic trends despite some scatter induced by alteration processes. As mentioned previously, caution must be exercised in interpreting these trends because of the closure problem, especially with negatively correlated trends. A closure problem most likely exists, but does not matter if one can find the petrogenetic process responsible for the trend (therefore, the trend is valid but in part spurious). In general, the NNE diabase dykes show a broad continuum from compositions with relatively high MgO and CaO contents to compositions with relatively low MgO and CaO contents. In addition, there exists an inverse correlation between MgO and CaO with TiO_2, FeO_T, K_2O, and P_2O_5. Similarly, there exists a positive correlation between MgO and CaO with most compatible elements (e.g. Ni and Cr), and a negative correlation between MgO and CaO with most incompatible elements (e.g. Ba, La, Ce). The compositions with relatively high MgO and CaO contents are comparable to low-K tholeiites, whereas those with low MgO and CaO contents are similar to Fe-tholeiites.

The NNE diabase dykes are mainly olivine normative tholeiites(44 of 53), the rest are either quartz normative (8 of 53) or nepheline normative (5 of 53, 3 of which are also olivine normative).

The above mentioned geochemical characteristics of the NNE diabase dykes, combined with petrographic observations, suggest

that the dykes can be divided into groups on the basis of TiO_2 (confirmed with FeO_T and P_2O_5 contents) and Al_2O_3 contents. This approach is similar to the one used by Bellieni et al. (1986), Fodor (1987), and others in identifying the existence of two types of basalt (a low-TiO_2-P_2O_5 type and a high-TiO_2-P_2O_5 type) in the Paraná flood basalt province.

The NNE dykes are subdivided into two major groups, including a subgroup, and one minor group, respectively: 1) a low-TiO_2 group, 2) a high-TiO_2 group, 3) a high-TiO_2 pegmatitic segregation subgroup, and 4) a high-Al_2O_3 group with very low TiO_2 contents.

The low-TiO_2 group, consisting of 19 samples, is predominantly olivine normative (16.06 - highest value) to slightly quartz normative (3.06 - highest value). This group has a Mg# (molecular $MgO/MgO+FeO_T$) ranging from 0.65 to 0.51. The characteristic oxides/elements of this group show values ranging as follows:

TiO_2	- 0.56	to 1.61	wt%	(average = 1.19 wt%)
K_2O	- 0.26	to 0.52	wt%	(average = 0.45 wt%)
P_2O_5	- 0.07	to 0.21	wt%	(average = 0.13 wt%)
Y	- 8	to 22	ppm	(average = 18 ppm)
Zr	- 54	to 137	ppm	(average = 93 ppm)
Yb	- 0.9	to 2.9	ppm	(average = 1.8 ppm)

The high-TiO_2 group, comprising 27 dyke analyses, ranges from olivine normative (19.46) to marginally quartz normative (12.2) and nepheline normative (6.56). This group is characterized by a

Mg# ranging from 0.56 to 0.28. The oxides/elements of this group are as follows:

TiO_2	-	1.38	to	3.22	wt%	(average = 2.24	wt%)
K_2O	-	0.58	to	1.63	wt%	(average = 0.82	wt%)
P_2O_5	-	0.11	to	0.57	wt%	(average = 0.33	wt%)
Y	-	23	to	84	ppm	(average = 34	ppm)
Zr	-	72	to	337	ppm	(average = 176	ppm)
Yb	-	2.4	to	7.6	ppm	(average = 3.3	ppm)

The NNE diabase dykes often have pegmatitic segregations (i.e. residual liquid pockets) of irregular shape. These segregations are composed of a mineralogical assemblage which is very similar to that of the host dyke. The chemical composition of six analyzed segregations have been classified as a subgroup of the high-TiO_2 group. This subgroup is olivine normative (13.21) to quartz normative (17.93) with its Mg# falling between 0.53 and 0.32. The characteristic oxides/elements are as follows:

TiO_2	-	1.12	to	3.78	wt%	(average = 2.63	wt%)
K_2O	-	0.32	to	1.40	wt%	(average = 0.97	wt%)
P_2O_5	-	0.17	to	0.95	wt%	(average = 0.58	wt%)
Y	-	23	to	75	ppm	(average = 51	ppm)
Zr	-	116	to	339	ppm	(average = 241	ppm)
Yb	-	2.3	to	7.3	ppm	(average = 5.1	ppm)

The pegmatitic segregations are typically depleted in Cr and Ni, but enriched in Ti, Fe, K, REE, Zr, Y, and Ba. The segregations are interpreted to represent mineral phases that have crystallized from late-stage residual liquids.

The third group is defined by extremely high-Al_2O_3 contents.

Two samples fall into this category and they are olivine normative (15.78) to quartz normative (1.97). The oxides/elements ranges as follows:

Al_2O_3	-	22.9	to	23.8	wt%	(average = 23.3	wt%)
TiO_2	-	0.26	to	0.28	wt%	(average = 0.27	wt%)
K_2O	-	0.36	to	0.38	wt%	(average = 0.37	wt%)
P_2O_3	-	0.03	to	0.05	wt%	(average = 0.04	wt%)
Y	-	3	to	11	ppm	(average = 7	ppm)
Zr	-	28	to	41	ppm	(average = 34	ppm)
Yb	-	0.3	to	1.2	ppm	(average = 0.8	ppm)

The characteristic features of the high-Al_2O_3 group are the high values of Mg# and Ni, and the low values of incompatible (e.g. Ti, Zr, Ba, Y, and possibly Nb) and partially compatible elements (e.g. V) when compared to the low- and high-TiO_2 groups. In addition, the low-TiO_2 group is distinguished from the high-TiO_2 group by its consistently lower contents of incompatible and moderately compatible elements and higher values of Mg# and Ni. The coarse-grained pegmatitic segregations, commonly found in the diabase dykes, have an enrichment in most incompatible and partially compatible elements.

The low-TiO_2 group represents the most primitive magma compositions, on the basis of its high MgO, CaO, Ni, and Cr values, and its low values of alkali, incompatible, partially compatible, and rare earth elements.

The high-Al_2O_3 group has the lowest values of trace and rare earth elements.

Figure 34 (backpocket) shows the distribution of the above mentioned geochemical groups with respect to sample locations. The distribution of those groups does not suggest any regional pattern or tectonic implications.

4.2.3 GEOCHEMICAL CLASSIFICATION DIAGRAMS:

As shown above the NNE dykes have been classified according to their TiO_2 and Al_2O_3 contents. How does this classification scheme relate to commonly used discrimination diagrams?

Conventional major element discrimination diagrams such as the AFM ternary plot (Alkalies-FeO_T-MgO) and the Jensen Cation Plot (Al-Fe+Ti-Mg) indicate the tholeiitic affinity of the NNE diabase dykes, despite some superimposed effects of alteration. The NNE diabase dykes show a distinct enrichment trend from low FeO (i.e the low-TiO_2 group) to high FeO (i.e. the high-TiO_2 group) on the [Na_2O + K_2O]-FeO_T-MgO triangular diagram (Figure 35, after Irvine and Baragar, 1971). Furthermore, on the Jensen Cation Plot (Jensen, 1976), the low-TiO_2 group plots in the high-magnesium tholeiite field, whereas the high-TiO_2 group plots mostly in the high-iron tholeiite field (Fig. 36). The two analyses from the high-Al_2O_3 group are characterized by a calc-alkaline affinity.

Figure 35. AFM ternary plot (Alk-FeO_T-MgO) form Irvine and Baragar (1971). The NNE diabase dykes shows an enrichment trend from the low-FeO (i.e. low-TiO_2 group) to high-FeO (i.e. high-TiO_2 group).

△ High-Al_2O_3

▲ Low-TiO_2

■ High-TiO_2

◊ Segregations

Figure 36. Jensen Cation Plot (Al-Fe+Ti-Mg) from Jensen (1976). The low-TiO_2 group plots in the high-Mg tholeiite field, whereas the high-TiO_2 group plots in the high-Fe tholeiite field.

Fig. 35

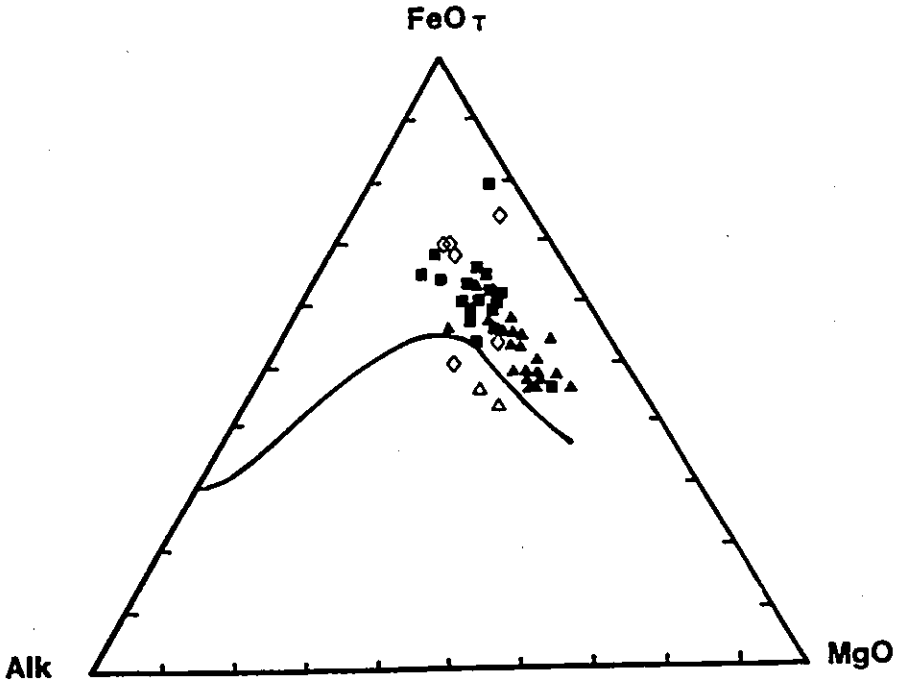

Fig. 36

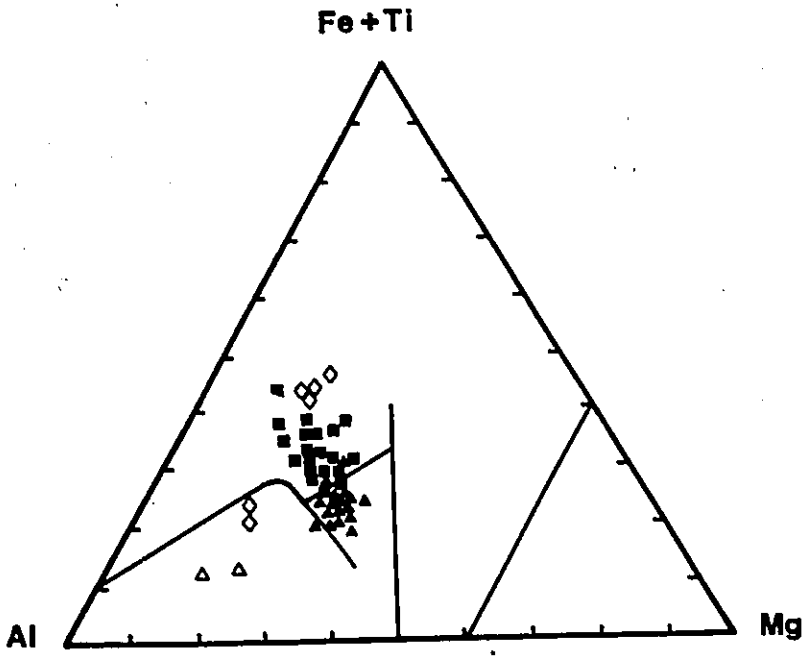

4.3 PETROGENESIS

In this section, I evaluate how the different types of NNE diabase dykes might be related to one another with respect to similar or different mantle source regions, and to variations in conditions of melting and fractional crystallization processes. Also, the author will attempt to answer the question whether the geochemical characteristics of the mantle source are retained in these rocks or whether processes of fractional crystallization and/or crustal contamination have destroyed the fingerprints of the mantle source.

Several questions must be answered in order to properly interpret the geochemical results of the NNE diabase dykes:

1) Do any of these rock compositions approximate silicate liquid compositions (i.e. a primary magma)?
2) Do the range of rock compositions reported herein represent a spectrum of differentiated (i.e. more SiO_2-rich and less mafic-rich) magmatic liquids? If so, how are they related to the primary magmas? - by processes of fractional crystallization, magma mixing, and/or crustal contamination.
3) Are the rock compositions original (i.e. have they been modified by alteration and metamorphic processes)? As mentioned above, most of the samples have not been modified substantially by these secondary processes.

None of the NNE diabase dykes have compositions that are

capable of coexisting with any proposed mantle compositions, even the most Fe-rich of acceptable mantle compositions. This conclusion is supported by several facts:

1) The most primitive NNE diabase dyke has a Mg# of 0.65. This Mg# is less than one of a primary basalt magma that is capable of being in equilibrium with olivine compositions of a residual mantle (Carter, 1970; Basaltic Volcanism Study Project, 1981).
2) The low Ni contents of the NNE diabase dykes are not compatible with mantle olivine compositions.
3) The NNE diabase dykes plot near the low pressure basalt cotectic of olivine-clinopyroxene-plagioclase, mostly within the plagioclase field or the boundary of the olivine and plagioclase fields at 1 atmosphere pressure.

Therefore, the most primitive NNE diabase dykes were likely evolved from magmas that had undergone limited differentiation.

The compositional variation of the NNE diabase dykes is large. This makes it necessary to evaluate the processes of fractional crystallization, magma mixing, and crustal contamination for establishing the origin(s) of the dykes. The general trend of increasing TiO_2 with increasing FeO_T and decreasing Mg# suggests that the NNE diabase dykes have compositions which are largely controlled by fractional crystallization plus or minus an assimilation component. This is supported by the following evidence:

1) The transition from Mg-rich to Fe-rich dykes is marked, in

most cases, by increasing incompatible and decreasing compatible elements.

2) Incompatible elements generally show positive correlations with one another (Figures 37a and 37b).

3) The NNE diabase dykes plot well below the field of liquid composition in the MgO versus total FeO "sail" diagram (Figure 38, from Hanson and Langmuir, 1978). This implies that if the dykes were generated from a mantle source of pyrolite composition, then they have undergone large degrees of fractional crystallization. This is also indicated by the distinct trend sub-parallel to the FeO (molar) axis. This trend is diagnostic of significant plagioclase fractionation, as well as some (%-?) Fe oxide fractionation.

4) The NNE diabase dykes define two parallel linear trends on the Ti/Zr versus Zr diagram (Figure 29a). Each trend is parallel to sub-parallel with the Z-axis and this is consistent with a fractionation relationship between compositions falling on the same linear trend. More evolved compositions lie to the right of primitive compositions. The position of the two parallel trends suggests a variation in parental magmas, either the result of different source regions, different degrees of partial melting, or crustal contamination.

5) The likelihood of a fractionation origin is also confirmed by comparing trends among incompatible and compatible

Figure 37a. Plot of Y (ppm) versus TiO_2 (wt%) for the NNE diabase dykes.

Figure 37b. Plot of Y (ppm) versus Zr (ppm) of the NNE diabase dykes.

Fig. 37a

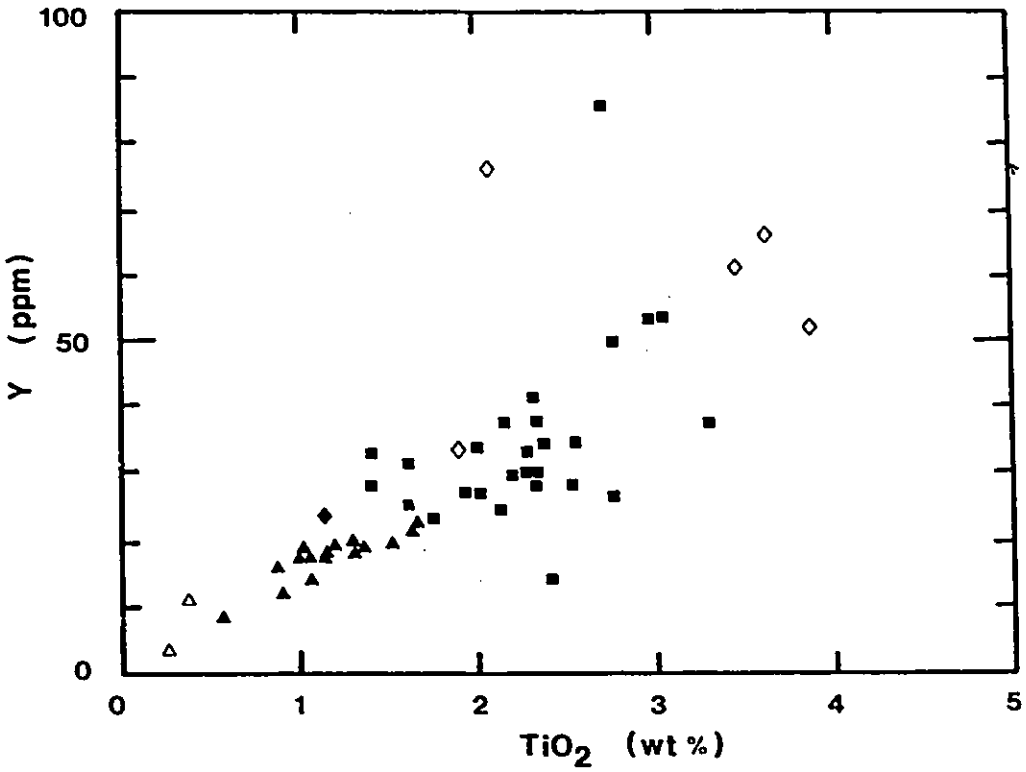

Fig. 37b

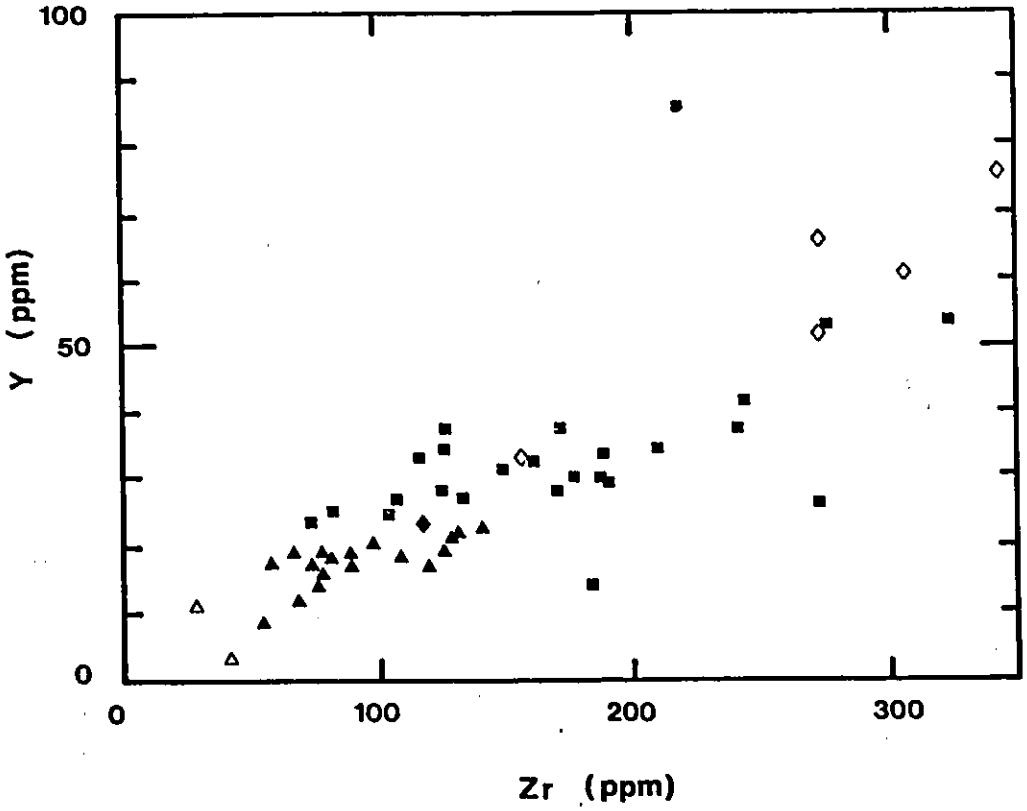

Figure 38. Plot of MgO versus total Fe as FeO (cation mole percent) for the NNE diabase dykes. The melt and residue fields (sail) are contoured on the basis of temperature and extent of melting to represent the olivine saturation surface in coexistence with a mantle source of pyrolite composition (after Hanson and Langmuir, 1978). The NNE diabase dykes plot outside the field of partial melting of a mantle source, hence they are not primary magmas.

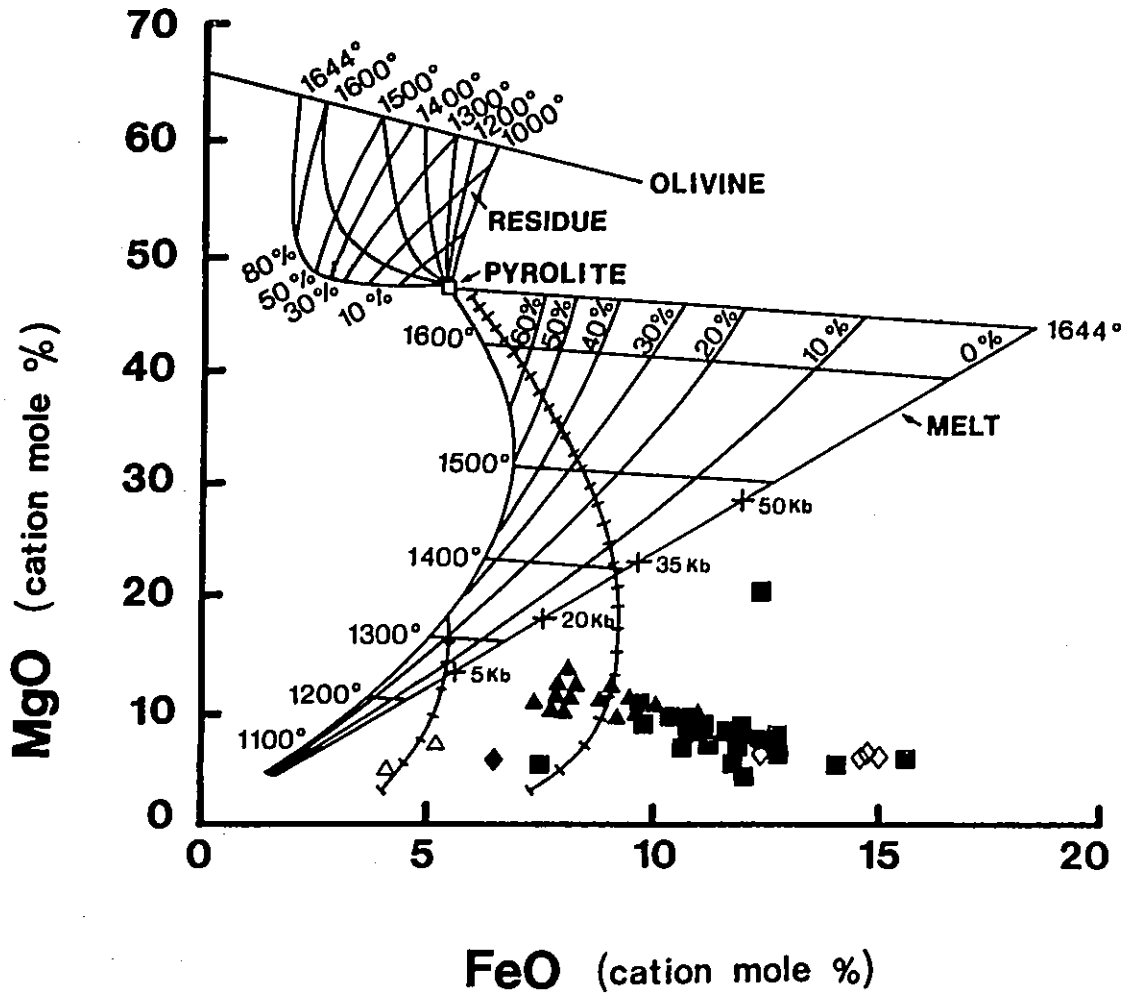
70
60
50
40
30
20
10
0
0
5
10
15
20
MgO (cation mole %)
FeO (cation mole %)
1644°
1600°
1500°
1400°
1300°
1200°
1000°
OLIVINE
RESIDUE
PYROLITE
80%
50%
30%
10%
60%
50%
40%
30%
20%
10%
0%
1644°
MELT
1600°
1500°
1400°
1300°
1200°
1100°
50Kb
35 Kb
20Kb
5Kb

elements. A Zr-log Ni diagram (Figure 39, after Rajamani et al. 1985) is quite suitable for readily distinguishing fractional crystallization and partial melting effects. Also, Ni and Zr are among the least mobile elements during alteration and metamorphic processes that affect mafic rocks. On this diagram, the NNE diabase dykes define several elongated clusters which suggest fractional crystallization processes were involved. The data array also indicates that crustal contamination was probably involved in the generation of some dyke rocks, most likely those with high Zr values.

6) The distinct correlation between Ni and MgO (and Cr and MgO) favours a fractional crystallization origin.

The next question to be answered is: What phases were involved in the fractional crystallization process? Petrographic observations indicate that olivine, plagioclase, and clinopyroxene were the major phases involved in the fractional crystallization processes that produced the compositions of the NNE diabase dykes. The involvement of these phases in the fractional crystallization processes can be rigorously confirmed by several methods:

1) graphically, using methods of Cox et al. (1979) and Wilson (1989),
2) mathematically, using mass balance calculations, and
3) statistically (also graphical and mathematical), using PER diagrams (Pearce, 1968; among others).

Figure 39. Plot of Zr (ppm) versus Ni (ppm, log scale) of the NNE diabase dykes. Solid lines I and II represent theoretical partial melting trends of a mantle source. Dotted lines III and IV correspond to theoretical fractional crystallization trends of the primary magma. Calculated trends and mantle source are from Rajamani et al. (1985).

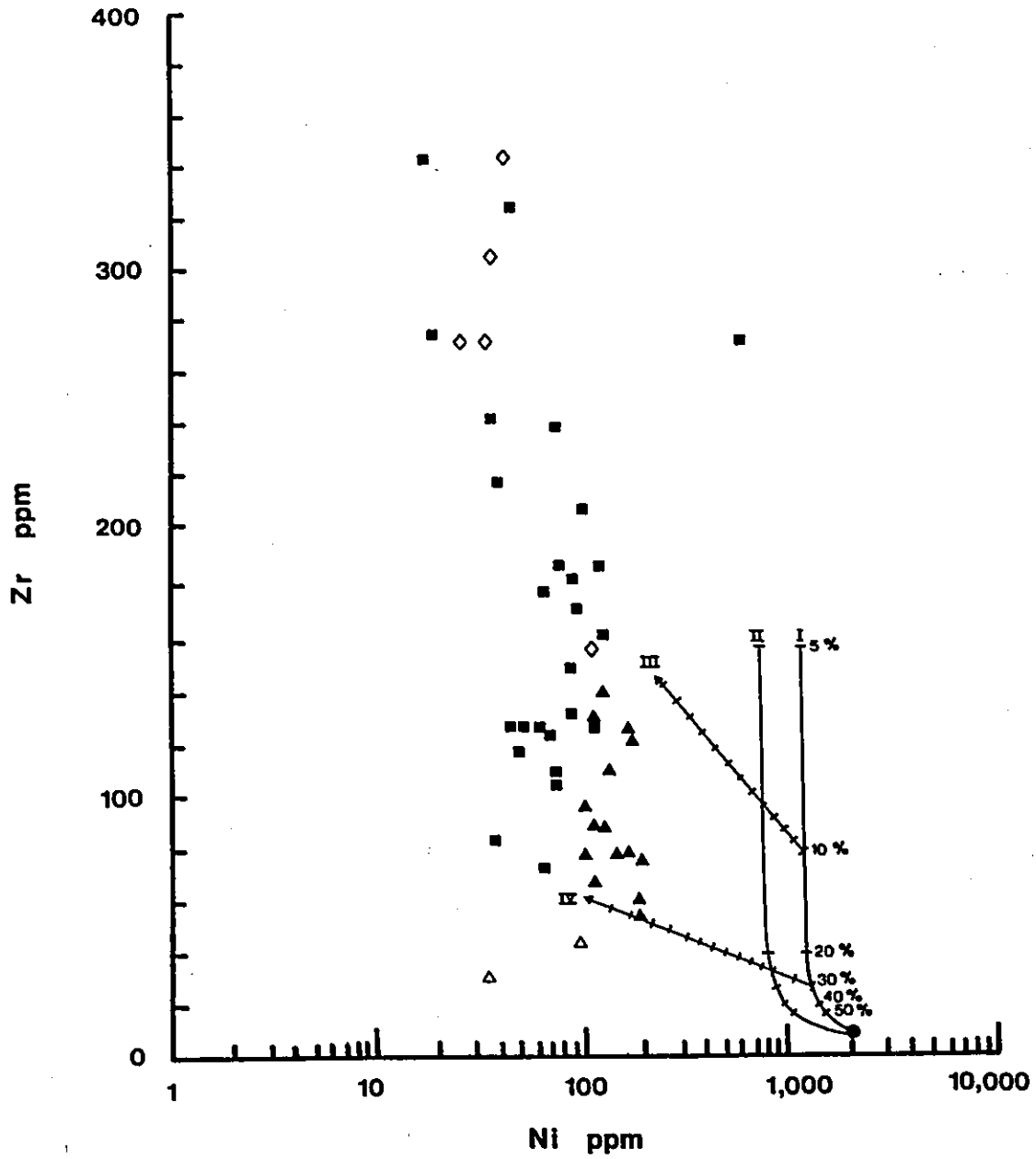
400
300
200
100
0
Zr ppm
1
10
100
1,000
10,000
Ni ppm
I
II
III
IV
5 %
10 %
20 %
30 %
40 %
50 %

Figures 40, 41a and 41b, graphically illustrating the variation in Al_2O_3 versus MgO, TiO_2 versus MgO, and FeO + Fe_2O_3 versus MgO indicate that the diversity of compositions in the NNE diabase dykes can be interpreted in terms of olivine plus plagioclase fractionation from primary magmas. These covariant plots also indicate that clinopyroxene, although present, did not participate significantly in the fractional crystallization process. Major element mass balance calculations (Tables 6a, 6b, 6c, and 6d) support, in general, these conclusions. However, clinopyroxene is a minor fractionating or accumulating phase in some of the fractionating assemblages.

Mass balance calculations (Tables 6a, 6b, 6c, and 6d) using the major elements indicate that the most primitive dykes are similarly related to one another by olivine or olivine and plagioclase fractionation.

The phases that control the fractional crystallization processes(es) can also be ascertained from PER diagrams. These diagrams which show variations in ratios of molecular proportions (MPR) are more direct because they facilitate comparisons between whole-rock compositions and mineral compositions. They also eliminate the closure effect (i.e. summing to 100%) by use of a constant parameter as a common denominator. In Figures 42a and 42b, and Figures 43a and 43b, the high Ti/Zr dykes and low Ti/Zr dykes, respectively, lie on trends intermediate between olivine and plagioclase control. These trends also lie closely to a clinopyroxene dominated fractionation trend, but other PER

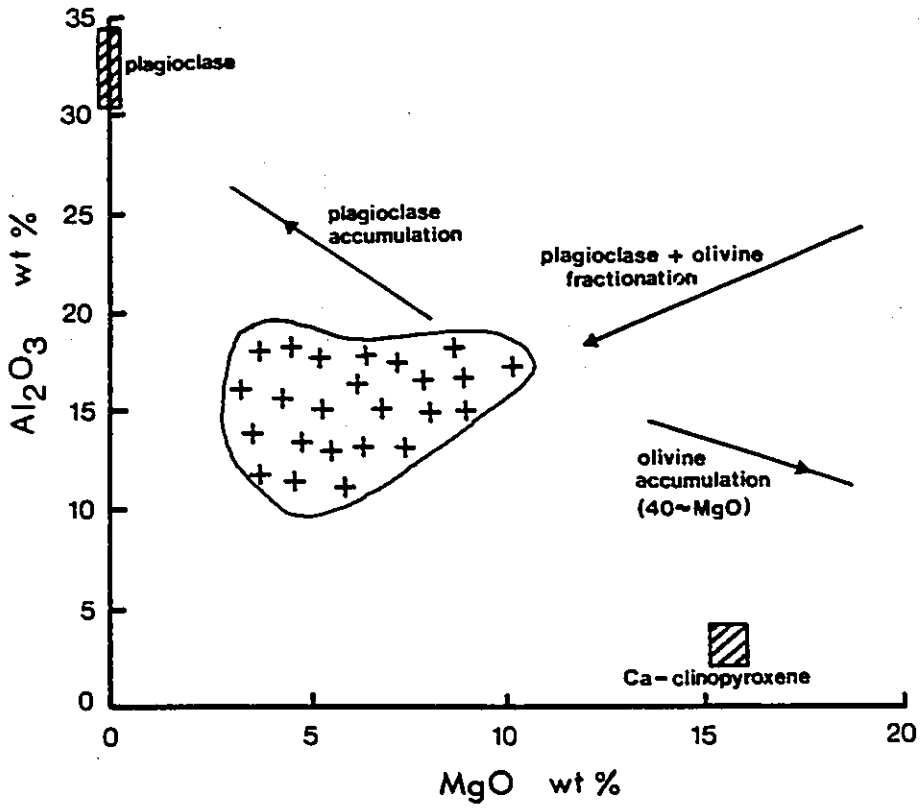

Figure 40. Al_2O_3 versus MgO diagram of the NNE diabase dykes. Most of the data (field defined by crosses) can be explained in terms of plagioclase and olivine fractional crystallization. The bulge in the data array is interpreted in terms of combined assimilation-fractional crystallization (AFC).

Figure 41a. Harker-type diagram of TiO_2 versus MgO for the NNE diabase dykes (field denoted as in Figure 40) Note the titanium enrichment trend, which is explained by plagioclase and olivine fractionation.

Figure 41b. Harker-type diagram of $FeO+Fe_2O_3$ versus MgO for the NNE diabase dykes (field denoted as above). Note the iron enrichment trend. The extension of the data array past the Thingmuli fractionation trend can be explained in terms of:
1) plagioclase and olivine fractionation with plagioclase dominant over olivine,
2) crustal contamination, and/or
3) late fractional crystallization (hence, accumulation) of iron oxide minerals.

Fig. 41a

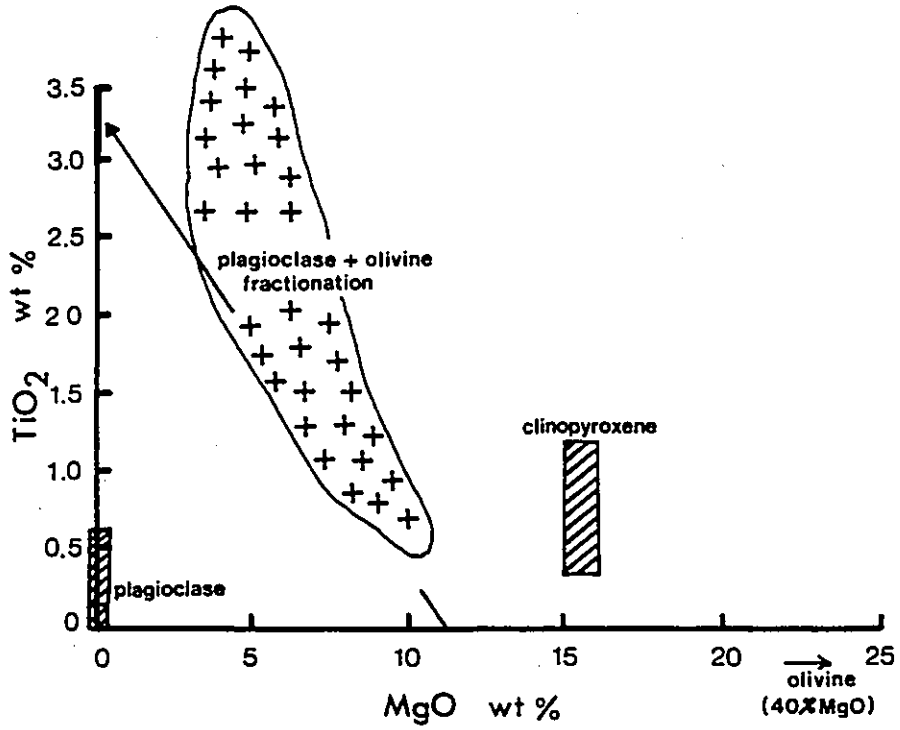

Fig. 41b

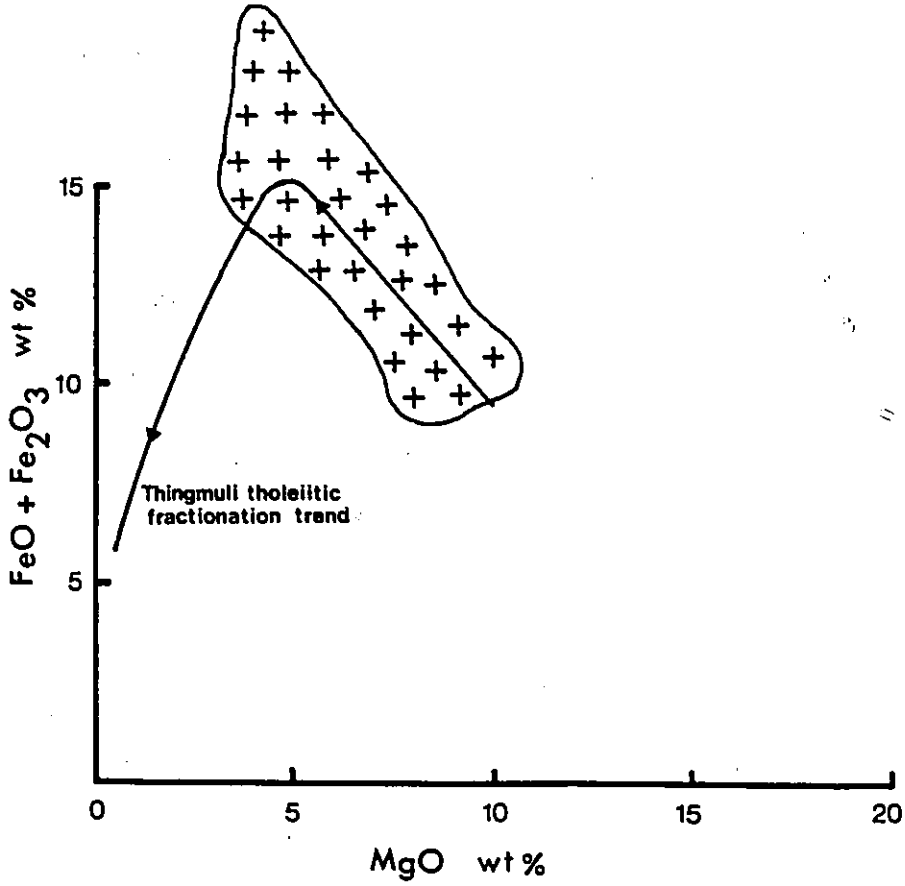

Table 6a. Results of mass balance fractional crystallization calculations involving olivine, plagioclase, and clinopyroxene.

INPUT DATA:

	PARENT	OL-75	PL-75	CPX3	DAUGHTER
SiO_2	47.30	38.40	49.27	49.53	47.30
TiO_2	0.56	0.00	0.00	1.00	0.87
Al_2O_3	17.80	0.00	32.51	3.61	17.90
FeO	10.46	22.96	0.00	11.65	10.64
MnO	0.16	0.00	0.00	0.24	0.18
MgO	10.22	38.65	0.00	14.54	9.30
CaO	9.81	0.00	15.33	18.85	10.12
Na_2O	2.00	0.00	2.71	0.00	2.20
K_2O	0.26	0.00	0.17	0.08	0.80

(PARENT - MINERALS = DAUGHTER)

PARENT: CMD-37
DAUGHTER: CMD-12

	SOLUTION	% CUMULATE
CMD-37	1.000	
OL-75	-0.048	44.567
PL-75	-0.058	53.011
CPX3	-0.003	2.422
CMD-12	0.891	

R SQUARED = 0.400

	PARENT ANALYSIS	DAUGHTER ANALYSIS	DAUGHTER CALC.	WEIGHTED RESID.
SiO_2	47.95	47.86	48.38	-0.53
TiO_2	0.57	0.88	0.63	0.25
Al_2O_3	18.05	18.11	18.13	-0.02
FeO	10.60	10.76	10.62	0.15
MnO	0.16	0.18	0.18	0.00
MgO	10.36	9.41	9.47	-0.06
CaO	9.95	10.24	10.11	0.13
Na_2O	2.03	2.23	2.10	0.13
K_2O	0.26	0.25	0.28	-0.03

Table 6b. Results of mass balance fractional crystallization calculations involving olivine, plagioclase, and clinopyroxene.

INPUT DATA:

	PARENT	OL-75	PL-70	CPX1	DAUGHTER
SiO_2	47.30	38.40	50.52	50.55	47.40
TiO_2	0.56	0.00	0.00	0.73	1.05
Al_2O_3	17.80	0.00	31.68	3.54	17.70
FeO	10.46	22.96	0.00	12.09	11.64
MnO	0.16	0.00	0.00	0.32	0.18
MgO	10.22	38.65	0.00	14.91	8.66
CaO	9.81	0.00	14.35	18.55	9.65
Na_2O	2.00	0.00	3.29	0.00	2.40
K_2O	0.26	0.00	0.17	0.00	0.39

(PARENT - MINERALS = DAUGHTER)

PARENT = CMD-37
DAUGHTER = CMD-01

	SOLUTION	% CUMULATE
CMD-37	1.000	
OL-75	-0.098	29.506
CPX1	-0.048	14.313
PL-70	-0.187	56.181
CMD-01	0.667	

R SQUARED = 0.671

	PARENT ANALYSIS	DAUGHTER ANALYSIS	DAUGHTER CALC.	WEIGHTED RESID.
SiO_2	47.95	47.80	48.48	-0.69
TiO_2	0.57	1.06	0.80	0.26
Al_2O_3	18.05	17.85	17.92	-0.07
FeO	10.60	11.74	11.67	0.07
MnO	0.16	0.18	0.22	-0.04
MgO	10.36	8.73	8.77	-0.04
CaO	9.95	9.73	9.57	0.16
Na_2O	2.03	2.42	2.12	0.30
K_2O	0.26	0.39	0.35	0.05

Table 6c. Results of mass balance fractional crystallization calculations involving plagioclase, clinopyroxene, and magnetite.

INPUT DATA:

	PARENT	PL-70	CPX3	MAG1	DAUGHTER
SiO_2	47.50	50.52	49.53	0.39	46.60
TiO_2	2.31	0.00	1.00	2.13	3.57
Al_2O_3	15.30	31.68	3.61	1.52	13.00
FeO	14.90	0.00	11.65	90.34	17.78
MnO	0.21	0.00	0.24	0.09	0.31
MgO	5.20	0.00	14.54	0.00	4.02
CaO	9.48	14.35	18.85	0.08	7.94
Na_2O	2.70	3.29	0.00	0.00	2.40
K_2O	0.85	0.17	0.08	0.00	1.40

(PARENT - MINERALS = DAUGHTER)

PARENT = CMA-LG7-87
DAUGHTER = CMA-79DI

	SOLUTION	% CUMULATE
CMA-LG7-87	1.000	
PL-70	-0.151	61.979
CPX3	-0.090	36.920
MAG1	-0.003	1.101
CMA-79DI	0.757	

R SQUARED = 3.002

	PARENT ANALYSIS	DAUGHTER ANALYSIS	DAUGHTER CALC.	WEIGHTED RESID.
SiO_2	48.13	47.57	47.62	-0.05
TiO_2	2.34	3.64	2.97	0.68
Al_2O_3	15.50	13.27	13.73	-0.46
FeO	15.10	18.15	18.23	-0.08
MnO	0.21	0.32	0.25	0.06
MgO	5.27	4.10	5.23	-1.12
CaO	9.60	8.10	7.58	0.52
Na_2O	2.74	2.45	2.76	-0.51
K_2O	0.86	1.43	1.09	0.33

Table 6d. Results of mass balance fractional crystallization calculations involving olivine, plagioclase, and clinopyroxene.

INPUT DATA:

	PARENT	OL-75	PL-75	CPX3	DAUGHTER
SiO_2	47.30	38.40	49.27	49.53	47.60
TiO_2	0.56	0.00	0.00	1.00	0.26
Al_2O_3	17.80	0.00	32.51	3.61	23.80
FeO	10.46	22.96	0.00	11.65	6.72
MnO	0.16	0.00	0.00	0.24	0.10
MgO	10.22	38.65	0.00	14.54	5.54
CaO	9.81	0.00	15.33	18.85	11.08
Na_2O	2.00	0.00	2.71	0.00	2.90
K_2O	0.26	0.00	0.17	0.08	0.38

(PARENT - MINERALS = DAUGHTER)

PARENT = CMD-37
DAUGHTER = CMD-49

	SOLUTION	% CUMULATE
CMD-37	1.000	
OL-75	-0.057	-30.653
PL-75	0.342	183.625
CPX3	-0.099	-52.973
CMD-49	1.186	

R SQUARED = 0.339

	PARENT ANALYSIS	DAUGHTER ANALYSIS	DAUGHTER CALC.	WEIGHTED RESID.
SiO_2	47.95	48.36	48.65	-0.29
TiO_2	0.57	0.26	0.39	-0.13
Al_2O_3	18.05	24.18	24.32	-0.14
FeO	10.60	6.83	6.84	-0.01
MnO	0.16	0.10	0.12	-0.01
MgO	10.36	5.63	5.63	-0.00
CaO	9.95	11.26	11.23	0.02
Na_2O	2.03	2.95	2.49	0.45
K_2O	0.26	0.39	0.27	0.12

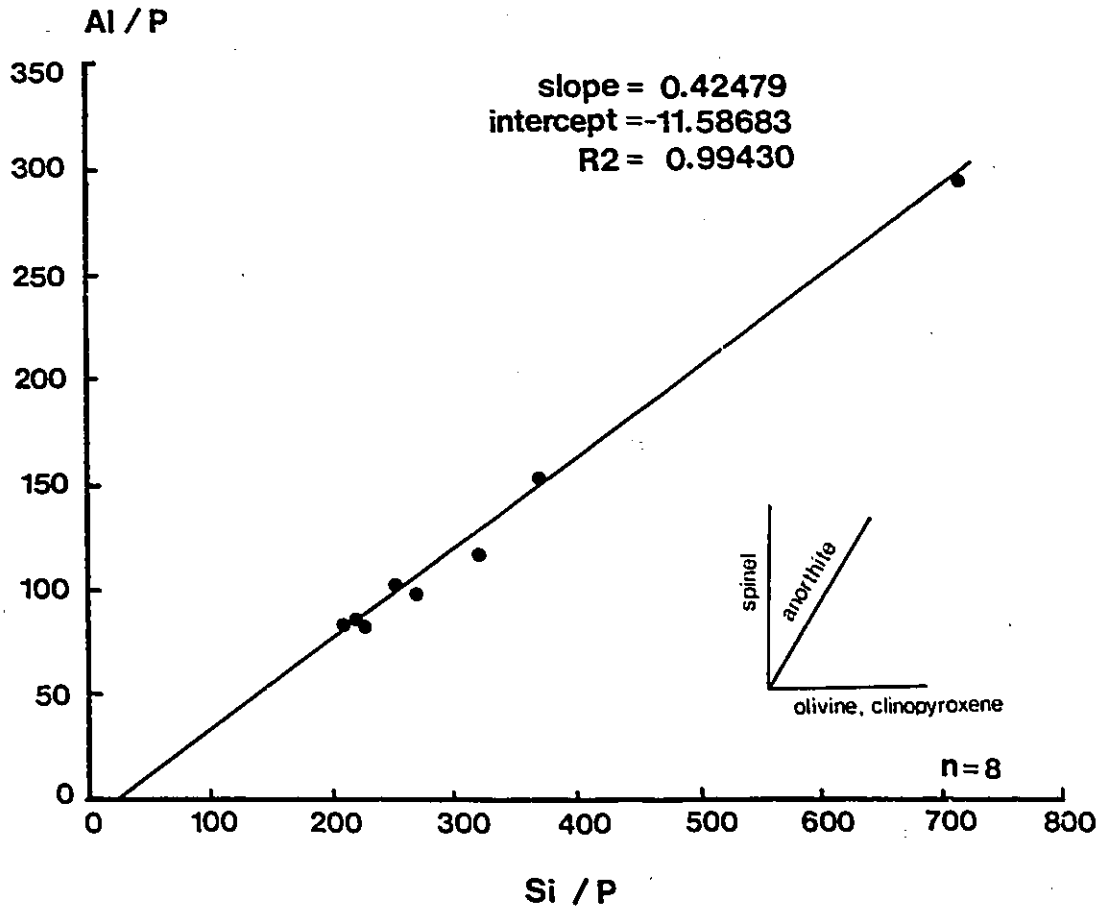

Figure 42a. PER diagram of Al and Si normalized to P for the high-Ti/Zr group.

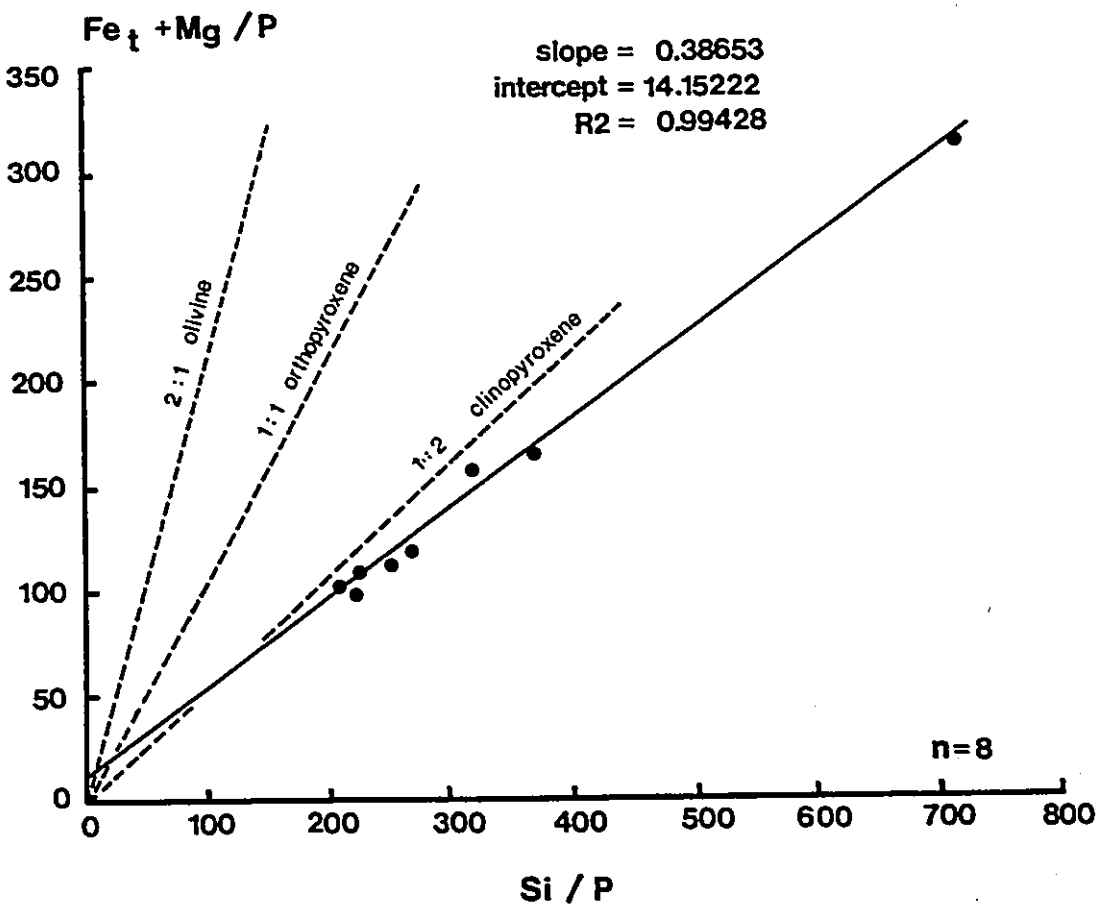

Figure 42b. PER diagram of Fe + Mg and Si normalized to P for the high-Ti/Zr group.

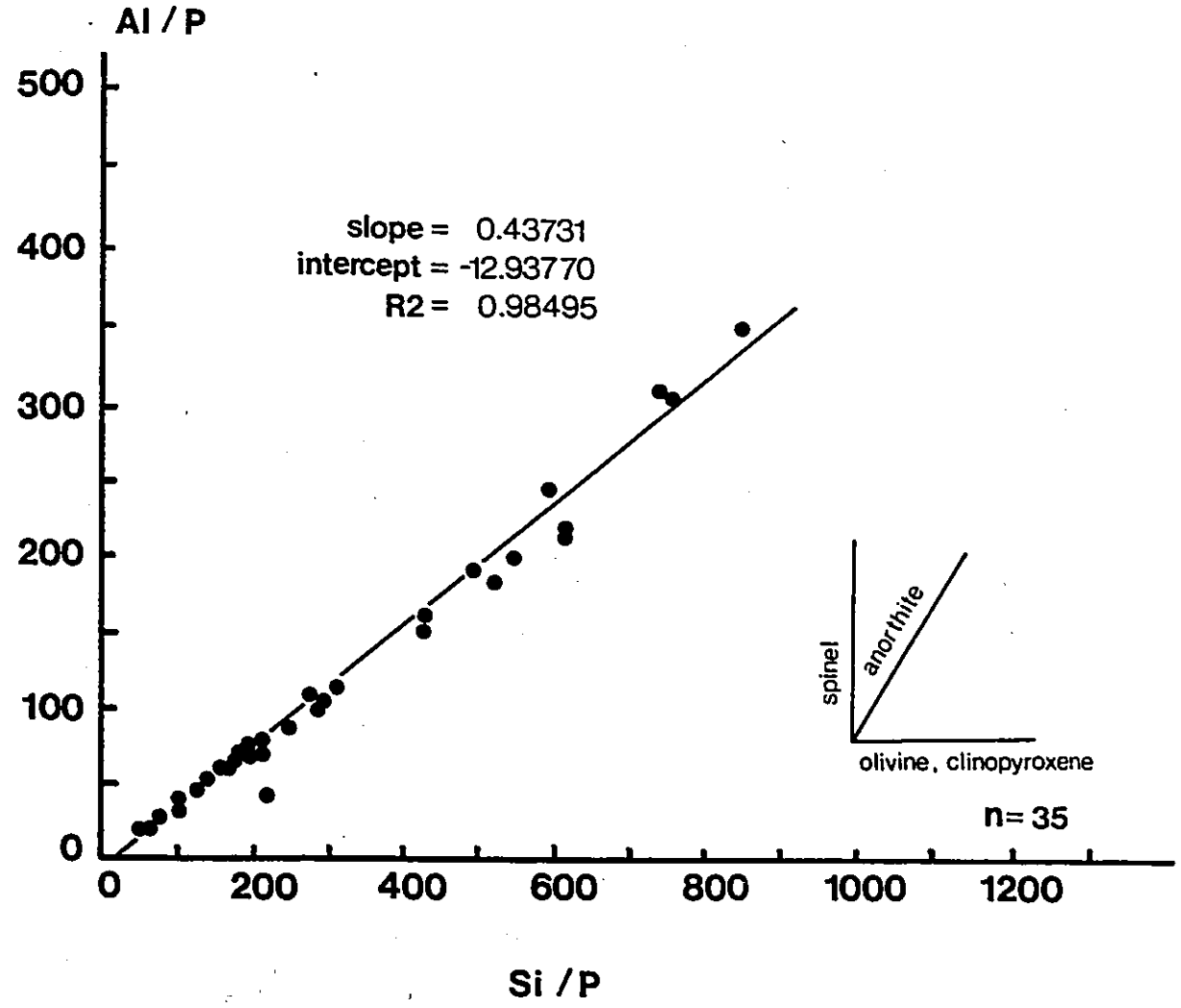

Figure 43a. PER diagram of Al and Si normalized to P for the low-Ti/Zr group.

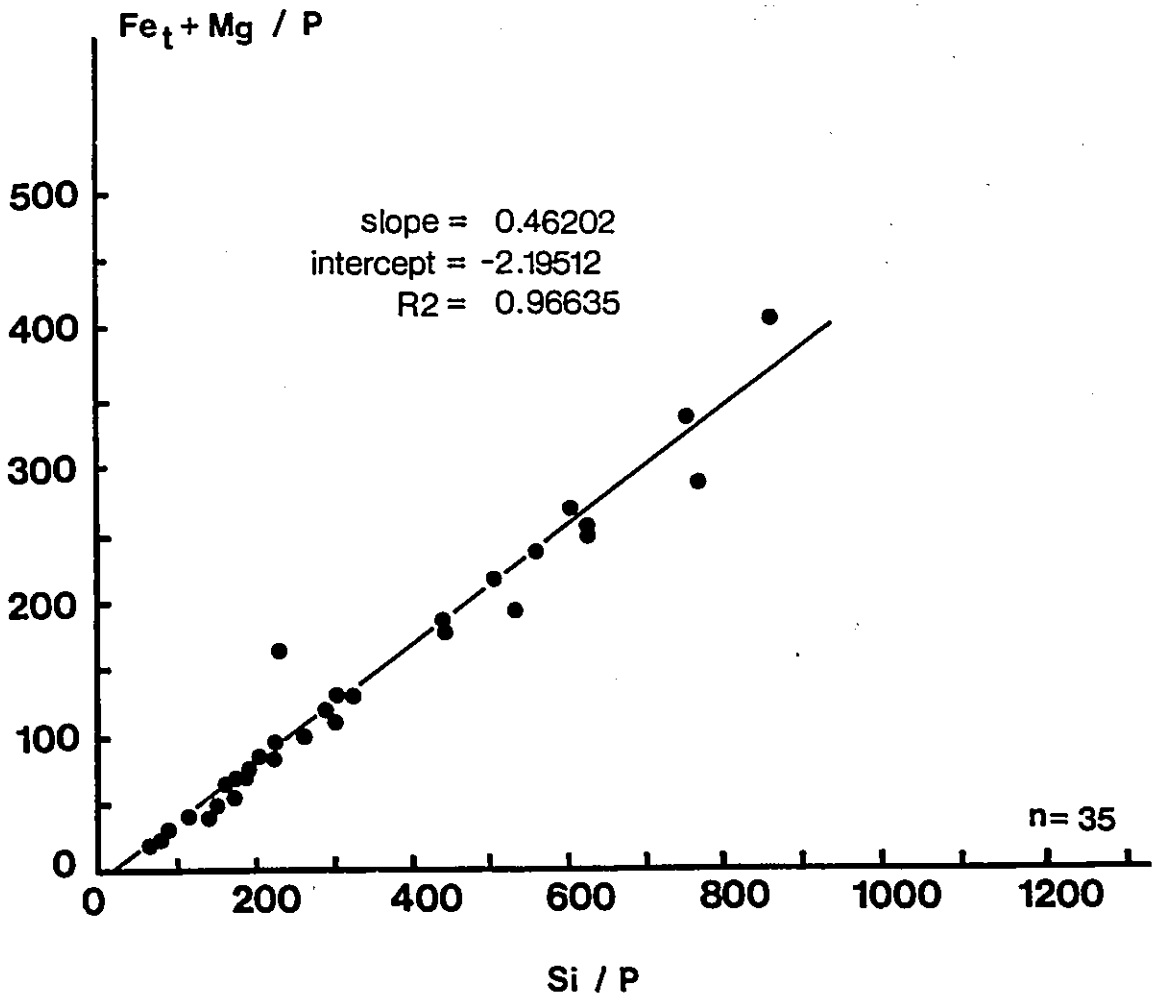

Figure 43b. PER diagram of Fe + Mg and Si normalized to P for the low-Ti/Zr group.

diagrams suggest that clinopyroxene is only a minor phase. It should be noted that the intercepts of the low Ti/Zr dyke trends are closer to zero then those of the high Ti/Zr dyke trends. This may imply that crustal contamination or alteration is affecting the fractional crystallization (AFC) trends to produce the same mineral assemblages but in differing proportions. The fractionating mineral assemblage tends to be enhanced in plagioclase (hence more siliceous and residual). Several petrological processes could account for the relative position of the trend lines of the low Ti/Zr dykes. However, evidence for crustal contamination is far greater. Some of this evidence includes:

1) the high Zr and LREE contents of the most evolved dykes,
2) the quartz normative nature of some evolved dykes (including pegmatitic segregations),
3) the position of some evolved dykes in the hypersthene field of CMAS diagrams (Figure 44),
4) the significant increase of Y/Zr ratios with increasing Zr (note: this cannot be explained by different degrees of partial melting or different source regions),
5) the presence of "balls" of similar composition to pegmatitic segregations (Ciesielski, per. comm., 1990, interprets these as partially digested xenoliths, either country rock material or fragments of an earlier dyke pulse)
6) the position of the pegmatitic gabbro segregations and the

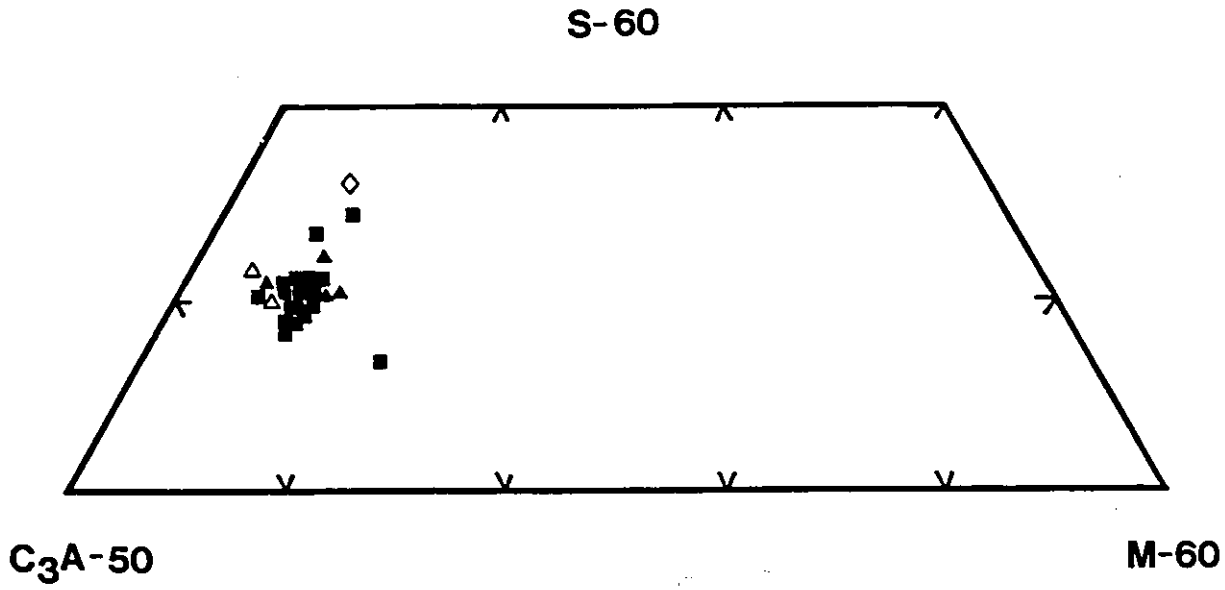

Figure 44. Analyses of NNE diabase dykes projected from or towards diopside onto the C_3A-S-M plane (wt%) using the CMAS system of O'Hara (1968).

high-Al_2O_3 dykes in Al-Si space (Figure 45, Francis et al. 1983).

In summary, olivine-plagioclase fractionation is the mechanism of fractional crystallization in the high Ti/Zr dykes, and olivine-plagioclase fractionation with variable crustal contamination is the mechanism of fractional crystallization in the low Ti/Zr dykes.

4.4 COMPARISON WITH DYKES OF THE GRENVILLE, SUPERIOR, AND OTHER PROVINCES

The average analyses of the NNE diabase dykes of this study are presented in Table 5 in comparison to other typical basaltic dykes and mafic volcanic suites of the Grenville Province, other continental provinces, and some modern-day environments.

The high-Al_2O_3 NNE diabase dykes are most similar to the Jurassic plagioclase-rich dolerites of the Ferrar Group (Antartica). There are, however, distinct differences such as slightly higher values of MgO, and Al_2O_3, and slightly lower values of TiO_2, V, Y, and Zr. They are also similar to the Atka basaltic lavas of Alaska, but are more evolved and therefore may represent residua or cumulates to primary high-Al_2O_3 basaltic liquids.

The low-TiO_2 NNE diabase dykes exhibit similar chemical compositions to other typical low-TiO_2 basalts and associated dykes of continental provinces, such as those of the Columbia

Figure 45. Al_2O_3 versus SiO_2 in cation mole percent for the NNE diabase dykes. The "sail" represents the field of liquid compositions that are capable of coexisting with a mantle source of pyrolite-3 composition.

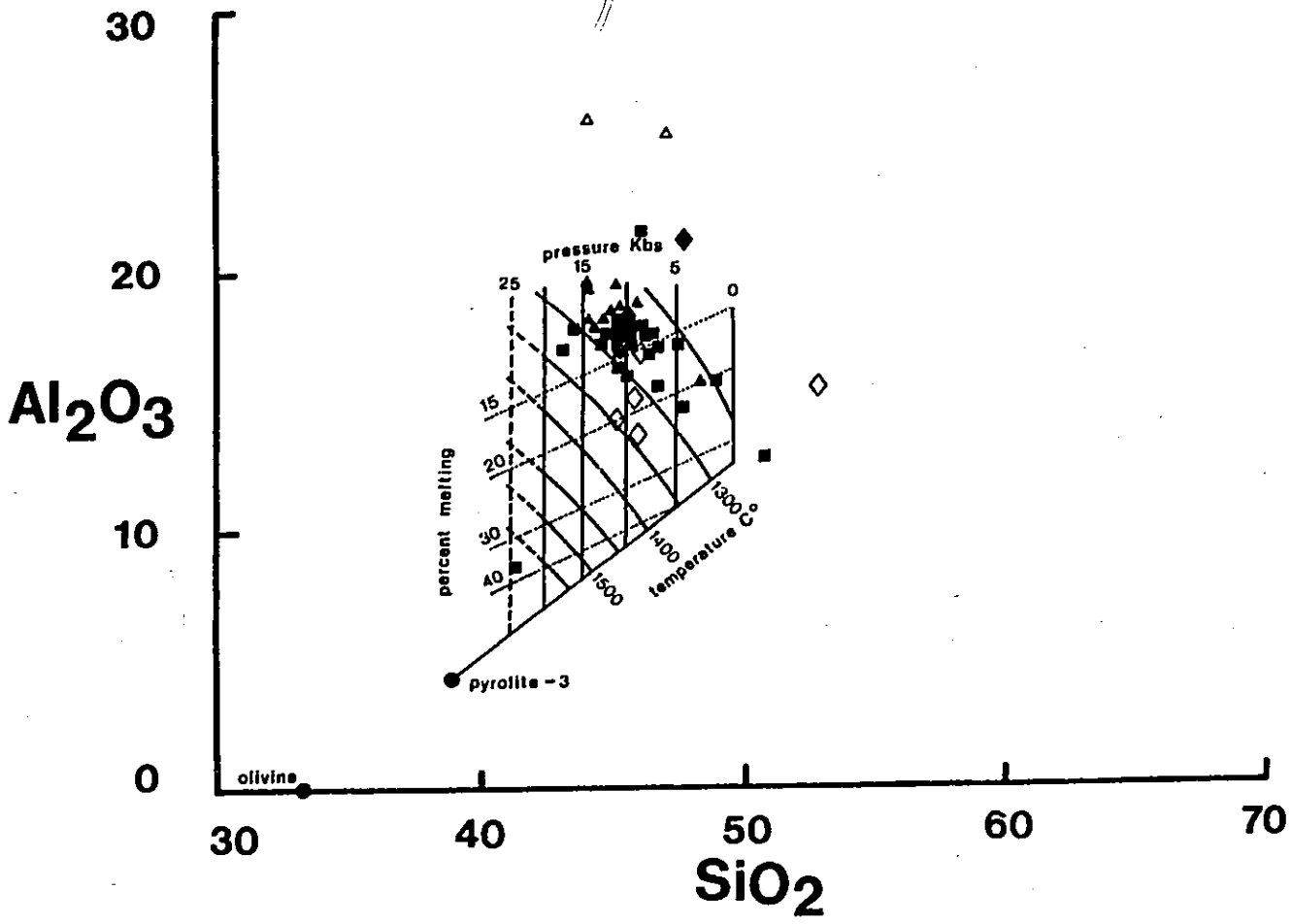
30
20
10
0
Al_2O_3
pressure Kbs
15
5
25
0
15
20
30
40
percent melting
1300°C
1400
1500
temperature C°
pyrolite - 3
olivine
30
40
50
60
70
SiO_2

River Basalt Province, the Taos Plateau, and the Parana Basin Plateau (i.e. analyses 11, 13, and 14, of Table 5). All of the continental low-TiO_2 basalts are characterized by low TiO_2, P_2O_5, and K_2O values, high Al_2O_3 values, and moderately high Mg numbers. Except for their light REE enrichment pattern, the least evolved members of the low-TiO_2 group are quite similar to N1-MORB (analysis 18). Fodor et al. (1985) have proposed a 9:1 mixture of N-type and P-type MORB components as the source material for the Parana Basin continental flood basalts.

High-TiO_2 NNE diabase dykes are the most abundant group within the parautochthonous domain. Based on the comparison of chemical compositions of other Grenville dykes, this appears to be the case throughout the Grenville Province. The high-TiO_2 NNE diabase dykes resemble high-TiO_2 basaltic rocks of other Grenville dyke localities (e.g. analyses 5, 6, and 7 of Table 5) and other typical continental provinces (e.g. analyses 8, 10, 12, 15 of Table 5; see Basaltic Volcanism Study Project, 1981, for others). All of the high-TiO_2 basalt suites are characterized by enrichment in highly to moderately incompatible elements (e.g. LREE). However, there are distinct variations from suite to suite, and these can only be explained by variably enriched mantle sources or assimilation fractional crystallization processes (AFC) or a combination of processes. This problem will not be assessed any further because isotopic data and additional geochemical data is needed to properly resolve this problem (Fodor, 1987; Condie et al., 1987) for the NNE diabase dykes.

Segregations occur mostly within high-TiO_2 NNE diabase dykes. As mentioned in section 4.4.2, their chemical composition is the most evolved of the rocks in this study. They are most similar to the high-TiO_2 basalts of the Colombia River Basalt Province (analysis 12 of Table 5).

MINERAL CHEMISTRY

5.1 ANALYTICAL METHODS

Eleven representative samples of the NNE diabase dykes were selected from the parautochthonous domain for microprobe analyses of minerals. Eight of these were chosen to study the evolution of corona structures through increasing metamorphic grade. Several thin section traverses across different types of corona structures were performed. Microprobe analyses were also carried out on mineral pairs of three non-coronitic samples for pressure-temperature (P-T) determinations. Several grains of the same mineral, from each thin section, were analyzed to determine grain to grain homogeneity. In addition, several analyses on single grains were also determined to study internal compositional zoning (i.e. if present) and to test analytical reproducibility.

The mineral analyses were obtained at the Geological Survey of Canada using a Materials Analysis Company electron microprobe equipped with a Kevex Model 5000A energy dispersive spectrometer, and automated to produce simultaneous multi-element analysis. Data reduction was calculated using the method of Plant and Lachance (1973), through the program SICOM on a Hewlett Packard 1000 computer. Operating conditions of the electron microprobe are 20 kv accelerating voltage, specimen current of 10 nanoamperes measured on a standard of kaersutite, and counting times of 100 and 50 seconds. Natural silicate and oxide standards

were used.

The amphibole, pyroxene, and garnet minerals were analyzed for 10 elements using kaersutite (Al, Mn, Mg, Ca, Ti), amphibole-1 (Fe,Si), labradorite (Al, Ca, Na), orthoclase (K), and chromite (Cr) as standards. Plagioclase, biotite, and olivine grains were analyzed, respectively, using the G.S.C. labradorite, biotite-20, and forsterite-60 standards. The opaque minerals were analyzed using the G.S.C. ilmenite and magnetite standards.

Counting times of 100 seconds were used on each of the standards and 50 seconds on each of the analyzed specimens. Mineral analyses have a precision (at 1 standard deviation) of 2 percent of the amount present in the samples for major elements. A beam diameter of approximately 1 um was used for most of the minerals being analyzed. Minerals not analyzed with this beam diameter were clouded plagioclase and dusty clinopyroxene grains, where a 10 to 20 um diameter beam was used to estimate the contribution of the minor phases to their host mineral.

5.1.1 STOICHIOMETRY

Olivine formulas have been calculated on the basis of 3 cations or 4 oxygen ions using the general formula of A_2BO_4, where A refers to octahedrally coordinated cations (Fe,Mg), B refers to tetrahedrally coordinated cations (Si) and O refers to anions (O).

Pyroxene formulas have been calculated on the basis of 4 cations or 6 oxygen ions using the general formula:

$$X_{1-p}Y_{1+p}T_2O_6$$

where X = Ca, Na
Y = Mg, Fe^{2+}, Mn, Al, Fe^{3+}, Cr, Ti
and T = Si, Al

Values of Fe_2O_3 have been assigned to satisfy the charge balance.

Plagioclase analyses have been recalculated on the basis of 32 oxygens using the general formula:

$$XY_2Z_2O_8$$

where X = Na, K
Y = Ca, Al
Z = Al, Si

Magnetite formulas have been calculated on the basis of 3 cations and 4 oxygens according to the formula:

$$Fe^{2+}Fe^{3+}{}_2O_4$$

Values of Fe_2O_3 are estimated on the basis of charge balance and idealized stoichiometry.

Ilmenite stoichiometry has been calculated on the basis of 2 cations and 3 oxygens according to the formula:

$$FeTiO_3$$

Biotite formulas have been calculated on the basis of 22 oxygens using the general formula:

$$X_2Y_{6-4}T_8O_{20}(OH)_4$$

where X = K, Na, Ca
Y = Al_{VI}, Ti, Cr, Fe^{3+}, Fe^{2+}, Mn, Mg
T = Al_{IV}, Si, Fe_{IV}, Ti_{IV}

The values of Fe_2O_3 are estimated assuming a ratio of 0.86 for FeO/FeO_T.

Amphibole stoichiometry has been calculated on the basis of 23 oxygens using the general formula of calcium-rich amphibole, which is expressed as:

$$A_{0-1}(M4)_2(M1,2,3)_5{}^{VI}(T1)_4{}^{VI}(T2)_4{}^{IV}O_{22}(OH)_2$$

where A = K, Na
T = Si, Al
M4 = Fe^{2+}, Mn, Ca, Na
M1,2,3 = Al, Fe^{3+}, Ti, Cr, Mg, Fe^{2+}

The Fe_2O_3 values were estimated using the method described by Stout (1972) and Robinson et al. (1982). First, the structural formalas were calculated on the basis of 13 cations, excluding K, Ca, Na, and Mn. This calculation generates the maximum value of Fe^{3+} that is permitted in the amphibole stoichiometry. Secondly, the structural formulas were calculated assuming 15 cations, excluding K and Na. The resulting calculated Fe^{3+} is the minimum value permitted in the amphibole stoichiometry. The mean value of Fe^{3+}, derived by averaging the Fe^{3+} from the two calculation methods (i.e. by 13 cations and 15 cations), gives the closest estimate of the real value of Fe^{3+} in the amphibole structural formula. An example of this method is given in Appendix G.

Garnet formulas have been calculated on the basis of 16 cations and 24 oxygens using the general formula:

$$X_3Y_2Z_3O_{12}$$

where X = Ca, Fe^{2+}, Mg, Mn
Y = Al, Fe^{3+}, Cr
Z = Si

The values of Fe^{3+} have been estimated assuming a full octahedral occupancy.

5.2 Introduction

Microprobe analyses of constituent minerals, igneous and/or metamorphic, were determined on the following samples: CMA-LA18, CMA-LGY, CMA-27.6.5, CMA-27.6.3, CMA-LG6, CMA-LG7, CMA-015A, CMA-M-V01, CMA-79DI86, CMA-M-R01A, and CMA-146. The analyses are listed in Appendix E. Average mineral composition of these samples is presented in Table 7.

Please note that "primary (igneous) minerals" are defined in this study as those crystals which because of textural criteria are presumed to have crystallized from a magmatic liquid (i.e. from a melt not in the solid state). Also, it should be noted that the composition of these primary minerals may have been variably modified by post-magmatic processes.

5.3 Primary (igneous) Minerals

Primary (igneous) minerals were analyzed for the following reasons:

1) to characterize the transformation of primary minerals to secondary minerals,
2) to characterize the late- to post-magmatic

Table 7. Average mineral composition of NNE diabase dykes

	OL	CPX(p)	PL(p)	PL(m)	OPX(m)	AMP	GRT
CMA-LA18	Fo_{43-60}	En_{40-44} Wo_{39-41} Fs_{17-20}	An_{46-60}	-	En_{46-59} $Wo_{0.4-2.1}$ Fs_{41-52}	Prg	-
CMA-LGY	Fo_{45-51}	En_{40-50} Wo_{32-41} Fs_{17-20}	An_{40-56}	-	En_{42-61} $Wo_{0.3-4}$ Fs_{39-54}	Prg	-
CMA-2765	-	En_{33-34} Wo_{37-39} Fs_{19-25}	An_{36-62}	An_{24-28}	En_{61-63} $Wo_{0.4-0.8}$ Fs_{36-39}	Prg	Al_{47-68} Py_{11-21} $Gros_{16-32}$
CMA-79DI	-	En_{28-42} Wo_{45-51} Fs_{8-25}	An_{51-72}	An_{10-25}	-	Prg Hbl	Al_{40-65} Py_{7-12} $Gros_{18-43}$
CMA-LG6	-	En_{41-45} Wo_{35-36} Fs_{19-24}	An_{34-60}	-	En_{31} $Wo_{0.6}$ Fs_{19-24}	Prg	-
CMA-LG7	-	En_{39-46} Wo_{16-33} Fs_{28-39}	An_{35-51}	-	En_{37-43} $Wo_{0.5-2}$ Fs_{55-62}	Prg	Al_{71-72} Py_{4-9} $Gros_{14-20}$
CMA-2763	-	En_{42-55} Wo_{38-49} Fs_{9-18}	An_{37-51}	-	En_{68} $Wo_{0.5}$ Fs_{32}	Prg	Al_{44-51} Py_{23-27} $Gros_{20-26}$
CMA-MV01	-	En_{41-43} Wo_{44-49} Fs_{10-13}	-	An_{20}	-	Hbl Ed Hbl	Al_{45-54} Py_{21-25} $Gros_{18-29}$
CMA-M015A	-	En_{40-48} Wo_{29-51} Fs_{28-39}	-	-	En_{64-80} $Wo_{0.3-0.7}$ Fs_{55-62}	Hbl Ed Hbl	Al_{38-46} Py_{20-30} $Gros_{14-20}$
CMA-MR01A	-	En_{26-40} Wo_{21-40} Fs_{21-52}	-	-	-	Hbl	Al_{67-72} Py_{2-3} $Gros_{17-19}$
CMA-146	-	En_{34-39} Wo_{30-47} Fs_{17-21}	-	An_{40-54}	-	Hlb	Al_{62-69} Py_{5-8} $Gros_{18-25}$

Pyroxene end-members
En = Mg/(Mg + Fe + Ca)
Wo = Ca/(Ca + Fe + Mg)
Fs = Fe/(Fe + Ca + Mg)

Garnet end-members
Al = Fe/(Fe + Mg + Ca)
Py = Mg/(Mg + Fe + Ca)
Gros = Ca/(Ca + Mg + Fe)

Abreviations
En = enstatite
Fs = ferrosilite
Wo = wollastonite
Hbl = hornblende
Ed Hbl = edenitic hornblende
Prg = pargasite

(m) = metamorphic
(p) = primary or igneous

crystallization events of the NNE diabase dykes,

3) to understand the evolution of corona structures from late-magmatic to early post-magmatic conditions to metamorphic conditions

5.3.1 Olivine

The olivine compositions range from Fo_{45} to Fo_{60} (Table 7). The olivine composition is overall uniform within individual grains, but is highly variable between some grains (e.g. CMA-LA18). Chemical zoning within grains is generally absent, but where detected, it is restricted to grain boundaries. The zoning is characterized by a slight decrease in magnesium from the core to the margin. Chemical zoning does not exceed 1 mole percent Fo, whereas grain to grain chemical variation ranges up to 7 mole percent Fo. The olivine composition in sample CMA-LA18 ranges from Fo_{60} to Fo_{53}, whereas the olivine composition in sample CMA-27.6.5, which contains metamorphic mineral assemblages, ranges from Fo_{51} to Fo_{45}. The chemical variation of olivine grains shown in sample CMA-LA18 appears to reflect magmatic (i.e. early) re-equilibration of olivine where in contact with plagioclase grains. The most magnesium-rich olivine grain (Fo_{60}) analyzed in sample CMA-LA18 is partly enclosed by primary augite and does not exhibit any disequilibrium textural features. This olivine composition is considered to be the closest estimate of the primary olivine composition. The iron-enriched olivine grains analyzed in CMA-27.6.5, most likely, represent re-equilibration

of primary olivine grains during metamorphic conditions.

5.3.2 Clinopyroxene

The composition of the primary (igneous) clinopyroxene grains in sample CMA-LA18, expressed as end member constituents, is relatively constant between $En_{40}Wo_{39}Fs_{21}$ and $En_{44}Wo_{39}Fs_{17}$ (Table 7) . The primary clinopyroxene grains are augite according to the pyroxene quadrilateral (Appendix F).

5.3.3 Plagioclase

Primary plagioclase ranges from An_{60} to An_{50} (Table 7) in the least metamorphosed samples (CMA-LA18 and CMA-LGY), Al:Si is consistently near 0.54 (An_{50-60}). This is suggestive of restricted mobility of Al and Si within these dyke samples. Minor amounts of spinel inclusions are responsible for the small amounts of FeO (i.e. 0.28 to 0.77 wt. percent) and MgO in the plagioclase analyses. Most grains show normal chemical zoning. Plagioclase laths found in contact with the least evolved olivine corona structures are not significantly different from those a few mm away.

5.3.4 Magnetite/Ilmenite

The opaque minerals analyzed (Appendix E) in the least metamorphosed NNE dykes are always Ti-magnetite with minor amounts of fine exsolution lamellae of ilmenite. They

occasionally contain tiny inclusions of hercynite. The igneous magnetite crystals are titaniferous and are richer in chromium and aluminum than the metamorphic magnetite crystals.

5.3.5 Biotite

The composition of the primary biotite grains is uniform within and between individual samples (Appendix E). Within the least altered samples, their TiO_2, Al_2O_3, Fe_2O_3, FeO, and MgO contents, respectively, are 3.14 - 3.19 wt. percent, 14.45 - 15.09 wt. percent, 2.87 - 3.31 wt. percent, 15.87 - 18.29 wt. percent, and 11.49 - 14.38 wt. percent.

5.3.6 Amphibole

Based on the nomenclature of Leake (1978), the analyzed calcic amphiboles (Appendix E) fall into the pargasite field. They are typically characterized by low TiO_2 (0.02 - 0.18 wt.%) and high Al_2O_3 (17.0 - 21.0 wt>%) values.

5.3.7 Apatite

Apatite is the only analysed accessory mineral (Appendix E). Its composition is close to a fluor-apatite (Deer et al., 1978), as indicated by 3.5 wt% (average value) Fl. Minor chlorine (0.25 wt%) is present.

5.4 Metamorphic Minerals

Metamorphic minerals were analyzed for the following reasons:

1) to characterize the metamorphic mineral assemblages,
2) to study the metamorphic paragenesis in order to decipher the evolution of corona structures,
3) to be able to write quantitative mineral equations for the corona reactions,
4) to compare the P-T conditions of coronitic assemblages with those of noncoronitic assemblages

5.4.1 Orthopyroxene

Orthopyroxene is homogeneous within individual grains (Table 7), but composition varies with respect to grain location in the samples (i.e. dependant on association with different corona types). For example, the orthopyroxene that forms around olivine grains is more magnesium-rich (En_{61-72} Fs_{27-39}) than the orthopyroxene that is associated with magnetite crystals (En_{38-64} Fs_{36-62}). The composition also varies within the orthopyroxene aggregates, which are slightly more magnesium-rich (En_{65-80} Fs_{20-35}) than those surrounding the olivine grains. The Mg/Fe+Mg ratio (X_{Mg}) of the orthopyroxene within the olivine corona structure is characteristically higher than that of the associated olivine grains. Although the X_{Mg} of olivine and orthopyroxene are variable, the $K_D = X^{ol}/1-X^{ol} \cdot 1-X^{opx}/X^{opx}$ varies from 0.56 to 0.64 in sample CMA-LA18 and from 0.52 to 0.59 in sample CMA-27.6.5. The Al_2O_3 content of the orthopyroxene within

the olivine corona structure ranges from 0.01 to 0.54 wt%. Orthopyroxene elsewhere is extremely aluminum-rich, as much as 5.61 wt% in the orthopyroxene and magnetite symplectite layers of more evolved corona structures.

5.4.2 Clinopyroxene

The composition of the metamorphic clinopyroxene grains, expressed as pyroxene type with X_{Mg} (= molecular ratio Mg/Mg+Fe) values, ranges from salitic augite (0.64 - 0.71) to diopside (0.73 - 0.81), salite (0.50 - 0.75), ferrosalite (0.45 - 0.50), and ferroaugite (0.35 - 0.45). The variable mineral chemistry is characterized, in general, by a loss of Al_2O_3 and TiO_2, and a gain of CaO and Na_2O as the metamorphic clinopyroxene evolves from salitic augite to other varieties, especially those of the diopside-hedenbergite series.

5.4.3 Plagioclase

Metamorphic plagioclase is common in all of the more evolved samples (i.e. those either than CMA-LA18 and CMA-LGY). In the less metamorphosed samples, it occurs at the edges of and along fractures within magmatic plagioclase crystals. In most cases, it is depleted in the anorthite component when compared to the nearby primary plagioclase crystals. In more metamorphosed samples, magmatic plagioclase crystals are characterized by spinel- and corundum-bearing clouds. In general, the clouding is more intense in the plagioclase cores and it is pseudomorphic

after the original zoning within the magmatic plagioclase laths. The clouded plagioclase cores are typically calcium-rich, but they exhibit distinct chemical differences within and between individual grains (An_{34-60}). This is indicative of their highly variable degree of alteration and recrystallization. Some of the more highly altered and heavily clouded cores have very fresh rims. These clear grain margins are more sodic in composition (An_{20-50}). Several samples contain plagioclase grains with extreme variations in composition between grains, as indicated by their highly variable Al:Si ratios (0.32 to 0.69). Samples CMA-27.6.5 and CMA-146 are characterized by more stable plagioclase compositions with Al:Si ratios of 0.47 to 0.54.

Sample CMA-79DI exhibits extreme variation in composition between plagioclase grains. Plagioclase grains analysed in the coarse-grained segregations are characterized by very calcic cores (An_{72-83}) and sodic rims (An_{10-59}). However, for plagioclase laths adjacent to the clinopyroxene corona structure, a reverse zoning is observed. The plagioclase cores, which are relatively inclusion-free, become calcium depleted, whereas the margins, which are spinel clouded, become calcium enriched. It appears that the nucleation of garnet crystals near the plagioclase cores is responsible for the annealing of the spinel dust and progressive loss of calcium in the plagioclase cores.

Sample CMA-79DI is also characterized by the presence of complex exsolution morphologies developed within primary plagioclase laths. This particular texture has been described in

Chapter 3. The chemical composition of the microcrystals could not be determined using the electron microprobe; however, qualitative determination by Scanning Electron Microprobe (SEM) reveals that the exsolutions are more sodic than their host plagioclase grains (Fig. 46)

5.4.4 Biotite

Its chemical composition does not show significant variations of TiO_2, Al_2O_3, and Fe_2O_3. The principal oxides that vary are FeO and MgO, which suggests $FeMg_{-1}$ exchange within the octahedral site. FeO varies from 11.7 to 13.1 wt% and MgO from 9.22 to 29.2 wt%.

Sample CMA-79DI with segregations contains biotite grains with the highest titanium content (5.79 wt%). The biotite making up the matrix is generally more Fe-rich (19.7 wt%) than the biotite found within the segregations (16.3 wt%). On the other hand, MgO and Al_2O_3 are slightly depleted in the matrix (9.22 to 11.5 wt%) compare to the segregation (12.9 to 15.1 wt%).

5.4.5. Amphibole

Amphibole grains from the NNE diabase dykes show a wide range of compositions, which are distributed about a "pargasite trend", that connects pargasite and actinolite end-members (Fig. 47). Amphibole grains from the least altered samples plot mainly

Figure 46. Plagioclase crystal showing randomly oriented exsolution of more sodic plagioclase. Qualitative analysis by Scanning Electron Microprobe shows that the exsolution are more sodic than their host plagioclase. Two dots on the photograph indicate the position of the analyses.(G.S.C.)

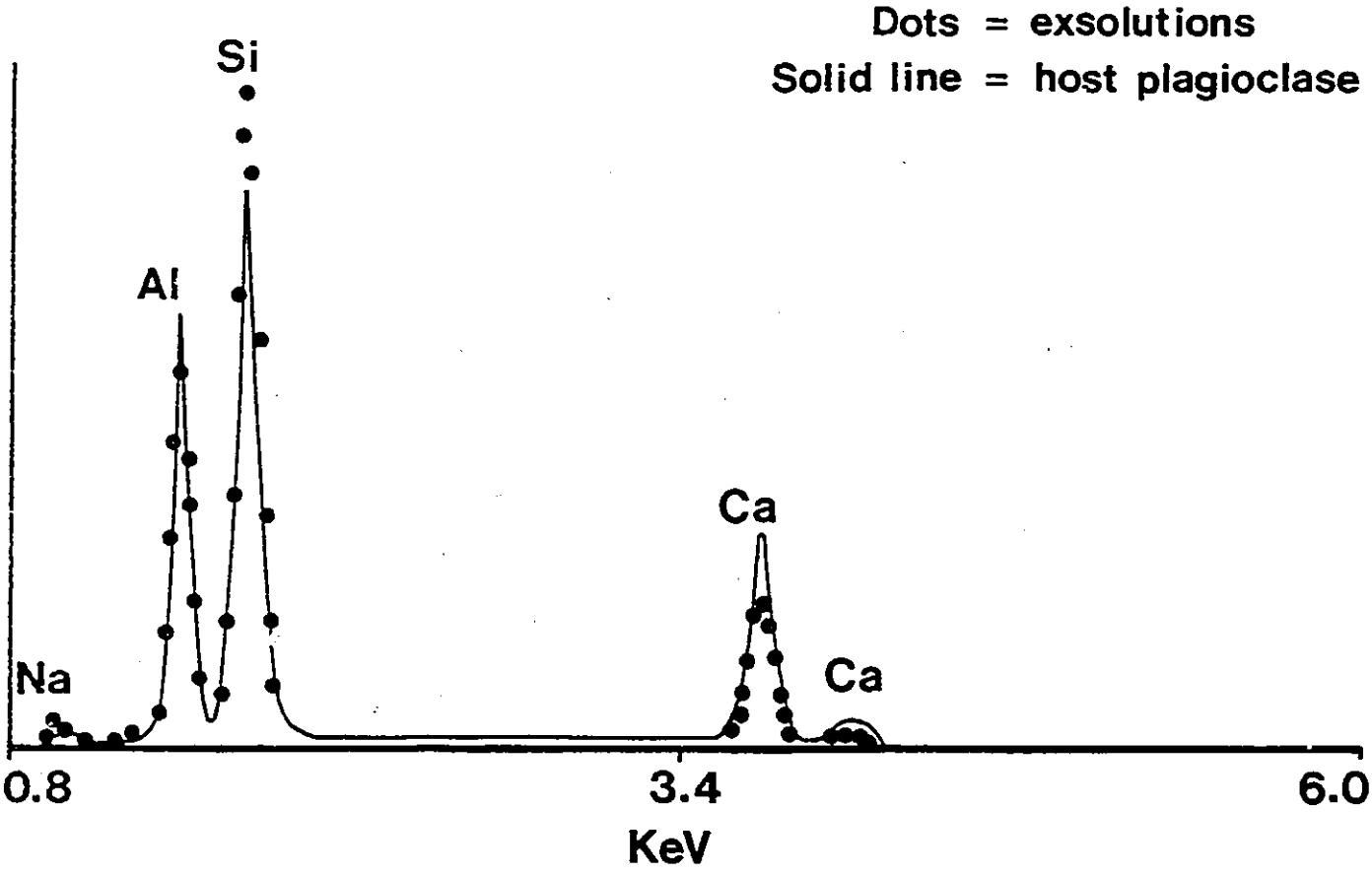
Dots = exsolutions
Solid line = host plagioclase
Si
Al
Ca
Na
Ca
0.8
3.4
6.0
KeV

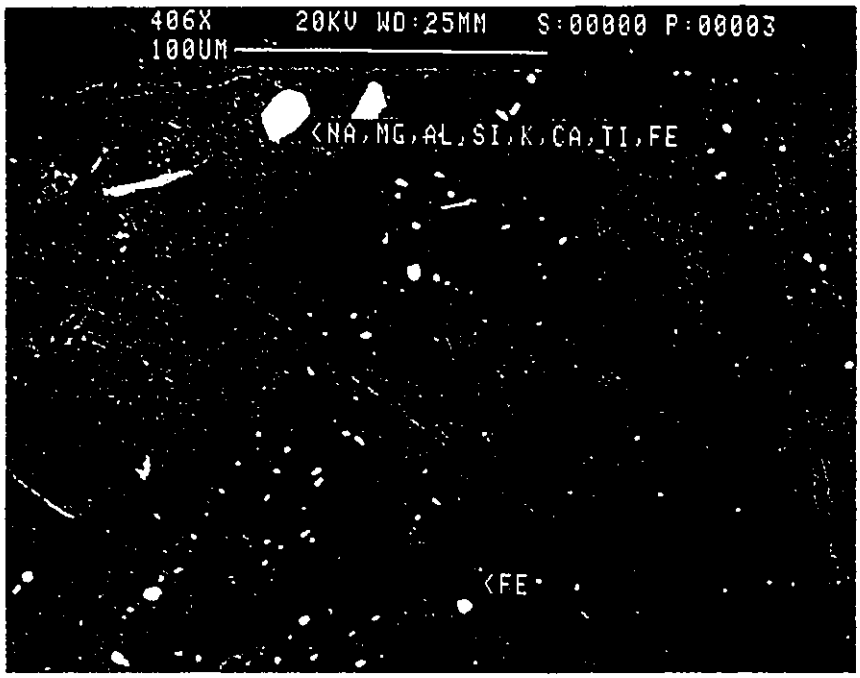
406X 20KV WD:25MM S:00000 P:00003
100UM
(NA,MG,AL,SI,K,CA,TI,FE
(FE

within the pargasite field, whereas those of the most metamorphosed samples plot within the edenitic hornblende to actinolite fields. Based on the nomenclature of Leake (1978), the amphibole compositions may be divided into two main groups : 1) the pargasite group, which comprises pargasite and parcasitic hornblende, and 2) the hornblende group, which includes edenitic hornblende, tschermakitic hornblende, hornblende, actinolitic hornblende, and actinolite.

Amphibole grains from the pargasite group contain low TiO_2 values, ranging from 0.02 to 0.28 wt%, and high Al_2O_3 values, ranging from 17.0 to 21.0 wt%. The Fe/Mg ratio of these amphibole varies from 0.31 to 0.48. Characteristically, they show a decrease in TiO_2 content that is accompanied by an increase in Al_2O_3 values and Fe/Mg ratios. Pargasitic amphibole layers that form within olivine corona structures and orthopyroxene/magnetite symplectite corona structures have similar Fe/Mg ratios as sudjacent orthopyroxene layers of these corona. The pargasitic amphibole layers that form within corona structure around primary augite are characterized by higher values of TiO_2 (0.77 to 0.79) and Al_2O_3 (16.0 wt%). The Fe/Mg ratio of these pargasitic amphibole layers is higher than the adjacent primary augite grains.

Amphiboles comprising the hornblende group are characteristic of the most metamorphosed samples. These amphiboles are defined by higher TiO_2 (0.79 to 1.25 wt%) and lower Al_2O_3 (3.0 to 11.0 wt%) values when compared to those of the pargasite group. The

Figure 47. Plot of Al^{IV} versus $(Na+K)_A$. The symbols refers to the amphibole layer surrounding different corona structures. The solid line represents the pargasite trend tying pargasite and actinolite end-members.
Pg Hbl = pargasitic hornblende; Ed Hbl = edenitic hornblende; Act Hbl = actinolitic hornblende; and Ts Hbl = tschermakitic hornblende.

Figure 48. Plot of Al^{IV} versus A site ions + Al^{VI} + Fe^{3+} + 2Ti. The trend line shows predicted values for perfect substitution. Diagram after Pe-Piper G. (1988)

Fig. 47

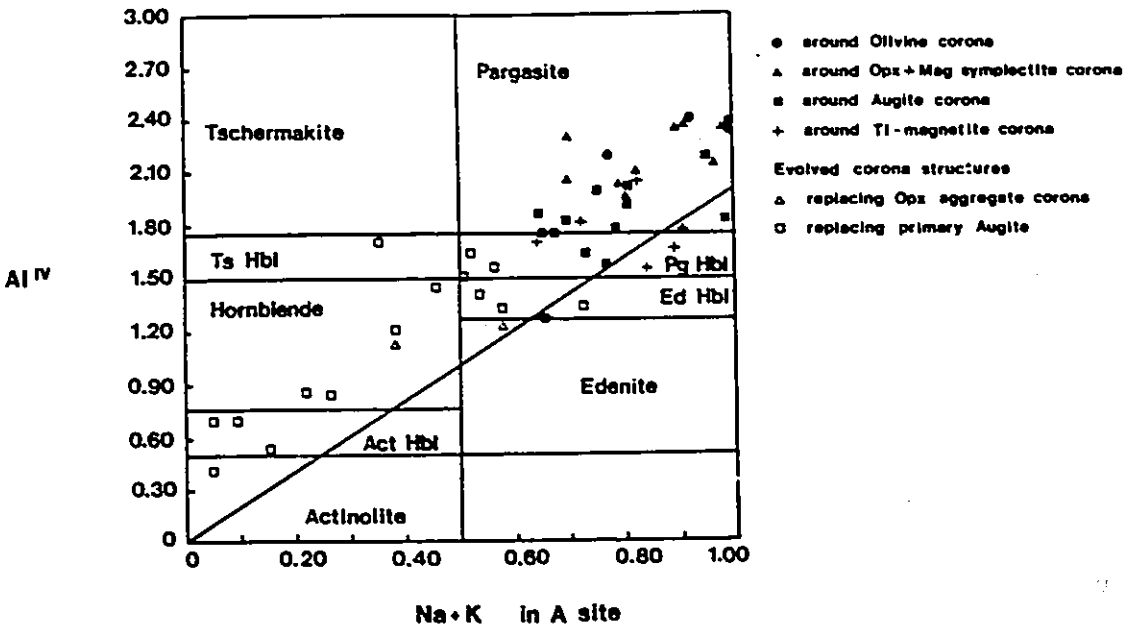
3.00
2.70
2.40
2.10
1.80
1.50
1.20
0.90
0.60
0.30
0
0.20
0.40
0.60
0.80
1.00
Al IV
Na+K in A site
Tschermakite
Pargasite
Ts Hbl
Pg Hbl
Hornblende
Ed Hbl
Edenite
Act Hbl
Actinolite
around Olivine corona
around Opx+Mag symplectite corona
around Augite corona
around Ti-magnetite corona
Evolved corona structures
replacing Opx aggregate corona
replacing primary Augite

Fig. 48

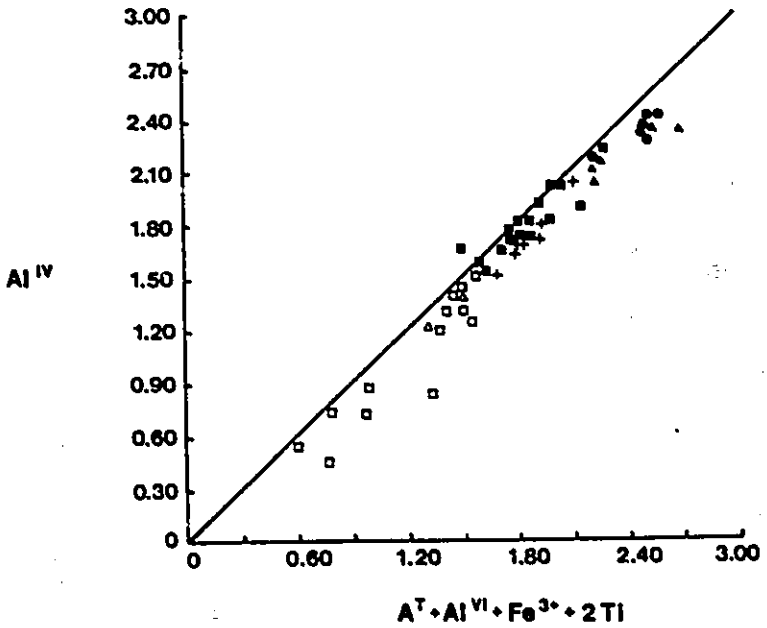
3.00
2.70
2.40
2.10
1.80
1.50
1.20
0.90
0.60
0.30
0
0.60
1.20
1.80
2.40
3.00
Al IV
A^T+Al^VI+Fe^3+ +2Ti

Fe/Mg ratios of the amphiboles of the hornblende group are generally lower than the adjacent pyroxenes. In addition, these Fe/Mg ratios are lower than those of the pargasite group.

Substitution:

It has been proposed by Pe-Piper (1988) that there is continuous chemical variation from pargasite to hornblende and from actinolitic hornblende to actinolite. The expression of those variations are illustrated by coupled substitutions.

Substitution of Al^{IV} for Si in tetrahedral sites in both amphibole groups is mainly compensated by substitution of Al^{VI}, Fe^{3+}, and Ti in octahedral sites and partial occupancy of the A site by Na and K, as illustrated by the linear relationship in Figure 48. The trend line with a slope of 1.0 on Figure 48 defines perfect substitution. The excess charges produced by this substitution is balanced by the substitution of Na for Ca in the M4 site. In addition, with increasing metamorphic grade, the values of Al^{VI} in the octahedral site decreases with increasing Ti and Mg values from the same site. Therefore, it is suggested that the substitution of Ti for Al^{VI} is accompanied by a decrease of Na within the M4 site from post magmatic pargasite to metamorphic hornblende. Furthermore, the Fe^{2+} content within the M4 site decreases with increasing Si values, which suggests the coupled substitution of Fe^{2+} and Na for Ca in the M4 site.

Substitutions of Al^{IV} plus $(Na+K)_A$ for Si and A-site vacancy is illustrated in Figure 49. The amphibole grains, analysed from

Figure 49. Plot of Al^{IV} versus A site - Na (M4).

Blue = CMA-27.6.3
Red = CMA-146
Green = CMA-M-R01A

sample	slope	correlation	number of analyses	colour coefficient
CMA-27.6.3	0.97±0.25	0.913	5	blue
CMA-146	0.46±0.28	0.502	10	red ■
	1.49±0.84	0.662	6	□
CMA-M-R01A	1.04±0.19	0.943	6	green

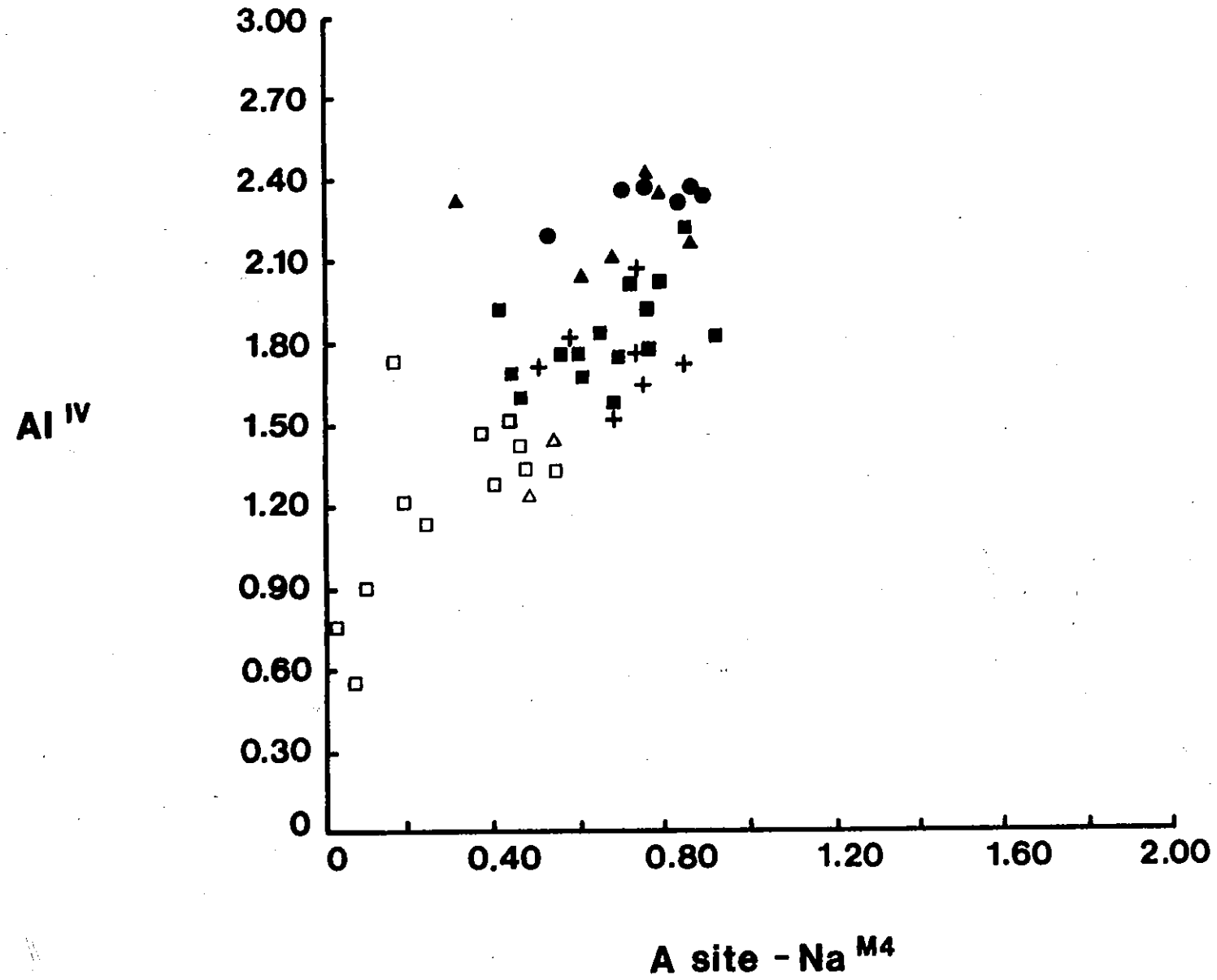
3.00
2.70
2.40
2.10
1.80
1.50
1.20
0.90
0.60
0.30
0
Al IV
0
0.40
0.80
1.20
1.60
2.00
A site - Na M4

the least to the most metamorphosed dykes, define linear trends which have slopes that vary from 0.46 ± 0.28 to 1.23 ± 0.76 for pargasite and hornblende, to 1.49 ± 0.84 for actinolite. The analysed amphiboles of the least metamorphosed dyke (CMA-LA18) define a trend with a slope of 1.23 ± 0.76 and a correlation coefficient of 0.752. This trend line shows the substitution within pargasite in the olivine and orthopyroxene/magnetite corona structures. Within more metamorphosed dykes (CMA-LG7, CMA-27.6.3, CMA-R01A, and CMA-146) the trend lines define the substitution within pargasite and hornblende layers formed around primary augite and oxide minerals. The slopes and correlation coefficients of these trend lines are 0.63 ± 0.59 and 0.468 in CMA-LG7; 0.97 ± 0.25 and 0.913 in CMA-27.6.3 and CMA-R01A; and 0.46 ± 0.28 and 0.502 for pargasite/hornblende, with 1.49 ± 0.84 and 0.663 for actinolite in CMA-146.

The diagram (Figure 50) display substitution of Al^{IV} for Ti (octahedral) illustrates two different trends. The positive trend is defined by actinolitic compositions and the negative trend is defined by pargasitic/hornblendic compositions. This substitution is observed in pargasitic amphibole around primary augite and oxide minerals, but does not occur in pargasitic amphibole around olivine or orthopyroxene/magnetite symplectite corona structures. The trend displayed by the pargasitic amphibole exhibits a slope of -4.86 ± 1.53 and a correlation coefficient of -0.747. Contrastly, the actinolitic amphiboles from sample CMA-146 display a positive trend with a slope of 16.69 ± 6.54 and a

Figure 50. Plot of Al^{IV} versus Ti showing different trends for a) pargasite and hornblende, and b) for actinolite.

sample	slope	correlation coefficient	number of analyses	colour
CMA-27.6.3	2.22±0.52	0.928	5	blue
CMA-146	-4.84±1.53	-0.747	10	red ■
	16.69±6.54	0.787	6	red □
CMA-M-R01A	-1.98±1.56	-0.536	6	green

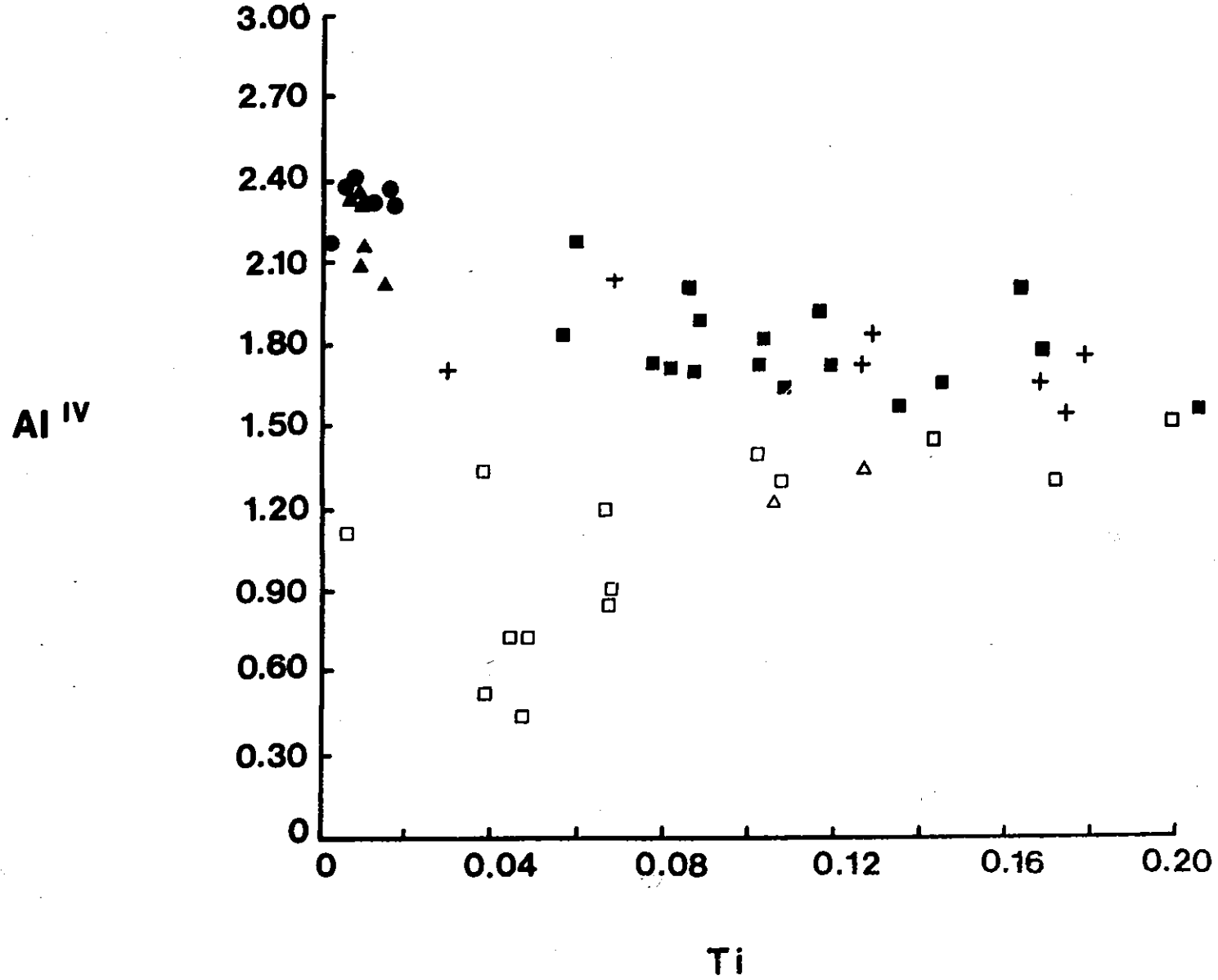
3.00
2.70
2.40
2.10
1.80
1.50
1.20
0.90
0.60
0.30
0
Al IV
0
0.04
0.08
0.12
0.16
0.20
Ti

correlation coefficient of 0.787.

In Figure 51, pargasite shows a positive correlation between Al^{IV} and Mg ratio (Mg/Mg + Fet) in sample CMA-LA18, whereas pargasite and hornblende show strong negative correlations in samples CMA-27.6.3, CMA-R01A, and CMA-146. The negative trends are characterized by similar slopes but different intercepts along the X axis (i.e. at different Mg ratios: CMA-R01A > CMA-146 > CMA-27.6.3).

In Figure 52, the Mg ratio increases from pargasite to hornblende and actinolite; however, it also decreases with increasing metamorphic grade. The diagram of Mg ratio versus Si reveals a coherent positive trend for sample CMA-146 and a negative trend for sample CMA-LA18. The positive trend indicates an increase in Mg ratio with increasing Si content from late- to post-magmatic pargasite to metamorphic hornblende and actinolite.

5.4.6. Garnet:

Garnet has a constant composition within individual grains but the composition varies depending upon the corona types. For instance, garnet crystals forming around olivine corona structures generally contain more Mg ($Fe_{47-55}Mg_{16-22}Ca_{19-32}$), whereas Fe enrichment ($Fe_{68-72}Mg_{7-11}Ca_{16-20}$) is observed around oxide mineral corona structures. Also, a distinct chemical variation of garnet compositions is observed with further recrystallization (i.e. with changing metamorphic conditions), as

Figure 51. Plot of Al^{IV} versus $Mg/(Mg + Fe_T)$ which exhibit three trends of similar slope, defined by samples CMA-R01A, CMA-146, and CMA-27.6.3.

samples	slope	correlation coefficient	number of analyses	colour
CMA-27.6.3	-3.72±1.18	-0.876	5	blue
CMA-146	-5.87±0.36	-0.975	16	red
CMA-M-R01A	-8.45±4.03	-0.723	6	green

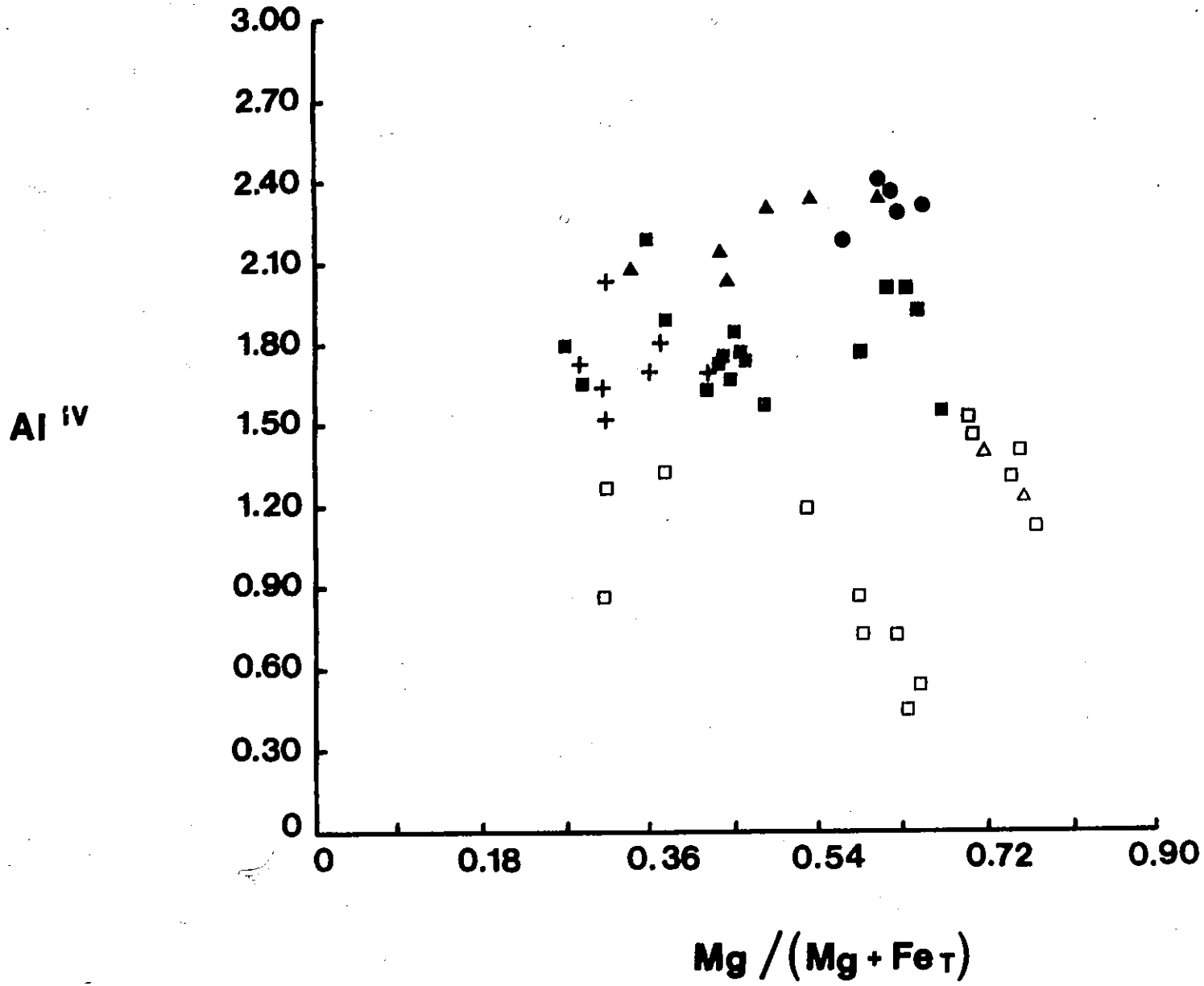
3.00
2.70
2.40
2.10
1.80
1.50
1.20
0.90
0.60
0.30
0
Al IV
0
0.18
0.36
0.54
0.72
0.90
Mg /(Mg + Fe T)

Table 52. Amphibole plotted on a $Mg/(Mg + Fe_T)$ versus Si^{IV} diagram. Metamorphic amphibole are commonly enriched in silica.

samples	slope	correlation coefficient	number of analyses	colour
CMA-27.6.3	0.21±0.06	0.876	5	blue
CMA-146	0.17±0.01	0.976	16	red
CMA-M-R01A	0.06±0.03	0.723	6	green

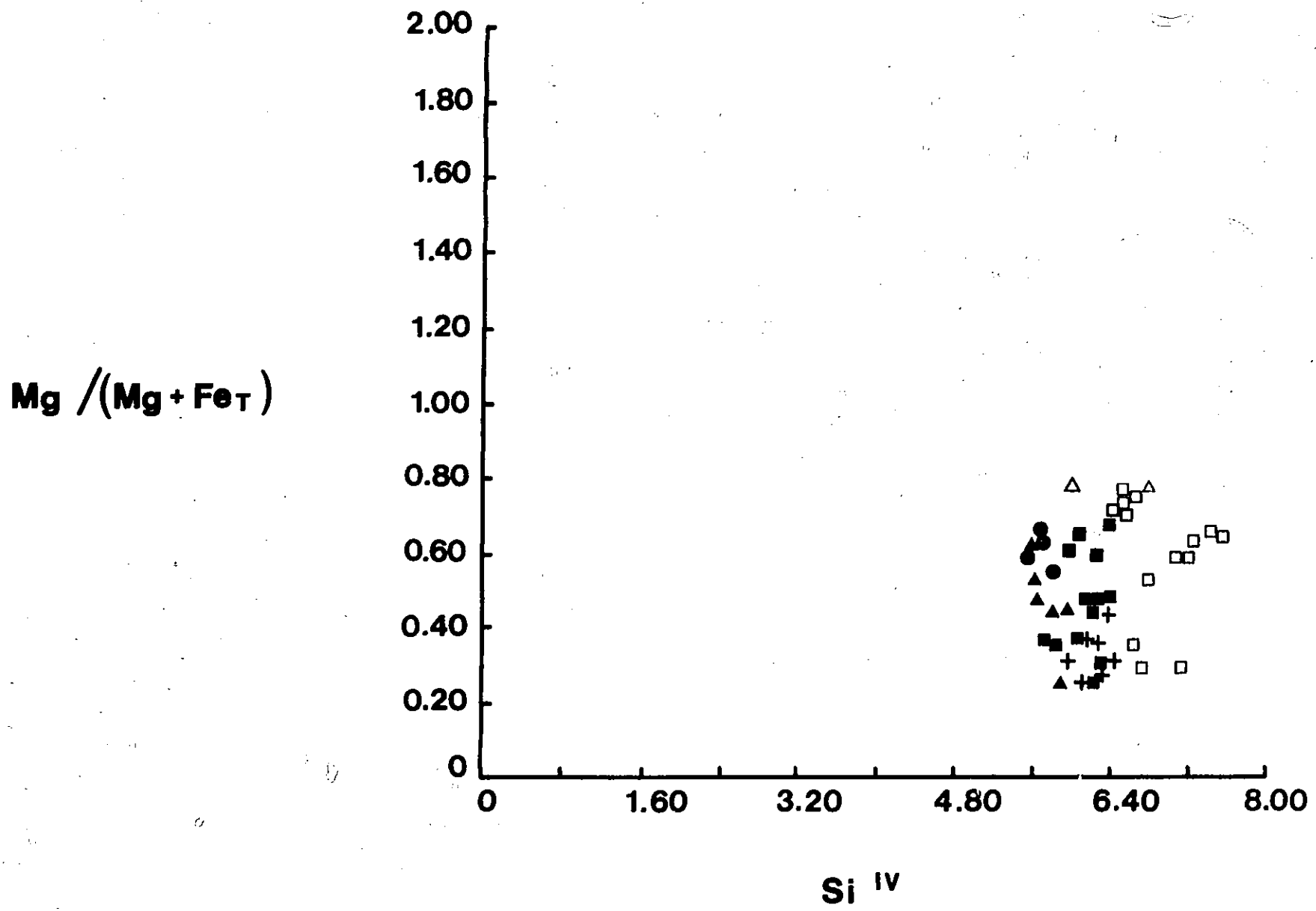
Mg /(Mg + FeT)
2.00
1.80
1.60
1.40
1.20
1.00
0.80
0.60
0.40
0.20
0
0
1.60
3.20
4.80
6.40
8.00
Si IV

indicated by the increase in FeO content and the decrease in MgO content. The chemical variation observed in garnet crystals from dyke to dyke is also a reflection of the bulk rock chemistry. In fact, garnet is more magnesian within dykes with higher Mg numbers. The MnO content of the garnet crystals does not exceed 1.0 wt% in all samples and characteristically decreases with increasing CaO content.

The chemical compositions of coronitic garnet crystals and non-coronitic garnet crystals are similar for most samples. Some differences are observed in CMA-79DI between garnet crystals from the host dyke and those from the segregations. In general, garnet compositions from the host dyke are more Fe-rich ($Fe_{60-65}Mg_{9-11}Ca_{19-23}$), whereas garnet compositions from the segregations are more calcium-rich ($Fe_{41}Mg_{12}Ca_{43}$). The chemical compositions of the different minerals within a thin section are plotted together in Figures 53a, 53b, and 53c.

Figures 53a, 53b, and 53c.

Chemical composition of co-existing mineral phases from representative dyke samples (CMA-LA18, CMA-LGY, CMA-LGY, CMA-27.6.5, CMA-79Di, CMA-27.6.3, CMA-M-V01, CMA-LG6, CMA-LG7, CMA-M-R01A, CMA-146, and CMA-M-015a) plotted on a Ca-Mg-Fe quadrilateral diagram. Each analysis plotted on the quadrilateral diagram represents an individual mineral grain in the thin section (e.g. 4 individual amphibole grains were analysed in sample CMA-LA18). Solid solution diagrams of olivine and plagioclase are plotted beneath their respective quadrilateral diagrams. On the plagioclase diagram, the open circles represent the core compositions, whereas the filled circles are margin compositions.

Note: For sample CMA-79Di, a) corresponds to the chemical composition of minerals from the pegmatitic portion of the dyke, whereas b) corresponds to mineral compositions from the host dyke portion.

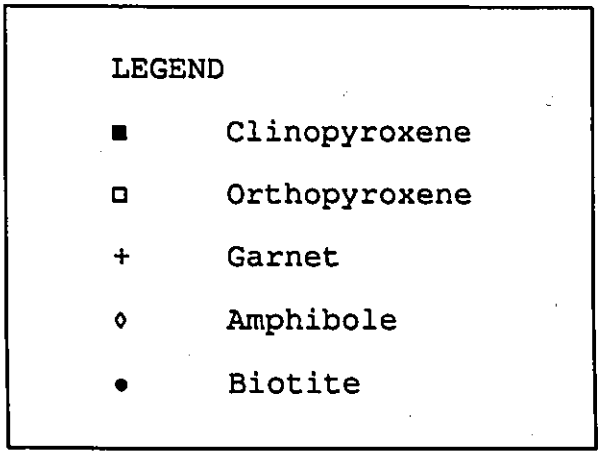

Figure 53a

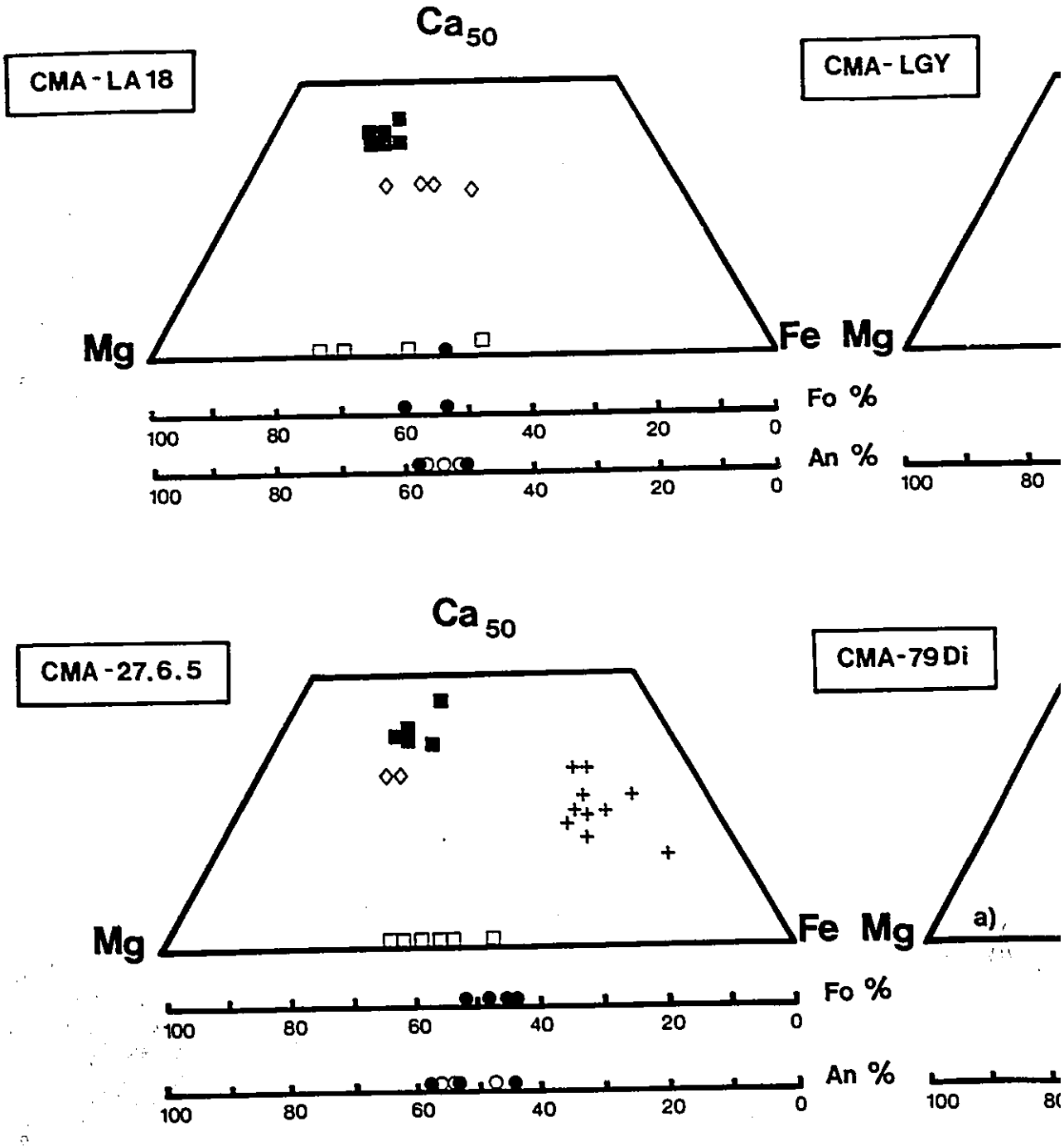
Ca50
CMA-LA18
Mg
Fe Mg
Fo %
100 80 60 40 20 0
An %
100 80 60 40 20 0
CMA-LGY
100 80
Ca 50
CMA-27.6.5
Mg
Fe Mg
Fo %
100 80 60 40 20 0
An %
100 80 60 40 20 0
CMA-79Di
a)
100 80

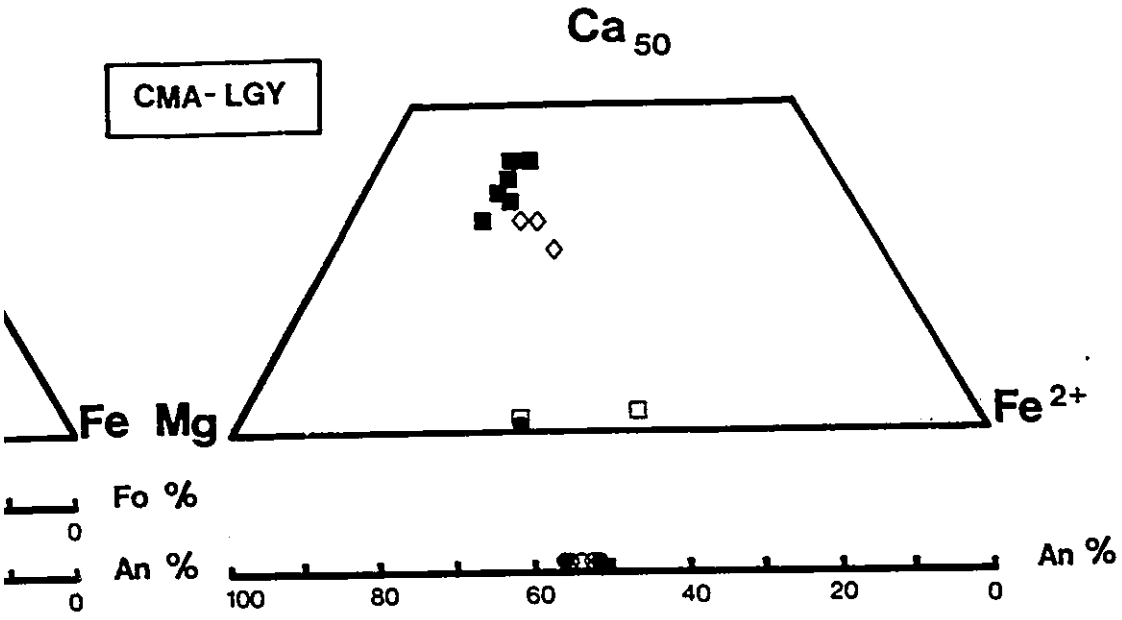
Ca 50
CMA- LGY
Fe Mg
Fe 2+
Fo %
0
An %
0
100
80
60
40
20
0
An %

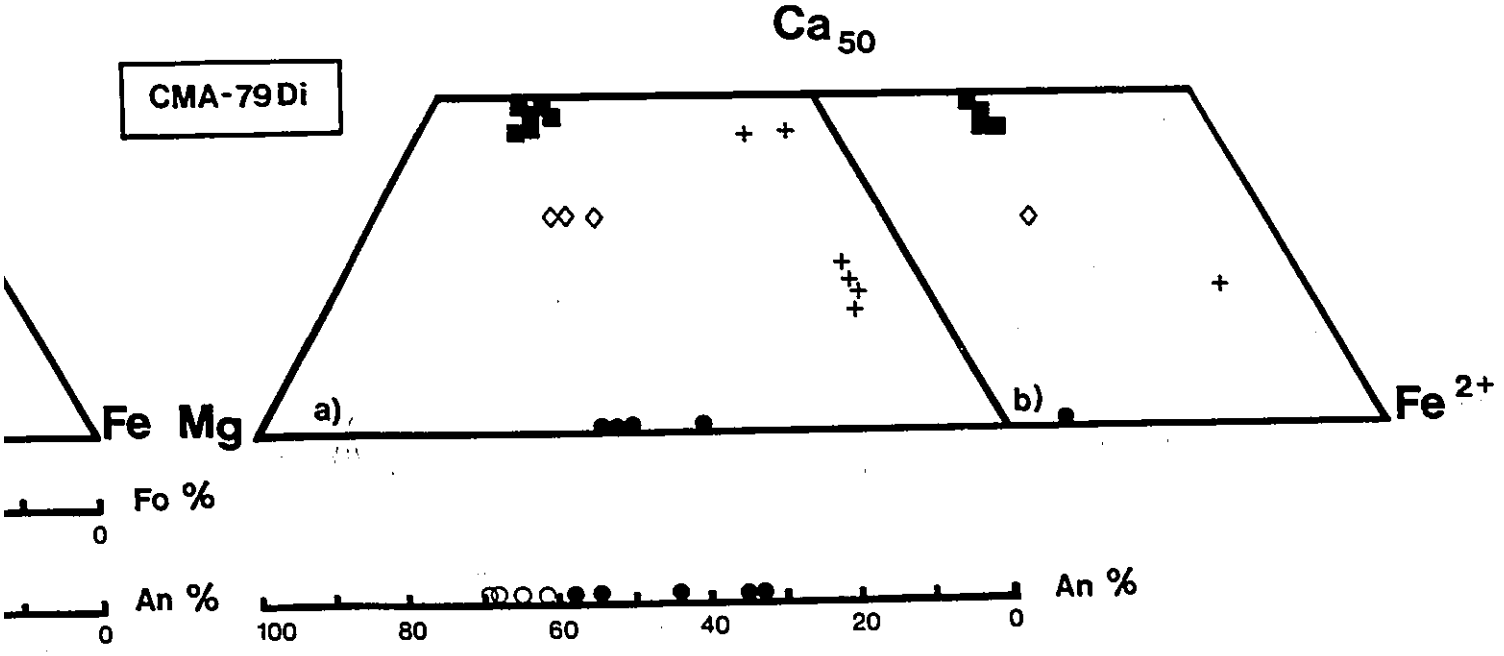
Ca 50
CMA-79 Di
Fe Mg
a)
b)
Fe 2+
Fo %
0
An %
0
100
80
60
40
20
0
An %

Figure 53b

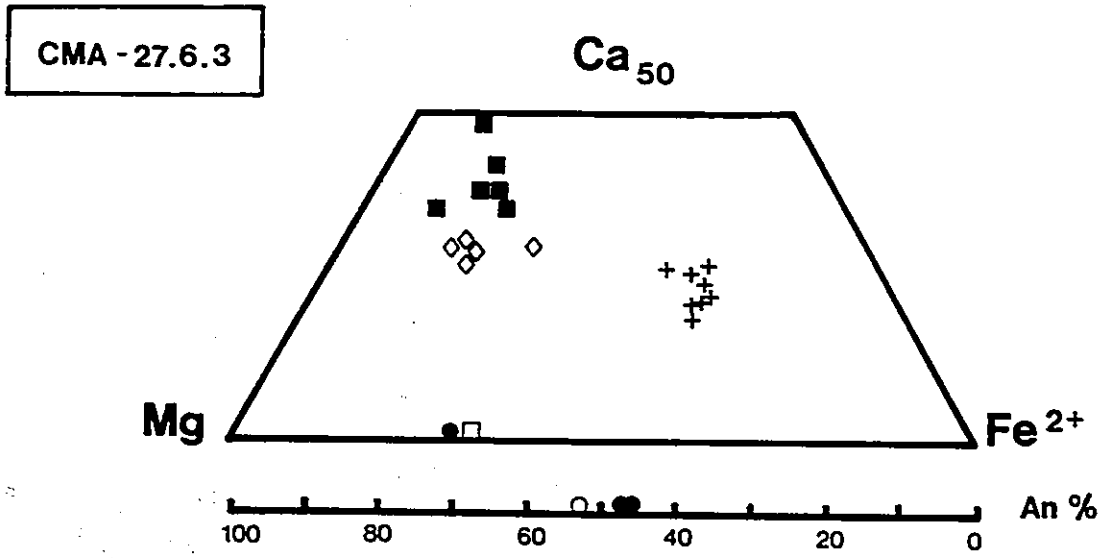
CMA - 27.6.3
Ca 50
Mg
Fe 2+
An %
100
80
60
40
20
0

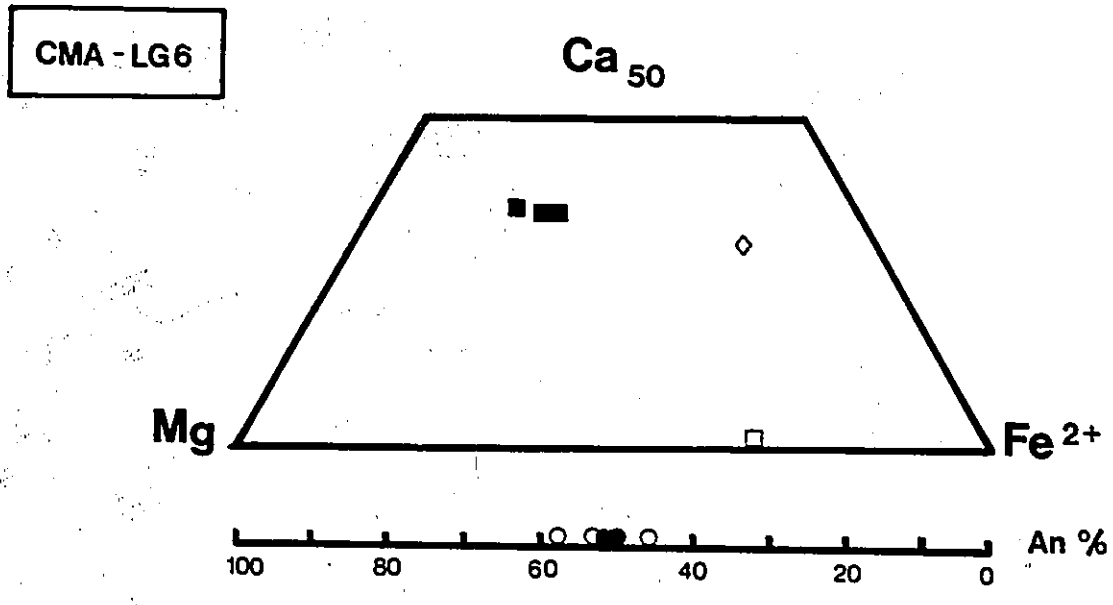
CMA - LG6
Ca 50
Mg
Fe 2+
An %
100
80
60
40
20
0

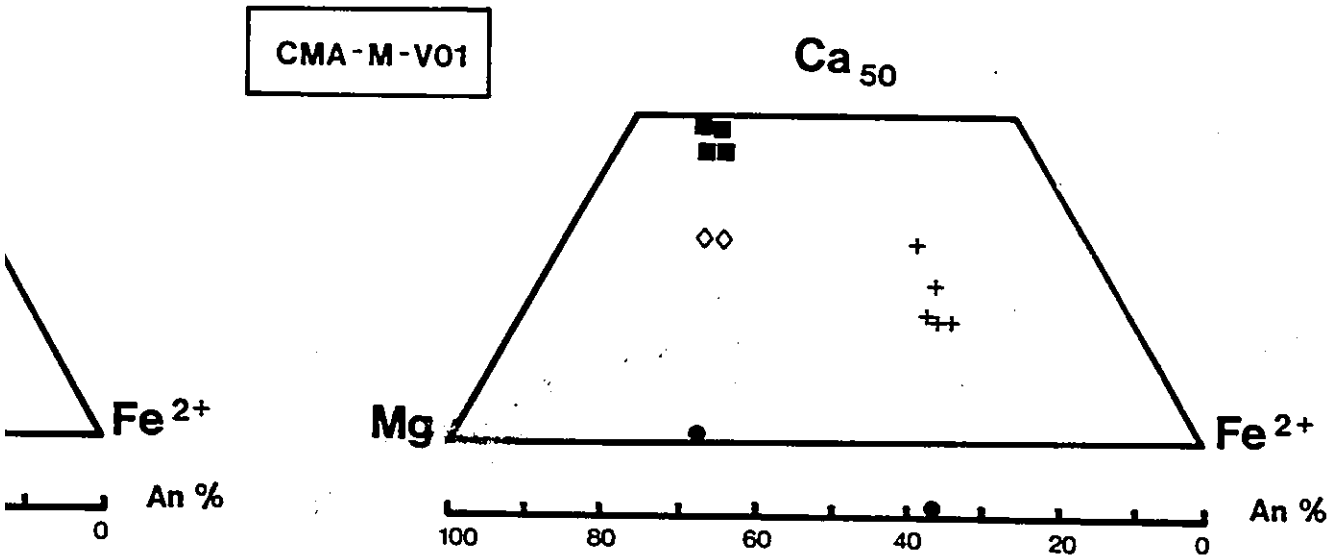
CMA - M - V01
Ca 50
Mg
Fe 2+
Fe 2+
An %
0
100
80
60
40
20
0
An %

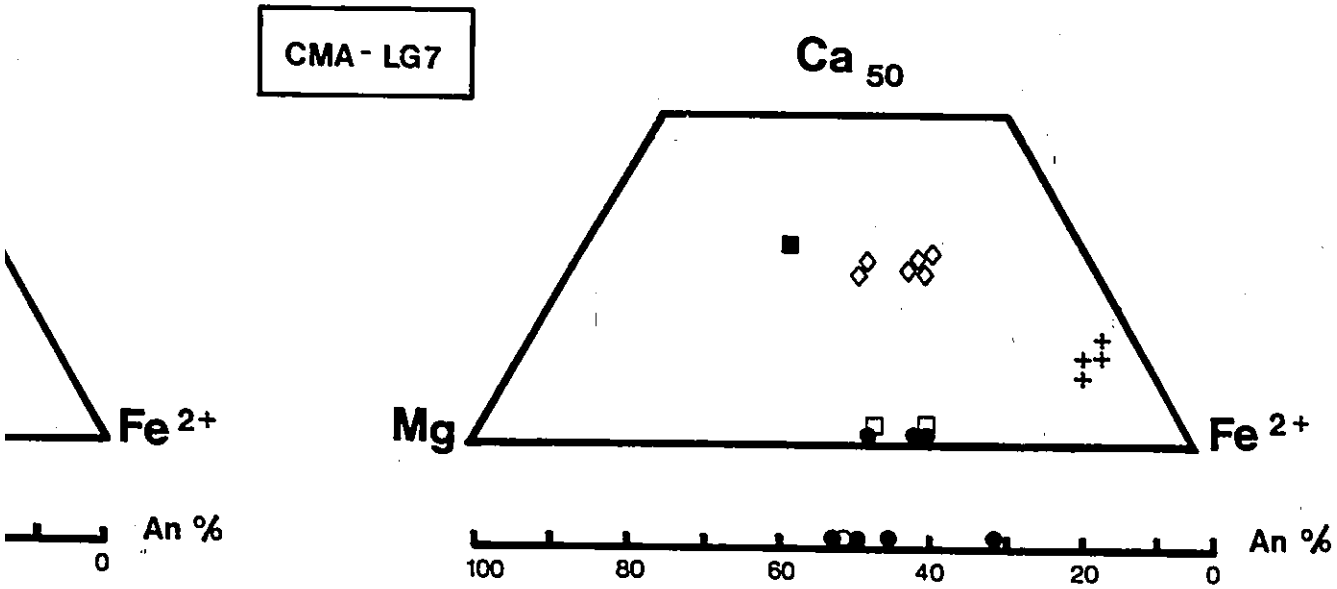
CMA - LG7
Ca 50
Mg
Fe 2+
Fe 2+
An %
0
100
80
60
40
20
0
An %

Figure 53c

CMA - M - R01a

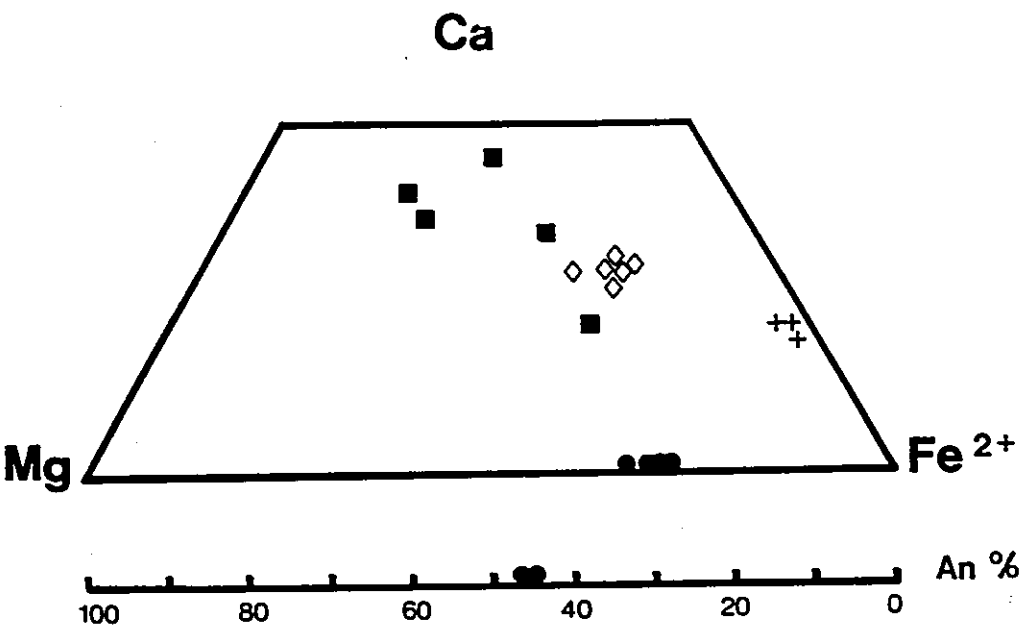

CMA - 146

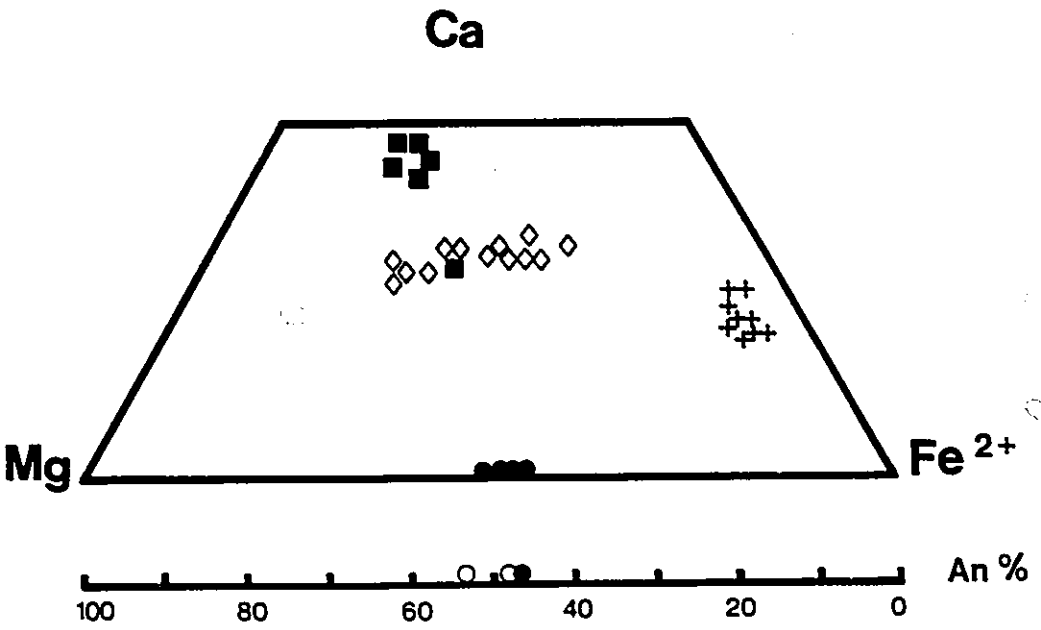

CMA - M - 015a

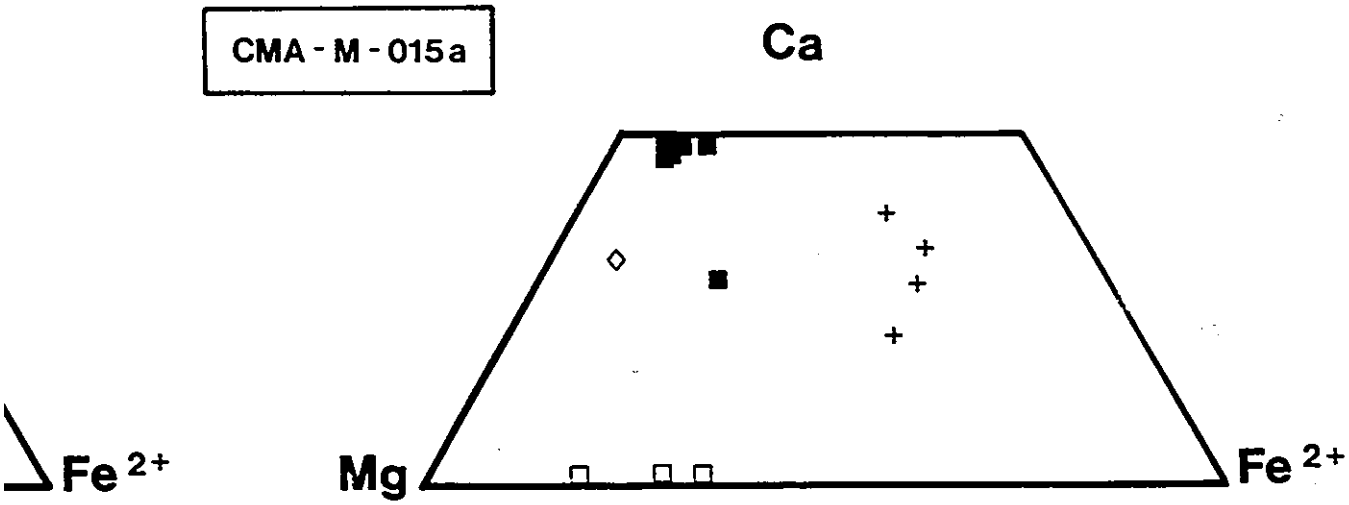

Fe 2+

An %

0

Fe 2+

An %

0

ORIGIN AND IMPLICATION OF CORONA STRUCTURES

6.1 INTRODUCTION

In this chapter, the petrographic observations of Chapter 3 and the mineral analyses presented in Chapter 5 will be used to examine and model the development of corona structures in the NNE diabase dykes. First, to facilitate this examination and modelling of corona structures, a review of the origin and development of corona formation, including the responsible variables and mechanisms, is presented. Finally, in combination with P-T estimate work, the physicochemical changes recorded by the corona structures will be used in an attempt to locate the P-T path (i.e. the reaction history) of the NNE diabase dykes. Ultimately, this can be related to the metamorphic conditions established elsewhere for the latter stages of the Grenvillian Orogeny.

6.2 ORIGIN AND DEVELOPMENT OF CORONA STRUCTURES

Corona structures are formed when two or more minerals are no longer stable together under the ambient conditions. The mechanism of corona formation is controversial, not well understood, and generally considered to be complex.

Many different origins have been proposed for corona

formation. Sederholm (1916) discussed this problem in terms of a secondary origin versus a primary magmatic origin. He concluded on textural grounds that corona formation is metamorphic (i.e. subsolidus) rather than magmatic. He favoured regional metamorphism over other types of metamorphism because of the widespread occurrence of corona structures in many different metamorphic terrains. Vogt (1921) suggested their formation as being a "deuteric" process, and Broegger (1934) also suggested a deuteric origin, but in a much broader sense. Later work by Shand (1945) and Murthy (1958) rejected this deuteric origin and suggested instead thermal metamorphism and regional metamorphism, respectively. Later, Griffin and Heir (1973) provided evidence that corona textures are the consequence of cooling from high-T conditions during constant or increasing pressure (i.e. subsolidus re-equilibration). Esbensen (1978) examined some coronites from Norway and concluded that corona formation was the result of extended magmatic cooling from high-T, possibly synchronous with regional metamorphism. Hence, the formation of coronas was one continuous process. Esbensen could not distinguish between a syn-to post-magmatic (i.e. deuteric) and a regional metamorphic process being responsible. Whitney and McLelland (1973) suggested a sequential growth origin for the garnet-bearing coronas of the Adirondacks. Mongkoltip and Ashworth (1983) examined some coronitic intrusions in NE Scotland from a physicochemical point of view. They concluded that the corona reactions took place during slow cooling within

retrograde conditions of regional metamorphism. However, Emslie (1983) and Whitney and McLelland (1983) argued that the time sequence of various corona reactions is difficult to establish with certainty. Hence, the conventional, favoured interpretation of corona development by regional metamorphism (i.e. either prograde or retrograde) is not conclusive. However, the consistent textural relationships observed in gabbros from high-grade metamorphic terranes have tended to support the general idea of a metamorphic origin for corona structures by reaction and exchange between solid olivine and plagioclase. This interpretation is strongly favoured by Grieve and Gittins (1975), Mork (1986), and Bhattacharyya and Mukherjee (1987). Furthermore, Mongkoltip and Ashworth (1983) and Nishiyama (1983) have pointed out that an inter-granular fluid (i.e. metamorphic) is a necessary catalyst for dissolution and reaction in corona development.

Griffin and Heier (1973) challenged earlier hypotheses of metamorphic origin and proposed that corona structures formed during post-emplacement cooling of a deep-seated body and that subsequent metamorphism would tend to destroy the delicate corona structure. This other alternative has been accepted by Gardner and Robins (1974), Johnson and Essene (1982), and Joesten (1986a), among others. Joesten (1986a) argued on the basis of textural evidence that some corona textures are of magmatic origin. He discussed the definition and the role of sequential and simultaneous growth in the formation of corona structures.

Simultaneous growth would be responsible for the early corona structure of orthopyroxene - amphibole and spinel - plagioclase around olivine, whereas sequential growth would be the cause of garnet-bearing corona layers. On this basis, Joesten (1986a) proposed a magmatic origin followed by annealing for the coronas from Risor, Norway. Ashworth (1986) replied vehemently to this interpretation of Joesten (1986a and 1986b) and proposed that the coronas in question are consistent with the widely accepted metamorphic origin.

An alternative to the igneous and metamorphic hypotheses is one that favours a combined igneous and metamorphic origin for corona structures (Esbensen, 1978; Emslie, 1983; Grant, 1988). This would involve a late magmatic crystallization and cooling stage (i.e. by interaction with a late residual melt or hydrous phase) for the formation of simple corona structures followed by a second more evolved metamorphic stage, which overprinted the earlier structure with a more complex corona structure consisting of metamorphic minerals.

Recently, Grant (1988) considered and evaluated the merits of the igneous and metamorphic origins for corona formation. She suggested a single stage subsolidus cooling mechanism for corona growth during cooling and subsequent high-grade metamorphism of the coronitic metagabbros. This hypothesis agrees with the single step cooling process from igneous temperatures, proposed earlier by Griffin and Heier (1973). However, Grant (1988) has not ruled out the prograde regional metamorphic origin for corona growth,

until some age dates become available. Emslie (1983) also suggested that isotopic dating of amphibole and biotite would help to confirm or reject one or the other of these hypotheses.

6.2.1 Mechanism(s) of corona formation

As mentioned above, the debate on whether the coronas represent an igneous history or a metamorphic phenomenon continues. Recent work by Joesten (1977, 1986a, and 1986b), Foster (1981), Mongkoltip and Ashworth (1983), Nishiyama (1983), and Grant (1988) has attempted to model the disequilibrium corona structures by use of irreversible thermodynamics. This work demonstrated that many factors are the cause of corona structures. These factors include:

1) pressure (P),
2) temperature (T),
3) P_{H2O},
4) the bulk composition of the system under consideration,
5) the chemical composition of the corona minerals and the primary minerals,
6) kinetics (i.e. reaction and diffusion kinetics) of the corona structure, and
7) the nature of the system (i.e. open or closed) under consideration.

The pressure, temperature and P_{H2O} conditions would control the stability fields of the mineral phases of the corona structure.

Temperature and pressure appear to be the two most important factors controlling the growth of corona structures. They contribute to the stability fields of the mineral phases of the corona structure. Vernon (1976) discussed the influence of physical conditions on the morphology of corona structures. Emplacement of the gabbros at shallow depth does not permit the formation of corona structures, whereas emplacement at intermediate and great depths will tend to produce spherulitic and granular corona structures, respectively. The depth of emplacement of diabase dykes is regarded as an important factor in controlling the mineralogy of corona structures. Whitney and McLelland (1978) observed the development of spinel symplectite layers (amphibole and spinel) around olivine in basic rocks from the Adirondack Lowlands (estimated pressure of 6-7 kbars) and the presence of garnet shells around olivine in similar rocks from the Adirondack Highlands (estimated pressure of 7-8 kbars). The garnet shells around olivine indicate emplacement at greater depths, and suggest that the rock never entered the spinel stability field or the rock passed through it and re-equilibrated. If spinel was once present, then upon entering the garnet stability field, the spinel symplectite assemblage would become unstable and breakdown to garnet.

The fluid phase would control the reaction rates of minerals, hence the development of corona structures. Water is an important factor which can greatly control the reaction rates of minerals, and hence the growth of minerals. Water is an excellent catalyst

which can speed up the reactions, which are otherwise extremely slow. The absence of water may arrest the formation of coronas, so that each corona layer may represent a new supply of H_2O. The compositions of the primary minerals (i.e. reactants) and corona minerals (i.e. products or later on as reactants) are needed in order to establish and understand the variation in bulk composition across the corona structure. Recent work on coronas shows that the composition of the corona minerals have a certain interdependence to the composition of the primary minerals. This interdependence is complex and not fully understood, but is somewhat ordered, since the concentrations of oxides vary in a systematic, stepwise fashion across the corona structure (Grant, 1988). The corona structure probably represents a series of mineral phases that were in equilibrium at a particular point or increment in time. Therefore, the corona structure is a reaction zone that records the increments of changes in compositional gradients produced and controlled by the reaction and diffusion kinetics of the system.

For example, the early reaction of olivine and plagioclase results in a double layered corona structure consisting of orthopyroxene and pargasite plus spinel. This corona structure and other types are interpreted as disequilibrium textures (Barker, 1990; among others) which formed as a result of different elements diffusing along chemical potential gradients in an attempt to maintain local equilibrium between adjacent minerals by eliminating incompatibilities. The resulting product

is composed of a two layer mineral assemblage in which each layer is in equilibrium with the layer and mineral bounding it. These reaction layers (i.e. reaction zones) record in part (possibly reset) the increments of changes in compositional gradients produced and controlled by the reaction and diffusion kinetics of the system.

Presently, most workers regard the great variety of corona structures as products of high-temperature subsolidus re-equilibration (meta-stable --> stable) during changing physicochemical conditions. It is generally considered that the growth of coronas is highly diffusion-controlled. Vernon (1976) proposed that the rate of diffusion is the major controlling factor responsible for growth of corona structures. It is known that this diffusion-controlled growth mechanism varies with pressure, temperature, and water activity, and is possibly initiated during cooling from magmatic temperatures. Later growth (i.e. reactions) is complex and multistage with the diffusion-controlled mechanism of corona formation being under the influence of amphibolite or granulite facies conditions (either <u>retrograde</u> or prograde). The next section (6.2.2) will review the diffusion and reaction conditions of this corona growth mechanism.

Determination of corona structure reactions invariably leads to the question of open versus closed systems. For instance, a closed system would imply no transfer of matter into or out of the system. Hence, the corona structure would be considered as an

isochemical system (i.e. closed with element migration only between the reactant minerals (e.g. olivine and plagioclase) and their products of the corona structure). Alternatively, the system could be open, thus permitting the introduction of components transported over large distances. A more realistic approach would be a hybrid of the two mentioned above, in which one considers the system in terms of partial ionic (open system) reactions taking place at the site(s) of the mineral(s) in question. The ions produced by the partial ionic reactions in one part of the corona structure would be consumed elsewhere in the corona structure. The result in the sum of the different partial ionic reactions would yield mass-balanced reactions, hence in essence closed system reactions (Rivers and Mengel, 1988). This concept has been confirmed by Kretz et al. (1989) who concluded that corona reactions behave essentially as closed systems, except for volatiles such as F and Cl.

6.2.2 Diffusion And Reaction Conditions (i.e. thermodynamics) Of Corona Formation

If coronas form by subsolidus reaction and mass transport (i.e. ion exchange) between primary minerals (and their products; i.e. reactant dissolution and/or product absorption), then the conditions of diffusion and reaction are the most important factors of corona formation. More explicitly, the rate-determining factors of corona formation, according to Fisher

(1977), are:

1) the diffusion of chemical components between two reactants in which the diffusive flux of the slowest diffusing chemical component controls the reaction rate, and
2) the rate of reaction or chemical potential gradient at each interface or reaction boundary.

The rate of reaction is a function of the differences (i.e. relative chemical potential) between the diffusive fluxes of each of the chemical components on each side of the reaction interface. Therefore, the change in concentration at the reaction interface of a given component results from the difference between its rate of production and its net loss by diffusion. It is the slowest of these two processes (diffusion or reaction rates) that determines the rate of consumption and production of a component at an interface, and ultimately controls the overall rate of reaction. Hence, each corona layer grows concurrently within a set of diffusion-controlled reactions at their respective reaction interfaces. Therefore, adjacent layers are linked by diffusing components that are added or subtracted in the proportions necessary for re-equilibration and growth of the corona structure.

The spatial organization of corona structures indicates that the diffusion rate(s) is the principal controlling variable for corona growth. A large diffusion coefficient would tend to eliminate chemical potential gradients and then nucleation could occur at any suitable low energy sites, hence inhibiting the

formation of corona structures.

The diffusion of Al and Si is also considered to be a major controlling factor on corona nucleation and growth. The restricted mobility of Al has the effect of controlling the nucleation of garnet within aluminum-rich phases such as plagioclase or amphibole-spinel symplectites. Also, the occurrence of spinel-clouded plagioclase is similarly explained by the relative immobility of Al and Si in plagioclase. When the diffusion paths become too long and the chemical potential gradients too low to drive significant diffusion, the growth of corona structures will slow down and eventually stop. A drop in temperature inhibits diffusion and may be important in arresting corona growth and allowing corona structures to persist metastably during subsolidus cooling from magmatic temperatures. In some cases, H_2O or H^+ is needed and the reaction could be controlled or arrested by the availability of H^+.

According to Joesten (1977) and Fisher (1977), each corona structure can be modelled quantitatively by solving an algebraic system of linear mass balance, conservation, and flux ratio equations. These equations describe the diffusion-controlled growth of corona structures, and are based solely on the reaction components and the ratios of the Onsager diffusion coefficients. Each corona layer interface has a ratio of chemical potential gradients which is solved by the Gibbs-Duhem equations for each component. Therefore, the mass-balance chemical reaction at each interface is a function of the ratio of the Onsager diffusion

constants (Joesten, 1977).

Nishiyama (1983) and Grant (1988) have excellently reviewed the essential features, constraints, and assumptions of the steady state diffusion model that is used in simulating the formation of corona structures. It is necessary to make several assumptions when using the steady state diffusion model to simulate disequilibrium corona structures, and these are:

1) the chemical reactions involved in forming corona structures occur in a steady state,
2) the corona layer interfaces were filled with an intergranular fluid (most likely H_2O),
3) the chemical reactions do not take place within the corona layers, but only occur at the interfaces (i.e. no volume diffusion),
4) the steady state system operates within a condition of minimum entropy production,
5) the steady state system is not far from equilibrium, hence a low energy level. The system tends to approach as closely as possible the reversible state. Therefore, near equilibrium, there is a linear relationship between the chemical potential gradient and flux of each component,
6) diffusion is limited within corona layers (i.e. volume diffusion),
7) input of energy is needed to overcome the activation energy barriers of chemical reactions,
8) the growth of corona structures will stop when diffusion

paths of chemical components become too long and chemical potential gradients become extremely small for generating significant amounts of diffusion,

9) the diffusion coefficients vary exponentially with temperature, but over the temperature interval of the corona structure this effect is considered negligible,
10) the mass-balance equations require an overall fixed proportion of mineral phases,
11) the steady state system is essentially closed,
12) the possibility of up-hill diffusion, and
13) the observed proportions of mineral phases constrain Onsager coefficients of diffusion (or phenomenological coefficients, L_{ij}).

Some of the more important observations from these studies using the steady state diffusion model (Foster, 1981; Nishiyama, 1983; Joesten, 1986a and 1986b; Grant, 1988) are:

1) in simple models, Fe and Mg diffuse down chemical potential gradients from olivine towards plagioclase, and Si minor amounts of Al, Ca, Na diffuse down chemical potential gradients from plagioclase toward olivine. However, each of the elements has different diffusion paths,
2) chemical reactions and exchange are favoured at layer boundaries (interfaces) where chemical potential gradients and structural disorder are the most significant (i.e. at the interface of minerals that differ greatly in

composition),

3) models solve only for reactions at layer boundaries, since diffusion (D) is much faster and takes less activation energy (Q) along grain surfaces and boundaries than within corona layers (volume diffusion). However, these differences become negligible at very high temperatures,
4) the diffusion coefficients of chemical components are small and rate-determining within corona structures,
5) the overall rate of corona reactions is a function of extremely small increments of change(s) in chemical potential gradients, which in turn are produced and controlled by the reaction and diffusion kinetics of the system under examination,
6) the stability of each layer within a corona structure is controlled by the relative magnitude of the Onsager diffusion coefficient, and this can be expressed on a L (phenomenological coefficient)-ratio diagram,
7) the relative abundance of Al across corona structures is ordered and decreases in a step-like manner (Grant, 1988).
8) the ratio of Al:Si varies in a systematic fashion across corona structures (Grant, 1988),
9) Al and Si are extremely immobile (i.e. have short diffusion paths), and therefore, are rate-determining for corona structures and symplectites (Mongkoltip and Ashworth, 1983; Grant, 1988),
10) symplectites, in general, are an important textural

component of corona structures. As pointed out by Mongkoltip and Ashworth (1983) an understanding of symplectites is necessary to interpret the formation of corona structures,

11) according to Nishiyama (1983), the relative magnitude of L_{MgMg} and L_{AlAl} is the most important rate-controlling factor for corona structures,

12) at least two chemical components must have limited diffusion ranges,

13) Mg and Fe must have similar mobility. Up-hill diffusion possibly explains Ca diffusion. Na has little effect on corona stability. Mg must be as mobile, possibly more, as Ca. The value of L_{MgMg}/L_{AlAl} is highly dependent on the composition of reacting plagioclase (Grant, 1988),

14) corona structures vary from "diffusionally unstable" to "diffusionally stable"; suggestive of a magmatic origin (Joesten, 1986), and

15) corona formation has either:

    a) a retrograde, regional metamorphic origin (Nishiyama, 1983; Mongkoltip and Ashworth, 1983),

    b) a prograde, regional metamorphic origin,

    b) a magmatic origin (Joesten, 1986a), or

    c) a single stage subsolidus origin from magmatic temperatures (Grant, 1988).

Some problems and restrictions exist with using the steady state diffusion models, and these may be the cause of the

controversy over the origin of corona structures. Some of the problems and restrictions are:

1) inaccurate volume estimates of the proportions of corona layers and minerals,
2) the assumption of a closed system. Mongkoltip and Ashworth (1983) pointed out that the growth of symplectites is not restricted to closed systems, and this is probably true for corona structures. They showed all the possibilities of symplectite growth within closed and open systems (Fig. 1, after Fig. 2 of Mongkoltip and Ashworth, 1983, p. 638). Hence, more assumptions are needed for the steady state diffusion models (i.e. possibly an incremental model to accomodate an open system) like changing the ratios of Al:Si or the activity of H_2O or the introduction of other chemical components,
3) the ratios of diffusion coefficients are possibly not constant over the whole temperature interval of corona formation,
4) the rates of reaction (nucleation/growth) become rate-determining, instead of diffusion,
5) other properties, such as surface energy or surface reaction rates or local stresses (growth of new phases will cause stresses around these phases), will alter equilibria, and produce effects on diffusion kinetics, chemical reactions, and resulting textures, and
6) volume diffusion, grain boundary migration, and volume

changes, most likely, are important in corona formation, as in symplectites (Mongkoltip and Ashworth, 1983), and should be incorporated into the steady state diffusion model.

6.3 CORONA REACTIONS IN THE NNE DIABASE DYKES

A multitude of corona reactions have been investigated by several workers (Kretz et al., 1989; among others) in order to explain the different types of corona structures. It should be noted here that none of the earlier studies (before Kretz et al., 1989) succeeded in defining a local balance for most elements, and this has been a perplexing problem in understanding corona structures. Several of these reactions are examined herein using the mineral analyses presented in Chapter 5. Each corona reaction will be presented and discussed separately, and then they will be discussed together in order to reconstruct the evolutionary path of the corona reactions and their resulting corona structures.

6.3.1 Olivine Corona Structure (double layer)

Reaction zones consisting of orthopyroxene, light green amphibole, and spinel are observed between grains of olivine and calcic plagioclase in the best preserved diabase dykes from along the Grenville Front (northeastern part of study area). The

reaction considered responsible for these reaction zones is:

olivine + plagioclase --> orthopyroxene + amphibole ±
spinel ± corundum

This reaction is always accompanied by the alteration of olivine to serpentine and iddingsite. The relative timing of the formation of serpentine and iddingsite is not conclusive on textural grounds, but it is known that hydrothermal alteration of ferromagnesian minerals produces serpentine below 400-500°C. Therefore, the serpentine and iddingsite most likely formed late, but why did the orthopyroxene not also alter to bastite at the same time. The above mentioned equation implies hydration of the igneous assemblage under hornblende granulite facies conditions (Rivers and Mengel, 1988). Table 8 presents analyses of the mineral phases involved in the reaction and Figure 54 gives the location of probe analyses across the corona structure under consideration. The probe analysis of spinel was taken from Grieve and Gittins (1975), and is considered to be representative on the basis of similar mineral chemistry in sample MG-101A of Grieve and Gittins and in sample CMA-LA18 of this study.

A balanced equation was calculated using independant end-members of plagioclase and olivine as reactants, and this is as follows:

$$(1)\ 6.67\ \underset{\text{Olivine}}{(Mg_{1.20}Fe_{0.80})Si_{1.02}O_4} + 1.80\ \underset{\text{Anorthite}}{(CaAl_2Si_2O_8)} + 0.98\ \underset{\text{Albite}}{(NaAlSi_3O_8)} +$$

$$0.003\ \underset{\text{Orthoclase}}{(KAlSi_3O_8)} + [0.128\ K + 0.02\ Ti + 0.065\ Mn] + H_2O$$

$$\longrightarrow 1.00\ (Na_{0.98}K_{0.13})Ca_{1.80}(Fe_{2.02}Mg_{2.52}Mn_{0.04}Ti_{0.02}Al_{0.93})Al_{2.31}Si_{5.69}O_{22}(OH,Cl)_2 +$$

Pargasite

$$7.93\ (Fe_{0.37}Mg_{0.68}Mn_{0.007}Ca_{0.002})Al_{0.001}Si_{0.98}O_3 +$$

Orthopyroxene

$$0.503\ (Fe_{0.66}Mg_{0.34}Mn_{0.02})(Al_{1.90}Fe_{0.10})O_4 + 0.19\ Al_2O_3$$

Spinel Corundum

Plagioclase reacting with olivine contains small amount of spinel and corundum inclusions. The volume proportion of spinel to corundum is estimated to be 3:2 on the basis of thin section observations. This observation suggests the production of corundum in reaction (1). Also note that some Fe is oxidized in this reaction.

The composition of plagioclase required by the equation is estimated to be An_{65}. This is higher than the actual composition of An_{60} which implies that the original composition of plagioclase was approximately An_{63}. This slight deviation may explain the presence of normal zoning in plagioclase grains adjacent to the olivine corona structure. The analyzed olivine composition is approximately Fo_{53}. This is noticeably lower than the Fo_{60} value calculated from the balanced equation, which suggests that the original olivine composition was approximately Fo_{57}. The X_{Mg} (Mg/(Mg+Fe)) of reactant olivine (0.600) is characteristically lower than that of orthopyroxene (X_{Mg} = 0.68) but similar to that of pargasite (X_{Mg} = 0.555). This indicates that the extraction of Fe was slightly greater than Mg in olivine. The X_{Al} (Al/(Al+Si) of hornblende (X_{Al} = 0.364) in the olivine corona structure is similar to that of the adjacent

LEGEND FOR TABLES 8 TO 13

Pl = plagioclase
Amp = amphibole
Opx = orthopyroxene
Cpx = clinopyroxene
Ilm = ilmenite
Grt = garnet
Bt = biotite
Ol = olivine
Spl = spinel

Box = Mineral analyses used in the reaction calculation

$Fe_T = Fe^{2+} + Fe^{3+}$
$FeMg = Fe^{2+}/(Fe^{2+} + Mg)$
$XCa_1 = Ca/(Ca + Fe^{2+} + Mg)$
$XCa_2 = Ca/(Ca + Na)$
XAl = Al/(Al + Si)
XNa = Na/(Na + Ca)

Table 8. Mineral chemistry across olivine corona structure from sample CMA-LA18

	Pl 1	Pl 2	Amp 3	Amp 4	Amp 5	Opx 6	Ol 7	Ol 8	Ol 9	Opx 11	Amp 12	Amp 13	Amp 14	Pl 15	Spl MG-101A
SiO_2	52.84	52.24	38.44	38.87	35.23	53.43	36.20	35.34	35.60	52.71	36.17	38.51	38.15	52.47	-
TiO_2	-	-	0.05	0.18	0.02	0.09	-	-	-	-	0.09	0.2	0.02	-	-
Al_2O_3	28.29	28.51	19.98	18.83	21.50	0.05	-	-	-	-	20.37	19.45	21.32	28.63	-
Cr_2O_3	-	-	0.05	0.07	-	-	-	-	-	0.02	-	-	0.09	0.08	-
Fe_2O_3	-	-	4.60	4.24	4.30	2.55	-	-	-	4.06	4.56	4.98	5.06	-	-
FeO	0.19	0.32	9.65	8.90	9.04	19.38	39.71	39.47	39.97	18.87	9.58	10.45	10.63	0.16	-
MgO	-	-	0.25	0.31	0.01	0.45	0.28	-	-	0.59	0.16	0.1	0.12	-	-
MnO	-	-	10.20	11.56	13.45	24.64	24.98	24.72	24.11	24.32	12.63	10.75	7.89	-	-
CaO	12.53	12.39	10.80	11.49	9.86	0.10	0.02	-	-	0.14	10.69	11.04	11.52	12.43	-
Na_2O	5.67	5.55	4.06	3.46	3.42	-	-	-	-	-	3.72	3.61	2.08	5.14	-
K_2O	0.19	0.06	0.32	0.70	0.48	-	-	-	-	0.01	0.57	0.8	1.13	0.15	-
Total	99.71	99.07	98.40	98.61	97.31	100.61	100.89	99.53	99.68	100.72	98.54	99.98	98	98.98	-
Si^{4+}	9.668	9.616	5.641	5.686	5.222	1.964	1.018	1.008	1.017	1.944	5.332	5.602	5.637	9.645	0.020
Ti^{4+}	0.006	0.020	0.002	0.003	-	-	-	-	-	-	0.01	0.022	0.002	-	-
Al^{3+}	6.100	6.185	3.456	3.247	3.756	0.002	0.005	-	-	-	3.539	3.334	3.713	6.203	1.903
Cr^{3+}	0.006	0.008	-	-	-	-	-	-	-	0.001	-	0.01	0.009	-	-
Fe^{3+}	3.000	0.508	0.467	0.480	0.071	1.563	-	-	-	0.113	0.506	0.545	0.563	-	-
Fe^{2+}	2.000	0.029	0.049	1.184	1.089	1.121	0.596	0.934	0.941	0.582	1.181	1.271	1.314	0.025	0.710
Mn^{2+}	0.031	0.038	0.001	0.014	0.009	-	-	-	-	0.018	0.02	0.012	0.015	-	0.020
Mg^{2+}	2.231	2.521	2.972	1.350	1.048	1.051	1.027	0.933	-	1.337	2.775	2.331	1.738	-	0.394
Ca^{2+}	2.456	2.444	1.698	1.801	1.566	0.004	0.001	-	-	0.006	1.688	1.721	1.833	2.448	-
Na^{+}	2.011	1.981	1.155	0.981	0.983	-	-	-	-	-	1.063	1.018	0.596	1.832	-
K^{+}	0.044	0.014	0.060	0.131	0.091	-	-	-	-	0.000	0.107	0.148	0.213	0.035	-
Total	20.310	20.290	15.980	15.990	16.190	4.000	3.000	3.000	3.000	4.000	16.220	16.010	15.63	20.19	3.05
Fe_T	-	-	1.44	1.32	1.36	0.63	-	-	-	0.64	1.43	1.54	1.59	-	-
FeMg	-	-	0.39	0.34	0.31	0.32	0.47	0.47	0.48	0.32	0.34	0.4	0.48	-	0.45
XCa_1	1.00	0.32	0.32	0.27	0.00	0.00	-	-	-	-	0.29	0.31	0.35	-	-
XCa_2	2.00	0.55	0.55	-	-	-	-	-	-	-	-	-	-	0.57	-
XAl	0.38	0.36	0.42	-	-	-	-	-	-	-	0.4	0.37	0.4	-	-
XNa	0.40	0.35	0.39	-	-	-	-	-	-	-	0.39	0.37	0.25	-	-

Fig. 54

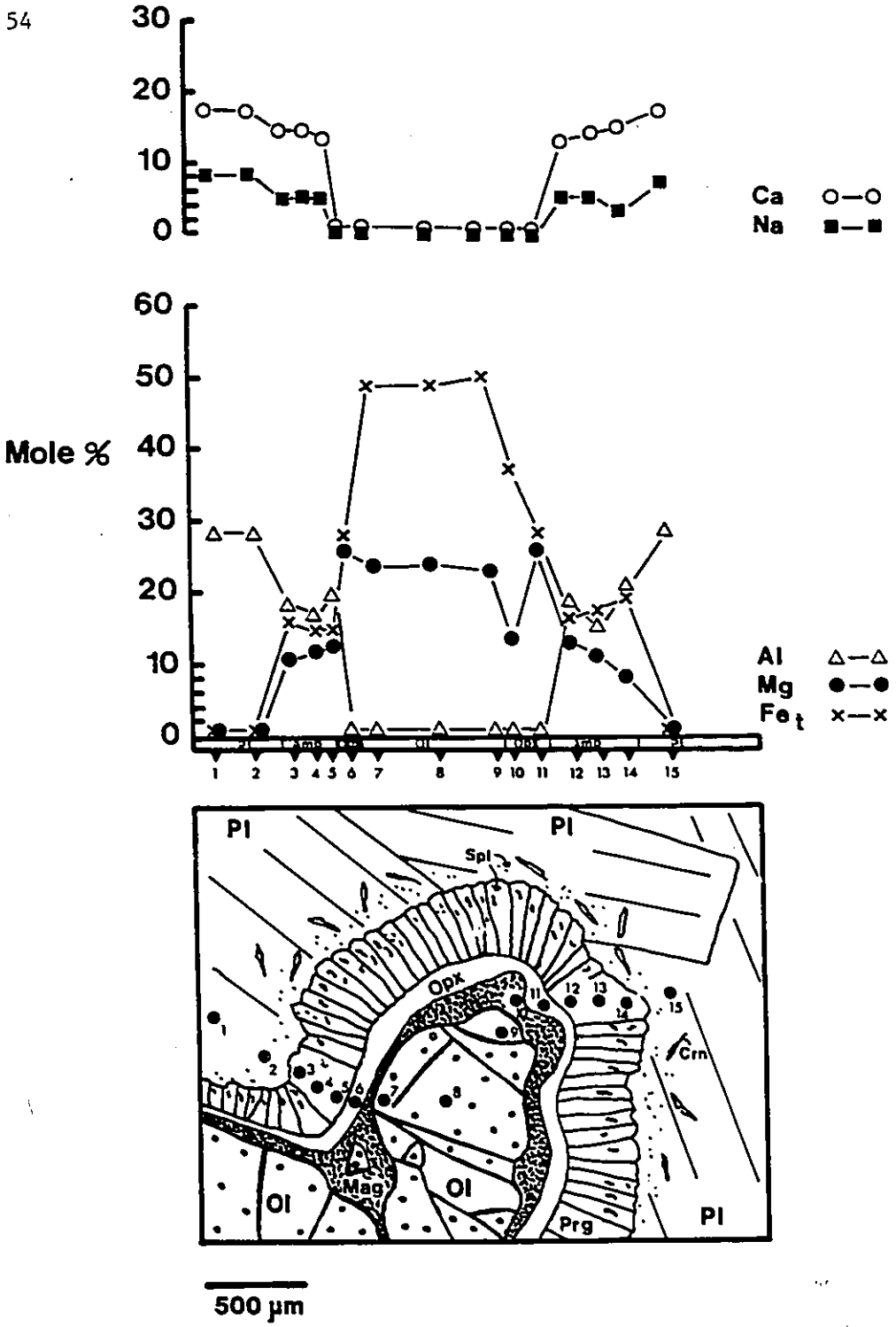

CMA - LA 18 - 87

plagioclase grains.

Equation (1) requires the introduction of elements such as K, Ti, Mn, Cl, and H but the source (i.e. adjacent mineral phases and/or fluids) and transport distance of these elements is not known.

A similar satisfactorily balanced equation was obtained in sample CMA-27.6.5, but with no spinel in the product. An acceptable balance required only the production of corundum. This agrees with petrographic observations in that no spinel inclusions are present in the hornblende corona layer and abundant corundum plates are present in the plagioclase grains next to the corona structure.

6.3.2 Orthopyroxene - Magnetite Symplectite-cored Corona Structure

The occurrence of an orthopyroxene-magnetite intergrowth replacing the olivine grain within an olivine corona structure and the depletion of Fe in the degenerating olivine grain suggests the breakdown of the olivine core by an oxidation such as:

olivine + O_2 ---> orthopyroxene + magnetite

The orthopyroxene-magnetite intergrowth is typically surrounded by the corona layers common to the normal olivine corona structure (i.e. corona layers composed of orthopyroxene and

pargasite). This suggests that the oxidation reaction occurred simultaneously with or sometime after the formation of the olivine corona structure (shown in Figure 55). This reaction requires the removal of the fayalite component from olivine and the extensive oxidation of Fe^{2+}. This would explain the presence of ferric iron in pargasite and possibly spinel. The mineral analyses of sample CMA-LGY are given in Table 9. The balanced equation using these data is:

$$(2)\ 1.03\ (\underset{\text{Olivine}}{Mg_{0.502}Fe_{1.498}})SiO_4 + 0.238\ O_2 + [0.005\ Mn + 0.008\ Ca]$$

$$\rightarrow 1.00\ (\underset{\text{Orthopyroxene}}{Mg_{0.517}Fe_{0.438}Mn_{0.005}Ca_{0.008}})Si_{1.031}O_3 + 0.369\ (\underset{\text{Magnetite}}{Fe_3O_4})$$

The olivine composition required by the equation is X_{Mg} = 0.250 (Fo_{25}), whereas the analyzed olivine composition is X_{Mg} = 0.470 (Fo_{47}). This suggests that the original composition of olivine was approximately X_{Mg} = 0.360.

An acceptable balanced equation for this reaction was also obtained in sample CMA-LG6. Rivers and Mengel (1988) surmised that the oxidation reaction of fayalite plus O_2 yielding magnetite plus quartz explains the presence of magnetite at the grain boundaries of olivine grains. The quartz that is produced would be subsequently consumed in the above mentioned olivine corona reaction (1). According to Rivers and Mengel (1988), the oxidation reaction would be a necessary ingredient for initiating the olivine corona reaction (1).

A single reaction has been proposed initially to explain the

Table 9. Mineral chemistry across orthopyroxene-magnetite symplectite corona structure from sample CMA-LGY

	Ol	Pl 1	Pl 2	Pl 3	Amp 4	Opx 5	Amp 7
SiO_2	-	53.59	52.26	53.99	38.91	52.53	39.15
TiO_2	-	-	-	-	0.09	0.05	-
Al_2O_3	-	27.89	28.98	27.84	18.16	0.76	18.11
Cr_2O_3	-	-	-	-	-	0.09	0.02
Fe_2O_3	-	-	-	-	6.57	-	5.83
FeO	-	0.31	0.38	0.24	13.79	26.43	12.24
MnO	-	-	-	-	0.23	0.50	0.16
MgO	-	-	-	-	8.47	17.42	8.69
CaO	-	11.66	12.82	11.38	8.15	0.64	10.64
Na_2O	-	6.14	5.45	6.06	3.59	3.25	-
K_2O	-	0.11	0.14	0.09	0.58	0.67	-
Total	-	99.70	100.03	99.60	98.54	98.42	98.86
Si^{4+}	1.001	9.785	9.546	9.843	5.796	2.046	5.795
Ti^{4+}	-	-	-	-	0.010	0.001	0.011
Al^{3+}	-	6.002	6.239	5.982	3.188	0.035	3.160
Cr^{3+}	-	-	-	-	-	0.003	0.002
Fe^{3+}	-	-	-	-	0.736	-	0.649
Fe^{2+}	1.049	0.047	0.058	0.037	1.718	0.861	1.515
Mn^{2+}	-	-	-	-	0.029	0.016	0.020
Mg^{2+}	0.948	-	-	-	1.881	1.011	1.918
Ca^{2+}	-	2.281	2.509	2.223	1.301	0.027	1.688
Na^{+}	-	2.174	1.930	2.142	1.037	-	0.933
K^{+}	-	0.026	0.033	0.021	0.110	-	0.127
Total	-	20.310	20.320	20.250	15.810	4.000	15.820
FeT	-	-	-	-	2.09	0.86	1.84
FeMg	0.53	-	-	-	0.53	0.46	0.49
XCa_1	-	-	-	-	0.25	-	0.31
XCa_2	-	0.51	0.57	0.51	-	-	-
XAl	-	-	-	-	0.35	-	0.35
XNa	-	-	-	-	0.44	-	0.36

Fig. 55

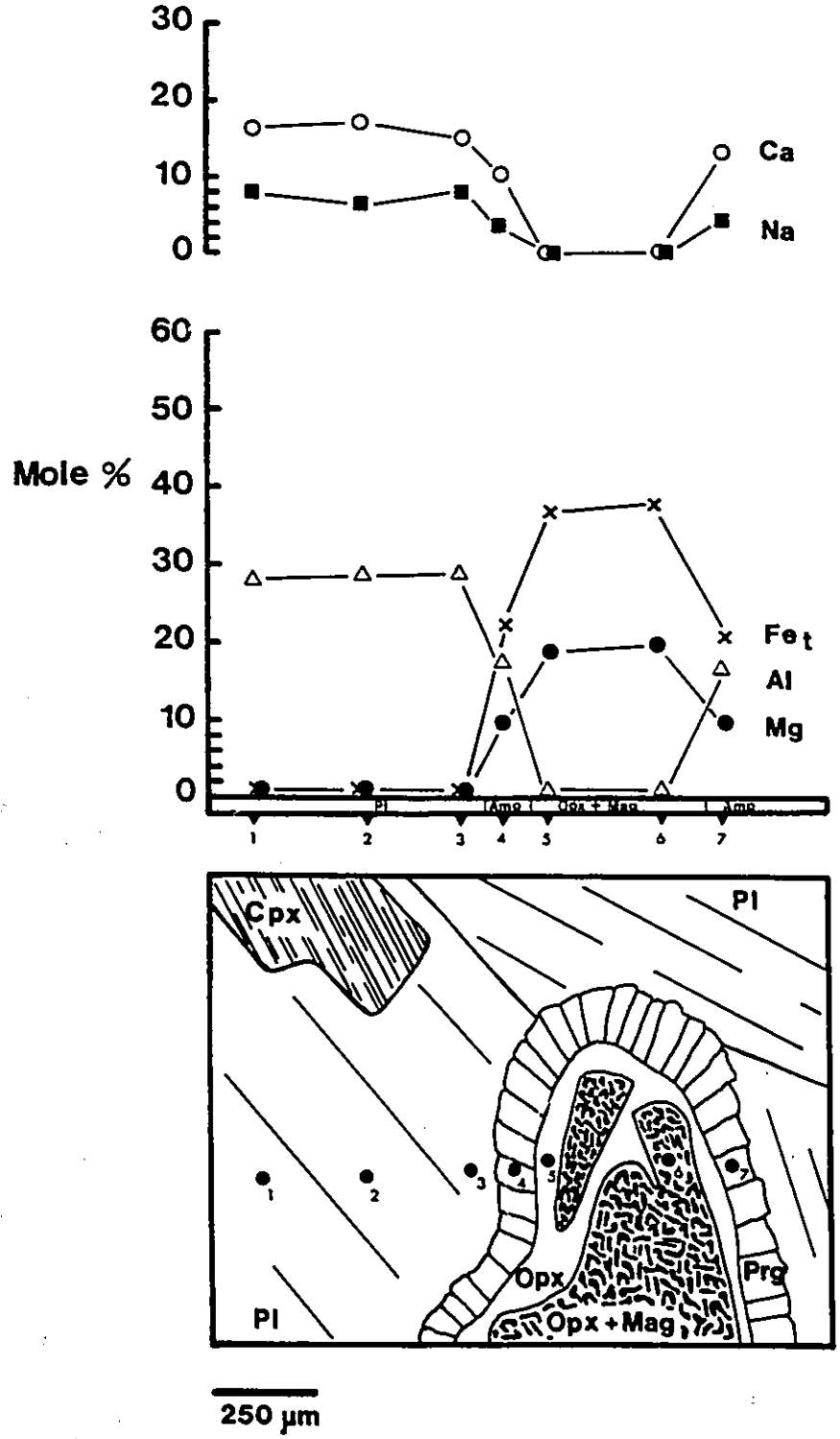

CMA - LGY - 87

presence of orthopyroxene-pargasite double corona layers and orthopyroxene-magnetite intergrcwth. However, a suitably balanced equation could not be derived and therefore two reaction stages are necessary to produce the mineral assemblage (products) observed in thin section. It is also proposed that reactions (1) and (2) are interdependant and that the observed corona structures are the final product of nucleation and growth of crystals via a complex series of diffusive mass-transfer reactions.

Barton and Van Gaans (1988) proposed different hypotheses to explain the formation of orthopyroxene and titaniferrous magnetite intergrowth. Based on petrologic and textural evidence, they were not able to reproduce this texture solely from the olivine corona reaction. They suggested that the occurence of orthopyroxene and Fe-Ti oxide symplectite was the result of olivine re-equilibration and that the presence of orthomagmatic Fe-Ti oxide and diffusion mechanism were crucial for the development of this texture. They concluded that orthopyroxene and Fe-Ti oxide would form during subsolidus re-equilibration of the original magmatic assemblage under high-grade retrogressive metamorphic condition.

6.3.3 Olivine Corona Structure (triple layer)

The presence of small anhedral garnet crystals nucleating in the pargasite and spinel corona layer has been observed in sample

CMA-27.6.5 (Fig. 56). Mineral analyses used in this reaction are given in Table 10. The modelled balanced reaction for this corona structure is:

$$(3)\ 6.60\ \underset{\text{Plagioclase}}{(Ca_{0.84}Na_{0.16})Al_{1.60}Si_{2.43}O_8} + 10.15\ \underset{\text{Olivine}}{(Fe_{1.39}Mg_{0.61})Si_1O_4} + 3.07\ \underset{\text{Corundum}}{Al_2O_3} +$$

$$1.33\ \underset{\text{Orthopyroxene}}{(Fe_{0.38}Mg_{0.61}Mn_{0.001}Ca_{0.004}Al_{0.02})Si_{0.98}O_3} + [\ 0.24\ K + 0.03\ Ti + 0.49\ Mn + H + Cl\ ]$$

$$\text{---> } 1.00\ \underset{\text{Pargasite}}{(K_{0.24}Na_{1.04})Ca_{1.73}(Fe_{2.33}Mg_{2.48}Ti_{0.02}Al_{0.82})Al_{2.33}Si_{5.67}O_{22}(OH,Cl)_2} +$$

$$6.95\ \underset{\text{Garnet}}{(Ca_{0.56}Fe_{1.81}Mg_{0.67}Ti_{0.001}Mn_{0.07})Al_{1.99}Si_{2.95}O_{12}}$$

This reaction is balanced for most major cations. This reaction involves the introduction of K, Ti, Mn, and H or H_2O. The composition of plagioclase required by the reaction is An_{84} which is much higher than the actual plagioclase composition of An_{61}. The plagioclase calculated from the reaction represents the selective removal of anorthite component from the plagioclase crystal. The olivine composition calculated from this equation is Fo_{31} which is much lower than the analyzed composition of Fo_{47}. This suggests that the original olivine composition was approximately Fo_{39}. The X_{Mg} of reactant orthopyroxene is 0.62, whereas the X_{Mg} of pargasite and garnet are 0.48 and 0.27, respectively. The X_{Al} ratio of reactant plagioclase (0.40) is similar to that of hornblende (0.36) and garnet (0.40), whereas the X_{Ca} of plagioclase (0.84) is much higher than the X_{Ca} ratio of pargasite (0.62). The equation (3) involves the consumption of corundum but there is no distinct petrographic evidence for decreasing amounts of corundum plates in the reactant plagioclase

Table 10. Mineral chemistry across olivine corona structure from sample CMA-27.6.5

	Pl 1	Pl 2	Grt 4	Amp 6	Amp 7	Amp 8	Ol 12	Ol 14	Opx 15	Opx 16	Amp 17
SiO_2	54.64	54.82	38.08	37.72	41.30	42.89	34.74	34.61	52.74	52.03	39.24
TiO_2	-	-	0.04	0.10	0.28	0.03	-	-	-	0.04	0.12
Al_2O_3	30.40	29.69	21.47	18.23	14.72	16.29	-	-	0.30	0.57	18.17
Cr_2O_3	-	-	0.10	-	0.03	0.05	-	-	-	0.02	-
Fe_2O_3	-	-	0.89	4.17	4.58	0.00	-	-	-	0.00	4.88
FeO	0.65	0.77	25.87	9.47	8.76	9.63	43.83	43.87	23.76	24.08	10.26
MnO	-	-	1.16	0.15	-	0.04	-	-	0.25	0.32	-
MgO	-	-	5.87	11.21	12.82	12.33	22.74	22.29	22.95	22.62	10.94
CaO	11.90	11.26	6.71	10.57	11.36	11.64	-	-	-	0.26	11.01
Na_2O	3.59	3.97	-	3.73	3.68	0.58	-	-	0.10	0.38	3.52
K_2O	0.54	0.44	-	0.75	1.06	0.01	-	-	-	-	1.50
Total	101.72	100.95	100.19	96.10	98.59	93.49	101.31	100.77	100.10	100.32	99.64
Si^{4+}	9.706	9.802	5.926	5.665	6.070	6.051	0.992	0.995	1.970	1.952	5.736
Ti^{4+}	-	-	0.005	0.011	0.031	0.003	-	-	-	0.001	0.013
Al^{3+}	6.365	6.257	3.938	3.227	2.550	2.708	-	-	0.013	0.025	3.130
Cr^{3+}	-	-	0.012	-	0.003	0.006	-	-	-	0.001	-
Fe^{3+}	-	-	0.120	0.510	0.461	0.486	-	-	-	0.000	0.537
Fe^{2+}	0.097	0.115	3.367	1.444	1.307	1.379	1.047	1.055	0.742	0.756	1.523
Mn^{2+}	-	-	0.153	0.019	-	0.005	-	-	0.008	0.010	-
Mg^{2+}	-	-	1.362	2.510	2.809	2.593	0.968	0.955	1.278	1.265	2.384
Ca^{2+}	2.265	2.157	1.119	1.701	1.789	1.771	-	-	0.009	0.010	1.724
Na^{+}	1.236	1.376	-	1.060	1.063	1.007	-	-	0.007	0.028	0.998
K^{+}	0.122	0.100	-	0.184	0.141	0.191	-	-	-	-	0.280
Total	19.79	19.81	16.00	16.33	16.22	16.20	3.01	3.01	4.03	4.05	16.32
Fe_T	-	-	3.43	1.70	1.54	1.62	-	-	0.74	0.76	1.79
FeMg	-	-	0.72	0.40	0.35	0.38	0.52	0.52	0.37	0.37	0.43
XCa_1	-	-	0.19	0.29	0.29	0.30	-	-	0.00	0.01	0.29
XCa_2	0.65	0.61	-	-	-	-	-	-	-	-	-
XAl	-	-	-	0.36	0.30	0.31	-	-	-	-	0.35
XNa	-	-	-	0.38	0.37	0.36	-	-	-	-	-

Fig. 56

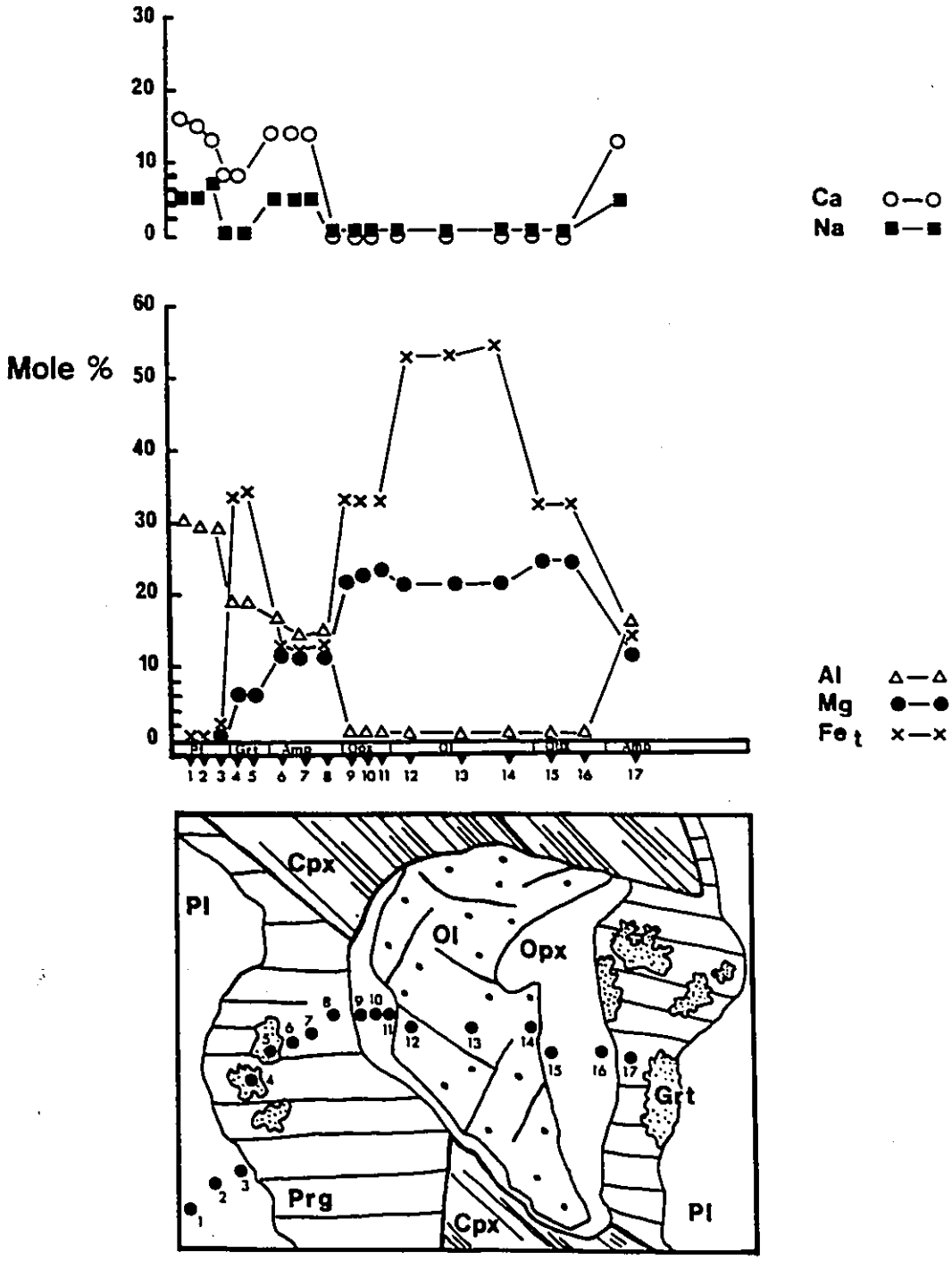

CMA - 27.6.5 - 87

corunmdum plates in the reactant plagioclase crystals.

Textural changes associated with reaction (3) are: 1) the coarsening of spinel grains in an orientation generally parallel to the plagioclase twin planes, and 2) the progressive replacement of pargasite layers by garnet. This results in the formation of an inner turbid part and an outer inclusion-free part displaying idioblastic terminations against plagioclase laths.

6.3.4 Clinopyroxene Corona Structure

Corona structures which form between primary clinopyroxene (augite) and calcic plagioclase are composed of pargasite, sodic plagioclase, and minor quartz grains (shown in Figure 57). Analyses of the reactants and products of this corona structure are given in Table 11. A proposed balanced equation for the formation of this corona structure is:

$$(4)\ 5.53\ \underset{\text{Clinopyroxene}}{(Ca_{0.14}Fe_{0.42}Mg_{0.44}Ti_{0.003}Mn_{0.004})Si_{0.98}O_3} + 2.29\ \underset{\text{Plagioclase}}{(Ca_{0.59}Na_{0.41}K_{0.03})Al_{1.82}Si_{2.20}O_8} +$$

$$[\,0.07\,Ti + 0.30\,K + H + Cl\,] \longrightarrow$$

$$1.00\ \underset{\text{Pargasite}}{(K_{0.33}Na_{0.54})Ca_{1.91}(Fe_{2.32}Mg_{2.43}Ti_{0.09}Mn_{0.01}Al_{0.34})Al_{2.06}Si_{5.94}O_{22}(OH,Cl)_2} +$$

$$0.64\ \underset{\text{Plagioclase}}{(Ca_{0.34}Na_{0.61}K_{0.06})Al_{1.36}Si_{2.63}O_8} + 2.83\ \underset{\text{Quartz}}{SiO_2} + 0.45\ \underset{\text{Corundum}}{Al_2O_3}$$

The equation indicates that an acceptable balance was achieved for most major cations, the exception being aluminum. This reaction requires the introduction of Ti, Mn, K, and H^+ and the

Table 11. Mineral chemistry across clinopyroxene corona structure from sample CMA-79DI86

	Pl 2	Amp 3	Pl 5	Amp 6	Cpx 7	Cpx 8	Cpx 9
SiO_2	48.27	40.34	59.73	40.50	51.86	51.99	52.53
TiO_2	-	0.79	-	0.77	0.48	0.18	0.09
Al_2O_3	33.81	14.96	26.22	15.64	2.43	2.09	2.62
Cr_2O_3	-	0.15	-	0.03	0.28	0.20	0.14
Fe_2O_3	-	5.13	-	4.85	1.57	0.00	0.60
FeO	0.15	10.77	0.20	10.19	7.53	8.41	7.87
MnO	-	0.06	-	0.11	0.23	0.21	0.11
MgO	-	11.24	-	11.29	12.85	13.31	12.70
CaO	16.03	12.09	7.22	12.15	21.11	21.76	22.04
Na_2O	1.67	1.40	7.73	1.89	1.02	0.42	0.87
K_2O	0.55	1.78	1.14	1.75	-	0.03	-
Total	100.48	98.71	102.24	99.17	99.36	98.60	99.57
Si^{4+}	8.797	5.965	10.506	5.943	1.944	1.962	1.961
Ti^{4+}	-	0.088	-	0.085	0.014	0.005	0.003
Al^{3+}	7.262	2.607	5.435	2.705	0.107	0.093	0.115
Cr^{3+}	-	0.018	-	0.003	0.008	0.006	0.004
Fe^{3+}	-	0.571	-	0.536	0.044	0.000	0.017
Fe^{2+}	0.023	1.332	0.029	1.251	0.236	0.265	0.246
Mn^{2+}	-	0.008	-	0.014	0.007	0.007	0.003
Mg^{2+}	-	2.478	-	2.470	0.718	0.749	0.707
Ca^{2+}	3.130	1.915	1.361	1.910	0.848	0.880	0.881
Na^{+}	0.590	0.401	2.636	0.538	0.074	0.031	0.063
K^{+}	0.128	0.336	0.256	0.328	-	0.001	-
Total	19.930	15.720	20.220	15.780	4.000	4.000	4.000
Fe_T	-	1.62	-	1.52	0.26	0.27	0.25
FeMg	-	0.39	-	0.38	0.26	0.26	0.26
XCa_1	-	0.32	-	0.32	0.46	0.46	0.48
XCa_2	0.84	-	0.34	-	-	-	-
XAl	-	0.30	-	0.31	-	-	-
XNa	-	0.17	-	0.22	-	-	-

Fig. 57

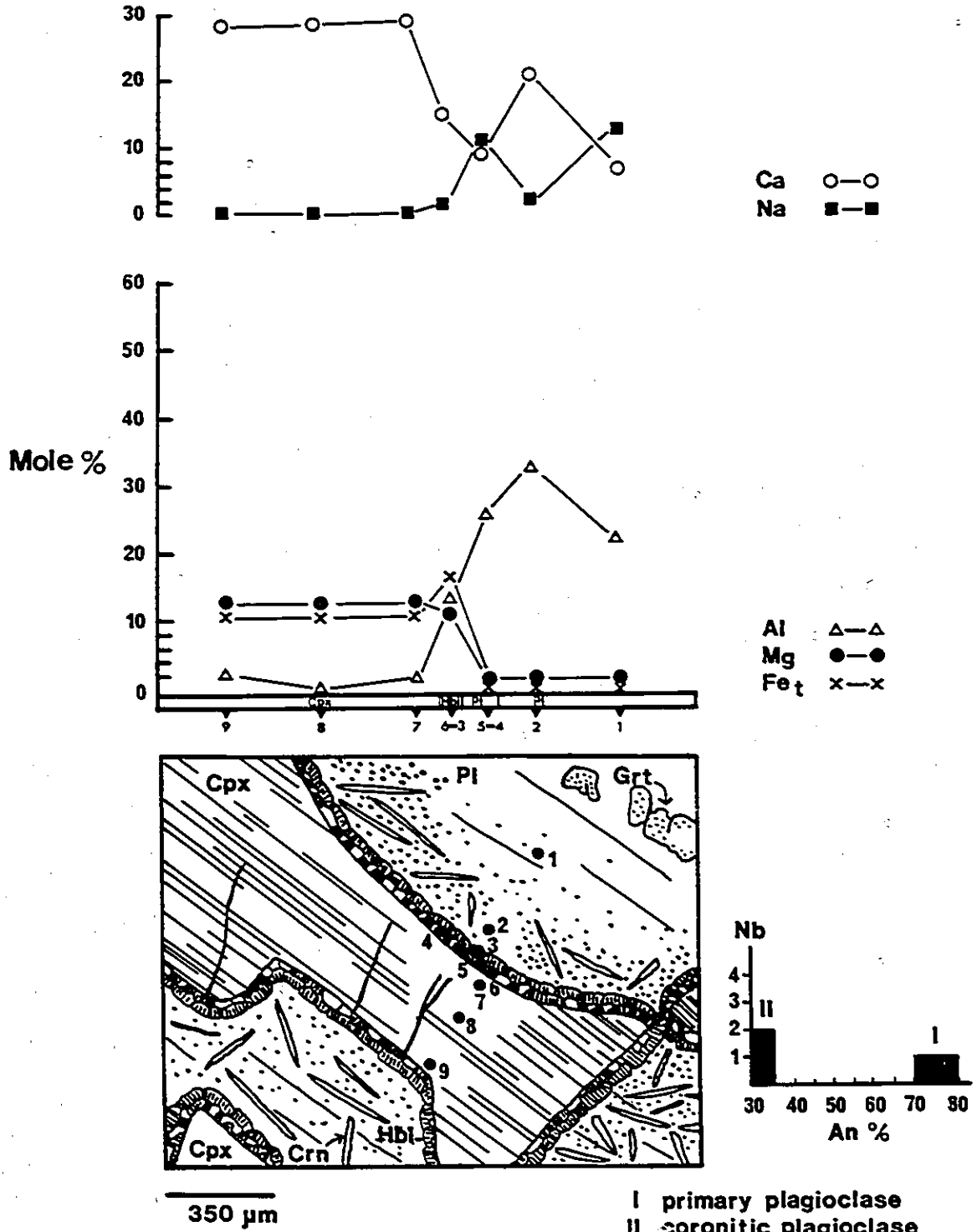

CMA-79 Di (B)-86

removal of aluminum. Hydrogen was most likely present in the form of H_2O. The excess aluminum may be responsible for the presence of corundum plates in the vicinity of the augite corona structure. The X_{Mg} ratio of augite is 0.44 and the X_{Mg} ratio of pargasite is 0.69; therefore the equation necessitates the extensive loss of Mg from augite, possibly by the exchange Fe = Mg. The X_{Al} ratio of calcic plagioclase (0.45) is higher than that of pargasite (0.31), whereas the X_{Ca} ratio of calcic plagioclase, pargasite, and sodic plagioclase are respectively 0.59, 0.78, and 0.34. The pargasite produced in augite corona is characteristically less sodic than the pargasite around the olivine corona structure.

6.3.5 Ti-magnetite Corona Structure

Corona layers consisting of biotite, pargasite, and garnet are common around Ti-magnetite grains in most thin sections. The innermost layer of the corona structure is generally composed of biotite. This biotite is similar optically and chemically to that found interstitially to plagioclase laths in an intimate relationship with apatite and Ti-magnetite crystals. The close association with apatite and Ti-magnetite suggest that the biotite crystallizes at a relatively late magmatic stage (i.e. at or slightly later than the opaque minerals). Figure 58 illustrates the corona structure from sample CMA-LG7 and Table 12 gives the corresponding chemistry of the mineral phases involved.

Table 12. Mineral chemistry of oxide corona structure from sample CMA-LG7

	Ilm 1	Grt 2	Grt 3	Grt 4	Bt 5	Amp 6
SiO_2	0.10	37.84	37.77	38.08	35.53	41.07
TiO_2	49.03	0.07	0.12	0.12	4.57	0.25
Al_2O_3	-	20.99	20.90	20.95	14.42	12.15
Cr_2O_3	0.06	-	-	-	-	-
Fe_2O_3	-	0.65	0.84	0.80	3.65	7.37
FeO	48.02	32.93	32.78	32.93	20.15	15.48
MnO	0.26	1.40	1.35	1.18	0.03	0.02
MgO	-	1.68	2.01	1.97	9.50	7.74
CaO	-	6.20	5.90	5.85	-	10.47
Na_2O	-	-	-	-	-	1.90
K_2O	-	-	-	-	8.78	1.12
Total	97.47	101.75	101.67	101.88	96.63	97.57
Si^{4+}	0.003	5.995	5.983	6.000	5.421	6.278
Ti^{4+}	0.953	0.008	0.014	0.014	0.524	0.029
Al^{3+}	-	3.919	3.902	2.189	4.482	3.890
Cr^{3+}	0.001	-	-	-	-	-
Fe^{3+}	0.088	0.077	0.100	0.095	0.419	0.848
Fe^{2+}	0.950	4.363	4.343	4.339	2.571	1.979
Mn^{2+}	0.006	0.188	0.181	0.157	0.004	0.003
Mg^{2+}	-	0.397	0.475	0.463	2.161	1.764
Ca^{2+}	-	1.052	1.001	0.988	-	1.715
Na^{+}	-	-	-	-	-	0.563
K^{+}	-	-	-	-	1.709	0.218
Total	2.00	16.00	16.00	15.95	15.40	15.58
Fe_T	0.99	4.40	4.39	4.39	2.78	2.40
FeMg	1.00	0.92	0.90	0.90	0.56	0.58
XCa_1	-	0.18	0.17	0.17	-	0.29
XCa_2	-	-	-	-	-	-
XAl	-	-	-	-	-	0.26
XNa	-	-	-	-	-	0.25

Fig. 58

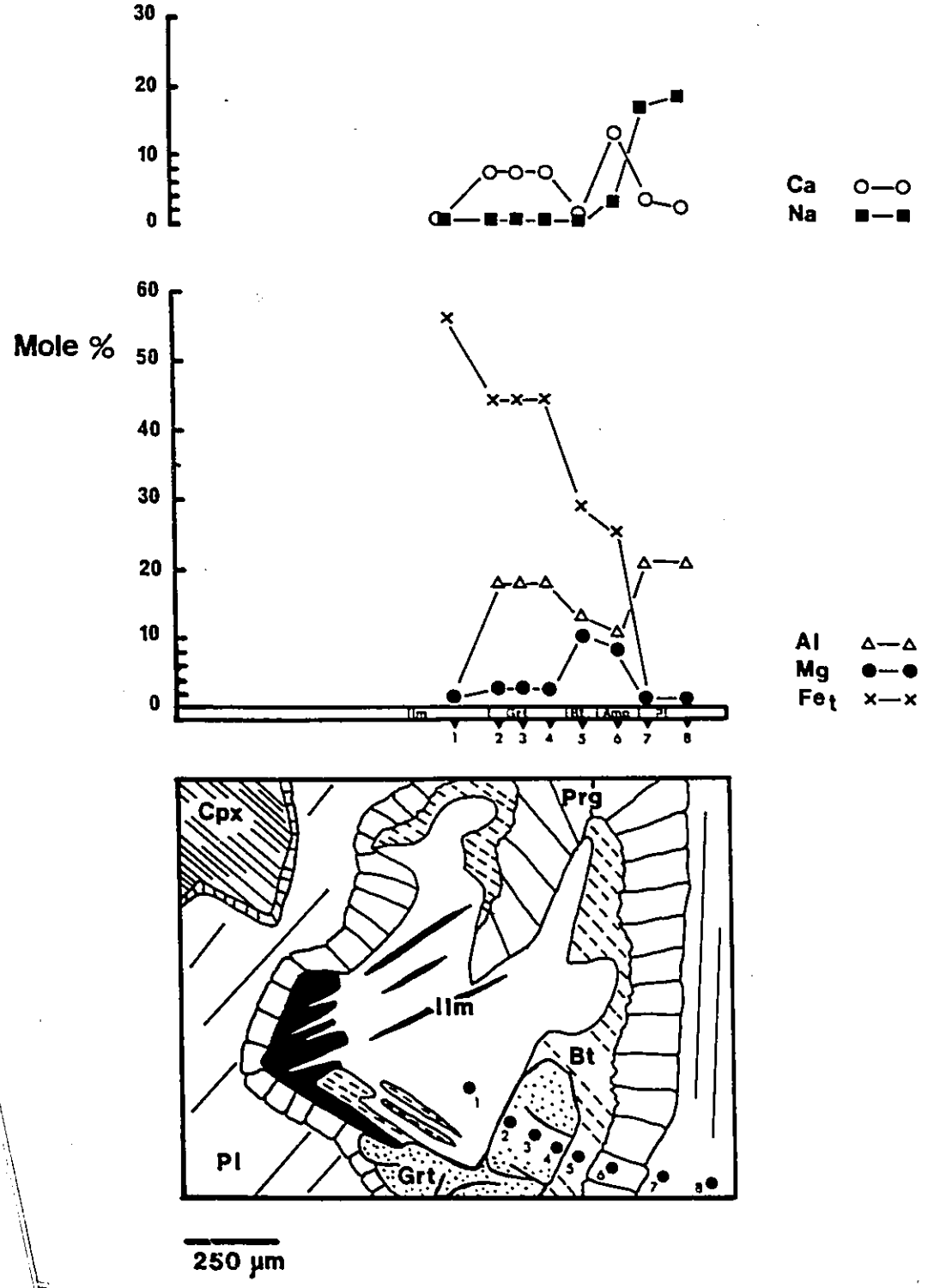

CMA - LG 7 - 86

Textural evidence suggests that biotite and plagioclase reacted to form pargasite. The balanced equation for this reaction is:

$$(5)\ 0.91\ \underset{\text{Biotite}}{K_{1.71}(Mg_{1.95}Fe_{4.06}Ti_{0.52}Mn_{0.004})Al_{2.59}Si_{5.42}O_{20}(OH,Cl)_4} +$$

$$2.28\ \underset{\text{Plagioclase}}{(Ca_{0.75}Na_{0.25}K_{0.006})Al_{1.06}Si_{2.89}O_8} \longrightarrow$$

$$1.00\ \underset{\text{Pargasite}}{(K_{0.22}Na_{0.56})Ca_{1.72}(Fe_{3.68}Mg_{1.76}Ti_{0.03}Mn_{0.003}Al_{0.47})Al_{1.72}Si_{6.28}O_{22}(OH.Cl)_2} +$$

$$[\ 1.35\ K + 2.59\ Al + 5.22\ Si + 0.50\ Ti + 1.63\ H + 6.69\ O_2\ ]$$

As one can notice, the balancing of reaction (5) gives poor results. The reaction requires the removal of K, Al, Si, Ti, H, and O, and in significant amounts for most of these elements. A satisfactorily balanced equation could not be achieved, possibly because some of the reactants or products of the reaction were not identified or because some of the reactants of the reaction were completely consumed.

6.3.6 Orthopyroxene Corona Structure

This corona structure is characterized by a core, composed of orthopyroxene grains, that is surrounded by blocky hornblende grains and idioblastic garnet crystals (Fig. 59). Table 13 presents the chemistry of mineral phases that occur across the orthopyroxene corona structure. Textural evidence suggests that the orthopyroxene grains have been replaced by hornblende. A balanced equation(s) could not be achieved for the proposed

Table 13. Mineral chemistry across orthopyroxene-cored corona structure from sample CMA-2763

	Opx 1	Amp 2	Grt 3	Pl 4	Pl 5	Grt 6	Grt 7
SiO_2	52.45	47.17	38.70	56.54	52.82	38.02	38.31
TiO_2	0.02	0.70	-	-	-	0.04	0.19
Al_2O_3	0.45	9.42	21.18	26.41	27.68	20.98	21.02
Cr_2O_3	0.02	0.14	0.01	-	-	-	0.08
Fe_2O_3	3.10	3.40	1.30	-	-	1.28	1.51
FeO	19.89	7.13	23.94	-	0.43	23.78	24.24
MnO	0.13	0.01	0.48	-	-	0.33	0.41
MgO	23.76	15.90	6.94	-	-	6.61	6.33
CaO	0.23	11.72	7.48	9.25	11.89	7.68	8.03
Na_2O	-	2.01	-	8.53	6.25	-	-
K_2O	0.02	0.54	-	0.18	0.19	-	-
Total	100.07	98.14	100.03	100.91	99.26	98.72	100.12
Si^{4+}	1.947	6.756	5.986	10.161	9.722	5.965	5.946
Ti^{4+}	0.001	0.075	-	-	-	0.005	0.022
Al^{3+}	0.020	1.590	3.861	5.594	6.005	3.879	3.845
Cr^{3+}	0.001	0.016	0.001	-	-	-	0.010
Fe^{3+}	0.086	0.366	0.151	-	-	0.151	0.177
Fe^{2+}	0.617	0.854	3.097	-	0.066	3.119	3.146
Mn^{2+}	0.004	0.001	0.063	-	-	0.044	0.054
Mg^{2+}	1.315	3.395	1.600	-	-	1.546	1.465
Ca^{2+}	0.009	1.799	1.240	1.781	2.345	1.291	1.335
Na^{+}	-	0.558	-	2.972	2.230	-	-
K^{+}	0.001	0.099	-	0.041	0.045	-	-
Total	4.00	15.51	16.00	20.55	20.41	16.00	16.00
Fe_T	0.66	1.04	3.17	-	-	3.20	3.23
FeMg	0.33	0.23	0.66	-	-	0.67	0.69
XCa_1	-	0.29	0.21	-	-	0.21	0.22
XCa_2	-	-	-	0.37	0.51	-	-
XAl	-	0.19	0.39	-	-	0.39	0.39
XNa	-	0.24	-	-	-	-	-

Fig. 59

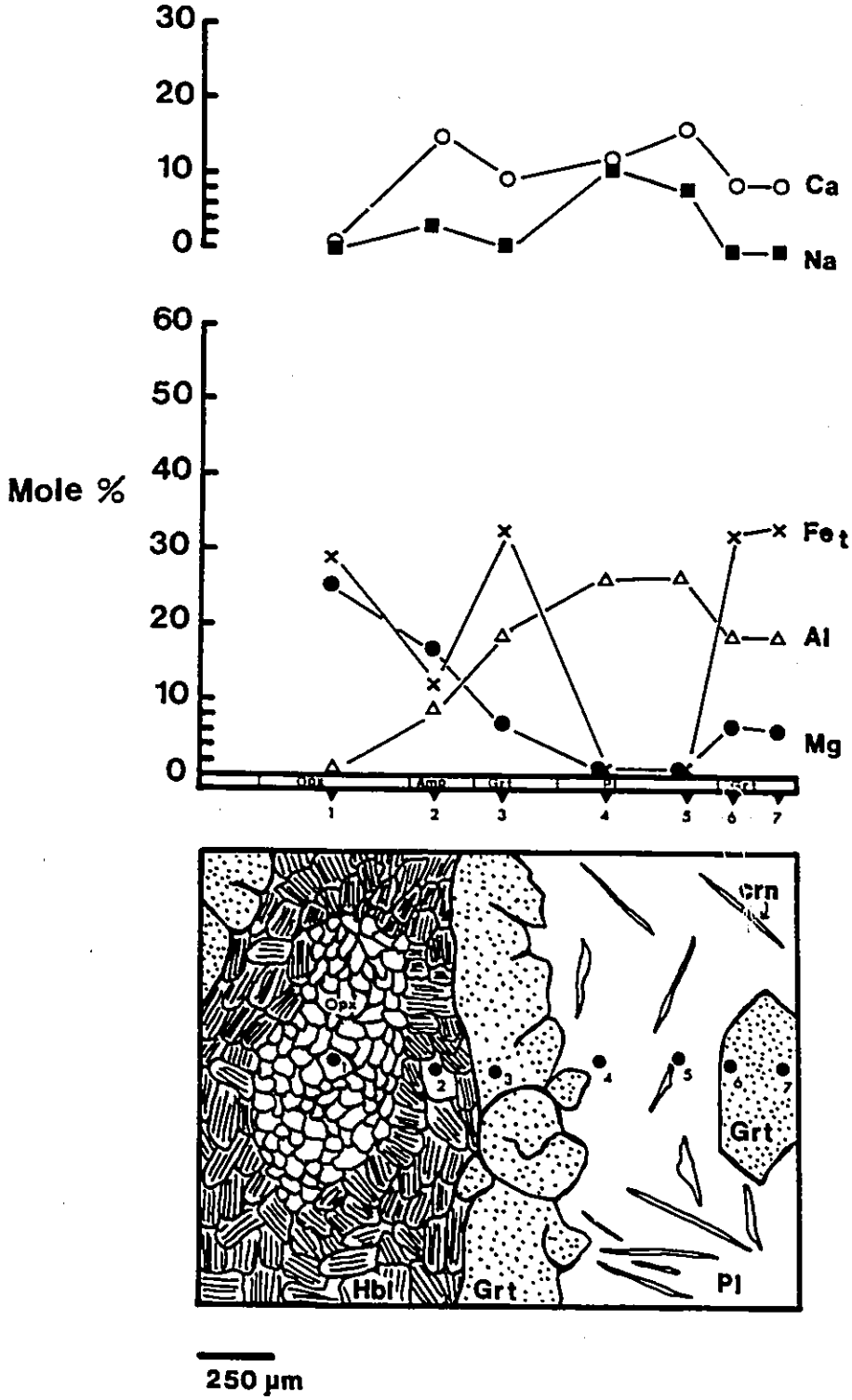

CMA - 27.6.3 - 87

reaction of this corona structure. This may suggest that some other (i.e. undetermined) mineral phases are necessary in order to derive the reaction responsible for this corona structure.

6.4 DISCUSSION OF MODELLED CORONA STRUCTURES

The formation of corona structures has been assigned to various subsolidus reactions which involve diffusion of cations. Three major hypotheses have been proposed: 1) an open system of subsolidus reactions which involves the introduction and removal of cations that have been transported from a distant source to the corona structure site, 2) a closed system of subsolidus reactions in which diffusion of material is restricted to the corona structure, and 3) a combined open/closed system of subsolidus reactions in which the corona structure is essentially closed for certain cations of restricted mobility, and mainly open for other cations with high mobility and high compatibility with the ongoing corona reaction (Grieve and Gittins, 1975; Rivers and Mengel, 1988; Grant, 1988). The combined open/closed system was suggested because the authors failed to balance their equations. However, this suggestion is not correct because the Grieve and Gittins equations can be balanced using the procedure of Kretz et al. (1989) that is used in the present study. In the case of an open system, a satisfactorily balanced reaction(s) has not been achieved by most workers. Again, it is possible to obtain a satisfactorily balanced equation; in this case by using

mass-balance (Gresens) equations. Likewise, in a closed system, there are apparent difficulties in balancing corona reactions. For example, reactions such as olivine and O_2 producing orthopyroxene and magnetite can not proceed without the availability of nearby Ti-magnetite grains or oxygen. Alternatively, the system could be considered as open at the scale of individual corona structures, and this would allow the introduction and removal of selective cations between different corona structures. Also in this latter case, the sum of cation diffusion from all the corona structures would result in a closed system on the scale of a thin section. The mobility of components is therefore an important factor in controlling the rate of reactions and consequently the rate of corona formation. In general, it is assumed that Fe and Mg diffuse rapidly, whereas Ca and Na are moderately mobile, and Al and Si are the slowest diffusing components.

6.4.1 Element Mobility In The Corona Structures

The corona layers (i.e. reaction zones), consisting of orthopyroxene, pargasite, and minor spinel, that develop between olivine and plagioclase grains, as modelled above, have formed by selective diffusion of Si, Al, Fe, Mg, Ca, and Na from the olivine and plagioclase crystals. The presence of K, Ti, Mn, and H in orthopyroxene and hornblende indicate the diffusion of these elements from an outside source. Kretz et al. (1989) proposed six

element migration paths for the mineral assemblage observed in their olivine corona structure. Figure 60 illustrates the following element migration paths that they recognized:

1) Fe, Mg, Mn, and O migrate along the olivine-orthopyroxene interface to the plagioclase-pargasite interface,

2) Si, Al, Ca, and Na migration in a direction opposite to path 1,

3) CaAl exchange with NaSi along the plagioclase-pargasite interface resulting in the normal zoning observed in plagioclase,

4) Fe-Mg exchange within the olivine structure to the olivine-orthopyroxene interface,

5) the introduction of K, Ti, Mn, H, and O from an outside source to the plagioclase-pargasite interface, and

6) the introduction of of Ti along the olivine-orthopyroxene interface from an outside source.

The presence of K and Ti in pargasite and orthopyroxene suggests their derivation from the biotite and Ti-magnetite grains that are present in the thin section.

The present boundary between orthopyroxene and pargasite most

Figure 60. Sketch illustrating the element migration paths of the olivine corona structure (Kretz et al, 1989).

Figure 61. Sketch illustrating the movement of elements during the formation of orthopyroxene-magnetite symplectite after olivine.

Fig. 60

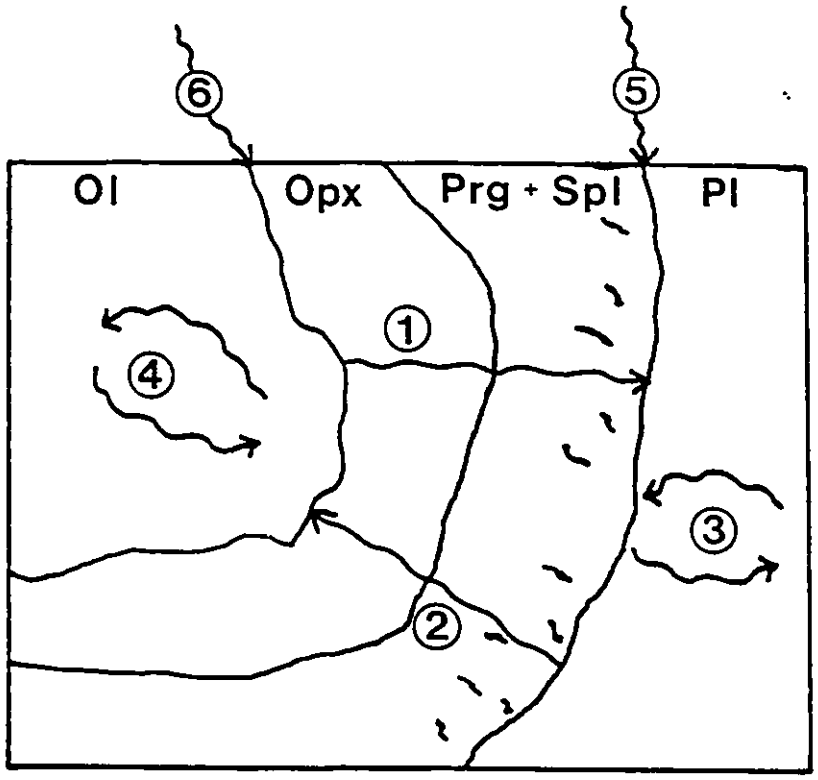

Fig. 61

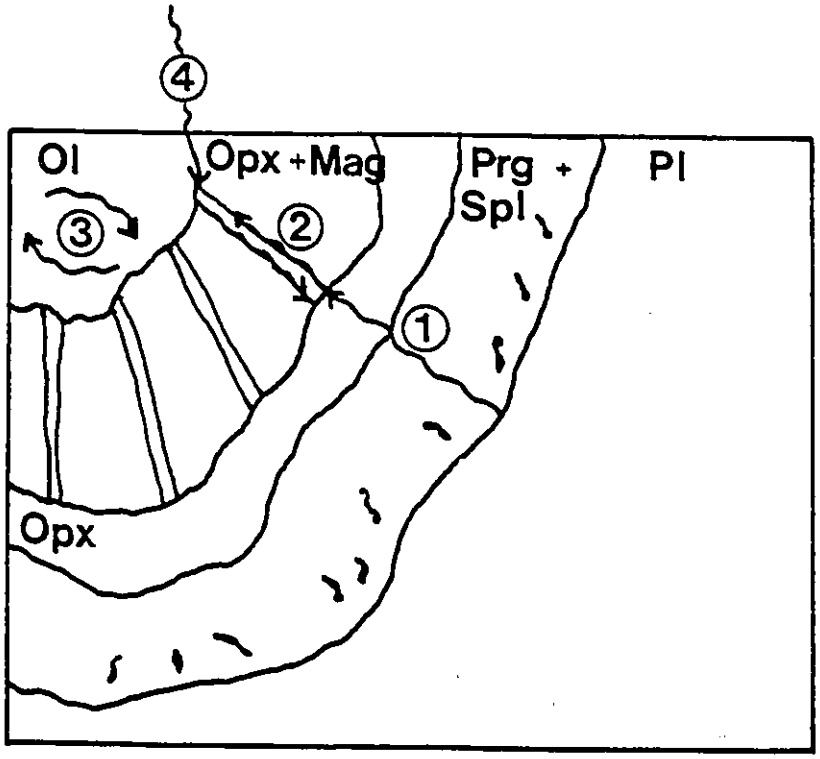

likely does not represent the exact position of the original interface between olivine and plagioclase because the diffusion rate controlling orthopyroxene growth is not the same as the one controlling pargasite growth (i.e. the boundary has shifted). The migration of the orthopyroxene-pargasite boundary takes place when the diffusion rates of components are different. For instance, the migration of the boundary towards olivine would indicate that the diffusion of Fe and Mg is more rapid than the diffusion of Ca and Al (Grieve and Gittins, 1975). However, quantitative calculations by Grieve and Gittins (1975) failed to provide a satisfactory balanced reaction or a satisfactory volume replacement model of the migrating reaction boundary. Recently, Kretz et al. (1989) have provided an estimate of the volume change for this reaction (near zero) and a quantification of the direction and magnitude of migration of the original olivine-plagioclase interface. The calculations of Kretz and co-workers are more realistic in explaining the migrating boundaries of each reaction zone in terms of mole volume data.

The replacement of olivine by the orthopyroxene - Ti-magnetite symplectite is initiated by the diffusion of Fe, Mg, and Si from the olivine grain. The presence of a small concentration of Ca in orthopyroxene indicates the introduction of this component from beyond the reaction site. A qualitative analysis of the oxide minerals intergrown with orthopyroxene, using the scanning electron microprobe, revealed the presence of Ti which suggests that the Ti was introduced to the reaction

site. Figure 61 illustrates the movement of elements during the formation of the orthopyroxene-magnetite symplectite. The diffusion of Ca is shown by the migration path 1 (same as path 2 of Figure 60 of Kretz et al., 1989) from the the plagioclase - hornblende interface to the orthopyroxene - Ti-magnetite symplectite interface. The diffusion of Fe and Ti probably followed the migration path 4 (same as path 6 in Figure 60) from the olivine - orthopyroxene - Ti-magnetite symplectite interface to the orthopyroxene - Ti-magnetite interface as shown by the migration path 2. The migration of atoms taking place in the olivine corona reaction was probably still operative during the olivine replacement reaction which suggests that both reactions probably used the same migration paths.

The presence of biotite and pargasite corona layers between Ti-magnetite and plagioclase grains is commonly observed with the olivine corona structure. Whitney and McLelland (1983) have recognized a direct correlation or association between these two types of corona structures. The magnesium introduced into the biotite and pargasite layers of the Ti-magnetite corona structure is provided by the breakdown reaction of olivine to orthopyroxene. At the same time, Fe and Ti ions migrate in the opposite direction, and this allows the reaction of olivine to orthopyroxene and Fe-Ti oxide symplectite to proceed.

The corona structures developed between augite and igneous plagioclase have formed by diffusion of Si, Al, Fe, Mg, Ca, and Na from augite and plagioclase grains, and this results in a

corona layer consisting of pargasite, Na-plagioclase, and minor quartz. The presence of Ti, Mn, K, and H in pargasite indicate the diffusion of these components from beyond the reaction site. The source of Ti and K is most likely a K-bearing mineral phase such as biotite. The excess Al produced by the reaction might be responsible for the presence of corundum plates occurring in primary plagioclase, adjacent to the corona structure. The lower concentration of sodium in pargasite around the augite corona structure may reflect the selective diffusion of sodium into secondary Na-plagioclase.

6.4.2 Summary Of Modelled Corona Reactions

It has been proposed that the mobility of Al and Si play an important role in the formation of early formed corona structures (Grieve and Gittins, 1975; McLelland and Whitney, 1980; Mongkoltip and Ashworth, 1983; Whitney and McLelland, 1983; Mork, 1986; Rivers and Mengel, 1988). Recent work by Grant (1988) and this study appear to confirm this proposal. During the early stages of corona formation, that is reactions (1), (2), and (5) above, the igneous plagioclase grains contain small amounts (< 1%) of spinel and corundum inclusions, and these are restricted within the plagioclase grains to areas adjacent to the corona structures. As these reactions proceed, the spinel clouding increases and sometimes to the point where the twinning of the plagioclase laths is completely obscured. The spinel clouding

results from the excess Al that is produced during the breakdown of plagioclase under low a_{SiO2} via the CaAl = NaSi exchange reaction. The slow diffusion of Si is probably the controlling factor in early corona development.

The formation of garnet by reaction (3) indicates the transition from the spinel stability field to that of garnet. Even in the garnet stability field, spinel persists metastably in the rocks because of the low mobility of Si and Al. On the basis of textural evidence, the nucleation of garnet is restricted to aluminum-rich regions such as corona layers consisting of pargasite and spinel, and spinel clouded plagioclase laths. The progressive replacement of pargasite corona layers, accompanied by the annealing of spinel clouds, suggests that the reaction is no longer diffusion controlled (Tracy and McLelland, 1985). The replacement of the pargasite corona layer by idioblastic garnet crystals suggests an interface controlled mechanism in which the rate of reactant dissolution and product absorption during recrystallization is rate controlling.

Corona reactions that took place around primary clinopyroxene grains (reaction (4)) are considered to have formed during similar conditions as reaction (3). Therefore this corona structure would have formed by interface controlled growth.

The early formed corona structures were generated by diffusion controlled growth, and this was probably initiated during magmatic cooling when there may have been some residual magmatic liquid occurring within grain interstices (i.e.

intergranular).

Corona structures which formed during peak Grenvillian metamorphism would include the double and triple layer olivine corona structures and the clinopyroxene corona structures.

Finally, corona structures that formed during retrogressive Grenvillian metamorphism would include the orthopyroxene corona structures, the diopside corona structures, and all other corona structures which resulted from replacement of early formed corona structures by variable amounts of retrogressive amphibole.

6.5 GEOTHERMOBAROMETRY

The initial temperature of crystallization of the NNE diabase dykes is inferred to be approximately 1100°C (at 10 kbars) by comparison with experimental work (Basaltic Volcanism Study Project, 1981).

The temperatures and pressures of metamorphic mineral assemblages and mineral equilibration can be estimated by key mineral assemblages. These approximations of P-T conditons may then be quantified by using a wide range of geothermometers and geobarometers. A comparison of P-T estimates from individual mineral assemblages using these different geothermobarometers allows a reconstruction of the evolution of corona structures through the thermal and barometric history of the diabase dykes.

The fundamental assumption that must be made when estimating temperatures of rocks is that the mineral assemblages used must

be in equilibrium. However in most rocks, this is generally not the case. For instance, if the equilibration rate of a particular mineral assemblage is more rapid than the change in temperature and pressure conditions, then the rock will retain the same P-T trajectory as the geological event taking place (Barker A.J., 1990). However, if the rate of equilibration is slower than the change of P-T conditions, the mineral assemblage will record some earlier stage of the P-T evolution. In this latter case, the mineral assemblage is considered to represent peak metamorphic conditions. In addition, the residency period of a particular rock at peak metamorphic condition will have an effect on how close to equilibrium the mineral assemblage will reach. The nature of the mineral pair(s) used for P-T estimates is also an important factor. For instance, pyroxene and garnet act as refractory minerals and do not re-equilibrate easily. On the other hand, biotite and Ti-magnetite will recrystallize fairly easily under changing metamorphic conditions.

6.5.1 Methods of Geothermometry and Geobarometry

Many different systems and approaches have been used to develop geothermometers and geobarometers for quantitatively estimating P-T conditions. The systems and approaches used in geothermobarometry fall into four main categories:

1) exchange thermometry
2) solvus thermometry

3) solution models for multiple systems

4) internally consistent thermodynamic data bases

In most cases, temperature estimates can be determined reasonably well, whereas pressure estimates are more difficult to determine, since geobarometers are commonly dependant upon temperature estimates.

In this study, temperatures were calculated using Fe^{2+} - Mg exchange reactions between garnet - clinopyroxene (Ellis and Green, 1979; Ganguly, 1979; Dahl, 1980), garnet - orthopyroxene (Powell, 1978; Harley, 1984; Sen and Bhattacharya, 1984;), garnet - hornblende (Graham and Powell, 1984), garnet - ilmenite (Pownceby et al., 1987); garnet - biotite (Thompson, 1978; Ferry and Spear, 1978; Hodges and Spear, 1982; Ganguly and Saxena, 1984) Perchuk et al., 1985), orthopyroxene - clinopyroxene (Kretz, 1982; Wood and Banno, 1973; Wells, 1977; Bertrand and Mercier, 1985), and clinopyroxene and hornblende (Kretz and Jen, 1978). Temperatures were also calculated using orthopyroxene - clinopyroxene solvus exchange reaction (Kretz, 1982), and equilibria between ulvospinel - magnetite and ilmenite - hematite (Spencer and Lindsley, 1981).

Pressures were estimated in this study using the aluminum content in hornblende (Hammastrom and Zen, 1986), the garnet - plagioclase - orthopyroxene - quartz barometer (Perkins and Newton, 1981), and the solubility of aluminum in orthopyroxene and co-existing garnet (Wood, 1974).

6.5.2 Results and Thermobarometric Evolution

The temperature of crystallization of the diabase dykes has been determined from the cores of primary clinopyroxene grains using the solvus equation of Kretz (1982). The estimated temperatures range from 1050°C to 1250°C at estimated pressures of 10.6 to 13.5 kbars. The pressures were estimated by using Al contents in hornblende (Hammarston and Zen, 1986). These results agree quite well with experimental work, as well as estimates from other fresh diabase dyke swarms. The temperatures calculated from the rims of clinopyroxene grains show a large variation, ranging from 1080°C down to 450°C. This is attributed to various stages of re-equilibration from magmatic conditions through retrogressive metamorphic conditions.

Table 14 summarizes the results (Appendix I) of pressure - temperature estimates obtained from ten samples using the geothermobarometers described above. Four major ranges of temperature are established from these estimates. The first range of temperature varies from 1050°C to 1250°C, using the Ca-Mg transfer reaction of Kretz (1982) within clinopyroxene cores. The next range of temperatures, from 800°C to 950°C, were estimated using the Ca-Mg transfer reaction of Kretz (1982) and the Fe-Mg exchange reaction between clinopyroxene and hornblende (Kretz and Jen, 1978). The Fe-Mg reactions involving garnet-clinopyroxene, garnet-hornblende, garnet-biotite, clinopyroxene-hornblende, and orthopyrxene-clinopyroxene provide

Table 14. Summary of temperature and pressure estimates.

1)	1050 - 1100 °C	- temperature of crystallization
		Ca-Mg transfer between Opx-Cpx
	10 - 13.5 kbars	- depth of emplacement (?); possibly maximum pressure conditions
2)	800 - 950°C	- peak metamorphic temperature
		Fe-Mg exchange between Cpx-Hbl Opx-Cpx
	6 - 9 kbars	Fe-Mg exchange from the assemblages Grt-Pl-Opx-Qtz Cpx-Pl-Qtz
3)	600 - 775°C	Fe-Mg exchange between Grt-Hbl Grt-Bt Opx-Cpx Grt-Cpx
	6 - 9 kbars	Fe-Mg exchange from the assemblages Grt-Pl-Opx-Qtz Cpx-Pl-Qtz
4)	400 - 600°C	Fe-Mg exchange between Grt-Opx Grt-Bt Grt-Ilm Mag-Ilm

the subsequent range of temperatures from 600°C to 775°C. The final temperature range is from 400°C to 600°C.

The different temperature estimates in the NNE diabase dykes may reflect the inaccuracies of one or more geothermometers or may be related to different closure temperatures for the various cation exchanges in different mineral pairs. The consistency of temperature estimates calculated in rocks with primary mineralogy, characterized by the presence of corona structures and exsolution in oxide minerals, provides some degree of confidence in the geothermometers used in this study.

The pressure estimates associated with the different temperature ranges were determined using the Al content in hornblende (Hammarstrom and Zen, 1986), the Cpx-Pl-Qtz assemblage of Ellis (1980) and the Grt-Pl-Opx-Qtz assemblage of Perkins and Newton (1981). The pressure estimates derived by these geobarometers range from 10 to 13.5 kbars, 6 to 9 kbars, and <6 kbars, respectively.

The estimated temperature of ≈1150°C from clinopyroxene cores and the pressure estimate of 10 - 13.5 kbars recorded in the freshest dykes (e.g. CMA-LA18 and CMA-LGY) most likely reflect the condition of crystallization of the diabase dykes. In these samples, pressures estimated (10 - 13.5 kbars) using the geobarometer of Hammarstrom and Zen (1986) are consistantly higher than the pressures calculated (9 to 10 kbars) using the geobarometers of Ellis (1980) and Perkins and Newton (1981). The higher pressure values recorded by the geobarometer of

Hammarstrom and Zen (1986) may reflect a difference in rock types from those used in the calibration of the geobarometer. Their work is based on mineral pairs from plutonic rocks of granodiorite to tonalite composition. The mineralogy of these rocks differ significantly from that of the NNE diabase dykes.

Temperature and pressure estimates for regional metamorphism are indicated by two groups of temperature estimates of 1) 800°C to 950°C and 2) 600°C to 775°C at pressures of 6 to 9 kbars. The 800°C to 950°C temperature range is provided by chemical re-adjustment within clinopyroxene cores and by Fe-Mg exchange reactions between clinopyroxene and hornblende pairs. The consistency of relative temperature differences calculated for mineral pairs such as garnet-clinopyroxene, garnet-hornblende, garnet-biotite, clinopyroxene-hornblende, and orthopyroxene-clinopyroxene is shown by the temperature range of 600°C to 775°C. Textures associated with these mineral pairs are the triple-layered corona structures around olivine and Ti-magetite and the double-layered corona structures around primary clinopyroxene.

The lowest temperatures recorded are from the Fe-Mg exchange reactions between magnetite-ilmenite and garnet-biotite, and these range from ~400°C to 600°C. This indicates that the oxide minerals and biotite continously re-equilibrated to lower temperatures with a closure temperature around 400°C, hence lower than that of the co-existing mineral assemblages.

6.6 Tectonic Implications of corona structures

The tectonic significance of corona structures has been discussed by Harley (1985) and Francis (1976), among others. The importance of studying corona structures is in the derivation of P-T-t paths of their host rock. The coronas most likely are a manifestation of some common crustal tectonic process. Several possibilities are: 1) environment of emplacement and cooling of a plutonic body (e.g. isobaric cooling), 2) crustal thickening (e.g. burial metamorphism, basalt to eclogite), and 3) isothermal crustal uplift after isobaric cooling of high-grade regional metamorphosed rocks or high-temperature intrusions. Corona structures are re-equilibration products which may record one or more events in a rock's history. Therefore, it is the textural evidence that will establish the P-T-t path of the corona structure, and ultimately allow modelling of the formation of corona structures. This along with careful geological mapping, structural interpretation, and isotopic data will establish whether the coronas are igneous or metamorphic (or a combination of) in origin. Only then, the corona structures can be used in establishing the P-T vector conditions and the tectonic environment.

The evolution of the corona structures in the NNE diabase dykes provide some constraints on the relative changes of temperature and pressure with time and reaction. The P-T

estimates obtained from the corona structures (Appendix I) have been summarized above in Table 14. The data presented there constrain a segment of the P-T-t path of the parautochthonous domain near Chibougamau. Temperatures >1050°C are consistent with crystallization temperatures of the dykes. The pressures ranging from 10 - 13.5 kbars are interpreted as either 1) high pressure crystallization conditions of the basic magmas or 2) relict pressure conditions of the magma chamber. Further work is needed to determine which of these hypotheses is correct, however, the former is the favoured interpretation. Although there is no supporting data, these high pressures may represent the peak pressures that were reached in the parautochthonous domain. No evidence of prograde metamorphism (i.e. increasing temperatures) is recorded in the corona structures. The data tentatively indicates that this part of the crust cooled from ≈ 850 - 900°C to 600 - 650°C with only a small to moderate decrease in pressure (i.e. from 9 kbars to 6 kbars). This would suggest a general decompression of the parautochthonous domain through approximately 2.5 kbars at temperatures greater than 650°C. In addition, the pressure estimates of 6 - 9 kbars indicate that this part of the parautochthonous domain was at 20 - 30 km depth during and after peak metamorphism. In other words, the parautochthonous domain experienced essentially isobaric (<10 km) cooling at depth after reaching peak metamorphic conditions. However, how does this fit into the regional tectonic framework? The results presented here would support the uplift model

advocated, 100 km to the north, by Neale (1952). This is in agreement with recent detailed geological mapping by Ciesielski (1988).

In summary, this study alone does not provide enough information to resolve the tectonic framework of the parautochthonous domain in this region. But combined with data of Ciesielski (1988) and others to come, this study will contribute to the understanding of the tectonic conditions under which the granulite grade metamorphism took place.

Main Conclusions

1) A distinct group of NNE-trending coronitic diabase dykes is present in the Grenville parautochthonous domain near Chibougamau.

2) The NNE diabase dykes vary in mineralogy and textures across the parautochthonous domain.

3) The NNE diabase dykes are tholeiitic (low TiO_2) to weakly alkaline (high-TiO_2) in composition. The low-TiO_2 group is similar to N-type MORB and low-TiO_2 flood basalt, and the high-TiO_2 group is similar to high-Fe-Ti continental flood basalts.

4) Textural evidence indicates that the simple corona structures (i.e. single layers) are possibly late magmatic in origin.

5) All complex corona structures are interpreted to be metamorphic in origin.

6) The evolution of the primary minerals to secondary minerals can be followed through variable complex reactions of a two stage corona growth.

7) Corona structure formation took place during a prolonged cooling event (i.e. from magmatic through regional metamorphic conditions).

8) Two-way diffusion has taken place across olivine - plagioclase, Ti-magnetite - plagioclase, and clinopyroxene - plagioclase interfaces.

9) Al and Si mobility is important in the formation of corona structures.

10) Early corona development is controlled in part by slow diffusion of Si.

11) Material has been transported from and to the different types of corona structures as they grew. Therefore, the corona structures are not individually but instead collectively isochemical.

12) H_2O and/or (OH^-) have played an integral part in the formation of some corona structures, especially the early formed ones. The origin of the water is uncertain, but primary biotite contributed in part.

13) Advanced corona development is controlled by reactant dissolution and product absorption during recrystallization.

14) A tentative P-T path from corona reactions across the parautochthonous domain extends from 950°C to 600°C at 6 to 9 kbars.

REFERENCES

Ashworth, J.R. (1986)
The role of magmatic reaction, diffusion, and annealing in the evolution of coronitic microstructure in troctolitic gabbro from Risor, Norway: a discussion, Mineralogical Magazine 50, pp. 469-473.

Avrantchev, L. (1979)
Suzanne Lebel-Drolet, carte n° M-307, Gîte minéraux du Québec, Région de l'Abitibi.

Barker, A.J. (1990)
Introduction to metamorphic textures and microstuctures, Blackie, Chapman and Hall, New York, 162 p.

Barnes, S.-J. (1985)
The petrography and geochemistry of komatiite flows from the Abitibi Greenstone Belt and a model for their formation. Lithos 18, pp. 241-270.

Barton, M. and Van Gaans, C. (1988)
Formation of orthopyroxene-Fe-Ti oxide symplectites in Precambrian intrusives, Rogaland, southwestern Norway. American Mineralogist 73, pp. 1046-1059.

Basaltic Volcanism Study Project (1981)
Basaltic Volcanism on the Terrestrial Planets, Pergamon Press, New York, 1, 286 p.

Bellini G.; Comin-Chiaramonti P.; Marques L.S.; Melfi A.J. Nardy, A.J.R., Papatrechas, C., Piccirillo, E.M., Roisenberg, A. and Stolfa, D. (1986)
Petrogenetic aspects of acid and basaltic lavas from the Parana Plateau (Brazil): geological, mineralogical and petrochemical relationships, Journal of Petrology 27, pp. 915-944.

Bertrand, P. and Mercier, J.C. (1985)
The mutual solubility of coexisting ortho- and clinopyroxene toward an absolute geothermometer for the natural system?, Earth and Planetary Science Letters 76, pp. 109-122.

Beswick, A.E. (1982)
Some geochemical aspects of alteration and genetic relations in komatiite suites, in Komatiites, N.T. Arndt and E.G. Nisbet (eds.), George Allen and Unwin, London, pp. 281-308.

Beswick, A.E. (1983)
Primary fractionation and secondary alteration within an Archean ultramafic flow, Contributions to Mineralogy and Petrology 82, pp. 221-231.

Bethune, K.M., and Davidson, A. (1988)
Diabase dykes and the Grenville Front southwest of Sudbury, Ontario. in Current Research, Part C, Geological Survey of Canada, Paper 88-1C, pp. 151-159.

Bhattacharyya, P.K. and Mukherjee, S. (1987)
Granulites in and around the Bengal anorthosite, eastern India; genesis of corona garnet, and evolution of the granulite - anorthosite complex, Geological Magazine 124, pp. 21-32.

Bose, M.K. (1961)
Garnet coronites from Koraput, Orissa. Geological Magazine 98, p. 409.

Brögger, W.C. (1934)
The South Norwegian hyperites and their metamorphism. Skrifter utgitt av Det Norske Videnskaps-Akademi i Oslo 1 Mat.-Nat. Klasse 1, 421 p.

Buddington, A.F. (1939)
Adirondack igneous rocks and their metamorphism. Memoire Geological Society of America 7, pp.

Buddington, A.F. (1952)
Chemical petrology of some metamorphosed Adirondack gabbroic, syenitic and quartz-syenitic rocks. American Journal of Sciences, Bowen Volume, pp. 37-84.

Carter, J.L. (1970)
Mineralogy and chemistry of the Earth's upper mantle based on the partial fusion - partial crystallization model, Bulletin of Geological Society of America 81, pp. 2021-2039.

Chown, E.H. and Archambault, G. (1987)
The transition from dyke to sill in the Otish Mountains, Québec; relations to host-rock characteristics. Canadian Journal of Earth Sciences 24, pp. 110-116.

Ciesielski, A. (1988)
Geological and structural context of the Grenville Front, southeast of Chibougamau, Québec; in Current Research, Part C, Geological Survey of Canada, Paper 88-1C, pp. 353-366.

Ciesielski, A. et Ouellet, E. (1985)
Le Front de Grenville dans la région de Chibougamau, Québec. dans Recherches en cours, partie B, Commission géologique du Canada, Étude 85-1B, pp. 303-317.

Ciesielski, A., Bellavance, Y. et Joly, M. (1986)
Le front de Grenville, à l'est de Chibougamau, Québec. Commission Géologique du Canada, Dossier public 1239.

Condie, K.C. and Bobrow, D.J. (1987)
Geochemistry of Precambrian mafic dykes from the Southern Superior Province of the Canadian Shield. in Mafic Dyke Swarms, Halls, H.C., and Fahrig, W.F. (eds.), Geological Survey of Canada, Special paper 34, pp. 95-108.

Cox, K.G., Bell, J.D. and Pankhurst, R.J. (1979)
The interpretation of igneous rocks, Allen and Unwin, London.

Dahl, P.S. (1980)
The thermal-compositional dependence of Fe^{2+}-Mg distributions between coexisting garnet and pyroxene applications to geothermometry, American Mineralogist 65, pp. 854-866.

Daigneault, R. et Allard, G.O. (1984)
Evolution Tectonique d'une Portion du Sillon de Roches Vertes de Chibougamau. Canadian Institute of Mining and Metallurgy, Special volume 34, pp. 212-228.

Davidson, A. and Bethune, K.M. (1988)
Geology of the north shore of Georgian Bay, Grenville Province of Ontario. in Current Research, Part C, Geological Survey of Canada, Paper 88-1C, pp. 135-144.

Davidson, A. and Grant, S.M. (1986)
Reconnaissance geology of western and central Algonquin Park and detailed study of coronitic olivine metagabbro, Central Gneiss Belt, Grenville province of Ontario. in Current Research, Part B, Geological Survey of Canada, Paper 86-1B, pp. 837-848.

Deer, W.A., Howie, R.A., and Zussman, J. (1978)
An Introduction to the Rock forming minerals. Longman, London, vol. 2A, 528 p.

Deland, A.N. (1953)
Carte géologique N° 1241, Région de Hazeur-Druillettes, feuillet Lac Surprise (Abitibi est), Ministère des Mines du Québec.

Ellis, D. J. (1980)
Osamilite-sapphirine-quartz granulites from Enderby Land Antartica, P-T conditions of metamorphism, implications for garnet-cordierite equilibria and the evolution of the deep crust, Contributions to Mineralogy and Petrology 74, pp. 201-210.

Ellis, D.J. and Green, D.H. (1979)
An experimental study of the effect of Ca upon garnet-clinopyroxene Fe-Mg exchange equilibria, Contributions to Mineralogy and Petrology 71, pp. 13-22.

Emslie, R.F. (1983)
The coronitic Michael gabbros, Labrador: assessment of Grenvillian metamorphism in northeastern Grenville Province. in Current Research, Part A, Geological Survey of Canada , Paper 83-1A, pp. 139-145.

Esbensen, K.H. (1978)
Coronites from the Fongen gabbro complex, Trondheim region, Norway: Role of water in the olivine-plagioclase reaction. Neues Jahrbuch für Mineralogie Abhandlungen 132, pp. 113-135.

Fahrig, W.F. (1987)
The tectonic settings of continental mafic dyke swarms: failed arm and early passive margin. in Mafic dyke swarms, Halls, H.C. and Fahrig, W.F. (eds.), Geological Association of Canada, Special Paper 34, pp. 331-348.

Ferry, J.M. and Spear, F.S (1978)
Experimental calibration of the partitioning of Fe and Mg between biotite and garnet, Contributions to Mineralogy and Petrology 66, pp. 113-117.

Fisher, G.W. (1977)
Nonequilibrium thermodynamics in metamorphism. in Thermodynamics in geology. Fraser, D.G. (ed.), D. Reidal Publ. Co., Dordrecht, Holland, pp.381-403.

Fodor, R.V. (1987)
Low- and high-TiO_2 flood basalts of southern Brazil: origin from picritic parentage and a common mantle source. Earth and Planetary Science Letters 84, pp. 423-430.

Fodor, R.V., Corwin, C., and Roisenberg, A. (1985)
Petrology of Serra Geral (Paraná) continental flood basalts, southern Brazil: crustal contamination, source material, and South Atlantic magmatism, Contributions to Mineralogy and Petrology 91, pp. 54-65.

Foster, C.T. (1981)
A thermodynamic model of mineral segregations in the lower sillimanite zone near Rangeley, Maine, American Mineralogist 66, pp. 260-277.

Francis, D.M. (1976)
Corona-bearing pyroxene granulite xenoliths and the lower crust beneath Nunivak Island, Alaska, Canadian Mineralogist 14, pp. 291-298.

Francis, D., Ludden, J. and Hynes, A. (1983)
Magma evolution in the Proterozoic rifting environment, Journal of Petrology 24, pp. 556-582.

Frodesen, S. (1968)
Coronas around olivine in a small gabbro intrusion, Bamble area, south Norway. Norsk Geologisk Tidsskrift 48, pp.201-206.

Ganguly, J. (1979)
Garnet and clinopyroxene solid solutions, and geothermometry based on Fe-Mg distribution coefficient, Geochimica et Cosmochimica Acta 43, pp. 1021-1029.

Ganguly, J. and Saxena, J.K. (1984)
Mixing properties of aluminosilicate garnets: constraints from natural and experimental data and applications to geothermobarometry, American Mineralogist 69, pp. 88-97.

Gardner, P.M. and Robins, B. (1974)
The olivine-plagioclase reaction: geological evidence from the Seiland petrographic province, Northern Norway. Contributions to Mineralogy and Petrology 44, pp. 149-156.

Gilbert, J.E. (1951)
Carte géologique n° 1239, Région de Rohault, District d'Abitibi est et De Roberval, Ministère des Mines du Québec.

Gjelsvik, T. (1952)
Metamorphosed dolerites in the gneiss area of Sunnmore on the west coast of southern Norway. Norsk Geologisk Tidsskrift 30, pp. 33-134.

Goode, A.D.T. (1974)
Oxidation of natural olivines. Nature 248, pp. 500-501.

Graham, C. and Powell, R. (1984)
A garnet-hornblende geothermometer: calibration, testing, and application to the Palona Schist, southern California, Journal of Metamorphic Petrology 2, pp. 13-31.

Grant, S.M. (1985)
Coronitic gabbro and meta-anorthosite in the Central Gneiss Belt, Grenville Province of Ontario. in Davidson, A., Nadeau, L., Grant, S.M., and Pryer, L.L., Studies in the Grenville Province of Ontario. in Current Research, Part A., Geological Survey of Canada, Paper 85-1A, pp. 474-478

Grant, S.M. (1988)
Diffusion models for corona formation in metagabbros from the western Grenville Province, Canada. Contributions to Mineralogy and Petrology 98, pp. 49-63.

Grenier, P.E. (1952)
Carte géologique n° 1240, Région de Hazeur-Druillettes, feuillet Gamache (Abitibi est), Ministère des Mines du Québec.

Grieve, R.A.F., and Gittins, J. (1975)
Composition and formation of coronas in the Hadlington gabbro, Ontario. Canadian Journal of Earth Sciences 12, pp. 289-299.

Griffin, W.L and Heier, K.S. (1973)
Petrological implications of some corona structures. Lithos 6, pp. 315-335.

Halls, H.C. (1988)
Precambrian dyke swarms: Status and progress of IGCP project 257. Episodes 11, pp. 286-288.

Hammarstrom, J.M. and Zen, E. (1986)
Aluminum in hornblende: an experimental igneous geobarometer, American Mineralogist 71, pp. 1297-1313.

Hanson, G.N. and Langmuir, C.H. (1978)
Modelling of major elements in mantle-melt systems using trace element approaches, Geochimica et Cosmochimica Acta 42, pp. 725-741.

Harley, S.L. (1984)
Comparison of the garnet-orthopyroxene geobarometer with recent experimental studies, and applications to natural assemblages, Journal of Petrology 25, pp. 697-712.

Harley, S.L. (1985)
Garnet-orthopyroxene bearing granulites from Enderby Land, Antartica, metamorphic pressure-temperature-time evolution of the Archean Napier Complex, Journal of Petrology 26, pp. 819-856.

Hergt, J.M., Chapell, B.W., Faure, G., and Mensing, T.M. (1989)
The geochemistry of Jurassic dolerites from Portal Peak, Antactica, Contributions to Mineralogy and Petrology 102, pp. 298-305.

Hodges, K.V. and Spear, F.S. (1982)
Geothermometry, geobarometry and the Al_2SiO_5 triple point at Mt. Moosilauke, New Hampshire, American Mineralogist 67, pp. 1118-1134.

Holland, T. (1896)
On the origin and growth of garnets. Rec. Geological Survey of India 29, p.20.

Holm, P.E., Smith, T.E., Huang, C.H., Gerasimoff, M., Grant, B. and McLaughlin, K. (1986)
Geochemistry of metavolcanic rocks and dykes from the central metasedimentary belt, Grenville Province, Southeastern Ontario. in The Grenville Province, Moore, J.M., Davidson, A. and Baer, A.J. (eds.), Geological Survey of Canada, Special paper 31, pp. 255-269.

Huang, W.T. and Merritt, C.A. (1954)
Petrography of the troctolite of the Wichita Mountains, Oklahoma. American Mineralogist 39, pp. 549-565.

Imbault, P.E. (1950)
Carte géologique n° 1236, Région de Queylus, District d'Abitibi est et De Roberval, Ministère des Mines du Québec.

Irvine, T.N. and Baragar, W.R.A (1971)
A guide to chemical classification of the common volcanic rocks, Canadian Journal of Earth Sciences 8, pp. 523-548.

Jensen, L.S. (1976)
A new cation plot for classifying subalkaline volcanic rocks, Ontario Division of Mines, Miscalleneous Paper 66, 22 p.

Joesten, R. (1977)
Evolution of mineral assemblage zoning in diffusion metasomatism. Geochimica Cosmochimica Acta 41, pp. 649-670.

Joesten, R. (1986a)
The role of magmatic reaction, diffusion and annealing in the evolution of coronitic microstructures in troctolitic gabbro from Risor, Norway. Mineralogical Magazine 50, pp. 441-467.

Joesten, R. (1986b)
The role of magmatic reaction, diffusion and annealing in the evolution of coronitic microstructures in troctolitic gabbro from Risor, Norway: A reply. Mineralogical Magazine 50, pp. 474-479.

Johnson C.A. and Essene E.J. (1982)
The formation of garnet in olivine-bearing metagabbros from the Adirondacks, Contributions to Mineralogy and Petrology 81, pp. 240-251.

Kretz R. (1982)
Transfer and exchange equilibria in a portion of the pyroxene quadrilateral as deduced from natural and experimental data, Geochimica et Cosmochimica Acta 46, pp. 411-421.

Kretz R. and Jen S. (1978)
Effect of temperature on the distribution of Mg and Fe^{2+} between calcic pyroxene and hornblende, Canadian Mineralogist 16, pp. 533-537.

Kretz, R., Jones, P., Hartree, R. (1989)
Grenville metagabbro complexes of the Otter Lake area, Québec. Canadian Journal of Earth Science 26, pp. 215-230.

Kretz, R., Hartree, R., Garrett, D., and Cermignani, C. (1985)
Petrology of the Grenville swarm of gabbro dikes, Canadian Precambrian Shield. Canadian Journal of Earth Sciences 22 pp. 53-71.

Laurin, A.F. (1954)
Carte préliminaire n° 1069, Région De Ducharme-Bouteroue, Comtés d'Abitibi Est et De Roberval, Ministère des Mines du Québec.

Leake, B.E. (1978)
Nomenclature of amphiboles. Mineralogical Magazine 42, pp. 533-563.

Mongkoltip, P. and Ashworth, J.R. (1983)
Quantitative estimation of and open-system symplectite-forming reaction: restricted diffusion of Al and Si in coronas around olivine. Journal of Petrology 24, pp. 635-661.

Mork, M.E. (1986)
Coronite and eclogite formation in olivine gabbro, Western Norway: reaction paths and garnet zoning. Mineralogical Magazine 50, pp. 417-426.

Murthy, M.V.N. (1958)
Coronites from India and their bearing on the origin of coronas. Geological Society of America Bulletin 69, No. 1, pp. 23-38.

Myers, J.D., Marsh, B.D., and Sinha, A.K. (1986)
Geochemical and strontium isotopic characteristics of parental Aleutian Arc magmas: evidence from the basaltic lavas of Atka, Contributions to Mineralogy and Petrology 94, pp. 1-11.

Neale, E.R.W. (1952)
Geology of the Bathoulat Lake area, Mistassini Territory, Québec; unpublished PhD thesis, Yale University, 345 p.

Neale, E.R.W. (1953)
Carte géologique n° 1235, Région De Dollier-Charron, District Abitibi Est et De Roberval, Ministère des Mines du Québec.

Nishiyama, T. (1983)
Steady diffusion model for olivine-plagioclase corona growth, Geochimica et Cosmochimica Acta 47, pp. 283-294.

O'Hara, M.J. (1968)
The bearing of phase equilibria studies in synthetic and natural systems on the origin and evolution of basic and ultrabasic rocks, Earth Science Reviews 4, pp. 69-133.

Pearce, T.H. (1968)
A contribution to the theory of variation diagrams, Contributions to Mineralogy and Petrology 19, pp. 142-157.

Pearce, T.H. (1987)
The identification and assessment of spurious trends in Pearce-type ratio variation diagrams: A discussion of some statistical arguments, Contributions to Mineralogy and Petrology 97, pp. 529-534.

Pearce, J.A. and Norry, M.J. (1979)
Petrogenetic implications of Ti, Zr, Y, and Nb variations in volcanic rocks, Contributions to Mineralogy and Petrology 69, pp. 33-47.

Pe-Piper, G. (1988)
Calcic amphiboles of mafic rocks of the Jeffers Brook plutonic complex, Nova Scotia, Canada. American Mineralogist 73, pp. 993-1006.

Perchuk L.L., Aranovich, L.Ya., Podlesskii, K.K, Lavrent'eva, V., Gerasimov, V.Ya., Fedkin, V.V., Kitsul, V.I., Karsakov, L.P., and Bernikov, N.V. (1985)
Precambrian granulites of the Aldan shield, eastern Siberia, USSR, Journal of Metamorphic Geology 3, pp. 265-310.

Perkins, D. III and Newton, R.C. (1981)
Charnokite geobarometer based on coexisting garnet-pyroxene-plagioclase-quartz, Nature 292, pp.144-146.

Plant , A.G. and Lachance, G.R. (1973)
Quantitative electron microprobe analysis using an energy dispersive spectrometer, Proceeding of the Eighth National Conference on Electron Probe Analysis, New Orleans, Paper 13.

Poldervaart, A. and Gilkey, A.K. (1954)
On clouded plagioclase, American Mineralogist 39, p. 75.

Powell, R. (1978)
The thermodynamics of pyroxene geotherms, Philosophical Transactions of the Royal Society of London A 288, pp. 457-469.

Pownceby, M.I., Wall, V.J., and O'Neil, H.St.C. (1987)
Fe-Mn partitioning between garnet and ilmenite: experimental calibration and applications, Contributions to Mineralogy and Petrology 97, pp. 116-176.

Rajamani, V., Shivkumar, K., Hanson, G.N., and Shirey, S.B. (1985)
Geochemisrty and petrogenesis of amphibolites, Kolar Schist Belt, South India: evidence for komatiitic magma derived by low percentages of melting of the mantle, Journal of Petrology 26, pp. 92-123.

Rivers, T. and Chown, E.H. (1986)
The Grenville Orogen in eastern Quebec and western Labrador definition, identification and tectonometamorphic relationship of autochthonous, parautochthonous and allochthonous terranes. in The Grenville Province, ed. J.M. Moore, A. Davidson, and A.J. Baer; Geological Association of Canada, Special Paper 31, pp. 31-50.

Rivers, T. and Mengel, F.C. (1988)
Contrasting assemblages and petrogenetic evolution of corona and noncorona gabbros in the Grenville Province of western Labrador, Canadian Journal of Earth Sciences 25, pp. 1629-1648.

Rivers, T., Martignole, J., Gower, C.F., Davidson, A. (1989)
New tectonic divisions of the Grenville Province, Southeast canadian shield. Tectonics 8, pp. 63-84.

Robinson, P., Spear, F.S., Schumacher, J.C., Laird, J., Klein, C., Evans, B.W., and Doolan, B.L. (1982)
Phase relations of metamorphic amphiboles: Natural occurrences and theory. Mineralogical Society of America Reviews in Mineralogy 9B, pp. 1-227.

Rollinson, H.R. and Roberts, C.R. (1986)
Ratio correlations and major element mobility in altered basalts and komatiites, Contributions to Mineralogy and Petrology 93, pp. 89-97.

Sederholm, J. (1916)
On synantetic minerals, Comm. Geol. Finlande Bull. 48, pp. 1-59.

Sen, S.K. and Bhattacharyya, P.K. (1984)
An orthopyroxene-garnet thermometer and its application to the Madras charnockites, Contribution to Mineralogy and Petrology 88, pp. 64-71.

Shand, S.J. (1945)
Coronas and coronites, Geological Society of America Bulletin 56, No. 3, pp. 247-266.

Smith, R.E. and Smith, S.E. (1976)
Comments on the use of Ti, Zr, Y, Sr, K, P, and Nb in classification of basaltic magmas, Earth and Planetary Science Letters 32, pp. 114-120.

Spencer, K.J. and Lindsley, D.H. (1981)
A solution model for coexisting iron-titanium oxides, American Mineralogist 66, pp. 1189-1201.

Spry, A. (1969)
Coronas, reaction rim. in Metamorphic textures, Pergamon Press, Oxford, pp. 104-108.

Stout, J.H. (1972)
Phase petrology and mineral chemistry of co-existing amphiboles from Telemark, Norway. Journal of Petrology 13, pp. 99-145.

Sutcliffe, R.H. (1987)
Petrology of Middle Proterozoic diabase and picrites from Lake Nipigon, Canada. Contributions to Mineralogy and Petrology 96, pp. 201-211.

Thompson, A.B. (1976)
Mineral reactions in pelitic rocks: II. Calculation of some P-T-X (Fe-Mg) phase relations, American Journal of Science 276, pp. 425-454.

Törnebohm, A.E. (1877)
Om Sveriges viktigare Diabas-och Gabbro-Arter, Kgl. Sveska Vetenskaps-Akademiens Handlingar, B.14, No. 13

Tracy and McLelland (1985)
A natural example of the kinetic controls of compositional and textural equilibration, in Metamorphic Reactions: Kinetics, textures, and deformation, A.B. Thompson and D.C. Rubie (eds.) Advance in Physical Geochemistry vol.4, pp. 118-137.

Vernon R.H. (1976)
Metamorphic processes and microstructure development, George Allan and Unwin, London, 247 p.

Viereck, L.G., Flower, M.F.J., Hertogen, J., Schmincke,H.-U., and Jenner, G.A. (1989)
The genesis and significance of N-MORB sub-types, Contributions to Mineralogy and Petrology 102, pp. 112-126.

Vogt, J.H.L. (1921)
The physical chemistry of the crystallization and the magmatic differentiation of igneous rocks, Journal of Geology 24, pp. 627-649.

Wells P.R.A. (1977)
Pyroxene thermometry in simple and complex systems, Contributions to Mineralogy and Petrology 62, pp. 129-139.

Whitney, P.R. and McLelland, J.M. (1973)
Origin of coronas in metagabbros of the Adirondacks Mts., N.Y. Contributions to Mineralogy and Petrology 39, pp. 81-98.

Wilson, M. (1989)
Igneous Petrogenesis: A Global Tectonic Approach, London, Allen & Unwin, 466 p.

Wood, B.J. (1974)
The solubility of alumina in orthopyroxene coexisting with garnet, Contribution to Mineralogy and Petrology 46, pp. 1-15.

Wood B.J. and Banno S. (1973)
Garnet-orthopyroxene and orthopyroxene-clinopyroxene relationships in simple and complex systems, Contributions to Mineralogy and Petrology 42, pp. 109-124.

APPENDIX A

Petrographic Descriptions

SAMPLE NUMBER: CMA-LA18-87

MINERALS:

1. Olivine	2 - 3	8. Iddingsite	1- 2
2. Plagioclase	20-30	9. Cummingtonite	tr
3. Clinopyroxene	10-15	10. Apatite	1-tr
4. Pargasite	10-15		
5. Biotite	3- 5		
6. Orthopyroxene	3- 5		
7. Magnetite	10-15		

DESCRIPTION:

- The rock exhibits a subophitic to ophitic texture which consists of plagioclase laths intergrown with olivine, clinopyroxene, magnetite, and biotite grains.

- The olivine and magnetite grains typically comprise the cores of symetrical and assymetrical corona structures where in contact with plagioclase laths. The olivine corona structures are composed of a double corona layer consisting of orthopyroxene and pargasite. Single corona layers are developed around magnetite, and consist of pargasite and/or biotite.

- Plagioclase forms randomly oriented laths that exhibit well developed Carlsbad and albite twins. They contain trace amounts of spinel in the vicinity of olivine corona structures. Minor amounts of corundum are also present.

- Clinopyroxene grains are abundant and form grains up to 4 mm in diameter. They do not show any corona structures.

- Magnetite grains are often associated with clinopyroxene, partly enclosed in clinopyroxene. Where in contact with plagioclase, magnetite grains have developed single corona structures. Magnetite crystals are also found forming intimate intergrowths with biotite flakes and apatite grains.

- Trace amounts of cummingtonite are found in interstices between plagioclase laths. The amphibole grains exhibit distinct twinning in cross polarized light.

CORONA TYPES

OLIVINE CORONA: Ol / Opx / Prg / Pl

OXIDE CORONA: Mag / Prg / Pl
Mag / Bt / Pl

SAMPLE: CMA-LGY-87

MINERALS:

1. Plagioclase	30-35	8. Epidote	tr-1
2. Clinopyroxene	25-30	9. Apatite	tr-1
3. Pargasite	5-10	10. Calcite	tr
4. Biotite I	3- 5	11. Garnet	tr
5. Magnetite	10-15		
6. Orthopyroxene	tr- 1		
7. Zircon	tr		

DESCRIPTION:

- An ophitic to subophitic texture is well developed. It consists of randomly oriented plagioclase laths intergrown with clinopyroxene, magnetite, and biotite grains.

- Plagioclase laths are well preserved, and exhibit albite and Carlsbad twins. Spinel and corundum microcrystals are present in plagioclase grains that are adjacent to orthopyroxene - magnetite symplectite-cored corona structures.

- The clinopyroxene grains are subhedral to anhedral. They display yellow to brown pleochroism. The clinopyroxene grains do not exhibit any corona structures.

- Reaction rims or corona structures have developed around some of the opaque oxide minerals and orthopyroxene - magnetite symplectite cores.

- The orthopyroxene - magnetite symplectite-cored corona structures are composed of a double corona layer of orthopyroxene and pargasite adjacent to plagioclase grains. Iddingsite is found in some cores of this corona type.

- Biotite crystals are found forming a corona layer around primary magnetite crystals. A double layered corona structure, consisting of biotite and pargasite, is observed around most magnetite crystals. The magnetite grains often display abundant exsolutions of ilmenite.

CORONA TYPES

OXIDE CORONA:	Mag / Bt / Prg / Pl Mag / Prg / Pl
OPX + MAG CORONA:	Opx + Mag / Opx / Prg / Pl

SAMPLE: CMA-LG7-87

MINERALS:

1. Plagioclase	25-30	8. Rutile	1
2. Clinopyroxene	20-25	9. Apatite	1-2
3. Biotite II	3- 5	10. Epidote	5- 7
4. Pargasite	10-15		
5. Orthopyroxene	5-10		
6. Garnet	2- 3		
7. Magnetite	10-15		

DESCRIPTION:

- The rock displays a well preserved ophitic to subophitic texture consisting of plagioclase, clinopyroxene, magnetite, and biotite.

- Plagioclase occurs as randomly oriented laths up to 2 mm in length. They show well developed twins that are bent (i.e. deformed). The plagioclase grains exhibit undulatory extinction. Inclusions of spinel and corundum are present and result in a weak clouding of the plagioclase laths. Intimate intergrowths of plagioclase and clinopyroxene grains are observed.

- Clinopyroxene grains are subhedral to anhedral. Microcrystals of spinel and rutile are found along cleavage planes. Clinopyroxene grains are replaced by hornblende along grain margins. Clinopyroxene grains range from 500 μm to 2 mm in diameter.

- Double layered corona structures are observed around the orthopyroxene - magnetite symplectite cores. The corona layers are composed of orthopyroxene and pargasite in contact with plagioclase laths. The orthopyroxene - magnetite symplectite cores vary from 0.05 mm to 0.5 mm in diameter.

- Ti-magnetite crystals are anhedral and range from 0.05 mm to 1 mm in diameter. They commonly exhibit ilmenite exsolutions. The Ti-magnetite crystals are surrounded by a double corona layer composed of biotite and pargasite. Minor amounts of garnet are observed in the pargasite layer. Dendritic to skeletal magnetite crystals are also observed intimately associated with biotite flakes.

CORONA TYPES

OPX+MAG CORONA:	opx + Mag / Opx / Prg / Pl
OXIDE CORONA:	Mag / Bt / Prg / Pl
	Mag / Bt / Prg + Grt / Pl

SAMPLE: CMA-LG6-87

MINERALS:

1. Plagioclase	30-35	8. Apatite	tr
2. Clinopyroxene	20-25		
3. Pargasite	5-10		
4. Orthopyroxene	2- 3		
5. Biotite	3- 5		
6. Magnetite	5-10		
7. Garnet	tr- 1		

DESCRIPTION:

- A well developed ophitic to subophitic texture is present It is composed of randomly oriented plagioclase laths intimately intergrown with clinopyroxene, magnetite, and biotite grains.

- The primary plagioclase laths display albite and Carlsbad twins. They show minor amounts of recrystallization along their grain boundaries. Some evidence of deformation is expressed by the presence of bent twin lamellae.

- Large crystals of primary (igneous) clinopyroxene are present. They are fine- to medium-grained. Minor alteration to amphibole occurs along grain margins. Magnetite crystals are often closely associated with the clinopyroxene grains.

- Corona structures are developed around the magnetite grains. They consist of a double corona layer of biotite and pargasite. Triple layered corona structures are locally observed around the magnetite grains and consist of an additional layer of garnet crystals about the biotite and pargasite layers. Skeletal grains of ilmenite are intimately intergrown within biotite flakes.

- Orthopyroxene aggregates are found as cores to double layered corona structures. The corona layers are composed of hornblende and garnet grains. The hornblende corona layers are replacing the orthopyroxene cores.

CORONA TYPES

OPX CORONA: Opx / Hbl / Grt / Pl

OXIDE CORONA: Mag / Bt / Prg / Pl
Mag / Bt / Prg / Grt / Pl

SAMPLE: CMA-27.6.3-87

MINERALS:

1. Plagioclase	25-30	8. Calcite	tr
2. Clinopyroxene	30-35		
3. Hornblende	15-20		
4. Biotite II	1- 3		
5. Garnet	5-10		
6. Ti-magnetite	1- 3		
7. Epidote	tr		

DESCRIPTION:

- The rock displays a well preserved ophitic to subophitic texture that is composed of randomly oriented plagioclase laths and clinopyroxene, biotite, and magnetite grains.

- The plagioclase laths vary from 0.5 to 1 mm in length. They show well developed albite and Carlsbad twins, some of which show strain extinction. The plagioclase laths contain variable amounts of spinel and corundum microcrystals (i.e. inclusions).

- Clinopyroxene grains are common. They are typically medium-grained and light green to brown in color. The clinopyroxene grains are partly replaced by amphibole crystals along grain boundaries and along fractures.

- Amphibole crystals are also found as aggregates generally surrounded by garnet crystals. Garnet atolls mark the position of relict corona structures. The garnet grains are euhedral and contain abundant inclusions of biotite, clinopyroxene (diopside), and amphibole. Garnet atolls also surround primary clinopyroxene and magnetite grains.

- The garnet crystals that are in contact with clinopyroxene grains are idioblastic and contain inclusion of hornblende. They do not show any zoning. However, the garnet crystals that occur around Ti-magnetite grains are well zoned, and contain inclusion zones consisting of biotite, hornblende, and pyroxene.

- Reddish brown biotite flakes are less then 0.5 mm in length. They are randomly distributed throughout the sample, and are generally intimately associated with the magnetite and ilmenite grains.

CORONA TYPES

CPX CORONA: Cpx / Hlb / Pl

OXIDE CORONA: Mag / Hbl / Grt / Pl

HORNBLENDE CORONA: Hbl / Grt / Pl

SAMPLE: CMA-27.6.5-87

MINERALS:

1. Olivine	1- 2	8. Garnet	10-15
2. Plagioclase	25-30	9. Apatite	1
3. Clinopyroxene	20-25	10. Epidote	5- 7
4. Amphibole	3- 5		
5. Orthopyroxene	10-15		
6. Magnetite	3- 5		
7. Biotite	1- 2		

DESCRIPTION:

- The rock consists of a well developed ophitic to subophitic texture, consisting of subhedral clinopyroxene, biotite, and anhedral magnetite grains enclosed by randomly oriented plagioclase laths.

- Anhedral olivine crystals are present, either enclosed by plagioclase laths or clinopyroxene grains. They are 0.25 to 0.75 mm in diameter, and are characteristically strongly fractured. The olivine grains are partly altered to iddingsite along grain boundaries and fractures. Double to triple layered corona structures are developed around the olivine grains where in contact with plagioclase laths. The corona layers consist of 1) orthopyroxene and pargasite, or 2) orthopyroxene, pargasite and garnet crystals. Spinel and corundum microcrystals are common in the plagioclase laths adjacent to the olivine corona structures. Where the olivine grains are completely enclosed by clinopyroxene, only a single layer of orthopyroxene has developed.

- Plagioclase laths exhibit albite and Carlsbad twins. The twins show weak evidence of deformation (i.e. bent and weakly undulose). The plagioclase laths are strongly clouded by spinel microcrystals, and this has resulted in their present brown color.

- Primary (igneous) clinopyroxene grains are subhedral to anhedral. They are brown to dark brown in color in plane light. The color has resulted from the minute inclusions of Ti-Fe oxide crystals that are distributed along the clinopyroxene cleavage planes.

- Magnetite grains are anhedral. They crystals vary from 0.25 to 1.5 mm in diameter. Magnetite grains are surrounded by a double to triple corona structure composed of biotite - pargasite, and biotite - pargasite - garnet, respectively. Garnet grains are generally zoned.

- Garnet crystals are found within pargasite layers and in nucleating in plagioclase laths.

- Orthopyroxene - magnetite symplectites are common and occur as cores to double and triple layered corona structures. The corona layers are composed of orthopyroxene - pargasite and orthopyroxene - pargasite - garnet crystals.

- Diopside corona structures are also present. They consist of thin sodic plagioclase moats with idioblastic garnet rims in contact with plagioclase laths.

CORONA TYPES

OLIVINE CORONA:	Ol / Opx / Prg / Pl
	Ol / Opx / Prg / Grt / Pl
OXIDE CORONA:	Mag / Bt / Prg / Pl
	Mag / Bt / Prg / Grt / Pl
OPX+MAG CORONA:	Opx+Mag / Opx / Prg / Pl
	Opx+Mag / Opx / Prg / Grt / Pl
DIOPSIDE CORONA:	Di / Na-Pl / Grt / Pl

SAMPLE: CMA-M-D'-05-86

similar to: CMA-146

MINERALS:

1. Plagioclase	25-30	8. Tremolite	tr
2. Augite	20-25		
3. Biotite II	2- 5		
4. Hornblende	15-20		
5. Magnetite/Ilmenite	5-10		
6. Garnet	5-10		
7. Diopside	tr		

DESCRIPTION:

- This sample is representative of a partially metamorphosed diabase dyke.

- Plagioclase grains are equidimensional and in part define a granoblastic texture. They are partly altered to sericite and epidote.

- Primary clinopyroxene (augite) grains are partly replaced by hornblende along grain margins and along fractures. The hornblende grains are equidimensional and form part of the granoblastic texture.

- Idioblastic garnet crystals commonly occur in recrystallized plagioclase grains. They also occur along the original plagioclase grain boundaries.

- Secondary biotite grains are found associated with opaque minerals such as magnetite and ilmenite.

- A relict ophitic texture is present, but has been nearly obliterated by recrystallization.

- Most plagioclase grains are recrystallized except for large phenocrysts (> 2mm in length) that show partial recrystallization along their grain boundaries.

SAMPLE: CMA-015A-86

MINERALS:

1. Plagioclase	25-30	8. Iddingsite	1- 2
2. Clinopyroxene	15-20	9. Rutile	tr
3. Biotite II	2- 3	10. Garnet	10-15
4. Magnetite	5-10		
5. Amphibole	5-10		
6. Orthopyroxene	5-10		

DESCRIPTION:

- A subophitic to ophitic texture is well preserved in the rock. It is defined by randomly oriented plagioclase laths which partly to completely enclose clinopyroxene, biotite, and magnetite crystals.

- The plagioclase laths exhibit well formed twins. They are typically clouded by microcrystals of spinel and corundum, the effect of which has imparted a brown color.

- Clinopyroxene grains are subhedral to anhedral. They show a green to salmon-brown pleochroism. They are partially replaced by hornblende crystals along grain margins. Small idioblastic garnet crystals are found along clinopyroxene grain margins.

- Reddish brown biotite is common as flakes ranging in size from <0.5 up to 2.0 mm in length. They are intimately intergrown with opaque oxide and amphibole grains. Some aggregates of biotite are rimmed by garnet crystals.

- Orthopyroxene crystals form as granoblastic aggregates that are surrounded by a double corona structure of hornblende and garnet grains. Iddingsite may be present in the core of some orthopyroxene aggregates.

- Diopside aggregates form the cores of double layered corona structures. The corona structure consists of an inner sodic plagioclase layer surrounded by an immediate layer of hornblende and an outer layer of idioblastic garnet crystals in contact with plagioclase laths.

- Magnetite grains are present as central cores to triple layered corona structures. The corona layers are composed of biotite, hornblende, and garnet.

CORONA TYPES

OPX CORONA: Opx / Hbl / Grt / Pl

OXIDE CORONA: Mag / Bt / Hbl / Grt / Pl

CPX CORONA: Cpx / Hbl / Pl

DIOPSIDE CORONA: Di / Hbl / Grt / Pl
Di / Pl / Grt / Pl

SAMPLE: CMA-M-V01-86

MINERALS:

1. Plagioclase	30-35
2. Clinopyroxene	20-25
3. Amphibole	5-15
4. Biotite II	2- 5
5. Magnetite/Ilmenite	2- 5
6. Garnet	15-20

DESCRIPTION:

- This sample is a partly metamorphosed and recrystallized diabase dyke.

- The metamorphic texture is granoblastic and is characterized by clear equidimensional plagioclase crystals intergrown with the mafic minerals.

- Large crystals of clinopyroxene are present and are green to yellowish green in color. They are partly replaced by hornblende grains along their grain margins. The hornblende crystals are also equidimensional and form part of the granoblastic texture. The clinopyroxene crystals contain abundant inclusions of oxide minerals.

- Garnet atolls are found around aggregates of hornblende and mixed aggregates consisting of hornblende, biotite, and oxide crystals.

- Oxide minerals, magnetite and ilmenite, occur as small grains disseminated throughout the rock.

SAMPLE: CMA-M-RO1A-85

MINERALS:

1. Plagioclase	45-50	8. Apatite	tr
2. Clinopyroxene	25-30	9. Epidote	tr
3. Hornblende	10-15		
4. Biotite	5- 7		
5. Magnetite/ilmenite	10-15		
6. Garnet	2- 3		
7. Rutile	tr		

DESCRIPTION:

- An ophitic to subophitic texture is well developed. This texture is composed of randomly oriented plagioclase laths enclosing clinopyroxene, biotite, opaque oxide, and hornblende grains.

- Plagioclase occurs as laths up to 2.5 mm in length. They display albite and Carlsbad twins and are generally free of inclusions.

- Clinopyroxene crystals are 0.75 to 1.5 mm in diameter. They exhibit a brown to green color in plane light. Amphibole crystals are replacing clinopyroxene along grain boundaries. The hornblende are equidimensional and form part of the granoblastic texture.

- Magnetite occurs occasionally as dendritic grains within biotite flakes, but more often as anhedral grains associated with ferromagnesian minerals. The magnetite grains vary from 0.10 to 0.25 mm in diameter. They are rounded and are accompanied by ilmenite grains and trace amounts of sulfide minerals.

- Garnet grains are xenoblastic to idioblastic and contain abundant inclusions. They form around oxide minerals and around mixed aggregates of ferromagnesian minerals such as hornblende, biotite, and clinopyroxene.

SAMPLE: CMA-146-86

MINERALS:

1. Plagioclase	15-20	8. Apatite	1-tr
2. Clinopyroxene	3- 5	9. Quartz	2- 5
3. Biotite II	5-10	10. Corundum	1-tr
4. Magnetite/ilmenite	5-10	11. Calcite	tr
5. Amphibole	50-55		
6. Garnet	3- 5		
7. Epidote	tr		

DESCRIPTION:

- A recrystallized ophitic to subophitic texture is present in this sample. This texture is similar to those described above.

- The plagioclase crystals are medium- to coarse-grained and inclusion-free, ranging from 0.50 to 2.5 mm in length. A weakly to moderately developed mortar texture is present along plagioclase grain boundaries.

- Large crystals of clinopyroxene (up to 1.5 mm in diameter) are common and are partly replaced by hornblende grains. In some cases, the clinopyroxene crystals are almost completely pseudomorphed by hornblende aggregates.

- Garnet occurs as coarse-grained crystals nucleating in hornblende aggregates. They do not form as part of the corona structures.

- Biotite crystals occur within small aggregates consisting of variable amounts of ferromagnesian minerals, such as hornblende and magnetite.

- Magnetite grains are generally anhedral and up to 1.5 mm in diameter. Biotite and hornblende grains are common adjacent to the magnetite grains. The magnetite grains contain exsolutions of ilmenite (Note: observed in reflected light).

Legend to Appendix B

Ol = Olivine
Pl = Plagioclase
Bt = Biotite
Prg = Pargasite
Hbl = Hornblende
Opx = Orthopyroxene
Cpx = Clinopyroxene
Grt = Garnet
Ilm = Ilmenite
Mag = Magnetite

$Fe_T = Fe^{2+} + Fe^{3+}$
$FeMg = Fe^{2+} / (Fe^{2+} + Mg)$
$XCa_1 = Ca / (Ca + Fe^{2+} + Mg)$
$XCa_2 = Ca / (Ca + Na)$
$XAl = Al / (Al + Si)$
$XNa = Na / (Ca + Na)$

Appendix B1. Figure and mineral analyses of corona structure from sample CMA-LA18-87

	Pl 1	Pl 2	Cpx 3	Cpx 4	Cpx 5	Cpx 6	Ol 7	Ol 9	Ol 10	Cpx 11	Cpx 12	Cpx 13
SiO_2	51.42	53.85	47.90	48.68	49.75	49.53	35.40	34.89	35.44	49.18	49.08	56.24
TiO_2	-	-	1.07	1.16	1.01	1.00	-	-	-	0.81	0.77	-
Al_2O_3	28.93	28.59	3.44	3.71	3.82	3.61	-	-	-	3.14	2.84	28.79
Cr_2O_3	-	-	0.05	0.16	0.21	0.33	-	-	-	0.07	0.05	-
Fe_2O_3	-	-	1.73	3.64	1.21	2.31	-	-	-	1.34	2.62	-
FeO	0.54	0.42	11.22	9.73	10.55	9.57	38.73	38.18	38.51	12.14	11.10	0.31
MnO	-	-	0.28	0.34	0.28	0.24	-	-	-	0.33	0.50	-
MgO	-	-	13.05	13.73	14.26	14.54	25.52	25.30	25.06	13.88	13.97	-
CaO	13.23	11.92	18.32	18.66	18.82	18.85	-	-	-	17.30	17.78	10.20
Na_2O	4.74	5.63	-	0.10	-	-	-	-	-	-	-	6.10
K_2O	0.34	0.59	-	0.11	0.01	0.08	-	-	-	0.05	0.03	0.68
Total	99.20	101.00	97.06	100.01	99.92	100.06	99.65	98.37	99.01	98.24	98.74	102.32
Si^{4+}	9.488	9.725	1.864	1.837	1.867	1.856	1.003	1.001	1.013	1.886	1.876	9.948
Ti^{4+}	-	-	0.031	0.033	0.029	0.028	-	-	-	0.023	0.022	-
Al^{3+}	6.291	6.085	0.158	0.165	0.169	0.159	-	-	-	0.142	0.128	6.002
Cr^{3+}	-	-	0.002	0.005	0.006	0.010	-	-	-	0.002	0.002	-
Fe^{3+}	-	-	0.051	0.103	0.034	0.065	-	-	-	0.039	0.075	-
Fe^{2+}	0.083	0.063	0.365	0.307	0.331	0.300	0.918	0.916	0.920	0.390	0.355	0.046
Mn^{2+}	-	-	0.009	0.011	0.009	0.008	-	-	-	0.011	0.016	-
Mg^{2+}	-	-	0.757	0.772	0.798	0.812	1.078	1.082	1.067	0.794	0.796	-
Ca^{2+}	2.616	2.306	0.764	0.754	0.757	0.757	-	-	-	0.711	0.728	1.933
Na^{+}	1.696	1.971	-	0.007	-	-	-	-	-	-	-	2.092
K^{+}	0.080	0.136	-	0.005	0.000	0.004	-	-	-	0.002	0.001	0.153
Total	20.250	20.290	4.000	4.000	4.000	4.000	3.000	3.000	3.000	4.000	4.000	20.170
Fe_T	-	-	0.39	0.36	0.35	0.33	-	-	-	0.41	0.39	-
FeMg	-	-	0.34	0.32	0.30	0.29	0.46	0.46	0.46	0.34	0.33	-
XCa_1	-	-	0.40	0.40	0.40	0.40	-	-	-	0.37	0.38	-
XCa_2	0.61	0.54		-			-	-	-	-	-	0.48
XAl	-	-	-	-	-	-	-	-	-	-	-	-
XNa	-	-	-	-	-	-	-	-	-	-	-	-

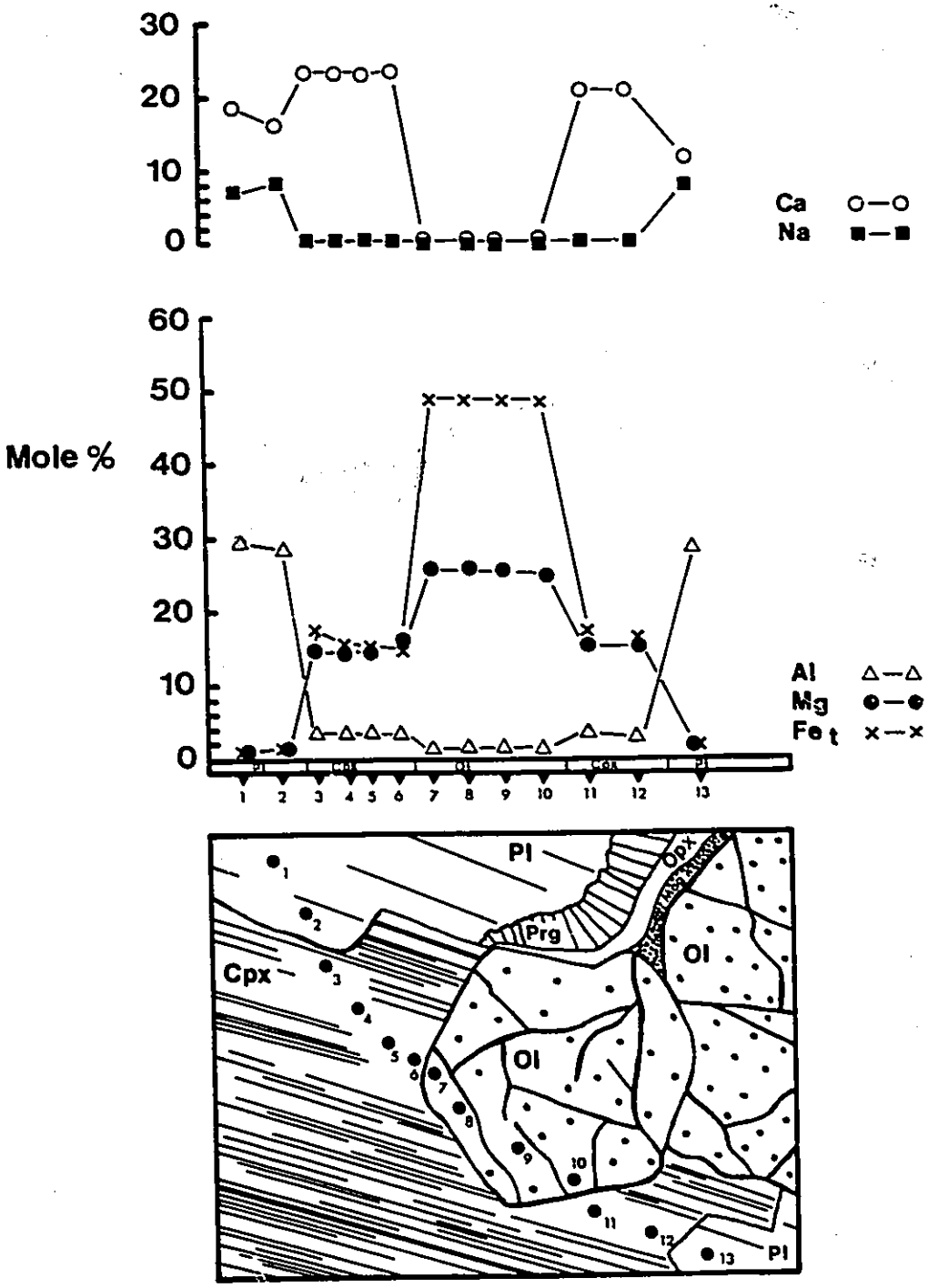
30
20
10
0
Ca
Na
60
50
40
30
20
10
0
Mole %
Al
Mg
Fe t
Pl
Cpx
Ol
Cpx
Pl
1 2 3 4 5 6 7 8 9 10 11 12 13
Pl
Opx
Prg
Ol
Cpx
Ol
Pl
450 µm

CMA - LA 18 - 87

Appendix B2. Figure and mineral analyses of corona structure from sample CMA-27.6.3-87

	Opx 1	Opx 2	Opx 3	Hbl 4	Hbl 5	Grt 6	Pl 9
SiO_2	53.10	53.58	53.36	46.84	45.33	39.59	57.21
TiO_2	0.05	0.06	0.03	1.27	0.81	0.07	-
Al_2O_3	1.67	1.20	1.48	9.56	11.36	21.62	27.35
Cr_2O_3	0.05	0.11	0.09	-	-	-	-
Fe_2O_3	2.22	-	1.26	3.63	7.77	1.19	-
FeO	4.72	6.55	5.37	7.62	8.16	23.99	0.02
MnO	-	0.06	0.04	0.09	0.08	0.62	-
MgO	14.19	14.37	14.46	15.27	14.58	6.38	-
CaO	22.89	23.08	23.02	11.91	11.80	8.58	9.84
Na_2O	0.88	-	0.68	2.18	1.45	-	8.58
K_2O	0.04	-	-	0.71	0.82	-	0.15
Total	99.80	99.01	99.79	99.08	102.16	102.04	103.15
Si^{4+}	1.963	2.007	1.973	6.686	6.360	5.997	10.073
Ti^{4+}	0.001	0.002	0.001	0.136	0.085	0.008	-
Al^{3+}	0.073	0.053	0.064	1.608	1.878	3.860	5.675
Cr^{3+}	0.001	0.003	0.003	-	-	-	-
Fe^{3+}	0.062	-	0.035	0.390	0.820	0.135	-
Fe^{2+}	0.146	0.205	0.166	0.910	0.957	3.039	0.003
Mn^{2+}	-	0.002	0.001	0.011	0.010	0.080	-
Mg^{2+}	0.782	0.802	0.797	3.249	3.050	1.442	-
Ca^{2+}	0.907	0.926	0.912	1.821	1.774	1.393	1.856
Na^{+}	0.063	-	0.049	0.603	0.394	-	2.929
K^{+}	0.002	-	-	0.129	0.147	-	0.034
Total	4.000	4.000	4.000	15.540	15.480	15.950	20.570
Fe_T	0.18	0.21	0.18	1.10	1.37	3.11	-
FeMg	0.18	0.20	0.19	0.25	0.31	0.68	-
XCa_1	-	-	-	0.29	0.29	0.23	-
XCa_2	-	-	-	-	-	-	0.39
XAl	-	-	-	-	-	0.19	0.40
XNa	-	-	-	-	-	0.25	-

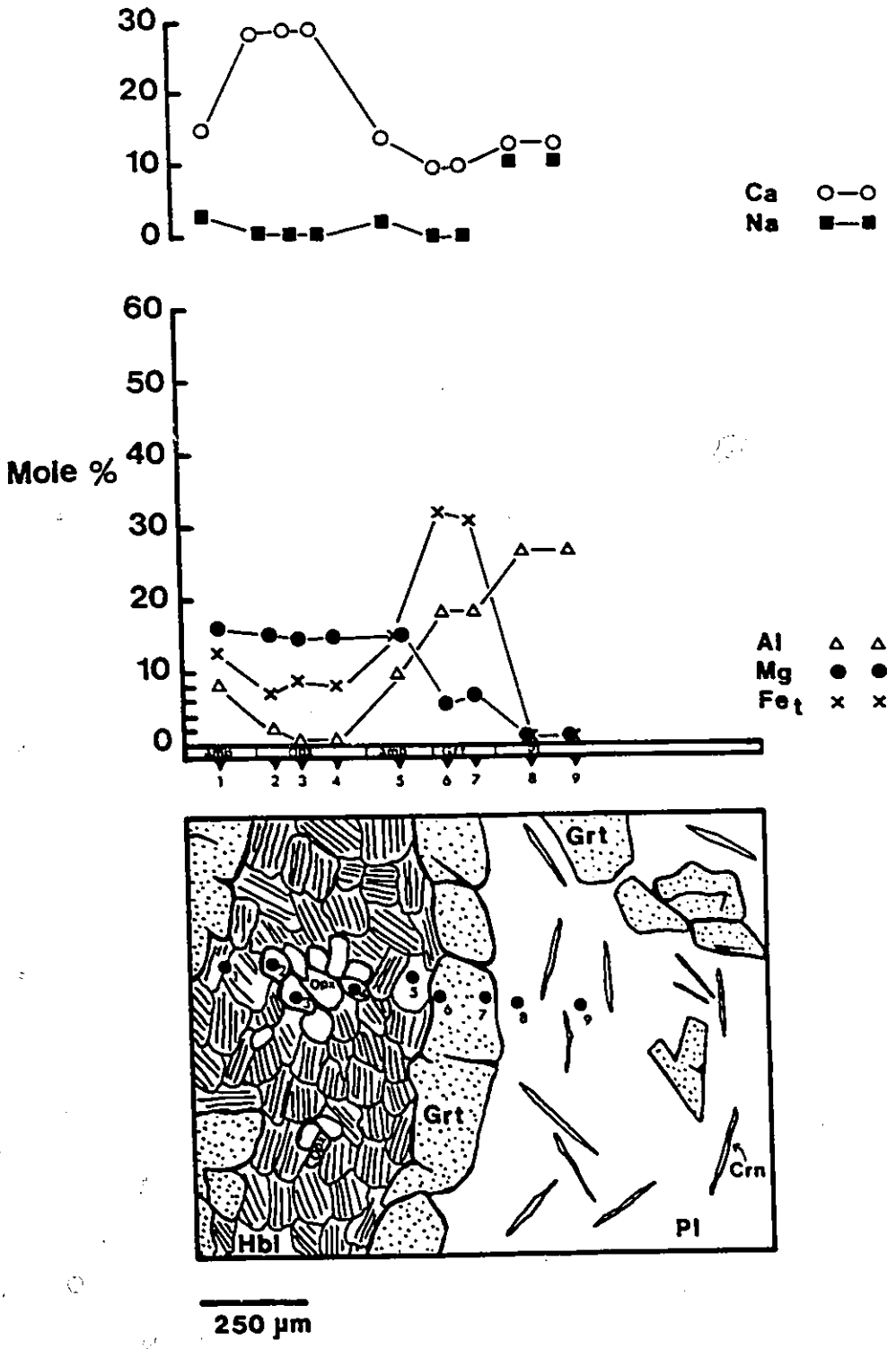
30
20
10
0
Ca
Na
60
50
40
30
20
10
0
Mole %
Al
Mg
Fe t
1 2 3 4 5 6 7 8 9
Grt
Grt
Hbl
Pl
Crn
250 µm

CMA - 27.6.3 - 87

Appendix B3. Figures and mineral analyses of corona structures from sample CMA-27.6.5-87

	Ol 1	Ol 2	Opx 3	Opx 4	Opx 5	Opx 6	Prg 7	Prg 8	Prg 9	Pl 10	Pl 11	Pl 12
SiO_2	33.57	34.44	51.86	51.75	52.03	51.91	39.45	36.80	36.60	51.70	54.12	53.50
TiO_2	-	-	0.02	0.06	0.05	-	0.16	0.06	0.18	0.10	0.07	0.14
Al_2O_3	-	-	0.15	0.59	0.34	0.32	16.88	19.34	20.27	28.88	27.85	28.41
Cr_2O_3	-	-	-	0.12	-	0.03	0.07	0.05	-	-	-	-
Fe_2O_3	-	-	0.00	-	-	-	4.66	4.79	4.82	-	-	-
FeO	44.92	46.10	24.71	25.40	25.33	25.64	9.79	10.06	10.12	2.07	0.89	1.47
MnO	0.30	0.45	0.19	0.41	0.03	0.06	0.05	-	-	-	-	-
MgO	20.62	20.44	22.12	21.63	22.31	21.10	11.48	9.96	10.24	-	-	-
CaO	-	-	0.29	0.37	0.21	0.33	11.03	10.43	10.18	9.41	10.06	9.04
Na_2O	-	-	-	-	0.43	0.06	4.22	3.61	4.00	8.27	6.53	8.24
K_2O	-	-	0.05	0.08	-	0.08	1.55	1.46	1.59	0.13	0.12	0.17
Total	99.11	100.98	99.50	100.45	100.89	99.88	99.32	96.62	98.05	100.56	99.64	100.97
Si^{4+}	0.991	0.999	1.966	1.952	1.951	1.970	5.796	5.559	5.455	9.480	9.867	9.703
Ti^{4+}	-	-	0.001	0.002	0.001	-	0.018	0.007	0.020	0.014	0.010	0.019
Al^{3+}	-	-	0.007	0.026	0.015	0.014	2.923	3.443	3.561	6.241	5.985	6.072
Cr^{3+}	-	-	-	0.004	-	0.001	0.008	0.006	-	-	-	-
Fe^{3+}	-	-	0.000	-	-	-	0.515	0.544	0.541	-	-	-
Fe^{2+}	1.109	1.118	0.783	0.801	0.794	0.814	1.460	1.543	1.532	0.317	0.136	0.223
Mn^{2+}	-	-	0.010	0.014	0.006	0.013	0.004	0.008	0.006	-	-	-
Mg^{2+}	0.908	0.884	1.250	1.216	1.247	1.194	2.514	2.243	2.275	-	-	-
Ca^{2+}	-	-	0.012	0.015	0.008	0.013	1.755	1.688	1.626	1.849	1.965	1.757
Na^{+}	-	-	-	-	0.031	0.004	1.202	1.057	1.156	2.940	2.308	2.897
K^{+}	-	-	0.002	0.004	-	0.004	0.291	0.281	0.302	0.030	0.028	0.039
Total	3.010	3.000	4.030	4.030	4.060	4.030	16.490	16.380	16.470	20.870	20.300	20.710
Fe_T	-	-	0.78	0.80	0.79	0.81	1.72	1.82	1.80	-	-	-
FeMg	0.55	0.56	0.39	0.40	0.39	0.41	0.41	0.45	0.44	-	-	-
XCa_1	-	-	0.01	0.01	0.00	0.01	0.29	0.29	0.29	-	-	-
XCa_2	-	-	-	-	-	-	-	-	-	0.39	0.46	0.38
XAl	-	-	-	-	-	-	0.34	0.38	0.39	-	-	-
XNa	-	-	-	-	-	-	0.41	0.39	0.42	-	-	-

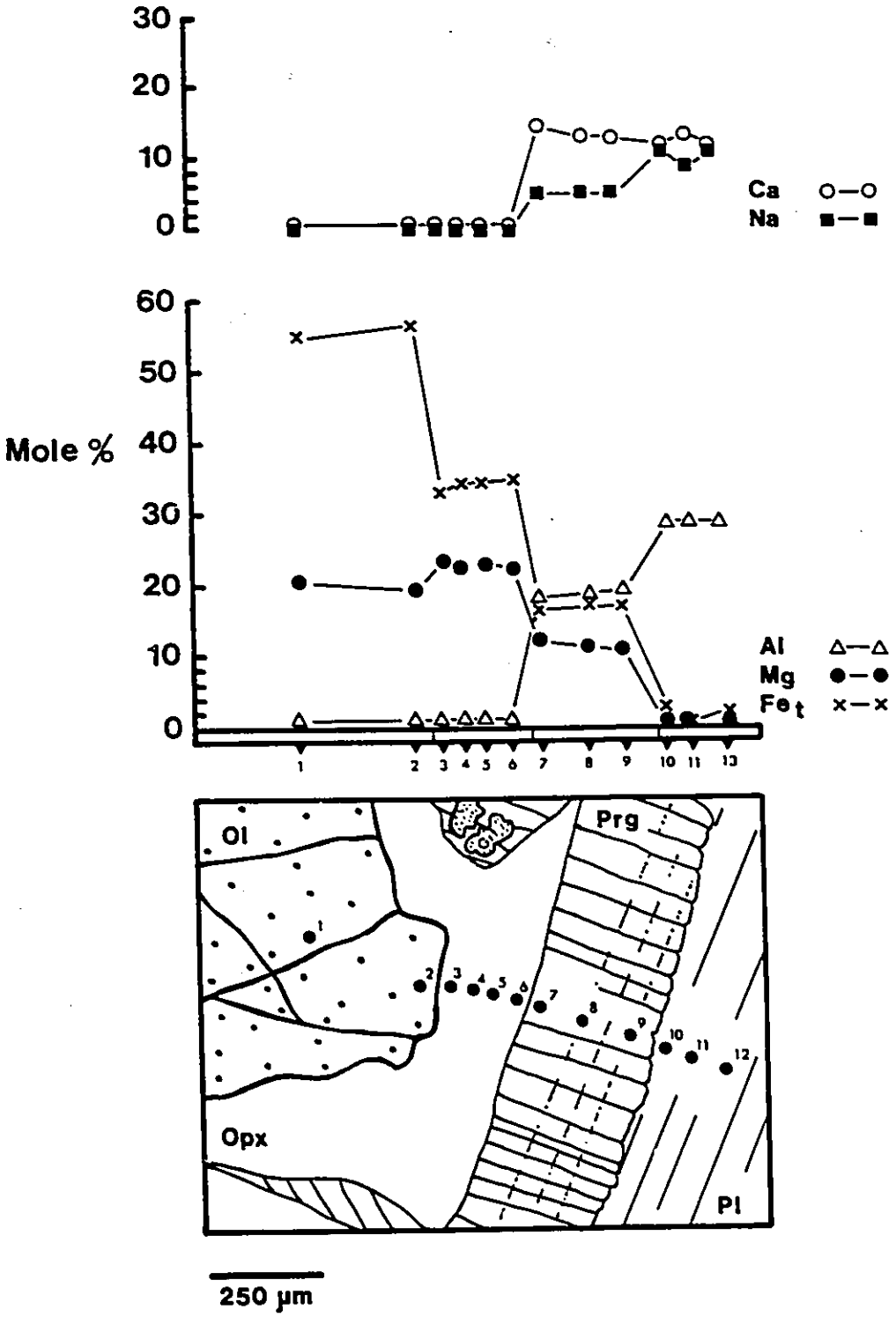
30
20
10
0
Ca
Na
60
50
40
30
20
10
0
Mole %
Al
Mg
Fe t
1
2
3
4
5
6
7
8
9
10
11
13
Ol
Prg
Opx
Pl
250 µm

CMA - 27.6.5 - 87

Appendix B3 (continued)

	Ol 1	Ol 2	Ol 3	Opx 4	Opx 5	Opx 6	Prg 7	Prg 8	Prg 9	Pl 10	Pl 11	Pl 12	Pl 13
SiO_2	34.47	34.40	34.29	52.52	52.38	51.97	39.24	37.84	36.78	51.37	51.74	52.08	52.14
TiO_2	0.11	-	0.07	-	0.06	-	0.03	0.09	0.07	0.08	0.12	0.10	0.07
Al_2O_3	-	-	-	0.14	0.39	0.22	17.66	18.86	21.98	29.93	29.34	29.38	28.96
Cr_2O_3	0.02	-	-	-	0.02	-	0.02	0.08	-	-	-	-	-
Fe_2O_3		-	-	-	0.00	0.00	4.41	4.56	4.97	-	-	-	-
FeO	41.59	41.52	41.02	22.89	23.49	24.46	9.27	9.57	10.44	2.83	0.19	1.88	0.50
MnO	-	-	-	0.31	0.33	0.30	-	-	0.10	-	-	-	-
MgO	24.58	24.30	24.18	23.58	22.74	22.69	11.35	11.29	10.51	-	-	-	-
CaO	-	-	-	0.23	1.00	0.14	11.15	10.68	10.00	8.60	12.44	9.89	11.82
Na_2O	-	-	-	-	-	-	3.25	3.77	3.59	7.28	5.18	6.94	5.64
K_2O	-	-	-	-	0.04	-	1.03	1.12	1.19	0.12	0.15	0.16	0.17
Total	100.77	100.22	99.56	99.67	100.45	99.78	97.41	97.86	99.63	100.21	99.16	100.43	99.30
Si^{4+}	0.982	0.985	0.987	1.968	1.958	1.961	5.816	5.613	5.369	9.421	9.508	9.510	9.576
Ti^{4+}	-	-	-	-	0.002	-	0.003	0.010	0.008	0.011	0.017	0.014	0.010
Al^{3+}	-	-	-	0.006	0.017	0.010	3.085	3.297	3.781	6.469	6.355	6.323	6.268
Cr^{3+}	0.000	-	-	-	0.001	-	0.002	0.009	-	-	-	-	-
Fe^{3+}	-	-	-	-	0.000	0.000	0.492	0.509	0.546	-	-	-	-
Fe^{2+}	0.991	0.994	0.988	0.717	0.734	0.772	1.395	1.442	1.547	0.434	0.029	0.287	0.077
Mn^{2+}	-	-	-	0.010	0.010	0.010	-	-	0.012	-	-	-	-
Mg^{2+}	1.044	1.037	1.038	1.317	1.267	1.276	2.508	2.497	2.287	-	-	-	-
Ca^{2+}	-	-	-	0.009	0.040	0.006	1.771	1.697	1.564	1.690	2.449	1.935	2.326
Na^{+}	-	-	-	-	-	-	0.934	1.084	1.016	2.589	1.846	2.457	2.008
K^{+}	-	-	-	-	0.002	-	0.195	0.212	0.222	0.028	0.035	0.037	0.040
Total	3.020	3.020	3.010	4.030	4.030	4.030	16.200	16.370	16.350	20.640	20.240	20.560	20.300
Fe_T	-	-	-	0.72	0.73	0.77	1.64	1.7	1.82	-	-	-	-
FeMg	0.49	0.49	0.49	0.35	0.37	0.38	0.4	0.4	0.44	-	-	-	-
XCa_1	-	-	-	0	0.02	0	0.3	0.29	0.28	-	-	-	-
XCa_2	-	-	-	-	-	-	-	-	-	0.39	0.57	0.44	0.54
XAl	-	-	-	-	-	-	0.35	0.37	0.41	-	-	-	-
XNa	-	-	-	-	-	-	0.35	0.39	0.39	-	-	-	-

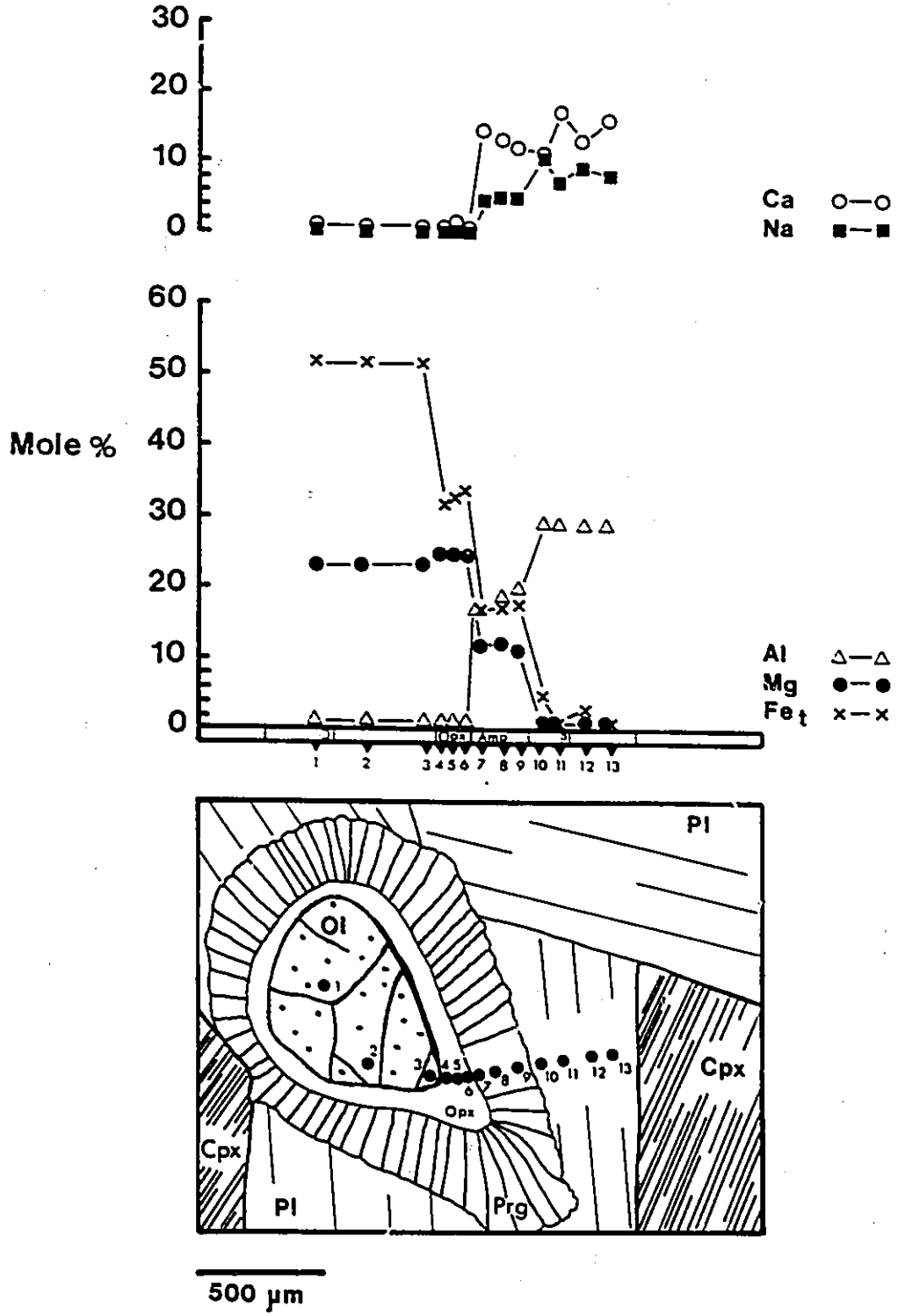
30
20
10
0
Ca
Na
60
50
40
30
20
10
0
Mole %
Al
Mg
Fe t
Opx
Amp
1 2 3 4 5 6 7 8 9 10 11 12 13
Pl
Ol
Cpx
Opx
Cpx
Pl
Prg
500 µm

CMA - 27.6.5 - 87

Appendix B4. Figures and mineral analyses of corona structures from sample CMA-LG6-87

	Ilm 1	Opx 2	Prg 3	Prg 4	Pl 5	Pl 6
SiO_2	47.93	47.37	33.14	37.99	56.25	57.23
TiO_2	0.04	0.02	0.58	0.05	-	-
Al_2O_3	0.25	0.38	16.69	16.52	26.98	26.17
Cr_2O_3	0.11	0.10	-	0.04	-	-
Fe_2O_3	-	3.08	8.81	7.98	-	-
FeO	41.44	37.97	18.50	16.76	0.40	0.26
MnO	0.89	1.02	0.04	0.25	-	-
MgO	9.74	9.56	7.24	4.07	-	-
CaO	0.31	0.34	0.04	10.48	9.18	8.49
Na_2O	-	-	-	2.53	8.44	9.13
K_2O	-	0.06	8.72	1.42	0.22	0.27
Total	100.71	99.90	93.75	98.08	101.47	101.55
Si^{4+}	0.972	1.943	5.503	5.856	10.073	10.228
Ti^{4+}	0.001	0.001	0.073	0.005	-	-
Al^{3+}	0.006	0.018	3.267	3.001	5.694	5.512
Cr^{3+}	0.002	0.003	-	0.005	-	-
Fe^{3+}	0.047	0.095	1.101	0.926	-	-
Fe^{2+}	0.656	1.302	2.569	2.162	0.060	0.039
Mn^{2+}	0.015	0.035	0.006	0.032	-	-
Mg^{2+}	0.295	0.584	1.791	0.937	-	-
Ca^{2+}	0.007	0.015	0.006	1.806	1.761	1.626
Na^{+}	-	-	-	0.756	2.930	3.163
K^{+}	-	0.003	1.846	0.280	0.050	0.062
Total	2.000	4.000	16.160	15.770	20.570	20.630
Fe_T	0.68	1.35	3.12	2.62	-	-
FeMg	0.70	0.70	0.64	0.74	-	-
XCa_1	-	0.01	0.00	0.34	-	-
XCa_2	-	-	-	-	0.38	0.34
XAl	-	-	0.37	0.34	-	-
XNa	-		-	0.30	-	-

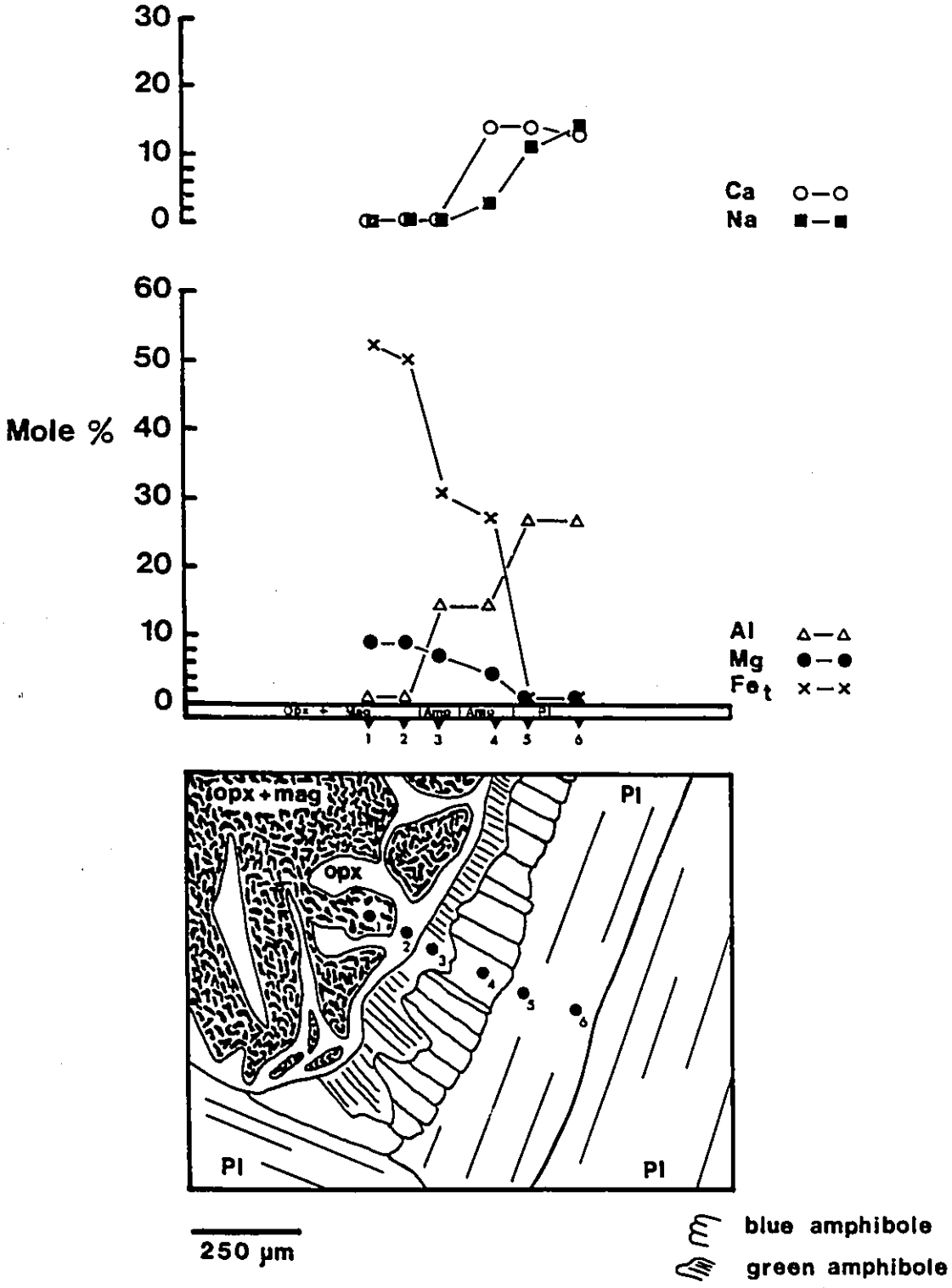
30
20
10
0
Ca
Na
60
50
Mole %
40
30
20
10
0
Al
Mg
Fe t
Opx + Mag
Amp
Amp
Pl
1
2
3
4
5
6
opx + mag
opx
Pl
Pl
Pl
250 µm
blue amphibole
green amphibole

CMA - LG6 - 87

Appendix B4 (continued)

	Mag 1	Pl 3	Pl 4	Pl 5
SiO_2	0.38	53.26	51.23	51.93
TiO_2	0.94	-	-	-
Al_2O_3	0.46	28.72	29.80	30.11
Cr_2O_3	0.26	-	-	-
Fe_2O_3	66.62	-	-	-
FeO	32.94	0.41	0.56	0.37
MnO	-	-	-	-
MgO	-	-	-	-
CaO	0.06	12.32	13.66	13.37
Na_2O	-	6.02	4.78	5.03
K_2O	-	0.18	0.20	0.15
Total	101.66	100.91	100.23	100.96
Si^{4+}	0.014	9.641	9.367	9.405
Ti^{4+}	0.027	-	-	-
Al^{3+}	0.020	6.127	6.422	6.427
Cr^{3+}	0.008	-	-	-
Fe^{3+}	1.890	-	-	-
Fe^{2+}	1.039	0.062	0.086	0.056
Mn^{2+}	-	-	-	-
Mg^{2+}	-	-	-	-
Ca^{2+}	0.002	2.389	2.676	2.594
Na^{+}	-	2.113	1.695	1.766
K^{+}	-	0.042	0.047	0.035
Total	3.000	20.370	20.290	20.280
Fe_T	1.98	-	-	-
FeMg	1.00	-	-	-
XCa_1	0.00	-	-	-
XCa_2	-	0.53	0.61	0.59
XAl	-	-	-	-
XNa	-	-	-	-

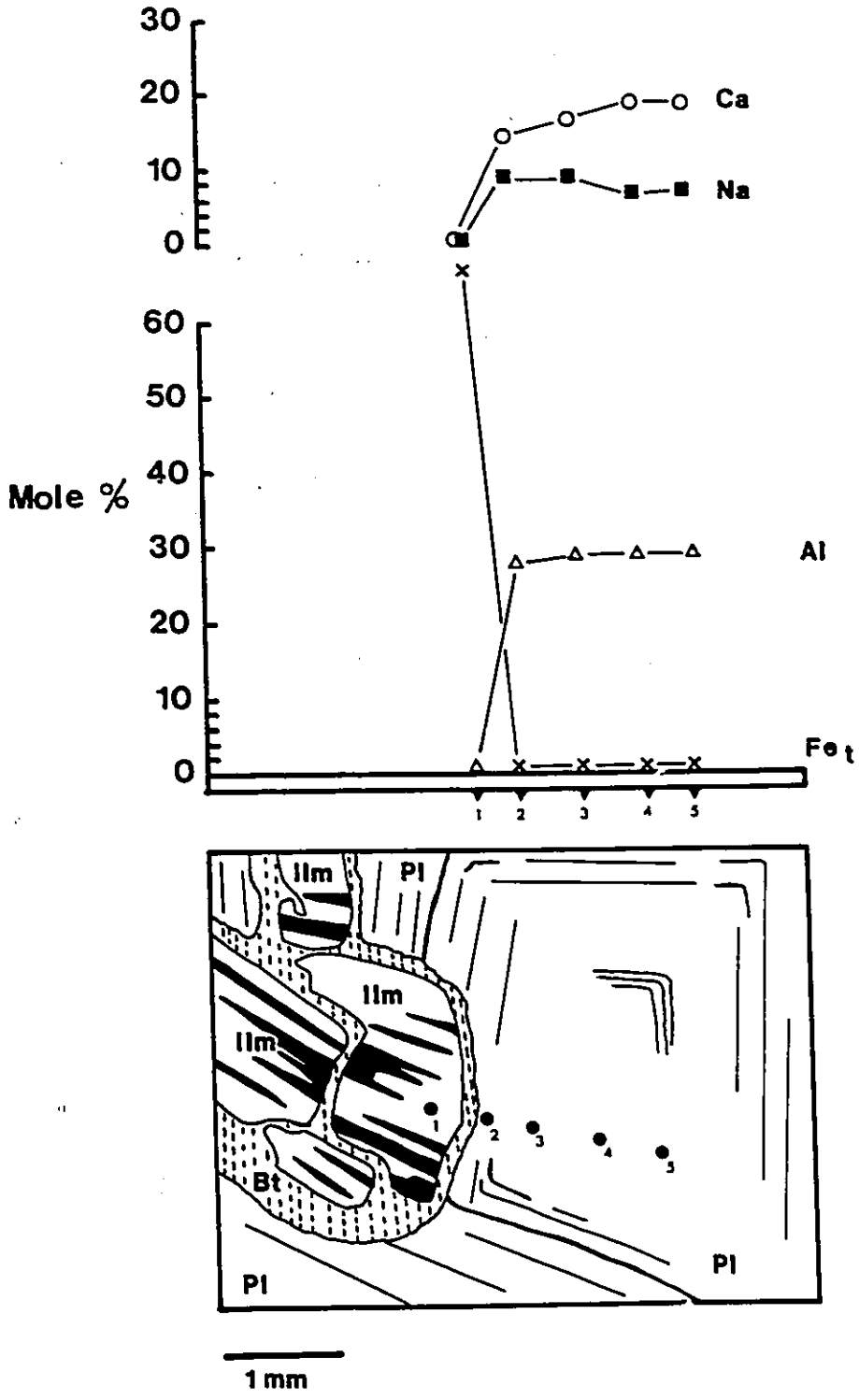
30
20
10
0
Ca
Na
60
50
40
30
20
10
0
Mole %
Al
Fe t
1
2
3
4
5
Ilm
Pl
Ilm
Ilm
Bt
Pl
Pl
1 mm

CMA - LG6 - 87

Appendix B5. Figures and mineral analyses of corona structures from sample CMA-LG7-87

	Ilm 2	Ilm 3	Ilm 4	Grt 5	Grt 6	Bt 7
SiO_2	0.32	0.32	0.18	37.45	37.38	35.66
TiO_2	49.48	48.79	49.03	0.01	0.10	4.31
Al_2O_3	-	-	-	20.67	20.42	14.01
Cr_2O_3	0.10	0.13	0.09	-	0.05	-
Fe_2O_3	-	-	-	1.01	0.99	3.95
FeO	49.02	48.54	48.61	33.37	33.15	21.83
MnO	0.31	0.41	0.28	1.58	1.41	-
MgO	-	-	-	1.23	1.06	8.15
CaO	0.06	0.09	0.04	6.04	6.43	-
Na_2O	-	-	-	-	-	-
K_2O	-	-	-	-	-	9.30
Total	99.29	98.28	98.23	101.36	100.99	97.21
Si^{4+}	0.008	0.008	0.005	5.984	5.999	5.472
Ti^{4+}	0.943	0.939	0.945	0.001	0.012	0.497
Al^{3+}	-	-	-	3.893	3.863	2.534
Cr^{3+}	0.002	0.003	0.002	-	0.006	-
Fe^{3+}	0.096	0.103	0.099	0.122	0.120	0.456
Fe^{2+}	0.943	0.936	0.942	4.459	4.449	2.801
Mn^{2+}	0.007	0.009	0.006	0.214	0.192	-
Mg^{2+}	-	-	-	0.293	0.254	1.864
Ca^{2+}	0.002	0.002	0.001	1.034	1.106	-
Na^{+}	-	-	-	-	-	-
K^{+}	-	-	-	-	-	1.821
Total	2.000	2.000	2.000	16.000	16.000	15.450
Fe_T	0.99	0.99	0.99	4.52	4.51	3.03
FeMg	1.00	1.00	1.00	0.94	0.95	0.62
XCa_1	-	-	-	0.18	0.19	-
XCa_2	-	-	-	-	-	-
XAl	-	-	-	-	-	-
XNa	-	-	-	-	-	-

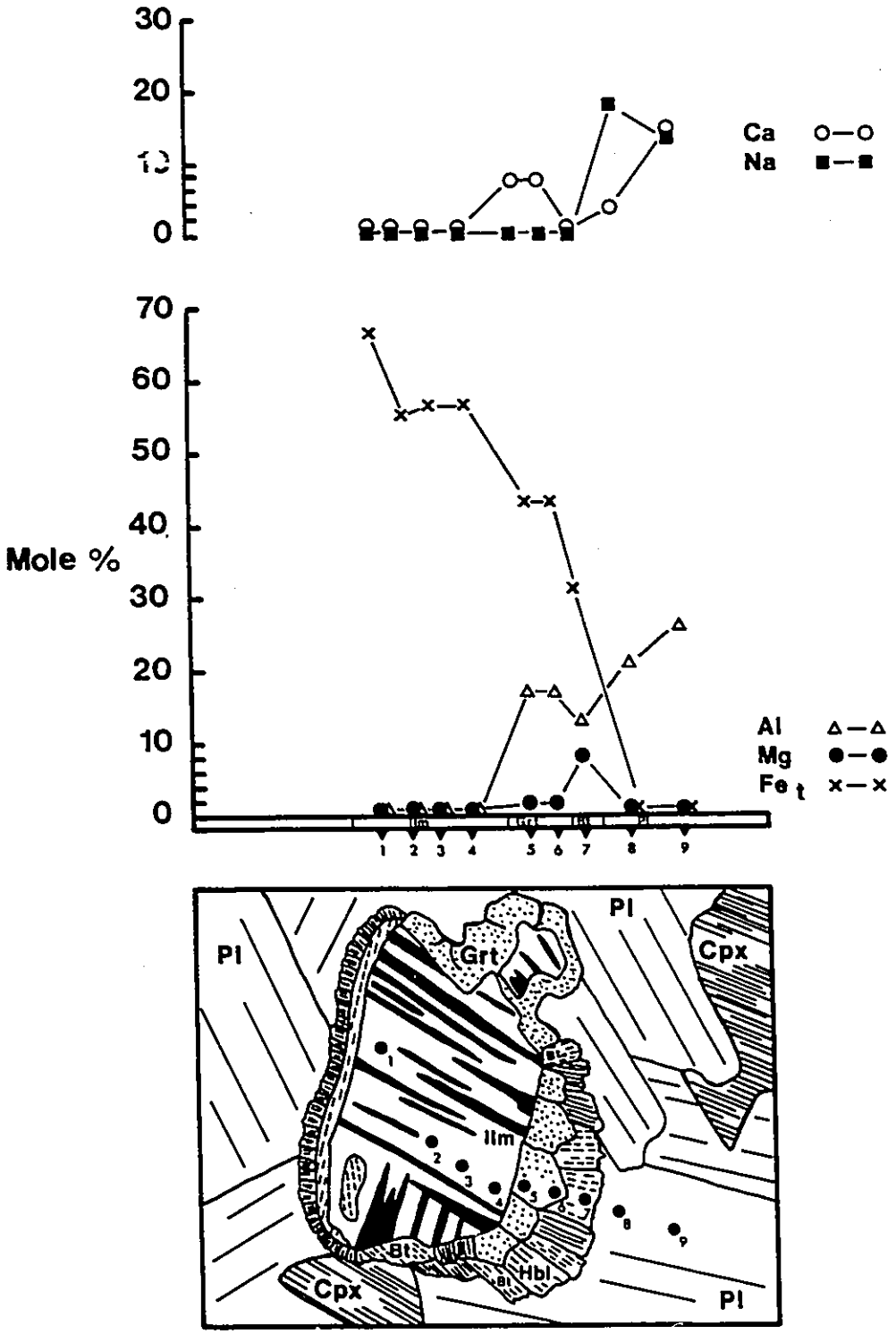
30
20
10
0
Ca
Na
70
60
50
40
30
20
10
0
Mole %
Al
Mg
Fe t
1 2 3 4 5 6 7 8 9
Pl
Grt
Cpx
Ilm
Bt
Hbl
Pl
Cpx
Pl
500 µm

CMA - LG 7 - 87

Appendix B5 (continued)

	Pl 1	Pl 2	Prg 3	Prg 4	Opx 5	Ilm 6
SiO_2	54.83	54.93	37.86	39.61	49.02	42.12
TiO_2	-	-	0.09	0.07	-	0.10
Al_2O_3	28.18	28.37	18.92	16.10	0.04	0.33
Cr_2O_3	-	-	-	0.12	-	0.08
Fe_2O_3	-	-	7.23	7.42	1.79	-
FeO	0.23	0.04	15.18	15.58	35.99	45.44
MnO	-	-	0.19	0.22	0.63	0.66
MgO	-	-	5.14	5.61	12.10	10.50
CaO	11.09	10.91	10.46	10.79	0.33	0.21
Na_2O	6.44	6.23	2.52	2.26	-	-
K_2O	0.20	0.10	1.44	1.33	-	-
Total	100.97	100.58	99.03	99.11	99.90	99.44
Si^{4+}	9.861	9.884	5.712	5.979	1.972	0.868
Ti^{4+}	-	-	0.010	0.008	-	0.002
Al^{3+}	5.973	6.016	3.364	2.864	0.002	0.008
Cr^{3+}	-	-	-	0.014	-	0.001
Fe^{3+}	-	-	0.821	0.843	0.054	0.252
Fe^{2+}	0.035	0.006	1.915	1.967	1.211	0.531
Mn^{2+}	-	-	0.024	0.028	0.021	0.012
Mg^{2+}	-	-	1.156	1.262	0.726	0.322
Ca^{2+}	2.137	2.103	1.691	1.779	0.014	0.005
Na^{+}	2.246	2.173	0.737	0.661	-	-
K^{+}	0.046	0.023	0.277	0.256	-	-
Total	20.300	20.210	15.710	15.660	4.000	2.000
Fe_T	-	-	2.33	2.39	1.24	0.66
FeMg	-	-	0.67	0.65	0.63	0.67
XCa_1	-	-	0.33	0.33	0.01	-
XCa_2	0.49	0.49	-	-	-	-
XAl	-	-	0.37	0.32	-	-
XNa	-	-	0.30	0.27	-	-

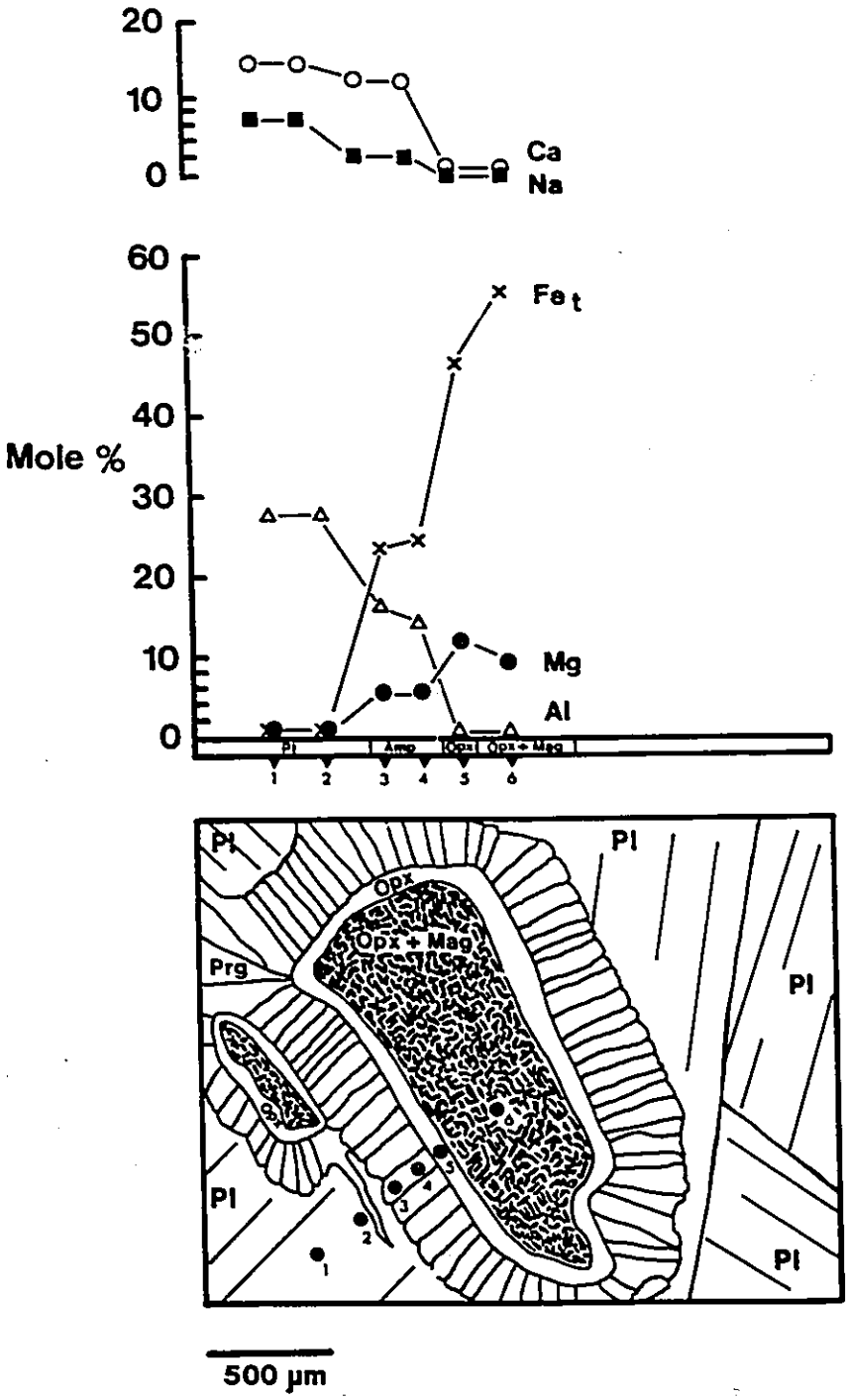
20
10
0
Ca
Na
60
50
40
30
20
10
0
Mole %
Fe t
Mg
Al
Pl
Amp
Opx
Opx + Mag
1
2
3
4
5
6
Pl
Opx
Opx + Mag
Prg
Pl
Pl
Pl
Pl
500 µm

CMA - LG 7 - 87

Appendix B6. Figures and mineral analyses of corona structures from sample CMA-146-86

	Prg 1	Prg 2	Prg 3	Cpx 4	Cpx 5	Cpx 6	Cpx 7	Prg 8	Prg 9	Pl 10	Pl 11	Pl 12
SiO_2	41.11	50.05	49.73	46.50	51.07	51.12	51.22	51.50	41.11	57.28	56.47	55.75
TiO_2	0.91	0.44	0.40	3.59	0.73	0.64	0.19	0.35	1.25	-	-	-
Al_2O_3	12.80	3.74	4.53	4.10	0.87	1.10	1.43	3.27	11.61	27.13	27.62	27.65
Cr_2O_3	0.12	0.05	0.06	0.08	0.05	0.09	0.10	0.06	0.24	-	-	-
Fe_2O_3	6.93	5.62	5.70	0.45	0.44	0.23	-	5.39	6.83	-	-	-
FeO	14.56	11.80	11.96	17.21	10.16	11.95	12.57	11.31	14.34	0.14	0.13	0.32
MnO	0.18	0.09	0.11	0.17	0.16	0.24	0.12	0.17	0.14	-	-	-
MgO	8.42	13.90	13.41	12.24	12.61	12.42	11.70	14.18	7.81	-	-	-
CaO	11.46	11.51	11.68	13.29	22.43	21.15	21.27	11.81	11.37	9.27	9.97	10.03
Na_2O	1.77	0.38	0.38	0.39	-	-	-	0.62	1.83	7.57	7.39	6.74
K_2O	1.05	0.24	0.28	0.26	0.06	0.09	0.15	0.24	1.14	0.13	0.18	0.22
Total	99.31	97.82	98.25	98.29	98.58	99.03	98.75	98.90	97.67	101.52	101.76	100.71
Si^{4+}	6.151	7.318	7.252	1.814	1.954	1.954	1.967	7.421	6.259	10.184	10.048	10.019
Ti^{4+}	0.102	0.048	0.044	0.105	0.021	0.018	0.005	0.038	0.143	-	-	-
Al^{3+}	2.257	0.645	0.779	0.188	0.039	0.050	0.065	0.555	2.083	5.685	5.792	5.856
Cr^{3+}	0.014	0.006	0.007	0.002	0.002	0.003	0.003	0.007	0.029	-	-	-
Fe^{3+}	0.780	0.618	0.625	0.013	0.013	0.007	-	0.584	0.783	-	-	-
Fe^{2+}	1.822	1.443	1.458	0.561	0.325	0.382	0.404	1.363	1.826	0.021	0.019	0.048
Mn^{2+}	0.023	0.011	0.014	0.006	0.005	0.008	0.004	0.021	0.018	-	-	-
Mg^{2+}	1.878	3.030	2.915	0.712	0.719	0.708	0.670	3.046	1.773	-	-	-
Ca^{2+}	1.837	1.803	1.824	0.555	0.919	0.866	0.875	1.823	1.941	1.766	1.901	1.931
Na^{+}	0.513	0.108	0.107	0.029	-	-	-	0.173	0.540	2.609	2.550	2.348
K^{+}	0.200	0.045	0.053	0.013	0.003	0.004	0.007	0.044	0.221	0.029	0.041	0.050
Total	15.580	15.080	15.080	4.000	4.000	4.000	4.000	15.080	15.620	20.290	20.350	20.250
Fe_T	2.21	1.75	1.77	0.57	0.33	0.39	0.40	1.66	2.22	-	-	-
FeMg	0.54	0.37	0.38	0.44	0.32	0.35	0.38	0.35	0.56	-	-	-
XCa_1	0.31	0.27	0.28	0.30	0.47	0.44	0.45	0.28	0.33	-	-	-
XCa_2	-	-	-	-	-	-	-	-	-	0.40	0.43	0.45
XAl	0.27	0.08	0.10	-	-	-	-	0.07	0.25	-	-	-
XNa	0.22	0.06	0.05	-	-	-	-	0.09	0.22	-	-	-

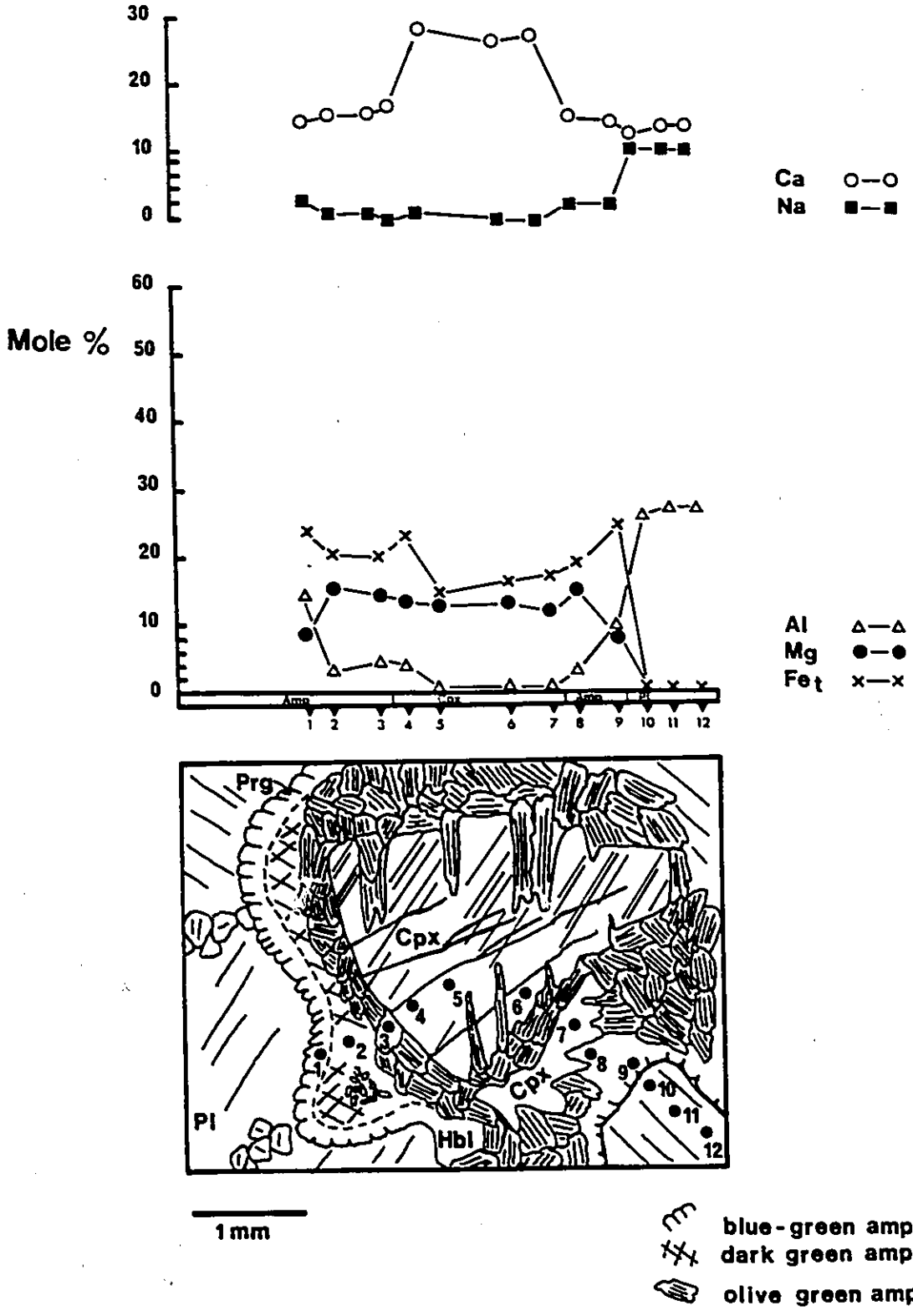
30
20
10
0
Ca
Na
Mole %
60
50
40
30
20
10
0
Al
Mg
Fe t
Amp
Cpx
Amp
Pl
1 2 3 4 5 6 7 8 9 10 11 12
Prg
Cpx
Pl
Hbl
Cpx
1 mm
blue-green amphibole
dark green amphibole
olive green amphibole

CMA - 146 - 86

Appendix B6 (continued)

	Hbl 1	Cpx 2	Cpx 3	Cpx 4	Cpx 5	Hbl 6	Hbl 7	Pl 8	Grt 9	Grt 10
SiO_2	51.00	51.48	50.10	49.62	50.76	42.07	37.73	52.79	37.28	37.24
TiO_2	0.46	0.16	0.63	1.66	0.34	0.73	0.51	-	0.03	0.06
Al_2O_3	3.89	0.91	2.80	2.89	2.11	12.93	16.64	28.50	20.40	20.45
Cr_2O_3	0.12	0.06	0.08	0.13	0.15	0.09	-	-	0.03	-
Fe_2O_3	5.82	0.30	0.87	1.03	1.57	7.11	7.45	-	1.02	0.90
FeO	12.23	12.12	12.79	11.61	11.66	14.94	15.65	-	28.98	29.22
MnO	0.13	0.22	0.13	0.20	0.13	0.02	-	-	1.30	1.20
MgO	13.11	11.22	12.59	13.87	11.80	8.04	5.84	-	1.91	1.63
CaO	11.49	22.63	17.91	17.95	20.24	11.52	11.02	11.73	8.10	8.73
Na_2O	0.94	-	0.36	0.20	0.38	2.16	2.50	5.57	-	-
K_2O	0.28	0.12	0.17	0.12	0.16	1.08	1.54	0.06	-	-
Total	99.47	99.22	98.42	99.28	99.30	100.69	98.88	98.65	99.04	99.43
Si^{4+}	7.351	1.973	1.922	1.882	1.936	6.209	5.745	9.710	6.000	6.000
Ti^{4+}	0.050	0.005	0.018	0.047	0.010	0.081	0.058	-	0.004	0.007
Al^{3+}	0.661	0.041	0.127	0.129	0.095	2.249	2.986	6.178	3.870	3.883
Cr^{3+}	0.014	0.002	0.002	0.004	0.005	0.011	-	-	0.004	-
Fe^{3+}	0.631	0.009	0.025	0.030	0.045	0.790	0.854	-	0.123	0.110
Fe^{2+}	1.474	0.388	0.410	0.368	0.372	1.844	1.993	-	3.900	3.937
Mn^{2+}	0.016	0.007	0.004	0.006	0.004	0.002	-	-	0.177	0.164
Mg^{2+}	2.817	0.641	0.720	0.784	0.671	1.769	1.326	-	0.458	0.392
Ca^{2+}	1.774	0.929	0.736	0.729	0.827	1.868	1.837	2.312	1.397	1.507
Na^{+}	0.263	-	0.027	0.015	0.028	0.618	0.738	1.986	-	-
K^{+}	0.051	0.006	0.008	0.006	0.008	0.203	0.299	0.014	-	-
Total	15.100	4.000	4.000	4.000	4.000	15.640	15.830	20.200	15.930	16.000
Fe_T	1.79	0.39	0.42	0.38	0.39	2.24	2.42	-	3.96	3.99
FeMg	0.39	0.38	0.37	0.33	0.37	0.56	0.65	-	0.90	0.91
XCa_1	0.28	0.47	0.39	0.38	0.44	0.32	0.33	-	0.24	0.26
XCa_2	-	-	-	-	-	-	-	0.54	-	-
XAl	0.08	-	-	-	-	0.27	0.34	-	-	-
XNa	0.13	-	-	-	-	0.25	0.29	-	-	-

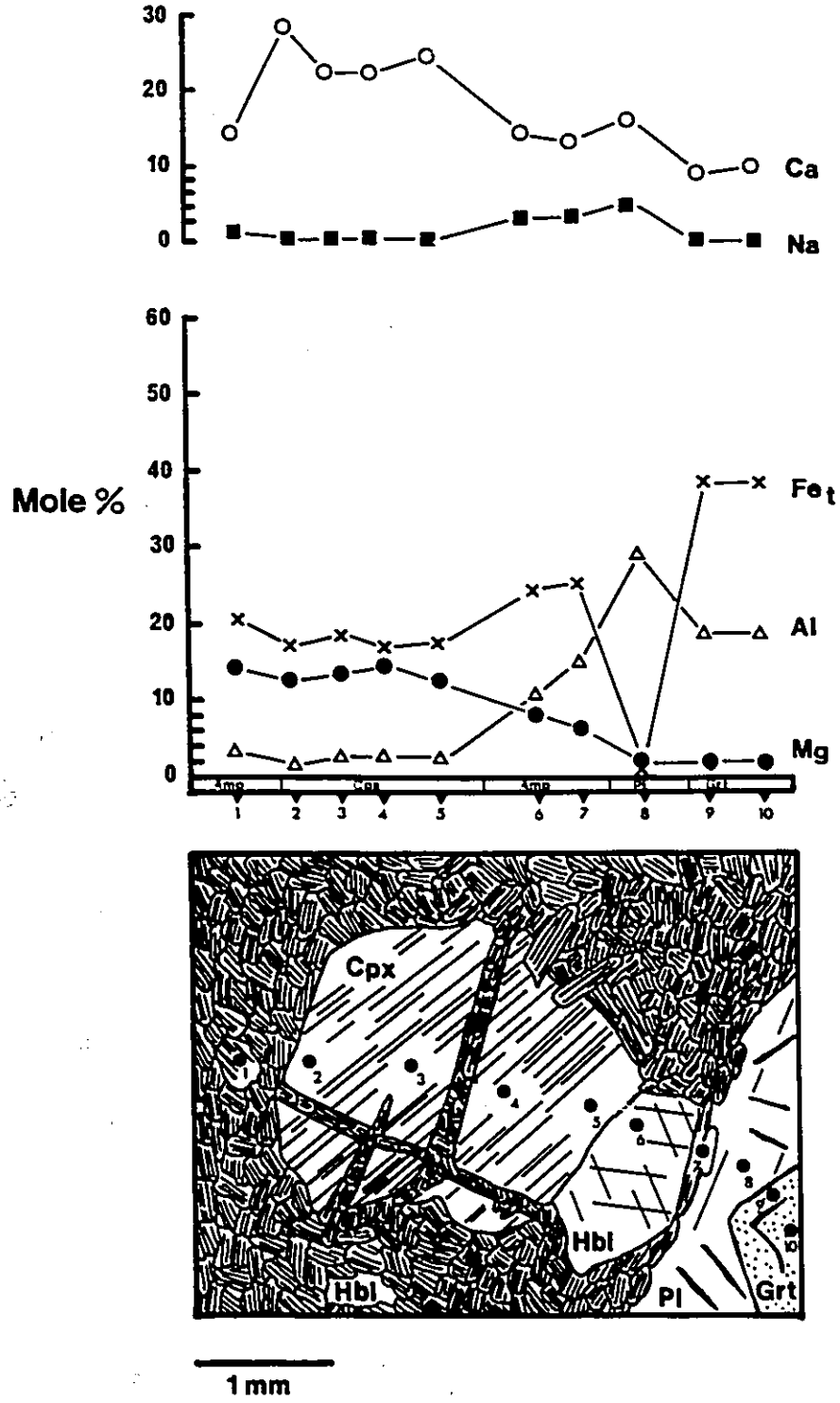
30
20
10
0
Ca
Na
60
50
40
30
20
10
0
Mole %
Fe t
Al
Mg
Amp
Cpx
Amp
Pl
Grt
1
2
3
4
5
6
7
8
9
10
Cpx
Hbl
Hbl
Pl
Grt
1 mm

CMA -146 - 86

Appendix B6 (continued)

	Prg 1	Prg 2	Prg 3	Grt 4	Grt 5
SiO_2	48.33	40.94	41.35	37.68	37.12
TiO_2	0.43	0.67	0.73	0.07	-
Al_2O_3	4.18	11.58	10.30	20.80	20.34
Cr_2O_3	0.06	0.11	0.12	0.02	-
Fe_2O_3	6.29	7.29	6.84	0.89	1.03
FeO	13.20	15.30	14.36	30.59	30.58
MnO	0.13	0.18	0.14	1.51	1.39
MgO	12.74	8.18	8.24	2.19	1.76
CaO	10.28	10.94	10.71	7.12	6.63
Na_2O	0.64	2.02	1.36	-	-
K_2O	0.25	0.85	0.64	-	-
Total	96.53	98.06	94.79	100.87	98.85
Si^{4+}	7.227	6.232	6.449	5.988	6.000
Ti^{4+}	0.048	0.077	0.086	0.008	-
Al^{3+}	0.737	2.078	1.893	3.896	3.875
Cr^{3+}	0.007	0.013	0.015	0.003	-
Fe^{3+}	0.708	0.835	0.803	0.106	0.125
Fe^{2+}	1.651	1.948	1.873	4.066	4.134
Mn^{2+}	0.016	0.023	0.018	0.203	0.190
Mg^{2+}	2.840	1.856	1.916	0.519	0.424
Ca^{2+}	1.647	1.784	1.790	1.212	1.148
Na^{+}	0.186	0.596	0.411	-	-
K^{+}	0.048	0.165	0.127	-	-
Total	15.120	15.610	15.380	16.000	15.900
Fe_T	2.00	2.37	2.27	4.12	4.20
FeMg	0.41	0.56	0.54	0.89	0.91
XCa_1	0.25	0.30	0.30	0.21	0.20
XCA_2	-	-	-	-	-
XAl	0.09	0.25	0.23	-	-
XNa	0.10	0.25	0.19	-	-

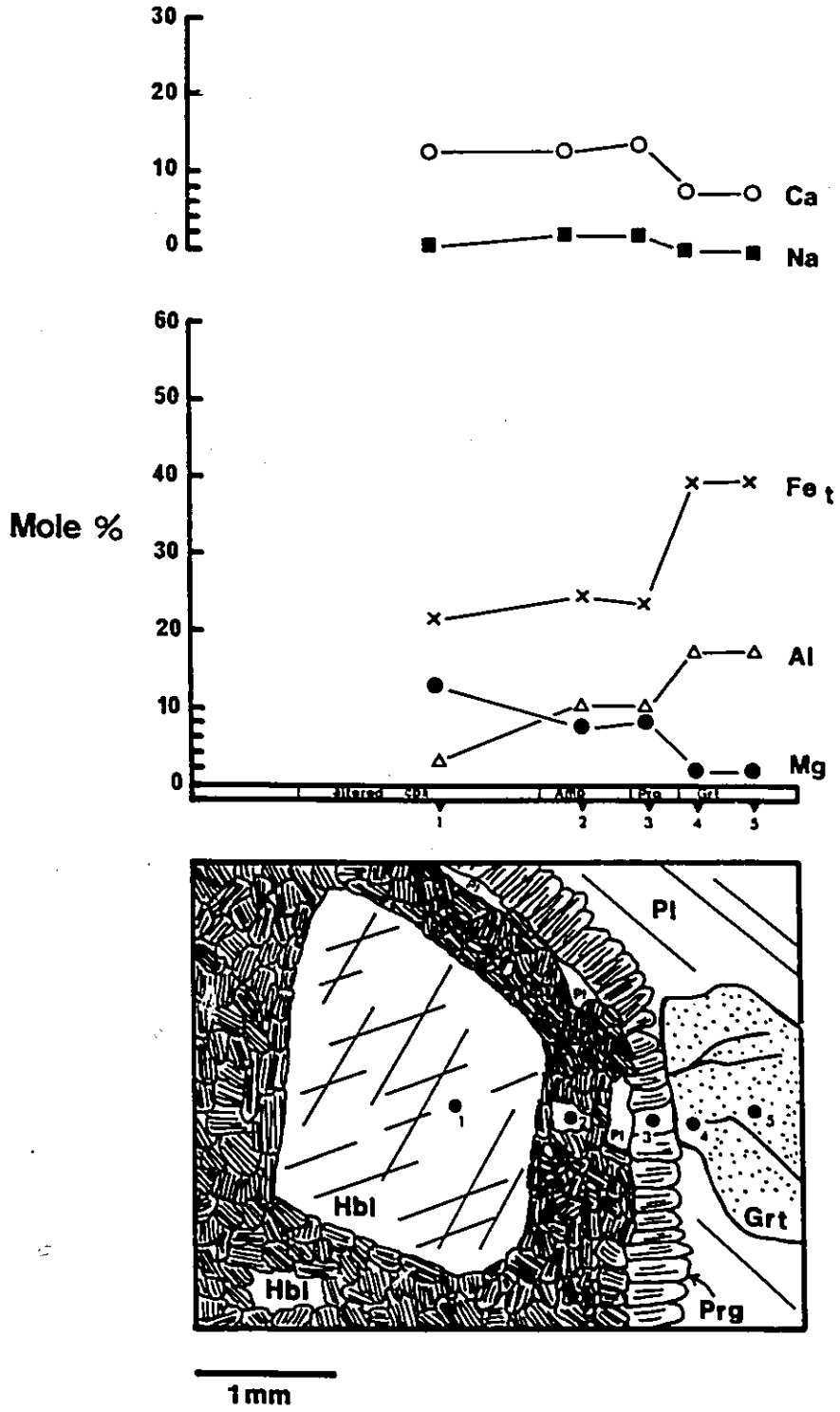
30
20
10
0
Ca
Na
60
50
40
30
20
10
0
Mole %
Fe t
Al
Mg
altered
Cpx
Amp
Pre
Grt
1
2
3
4
5
Pl
Hbl
Hbl
Grt
Prg
1mm

CMA - 146 - 86

Legend to Appendix C

Mineral Symbols:

Ol	= Olivine
Pl	= Plagioclase
Kfs	= K-feldspar
Cpx	= Clinopyroxene
Opx	= Orthopyroxene
Ti-Mag	= Ti-magnetite
Ilm	= Ilmenite
Bt	= Biotite
Hbl	= Hornblende
Grt	= Garnet
Di	= Diopside
Tr	= Tremolite
Act	= Actinolite
Qtz	= Quartz
Ap	= Apatite
Spl	= Spinel
Crn	= Corundum
Hem	= Hematite
Ep	= Epidote
Spn	= Sphene
Cal	= Calcite
Srp	= Serpentine
Id	= Iddingsite
Chl	= Chlorite
Sc	= Sericite
Bw	= Bowlingite
Ms	= Muscovite
Hc	= Hyrcenite
Rt	= Rutile

Appendix C. Visual estimates of mineral proportions in the MHB diabase dykes.

	CMD-01	CMD-02a	CMD-03a	CMD-03b	CMD-03c	CMD-03d	CMD-04	CMD-05	CMD-06
Ol	-	-	1	-	-	-	-	tr	-
Pl	55-60	55-60	45-50	45-50	45-50	15-20	30-35	40-45	20-25
Kfs	tr	tr	tr	tr	tr	-	-	tr	-
Cpx	10-15	10-15	25-29	25-29	1-2	-	15-20	20-25	-
Ti-Mag	2-3	1-2	1-2	1-2	2-3	1-2	1-5	2-3	1-2
Ilm	5-7	2-3	5-8	5-8	1-2	1-2	1-5	2-3	1-2
Bt	5-7	3-5	2-3	2-3	tr-1	1	5-7	5-8	tr-1
Hbl	5-7	5-10	5-7	5-7	25-30	45-50	7-10	3-6	40-45
Grt	tr-1	3-5	tr-1	tr-1	2-3	15-20	7-10	tr-1	3-5
Opx	3-5	-	tr-1	tr-1	-	-	3-5	-	-
Di	-	-	-	1-2	-	-	tr-1	-	-
Tr	-	tr	-	-	-	-	-	-	-
Qtz	tr-1	tr	-	-	tr-1	tr-1	tr	1	1-2
Ap	tr	tr	tr	tr	tr	tr	tr	tr	tr
Spl	-	tr	tr	tr-1	-	tr	-	-	-
Crn	tr	tr	-	tr	tr	tr	tr	-	-
Hem	-	tr	tr	tr	tr	-	-	-	-
Ep	-	-	tr	tr	tr	1-2	tr	tr	-
Spn	-	-	-	-	1-2	1-2	-	-	-
Cal	-	-	-	-	tr	1-2	tr	tr	tr
Srp	-	-	tr	-	-	-	-	tr	-
Id	-	-	tr-1	-	-	-	-	tr	-

Appendix C (continued)

	CMD-07a	CMD-07b	CMD-08a	CMD-08b	CMD-09	CMD-10	CMD-11	CMD-12	CMD-13	CMD-14
Ol	40-45	-	-	-	-	-	-	-	-	-
Pl	10-15	15-20	35-40	45-50	10-15	15-20	30-35	45-50	25-30	30-35
Kfs	-	-	tr	tr	tr	-	-	tr	-	tr
Cpx	10-15	tr	1-3	5-10	-	-	-	5-10	5-10	10-15
Ti-Mag	5-10	2-3	3-5	5-7	2-4	1-3	tr-1	1-2	2-3	1-2
Ilm	?	2-3	3-5	?	2-4	1-3	tr-1	1-2	?	1-2
Bt	5-10	tr-1	1-2	3-5	1	tr-1	tr-1	5-7	3-7	2-3
Hbl	-	60-65	30-35	10-15	65-70	55-60	50-55	5-10	35-40	20-25
Grt	-	3-7	5-10	5-10	tr-1	10-15	1-2	5-10	10-15	20-25
Opx	-	-	-	-	-	-	-	5-8	-	3-5
Di	-	-	-	-	-	-	-	1-2	-	1-2
Act/Tr	tr-1	-	-	-	-	-	-	-	-	-
Act/Hbl	-	-	-	-	-	-	tr	-	-	-
Qtz	-	1-2	tr	tr	2-3	2-3	2-3	tr	-	tr
Ap	-	tr	tr	tr	tr-1	tr	tr	tr	-	tr
Crn	-	-	-	-	-	-	-	tr	-	-
Hem	-	-	-	-	tr	-	-	tr	-	-
Rp	1	-	tr-1	-	-	tr	-	-	-	-
Spn	-	-	-	-	tr	-	1-2	tr	tr	-
Cal	tr	tr	-	-	2-3	tr	2-4	tr	-	tr
Srp	tr	-	-	-	-	-	-	-	-	-
Chl	tr	-	-	-	-	-	-	-	-	-
Sc	1-2	-	-	-	tr	tr	tr	-	-	tr

Appendix C (continued)

	CMD-14a	CMD-15	CMD-16	CMD-18	CMD-19	CMD-20	CMD-28	CMA-55-86
Pl	35-40	40-45	30-35	50-57	20-25	40-45	25-30	20-25
Kfs	tr	tr	-	tr	-	-	tr	-
Cpx	25-30	20-25	1	20-25	35-40	25-30	3-5	3-5
Ti-Mag	1-2	2-3	1-2	3-5	1-2	2-4	tr-1	tr-1
Ilm	2-3	?	2-3	?	2-3	1-2	1-2	1-2
Bt	3-5	3-5	1-2	3-5	2-3	3-5	1-2	tr
Hbl	1-2	5-10	40-45	2-5	5-10	5-10	45-50	50-55
Grt	10-15	5-10	5-10	7-10	10-15	5-10	3-5	5-10
Opx	-	1-2	-	5-10	-	4-8	-	-
Di	1	1-2	-	1-2	2-3	2-3	-	-
Ap	tr	tr	-	tr	tr	tr	tr	tr-1
Qtz	tr	tr	-	tr	-	tr	1-2	1-2
Crn	tr-1	tr-1	-	tr-1	tr-1	tr-1	-	-
Hem	tr	-	tr	tr	-	tr	-	tr
Bp	tr	tr	-	-	-	-	-	-
Spn	tr	-	-	-	-	-	-	-
Cal	tr	tr	-	tr	tr	-	tr	-
Id	-	-	-	-	-	tr	-	-
Bw	-	-	-	-	-	tr	-	-
Sc	tr	tr	-	-	-	-	4-8	tr
Ms	-	-	-	-	-	-	tr	tr
Chl	-	-	-	-	-	-	2-3	-

Appendix C (continued)

	CMD-25	CMD-26	CMD-37a	CMD-38	CMD-40a	CMD-42	CMD-43	CMD-47
Ol	-	-	-	-	-	-	tr-1	-
Pl	40-45	25-30	15-20	50-55	20-25	25-30	50-55	15-20
Kfs	tr-1	-	tr	tr	tr	-	-	-
Cpx	3-5	1-2	3-5	20-25	5-10	15-20	20-25	25-30
Ti-Mag	tr-1	1-2	1-2	1-2	1-2	1-2	3-8	tr-1
Ilm	1-2	1-2	3-4	1-2	tr	2-3	?	tr
Bt	tr-1	1-5	3-5	1-2	3-5	3-5	1-2	-
Hbl (blue)	45-50	50-55	10-15	1-5	40-45	15-20	1-3	5-10
(green)			5-10					
Grt	5-7	-	10-15	3-5	5-10	5-10	3-5	20-25
Opx	-	-	10-15	5-8	-	2-3	5-10	-
Di	-	-	5-10	2-3	-	-	tr	-
Qtz	1-2	tr-1	tr	tr-1	tr-1	tr-1	tr-1	tr-1
Ap	tr-1	tr	tr	tr-1	tr	tr	tr	-
Spl	-	-	tr	-	-	1-2	-	-
Crn	-	tr	tr	2-3	-	1-5	tr-1	-
Hem	-	tr	tr	-	tr	tr	-	tr
Rp	-	tr	tr	tr-1	tr	1-2	-	tr-1
Spn	-	-	tr	-	tr-1	tr	-	1-2
Cal	tr-1	-	-	tr-1	tr-1	-	-	tr
Sc	tr	tr	-	-	-	-	-	-
Hc	-	-	-	-	-	-	tr-1	-
Id	-	-	-	-	-	-	tr	-
Ms	tr	-	-	-	-	-	-	-

Appendix C (continued)

	CMA-87-LA-10	CMA-M-L-09-86	CMA-P-12.30-86	CMA-M-R-01a-85	CMA-M-V-01-86	MJ-Di-86
Ol	2-3	-	-	-	-	-
Pl	20-30	50-55	50-55	45-50	30-35	65-70
Kfs	tr	tr	-	tr	tr	tr
Cpx	15-20	30-35	15-20	25-30	20-25	3-5
Ti-Maq	10-15	2-3	2-3	10-15	2-5	tr-1
Ilm						1-2
Bt	3-5	1-2	1-2	5-7	2-5	tr
Hbl	10-15	3-5	10-15	10-15	10-15	5-10
Grt	-	3-5	3-5	2-3	15-20	5-10
Opx	1-5	1-2	5-8	-	-	-
Di	-	tr-1	tr-1	tr	tr	-
Act/Tr	tr	-	-	-	-	-
Qtz	-	tr	-	-	-	tr
Ap	tr	tr	tr	tr-1	-	-
Spl	-	tr	-	-	-	-
Crn	-	tr-1	tr	-	-	tr
Hem	-	-	-	-	-	-
Ep	-	-	tr	tr-1	-	1-2
Cal	-	tr-1	tr	-	-	tr
Chl	tr	-	-	-	-	-
Id	1-2	-	-	-	-	-
Sc	-	-	-	-	-	tr

Appendix C (continued)

	CMA-LG-6-87	CMA-LG-7-87	CMA-LG-Y-87	CMA-27.6.3-87	CMA-27.6.5-87	CMA-82-86	CMA-45-86
Ol	-	-	-	-	1-2	-	-
Pl	25-30	30-35	30-35	30-35	25-30	50-55	50-55
Kfs	tr	tr	tr	tr	-	-	tr
Cpx	20-25	20-25	25-30	25-30	20-25	25-30	30-35
Ti-Mag	10-15	5-10	10-15	5-10	1-5	2-3	3-5
Ilm							
Bt	3-5	1-5	3-5	1-3	1-2	1-2	2-3
Hbl	10-15	5-10	5-10	15-20	3-5	5-10	1-2
Grt	2-3	tr-1	tr	5-10	10-15	5-7	3-5
Opx	5-10	2-3	tr-1	-	10-15	-	3-5
Di	-	-	-	-	-	-	1-3
Act/Tr	-	-	tr-1	-	-	-	-
Qtz	tr	tr	-	-	-	-	tr
Ap	2-3	tr	tr	tr	tr-1	tr-1	tr
Spl	-	-	-	-	-	-	tr-1
Crn	-	-	-	-	-	-	tr-1
Ep	5-7	-	tr-1	tr	5-7	-	-
Spn	-	-	-	-	tr-1	-	-
Cal	-	-	1-2	tr	-	-	tr
Rt	tr-1	-	tr	-	-	-	-
Chl	-	-	tr	-	-	-	-

Appendix C (continued)

	CMA-146-86	CMA-M5-86	CMA-M015A-86	CMA-79-DI (A)-86	CMA-79-DI (B)-86	B-79-DI-1	B-79-DI-2
Pl	15-20	25-30	25-30	30-35	30-35	30-35	20-25
Kfs	-	tr	tr	tr	tr	tr	tr
Cpx	1-5	20-25	15-20	20-25	15-20	20-25	1-2
Ti-Mag	1-3	3-5	3-5	5-10	1-2	5-10	5-10
Ilm	4-7	2-5	2-5	3-7	1-5	5-7	2-3
Bt	5-10	2-5	2-3	3-5	15-20	1-5	3-5
Hbl	50-55	15-20	5-10	tr	1-5	1-5	5-8
Grt	3-5	5-10	10-15	15-20	10-15	15-20	10-15
Opx	-	-	5-10	-	-	5-10	10-15
Di	-	tr	-	2-3	-	1-5	2-5
Qtz	2-5	tr	tr	tr	1-2	1-2	2-3
Ap	tr	tr	tr	tr	tr	tr	tr
Rt	-	-	tr	-	-	-	tr
Crn	tr-1	-	-	-	-	tr	tr-1
Ep	tr-1	-	-	tr	-	tr	tr-1
Cal	tr	-	-	-	tr-1	tr	tr
Tr	-	tr	-	-	-	-	-
Hc	-	-	-	-	-	-	tr-1
Id	tr-1	-	-	1-2	-	-	-

Legend to Appendix D1

$FeOT = FeO + Fe_2O_3$

Mg# = MgO / (MgO + FeO) x 100 (molecular)

bl = below detection limit

Ap = Apatite
Il = Ilmenite
Mt = Magnetite
Or = Orthoclase
Ab = Albite
An = Anorthite
Di = Diopside
Hy = Hypersthene
Ol = Olivine
Ne = Nepheline
Q = Quartz

Appendix D1. Geochemistry of the NNE diabase dykes, southeast of Chibougamau

	High-Al_2O_3		Low-TiO_2						
	D-49-2b	LA-6-87	D-37a	D-12	D-43	27-6-3	D-47	LA-5-87	D-01
SiO_2	47.60	50.00	47.30	47.30	48.10	49.00	51.00	49.20	47.40
TiO_2	0.26	0.38	0.56	0.87	0.89	1.00	1.01	1.03	1.05
Al_2O_3	23.80	22.90	17.80	17.90	17.70	17.00	14.10	15.80	17.70
Fe_2O_3	0.80	2.10	1.40	2.60	0.20	2.30	2.40	2.10	1.60
FeO	6.00	3.30	9.20	8.30	9.60	7.30	9.00	8.10	10.20
MnO	0.10	0.10	0.16	0.18	0.16	0.15	0.21	0.16	0.18
MgO	5.54	3.64	10.22	9.30	7.54	8.04	7.85	8.79	8.66
CaO	11.08	13.24	9.81	10.12	11.05	10.32	11.72	9.59	9.65
Na_2O	2.90	2.20	2.00	2.20	2.50	2.70	1.70	2.60	2.40
K_2O	0.38	0.36	0.26	0.25	0.31	0.47	0.09	0.66	0.39
P_2O_5	0.05	0.03	0.07	0.08	0.08	0.08	0.07	0.17	0.10
H_2O+	0.80	1.10	0.90	0.80	0.40	0.90	0.60	0.50	1.10
Total	99.31	99.[illegible]	99.68	99.90	98.53	99.26	99.75	98.70	100.43
CO_2	0.70	0.40	0.10	0.80	0.50	0.80	0.10	0.80	0.10
S	0.02	0.03	0.01	0.04	0.07	0.06	0.07	0.06	0.07
Ba	208	110	194	74	178	139	66	301	230
Nb	bl	bl	12	21	bl	bl	14	bl	1[illegible]
Rb	15	bl	18	30	20	bl	24	bl	30
Sr	370	215	294	235	294	319	102	321	297
Zr	41	28	54	77	67	57	78	73	76
Be	bl	bl	bl	bl	bl	1	bl	1	bl
Co	70	28	120	89	94	49	88	52	80
Cr	25	31	160	110	230	150	170	200	120
Cu	10	62	38	44	58	72	120	67	51
Ni	94	34	180	160	110	180	100	190	140
V	33	110	110	150	170	160	280	170	150
Zn	74	40	120	120	86	83	110	84	170
La	2.8	6.9	3.7	8.5	4.7	8.5	3.7	11.0	5.4
Ce	6.3	14.0	8.7	14.0	11.0	20.0	10.0	25.0	13.0
Nd	1.9	11.0	4.1	8.1	7.9	12.0	7.1	16.0	10.0
Sm	0.5	0.3	1.2	2.0	1.8	2.1	2.1	1.7	2.1
Eu	0.6	0.6	0.6	0.8	0.8	0.9	0.8	1.2	0.9
Gd	0.8	2.1	1.6	2.7	2.5	3.1	3.2	3.6	2.8
Dy	0.7	2.2	1.7	2.9	2.9	3.2	3.6	3.4	2.8
Yb	0.3	1.2	0.9	1.6	1.3	1.6	2.1	1.7	1.5
Y	3	11	8	16	12	17	19	17	14
FeOT	6.72	5.19	10.46	10.64	9.78	9.37	11.16	9.99	11.64
Mg#	61.0	61.0	65.1	63.9	58.1	63.5	58.4	63.6	58.7
Ap	0.11	0.07	0.15	0.18	0.18	0.18	0.15	0.37	0.22
Il	0.49	0.72	1.06	1.66	1.69	1.90	1.92	1.96	2.00
Mt	2.17	1.68	3.37	3.44	3.15	3.03	3.60	3.23	3.75
Or	2.24	2.13	1.53	1.48	1.83	2.78	0.53	3.90	2.30
Ab	24.51	18.63	16.90	18.61	21.10	22.84	14.38	21.99	20.28
An	50.74	51.59	38.78	38.22	36.07	32.87	30.57	29.48	36.32
Di	3.13	11.43	7.61	9.31	14.76	14.46	22.17	13.78	8.85
Hy	0.18	9.72	15.67	12.85	9.74	11.30	21.77	15.11	11.67
Ol	14.93	0.00	13.70	13.35	9.61	9.00	0.00	8.38	13.94
Ne	-	2.29	-	-	-	-	4.05	-	-
Q	-	-	-	-	-	-	-	-	-
Total	98.51	98.25	98.78	99.10	98.13	98.36	99.15	98.20	99.33

Appendix D1 (continued)

	Low-TiO_2									
	D-20	D-42	LA-3-87	D-41a	D-38	D-40	D-02	F-12134	D-48	D-14 (n=2)
SiO_2	48.00	48.90	49.20	49.00	47.80	49.70	47.20	47.40	47.30	47.05
TiO_2	1.13	1.12	1.13	1.18	1.28	1.29	1.33	1.34	1.49	1.61
Al_2O_3	16.40	15.70	15.80	15.80	15.40	16.00	16.40	16.50	15.60	15.95
Fe_2O_3	1.50	1.50	2.00	0.30	0.90	2.20	2.40	2.50	3.20	1.00
FeO	10.60	8.80	8.60	9.80	11.90	8.20	9.90	9.30	8.90	11.35
MnO	0.19	0.17	0.17	0.17	0.20	0.16	0.19	0.18	0.19	0.19
MgO	7.59	8.64	8.31	8.50	7.75	7.46	7.95	6.90	7.60	7.46
CaO	9.95	10.78	9.91	10.72	10.20	9.79	10.16	10.66	10.10	9.83
Na_2O	2.50	2.50	2.60	2.50	2.30	2.90	2.60	2.40	2.60	2.60
K_2O	0.47	0.43	0.74	0.45	0.51	0.56	0.45	0.47	0.50	0.52
P_2O_5	0.14	0.10	0.18	0.10	0.14	0.12	0.12	0.15	0.19	0.21
H_2O+	0.50	0.70	0.70	0.60	0.80	1.20	0.80	0.80	1.40	0.90
Total	98.97	99.34	99.34	99.12	99.18	99.58	99.50	98.60	99.07	98.67
CO_2	0.10	0.30	0.50	0.50	0.40	0.80	0.30	0.70	0.70	1.15
S	0.04	0.07	0.09	0.07	0.10	0.04	0.10	0.10	0.10	0.11
Ba	279	206	365	199	293	260	251	240	278	292
Nb	12	17	bl	12	11	9	20	bl	15	15
Rb	28	27	bl	29	21	30	26	bl	29	27
Sr	286	291	319	278	263	392	277	273	283	308
Zr	88	118	80	124	96	107	88	65	123	133
Be	1	1	1	1	1	1	1	1	1	1
Co	94	91	50	86	91	83	89	59	82	81
Cr	100	250	150	240	150	120	200	150	170	83
Cu	57	69	66	70	63	68	60	75	68	69
Ni	110	170	160	160	100	130	120	110	110	115
V	210	200	190	220	250	200	210	230	230	235
Zn	120	120	99	110	120	110	150	99	120	135
La	7.9	9.2	11.0	9.8	8.5	8.4	7.2	9.3	9.9	12.0
Ce	17.0	22.0	24.0	23.0	19.0	21.0	17.0	21.0	25.0	28.0
Nd	11.0	12.0	18.0	14.0	12.0	11.0	14.0	15.0	14.0	18.0
Sm	2.7	2.8	2.8	3.3	3.0	2.9	2.7	2.4	3.5	4.0
Eu	1.2	1.0	1.2	1.2	1.2	1.2	1.2	1.3	1.3	1.5
Gd	3.4	3.4	3.7	3.9	3.9	3.4	3.5	3.6	4.2	4.7
Dy	3.7	3.4	3.4	4.0	5.1	3.4	3.5	3.5	4.0	4.4
Yb	1.8	1.7	1.7	1.8	2.1	1.6	1.9	1.8	2.0	2.2
Y	17	17	18	19	20	18	19	19	19	22
FeOT	11.95	10.15	10.40	10.07	12.71	10.18	12.06	11.55	11.78	12.25
Mg#	54.7	62.1	61.1	60.4	53.0	59.4	56.6	54.4	57.1	53.1
Ap	0.31	0.22	0.40	0.22	0.31	0.26	0.26	0.33	0.42	0.46
Il	2.15	2.13	2.15	2.24	2.43	2.46	2.53	2.55	2.84	3.06
Mt	3.85	3.27	3.36	3.25	4.10	3.29	3.89	3.73	3.81	3.95
Or	2.77	2.54	4.37	2.65	3.01	3.31	2.66	2.78	2.95	3.04
Ab	21.12	21.13	21.99	21.10	19.42	24.53	21.98	20.30	22.00	21.95
An	32.09	30.31	29.24	30.49	30.12	28.98	31.72	32.85	29.43	30.27
Di	13.36	18.25	15.25	17.81	15.98	15.33	14.62	15.63	15.93	13.97
Hy	13.66	11.85	13.35	12.74	14.90	14.50	6.71	11.83	9.70	10.03
Ol	9.15	8.94	8.55	8.02	8.13	5.72	14.32	7.80	10.59	11.03
Ne	-	-	-	-	-	-	-	-	-	-
Q	-	-	-	-	-	-	-	-	-	-
Total	98.47	98.64	98.64	98.52	98.38	98.38	98.70	97.80	97.67	97.76

Appendix D1 (continued)

	Low-TiO_2	High-TiO_2							
	D-51	D-28	D-13a	B79DI	D-15	La-18-87	D-18	D-05	27-6-5
SiO_2	46.80	49.00	48.00	48.70	48.00	47.40	47.80	48.60	46.70
TiO_2	1.61	1.38	1.39	1.59	1.60	1.74	1.90	1.96	1.98
Al_2O_3	14.90	15.10	15.90	18.80	16.30	16.20	14.60	13.70	15.30
Fe_2O_3	2.80	2.00	2.70	2.00	2.40	4.60	1.40	1.90	4.40
FeO	11.20	10.40	9.90	7.70	10.30	9.70	12.70	12.00	11.10
MnO	0.23	0.21	0.21	0.16	0.21	0.19	0.21	0.23	0.22
MgO	7.33	6.61	7.71	3.97	6.80	5.94	6.76	6.24	6.19
CaO	10.01	10.00	9.47	11.51	9.82	9.55	9.49	9.64	9.18
Na_2O	2.40	2.40	2.70	3.10	2.60	2.70	2.60	2.60	2.60
K_2O	0.51	0.83	0.58	0.63	0.76	0.71	0.87	0.85	0.66
P_2O_5	0.20	0.21	0.11	0.30	0.32	0.22	0.30	0.28	0.26
H_2O+	0.80	1.70	1.10	0.60	0.70	0.80	0.60	0.70	0.60
Total	98.79	99.84	99.77	99.06	99.81	99.75	99.23	98.70	99.19
CO_2	0.40	0.40	0.10	0.20	0.20	0.20	0.60	0.20	0.10
S	0.12	0.12	0.03	0.10	0.11	0.03	0.15	0.15	0.00
Ba	319	394	178	346	398	403	476	401	324
Nb	12	6	20	bl	24	bl	13	15	bl
Rb	38	32	43	bl	35	bl	34	36	bl
Sr	272	316	237	289	289	278	300	245	246
Zr	126	122	159	81	147	72	131	184	105
Be	1	1	1	1	1	1	1	1	1
Co	98	75	99	35	87	52	92	75	58
Cr	86	260	120	150	160	80	150	170	73
Cu	76	47	63	54	47	65	72	67	110
Ni	110	69	120	37	88	65	86	75	74
V	260	210	230	230	180	290	300	310	290
Zn	140	120	280	72	140	120	150	160	130
La	11.0	11.0	12.0	13.0	14.0	11.0	15.0	18.0	15.0
Ce	25.0	26.0	27.0	30.0	33.0	26.0	33.0	41.0	35.0
Nd	15.0	18.0	16.0	22.0	21.0	21.0	21.0	25.0	23.0
Sm	3.5	4.1	4.2	3.5	5.0	2.9	3.7	5.6	3.9
Eu	1.4	1.6	1.5	1.7	1.7	1.5	1.7	1.8	1.8
Gd	4.2	5.1	5.1	5.0	5.4	4.5	5.6	6.5	5.3
Dy	4.1	5.3	5.7	4.8	5.5	4.3	5.7	6.8	5.1
Yb	2.1	2.9	3.2	2.5	2.9	2.4	2.7	3.4	2.7
Y	21	28	32	25	31	23	27	33	27
FeOT	13.72	12.20	12.33	9.50	12.46	13.84	13.96	13.71	15.06
Mg#	51.4	51.2	55.6	45.4	51.8	47.8	47.6	46.5	46.1
Ap	0.44	0.46	0.24	0.66	0.70	0.48	0.66	0.62	0.57
Il	3.06	2.63	2.65	3.03	3.04	3.32	3.61	3.73	3.77
Mt	4.43	3.94	3.98	3.07	4.02	4.48	4.50	4.42	4.87
Or	3.01	4.90	3.42	3.72	4.49	4.20	5.13	5.01	3.90
Ab	20.29	20.29	22.83	26.22	21.99	22.87	21.96	21.97	22.02
An	28.36	27.96	29.54	35.51	30.55	30.03	25.55	23.17	28.15
Di	16.45	16.68	13.70	16.26	13.22	13.25	16.09	18.84	13.07
Hy	11.94	19.27	11.04	5.11	12.56	11.24	13.03	18.10	13.12
Ol	10.00	2.02	11.27	4.88	8.54	9.08	8.10	2.14	9.12
Ne	-	-	-	-	-	-	-	-	-
Q	-	-	-	-	-	-	-	-	-
Total	97.99	98.14	98.67	98.46	99.11	98.95	98.63	98.00	98.59

Appendix D1 (continued)

High-TiO_2

	D-25	D-16	D-04	D-05	X287	LG-V-87	LG-6-87	LG-7-87	A-03	X187
SiO_2	46.60	47.00	46.20	46.60	48.20	47.60	48.70	47.50	48.00	46.50
TiO_2	2.07	2.12	2.16	2.24	2.25	2.28	2.30	2.31	2.29	2.31
Al_2O_3	14.30	15.00	15.80	16.00	14.70	16.10	15.70	15.30	14.90	14.40
Fe_2O_3	2.50	4.20	3.00	3.90	2.60	3.20	3.40	4.00	2.30	2.60
FeO	12.20	11.00	10.80	10.20	13.00	10.40	11.60	11.30	12.00	13.30
MnO	0.24	0.24	0.21	0.21	0.24	0.19	0.21	0.21	0.22	0.25
MgO	6.34	6.69	6.97	6.67	5.12	5.02	4.11	5.20	5.19	5.40
CaO	9.95	9.16	9.32	9.13	9.55	9.28	8.56	9.48	9.04	9.78
Na_2O	2.40	2.10	3.00	3.00	2.60	3.00	3.00	2.70	2.80	2.60
K_2O	0.56	0.62	0.65	0.67	0.27	0.88	1.27	0.85	1.07	0.28
P_2O_5	0.17	0.27	0.29	0.32	0.21	0.37	0.43	0.25	0.34	0.24
H_2O+	1.20	1.20	0.90	0.90	1.60	0.90	0.90	0.80	0.50	1.60
Total	98.53	99.60	99.30	99.84	100.34	99.22	100.18	99.90	98.65	99.26
CO_2	0.50	0.20	0.50	0.30	0.30	0.70	0.40	0.10	0.10	0.50
S	0.18	0.05	0.07	0.03	0.01	0.12	0.02	0.01	0.16	0.00
Ba	343	308	310	337	195	405	510	416	429	207
Nb	16	29	20	30	bl	bl	bl	bl	32	bl
Rb	35	43	40	41	bl	bl	23	bl	64	bl
Sr	254	213	309	307	284	271	233	231	252	225
Zr	101	168	186	185	115	174	242	124	237	123
Be	1	1	1	1	1	1	1	1	1	1
Co	97	89	95	86	56	47	41	44	76	61
Cr	140	120	91	100	55	93	65	98	100	62
Cu	150	59	59	60	44	74	57	72	67	34
Ni	72	92	120	120	49	63	36	44	74	55
V	400	270	220	230	290	270	230	310	290	320
Zn	150	170	210	140	130	120	140	130	180	140
La	9.8	13.0	17.0	17.0	14.0	22.0	26.0	16.0	26.0	15.0
Ce	23.0	33.0	40.0	41.0	34.0	49.0	61.0	38.0	56.0	35.0
Nd	15.0	21.0	24.0	25.0	28.0	30.0	38.0	26.0	34.0	25.0
Sm	3.6	5.4	5.5	5.7	4.5	5.8	6.3	3.6	6.8	5.5
Eu	1.4	1.8	1.9	2.0	2.0	2.1	2.4	1.8	2.2	2.1
Gd	4.5	6.1	5.9	6.2	6.5	6.4	8.2	5.7	7.7	6.6
Dy	5.0	6.5	5.6	5.9	6.3	5.8	7.8	5.5	8.4	6.7
Yb	2.5	3.5	2.6	2.8	3.1	2.9	4.2	2.9	3.7	3.2
Y	24	37	29	30	33	30	41	28	37	34
FeOT	14.45	14.78	13.50	13.71	15.34	13.28	14.66	14.90	14.07	15.64
Mg#	46.1	48.4	50.8	50.2	39.4	43.3	36.1	41.8	41.7	40.1
Ap	0.37	0.59	0.64	0.70	0.46	0.81	0.95	0.55	0.75	0.53
Il	3.94	4.04	4.11	4.27	4.28	4.34	4.38	4.40	4.36	4.39
Mt	4.66	4.78	4.36	4.43	4.95	4.29	4.74	4.81	4.54	5.05
Or	3.30	3.67	3.84	3.96	1.59	5.20	7.50	5.02	6.32	1.65
Ab	20.28	17.79	25.37	25.40	21.98	25.39	25.39	22.86	23.67	21.97
An	26.56	29.70	27.71	28.23	27.62	27.87	25.63	27.13	24.91	26.76
Di	17.92	11.60	13.67	12.37	15.33	13.10	11.80	15.26	14.72	16.81
Hy	14.06	24.38	1.80	4.93	21.51	10.65	16.38	13.27	14.91	16.78
Ol	6.22	1.85	16.90	14.66	-	6.67	2.52	5.80	3.99	3.72
Ne	-	-	-	-	-	-	-	-	-	-
Q	-	-	-	-	1.01	-	-	-	-	-
Total	97.33	98.40	98.40	98.94	98.74	98.32	99.28	99.10	98.15	97.66

High-TiO_2

	D-52	D-07	D-08a	D-13b	A-01	D-07a	MR-1A-87	D-08b	D-09
SiO_2	45.80	45.40	46.50	48.70	48.70	44.10	48.60	47.20	51.70
TiO_2	2.35	2.49	2.51	2.65	2.70	2.71	2.91	2.99	3.22
Al_2O_3	15.80	15.10	15.20	13.30	14.80	7.80	12.70	14.00	11.20
Fe_2O_3	3.90	2.90	3.50	1.20	2.80	2.40	4.40	3.30	2.50
FeO	9.50	11.40	11.30	17.50	12.30	13.70	13.20	12.80	11.30
MnO	0.19	0.21	0.23	0.36	0.23	0.22	0.26	0.27	0.20
MgO	6.80	6.41	5.97	3.94	3.34	14.64	3.80	4.51	5.61
CaO	8.31	9.18	8.80	8.65	7.67	8.00	7.60	7.93	8.79
Na_2O	3.70	3.90	3.10	0.70	3.20	2.70	2.70	3.50	2.10
K_2O	0.89	0.67	0.80	0.18	1.53	1.57	1.63	1.23	0.58
P_2O_5	0.55	0.32	0.36	0.57	0.46	0.25	0.56	0.56	0.41
H_2O+	1.00	1.30	1.10	0.40	1.00	0.90	1.30	1.00	1.30
Total	98.79	99.28	99.37	98.15	98.73	98.99	99.66	99.29	98.91
CO_2	0.30	0.20	0.50	0.60	0.00	0.60	0.40	0.10	0.40
S	0.07	0.12	0.08	0.19	0.02	0.07	0.03	0.07	0.08
Ba	898	330	385	298	681	669	679	514	145
Nb	15	12	31	49	52	41	bl	64	44
Rb	28	32	50	24	79	50	49	66	26
Sr	662	313	295	120	274	671	175	270	156
Zr	179	166	206	214	337	268	271	318	124
Be	1	1	1	1	2	2	2	2	1
Co	87	78	79	85	62	110	42	74	74
Cr	90	110	100	34	27	420	15	48	110
Cu	53	92	66	110	35	250	50	54	40
Ni	90	92	100	38	17	580	19	44	61
V	230	270	260	240	160	210	290	190	250
Zn	140	150	170	190	190	170	180	200	170
La	20.0	16.0	23.0	28.0	30.0	44.0	30.0	32.0	12.0
Ce	46.0	38.0	50.0	71.0	72.0	95.0	70.0	74.0	31.0
Nd	29.0	24.0	30.0	48.0	44.0	47.0	45.0	44.0	23.0
Sm	5.9	5.4	6.4	13.0	9.1	8.5	8.3	9.7	6.1
Eu	2.3	1.9	2.2	4.2	2.8	2.7	2.8	3.1	2.0
Gd	5.7	6.2	7.0	15.0	9.9	7.9	9.9	10.0	7.6
Dy	3.9	5.8	6.6	15.0	9.5	6.1	9.7	9.9	7.2
Yb	0.8	2.6	3.1	7.6	4.9	1.6	5.1	4.8	3.6
Y	14	28	34	84	49	26	52	53	37
FeOT	13.01	14.01	14.45	18.58	14.82	15.86	17.16	15.77	13.55
Mg#	52.2	47.6	45.6	28.1	30.7	64.0	31.1	36.2	44.8
Ap	1.21	0.70	0.79	1.25	1.01	0.55	1.23	1.23	0.90
Il	4.48	4.74	4.78	5.03	5.14	5.15	5.55	5.69	6.13
Mt	4.21	4.52	4.67	5.98	4.79	5.11	5.55	5.09	4.37
Or	5.26	3.95	4.73	1.06	9.04	9.25	9.64	7.26	3.42
Ab	27.03	23.60	26.23	5.91	27.07	11.78	22.86	29.61	17.76
An	23.90	21.70	25.20	32.53	21.49	4.52	17.73	18.85	19.41
Di	11.32	17.93	13.35	5.56	11.44	27.06	13.83	14.10	17.75
Hy	-	-	5.58	27.08	17.55	-	20.23	6.10	17.67
Ol	18.06	15.75	12.95	-	-	28.72	-	10.35	-
Ne	2.33	5.08	-	-	-	5.96	-	-	-
Q	-	-	-	13.35	0.20	0.00	1.74	-	10.19
Total	97.79	97.98	98.27	97.75	97.73	98.09	98.36	98.29	97.61

Appendix D1 (continued)

Segregations

	D-03-2	D-03	D-03-1	D-49-1	B79DI	D-49-2a
SiO_2	50.90	48.20	53.60	46.50	46.60	45.70
TiO_2	1.12	1.87	2.04	3.38	3.57	3.78
Al_2O_3	19.10	15.00	13.30	11.70	13.00	12.30
Fe_2O_3	1.10	1.70	3.30	4.50	6.20	4.40
FeO	7.30	10.70	12.10	13.80	12.20	14.20
MnO	0.14	0.20	0.27	0.31	0.31	0.29
MgO	4.40	7.15	4.32	4.47	4.02	4.28
CaO	10.33	10.05	8.33	8.62	7.94	8.53
Na_2O	3.60	2.90	0.90	2.50	2.40	2.60
K_2O	0.32	0.73	0.14	1.23	1.40	1.15
P_2O_5	0.17	0.24	0.54	0.85	0.95	0.70
H_2O+	0.90	0.80	0.70	0.60	0.80	0.50
Total	99.38	99.54	99.54	98.46	99.39	98.43
CO_2	0.40	0.20	0.50	0.20	0.50	0.50
S	0.00	0.07	0.03	0.12	0.22	0.27
Ba	341	361	220	683	735	660
Nb	13	14	57	34	bl	28
Rb	27	40	9	56	26	40
Sr	519	335	94	211	188	221
Zr	116	154	339	300	270	267
Be	1	1	1	2	1	1
Co	75	78	99	76	51	75
Cr	220	220	130	26	15	20
Cu	29	63	28	54	120	67
Ni	51	110	42	36	26	34
V	170	270	210	340	290	380
Zn	110	150	89	240	210	220
La	12.0	14.0	34.0	33.0	39.0	26.0
Ce	26.0	34.0	81.0	77.0	90.0	64.0
Nd	17.0	23.0	50.0	47.0	57.0	40.0
Sm	3.8	5.3	12.0	10.0	11.0	8.8
Eu	1.7	1.9	3.6	3.4	3.8	3.0
Gd	4.5	6.5	13.0	12.0	13.0	10.0
Dy	4.5	6.9	14.0	11.0	12.0	9.9
Yb	2.3	3.4	7.3	5.9	6.2	5.2
Y	23	33	75	60	65	51
FeOT	8.29	12.23	15.07	17.85	17.78	18.16
Mg#	50.3	52.8	36.4	33.8	32.8	32.3
Ap	0.37	0.53	1.19	1.87	2.10	1.54
Il	2.13	3.56	3.88	6.44	6.82	7.20
Mt	2.68	3.94	4.87	5.77	5.76	5.87
Or	1.89	4.31	0.83	7.27	8.30	6.80
Ab	30.44	24.50	7.62	21.18	20.37	22.01
An	34.98	25.72	31.84	17.09	20.63	18.51
Di	12.45	18.46	5.01	16.98	10.69	16.23
Hy	12.60	6.76	24.74	20.56	22.24	18.64
Ol	0.94	10.97	-	-	-	1.13
Ne	-	-	-	-	-	-
Q	-	-	18.86	0.70	1.70	-
Total	98.48	98.74	98.84	97.86	98.59	97.93

Legend to Appendix D2

Major elements (Al_2O_3, FeO_T, K_2O, P_2O_5), selected trace elements (V, Cr, Ni, Zr), and rare earth elements (La, Ce, Yb, Y) plotted versus TiO_2 and MgO on Harker diagrams.

△ High-Al_2O_3 group

▲ Low-TiO_2 group

■ High-TiO_2 group

◇ Segregations

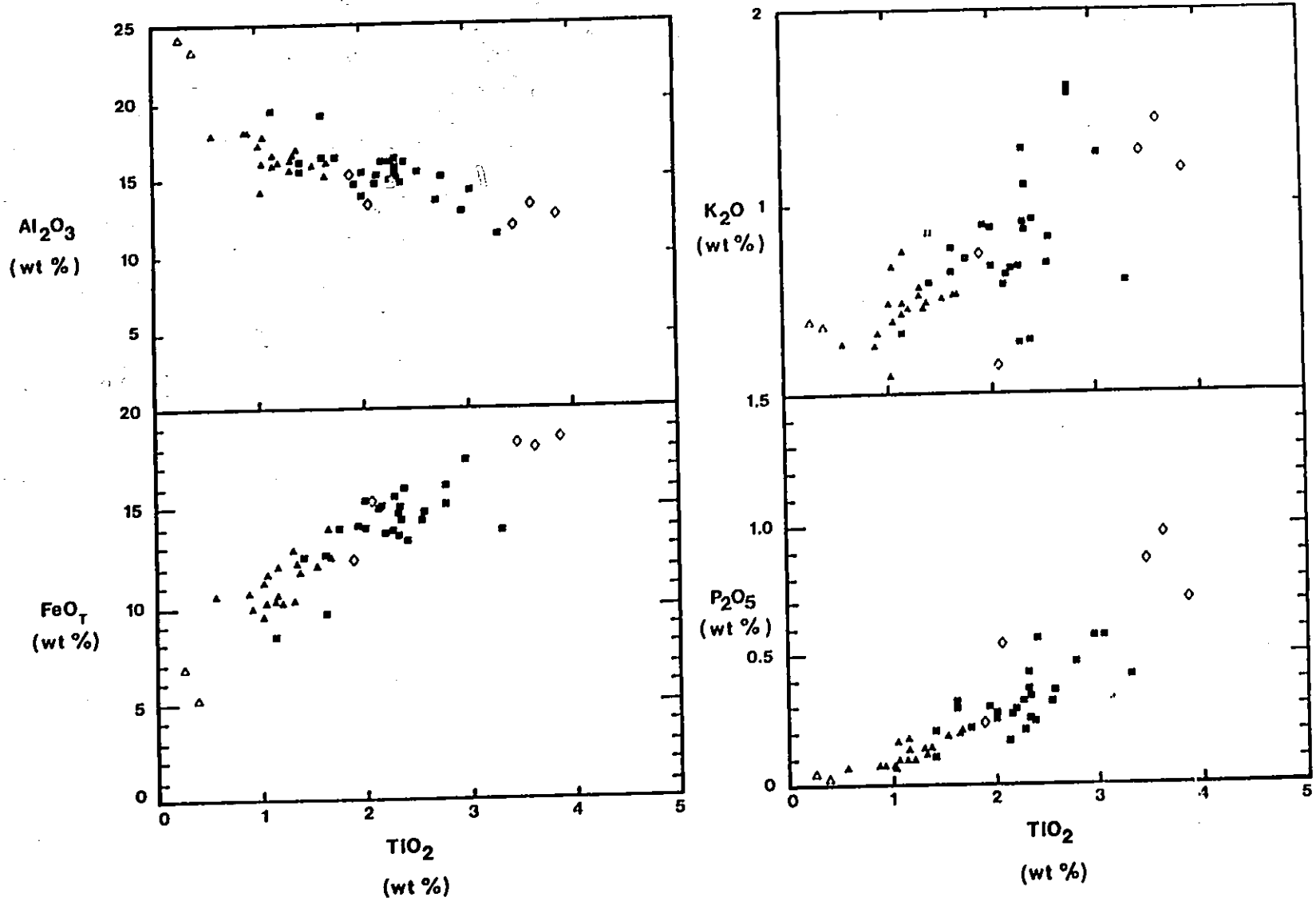
Al_2O_3 (wt %)
FeO_T (wt %)
TiO_2 (wt %)
K_2O (wt %)
P_2O_5 (wt %)
TiO_2 (wt %)

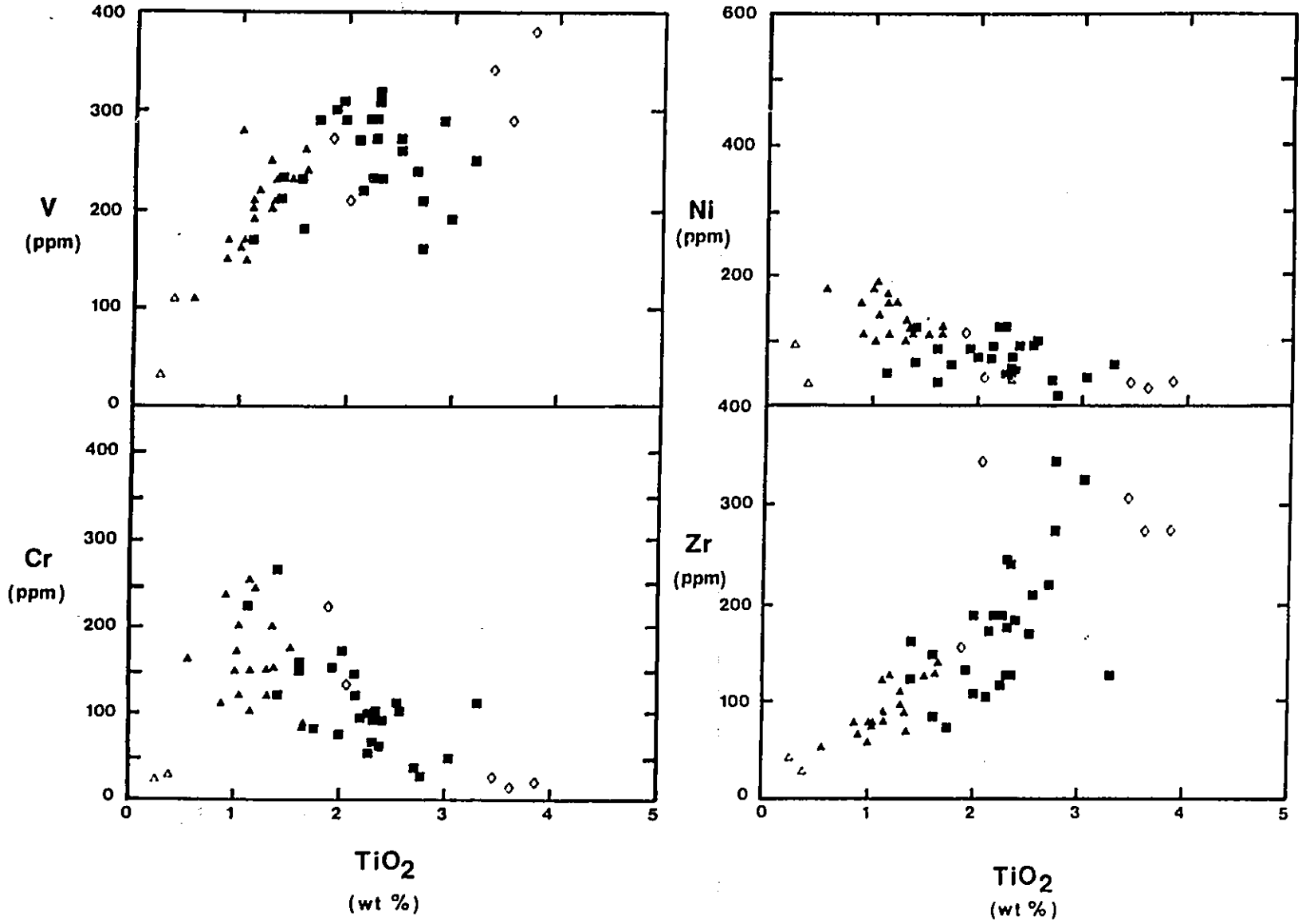
V
(ppm)
Cr
(ppm)
Ni
(ppm)
Zr
(ppm)
TiO2
(wt %)
TiO2
(wt %)

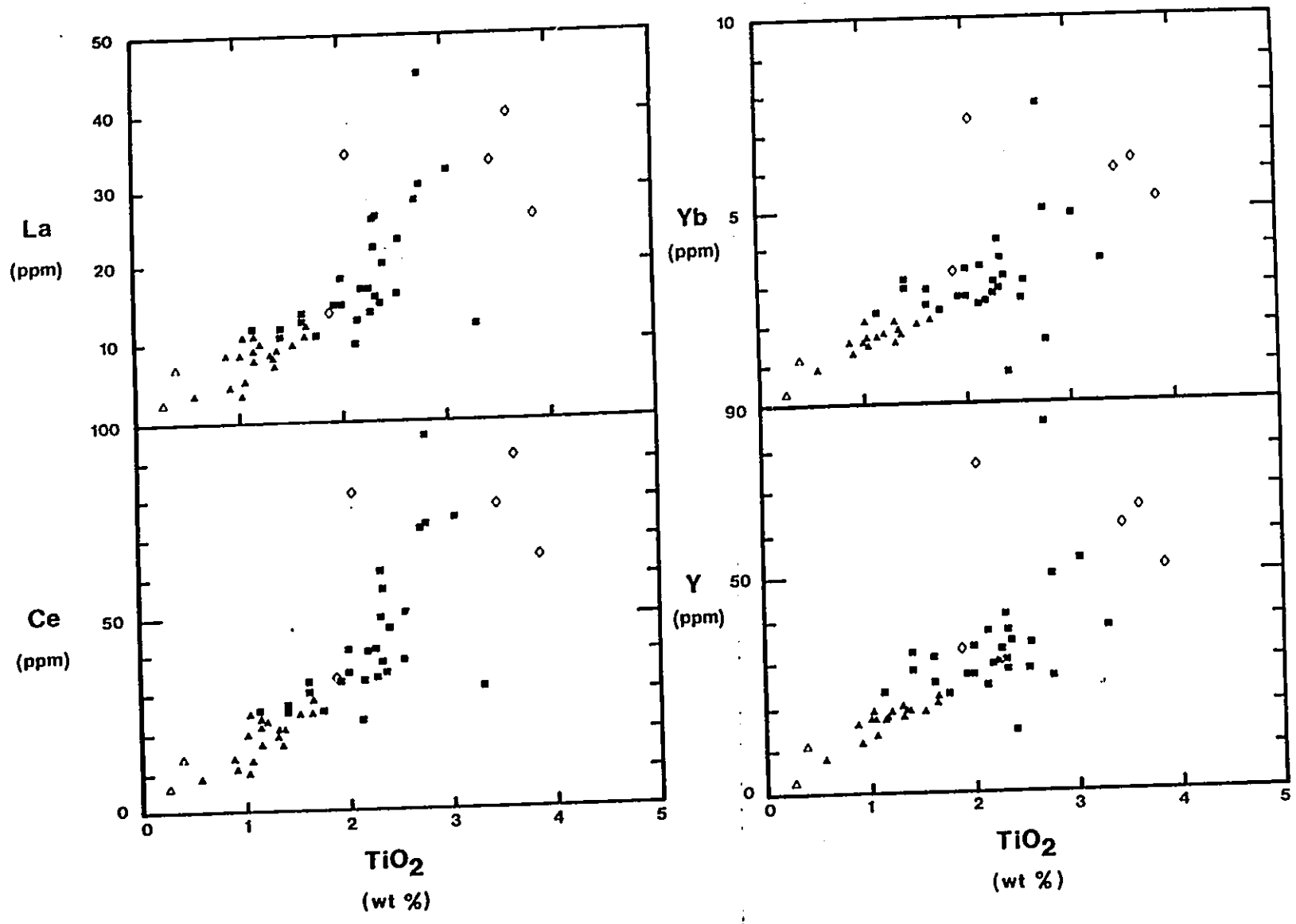
La
(ppm)
Ce
(ppm)
Yb
(ppm)
Y
(ppm)
TiO2
(wt %)
TiO2
(wt %)

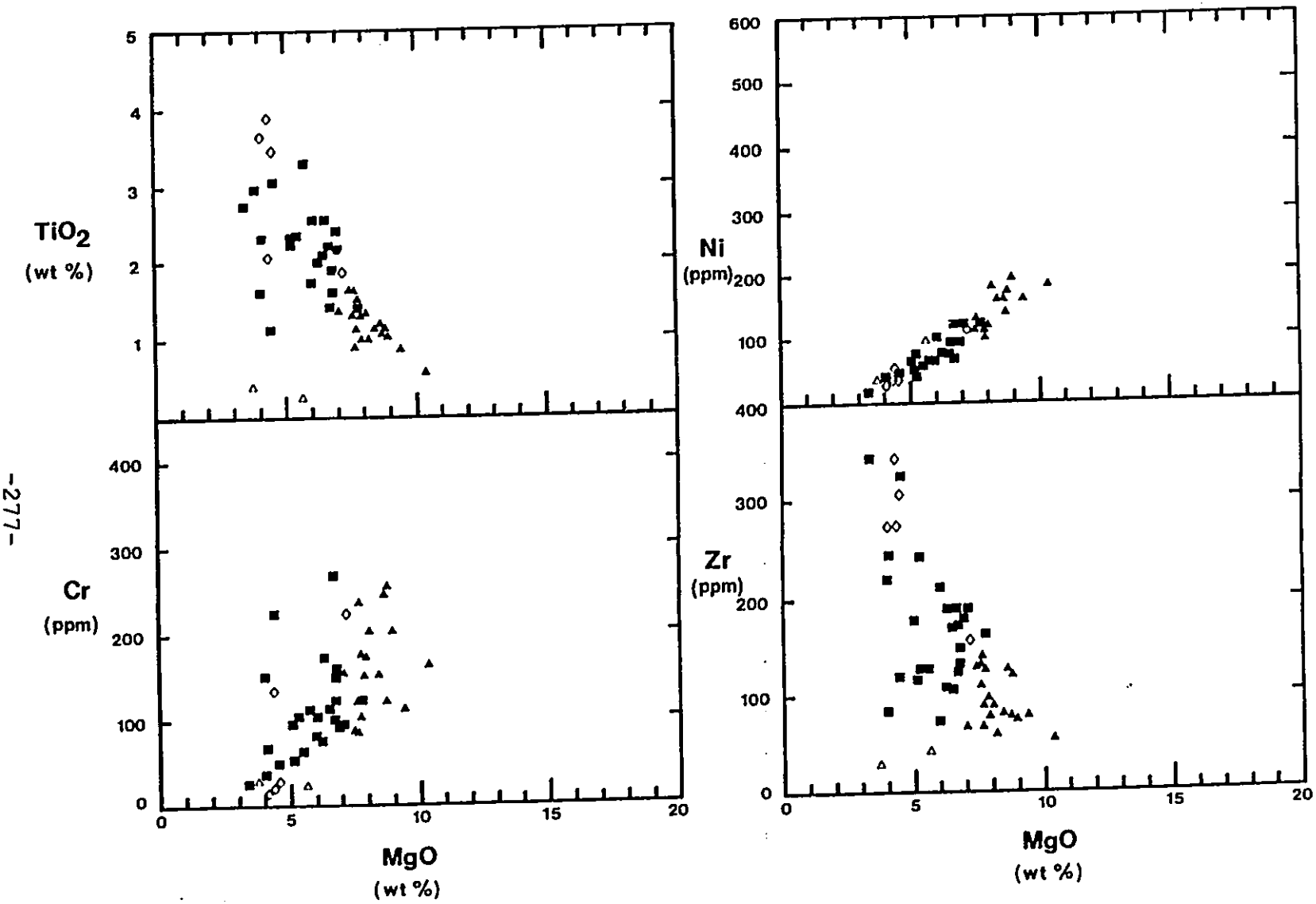
TiO2
(wt %)
Ni
(ppm)
Cr
(ppm)
Zr
(ppm)
MgO
(wt %)
MgO
(wt %)

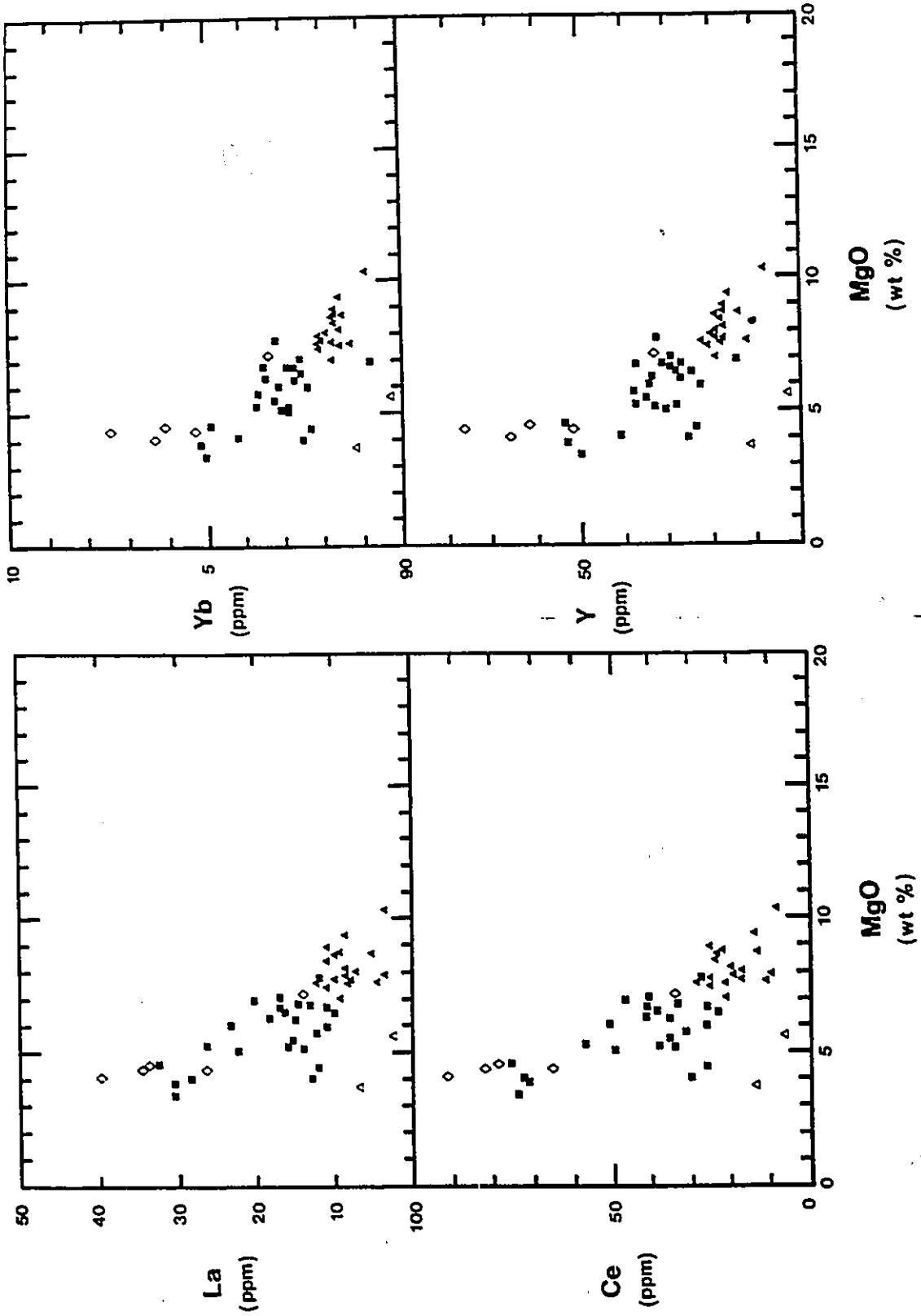
Yb (ppm)
Y (ppm)
MgO (wt %)
La (ppm)
Ce (ppm)
MgO (wt %)

Legend to Appendix E

Ol = Olivine
Pl = Plagioclase
Cpx = Clinopyroxene
Opx = Orthopyroxene
Bt = Biotite
Amp = Amphibole
Grt = Garnet
Mag = Magnetite
Ilm = Ilmenite
Ap = Apatite

c = core
m = margin

Prg = Pargasite
Hbl = Hornblende
Prg Hbl = Pargasitic hornblende
Ed Hbl = Edenitic hornblende
Act = Actinolite
Act Hbl = Actinolitic hornblende
Ts Hbl = Tschermakitic hornblende
En = Enstatite
Wo = Wollastonite
Fs = Ferrosilite
An = Anorthite
Ab = Albite
Or = Orthoclase
Almand = Almandine
Pyrop = Pyrope
Gross = Grossular
Spess = Spessartine
And = Andradite
Uvaro = Uvarovite

$XMg = Mg / (Mg+Fe_T)$ where $Fe_T = Fe^{2+} + Fe^{3+}$
$XNa = Na / (Na+Ca)$

$FeO^* = FeO + Fe_2O_3$

Mineral End Members

$En = Mg /(Mg+Fe+Ca)$
$Wo = Ca /(Mg+Fe+Ca)$ Pyroxene
$Fs = Fe /(Mg+Fe+Ca)$

$An = Ca /(Ca+Na+K)$
$Ab = Na /(Ca+Na+K)$ Plagioclase
$Or = K /(Ca+Na+K)$

$Almand = Fe^{2+} /(Ca+Fe^{2+}+Fe^{3+}+Mg+Ti+Cr+Mn)$
$Pyrop = Mg /(Ca+Fe^{2+}+Fe^{3+}+Mg+Ti+Cr+Mn)$
$Gross = Ca /(Ca+Fe^{2+}+Fe^{3+}+Mg+Ti+Cr+Mn)$
$Ti\ And = Ti /(Ca+Fe^{2+}+Fe^{3+}+Mg+Ti+Cr+Mn)$ Garnet
$Fe\ And = Fe^{3+} /(Ca+Fe^{2+}+Fe^{3+}+Mg+Ti+Cr+Mn)$
$Spess = Mn /(Ca+Fe^{2+}+Fe^{3+}+Mg+Ti+Cr+Mn)$
$Uvaro = Cr /(Ca+Fe^{2+}+Fe^{3+}+Mg+Ti+Cr+Mn)$

Appendix E1. Representative analyses of the principal minerals from sample CMA-LA18-87

	Ol1 n=4	Ol2 n=9
SiO_2	36.42	35.30
FeO	34.94	39.06
MgO	29.06	24.93
Total	100.41	99.28
Si4+	1.003	1.007
Fe2+	0.804	0.932
Mg2+	1.193	1.061
X site	1.997	1.993
Total	3.000	3.000
Charge	8.01	8.01
XMg	0.60	0.53

	Cpx1c n=1	Cpx1m n=2	Cpx2c n=1	Cpx2m n=2	Cpx3c n=2	Cpx3m n=1	Opx1 n=3	Opx2 n=4	Opx3 n=3	Opx4 n=5
SiO_2	50.55	50.96	49.08	49.60	49.22	49.53	53.89	52.81	51.36	50.20
TiO_2	0.73	0.74	0.77	0.79	1.09	1.00	0.08	-	0.02	0.08
Al_2O_3	3.54	3.56	2.84	2.80	3.77	3.61	0.33	0.01	0.31	0.53
Cr_2O_3	0.05	0.21	0.06	0.19	0.33	-	0.02	0.01	0.02	0.24
Fe_2O_3	1.84	1.25	2.62	1.54	2.42	2.31	3.49	3.30	3.39	3.44
FeO	10.43	10.19	11.10	12.41	10.14	9.57	17.43	19.18	24.85	30.43
MnO	0.32	0.31	0.50	0.36	0.31	0.24	0.52	0.54	0.87	1.01
MgO	14.91	15.15	13.97	13.45	13.99	14.54	25.98	24.28	19.87	15.13
CaO	18.55	18.75	17.78	17.98	18.74	18.85	0.16	0.09	0.20	0.96
Na_2O	-	-	-	0.02	0.05	-	-	-	-	-
K_2O	0.00	0.02	0.03	0.05	0.06	0.08	0.01	0.01	0.01	0.14
Total	101.08	101.17	98.74	99.05	99.97	100.06	101.92	100.24	100.89	101.95
Si IV	1.874	1.882	1.876	1.893	1.852	1.856	1.943	1.954	1.944	1.939
Al IV	0.126	0.118	0.124	0.107	0.148	0.144	0.014	0.001	0.014	0.024
T site	2.000	2.000	2.000	2.000	2.000	2.000	1.960	1.950	1.960	1.960
Al VI	0.028	0.037	0.004	0.019	0.019	0.016	-	-	-	-
Ti4+	0.020	0.020	0.022	0.023	0.031	0.028	0.002	-	0.001	0.002
Cr3+	0.002	0.006	0.002	0.006	0.010	-	0.001	-	0.001	0.007
Fe3+	0.051	0.035	0.075	0.044	0.069	0.065	0.095	0.092	0.097	0.100
Fe2+	0.323	0.315	0.355	0.396	0.319	0.300	0.526	0.593	0.787	0.983
Mn2+	0.010	0.010	0.016	0.012	0.010	0.008	0.016	0.017	0.028	0.033
Mg2+	0.824	0.834	0.796	0.766	0.785	0.812	1.397	1.339	1.121	0.871
Ca2+	0.737	0.742	0.728	0.735	0.756	0.757	0.006	0.004	0.008	0.040
Na+	-	-	-	0.001	0.004	-	-	-	-	-
K+	0.000	0.001	0.001	0.002	0.003	0.004	0.000	0.000	0.000	0.007
M1,M2	2.000	2.000	2.000	2.000	2.000	2.000	2.040	2.050	2.040	2.040
O	6.000	6.000	6.000	6.000	6.000	6.000	6.000	6.000	6.000	6.000
En	43.73	44.11	42.36	40.37	42.21	43.46	72.41	69.16	58.51	46.03
Wo	39.10	39.24	38.75	38.75	40.64	40.49	0.33	0.19	0.42	2.09
Fs	17.17	16.65	18.88	20.88	17.15	16.05	27.26	30.65	41.06	51.88
XMg	0.70	0.71	0.66	0.64	0.68	0.70	0.70	0.67	0.57	0.45

Appendix E1 (continued)

	Bt1 n=3
SiO_2	36.34
TiO_2	3.19
Al_2O_3	14.45
Cr_2O_3	0.01
Fe_2O_3	3.31
FeO	18.29
MnO	0.10
MgO	11.49
CaO	0.13
Na_2O	-
K_2O	9.74
H_2O	3.93
Total	100.98
Si IV	5.489
Al IV	2.511
T site	8.000
Al VI	0.062
Ti VI	0.363
Cr3+	0.001
Fe3+	0.376
Fe2+	2.311
Mn2+	0.012
Mg2+	2.589
O site	5.710
Ca2+	0.021
Na+	-
K+	1.876
A site	1.900
O	20.000
OH	4.000
XMg	0.51

	Pl1c n=1	Pl2c n=1	Pl3c n=1	Pl3m n=1	Pl4m n=1	Pl5m n=1	Pl6c n=1	Pl7c n=5	Pl7m n=1
SiO_2	53.79	54.51	53.07	53.20	55.15	56.24	52.69	51.42	52.79
Al_2O_3	28.93	28.53	30.32	30.14	28.66	28.79	30.16	28.93	28.53
CaO	11.09	10.87	12.41	12.37	10.30	10.20	11.54	13.23	12.36
Na_2O	6.33	5.52	5.10	5.27	6.48	6.10	5.93	4.74	5.48
K_2O	0.87	0.67	0.50	0.43	0.51	0.68	0.57	0.34	0.24
FeO	0.46	0.77	0.42	0.75	0.39	0.31	0.62	0.54	0.28
Total	101.47	100.87	101.82	102.16	101.49	102.32	101.51	99.20	99.68
Si4+	9.687	9.826	9.506	9.513	9.863	9.948	9.489	9.488	9.655
Al3+	6.141	6.061	6.401	6.352	6.041	6.002	6.401	6.291	6.150
Z site	15.828	15.887	15.907	15.866	15.903	15.950	15.890	15.779	15.806
Ca2+	2.140	2.099	2.382	2.370	1.974	1.933	2.227	2.616	2.422
Na+	2.210	1.929	1.771	1.827	2.247	2.092	2.071	1.696	1.942
K+	0.200	0.154	0.114	0.098	0.116	0.153	0.131	0.080	0.055
Fe2+	0.069	0.116	0.063	0.112	0.058	0.046	0.093	0.083	0.043
X site	4.619	4.299	4.330	4.407	4.395	4.224	4.521	4.475	4.462
Total	20.447	20.185	20.236	20.273	20.299	20.174	20.411	20.254	20.268
O	32.000	32.000	32.000	32.000	32.000	32.000	32.000	32.000	32.000
An	47.03	50.19	55.81	55.18	45.51	46.26	50.28	59.56	54.83
Ab	48.58	46.12	41.51	42.54	51.81	50.07	46.76	38.62	43.93
Or	4.39	3.68	2.68	2.28	2.68	3.67	2.96	1.82	1.24

Appendix E1 (continued)

	Amp1 n=1	Amp2 n=10	Amp3 n=4	Amp4 n=2
SiO_2	39.10	37.87	38.26	39.54
TiO_2	-	0.07	0.06	0.13
Al_2O_3	18.62	19.77	20.12	16.41
Cr_2O_3	0.06	0.04	0.08	0.12
Fe_2O_3	-	-	-	-
FeO*	15.00	14.41	16.27	20.10
MnO	0.23	0.18	0.36	0.23
MgO	9.41	10.75	9.17	7.77
CaO	10.51	10.45	10.21	10.09
Na_2O	2.50	3.28	3.48	1.84
K_2O	1.51	0.73	0.55	2.28
H_2O	2.01	2.03	2.04	2.00
Total	98.95	99.59	100.60	100.49
Si IV	5.800	5.580	5.640	5.950
Al IV	2.200	2.420	2.360	2.050
Tsite	8.000	8.000	8.000	8.000
Al VI	1.088	1.017	1.126	0.860
Fe3+	0.373	0.620	0.522	0.553
Ti4+	-	0.008	0.007	0.015
Cr3+	0.007	0.005	0.009	0.013
Mg2+	2.093	2.365	2.008	1.744
Fe2+	1.446	0.985	1.328	1.815
M1,M2,M3	5.000	5.000	5.000	5.000
Fe2+	0.054	0.175	0.150	0.164
Mn2+	0.029	0.023	0.045	0.029
Ca2+	1.677	1.647	1.610	1.627
Na+	0.237	0.155	0.195	0.180
M4	2.000	2.000	2.000	2.000
Na+	0.481	0.783	0.795	0.356
K+	0.288	0.136	0.103	0.438
A site	0.770	0.920	0.900	0.790
O	22.000	22.000	22.000	22.000
OH	2.000	2.000	2.000	2.000
XMg	0.56	0.60	0.53	0.44
XNa	0.30	0.36	0.38	0.25
Name	Prg	Prg	Prg	Prg

	Ap1 n=1	Ap2 n=1	Ap3 n=1
SiO_2	0.00	0.00	0.00
TiO_2	0.00	0.00	0.02
Al_2O_3	0.01	0.01	0.01
FeO*	0.24	0.55	0.29
MnO	0.08	0.04	0.05
MgO	0.01	0.05	0.00
CaO	57.01	56.75	56.50
Na_2O	0.00	0.00	0.00
K_2O	0.00	0.00	0.00
P_2O_5	43.31	43.41	42.85
F	2.91	2.45	2.65
Cl	0.08	0.13	0.20
Total	103.66	103.39	102.61
Si4+	0.000	0.000	0.000
Ti4+	0.000	0.000	0.000
Al3+	0.001	0.003	0.002
Fe	0.034	0.078	0.042
Mn2+	0.011	0.005	0.008
Mg2+	0.004	0.014	0.000
Ca2+	10.377	10.314	10.384
Na+	0.000	0.000	0.000
K+	0.000	0.000	0.000
P	6.229	6.234	6.222
F	1.566	1.315	1.438
Cl	0.024	0.037	0.058
Total	18.245	18.000	18.162

Contact between minerals

Ol1 - Cpx1
Cpx1 - Opx1
Opx1 - Pl6
Ol2 - Opx2
Opx2 - Cpx2
Cpx3 - Amp1
Amp2 - Pl4,5
Opx3 - Amp3
Amp3 - Pl2
Opx4 - Amp4
Amp4 - Bt1
Bt1 - Pl1

Appendix E2. Representative analyses of the principal minerals from sample CMA-LGY-87

	Cpx1c n=1	Cpx1m n=1	Cpx2c n=1	Cpx2m n=1	Cpx3c n=1	Cpx3m n=1	Opx1 n=4	Opx2 n=1
SiO_2	48.25	50.69	48.96	50.33	49.81	47.11	47.72	51.93
TiO_2	1.53	0.90	1.55	0.92	0.85	2.94	0.01	-
Al_2O_3	3.76	2.02	4.04	1.92	2.06	4.35	5.61	0.44
Cr_2O_3	0.08	0.07	0.08	0.09	0.28	0.27	0.03	0.02
Fe_2O_3	2.61	2.72	3.34	2.94	3.78	3.47	1.16	3.05
FeO	10.89	12.02	10.20	11.20	10.73	9.86	28.90	23.91
MnO	0.38	0.37	0.14	0.38	0.39	0.33	0.90	0.53
MgO	13.19	15.44	14.02	15.22	16.76	13.42	13.76	20.96
CaO	18.86	16.57	18.94	17.21	14.87	17.94	1.32	0.13
Na_2O	-	-	-	-	-	0.30	-	-
K_2O	0.04	0.09	0.11	0.08	0.09	0.16	0.02	0.04
Total	99.59	100.89	101.38	100.29	99.62	100.15	99.42	101.01
Si IV	1.834	1.893	1.823	1.890	1.875	1.781	1.867	1.948
Al IV	0.166	0.089	0.177	0.085	0.091	0.194	0.136	0.019
T site	2.000	1.980	2.000	1.980	1.970	1.970	2.000	1.970
Al VI	0.003	-	-	-	-	-	0.128	-
Ti4+	0.044	0.025	0.043	0.026	0.024	0.084	-	-
Cr3+	0.002	0.002	0.002	0.003	0.008	0.008	0.001	0.001
Fe3+	0.075	0.076	0.094	0.083	0.107	0.099	0.034	0.086
Fe2+	0.346	0.375	0.318	0.352	0.338	0.312	0.947	0.750
Mn2+	0.012	0.012	0.004	0.012	0.012	0.011	0.030	0.017
Mg2+	0.748	0.860	0.778	0.852	0.940	0.756	0.799	1.172
Ca2+	0.768	0.663	0.755	0.693	0.600	0.727	0.056	0.005
Na+	-	-	-	-	-	0.022	-	-
K+	0.002	0.004	0.005	0.004	0.004	0.008	0.001	0.002
M1,M2	2.000	2.020	2.000	2.020	2.030	2.030	2.000	2.030
O	6.000	6.000	6.000	6.000	6.000	6.000	6.016	6.000
En	40.15	45.29	42.03	44.93	50.08	42.15	42.31	60.82
Wo	41.26	34.93	40.81	36.52	31.93	40.49	3.79	0.27
Fs	18.59	19.78	17.16	18.55	17.98	17.36	53.90	38.91
XMg	0.65	0.67	0.68	0.68	0.70	0.67	0.42	0.59

	Bt1 n=1
SiO_2	37.54
TiO_2	3.14
Al_2O_3	15.09
Cr_2O_3	-
Fe_2O_3	2.87
FeO	15.87
MnO	-
MgO	14.38
CaO	-
Na_2O	-
K_2O	9.09
H_2O	4.01
Total	101.99
Si IV	5.498
Al IV	2.502
T site	8.000
Al VI	0.102
Ti VI	0.346
Cr3+	-
Fe3+	0.316
Fe2+	1.944
Mn2+	-
Mg2+	3.139
O site	5.850
Ca2+	-
Na+	-
K+	1.698
A site	1.700
O	20.000
OH	4.000
XMg	0.60

Appendix E2 (continued)

	Pl1c n=1	Pl1m n=2	Pl2c n=1	Pl2m n=1	Pl3m n=1	Pl4c n=1
SiO_2	52.26	53.79	53.21	53.00	52.94	53.45
Al_2O_3	28.98	27.86	28.47	28.73	28.65	28.58
CaO	12.82	11.52	11.60	11.99	12.01	11.30
Na_2O	5.45	6.10	6.22	6.12	6.52	6.68
K_2O	0.14	0.10	0.06	0.13	0.09	0.10
FeO	0.38	0.28	0.25	0.36	0.31	0.47
Total	100.03	99.65	99.81	100.33	100.52	100.58
Si4+	9.546	9.814	9.705	9.639	9.624	9.693
Al3+	6.239	5.992	6.120	6.158	6.138	6.108
Z site	15.785	15.806	15.824	15.797	15.762	15.801
Ca2+	2.509	2.252	2.267	2.336	2.339	2.195
Na+	1.930	2.158	2.199	2.158	2.298	2.349
K+	0.033	0.023	0.014	0.030	0.021	0.023
Fe2+	0.058	0.042	0.038	0.055	0.047	0.071
X site	4.530	4.475	4.518	4.579	4.705	4.639
Total	20.316	20.281	20.342	20.376	20.467	20.439
O	32.000	32.000	32.000	32.000	32.000	32.000
An	56.11	50.80	50.59	51.64	50.22	48.07
Ab	43.16	48.68	49.09	47.70	49.33	51.42
Or	0.73	0.52	0.31	0.67	0.45	0.51

	Amp1 n=4	Amp2 n=1	Amp3 n=1
SiO_2	38.42	39.43	38.26
TiO_2	0.09	0.17	0.14
Al_2O_3	18.57	20.52	20.02
Cr_2O_3	0.02	0.08	0.03
Fe_2O_3	-	-	-
FeO*	19.67	14.37	13.92
MnO	0.26	0.24	0.25
MgO	8.95	10.77	10.68
CaO	8.02	10.83	10.74
Na_2O	3.48	4.04	3.44
K_2O	0.52	0.41	0.46
H_2O	2.02	2.10	2.04
Total	100.04	102.96	99.98
Si IV	5.675	5.630	5.610
Al IV	2.325	2.370	2.390
T site	8.000	8.000	8.000
Al VI	0.902	1.081	1.063
Fe3+	1.087	0.431	0.516
Ti4+	0.010	0.009	0.016
Cr3+	0.002	0.009	0.004
Mg2+	1.968	2.292	2.334
Fe2+	1.031	1.178	1.067
M1,M2,M3	5.000	5.000	5.000
Fe2+	0.312	0.110	0.122
Mn2+	0.033	0.029	0.031
Ca2+	1.268	1.657	1.691
Na+	0.387	0.204	0.156
M4	2.000	2.000	2.000
Na+	0.607	0.912	0.830
K+	0.098	0.076	0.086
A site	0.700	0.990	0.920
O	22.000	22.000	22.000
OH	2.000	2.000	2.000
XMg	0.49	0.61	0.61
XNa	0.47	0.40	0.37
Name	Prg	Prg	Prg

Appendix E2 (continued)

	Ilm1
	n=1
SiO_2	0.12
TiO_2	50.76
Al_2O_3	-
Cr_2O_3	0.08
Fe_2O_3	-
FeO	47.90
MnO	0.59
MgO	-
CaO	0.01
Total	99.46
Si4+	0.003
Ti4+	0.967
Al3+	-
Cr3+	0.002
Fe3+	0.058
Fe2+	0.957
Mn2+	0.013
Mg2+	-
Ca2+	0.000
Total	2.000
O	3.000

Contact between minerals

Opx1 - Amp1
Amp1 - Pl1
Opx2 - Amp2
Amp2 - Pl2
Cpx3 - Pl4
Amp3 - Pl3
Ilm1 - Bt1

Appendix E3. Representative analyses of the principal minerals from sample CMA-79DI-86

	Cpx1 n=1	Cpx2 n=1	Cpx3 n=1	Cpx4c n=1	Cpx4m n=1	Cpx5 n=1	Cpx6c n=2	Cpx6m n=2	Cpx7 n=2	Cpx8c n=1	Cpx8m n=1	Cpx9c n=1	Cpx9m n=1	Cpx10 n=2
SiO_2	49.11	50.05	47.95	50.13	50.78	50.55	51.84	52.19	50.67	52.49	52.79	52.69	52.09	51.55
TiO_2	0.64	1.07	3.04	0.24	0.05	1.10	0.56	0.28	0.37	0.51	0.23	0.18	0.34	0.63
Al_2O_3	1.68	1.41	1.69	1.96	1.12	1.78	2.08	2.53	2.13	3.34	2.85	2.59	2.62	2.44
Cr_2O_3	0.06	0.12	0.03	0.02	0.03	0.06	0.33	0.21	0.13	0.30	0.38	0.13	0.32	0.24
Fe_2O_3	4.12	3.31	4.19	1.66	0.58	0.33	-	1.08	1.82	1.81	4.19	-	1.56	1.42
FeO	11.71	13.28	14.90	14.32	14.88	16.16	8.88	7.70	14.05	7.86	4.64	9.53	8.48	7.03
MnO	0.20	0.05	0.10	0.10	0.06	0.22	0.31	0.17	0.17	0.19	0.26	0.14	0.12	0.13
MgO	9.47	9.59	9.35	9.08	9.93	9.30	13.19	12.77	9.52	13.52	13.02	12.17	12.12	12.76
CaO	20.83	21.10	19.18	20.94	21.41	21.03	21.53	21.58	20.33	20.12	22.97	22.01	22.53	21.87
Na_2O	0.81	0.71	0.82	0.58	0.15	0.33	0.44	0.94	0.79	1.07	1.19	0.48	0.76	0.84
K_2O	0.02	0.02	0.01	0.01	0.00	0.00	0.03	0.00	0.00	0.11	0.09	0.05	0.00	0.12
Total	98.65	100.71	101.26	99.05	98.99	100.86	99.18	99.46	99.98	101.32	102.61	99.97	100.94	99.04
Si IV	1.912	1.915	1.844	1.946	1.970	1.935	1.951	1.952	1.943	1.925	1.914	1.974	1.934	1.938
Al IV	0.077	0.064	0.077	0.054	0.030	0.065	0.049	0.048	0.057	0.075	0.086	0.026	0.066	0.062
T site	1.990	1.980	1.920	2.000	2.000	2.000	2.000	2.000	2.000	2.000	2.000	2.000	2.000	2.000
Al VI	-	-	-	0.035	0.021	0.015	0.043	0.064	0.039	0.069	0.036	0.088	0.049	0.046
Ti4+	0.019	0.031	0.088	0.007	0.001	0.032	0.016	0.008	0.011	0.014	0.006	0.005	0.009	0.018
Cr3+	0.002	0.004	0.001	0.001	0.001	0.002	0.010	0.006	0.004	0.009	0.011	0.004	0.009	0.007
Fe3+	0.121	0.095	0.121	0.049	0.017	0.010	-	0.030	0.052	0.050	0.114	-	0.044	0.040
Fe2+	0.381	0.425	0.479	0.465	0.483	0.517	0.279	0.241	0.450	0.241	0.141	0.299	0.263	0.221
Mn2+	0.007	0.002	0.003	0.003	0.002	0.007	0.010	0.005	0.006	0.006	0.008	0.004	0.004	0.004
Mg2+	0.550	0.547	0.536	0.525	0.574	0.531	0.740	0.712	0.544	0.739	0.704	0.680	0.671	0.715
Ca2+	0.869	0.865	0.790	0.871	0.890	0.862	0.868	0.865	0.835	0.791	0.892	0.883	0.896	0.881
Na+	0.061	0.053	0.061	0.044	0.011	0.024	0.032	0.069	0.059	0.076	0.084	0.035	0.055	0.061
K+	0.001	0.001	0.000	0.000	0.000	0.000	0.001	0.000	0.000	0.005	0.004	0.002	0.000	0.006
M1,M2	2.010	2.020	2.080	2.000	2.000	2.000	2.000	2.000	2.000	2.000	2.000	2.000	2.000	2.000
O	6.000	6.000	6.000	6.000	6.000	6.000	6.001	6.000	6.000	6.000	6.000	6.019	6.000	6.000
En	30.54	29.78	29.69	28.23	29.50	27.78	39.20	39.19	29.72	41.74	40.52	36.51	36.65	39.36
Wo	48.28	47.09	43.77	46.79	45.71	45.14	46.00	47.56	45.64	44.65	51.38	47.45	48.97	48.48
Fs	21.19	23.13	26.54	24.98	24.79	27.08	14.80	13.25	24.63	13.61	8.10	16.04	14.38	12.15
XMg	0.55	0.54	0.50	0.52	0.54	0.50	0.73	0.74	0.53	0.74	0.78	0.69	0.70	0.75

Appendix E3 (continued)

	Bt1 n=5	Bt2 n=1	Bt3 n=1
SiO_2	35.96	35.93	37.33
TiO_2	5.89	5.37	6.01
Al_2O_3	12.86	15.40	14.82
Cr_2O_3	0.03	0.28	0.12
Fe_2O_3	3.56	2.95	2.95
FeO	19.66	16.31	16.30
MnO	-	-	0.01
MgO	9.22	11.05	11.93
CaO	0.20	0.25	0.21
K_2O	9.71	9.61	9.77
H_2O	3.89	3.97	3.98
Total	100.98	101.12	103.98
Si IV	5.488	5.365	5.430
Al IV	2.313	2.635	2.541
Fe IV	0.199	0.000	0.030
T site	8.000	8.000	8.000
Al VI	-	0.075	-
Ti VI	0.676	0.603	0.657
Cr3+	0.003	0.033	0.014
Fe3+	0.210	0.331	0.293
Fe2+	2.509	2.037	1.983
Mn2+	-	-	0.001
Mg2+	2.098	2.460	2.587
O site	5.500	5.540	5.540
Ca2+	0.032	0.040	0.033
K+	1.891	1.831	1.813
A site	1.920	1.870	1.850
O	20.000	20.000	20.000
OH	4.000	4.000	4.000
XMg	0.45	0.53	0.55

	Pl1c n=1	Pl2 n=1	Pl3c n=1	Pl3m n=1	Pl4m n=1	Pl5 n=1	Pl6c n=1	Pl6m n=1	Pl7c n=1
SiO_2	49.24	59.73	48.33	50.24	65.82	62.34	50.48	52.83	48.90
Al_2O_3	33.49	26.22	33.55	29.65	20.94	21.53	30.57	28.65	31.88
Na_2O	2.24	7.73	1.64	4.16	9.92	9.51	3.00	4.70	2.04
CaO	15.62	7.22	16.18	12.22	2.07	4.19	14.25	12.54	16.12
K_2O	0.52	1.14	0.22	0.70	0.55	0.82	0.19	0.29	0.10
FeO	0.12	0.20	0.01	0.10	0.85	1.20	0.32	0.85	0.29
Total	101.22	102.24	99.93	97.07	100.15	99.59	98.81	99.86	99.33
Si4+	8.901	10.506	8.835	9.426	11.572	11.137	9.304	9.595	9.004
Al3+	7.135	5.435	7.228	6.556	4.339	4.533	6.640	6.132	6.921
Z site	16.036	15.941	16.064	15.983	15.910	15.670	15.944	15.727	15.925
Ca2+	3.026	1.361	3.169	2.457	0.390	0.802	2.814	2.440	3.181
Na+	0.784	2.636	0.581	1.513	3.381	3.294	1.072	1.655	0.726
K+	0.120	0.256	0.051	0.168	0.123	0.187	0.045	0.067	0.024
Fe2+	0.018	0.029	0.002	0.016	0.125	0.179	0.049	0.129	0.045
X site	3.930	4.253	3.801	4.138	3.894	4.283	3.931	4.162	3.931
Total	19.984	20.223	19.867	20.136	19.998	20.302	19.935	20.189	19.906
O	32.000	32.000	32.000	32.000	32.000	32.000	32.000	32.000	32.000
An	77.10	32.00	83.36	59.37	10.01	18.73	71.59	58.62	80.99
Ab	19.85	61.99	15.29	36.58	86.82	76.91	27.27	39.76	18.40
Or	3.06	6.02	1.35	4.05	3.17	4.36	1.14	1.61	0.61

Contact between minerals

Cpx8 - Amp1
Amp5 - Pl1

Appendix E3 (continued)

	PL7m n=5
SiO_2	53.47
Al_2O_3	28.40
Na_2O	5.34
CaO	11.66
K_2O	0.24
FeO	0.45
Total	99.56
Si4+	9.754
Al3+	6.105
Z site	15.859
Ca2+	2.280
Na+	1.888
K+	0.056
Fe2+	0.068
X site	4.224
Total	20.164
O	32.000
An	54.08
Ab	44.60
Or	1.32

	Amp1 n=3	Amp2 n=2	Amp3 n=1	Amp4 n=1	Amp5 n=3
SiO_2	40.61	40.49	41.06	41.08	41.31
TiO_2	0.77	1.46	1.76	1.47	1.04
Al_2O_3	14.96	14.78	11.08	12.49	14.70
Cr_2O_3	0.13	0.26	-	0.08	0.05
Fe_2O_3	-	-	-	-	-
FeO*	15.02	14.10	22.26	15.64	13.68
MnO	0.11	0.08	0.06	0.16	0.01
MgO	11.29	11.38	8.11	10.45	11.82
CaO	12.11	12.27	11.22	12.04	12.04
Na_2O	1.64	1.78	1.69	1.86	1.93
K_2O	1.72	1.67	1.40	1.41	1.68
H_2O	2.03	2.04	1.99	1.99	2.04
Total	100.38	100.30	100.63	98.67	100.30
Si IV	5.990	6.000	6.229	6.230	6.080
Al IV	2.010	2.000	1.771	1.770	1.920
T site	8.000	8.000	8.000	8.000	8.000
Al VI	0.596	0.579	0.218	0.470	0.633
Fe3+	0.509	0.304	0.563	0.177	0.275
Ti4+	0.085	0.163	0.201	0.168	0.116
Cr3+	0.015	0.030	-	0.010	0.006
Mg2+	2.482	2.507	1.833	2.360	2.598
Fe2+	1.312	1.417	2.185	1.812	1.372
M1,M2,M3	5.000	5.000	5.000	5.000	5.000
Fe2+	0.035	0.023	0.077	-	0.038
Mn2+	0.014	0.010	0.008	0.002	0.001
Ca2+	1.914	1.947	1.824	1.967	1.906
Na+	0.037	0.020	0.091	0.031	0.055
M4	2.000	2.000	2.000	2.000	2.000
Na+	0.433	0.496	0.407	0.515	0.497
K+	0.324	0.314	0.272	0.274	0.316
A site	0.760	0.810	0.680	0.790	0.810
O	22.000	22.000	22.000	22.000	22.000
XMg	0.61	0.63	0.43	0.58	0.64
XNa	0.20	0.21	0.21	0.21	0.22
Name	Prg	Prg	Prg	Prg	Prg

	Grt1 n=1	Grt2 n=3	Grt3 n=1	Grt4 n=1
SiO_2	37.79	37.24	37.38	37.39
TiO_2	0.02	0.08	0.12	0.10
Al_2O_3	19.64	19.79	19.87	20.34
Cr_2O_3	0.02	0.01	0.03	-
Fe_2O_3	2.68	2.21	2.61	2.28
FeO	30.01	28.30	29.32	21.56
MnO	1.34	1.11	1.32	0.52
MgO	2.47	2.41	2.49	1.73
CaO	6.98	8.57	7.82	15.72
Total	100.95	99.72	100.96	99.64
Si IV	6.000	5.977	5.945	5.921
Al IV	0.000	0.023	0.055	0.079
T site	6.000	6.000	6.000	6.000
Al VI	3.675	3.722	3.669	3.716
Ti VI	0.002	0.010	0.014	0.012
Cr3+	0.003	0.002	0.004	-
Fe3+	0.320	0.267	0.313	0.272
O site	4.000	4.000	4.000	4.000
Fe2+	3.985	3.798	3.899	2.855
Mn2+	0.180	0.150	0.178	0.070
Mg2+	0.585	0.578	0.590	0.408
Ca2+	1.187	1.474	1.332	2.667
A site	5.940	6.000	6.000	6.000
O	23.938	23.993	23.980	23.966
Almand	63.64	60.49	61.59	45.43
Pyrop	9.34	9.20	9.32	6.50
Gross	18.96	23.48	21.05	42.44
Ti And	0.04	0.15	0.23	0.19
Fe And	5.11	4.25	4.94	4.32
Spess	2.88	2.40	2.81	1.11
Uvaro	0.04	0.03	0.06	-
XMg	0.12	0.13	0.13	0.12

Appendix E3 (continued)

	Grt5 n=2	Grt6 n=4	Grt7 n=1	Grt8 n=1
SiO_2	37.26	37.23	38.06	40.25
TiO_2	0.06	0.07	-	-
Al_2O_3	19.42	20.11	20.83	21.90
Cr_2O_3	-	0.03	-	0.03
Fe_2O_3	2.55	1.76	1.50	1.33
FeO	30.00	30.20	30.49	18.62
MnO	1.35	1.27	1.32	0.42
MgO	2.40	2.61	2.79	3.12
CaO	6.87	6.70	6.97	15.38
Total	99.91	99.98	101.96	101.04
Si IV	5.999	5.973	5.971	6.000
Al IV	0.001	0.027	0.029	0.000
T site	6.000	6.000	6.000	6.000
Al VI	3.683	3.776	3.823	3.848
Ti VI	0.008	0.009	-	-
Cr3+	-	0.003	-	0.004
Fe3+	0.309	0.212	0.177	0.149
O site	4.000	4.000	4.000	4.000
Fe2+	4.039	4.052	4.000	2.321
Mn2+	0.184	0.172	0.175	0.053
Mg2+	0.577	0.625	0.653	0.693
Ca2+	1.185	1.151	1.172	2.456
A site	5.990	6.000	6.000	5.520
O	23.990	23.991	23.986	23.523
Almand	64.09	65.11	64.76	40.89
Pyrop	9.16	10.04	10.56	12.22
Gross	18.80	18.49	18.97	43.28
Ti And	0.12	0.14	-	-
Fe And	4.90	3.41	2.87	2.62
Spess	2.92	2.77	2.84	0.93
Uvaro	-	0.05	-	0.06
XMg	0.12	0.13	0.14	0.22

Appendix E4. Representative analyses of the principal minerals from sample CMA-27.6.3-87

	Cpx1 n=3	Cpx2 n=1	Cpx3 n=1	Cpx4c n=1	Cpx4m n=1	Cpx5 n=1	Opx1 n=1
SiO_2	53.35	52.52	50.37	52.70	49.69	51.67	52.45
TiO_2	0.05	0.04	0.69	0.11	0.85	0.14	0.02
Al_2O_3	1.45	1.18	4.24	1.31	6.90	1.22	0.45
Cr_2O_3	0.08	0.02	0.09	0.13	0.10	0.12	0.02
Fe_2O_3	1.16	0.29	0.64	-	4.05	0.46	3.10
FeO	5.55	11.42	8.19	9.09	5.14	9.74	19.89
MnO	0.03	0.12	0.03	0.08	0.04	-	0.13
MgO	14.34	16.13	14.08	16.28	16.19	15.85	23.76
CaO	23.00	17.38	19.04	18.39	14.80	18.45	0.23
Na_2O	0.52	-	0.48	0.11	1.22	0.02	-
K_2O	0.01	0.09	0.30	0.06	0.50	0.06	0.02
Total	99.53	99.19	98.14	98.26	99.48	97.74	100.07
Si IV	1.981	1.971	1.901	1.982	1.825	1.962	1.947
Al IV	0.021	0.029	0.099	0.018	0.175	0.038	0.020
T site	2.000	2.000	2.000	2.000	2.000	2.000	1.970
Al VI	0.042	0.023	0.089	0.040	0.124	0.017	-
Ti4+	0.001	0.001	0.020	0.003	0.023	0.004	0.001
Cr3+	0.002	0.001	0.003	0.004	0.003	0.004	0.001
Fe3+	0.032	0.008	0.018	-	0.112	0.013	0.086
Fe2+	0.172	0.358	0.258	0.286	0.158	0.309	0.617
Mn2+	0.001	0.004	0.001	0.003	0.001	-	0.004
Mg2+	0.794	0.902	0.792	0.913	0.886	0.897	1.315
Ca2+	0.915	0.699	0.770	0.741	0.582	0.751	0.009
Na+	0.037	-	0.035	0.008	0.087	0.001	-
K+	0.001	0.004	0.014	0.003	0.023	0.003	0.001
M1,M2	2.000	2.000	2.000	2.000	2.000	2.000	2.030
O	6.012	6.000	6.000	6.011	6.000	6.000	6.000
En	42.21	46.05	43.51	47.06	54.50	45.84	67.72
Wo	48.65	35.66	42.29	38.20	35.80	38.35	0.47
Fs	9.14	18.29	14.19	14.74	9.70	15.81	31.81
XMg	0.81	0.71	0.75	0.76	0.81	0.74	0.67

	Bt1 n=1
SiO_2	36.85
TiO_2	4.88
Al_2O_3	14.25
Cr_2O_3	-
Fe_2O_3	2.11
FeO	11.66
MnO	0.05
MgO	15.32
CaO	-
Na_2O	-
K_2O	9.57
H_2O	4.07
Total	98.76
Si IV	5.502
Al IV	2.498
T site	8.000
Al VI	0.009
Ti VI	0.548
Cr3+	-
Fe3+	0.237
Fe2+	1.456
Mn2+	0.006
Mg2+	3.410
O site	5.670
Ca2+	-
Na+	-
K+	1.823
A site	1.820
O	20.000
OH	4.000
XMg	0.68

	Pl1 n=1	Pl2m n=1
SiO_2	54.71	57.21
Al_2O_3	28.50	27.35
CaO	10.99	9.84
Na_2O	6.04	8.58
K_2O	0.20	0.15
FeO	0.17	0.02
Total	100.61	103.15
Si4+	9.852	10.073
Al3+	6.049	5.675
Z site	15.900	15.749
Ca2+	2.120	1.856
Na+	2.109	2.929
K+	0.046	0.034
Fe2+	0.026	0.003
X site	4.301	4.822
Total	20.201	20.571
O	32.000	32.000
An	49.60	38.52
Ab	49.33	60.78
Or	1.07	0.70

Appendix E4 (continued)

	Pl3c n=1	Pl3m n=1
SiO_2	52.82	56.54
Al_2O_3	27.68	26.41
CaO	11.89	9.25
Na_2O	6.25	8.53
K_2O	0.19	0.18
FeO	0.43	0.00
Total	99.26	100.91
Si4+	9.722	10.161
Al3+	6.005	5.594
Z site	15.727	15.755
Ca2+	2.345	1.781
Na+	2.230	2.972
K+	0.045	0.041
Fe2+	0.066	0.000
X site	4.686	4.794
Total	20.413	20.549
O	32.000	32.000
An	50.75	37.15
Ab	48.28	61.99
Or	0.97	0.86

	Amp1 n=2	Amp2 n=1	Amp3 n=2	Amp4 n=1	Amp5 n=1
SiO_2	47.25	46.57	46.87	48.11	43.43
TiO_2	0.98	0.93	1.00	1.01	1.83
Al_2O_3	9.55	11.44	10.24	8.09	11.29
Cr_2O_3	0.13	0.16	-	0.01	0.05
Fe_2O_3	-	-	-	-	-
FeO	10.52	10.48	10.92	10.19	12.94
MnO	-	-	0.05	-	0.03
MgO	15.73	15.25	15.28	16.41	12.62
CaO	11.86	12.23	11.94	12.06	11.97
Na_2O	2.05	1.66	1.96	1.60	2.31
K_2O	0.58	0.84	0.73	0.54	1.07
H_2O	2.11	2.13	2.11	2.10	2.04
Total	100.75	101.69	101.10	100.12	99.58
Si IV	6.756	6.590	6.680	6.882	6.436
Al IV	1.244	1.410	1.320	1.118	1.564
T site	8.000	8.000	8.000	8.000	8.000
Al VI	0.366	0.495	0.410	0.247	0.412
Fe3+	0.177	0.241	0.235	0.268	0.056
Ti4+	0.106	0.102	0.108	0.006	0.205
Cr3+	0.015	0.017	-	0.001	0.006
Mg2+	3.352	3.214	3.245	3.497	2.786
Fe2+	0.984	0.931	1.002	0.954	1.535
M1,M2,M3	5.000	5.000	5.000	5.000	5.000
Fe2+	0.090	0.072	0.068	-	0.014
Mn2+	-	-	0.006	-	0.004
Ca2+	1.814	1.854	1.824	1.847	1.896
Na+	0.096	0.074	0.102	0.153	0.086
M4	2.000	2.000	2.000	2.000	2.000
Na+	0.472	0.382	0.440	0.291	0.572
K+	0.107	0.151	0.132	0.098	0.196
A site	0.580	0.530	0.570	0.390	0.770
O	22.000	22.000	22.000	22.000	22.000
OH	2.000	2.000	2.000	2.000	2.000
XMg	0.76	0.75	0.75	0.77	0.67
XNa	0.24	0.20	0.23	0.19	0.26
Name	Prg	Ed Hbl	Prg	Hbl	Prg Hbl

	Grt1 n=1	Grt2c n=1	Grt2m n=1
SiO_2	39.21	39.68	38.02
TiO_2	0.05	0.09	0.04
Al_2O_3	21.93	22.30	20.98
Cr_2O_3	0.01	0.15	-
Fe_2O_3	0.58	0.27	1.28
FeO	21.10	23.08	23.78
MnO	0.82	0.53	0.33
MgO	7.33	6.75	6.61
CaO	9.39	9.33	7.68
Total	100.42	102.18	98.72
Si IV	5.983	5.980	5.965
Al IV	0.017	0.020	0.035
T site	6.000	6.000	6.000
Al VI	3.926	3.942	3.844
Ti VI	0.006	0.010	0.005
Cr3+	0.001	0.018	-
Fe3+	0.067	0.030	0.151
O site	4.000	4.000	4.000
Fe2+	2.692	2.909	3.119
Mn2+	0.106	0.068	0.044
Mg2+	1.667	1.517	1.546
Ca2+	1.535	1.507	1.291
A site	6.000	6.000	6.000
O	23.994	23.995	23.985
Almand	44.32	48.02	50.67
Pyrop	27.45	25.03	25.11
Gross	25.27	24.87	20.97
Ti And	0.09	0.17	0.08
Fe And	1.10	0.50	2.46
Spess	1.74	1.12	0.71
Uvaro	0.02	0.30	-
XMg	0.37	0.34	0.32

Appendix E4 (continued)

	Grt3 n=3	Grt4 n=1	Grt5 n=2	Grt6c n=1	Grt7 n=1
SiO_2	39.59	38.12	38.79	38.31	38.70
TiO_2	0.07	0.05	0.06	0.19	-
Al_2O_3	21.62	24.55	21.04	21.02	21.18
Cr_2O_3	-	-	0.05	0.08	0.01
Fe_2O_3	1.19	-	1.47	1.51	1.30
FeO	23.99	22.03	24.03	24.24	23.94
MnO	0.62	0.46	0.63	0.41	0.48
MgO	6.38	5.64	7.29	6.33	6.94
CaO	8.58	9.06	6.67	8.03	7.48
Total	102.04	99.91	100.03	100.12	100.03
Si IV	5.997	5.682	5.987	5.946	5.986
Al IV	0.003	0.318	0.013	0.054	0.014
T site	6.000	6.000	6.000	6.000	6.000
Al VI	3.857	3.994	3.815	3.791	3.848
Ti VI	0.008	0.006	0.008	0.022	-
Cr3+	-	-	0.007	0.010	0.001
Fe3+	0.135	0.000	0.171	0.177	0.151
O site	4.000	4.000	4.000	4.000	4.000
Fe2+	3.039	2.746	3.102	3.146	3.097
Mn2+	0.080	0.058	0.082	0.054	0.063
Mg2+	1.442	1.253	1.677	1.465	1.600
Ca2+	1.393	1.447	1.103	1.335	1.240
A site	5.950	5.500	5.960	6.000	6.000
O	23.955	23.348	23.962	23.984	23.993
Almand	49.86	49.84	50.44	50.67	50.34
Pyrop	23.65	22.75	27.28	23.59	26.01
Gross	22.85	26.26	17.94	21.51	20.15
Ti And	0.12	0.10	0.12	0.36	-
Fe And	2.22	-	2.77	2.85	2.46
Spess	1.30	1.05	1.33	0.87	1.02
Uvaro	-	-	0.11	0.16	0.02
XMg	0.31	0.31	0.34	0.31	0.33

Contact between minerals

Opx1 - Amp1
Amp1 - Grt5
Grt7 - Pl3
Bt1 - Grt6
Cpx1 - Amp3
Amp3 - Grt3
Grt3 - Pl2
Cpx4 - Amp2
Grt1 - Pl1
Amp2 - Pl1
Grt1 - Pl1
Cpx3 - Amp5
Cpx5 - Grt4

Appendix E5. Representative analyses of the principal minerals from sample CMA-27.6.5-87

	Ol1 n=2	Ol2 n=2	Ol3 n=4	Ol4 n=1	Ol5 n=1
SiO_2	34.01	34.67	34.28	34.54	33.55
FeO	45.51	43.85	41.35	41.82	44.30
MgO	20.53	22.51	24.26	24.46	20.92
TiO_2	-	-	0.05	-	-
Cr_2O_3	0.00	0.00	0.00	0.06	0.00
Total	100.04	101.04	99.95	100.88	98.77
Si4+	0.994	0.992	0.979	0.977	0.989
Fe2+	1.112	1.049	0.987	0.990	1.092
Mg2+	0.894	0.960	1.033	1.032	0.919
Ti4+	-	-	0.001	-	-
Cr3+	0.000	0.000	0.000	0.001	0.000
Total	3.000	3.000	3.000	3.000	3.000
XMg	0.45	0.48	0.51	0.51	0.46

	Cpx1 n=3	Cpx2c n=3	Cpx2m n=3	Cpx3m n=1	Cpx4m n=1	Cpx5m n=1	Opx1 n=9	Opx2 n=5
SiO_2	49.50	50.28	50.15	49.99	49.18	50.06	52.14	52.16
TiO_2	0.69	1.21	0.96	0.53	0.93	0.52	0.03	0.01
Al_2O_3	4.58	4.39	3.49	2.49	3.89	2.61	0.49	0.54
Cr_2O_3	0.17	0.27	0.19	0.07	0.10	0.07	0.02	-
Fe_2O_3	-	-	-	-	-	-	-	-
FeO	12.42	12.04	12.56	14.84	11.39	12.94	25.03	23.81
MnO	0.31	0.23	0.13	0.19	0.20	0.07	0.31	0.27
MgO	14.41	14.04	13.86	13.14	14.45	10.71	22.00	22.49
CaO	18.35	18.66	18.27	17.36	17.84	19.86	0.30	0.21
Na_2O	0.02	0.62	0.94	0.70	0.32	1.57	0.09	0.10
K_2O	0.04	0.04	0.08	0.09	0.02	0.38	0.04	0.00
Total	100.49	101.79	100.64	99.40	98.32	98.79	100.45	99.60
Si IV	1.854	1.859	1.881	1.913	1.874	1.932	1.960	1.965
Al IV	0.146	0.141	0.111	0.087	0.126	0.068	0.022	0.022
T site	2.000	2.000	1.990	2.000	2.000	2.000	1.980	1.990
Al VI	0.048	0.050	0.043	0.026	0.049	0.050	-	0.002
Ti4+	0.020	0.034	0.027	0.015	0.027	0.015	0.001	0.000
Cr3+	0.005	0.008	0.006	0.002	0.003	0.002	-	-
Fe3+	-	-	-	-	-	-	-	-
Fe2+	0.390	0.373	0.395	0.475	0.363	0.418	0.787	0.750
Mn2+	0.010	0.007	0.004	0.006	0.006	0.002	0.010	0.009
Mg2+	0.805	0.774	0.776	0.750	0.821	0.616	1.232	1.263
Ca2+	0.737	0.739	0.734	0.712	0.728	0.821	0.012	0.009
Na+	0.052	-	-	-	0.024	0.117	0.006	0.007
K+	0.002	0.002	0.004	0.004	0.001	0.019	0.002	0.000
M1,M2	2.020	2.030	2.060	2.040	2.020	2.060	2.050	2.040
O	6.000	6.000	6.000	6.000	6.000	6.000	6.000	6.000
En	41.68	41.06	40.73	38.71	42.93	33.22	60.66	62.47
Wo	38.15	39.21	38.62	36.76	38.09	44.27	0.60	0.42
Fs	20.17	19.74	20.65	24.53	18.98	22.51	38.73	37.11
XMg	0.67	0.68	0.66	0.61	0.69	0.60	0.61	0.63

Appendix E5 (continued)

	Opx3 n=6	Opx4 n=6	Opx5 n=4	Opx6 n=2	Opx7 n=1
SiO_2	51.99	50.99	50.41	50.93	51.93
TiO_2	0.03	0.08	0.02	-	-
Al_2O_3	0.28	0.39	0.10	0.59	0.45
Cr_2O_3	0.03	0.02	-	-	-
Fe_2O_3	-	-	-	-	-
FeO	23.32	28.36	32.58	27.20	23.45
MnO	0.29	0.18	0.22	0.25	0.21
MgO	23.14	19.72	16.70	19.61	22.54
CaO	0.38	0.29	0.39	0.29	0.18
Na_2O	-	-	0.02	-	-
K_2O	0.01	0.08	0.01	0.01	0.00
Total	99.47	100.11	100.45	98.90	98.76
Si IV	1.959	1.956	1.967	1.966	1.969
Al IV	0.012	0.017	0.005	0.027	0.020
T site	1.970	1.970	1.970	1.990	1.990
Al VI	-	-	-	-	-
Ti4+	0.001	0.002	0.001	-	-
Cr3+	0.001	0.001	-	-	-
Fe3+	-	-	-	-	-
Fe2+	0.735	0.910	1.063	0.878	0.744
Mn2+	0.009	0.006	0.007	0.008	0.007
Mg2+	1.300	1.127	0.971	1.129	1.274
Ca2+	0.015	0.012	0.016	0.012	0.007
Na+	0.001	0.001	0.045	0.069	-
K+	0.001	0.004	0.000	0.000	0.000
M1,M2	2.060	2.060	2.060	2.030	2.030
O	6.000	6.000	6.000	6.000	6.000
En	63.40	55.01	47.38	55.90	62.92
Wo	0.75	0.59	0.79	0.60	0.36
Fs	35.85	44.39	51.83	43.49	36.72
XMg	0.64	0.55	0.48	0.56	0.63

	Pl1c n=1	Pl2c n=1	Pl2m n=1	Pl3m n=1	Pl4m n=1	Pl5 n=2	Pl6c n=1	Pl6m n=1
SiO_2	54.82	54.64	54.12	57.14	54.96	54.26	53.38	54.12
Al_2O_3	29.69	30.40	30.86	28.35	29.35	28.71	29.80	27.85
CaO	11.26	11.90	10.47	9.41	10.39	9.88	10.79	10.06
Na_2O	3.97	3.59	5.69	6.65	5.85	5.95	5.24	6.53
K_2O	0.44	0.54	0.74	0.87	1.09	0.62	0.71	0.12
FeO	0.77	0.65	1.61	0.70	0.70	0.85	0.79	0.89
Total	100.95	101.72	103.49	103.12	102.34	100.28	100.71	99.57
Si4+	9.802	9.706	9.550	10.043	9.777	9.824	9.640	9.867
Al3+	6.257	6.365	6.418	5.873	6.153	6.127	6.343	5.985
Z site	16.059	16.071	15.968	15.915	15.930	15.950	15.983	15.852
Ca2+	2.157	2.265	1.979	1.772	1.980	1.916	2.088	1.965
Na+	1.376	1.236	1.947	2.266	2.018	2.090	1.835	2.308
K+	0.100	0.122	0.167	0.195	0.247	0.143	0.164	0.028
Fe2+	0.115	0.097	0.238	0.103	0.104	0.130	0.119	0.136
X site	3.633	3.623	4.093	4.233	4.245	4.149	4.087	4.301
Total	19.808	19.791	20.298	20.251	20.279	20.230	20.188	20.299
O	32.000	32.000	32.000	32.000	32.000	32.000	32.000	32.000
An	59.36	62.50	48.36	41.86	46.65	46.21	51.09	45.69
Ab	37.88	34.12	47.56	53.53	47.53	50.33	44.90	53.66
Or	2.76	3.38	4.07	4.61	5.83	3.45	4.00	0.65

Appendix E5 (continued)

	Pl7 n=1	Pl8c n=2	Pl8m n=1	Pl9c n=1	Pl9m n=1	Pl10c n=1	Pl10m n=2	Pl11c n=1	Pl11m n=3	Pl12m n=1	Pl13c n=1	Pl13m n=2	Pl14m n=2
SiO_2	56.18	53.48	53.38	56.04	58.12	52.65	54.27	51.99	51.37	54.19	52.24	57.30	52.60
Al_2O_3	28.08	28.50	28.17	26.88	26.12	29.89	28.84	29.23	29.93	29.66	29.92	26.02	28.65
CaO	8.43	10.89	8.52	8.12	6.94	12.60	8.94	11.38	[illegible].60	5.90	12.01	7.82	9.23
Na_2O	6.94	6.47	7.55	8.47	9.49	5.34	7.16	5.92	[illegible].28	8.92	5.97	9.37	8.26
K_2O	0.59	0.21	0.26	0.33	0.30	0.22	0.26	0.16	0.12	0.21	0.22	0.36	0.15
FeO	0.87	0.30	2.35	1.20	1.09	0.44	2.07	0.86	2.83	2.87	0.81	1.28	1.77
Total	101.09	99.85	100.22	101.04	102.06	101.14	101.54	99.53	100.13	101.75	101.17	102.15	100.64
Si4+	10.051	9.737	9.748	10.080	10.319	9.495	9.755	9.531	9.421	9.725	9.442	10.203	9.591
Al3+	5.921	6.116	6.062	5.698	5.466	6.352	6.110	6.315	6.469	6.273	6.374	5.461	6.157
Z site	15.972	15.852	15.810	15.778	15.785	15.847	15.865	15.846	15.890	15.998	15.816	15.664	15.748
Ca2+	1.616	2.124	1.667	1.565	1.320	2.435	1.722	2.237	1.690	1.134	2.325	1.492	1.803
Na+	2.407	2.284	2.671	2.954	3.267	1.869	2.495	2.104	2.589	3.104	2.093	3.235	2.919
K+	0.135	0.049	0.061	0.076	0.068	0.051	0.060	0.037	0.028	0.048	0.050	0.082	0.035
Fe2+	0.130	0.046	0.358	0.181	0.162	0.065	0.311	0.131	0.434	0.431	0.122	0.191	0.270
X site	4.288	4.503	4.757	4.776	4.817	4.420	4.588	4.509	4.741	4.717	4.590	5.000	5.027
Total	20.260	20.363	20.576	20.569	20.609	20.277	20.460	20.368	20.642	20.715	20.424	20.694	20.791
O	32.000	32.000	32.000	32.000	32.000	32.000	32.000	32.000	32.000	32.000	32.000	32.000	32.000
An	38.86	47.66	37.75	34.06	28.36	55.91	40.26	51.14	39.24	26.47	52.04	31.03	37.89
Ab	57.90	51.24	60.86	64.29	70.18	42.93	58.35	48.00	60.11	72.41	46.85	67.27	61.37
Or	3.24	1.09	1.38	1.65	1.46	1.16	1.39	0.85	0.65	1.12	1.11	1.70	0.73

Appendix E5 (continued)

	Amp1 n=2	Amp2 n=8	Amp3 n=3
SiO_2	38.48	38.26	38.12
TiO_2	0.11	0.09	0.14
Al_2O_3	18.20	18.91	18.17
Cr_2O_3	-	0.02	0.04
Fe_2O_3	-	-	-
FeO*	14.09	13.93	13.29
MnO	0.08	0.04	0.07
MgO	11.07	11.78	10.79
CaO	10.79	10.65	10.66
Na_2O	3.58	3.65	3.87
K_2O	1.23	0.97	1.34
H_2O	2.02	2.03	2.01
Total	99.65	100.35	98.49
Si IV	5.690	5.671	5.630
Al IV	2.310	2.329	2.370
T site	8.000	8.000	8.000
A VI	0.871	0.822	0.918
Fe3+	0.587	0.576	0.555
Ti4+	0.012	0.017	0.006
Cr3+	-	0.005	0.002
Mg2+	2.444	2.476	2.581
Fe2+	1.086	1.104	0.938
M1,M2,M3	5.000	5.000	5.000
Fe2+	0.069	0.066	0.140
Mn2+	0.010	0.010	0.005
Ca2+	1.706	1.728	1.679
Na+	0.215	0.196	0.176
M4	2.000	2.000	2.000
Na+	0.813	0.844	0.866
K+	0.232	0.236	0.177
A site	1.050	1.080	1.130
O	22.000	22.000	22.000
XMg	0.62	0.65	0.62
XNa	0.38	0.38	0.40

	Grt1 n=4	Grt2 n=2	Grt3 n=3	Grt4 n=1	Grt5 n=1	Grt6 n=1	Grt7 n=2	Grt8 n=1	Grt9 n=1
SiO_2	38.08	38.49	37.73	39.29	37.23	37.99	37.81	37.17	38.08
TiO_2	0.02	0.03	0.07	0.02	0.49	0.07	-	0.11	0.02
Al_2O_3	22.01	21.22	21.83	21.03	20.11	21.07	21.24	21.00	21.06
Cr_2O_3	0.02	-	0.09	-	0.05	0.05	0.01	0.05	0.08
Fe_2O_3	0.97	0.99	0.95	1.85	1.35	1.30	0.90	0.77	0.65
FeO	25.20	26.36	25.97	22.51	31.38	27.41	23.77	23.63	22.68
MnO	0.77	0.75	1.08	0.82	0.97	0.92	0.86	0.67	0.74
MgO	5.29	4.38	5.77	4.80	2.80	2.87	5.39	4.84	4.01
CaO	8.45	8.67	6.85	11.48	5.76	9.66	8.53	9.36	11.22
Total	100.81	100.88	100.33	101.81	100.15	101.34	98.51	97.61	98.53
Si IV	5.878	5.989	5.869	6.000	5.971	5.946	5.951	5.935	6.000
Al IV	0.122	0.011	0.131	0.000	0.029	0.054	0.049	0.065	0.000
T site	6.000	6.000	6.000	6.000	6.000	6.000	6.000	6.000	6.000
Al VI	3.882	3.880	3.870	3.785	3.772	3.833	3.892	3.887	3.911
Ti VI	0.002	0.004	0.008	0.002	0.059	0.008	-	0.013	0.002
Cr3+	0.002	-	0.011	-	0.006	0.006	0.001	0.006	0.010
Fe3+	0.113	0.116	0.111	0.213	0.163	0.153	0.107	0.093	0.077
O site	4.000	4.000	4.000	4.000	4.000	4.000	4.000	4.000	4.000
Fe2+	3.253	3.430	3.378	2.875	4.209	3.588	3.129	3.156	2.988
Mn2+	0.100	0.098	0.142	0.106	0.132	0.122	0.115	0.091	0.099
Mg2+	1.216	1.016	1.338	1.093	0.669	0.670	1.265	1.152	0.942
Ca2+	1.398	1.446	1.142	1.878	0.990	1.620	1.440	1.601	1.894
A site	5.970	5.990	6.000	5.950	6.000	6.000	5.950	6.000	5.920
O	23.908	23.987	23.938	23.954	24.015	23.977	23.924	23.974	23.924
Almand	53.45	56.13	55.12	46.62	67.58	58.19	51.66	51.63	49.70
Pyrop	19.99	16.62	21.83	17.72	10.75	10.86	20.87	18.85	15.67
Gross	22.98	23.68	18.62	30.46	15.89	26.27	23.79	26.20	31.51
Ti And	0.04	0.06	0.13	0.04	0.95	0.13	-	0.22	0.04
Fe And	1.86	1.90	1.81	3.45	2.62	2.47	1.76	1.52	1.28
Spress	1.65	1.61	2.31	1.72	2.12	1.98	1.89	1.48	1.64
Uvaro	0.04	-	0.18	-	0.10	0.10	0.02	0.10	0.17
XMg	0.27	0.22	0.28	0.27	0.13	0.15	0.28	0.26	0.24

Appendix E5 (continued)

	Grt10 n=1	Grt11 n=1
SiO_2	38.15	38.37
TiO_2	0.02	0.05
Al_2O_3	21.20	19.26
Cr_2O_3	0.02	0.04
Fe_2O_3	0.55	3.74
FeO	23.90	23.11
MnO	0.77	0.77
MgO	4.99	5.98
CaO	9.23	7.66
Total	98.84	98.97
Si IV	6.000	6.000
Al IV	0.000	0.000
T site	6.000	6.000
Al VI	3.930	3.550
Ti VI	0.002	0.006
Cr3+	0.002	0.005
Fe3+	0.066	0.440
O site	4.000	4.000
Fe2+	3.144	3.022
Mn2+	0.103	0.102
Mg2+	1.170	1.394
Ca2+	1.555	1.283
A site	5.970	5.800
O	23.973	23.804
Almand	52.03	48.34
Pyrop	19.36	22.30
Gross	25.74	20.53
Ti And	0.04	0.09
Fe And	1.08	7.03
Spress	1.70	1.63
Uvaro	0.04	0.08
XMg	0.27	0.30

	Mag1 n=2	Mag2 n=3
SiO_2	0.39	0.16
TiO_2	2.13	1.73
Al_2O_3	1.52	1.04
Cr_2O_3	0.35	0.21
Fe_2O_3	62.63	63.96
FeO	33.98	33.07
MnO	0.09	-
MgO	-	-
CaO	0.08	0.02
Total	101.18	100.19
Si4+	0.015	0.006
Ti4+	0.060	0.050
Al3+	0.067	0.047
Cr3+	0.010	0.006
Fe3+	1.772	1.836
Fe2+	1.069	1.055
Mn2+	0.003	-
Mg2+	-	-
Ca2+	0.003	0.001
Total	3.000	3.000
O	4.000	4.000

	Ilm1 n=1	Ilm2 n=3
SiO_2	0.18	0.09
TiO_2	51.72	50.39
FeO	46.10	48.38
MnO	0.13	0.24
MgO	0.00	0.01
Total	98.13	99.12
Ti4+	1.003	0.965
Fe2+	0.994	1.030
Mn2+	0.003	0.005
Mg2+	0.000	0.000
Total	2.000	2.000
O	0.997	1.035
Charge	6.010	5.930

Appendix E5 (continued)

Contact between minerals

Ol1 - Opx1
Opx1 - Cpx1
Cpx1 - Amp2
Amp2 - Grt1
Grt1 - Pl5,6,7,14
Ol2 - Opx2
Opx2 - Cpx2
Cpx2 - Amp1
Amp1 - Grt3
Grt4 - Pl1,2,3,4
Ol3 - Opx3
Opx3 - Cpx5
Cpx5 - Amp3
Grt7 - Amp3
Grt9 - Pl11
Opx4 - Grt2
Grt11 - Pl12
Opx5 - Grt6
Grt6 - Pl10
Opx6 - Cpx3
Cpx3 - Pl13
Ilm1 - Grt5
Grt5 - Pl8
Mag2 - Ilm1
Mag1 - Ilm2

Appendix E6. Representative analyses of the principal minerals from sample CMA-LG6-87

	Cpx1c n=1	Cpx1m n=1	Cpx2c n=1	Cpx2m n=1	Opx1 n=2
SiO_2	49.04	48.97	48.50	49.30	47.43
TiO_2	1.04	0.83	0.80	0.97	0.01
Al_2O_3	3.16	2.91	2.52	2.55	0.31
Cr_2O_3	0.15	0.07	0.07	0.18	0.05
Fe_2O_3	3.96	1.83	2.49	2.70	3.00
FeO	11.33	13.61	13.98	13.43	38.24
MnO	0.36	0.38	0.42	0.41	1.00
MgO	14.60	13.58	13.25	13.94	9.54
CaO	16.23	15.94	16.03	16.18	0.27
Na_2O	0.17	0.10	-	-	-
K_2O	0.09	0.07	0.05	0.13	0.04
Total	100.13	98.29	98.11	99.79	99.89
Si IV	1.850	1.888	1.883	1.877	1.946
Al IV	0.141	0.112	0.115	0.114	0.015
T site	1.990	2.000	2.000	1.990	1.960
Al VI	-	0.020	-	-	-
Ti4+	0.030	0.024	0.023	0.028	-
Cr3+	0.004	0.002	0.002	0.005	0.002
Fe3+	0.112	0.053	0.073	0.077	0.093
Fe2+	0.357	0.439	0.454	0.428	1.312
Mn2+	0.012	0.012	0.014	0.013	0.035
Mg2+	0.821	0.780	0.767	0.791	0.584
Ca2+	0.656	0.658	0.667	0.660	0.012
Na+	0.012	0.007	-	-	-
K+	0.004	0.003	0.002	0.006	0.002
M1,M2	2.010	2.000	2.000	2.010	2.040
O	6.000	6.000	6.000	6.000	6.000
En	44.76	41.56	40.63	42.11	30.59
Wo	35.76	35.06	35.33	35.13	0.62
Fs	19.48	23.37	24.05	22.76	68.78
XMg	0.66	0.62	0.60	0.62	0.30

	Pl1c n=1	Pl2m n=2	Pl3c n=1	Pl4c n=2	Pl4m n=1
SiO_2	53.03	55.15	57.23	51.58	55.34
Al_2O_3	28.37	27.58	26.17	29.95	28.68
CaO	11.92	10.10	8.49	13.52	11.37
Na_2O	5.58	7.57	9.13	4.91	6.90
K_2O	0.20	0.22	0.27	0.17	0.15
FeO	0.14	0.41	0.26	0.47	0.37
Total	99.24	101.02	101.55	100.60	102.81
Si4+	9.717	9.932	10.228	9.386	9.802
Al3+	6.127	5.853	5.512	6.424	5.987
Z site	15.844	15.785	15.740	15.810	15.790
Ca2+	2.340	1.951	1.626	2.635	2.158
Na2+	1.982	2.640	3.163	1.730	2.370
K+	0.047	0.049	0.062	0.041	0.034
Fe2+	0.021	0.061	0.039	0.071	0.055
X site	4.391	4.701	4.889	4.477	4.616
Total	20.234	20.486	20.629	20.287	20.406
O	32.000	32.000	32.000	32.000	32.000
An	53.56	42.15	33.51	59.80	47.31
Ab	45.37	56.78	65.22	39.27	51.95
Or	1.07	1.06	1.27	0.92	0.74

Appendix E6 (continued)

	Amp1 n=2
SiO_2	37.99
TiO_2	0.05
Al_2O_3	16.52
Cr_2O_3	0.04
Fe_2O_3	-
FeO*	23.94
MnO	0.25
MgO	4.07
CaO	10.48
Na_2O	2.53
K_2O	1.42
H_2O	1.94
Total	99.22
Si IV	5.941
Al IV	2.059
T site	8.000
Al VI	0.986
Fe3+	0.271
Ti4+	0.005
Cr3+	0.006
Mg2+	0.949
Fe2+	2.783
M1,M2,M3	5.000
Fe2+	0.074
Mn2+	0.033
Ca2+	1.758
Na+	0.135
M4	2.000
Na+	0.631
K+	0.071
A site	0.700
O	22.000
OH	2.000
XMg	0.26
XNa	0.30
Name	Prg

	Mag1 n=1
SiO_2	0.38
TiO_2	0.94
Al_2O_3	0.46
Cr_2O_3	0.26
Fe_2O_3	66.62
FeO	32.94
CaO	0.06
Total	101.66
Si4+	0.014
Ti4+	0.027
Al3+	0.020
Cr3+	0.008
Fe3+	1.890
Fe2+	1.039
Ca2+	0.002
Total	3.000
O	4.000

Contact between minerals

Ilm1 - Opx1
Opx1 - Amp1
Amp1 - Pl2
Mag5 - Pl4

Appendix E7. Representative analyses of the principal minerals from sample CMA-LG7-87

	Cpx1c n=2	Cpx1m n=1	Opx1 n=2	Opx2 n=2
SiO_2	48.90	50.58	49.62	48.81
TiO_2	0.66	0.50	0.04	0.02
Al_2O_3	2.44	1.37	0.22	0.28
Cr_2O_3	0.05	-	0.00	0.00
Fe_2O_3	1.95	1.97	2.89	2.21
FeO	16.09	23.27	32.41	35.86
MnO	0.44	0.47	0.38	0.71
MgO	12.72	15.57	14.34	12.06
CaO	15.35	7.34	0.80	0.25
Na_2O	0.03	-	-	-
K_2O	0.03	0.01	0.00	0.00
Total	98.64	101.08	100.68	100.20
Al IV	0.103	0.062	0.010	0.013
T site	2.000	1.990	1.960	1.970
Al VI	0.009	-	-	-
Ti4+	0.019	0.014	0.001	0.001
Cr3+	0.002	-	-	-
Fe3+	0.057	0.057	0.085	0.067
Fe2+	0.522	0.741	1.066	1.204
Mn2+	0.014	0.015	0.012	0.024
Mg2+	0.736	0.884	0.840	0.722
Ca2+	0.638	0.300	0.033	0.011
Na+	0.002	-	-	-
K+	0.001	0.000	0.000	0.000
M1,M2	2.000	2.010	2.040	2.030
O	6.000	6.000	6.000	6.000
En	38.80	45.93	43.32	37.28
Wo	33.67	15.56	1.73	0.54
Fs	27.53	38.50	54.95	62.18
XMg	0.57	0.53	0.43	0.36

	Bt1 n=2	Bt2 n=1	Bt3 n=2
SiO_2	35.04	34.77	35.51
TiO_2	4.32	3.92	4.36
Al_2O_3	14.05	15.17	14.58
Cr_2O_3	2.00	3.00	0.03
Fe_2O_3	3.95	3.94	3.65
FeO	21.83	21.77	20.19
MnO	-	-	0.01
MgO	7.97	7.61	9.37
CaO	-	-	0.01
K_2O	9.20	9.16	9.02
H_2O	3.86	3.86	3.90
Total	100.21	100.20	100.64
Al IV	2.564	2.617	2.580
Fe IV	0.002	0.000	0.000
T site	8.000	8.000	8.000
Al VI	0.003	0.151	0.043
Ti VI	0.504	0.456	0.501
Cr3+	-	-	0.003
Fe3+	0.459	0.459	0.420
Fe2+	2.831	2.819	2.577
Mn2+	-	-	0.002
Mg2+	1.842	1.756	2.132
O site	5.640	5.640	5.680
Ca2+	-	-	0.001
K+	1.821	1.809	1.756
A site	1.820	1.810	1.760
O	20.000	20.000	20.000
OH	4.000	4.000	4.000
XMg	0.38	0.37	0.43

	Pl1c n=1	Pl1m n=1	Pl2c n=1
SiO_2	54.38	53.94	54.83
Al_2O_3	27.98	26.84	28.18
CaO	11.43	10.74	11.09
Na_2O	6.98	6.85	6.44
K_2O	0.19	0.13	0.20
FeO	0.49	0.73	0.23
Total	101.45	99.23	100.97
Si4+	9.789	9.910	9.861
Al3+	5.936	5.812	5.973
Z site	15.725	15.722	15.835
Ca2+	2.204	2.114	2.137
Na+	2.436	2.440	2.246
Fe2+	0.074	0.112	0.035
X site	4.758	4.697	4.463
Total	20.483	20.419	20.298
O	32.000	32.000	32.000
An	47.06	46.11	48.25
Ab	52.01	53.22	50.71
Or	0.93	0.66	1.04

Appendix E7 (continued)

	Pl2m n=1	Pl3 n=1	Pl4m n=1
SiO_2	54.93	57.97	66.86
Al_2O_3	28.37	26.66	20.85
CaO	10.91	8.82	2.00
Na_2O	6.23	8.63	12.59
K_2O	0.10	0.24	0.12
FeO	0.04	0.21	0.10
Total	100.58	102.53	102.52
Si4+	9.884	10.237	11.559
Al3+	6.016	5.548	4.248
Z site	15.900	15.785	15.808
Ca2+	2.103	1.669	0.370
Na+	2.173	2.955	4.220
Fe2+	0.006	0.031	0.014
X site	4.306	4.708	4.632
Total	20.206	20.494	20.440
O	32.000	32.000	32.000
An	48.92	35.68	8.02
Ab	50.55	63.17	91.40
Or	0.53	1.16	0.57

	Amp1 n=1	Amp2 n=2	Amp3 n=1	Amp4 n=1	Amp5 n=1	Amp6 n=1
SiO_2	38.85	38.73	40.75	38.42	41.07	40.48
TiO_2	0.09	0.08	1.09	0.57	0.25	1.12
Al_2O_3	16.87	17.51	12.34	15.65	12.15	13.90
Cr_2O_3	0.02	0.06	0.04	0.08	-	0.07
Fe_2O_3	-	-	-	-	-	-
FeO*	20.43	21.97	23.21	22.86	22.11	22.51
MnO	0.04	0.20	0.09	-	0.02	0.11
MgO	7.49	5.38	6.16	4.97	7.74	6.26
CaO	11.09	10.63	11.46	11.36	10.47	10.72
Na_2O	2.82	2.39	2.37	1.97	1.90	2.84
K_2O	1.38	1.38	1.35	1.62	1.12	0.17
H_2O	1.97	1.95	1.94	1.92	1.93	1.95
Total	101.05	100.29	100.80	99.42	98.76	100.13
Si IV	5.850	5.906	6.268	5.957	6.294	6.174
Al IV	2.150	2.094	1.732	2.043	1.706	1.826
T site	8.000	8.000	8.000	8.000	8.000	8.000
Al VI	0.832	1.055	0.505	0.828	0.492	0.665
Fe3+	0.427	0.326	0.131	0.343	0.656	0.319
Ti4+	0.010	0.009	0.126	0.068	0.029	0.128
Cr3+	0.003	0.007	0.005	0.010	-	0.008
Mg2+	1.682	1.218	1.414	1.147	1.769	1.420
Fe2+	2.046	2.385	2.819	2.604	2.054	2.460
M1,M2,M3	5.000	5.000	5.000	5.000	5.000	5.000
Fe2+	0.097	0.087	0.038	0.015	0.130	0.086
Mn2+	0.005	0.026	0.012	-	0.003	0.014
Ca2+	1.790	1.740	1.886	1.892	1.723	1.750
Na+	0.108	0.147	0.064	0.093	0.144	0.150
M4	2.000	2.000	2.000	2.000	2.000	2.000
Na+	0.706	0.559	0.642	0.499	0.422	0.690
K+	0.264	0.268	0.264	0.320	0.220	0.033
A site	0.970	0.830	0.910	0.820	0.640	0.720
O	22.032	22.035	22.037	22.037	22.035	22.035
OH	1.968	1.965	1.963	1.963	1.965	1.965
XMg	0.43	0.34	0.36	0.31	0.42	0.37
XNa	0.32	0.29	0.29	0.25	0.25	0.33
Name	Prg	Prg	Prg	Prg	Prg	Prg

Appendix E7 (continued)

	Grt1 n=1	Grt2 n=4	Grt3 n=1	Grt4 n=3
SiO_2	37.45	37.34	37.07	37.90
TiO_2	0.06	0.05	0.21	0.10
Al_2O_3	21.06	20.46	20.72	20.95
Cr_2O_3	0.06	0.01	0.05	-
Fe_2O_3	0.76	1.03	0.54	0.76
FeO	32.80	32.84	32.27	32.88
MnO	1.72	1.43	1.48	1.31
MgO	2.30	1.20	1.00	1.89
CaO	5.08	6.28	7.02	5.98
Total	101.30	100.66	100.36	101.77
Si IV	5.950	5.995	5.970	5.993
Al IV	0.050	0.005	0.030	0.007
T site	6.000	6.000	6.000	6.000
Al VI	3.894	3.867	3.903	3.897
Ti VI	0.007	0.006	0.025	0.012
Cr3+	0.008	0.002	0.006	-
Fe3+	0.091	0.125	0.065	0.091
O site	4.000	4.000	4.000	4.000
Fe2+	4.359	4.409	4.347	4.348
Mn2+	0.231	0.195	0.202	0.175
Mg2+	0.545	0.287	0.240	0.445
Ca2+	0.865	1.081	1.211	1.014
A site	6.000	5.970	6.000	5.980
O	23.979	23.974	23.998	23.985
Almand	71.39	72.21	71.29	71.45
Pyrop	8.92	4.70	3.94	7.31
Gross	14.16	17.71	19.87	16.66
Ti And	0.12	0.10	0.42	0.20
Fe And	1.49	2.04	1.07	1.50
Spess	3.79	3.20	3.31	2.88
Uvaro	0.12	0.03	0.10	-
XMg	0.11	0.06	0.05	0.09

	Ilm1 n=1	Ilm2c n=1	Ilm2m n=1	Ilm3m n=1
SiO_2	0.11	0.32	0.51	0.10
TiO_2	49.73	49.48	44.89	49.03
Al_2O_3	-	-	0.04	-
Cr_2O_3	-	0.10	0.11	0.06
FeO	48.68	49.02	51.73	48.02
MnO	0.65	0.31	0.35	0.26
CaO	0.00	0.06	0.05	0.00
Total	99.17	99.29	97.68	97.47
Si4+	0.003	0.008	0.013	0.003
Ti4+	0.950	0.943	0.865	0.953
Al3+	-	-	0.001	-
Cr3+	0.002	0.002	0.001	-
Fe2+	0.938	0.943	0.869	0.950
Mn2+	0.014	0.007	0.008	0.006
Ca2+	0.000	0.002	0.001	0.000
Total	2.000	2.000	2.000	2.000
O	3.000	3.000	3.000	3.000

Appendix E7 (continued)

Contact between minerals

Ilm1 - Opx1
Opx1 - Amp1
Amp1 - Grt1
Grt1 - Pl1
Ilm2 - Opx2
Opx2 - Amp2
Ilm4 - Amp3,4
Amp3,4 - Grt2
Grt3 - Bt1
Bt2 - Pl3
Ilm3 - Amp6
Amp6 - Cpx1
Ilm5 - Amp5
Amp5 - Grt4
Grt4 - Bt3

Appendix E8. Representative analyses of the principal minerals from sample CMA-M-015A-86

	Cpx1 n=2	Cpx2c n=1	Cpx2m n=1	Cpx3 n=1	Cpx4 n=1	Opx1 n=3	Opx2 n=1	Opx3 n=1
SiO_2	54.26	49.91	49.69	52.28	51.03	53.21	51.95	52.42
TiO_2	0.05	1.28	3.01	0.19	0.24	0.01	-	-
Al_2O_3	1.92	3.64	2.10	1.96	1.78	0.48	0.32	0.31
Cr_2O_3	0.16	0.37	0.12	0.14	0.19	0.01	0.02	-
Fe_2O_3	2.39	4.57	2.8	4.35	3.15	5.5	3.52	4.18
FeO	3.98	3.80	13.16	3.52	6.75	12.52	21.74	18.61
MnO	0.04	-	0.06	0.03	0.03	0.26	0.12	0.16
MgO	14.36	12.71	15.80	13.60	12.76	28.37	22.33	24.51
CaO	22.10	20.80	13.47	22.40	21.81	0.22	0.33	0.17
Na_2O	1.47	1.58	0.75	1.21	0.76	-	-	-
K_2O	0.06	0.13	0.00	0.19	0.08	0.00	0.00	0.00
Total	100.80	98.80	100.96	99.88	98.58	100.57	100.34	100.36
Si IV	1.976	1.874	1.855	1.937	1.936	1.915	1.943	1.935
Al IV	0.024	0.126	0.092	0.063	0.064	0.020	0.014	0.013
T site	2.000	2.000	1.950	2.000	2.000	1.940	1.960	1.950
Al VI	0.058	0.035	-	0.023	0.015	-	-	-
Ti4+	0.001	0.036	0.085	0.005	0.007	0.000	-	-
Cr3+	0.004	0.011	0.004	0.004	0.006	0.000	0.001	-
Fe3+	0.066	0.129	0.079	0.121	0.090	0.149	0.099	0.116
Fe2+	0.121	0.119	0.411	0.109	0.214	0.377	0.680	0.575
Mn2+	0.001	-	0.002	0.001	0.001	0.008	0.004	0.005
Mg2+	0.780	0.711	0.879	0.751	0.721	1.522	1.245	1.349
Ca2+	0.862	0.837	0.539	0.889	0.886	0.008	0.013	0.007
Na+	0.103	0.115	0.054	0.087	0.056	-	-	-
K+	0.003	0.006	0.000	0.009	0.004	0.000	0.000	0.000
M1,M2	2.000	2.000	2.050	2.000	2.000	2.060	2.040	2.050
O	6.000	6.000	6.000	6.000	6.000	6.000	6.000	6.000
En	44.22	42.66	48.07	42.94	39.60	79.80	64.24	69.88
Wo	48.90	50.18	29.46	50.82	48.65	0.45	0.68	0.35
Fs	6.88	7.16	22.47	6.24	11.75	19.75	35.08	29.77
XMg	0.83	0.79	0.66	0.81	0.74	0.77	0.63	0.68

	Amp1 n=2
SiO_2	41.46
TiO_2	0.38
Al_2O_3	14.24
Cr_2O_3	0.06
Fe_2O_3	-
FeO*	9.25
MnO	0.03
MgO	15.73
CaO	11.96
Na_2O	2.66
K_2O	0.74
H_2O	2.05
Total	98.56
Si IV	6.030
Al IV	1.970
T site	8.000
Al VI	0.477
Fe3+	0.664
Ti4+	0.042
Cr3+	0.007
Mg2+	3.408
Fe2+	0.402
M1,M2,M3	5.000
Fe2+	0.059
Mn2+	0.002
Ca2+	1.861
Na+	0.078
M4	2.000
Na+	0.672
K+	0.137
A site	0.810
O	22.000
OH	2.000
XMg	0.78
XNa	0.29
Name	Prg

Appendix E8 (continued)

	Grt1c n=2	Grt1m n=2	Grt2 n=1	Grt3 n=1
SiO_2	35.56	38.34	38.36	39.05
TiO_2	0.07	0.03	0.10	0.05
Al_2O_3	24.60	21.84	21.85	18.45
Cr_2O_3	0.03	0.04	-	0.05
Fe_2O_3	0.39	0.94	1.11	5.6
FeO	21.79	17.89	21.06	20.06
MnO	1.00	0.41	0.61	0.62
MgO	7.84	5.80	5.23	5.66
CaO	7.66	13.82	12.22	9.50
Total	98.93	99.12	100.54	99.04
Si IV	5.478	5.912	5.899	6.000
Al IV	0.522	0.088	0.101	0.000
T site	6.000	6.000	6.000	6.000
Al VI	3.944	3.883	3.859	3.341
Ti VI	0.008	0.003	0.012	0.006
Cr3+	0.003	0.005	-	0.006
Fe3+	0.045	0.109	0.129	0.647
O site	4.000	4.000	4.000	4.000
Fe2+	2.807	2.308	2.708	2.578
Mn2+	0.130	0.054	0.079	0.081
Mg2+	1.799	1.333	1.199	1.296
Ca2+	1.265	2.284	2.013	1.564
A site	6.000	5.980	6.000	5.520
O	23.743	23.937	23.955	23.522
Almand	46.34	37.86	44.10	41.73
Pyrop	29.70	21.87	19.53	20.98
Gross	20.90	37.47	32.79	25.31
Ti And	0.13	0.05	0.19	0.09
Fe And	0.74	1.79	2.10	10.47
Spess	2.14	0.89	1.29	1.31
Uvaro	0.05	0.08	-	0.10
XMg	0.38	0.35	0.30	0.30

	Mag1 n=3
SiO_2	0.30
TiO_2	0.69
Al_2O_3	0.82
Cr_2O_3	0.17
Fe_2O_3	67.67
FeO	32.66
MnO	0.02
MgO	0.18
CaO	0.04
Total	102.53
Si4+	0.011
Ti4+	0.019
Al3+	0.036
Cr3+	0.005
Fe3+	1.899
Fe2+	1.018
Mn2+	0.001
Mg2+	0.010
Ca2+	0.001
Total	3.000
O	4.000

	Ilm1 n=2
SiO_2	0.04
TiO_2	50.83
Al_2O_3	-
Cr_2O_3	-
FeO	45.44
MnO	0.74
MgO	1.32
CaO	0.00
Total	98.37
Si4+	0.001
Ti4+	0.970
Al3+	-
Cr3+	-
Fe2+	0.905
Mn2+	0.016
Mg2+	0.050
Ca2+	0.000
Total	2.000
O	3.000

Contact between minerals

Opx1 - Amp1
Amp1 - Ilm1
Ilm1 - Mag1
Mag1 - Grt1
Opx2 - Cpx3
Opx3 - Grt2
Cpx4 - Grt3

Appendix E9. Representative analyses of the principal minerals from sample CMA-M-R01A-87

	Cpx1c n=1	Cpx1m n=1	Cpx2m n=1	Cpx3 n=1	Cpx4c n=1	Cpx4m n=1
SiO_2	50.10	49.62	48.61	49.51	51.26	50.37
TiO_2	1.03	0.87	0.73	0.12	0.96	0.68
Al_2O_3	2.32	0.88	3.76	1.04	1.94	1.41
Cr_2O_3	0.11	0.01	0.05	0.07	0.07	-
Fe_2O_3	1.46	-	4.69	-	0.95	0.89
FeO	12.39	23.44	14.53	30.04	12.77	14.87
MnO	0.29	0.59	0.25	0.53	0.28	0.37
MgO	13.48	8.57	7.72	8.62	13.83	13.43
CaO	18.64	15.29	17.90	9.50	18.97	16.83
Na_2O	-	0.22	1.51	-	-	-
K_2O	0.08	0.04	0.10	0.13	0.05	0.03
Total	99.90	99.53	99.85	99.56	101.08	98.88
Si IV	1.898	1.964	1.883	1.987	1.917	1.936
Al IV	0.102	0.036	0.117	0.013	0.083	0.064
T site	2.000	2.000	2.000	2.000	2.000	2.000
Al VI	0.002	0.005	0.055	0.037	0.003	0.000
Ti4+	0.029	0.026	0.021	0.004	0.027	0.020
Cr3+	0.003	0.000	0.002	0.002	0.002	-
Fe3+	0.042	-	0.137	-	0.027	0.026
Fe2+	0.392	0.776	0.471	1.008	0.399	0.478
Mn2+	0.009	0.020	0.008	0.018	0.009	0.012
Mg2+	0.761	0.506	0.446	0.516	0.771	0.770
Ca2+	0.757	0.648	0.743	0.409	0.760	0.693
Na+	-	0.017	0.113	-	-	-
K+	0.004	0.002	0.005	0.007	0.002	0.001
M1,M2	2.000	2.000	2.000	2.000	2.000	2.000
	6.000	6.001	6.000	6.013	6.000	6.000
En	39.85	26.20	26.87	26.69	39.94	39.65
Wo	39.61	33.60	44.77	21.14	39.38	35.71
Fs	20.54	40.20	28.36	52.17	20.68	24.64
XMg	0.64	0.39	0.45	0.33	0.65	0.60

	Bt1 n=1	Bt2 n=1	Bt3 n=1	Bt4 n=1	Bt5 n=1
SiO_2	35.27	34.83	35.03	34.46	35.44
TiO_2	4.65	4.63	4.84	4.94	3.86
Al_2O_3	13.30	13.54	13.70	12.66	12.85
Cr_2O_3	0.04	0.03	-	-	-
Fe_2O_3	4.44	4.41	4.28	4.41	4.28
FeO	24.56	24.36	23.68	24.36	23.68
MnO	0.08	-	-	0.10	0.02
MgO	5.70	5.70	5.83	5.30	6.64
CaO	-	0.10	0.07	0.06	0.17
K_2O	8.80	9.22	9.60	9.03	9.07
H_2O	3.81	3.80	3.81	3.79	3.82
Total	100.57	100.70	100.84	99.11	99.83
Si IV	5.513	5.454	5.462	5.498	5.572
Al IV	2.450	2.499	2.518	2.381	2.381
Fe IV	0.037	0.047	0.020	0.121	0.046
T site	8.000	8.000	8.000	8.000	8.000
Ti VI	0.547	0.545	0.568	0.593	0.456
Cr3+	0.005	0.004	-	-	-
Fe3+	0.485	0.472	0.482	0.408	0.460
Fe2+	3.210	3.190	3.088	3.250	3.114
Mn2+	-	0.011	-	0.014	0.003
Mg2+	1.328	1.331	1.355	1.261	1.556
O site	5.570	5.550	5.490	5.530	5.590
Ca2+	-	0.017	0.012	0.010	0.029
K+	1.755	1.842	1.910	1.838	1.819
A site	1.750	1.860	1.920	1.850	1.850
O	20.000	20.000	20.000	20.000	20.000
OH	4.000	4.000	4.000	4.000	4.000
XMg	0.28	0.28	0.29	0.26	0.32

Appendix E9 (continued)

	Pl1 n=2	Pl2 n=1
SiO_2	58.40	57.96
Al_2O_3	26.00	25.50
CaO	8.78	8.01
Na_2O	7.89	8.53
K_2O	0.25	0.16
FeO	0.34	0.27
Total	101.67	100.43
Si4+	10.366	10.409
Al3+	5.440	5.397
Z site	15.806	15.807
Ca2+	1.670	1.541
Na+	2.717	2.970
K+	0.057	0.037
Fe2+	0.051	0.041
X site	4.495	4.589
Total	20.301	20.395
O	32.000	32.000
An	37.57	33.89
Ab	61.15	65.31
Or	1.27	0.81

	Amp1 n=1	Amp2 n=1	Amp3 n=3	Amp4 n=2	Amp5 n=1	Amp6 n=1	Amp7 n=1	Amp8 n=1
SiO_2	43.63	47.58	40.86	41.45	40.14	43.61	40.04	39.35
TiO_2	0.33	0.59	1.43	1.49	0.73	1.46	1.51	0.48
Al_2O_3	9.77	9.22	11.20	10.34	11.25	10.09	12.19	12.92
Cr_2O_3	-	0.12	0.06	0.03	0.02	0.08	-	-
Fe_2O_3	-	-	-	-	-	-	-	-
FeO*	24.20	24.51	25.25	24.94	25.65	23.91	25.05	25.84
MnO	0.16	0.21	0.07	0.11	0.11	0.12	0.08	0.15
MgO	6.70	5.08	5.25	5.36	4.97	4.96	4.63	4.49
CaO	10.48	8.97	10.75	10.64	10.92	10.51	10.62	10.58
Na_2O	2.39	1.90	2.67	2.61	2.23	2.22	2.53	2.87
K_2O	1.03	1.02	1.20	1.06	1.53	1.21	1.51	1.49
H_2O	1.99	2.03	1.97	1.96	1.93	1.98	1.95	1.94
Total	100.68	101.23	100.70	99.97	99.48	100.15	100.11	100.11
Si IV	6.666	7.135	6.343	6.470	6.333	6.731	6.255	6.177
Al IV	1.334	0.865	1.657	1.530	1.667	1.269	1.745	1.823
T site	8.000	8.000	8.000	8.000	8.000	8.000	8.000	8.000
Al VI	0.423	0.762	0.395	0.364	0.419	0.566	0.509	0.572
Fe3+	3.000	0.292	0.176	0.183	0.141	0.222	0.155	0.234
Ti4+	0.038	0.067	0.168	0.174	0.087	0.172	0.178	0.057
Cr3+	-	0.014	0.007	0.004	0.003	0.010	-	-
Mg2+	1.524	1.135	1.212	1.247	1.166	1.140	1.080	1.047
Fe2+	2.723	2.846	3.035	3.070	3.103	3.087	3.078	3.090
M1,M2,M3	5.000	5.000	5.000	5.000	5.000	4.970	5.000	5.000
Fe2+	0.077	0.046	0.052	0.043	0.064	-	0.049	0.069
Mn2+	0.021	0.027	0.009	0.015	0.015	0.016	0.011	0.020
Ca2+	1.717	1.441	1.791	1.781	1.849	1.734	1.775	1.782
Na+	0.185	0.486	0.148	0.161	0.072	0.250	0.165	0.129
M4	2.000	2.000	2.000	2.000	2.000	2.000	2.000	2.000
Na+	0.523	0.068	0.656	0.629	0.610	0.414	0.601	0.745
K+	0.200	0.195	0.236	0.212	0.308	0.238	0.300	0.298
A site	0.720	0.260	0.890	0.840	0.920	0.650	0.900	1.040
O	22.000	22.000	22.000	22.000	22.000	22.000	22.000	22.000
OH	2.000	2.000	2.000	2.000	2.000	2.000	2.000	2.000
XMg	0.37	0.30	0.30	0.31	0.29	0.30	0.28	0.27
XNa	0.29	0.28	0.31	0.31	0.27	0.28	0.30	0.33
Name	Ed Hbl	Hbl	Ed Hbl	Ed Hbl	Prg Hbl	Ed Hbl	Prg Hbl	Prg

Appendix E9 (continued)

	Grt1m n=1	Grt1c n=1	Grt2 n=1
SiO_2	37.02	37.61	37.34
TiO_2	0.19	0.15	0.02
Al_2O_3	19.68	20.12	20.26
Cr_2O_3	0.11	0.07	-
Fe_2O_3	2.67	1.76	1.33
FeO	31.60	32.89	31.95
MnO	2.70	2.04	2.53
MgO	0.93	0.69	0.54
CaO	6.88	6.93	5.92
Total	101.78	102.27	99.89
Si IV	5.928	5.987	6.000
Al IV	0.072	0.013	0.000
T site	6.000	6.000	6.000
Al VI	3.642	3.762	3.837
Ti VI	0.023	0.018	0.002
Cr3+	0.014	0.009	-
Fe3+	0.321	0.211	0.161
O site	4.000	4.000	4.000
Fe2+	4.231	4.379	4.294
Mn2+	0.366	0.275	0.344
Mg2+	0.222	0.164	0.129
Ca2+	1.180	1.182	1.019
A site	6.000	6.000	5.790
O	23.975	24.003	23.788
Almand	66.55	70.20	72.17
Pyrop	3.49	2.63	2.17
Gross	18.56	18.95	17.13
Ti And	0.36	0.29	0.04
Fe And	5.06	3.38	2.70
Spess	5.76	4.41	5.79
Uvaro	0.22	0.14	-
XMg	0.04	0.03	0.03

	Mag1 n=3
SiO_2	0.34
TiO_2	3.49
Al_2O_3	0.09
Cr_2O_3	0.28
Fe_2O_3	61.74
FeO	34.97
MnO	0.01
CaO	0.06
Total	100.99
Si4+	0.013
Al3+	0.100
Ti4+	0.004
Cr3+	0.008
Fe3+	1.762
Fe2+	1.110
Mn2+	0.000
Ca2+	0.002
Total	3.000
O	4.000

	Ilm1 n=3	Ilm2 n=3	Ilm3 n=1	Ilm4 n=1	Ilm5 n=2
SiO_2	0.09	0.16	0.25	0.10	0.10
TiO_2	48.90	49.06	49.37	48.73	49.13
Al_2O_3	-	-	-	-	-
Cr_2O_3	0.04	0.16	0.09	0.10	0.07
FeO	47.93	48.37	48.97	46.54	47.97
MnO	0.63	0.67	0.63	0.72	0.75
MgO	-	-	-	-	-
CaO	0.03	0.06	0.00	0.13	0.01
Total	97.63	98.48	99.31	96.32	98.04
Si4+	0.002	0.004	0.006	0.003	0.003
Ti4+	0.948	0.943	0.941	0.958	0.949
Al3+	-	-	-	-	-
Cr3+	0.001	0.003	0.002	0.002	0.001
Fe2+	0.936	0.931	0.934	0.941	0.935
Mn2+	0.014	0.015	0.014	0.016	0.016
Mg2+	-	-	-	-	-
Ca2+	0.001	0.002	0.000	0.004	0.000
Total	2.000	2.000	2.000	2.000	2.000
O	3.000	3.000	3.000	3.000	3.000

Contact between minerals

Cpx1 - Amp8
Ilm1 - Amp3
Amp3 - Cpx2
Ilm2 - Cpx3
Cpx3 - Amp4
Ilm3 - Amp7
Ilm5 - Mag1
Ilm4 - Bt3
Amp5 - Grt1
Bt4 - Grt2

Appendix E10. Representative analyses of the principal minerals from sample CMA-M-V01-86

	Cpx1 n=1	Cpx2 n=1	Cpx3 n=1	Cpx4 n=1
SiO_2	52.59	52.68	51.63	51.14
TiO_2	0.23	0.39	0.46	0.30
Al_2O_3	2.32	1.72	2.83	1.85
Cr_2O_3	0.12	0.24	0.17	0.13
Fe_2O_3	0.05	1.10	-	2.16
FeO	7.31	8.09	8.11	5.81
MnO	0.02	0.10	-	0.08
MgO	14.40	15.19	14.41	13.88
CaO	23.13	21.42	20.85	22.71
Na_2O	0.04	0.07	0.06	0.30
K_2O	0.09	0.10	0.28	0.10
Total	100.29	101.10	98.80	98.46
Si IV	1.944	1.938	1.939	1.931
Al IV	0.056	0.062	0.061	0.069
T site	2.000	2.000	2.000	2.000
Al VI	0.045	0.013	0.064	0.013
Ti4+	0.006	0.011	0.013	0.009
Cr3+	0.004	0.007	0.005	0.004
Fe3+	0.001	0.030	-	0.061
Fe2+	0.226	0.249	0.255	0.183
Mn2+	0.001	0.003	-	0.003
Mg2+	0.794	0.833	0.807	0.781
Ca2+	0.916	0.844	0.839	0.919
Na+	0.003	0.005	0.004	0.022
K+	0.004	0.005	0.013	0.005
M1,M2	2.000	2.000	2.000	2.000
O	6.000	6.000	6.008	6.000
En	41.00	43.25	42.45	41.48
Wo	47.33	43.83	44.15	48.78
Fs	11.67	12.92	13.40	9.74
XMg	0.78	0.76	0.76	0.78

	Bt1 n=1
SiO_2	36.89
TiO_2	4.99
Al_2O_3	14.19
Cr_2O_3	0.07
Fe_2O_3	2.36
FeO	13.05
MnO	0.03
MgO	14.74
CaO	-
Na_2O	-
K_2O	9.47
H_2O	4.04
Total	99.83
Si IV	5.481
Al IV	2.485
Fe IV	0.034
T site	8.000
Al VI	-
Ti VI	0.558
Cr3+	0.008
Fe3+	0.230
Fe2+	1.622
Mn2+	0.004
Mg2+	3.265
O site	5.690
Ca2+	-
Na+	-
K+	1.795
A site	1.795
O	20.000
OH	4.000
XMg	0.65

	Pl1 n=4
SiO_2	62.78
Al_2O_3	23.15
CaO	4.78
Na_2O	10.35
K_2O	0.33
FeO	0.05
Total	101.43
Si4+	11.044
Al3+	4.800
Z site	15.844
Ca2+	0.902
Na+	3.529
K+	0.075
Fe2+	0.008
X site	4.513
Total	20.357
O	32.000
An	20.00
Ab	78.34
Or	1.66

	Amp1 n=1	Amp2 n=1
SiO_2	45.44	44.47
TiO_2	1.32	1.81
Al_2O_3	10.93	11.23
Cr_2O_3	0.10	0.08
Fe_2O_3	-	-
FeO*	12.36	12.20
MnO	-	-
MgO	14.04	13.57
CaO	12.14	11.97
Na_2O	1.26	1.28
K_2O	0.97	1.14
H_2O	2.09	2.06
Total	100.65	99.81
Si IV	6.545	6.487
Al IV	1.455	1.513
T site	8.000	8.000
Al VI	0.398	0.416
Fe3+	0.369	0.261
Ti4+	0.143	0.199
Cr3+	0.012	0.009
Mg2+	3.014	2.954
Fe2+	1.064	1.161
M1,M2,M3	5.000	5.000
Fe2+	0.053	0.066
Mn2+	-	-
Ca2+	1.870	1.867
Na+	0.077	0.067
M4	2.000	2.000
Na+	0.275	0.295
K+	0.178	0.210
A site	0.450	0.500
O	22.000	22.000
OH	2.000	2.000
XMg	0.70	0.70
XNa	0.16	0.16
Name	Hbl	Hbl

Appendix E10 (continued)

	Grt1 n=1	Grt2 n=1	Grt3 n=1	Grt4 n=1	Grt5 n=1
SiO_2	38.58	39.14	39.13	37.95	37.85
TiO_2	-	0.05	0.09	0.09	0.15
Al_2O_3	21.49	21.39	21.36	20.95	20.99
Cr_2O_3	-	-	-	0.01	0.08
Fe_2O_3	1.23	1.12	1.39	1.97	1.56
FeO	25.02	25.50	21.92	24.28	25.75
MnO	0.55	0.67	0.55	0.58	0.53
MgO	6.77	6.51	5.79	5.85	6.30
CaO	6.92	6.76	11.03	8.40	6.52
Total	100.56	101.14	101.26	100.08	99.73
Si IV	5.951	6.000	5.982	5.912	5.920
Al IV	0.049	0.000	0.018	0.088	0.080
T site	6.000	6.000	6.000	6.000	6.000
Al VI	3.857	3.865	3.830	3.758	3.789
Ti VI	-	0.006	0.010	0.011	0.018
Cr3+	-	-	-	0.001	0.010
Fe3+	0.143	0.130	0.159	0.230	0.183
O site	4.000	4.000	4.000	4.000	4.000
Fe2+	3.228	3.269	2.803	3.163	3.368
Mn2+	0.072	0.087	0.071	0.077	0.070
Mg2+	1.557	1.488	1.320	1.358	1.469
Ca2+	1.144	1.110	1.807	1.402	1.093
A site	6.000	5.950	6.000	6.000	6.000
O	23.975	23.957	23.996	23.961	23.969
Almand	52.55	53.68	45.43	50.67	54.23
Pyrop	25.34	24.43	21.39	21.76	23.65
Gross	18.62	18.23	29.28	22.46	17.59
Ti And	-	0.09	0.17	0.17	0.28
Fe And	2.32	2.13	2.58	3.69	2.95
Spess	1.17	1.43	1.15	1.23	1.13
Uvaro	-	-	-	0.02	0.16
XMg	0.32	0.31	0.31	0.29	0.30

	Ilm1 n=1
SiO_2	0.07
TiO_2	50.62
Al_2O_3	-
Cr_2O_3	0.03
FeO	45.32
MnO	0.21
MgO	0.07
CaO	0.04
Total	96.36
Si4+	0.002
Ti4+	0.937
Al3+	-
Cr3+	0.001
Fe2+	0.990
Mn2+	0.005
Mg2+	0.003
Ca2+	0.001
Total	2.000
O	3.000

Contact between minerals

Grt1 - Cpx1
Grt2 - Cpx2
Cpx3 - Amp1
Bt1 - Ilm1

Appendix E11. Representative analyses of the principal minerals from sample CMA-146-86

	Cpx1c n=3	Cpx1m n=4	Cpx2c n=1	Cpx2m n=1	Cpx3c n=1
SiO_2	49.82	50.61	51.42	51.22	51.07
TiO_2	0.90	0.44	0.47	0.19	0.73
Al_2O_3	2.52	2.15	1.18	1.43	0.87
Cr_2O_3	0.08	0.09	0.13	0.10	0.05
Fe_2O_3	1.68	0.90	1.60	-	0.44
FeO	10.26	12.34	10.26	12.57	10.16
MnO	0.17	0.15	0.23	0.12	0.16
MgO	13.05	12.05	12.20	11.70	12.61
CaO	19.95	19.67	21.73	21.27	22.43
Na_2O	0.15	0.28	0.31	-	-
K_2O	0.14	0.15	0.13	0.15	0.06
Total	98.72	98.84	99.66	98.75	98.58
Si IV	1.901	1.938	1.950	1.967	1.954
Al IV	0.099	0.062	0.050	0.033	0.039
T site	2.000	2.000	2.000	2.000	1.990
Al VI	0.015	0.036	0.003	0.032	-
Ti4+	0.026	0.013	0.014	0.005	0.021
Cr3+	0.002	0.003	0.004	0.003	0.002
Fe3+	0.048	0.026	0.045	-	0.013
Fe2+	0.327	0.395	0.326	0.404	0.325
Mn2+	0.006	0.005	0.007	0.004	0.005
Mg2+	0.742	0.688	0.690	0.670	0.719
Ca2+	0.816	0.807	0.883	0.875	0.919
Na+	0.011	0.020	0.023	-	-
K+	0.007	0.007	0.006	0.007	0.003
M1,M2	2.000	2.000	2.000	2.000	2.010
O	6.000	6.000	6.000	6.003	6.000
En	39.36	36.43	36.35	34.37	36.62
Wo	43.28	42.64	46.57	44.91	46.82
Fs	17.36	20.92	17.09	20.72	16.56
XMg	0.68	0.62	0.66	0.62	0.68

	Bt1 n=1	Bt2 n=1	Bt3 n=1	Bt4 n=1	Bt5 n=1
SiO_2	34.78	34.59	34.55	35.19	35.95
TiO_2	3.40	3.41	3.29	3.08	3.34
Al_2O_3	14.85	13.87	14.55	14.99	15.43
Cr_2O_3	0.02	-	0.03	-	0.13
Fe_2O_3	3.58	3.51	3.47	3.49	3.31
FeO	19.77	19.53	19.20	19.30	18.31
MnO	0.05	0.03	0.06	-	0.09
MgO	9.72	10.16	9.70	10.11	10.60
CaO	-	-	-	-	-
K_2O	9.08	8.70	9.24	8.81	8.90
H_2O	3.90	3.91	3.90	3.92	3.95
Total	99.15	97.71	97.99	98.89	100.01
Si IV	5.394	5.442	5.422	5.441	5.456
Al IV	2.606	2.558	2.578	2.559	2.544
T site	8.000	8.000	8.000	8.000	8.000
Al VI	0.109	0.013	0.113	0.173	0.216
Ti VI	0.397	0.403	0.388	0.358	0.381
Cr3+	0.002	-	0.004	-	0.016
Fe3+	0.417	0.416	0.410	0.406	0.378
Fe2+	2.565	2.569	2.520	2.496	2.324
Mn2+	0.007	0.004	0.008	-	0.012
Mg2+	2.246	2.383	2.269	2.330	2.398
O site	5.740	5.790	5.710	5.760	5.720
Ca2+	-	-	-	-	-
K+	1.797	1.746	1.850	1.738	1.723
A site	1.797	1.746	1.850	1.738	1.723
O	20.000	20.000	20.000	20.000	20.000
OH	4.000	4.000	4.000	4.000	4.000
XMg	0.42	0.45	0.43	0.45	0.50

Appendix E11 (continued)

	Pl1c	Pl1m	Pl2c
	n=2	n=1	n=1
SiO_2	56.11	57.28	52.79
Al_2O_3	27.64	27.13	28.50
CaO	10.00	9.27	11.73
Na_2O	7.06	7.57	5.57
K_2O	0.20	0.13	0.06
FeO	0.22	0.14	0.00
Total	101.24	101.52	98.65
Si4+	10.033	10.184	9.710
Al3+	5.824	5.685	6.178
Z site	15.858	15.868	15.889
Ca2+	1.916	1.766	2.312
Na+	2.449	2.609	1.986
K+	0.046	0.029	0.014
Fe2+	0.034	0.021	0.000
X site	4.444	4.425	4.312
Total	20.302	20.294	20.201
O	32.000	32.000	32.000
An	43.46	40.09	53.61
Ab	55.50	59.24	46.07
Or	1.04	0.67	0.33

	Amp1	Amp2	Amp3	Amp4	Amp5	Amp6	Amp7	Amp8	Amp9
	n=1	n=1	n=1	n=1	n=1	n=2	n=1	n=1	n=1
SiO_2	51.50	41.11	48.72	42.37	41.56	49.73	41.11	50.05	48.33
TiO_2	0.35	1.25	0.62	1.18	0.90	0.40	0.91	0.44	0.43
Al_2O_3	3.27	11.61	6.02	10.57	12.37	4.53	12.80	3.74	4.18
Cr_2O_3	0.06	0.24	0.02	0.17	0.08	0.06	0.12	0.05	0.06
Fe_2O_3	-	-	-	-	-	-	-	-	-
FeO*	16.16	20.49	18.24	20.21	20.65	17.09	20.80	16.86	18.86
MnO	0.17	0.14	0.12	0.12	0.13	0.11	0.18	0.09	0.13
MgO	14.18	7.81	12.18	8.99	8.60	13.41	8.42	13.90	12.74
CaO	11.81	11.37	11.31	11.27	11.63	11.68	11.46	11.51	10.28
Na_2O	0.62	1.83	0.87	1.53	1.83	0.38	1.77	0.38	0.64
K_2O	0.24	1.14	0.46	0.97	0.90	0.28	1.05	0.24	0.25
H_2O	2.08	1.97	2.06	1.99	2.01	2.06	2.00	2.05	2.00
Total	100.44	98.96	100.62	99.37	100.66	99.73	100.62	99.31	97.90
Si IV	7.452	6.331	7.114	6.429	6.247	7.261	6.182	7.550	7.196
Al IV	0.548	1.669	0.886	1.571	1.753	0.739	1.818	0.450	0.734
T site	8.000	8.000	8.000	8.000	8.000	8.000	8.000	8.000	8.000
Al VI	0.010	0.441	0.151	0.326	0.432	0.038	0.459	0.177	-
Fe3+	0.383	0.252	0.491	0.459	0.509	0.584	0.473	0.465	0.837
Ti4+	0.038	0.145	0.069	0.135	0.102	0.044	0.103	0.047	0.048
Cr3+	0.007	0.029	0.002	0.015	0.010	0.007	0.014	0.006	0.007
Mg2+	3.061	1.796	2.649	2.034	1.923	2.920	1.889	2.779	2.828
Fe2+	1.501	2.337	1.638	2.031	2.024	1.407	2.062	1.526	1.280
M1,M2,M3	5.000	5.000	5.000	5.000	5.000	5.000	5.000	5.000	5.000
Fe2+	0.073	0.051	0.099	0.075	0.061	0.092	0.107	0.013	0.161
Mn2+	0.021	0.018	0.015	0.015	0.017	0.014	0.023	0.011	0.016
Ca2+	1.835	1.879	1.772	1.833	1.869	1.824	1.844	1.753	1.638
Na+	0.071	0.052	0.114	0.077	0.053	0.070	0.026	0.105	0.184
M4	2.000	2.000	2.000	2.000	2.000	2.000	2.000	1.880	2.000
Na+	0.103	0.494	0.132	0.373	0.479	0.038	-	-	0.490
K+	0.044	0.024	0.086	0.188	0.172	0.052	0.200	0.044	0.047
A site	0.150	0.520	0.220	0.560	0.650	0.090	0.690	0.040	0.050
O	22.000	22.000	22.000	22.000	22.000	22.000	22.000	22.000	22.000
OH	2.000	2.000	2.000	2.000	2.000	2.000	2.000	2.000	2.000
XMg	0.65	0.44	0.58	0.48	0.46	0.62	0.46	0.63	0.58
XNa	0.09	0.23	0.12	0.20	0.22	0.05	0.22	0.06	0.10
Name	Act Hbl	Prg Hbl	Hbl	Prg Hbl	Prg	Act Hbl	Prg	Act	Act Hbl

Appendix E11 (continued)

	Amp10 n=1	Amp11 n=2	Amp12 n=2	Amp13 n=1	Amp14 n=1	Amp15 n=2	Amp16 n=1
SiO_2	40.94	40.53	46.53	40.64	37.73	41.07	42.38
TiO_2	0.67	0.69	0.60	0.78	0.51	1.03	0.93
Al_2O_3	11.58	10.76	8.41	13.96	16.64	12.69	11.93
Cr_2O_3	0.11	0.08	0.10	0.03	-	0.00	0.12
Fe_2O_3	-	-	-	-	-	-	-
FeO*	21.86	21.28	19.41	22.48	22.35	20.82	22.29
MnO	0.18	0.12	0.08	-	-	0.14	0.12
MgO	8.18	8.92	10.57	6.57	5.84	7.59	7.65
CaO	10.94	9.93	11.51	11.09	11.02	11.07	11.26
Na_2O	2.02	1.38	1.55	2.17	2.50	2.46	2.25
K_2O	0.85	0.63	0.68	1.16	1.54	1.00	0.90
H_2O	1.97	1.92	2.06	2.00	1.97	1.99	2.02
Total	99.30	96.25	101.50	100.88	100.10	99.86	101.85
Si IV	6.255	6.273	6.798	6.105	5.802	6.276	6.347
Al IV	1.745	1.727	1.202	1.895	2.198	1.724	1.653
T site	8.000	8.000	8.000	8.000	8.000	8.000	8.000
Al VI	0.349	0.246	0.247	0.579	0.814	0.555	0.454
Fe3+	0.655	1.141	0.621	0.765	0.401	0.228	0.340
Ti4+	0.077	0.081	0.066	0.088	0.059	0.119	0.108
Cr3+	0.013	0.010	0.012	0.004	-	-	0.014
Mg2+	1.865	2.057	2.301	1.472	1.340	1.727	1.710
Fe2+	2.041	1.465	1.753	2.068	2.386	2.371	2.374
M1,M2,M3	5.000	5.000	5.000	4.980	5.000	5.000	5.000
Fe2+	0.090	0.154	0.003	-	0.090	0.064	0.075
Mn2+	0.023	0.016	0.010	-	-	0.018	0.015
Ca2+	1.791	1.647	1.800	1.788	1.820	1.810	1.809
Na+	0.096	0.183	0.187	0.212	0.090	0.108	0.101
M4	2.000	2.000	2.000	2.000	2.000	2.000	2.000
Na+	0.502	0.227	0.253	0.420	0.654	0.622	0.553
K+	0.165	0.125	0.127	0.222	0.304	0.195	0.172
A site	0.670	0.350	0.380	0.640	0.960	0.820	0.730
O	22.000	22.000	22.000	22.000	22.000	22.000	22.000
OH	2.000	2.000	2.000	2.000	2.000	2.000	2.000
XMg	0.44	0.47	0.53	0.38	0.35	0.43	0.42
XNa	0.25	0.20	0.19	0.26	0.29	0.29	0.27
Name	Prg	Ts Hbl	Hbl	Prg	Prg	Prg	Prg

	Grt1c n=2	Grt1m n=3	Grt2c n=1	Grt2m n=1	Grt3c n=1
SiO_2	37.22	37.14	37.12	37.68	37.24
TiO_2	0.13	0.12	-	0.07	0.06
Al_2O_3	20.49	20.24	20.34	20.80	20.45
Cr_2O_3	0.09	0.04	-	0.02	-
Fe_2O_3	1.31	1.27	1.03	0.89	0.90
FeO	28.87	30.45	30.58	30.59	29.22
MnO	2.31	2.26	1.39	1.51	1.20
MgO	1.34	2.00	1.76	2.19	1.63
CaO	8.79	6.39	6.63	7.12	8.73
Total	100.54	99.90	98.85	100.87	99.43
Si IV	5.954	5.984	6.000	5.988	6.000
Al IV	0.046	0.016	0.000	0.012	0.000
T site	6.000	6.000	6.000	6.000	6.000
Al VI	3.816	3.826	3.875	3.883	3.883
Ti VI	0.015	0.014	-	0.008	0.007
Cr3+	0.011	0.005	-	0.003	-
Fe3+	0.158	0.154	0.125	0.106	0.110
O site	4.000	4.000	4.000	4.000	4.000
Fe2+	3.862	4.103	4.134	4.066	3.937
Mn2+	0.312	0.308	0.190	0.203	0.164
Mg2+	0.320	0.480	0.424	0.519	0.392
Ca2+	1.506	1.103	1.148	1.212	1.507
A site	6.000	5.990	5.900	6.000	6.000
O	23.984	23.993	23.897	23.998	24.003
Almand	62.45	66.53	68.65	66.47	64.37
Pyrop	5.17	7.78	7.04	8.48	6.40
Gross	24.36	17.89	19.07	19.82	24.64
Ti And	0.24	0.23	-	0.14	0.12
Fe And	2.55	2.50	2.08	1.73	1.79
Spess	5.05	4.99	3.16	3.32	2.68
Uvaro	0.17	0.08	-	0.04	-
XMg	0.07	0.10	0.09	0.11	0.09

Appendix E11 (continued)

	Grt3m n=1	Grt4c n=1	Grt4m n=2	Grt5 n=1	Grt6 n=1
SiO_2	37.28	37.42	37.69	37.77	37.61
TiO_2	0.03	0.13	0.10	-	0.06
Al_2O_3	20.40	20.14	20.41	20.54	20.26
Cr_2O_3	0.03	0.07	0.07	0.10	-
Fe_2O_3	1.02	1.40	1.40	1.19	1.53
FeO	28.98	29.70	29.96	29.68	28.74
MnO	1.30	3.19	2.87	2.62	2.68
MgO	1.91	1.46	1.75	1.68	1.75
CaO	8.10	6.69	6.86	7.06	7.25
Total	99.04	100.20	101.12	100.64	99.88
Si IV	6.000	6.000	5.989	6.000	6.000
Al IV	0.000	0.000	0.011	0.000	0.000
T site	6.000	6.000	6.000	6.000	6.000
Al VI	3.870	3.806	3.812	3.846	3.809
Ti VI	0.004	0.016	0.013	-	0.007
Cr3+	0.004	0.009	0.009	0.013	-
Fe3+	0.123	0.170	0.167	0.142	0.184
O site	4.000	4.000	4.000	4.000	4.000
Fe2+	3.900	3.982	3.981	3.943	3.835
Mn2+	0.177	0.433	0.386	0.353	0.362
Mg2+	0.458	0.349	0.416	0.398	0.416
Ca2+	1.397	1.149	1.168	1.202	1.239
A site	5.930	5.910	5.950	5.900	5.850
O	23.934	23.921	23.952	23.895	23.856
Almand	64.33	65.20	64.85	65.18	63.46
Pyrop	7.56	5.71	6.77	6.58	6.89
Gross	23.04	18.82	19.02	19.86	20.51
Ti And	0.06	0.26	0.20	-	0.12
Fe And	2.03	2.78	2.72	2.35	3.04
Spess	2.92	7.09	6.28	5.83	5.99
Uvaro	0.06	0.15	0.14	0.21	-
XMg	0.10	0.07	0.09	0.08	0.09

	Ilm1 n=1	Ilm2 n=1
SiO_2	0.20	0.31
TiO_2	47.08	47.13
Al_2O_3	-	-
Cr_2O_3	0.05	0.15
FeO	50.45	49.44
MnO	0.47	0.57
MgO	-	-
CaO	0.02	0.12
Total	98.27	97.72
Si4+	0.005	0.008
Ti4+	0.905	0.911
Al3+	-	-
Cr3+	0.001	0.003
Fe2+	0.899	0.903
Mn2+	0.010	0.012
Mg2+	-	-
Ca2+	0.001	0.003
Total	2.000	2.000
O	3.000	3.000

Contact between minerals

Cpx1 - Amp12
Cpx2 - Amp1
Cpx3 - Amp6,7,8
Amp11 - Bt1
Amp13 - Grt3
Amp15 - Grt1
Grt1 - Bt5
Amp5 - Grt1
Bt2 - Amp16
Grt4 - Bt4
Bt4 - Mag1
Bt2 - Mag2

APPENDIX F

PYROXENE QUADRILATERAL

Formulas: Diopside = $Ca\ Mg\ Si_2\ O_6$

Hedenbergite = $Ca\ Fe\ Si_2\ O_6$

Clinoenstatite = $Mg_2\ Si_2\ O_6$

Clinoferrosilite = $Fe_2\ Si_2\ O_6$

Note: The composition of the primary (igneous) clinopyroxene grains in sample CMA-LA18 is relatively constant. These compositions plot within the augite field of the pyroxene quadrilateral shown on p. 318. However, the composition of metamorphic clinopyroxene is much variable, ranging from salitic augite to diopside, salite, ferrosalite, and ferroaugite (e.g. samples CMA-M-015A, CMA-M-R01A, CMA-M-V01, and CMA-146). The variation in composition of metamorphic clinopyroxene is a result of the degree of equilibration reached in the dyke, and thus a function of the chemical composition of the mineral phases adjacent to the clinopyroxene grain.

The composition of orthopyroxene varies from magnesium-rich to iron-rich. The corona type that the orthopyroxene is found within explains this variation. For example, orthopyroxene associated with olivine corona is characterized by a more magnesian composition, whereas orthopyroxene associated with magnetite corona is more iron-rich.

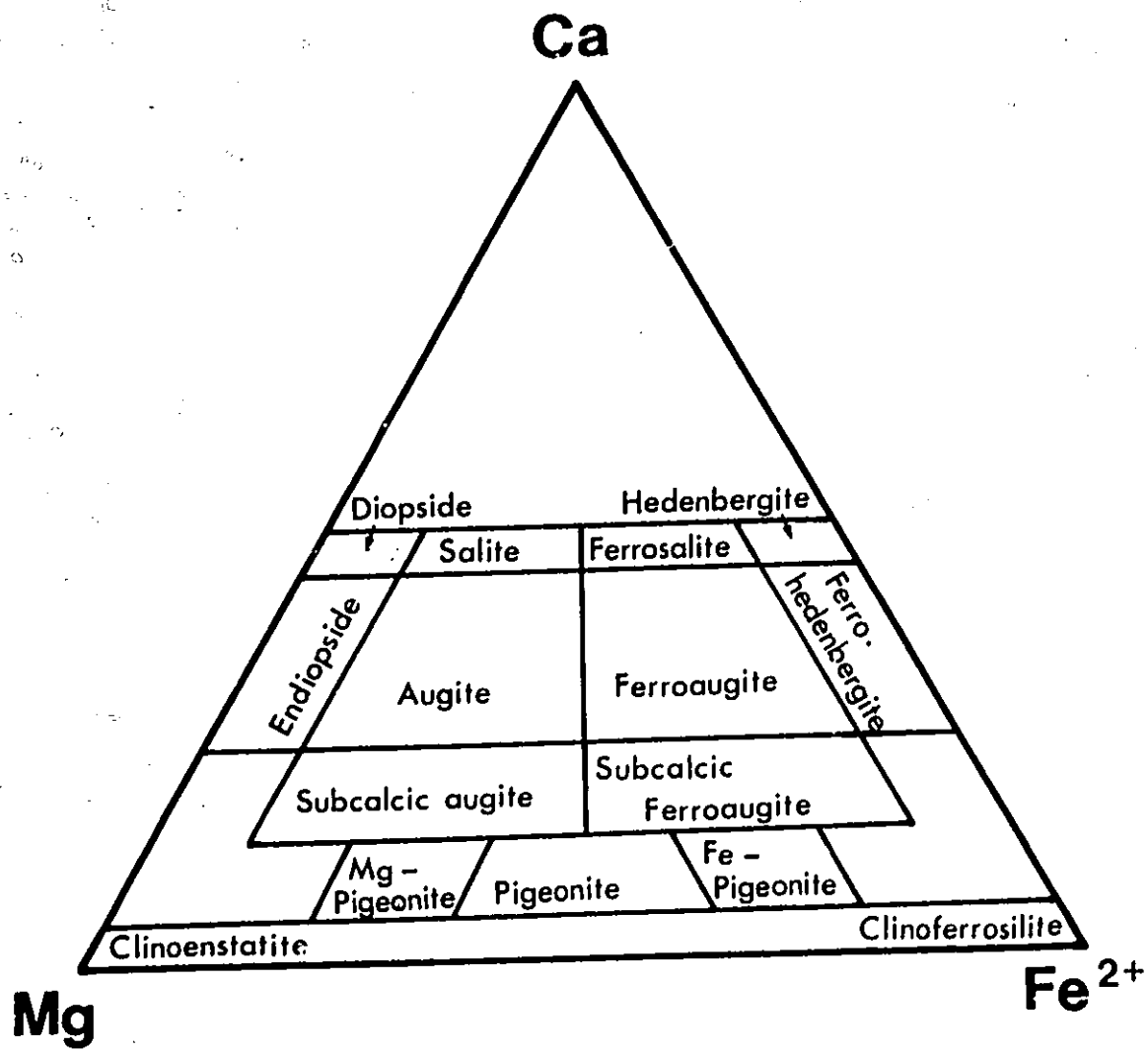
Ca
Diopside
Hedenbergite
Salite
Ferrosalite
Endiopside
Ferro-hedenbergite
Augite
Ferroaugite
Subcalcic augite
Subcalcic Ferroaugite
Mg – Pigeonite
Pigeonite
Fe – Pigeonite
Clinoenstatite
Clinoferrosilite
Mg
Fe 2+

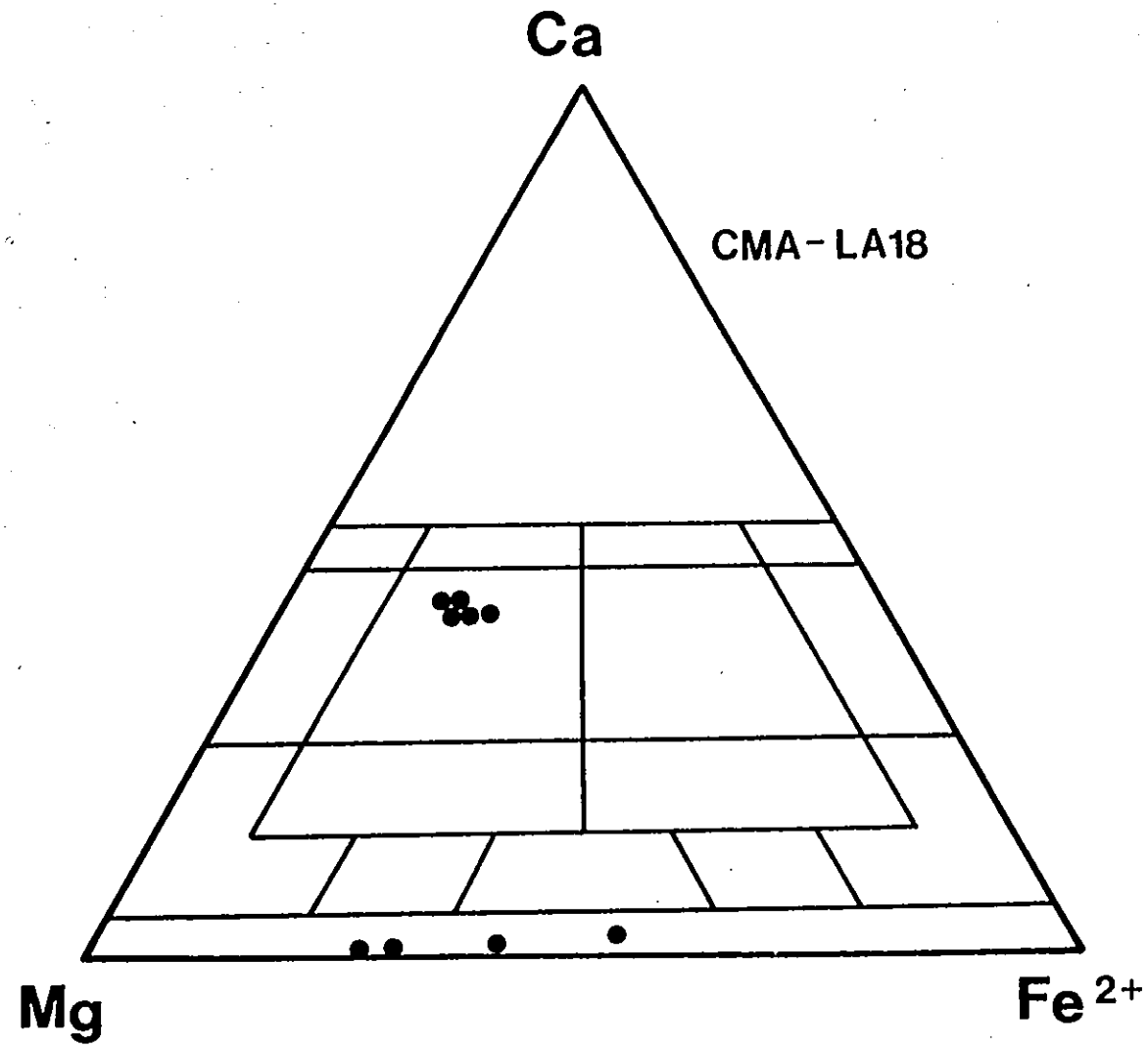
Ca
CMA-LA18
Mg
Fe 2+

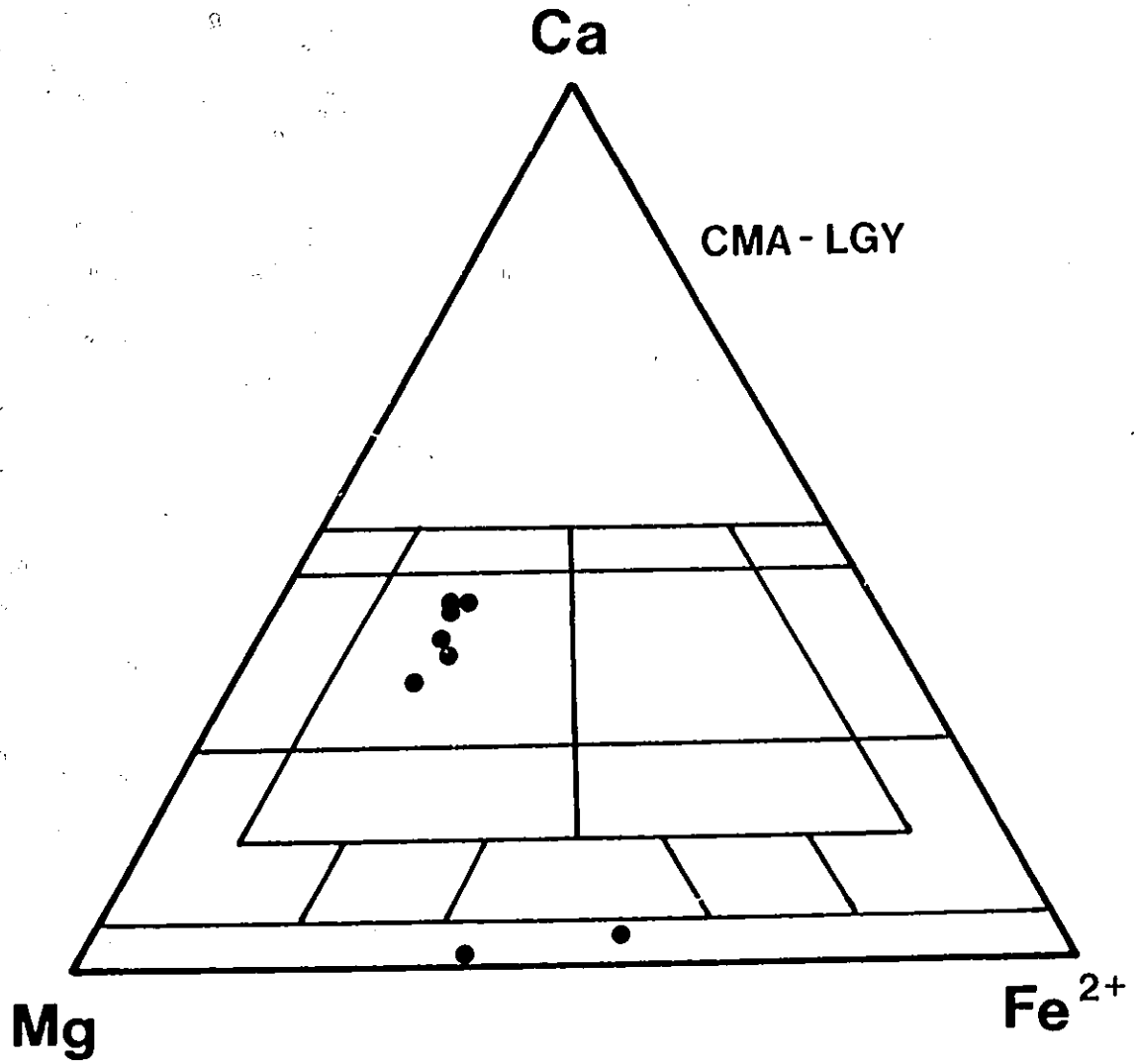
Ca
CMA - LGY
Mg
Fe 2+

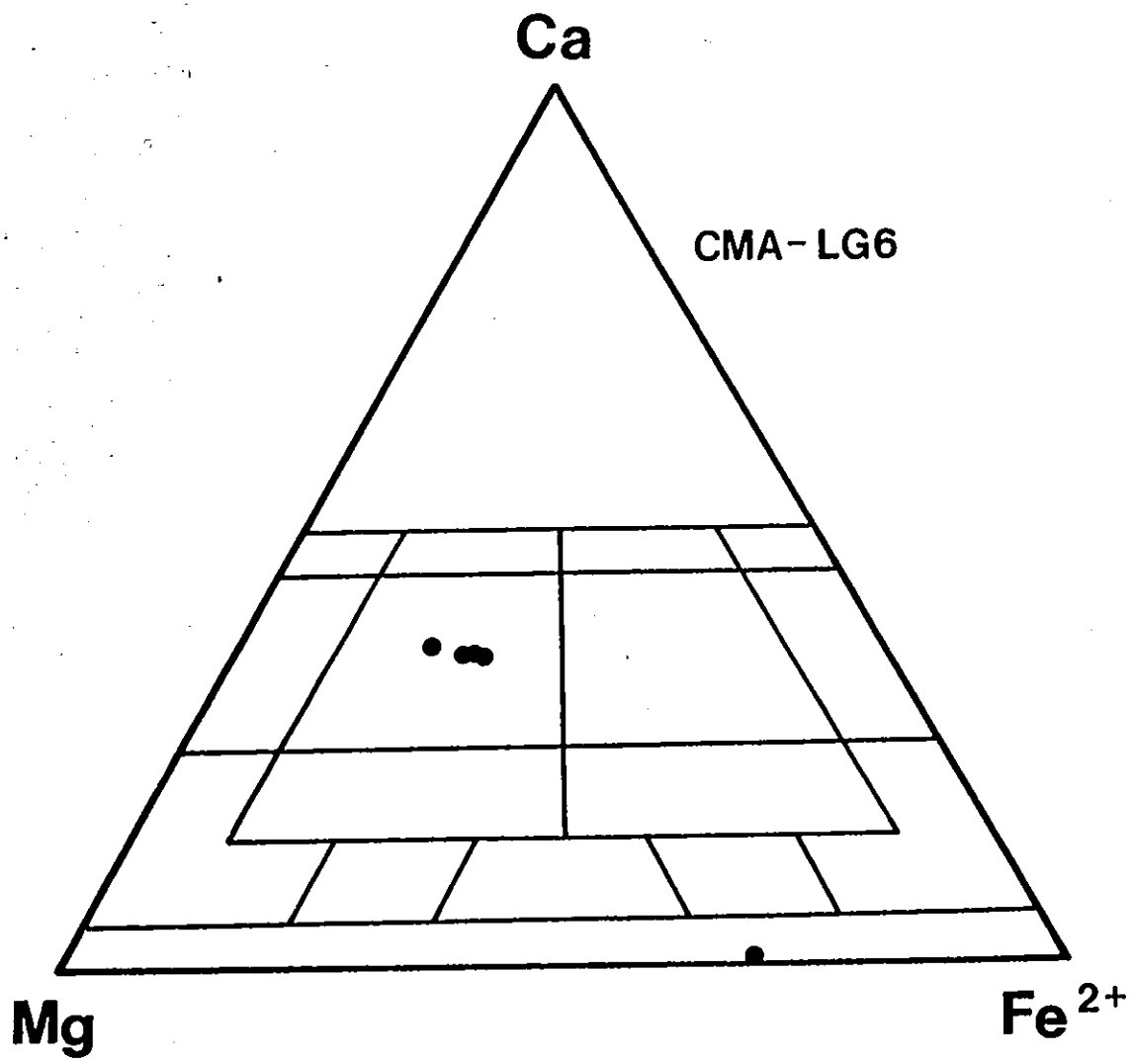
Ca
CMA-LG6
Mg
Fe 2+

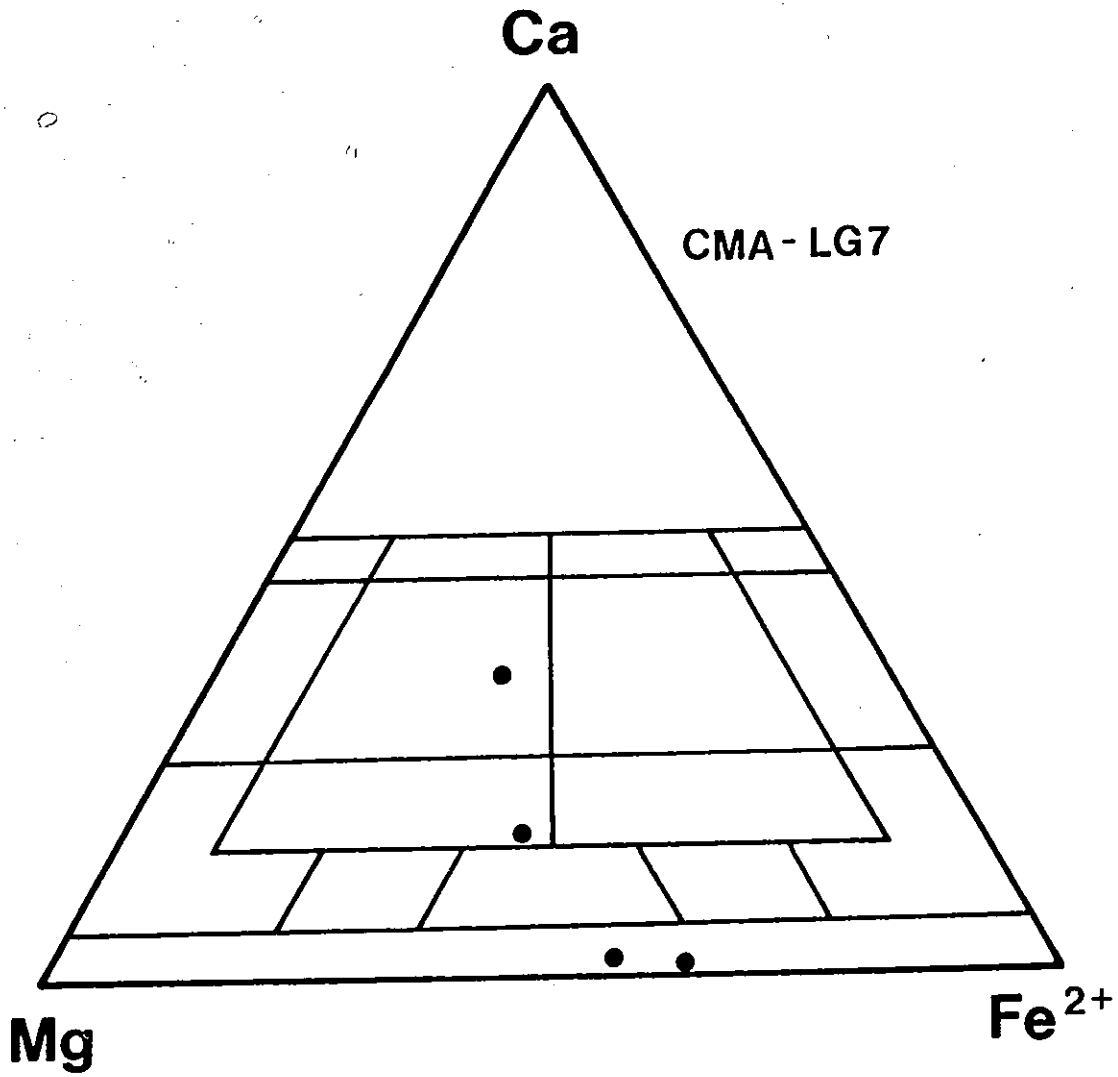
Ca
CMA - LG7
Mg
Fe2+

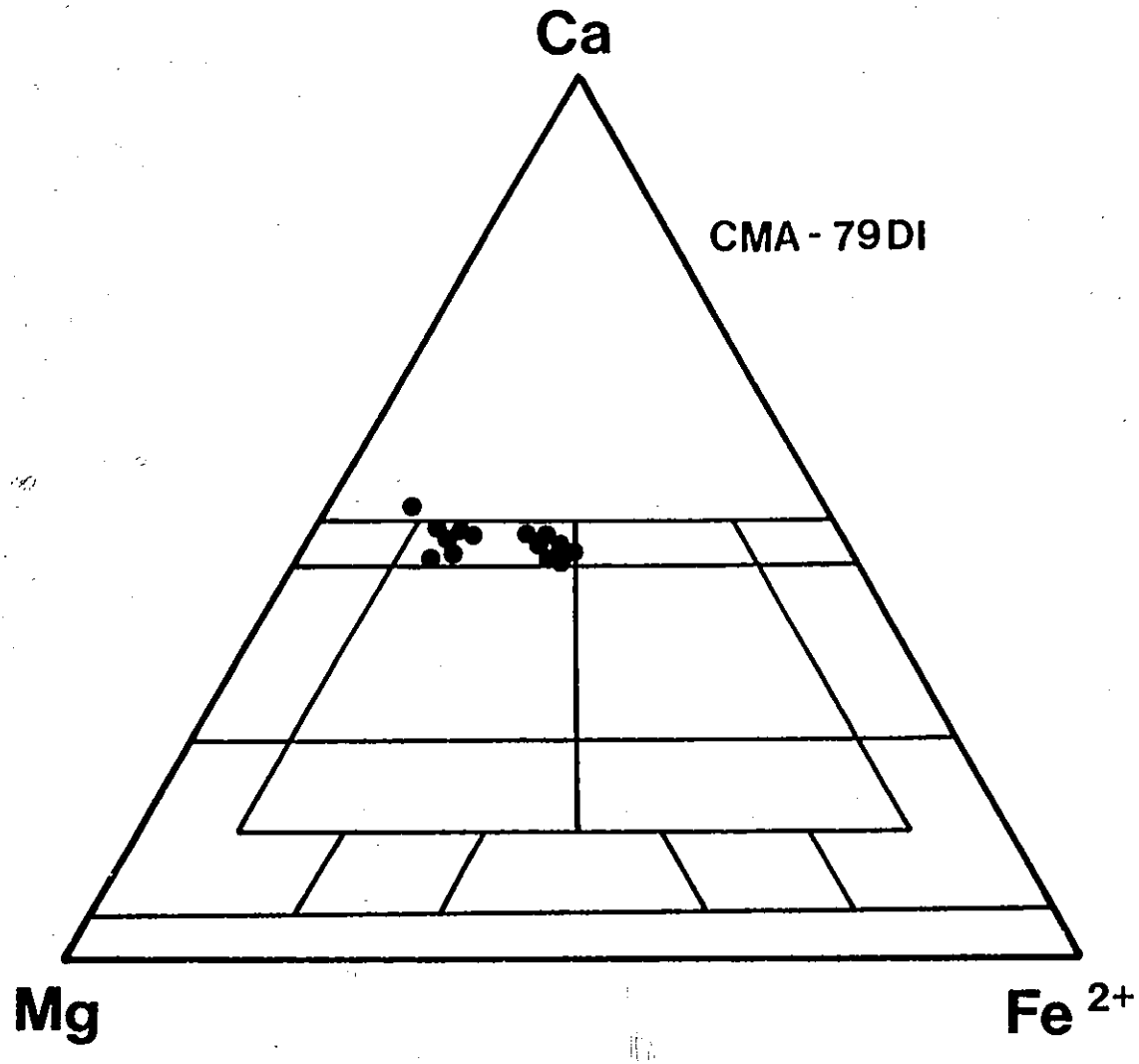
Ca
CMA - 79DI
Mg
Fe 2+

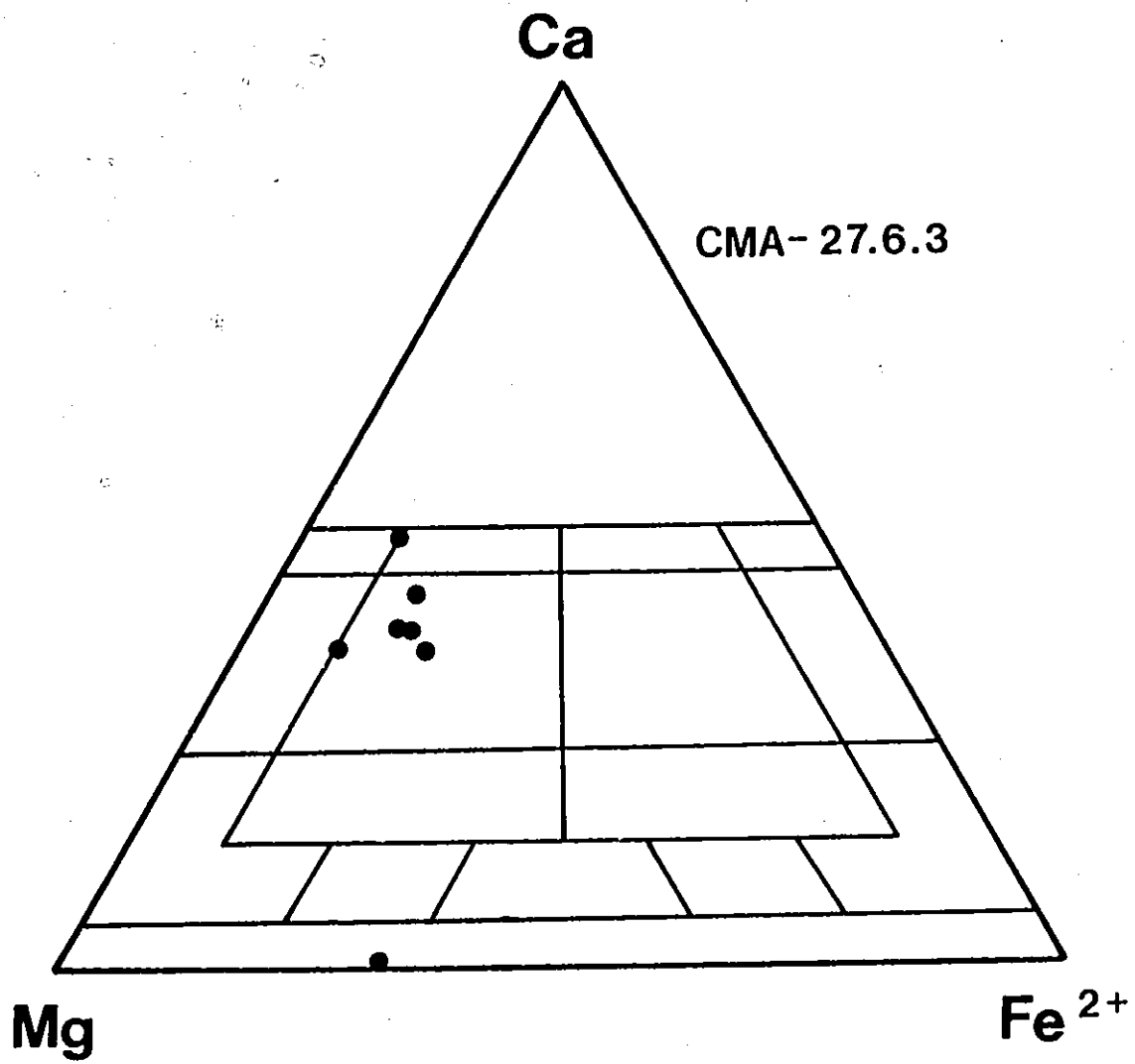
Ca
CMA- 27.6.3
Mg
Fe 2+

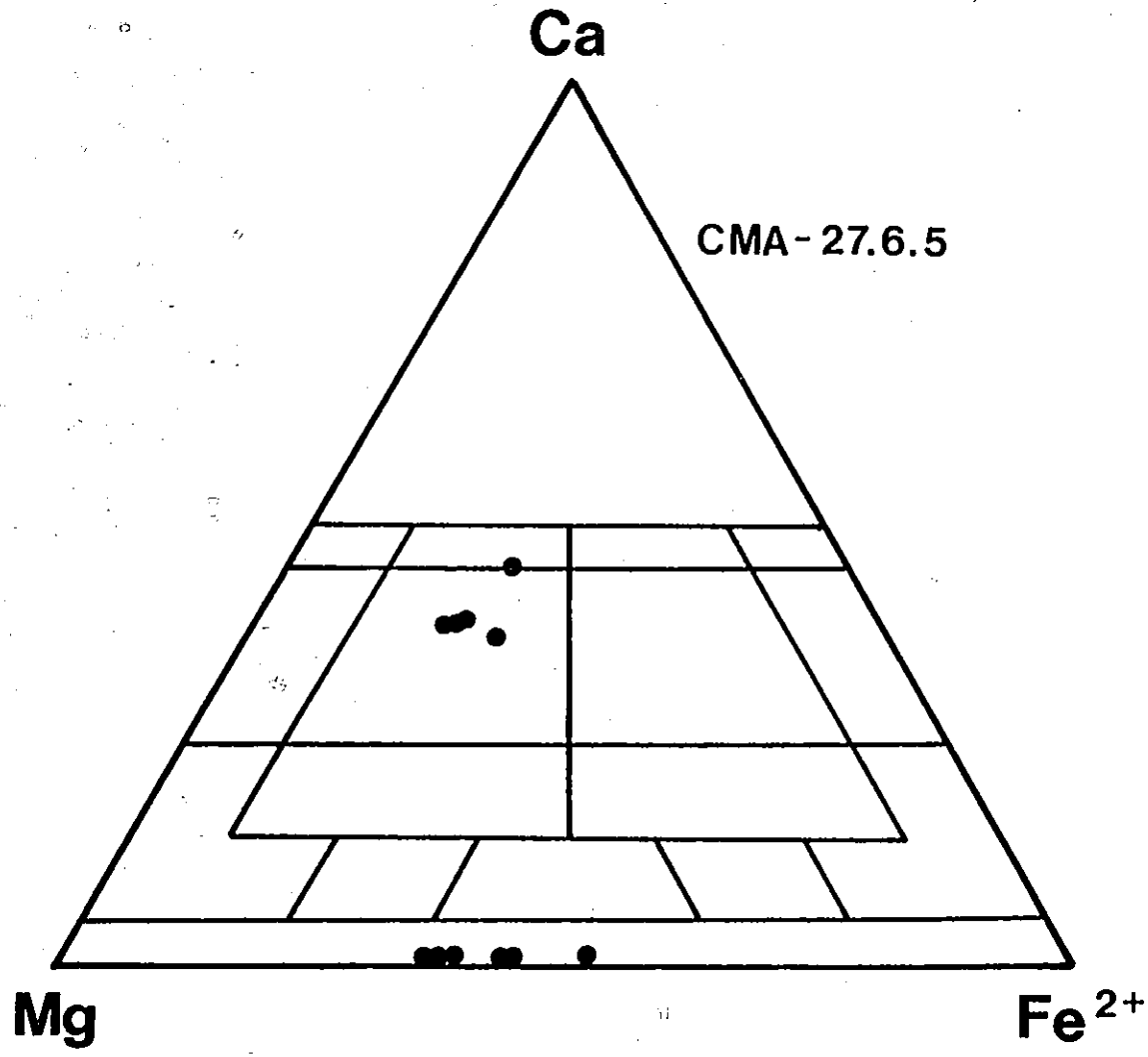
Ca
CMA-27.6.5
Mg
Fe 2+

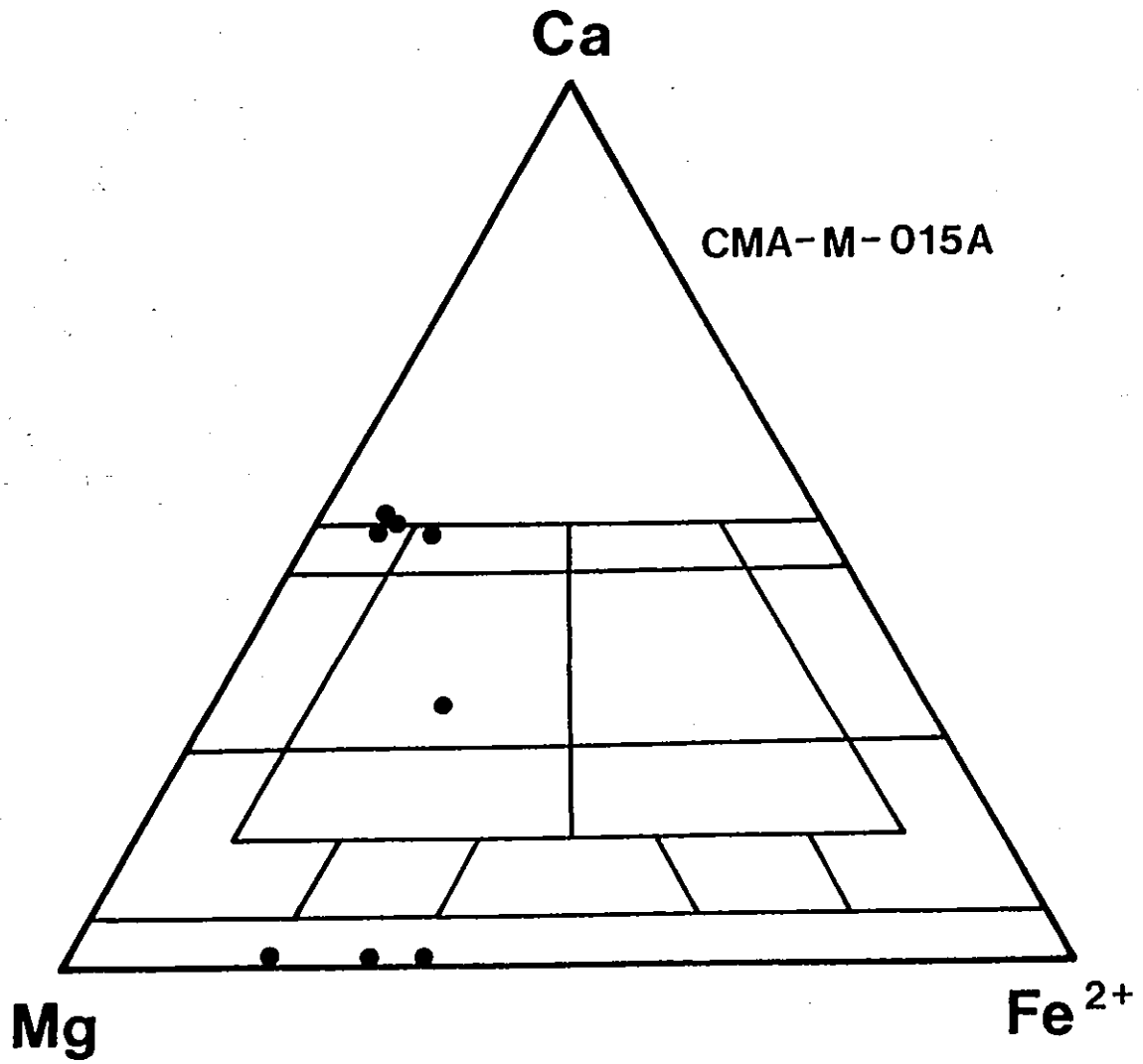
Ca
CMA-M-015A
Mg
Fe 2+

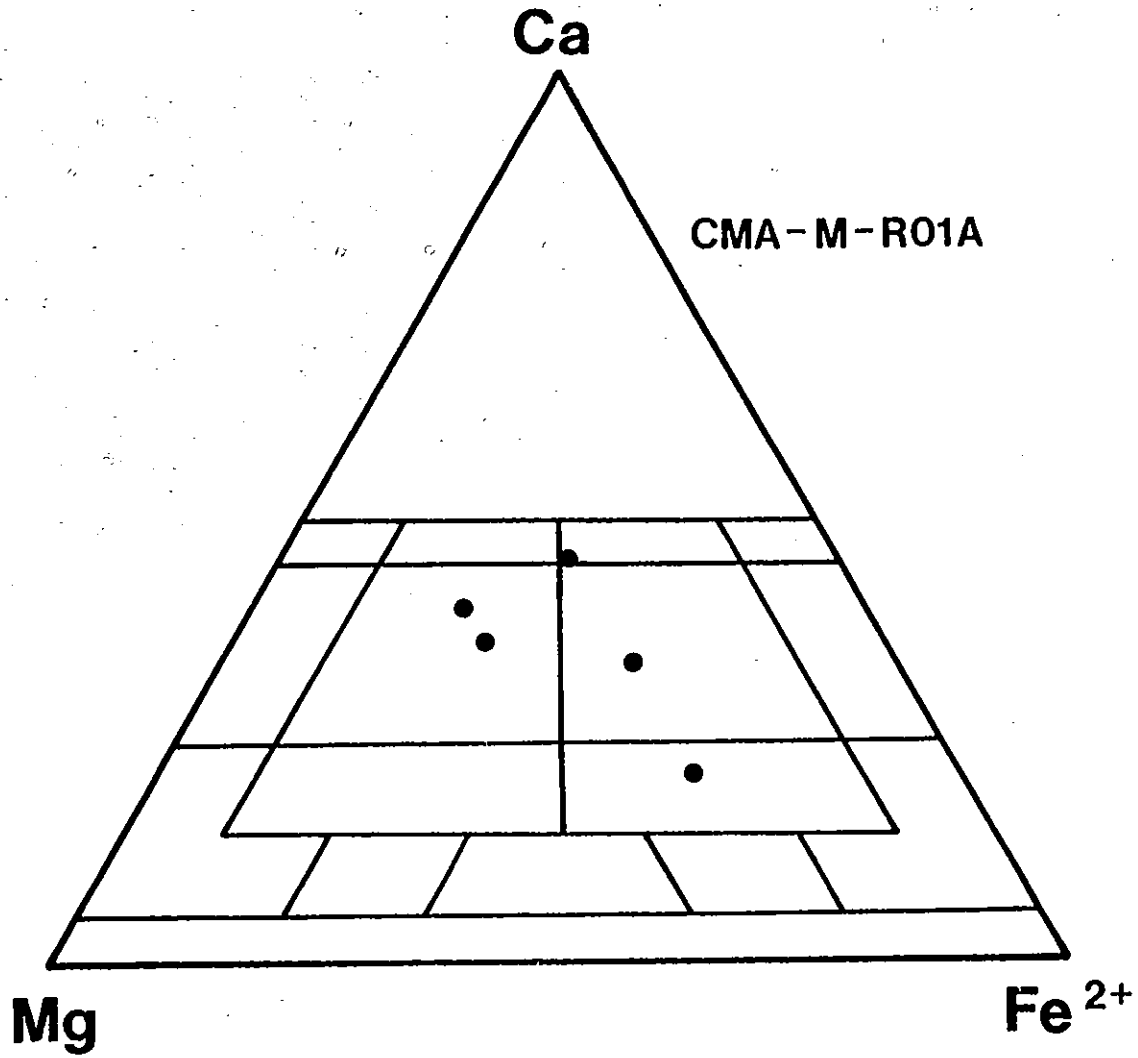
Ca
CMA-M-R01A
Mg
Fe 2+

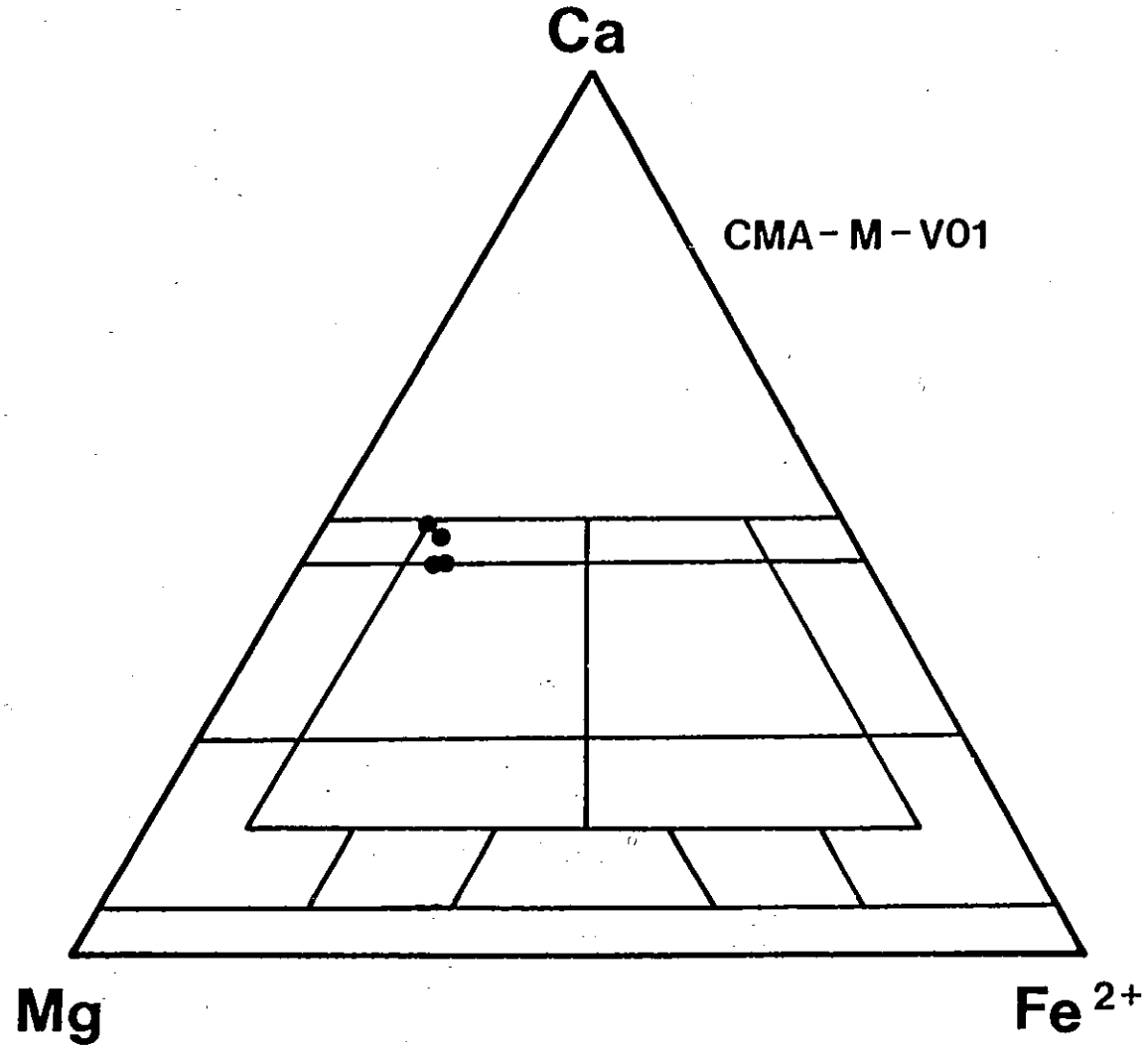
Ca
CMA - M - V01
Mg
Fe 2+

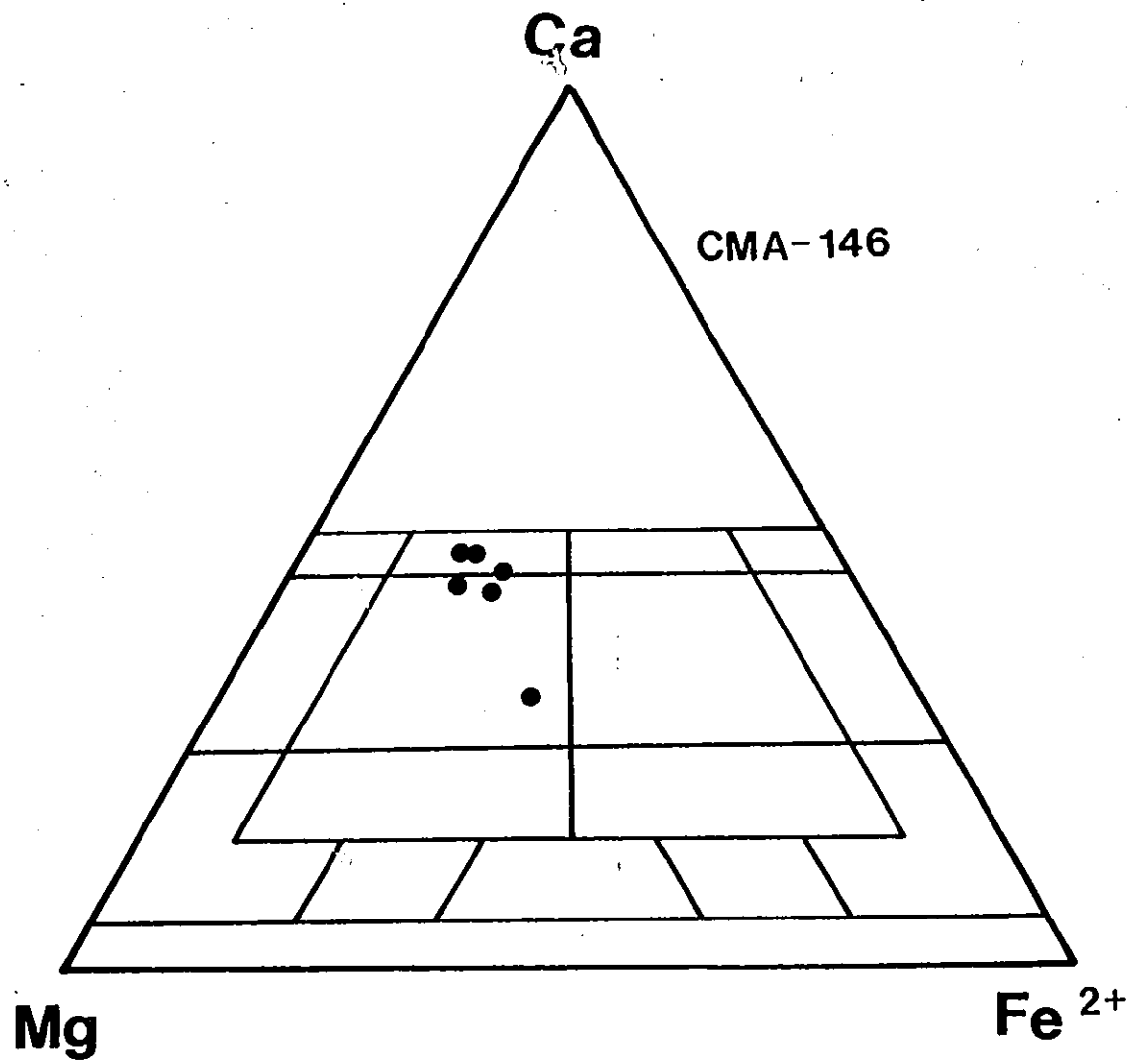
Ca
CMA-146
Mg
Fe 2+

Appendix G. Example of amphibole formulae calculation from microprobe analyses.
using the method of P. Robinson et al. (1982) and Stout (1972)

A series of recalculations can be done on fixed numbers of cations to derive amphibole formulae. First, the analysis is normalized on the basis of 13 cations excluding K, Na, Ca, Mn and with all Fe as Fe^{2+}. This calculation generates the maximum value of Fe^{3+} that is permitted in the amphibole stoichiometry. The amount of oxygen is then calculated for each cation. The oxygen values are obtained by multiplying 2 for R^{4+} ions, 1.5 for R^{3+} ions, 1.0 for R^{2+} ions, and 0.5 for R^{+} ions values. The sum of oxygen should be less than 23.
If the sum is greater than 23, then the analyses must be rejected.
Oxygen is then added to bring the total to 23. For each amount of oxygen added, convert twice that amount of Fe^{2+} to Fe^{3+} and so reduce the Fe^{2+} in the list.
Secondly, the structural formula is calculated assuming 15 cations, excluding K and Na. The resulting calculated Fe^{2+} is the minimum value permitted in the amphibole stoichiometry.
The mean value of Fe^{3+} is then calculated and converted into Fe_2O_3.
The final stage is to calculate the analysis on the basis of 23 oxygens incorporating the value c Fe_2O_3 obtained in the previous calculation.

	Wt%	Molecular Proportion	Cations	1 Cations x 8.740	Oxygens	2 Cations x 8.950	Oxygens
SiO_2	37.87	0.630	0.630	5.506	11.010	5.638	11.276
TiO_2	0.07	0.001	0.001	0.008	0.015	0.008	0.016
Al_2O_3	19.77	0.194	0.388	3.392	5.087	3.473	5.210
Cr_2O_3	0.04	0.000	0.001	0.005	0.007	0.005	0.007
Fe_2O_3							
FeO	14.41	0.201	0.201	1.757	1.757	1.799	1.799
MnO	0.18	0.003	0.003	0.022	0.022	0.023	0.023
MgO	10.75	0.267	0.267	2.334	2.334	2.390	2.390
CaO	10.45	0.186	0.186	1.626	1.626	1.665	1.665
Na_2O	3.28	0.053	0.106	0.925	0.462	0.947	0.974
K_2O	0.73	0.008	0.015	0.135	0.067	0.138	0.069
			1.487		22.388		23.430
					(+0.612)		

13 cations 1 -> 13 / 1.487 = 8.740
15 cations 2 -> 15 / 1.676 = 8.950

Fe_T= 1.757 then Fe^{2+}= 1.145 and Fe^{3+}= 0.612

Appendix G. Example of amphibole formulae calculation from microprobe analyses.
using the method of P. Robinson et al. (1982) and Stout (1972)

A series of recalculations can be done on fixed numbers of cations to derive amphibole formulae. First, the analysis is normalized on the basis of 13 cations excluding K, Na, Ca, Mn and with all Fe as Fe^{2+}. This calculation generates the maximum value of Fe^{3+} that is permitted in the amphibole stoichiometry. The amount of oxygen is then calculated for each cation. The oxygen values are obtained by multiplying 2 for R^{4+} ions, 1.5 for R^{3+} ions, 1.0 for R^{2+} ions, and 0.5 for R^{+} ions values. The sum of oxygen should be less than 23.
If the sum is greater than 23, then the analyses must be rejected.
Oxygen is then added to bring the total to 23. For each amount of oxygen added, convert twice that amount of Fe^{2+} to Fe^{3+} and so reduce the Fe^{2+} in the list.
Secondly, the structural formula is calculated assuming 15 cations, excluding K and Na. The resulting calculated Fe^{3+} is the minimum value permitted in the amphibole stoichiometry.
The mean value of Fe^{3+} is then calculated and converted into Fe_2O_3.
The final stage is to calculate the analysis on the basis of 23 oxygens incorporating the value c Fe_2O_3 obtained in the previous calculation.

	Wt%	Molecular Proportion	Cations	1 Cations x 8.740	Oxygens	2 Cations x 8.950	Oxygens
SiO_2	37.87	0.630	0.630	5.506	11.010	5.638	11.276
TiO_2	0.07	0.001	0.001	0.008	0.015	0.008	0.016
Al_2O_3	19.77	0.194	0.388	3.392	5.087	3.473	5.210
Cr_2O_3	0.04	0.000	0.001	0.005	0.007	0.005	0.007
Fe_2O_3							
FeO	14.41	0.201	0.201	1.757	1.757	1.799	1.799
MnO	0.18	0.003	0.003	0.022	0.022	0.023	0.023
MgO	10.75	0.267	0.267	2.334	2.334	2.390	2.390
CaO	10.45	0.186	0.186	1.626	1.626	1.665	1.665
Na_2O	3.28	0.053	0.106	0.925	0.462	0.947	0.974
K_2O	0.73	0.008	0.015	0.135	0.067	0.138	0.069
			1.487		22.388		23.430
					(+0.612)		

13 cations 1 -> 13 / 1.487 = 8.740 Fe_T= 1.757 then Fe^{2+}= 1.145 and
15 cations 2 -> 15 / 1.676 = 8.950 Fe^{3+}= 0.612

	Cations	Oxygens	Oxygens x 8.857
SiO_2	0.630	1.260	11.160
TiO_2	0.001	0.002	0.016
Al_2O_3	0.194	0.582	5.155
Cr_2O_3	0.000	0.001	0.007
Fe_2O_3	0.035	0.105	0.930
FeO	0.131	0.131	1.160
MnO	0.003	0.003	0.023
MgO	0.267	0.267	2.365
CaO	0.186	0.186	1.647
Na_2O	0.053	0.053	0.469
K_2O	0.008	0.008	0.068
		2.597	

23 oxygen

23 / 2.597 = 8.857

Amphibole Formula

Si IV	5.580
Al IV	2.420
T site	8.000
Al VI	1.017
Ti^{4+}	0.008
Cr^{3+}	0.005
Fe^{3+}	0.620
Fe^{2+}	0.985
Mg^{2+}	2.365
M1,M2,M3	5.000
Fe^{2+}	0.175
Mn^{2+}	0.023
Ca^{2+}	1.647
Na^{+}	0.155
M4	2.000
Na^{+}	0.783
K^{+}	0.136
A site	0.919

Appendix H. Example of modelled reaction using the method of Kretz et al. (1989)

Olivine + Plagioclase ---> Orthopyroxene + Pargasite + Spinel + Corundum

Plagioclase		Olivine		Orthopyroxene		Pargasite	
O	8.000	O	4.000	O	3.000	O	22.000
Si	2.404	Si	1.018	Si	0.982	Si	5.686
Al	1.546	Al	-	Al	0.001	Al	3.247
Ca	0.611	Fe	0.934	Ti	-	Ti	0.020
Na	0.425	Mg	1.048	Fe	0.369	Fe	2.023
K	0.003	Mn	-	Mg	0.675	Mg	2.521
Fe	0.001			Mn	0.007	Mn	0.038
		Spinel		Ca	0.002	Ca	1.801
		O	4.000			Na	0.981
		Si	0.020			K	0.131
		Al	1.903				
		Ti	-				
		Fe	0.710				
		Mg	0.394				
		Mn	0.020				

$$a\,(Mg_2SiO_4) + b\,(Fe_2SiO_4) + c\,(CaAlSi_3O_8) + d\,(NaAlSi_3O_8) = 1.00\ Prg + e\ Opx + f\ Spl$$

Na							d	=	0.981
Ca					c			=	1.801
Mg	2a							=	2.521 + 0.675e + 0.394f
Fe			2b					=	2.023 + 0.369e + 0.710f
Al					2c	+	d	=	3.247 + 1.903f
Si	a	+	b	+	2c	+	3d	=	5.686 + 0.982e

Equations:

(1) $d = 0.981$

(2) $c = 1.801$

(3) $2a = 2.521 + 0.675\,e + 0.394\,f$

(4) $2b = 2.023 + 0.369\,e + 0.710\,f$

(5) $2c + d = 3.247 + 1.903\,f$

(6) $a + b + 2c + 3d = 5.686 + 0.982\,e$

(5) $2c + d = 3.247 + 1.903\,f$
$4.583 = 3.247 + 1.903\,f$
$1.336 = 1.903\,f$
$f = 0.702$

(1) $c = 1.801$
(2) $d = 0.981$

(3) $2a = 2.521 + 0.675\,e + 0.394\,(0.702)$
$2a = 2.521 + 0.657\,e + 0.277$
$2a = 2.798 + 0.675\,e$
$a = 1.399 + 0.338\,e$ (7)

(4) $2b = 2.023 + 0.369\,e + 0.710\,f$
$2b = 2.023 + 0.369\,e + 0.710\,(0.702)$
$2b = 2.023 + 0.369\,e + 0.498$
$2b = 2.521 + 0.369\,e$
$b = 1.261 + 0.185\,e$ (8)

(6) $a + b + 2c + 3d = 5.686 + 0.982\,e$
$a + b + (3.602) + (2.943) = 5.686 + 0.982\,e$
$a + b + 6.545 = 5.686 + 0.982\,e$

including equations (7) and (8)

$1.399 + 0.338\,e + 1.261 + 0.185\,e + 0.859 = 0.982\,e$
$3.519 = 0.459\,e$
$e = 7.67$

(7) $a = 1.399 + 0.338\,e$
$a = 1.399 + 0.338\,(7.67)$
$a = 1.399 + 2.592$
$a = 3.99$

(8) $b = 1.261 + 0.185\,e$
$b = 1.261 + 0.185\,(7.67)$
$b = 1.261 + 1.419$
$b = 2.68$

The reaction can be writen as

Ol An Ab Or

$6.67\ (Mg_{1.20}Fe_{0.80})Si_{1.02}O_4 + 1.8\ (CaAl_2Si_2O_8) + 0.98\ (NaAlSi_3O_8) + 0.003\ (KAlSi_3O_8)$

$+ [\ 0.128\ K + 0.02\ Ti + 0.065\ Mn + OH] + H_2O$ --->

Prg

$1.00\ (K_{0.13}Na_{0.98})Ca_{1.80}(Fe_{2.02}Mg_{2.52}Mn_{0.04}Ti_{0.02}Al_{0.93})(Al_{2.31}Si_{5.69})O_{22}(OH)_2 +$

Opx Spl

$7.93\ (Fe_{0.37}Mg_{0.68}Mn_{0.01}Ca_{0.002})(Al_{0.001}Si_{0.98})O_3 + 0.503\ (Fe_{0.66}Mg_{0.34}Mn_{0.02})(Al_{1.90}Fe_{0.10})O_4$

Crn

$+ 0.19\ Al_2O_3$

<u>Verification:</u>

	Reactants	=	Products
Mg	8.004	=	8.007
Fe	5.336	=	5.286
Na	0.973	=	0.981
Ca	1.807	=	1.800
Al	4.583	=	4.620
Si	13.350	=	13.460
O	49.940	=	50.170

Legend for Appendix I

T^1 = Fe^{2+}-Mg exchange between orthopyroxene and clinopyroxene assemblage by Kretz (1982)
T^2 = Ca-Mg transfer reaction between orthopyroxene and clinopyroxene by Kretz (1982)
T^3 = Fe^{2+}-Mg exchange between garnet and hornblende by Graham and Powell (1984)
T^4 = Fe^{2+}-Mg exchange between garnet and ilmenite of Pownceby and O'Neil (1987)
T^5 = Ilmenite - Magnetite geothermometer of Spencer and Lindsley (1981)
T^6 = Fe^{2+}-Mg exchange between clinopyroxene and hornblende by Kretz and Jen (1978)
T^7 = Fe^{2+}-Mg exchange between garnet and biotite by Thompson (1976)
T^8 = Fe^{2+}-Mg exchange between garnet and biotite by Perry and Spear (1978)
T^9 = Fe^{2+}-Mg exchange between garnet and biotite by Hodges and Spear (1982)
T^{10}= Fe^{2+}-Mg exchange between garnet and biotite by Ganguly and Saxena (1984)
T^{11}= Fe^{2+}-Mg exchange between garnet and biotite by Perchuck et al. (1985)
T^{12}= Fe^{2+}-Mg exchange between garnet and clinopyroxene by Ellis and Green (1979)
taking into consideration the effect of Ca in Grt and Cpx.
T^{13}= Fe^{2+}-Mg exchange between garnet and clinopyroxene by Ganguly (1979)
T^{14}= Fe^{2+}-Mg exchange between garnet and clinopyroxene by Dahl (1980)
T^{15}= Fe^{2+}-Mg exchange between garnet and orthopyroxene by Powell (1978)
T^{16}= Fe^{2+}-Mg exchange between garnet and orthopyroxene by Harley (1984)
T^{17}= Fe^{2+}-Mg exchange between garnet and orthopyroxene by Sen and Bhattacharya (1984)
T^{18}= Fe^{2+}-Mg exchange between orthopyroxene and clinopyroxene by Wood and Banno (1973)
T^{19}= Fe^{2+}-Mg exchange between orthopyroxene and clinopyroxene by Well (1977)
T^{20}= Fe^{2+}-Mg exchange between orthopyroxene and clinopyroxene by Bertrand and Mercier (1985)

P^1 = Aluminum in hornblende by Hammarstrom and Zen (1986)
P^2 = Cpx-Plag-Qtz geobarometer by Ellis (1980)
P^3 = Grt-Plag-Opx-Qtz geobarometer by Perkins and Newton (1981)

Abbreviations:

Opx = orthopyroxene
Cpx = clinopyroxene
Prg = pargasite
Hbl = hornblende
Grt = garnet
Mag = magnetite
Ilm = ilmenite
Plag = plagioclase
Bt = biotite
(m) = metamorphic
(p) = primary, igneous

Appendix I. Pressure-Temperature estimates for the NMB diabase dykes.

Sample Number	Assemblage	Temperature (°C)	Pressure (kbar)
		T^2	P^1
CMA-LA18	Opx(m)-Cpx(p) $Cpx_{core(rim)}$	1103 (1088)	
	Opx(m)-Cpx(p)	1069 (1082)	
	Opx(m)-Cpx(p)	1108 (1088)	
	Al in Pargasite around olivine corona		13.2
	Al in Pargasite around olivine corona		12.5
	Al in Pargasite around olivine corona		13.5
	Al in Pargasite around olivine corona		10.6
CMA-LGY	Opx(m)-Cpx(p) $Cpx_{core(rim)}$	1057 (1177)	
	Opx(m)-Cpx(p)	1082 (1158)	
	Opx(m)-Cpx(p)	1240 (1088)	
	Al in Pargasite around olivine corona		12.3
	Al in Pargasite around olivine corona		13.4
	Al in Pargasite around olivine corona		13.5

Sample Number	Assemblage	Temperature (°C)				Pressure (kbar)
		T^2	T^3	T^4	T^5	P^1
CMA-27.6.5	Opx(m)-Cpx(p) $Cpx_{(rim)}$	(1062)				
	Opx(m)-Cpx(p) $Cpx_{core(rim)}$	1060 (1093)				
	Opx(m)-Cpx(p) $Cpx_{(rim)}$	(1086)				
	Opx(m)-Cpx(p) $Cpx_{(rim)}$	(1196)				
	Grt in Prg corona layer		692			11.8
			672			12.0
			771			12.0
			686			12.3
	Grt-Ilm, garnet corona layer			611		
	Ilm-Mag, ilmenite exsolution in magnetite				488	
					543	

Appendix I (continued)

Sample Number	Assemblage	Temperature (°C)		Pressure (kbar)
		T[2]	T[6]	P[1]
CMA-79DI86	In Host Rock			
	Opx(m)-Cpx(p)	(478)		
	$Cpx_{(rim)}$	(570)		
		(752)		
		(670)		
	Al in Prg corona			6.1
	In the Segregations			
	$Opx(m)-Cpx(p)_{core}$	577		
	$Cpx_{(rim)}$	(655)		
	Cpx_{core}	738		
	$Cpx_{(rim)}$	(611)		
		(657)		
	Cpx_{core}	856		
		606		
		(434)		
	Cpx_{core}	519		
	Cpx(p)-Prg corona		654-927	9.2
	K_D= 1.66			
	Cpx(p)-Prg corona		986	7.4
	K_D= 2.71			
	Al in Prg corona			8.9

Appendix I (continued)

Sample Number	Assemblage	Temperature (°C)								Pressure (kbar)		
		T^2	T^3	T^6	T^7	T^8	T^9	T^{10}	T^{11}	P^1		
CMA-27.6.3	Opx(m)-Cpx(p)$_{rim}$	(528)										
	Opx(m)-Cpx(p)$_{core}$	1172										
	Opx(m)-Cpx(p)$_{core}$	1021										
	Opx(m)-Cpx(p)$_{rim}$	(1242)										
	Cpx(p)$_{core}$	1195										
	Opx(m)-Cpx(p)$_{core}$	1133										
	Grt-Hbl around		593							4.2		
	Opx+Mag symplectite		619							4.7		
	Cpx(p)-Prg corona											
	K_D= 1.52			727-905						4.7		
	K_D= 1.76			935						5.7		
	K_D= 1.70			654-927						6.0		
	Grt-Bt corona around Mag grain				620	655	747	650	725			
		T^{12}	T^{13}	T^{14}	T^{15}	T^{16}	T^{17}			P^1	P^2	P^3
	Grt-Cpx(p)$_{rim}$	775	840	775							6.5	8.8
		660	755	605							8.6	7.2
	Grt-Opx(m)				565	605	645				8.3	

Sample Number	Assemblage	Temperature (°C)							Pressure (Kbars)
		T^2	T^3	T^7	T^8	T^9	T^{10}	T^{11}	P^1
CMA-LG7	Opx(m)-Cpx(p)$_{core}$	1141							
	Grt-Hbl around		543						11.1
	Opx-Mag symplectite		533						7.1
			507						7.4
			544						10.5
	Al in Prg corona								8.6
	Grt-Bt corona layer			433	415	458	495	569	
				508	507	540	580	677	
				440	425	467	506	575	

Appendix I (continued)

Sample Number	Assemblage	Temperature (°C)						Pressure (kbar)
		T^{1}	T^{2}	T^{5}	T^{12}	T^{13}	T^{14}	P^{1}
CMA-015A	Opx(m)-Cpx(p)$_{(rim)}$		(464)					
	Opx(m)-Cpx(p)$_{core}$		1249					
	Opx(m)-Cpx(p)$_{(rim)}$		(495)					
	Opx(m)-Cpx(m)	345						
		399						
	Ilm-Mag, ilm exsolution in magnetite			366				
	Grt-Cpx(p)				695	775	647	
	Al in Hbl							8.4

		T^{15}	T^{16}	T^{17}	T^{18}	T^{19}	T^{20}
	Grt-Opx(m)	500	543	587			
	Opx(m)-Cpx(p)$_{(rim)}$				1053	1169	1205
	Opx(m)-Cpx(p)$_{core}$				777	759	695
	Opx(m)-Cpx(p)$_{core}$				681	634	598

Sample Number	Assemblage	Temperature (°C)					Pressure (kbar)
		T^{2}	T^{6}	T^{12}	T^{13}	T^{14}	P^{3}
CMA-M-V01	Opx(m)-Cpx(p)$_{core}$	656					
		933					
		903					
	Opx(m)-Cpx(m)	494					
	Cpx(p)-Hbl						
	K_D= 1.17	2					
	K_d= 1.76	638					
	Grt-Cpx(p)$_{(rim)}$			665	771	659	8.5
				660	770	659	8.6

Appendix I (continued)

Sample Number	Assemblage	Temperature (°C)					Pressure (kbar)
		T^2	T^3	T^5	T^6		P^1
CMA-M-R01A	Opx(m)-Cpx(p)$_{core}$	1069					
		1158					
		1073					
	Opx(m)-Cpx(m)	675					
	Grt-Hbl rims		524				6.6
			473				6.6
	Al in Hbl grains						8.1
							4.9
							4.3
							6.4
	Ilm-Mag, ilm exsolution in magnetite			648			
	Cpx(p)-Hbl corona layer						
	K_D= 1.97				949		
	K_D= 2.41				970		
	K_D= 1.28				800-859		
		T^7	T^8	T^9	T^{10}	T^{11}	
	Grt-Bt rims	413	390	425	477	540	

Appendix I (continued)

Sample Number	Assemblage	Temperature (°C)								Pressure (kbar)
		T^2	T^3	T^6	T^7	T^8	T^9	T^{10}	T^{11}	P^1
CMA-146	Opx(m)-Cpx(p)$_{core}$	902								
		673								
		654								
	Grt-Hbl rims		532							7.1
			557							7.6
			648							8.6
			675							11.2
	Grt-Hbl cores		517							
			540							
			625							
			650							
	Cpx(p)-Hbl									
	K_D= 1.33			791-870						
	Grt-Bt rims				485	478	525	551	605	
	cores				418	397	448	478	576	
	Grt-Bt rims				481	473	523	552	606	
	cores				447	436	474	510	576	

Figure 15

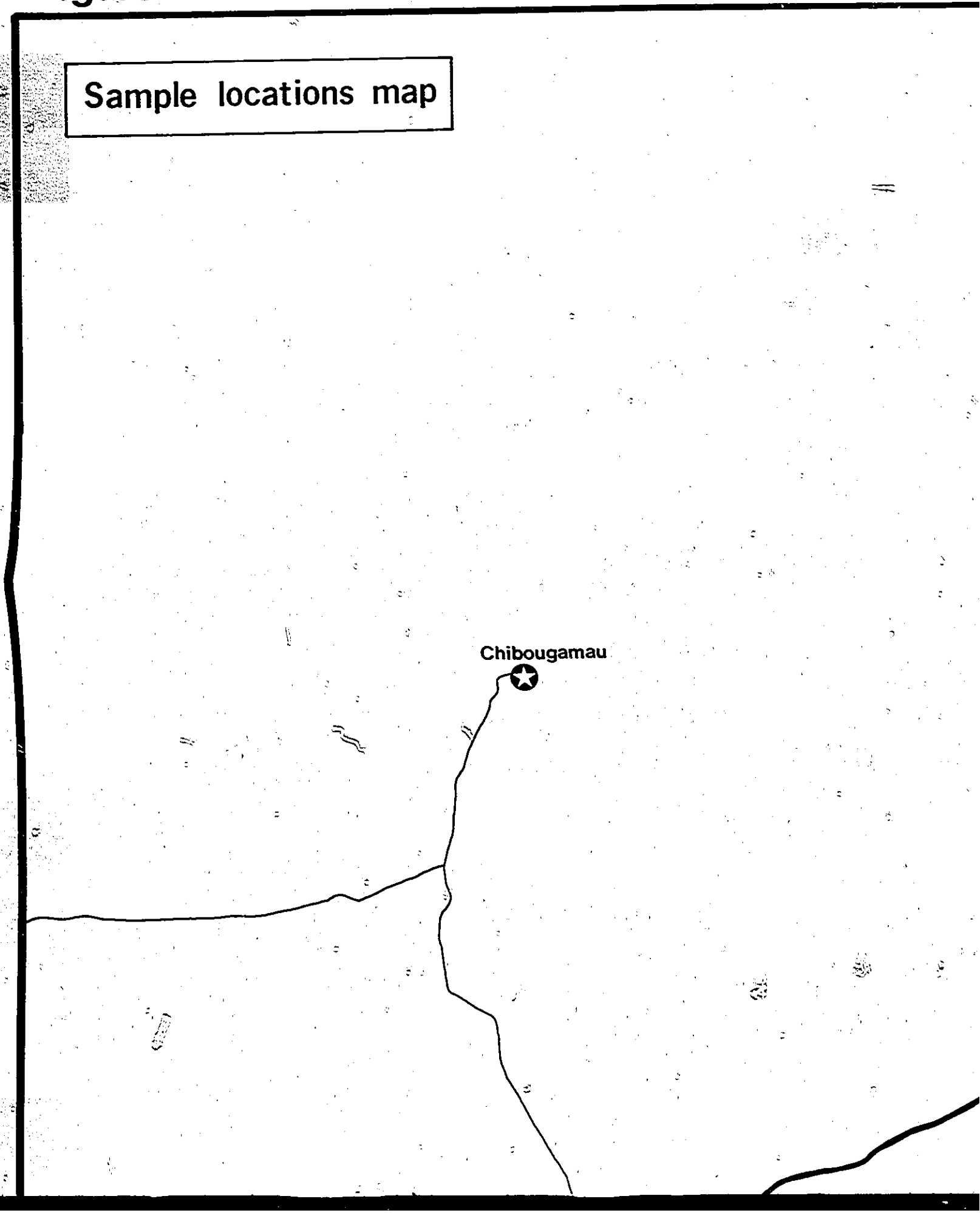

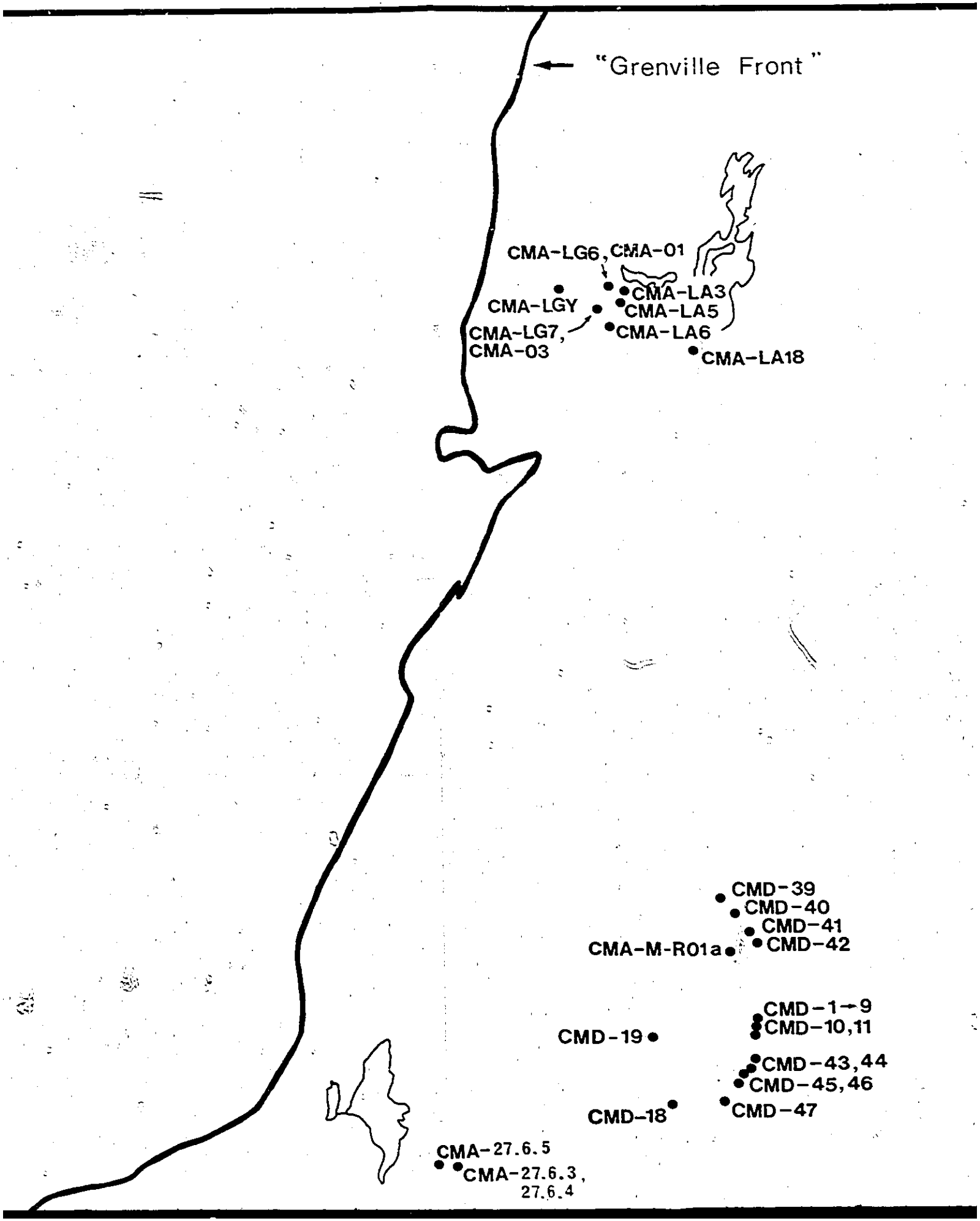
"Grenville Front"
CMA-LG6, CMA-01
CMA-LA3
CMA-LGY
CMA-LA5
CMA-LG7, CMA-03
CMA-LA6
CMA-LA18
CMD-39
CMD-40
CMD-41
CMA-M-R01a
CMD-42
CMD-1-9
CMD-10,11
CMD-19
CMD-43,44
CMD-45,46
CMD-18
CMD-47
CMA-27.6.5
CMA-27.6.3, 27.6.4


50° 15'

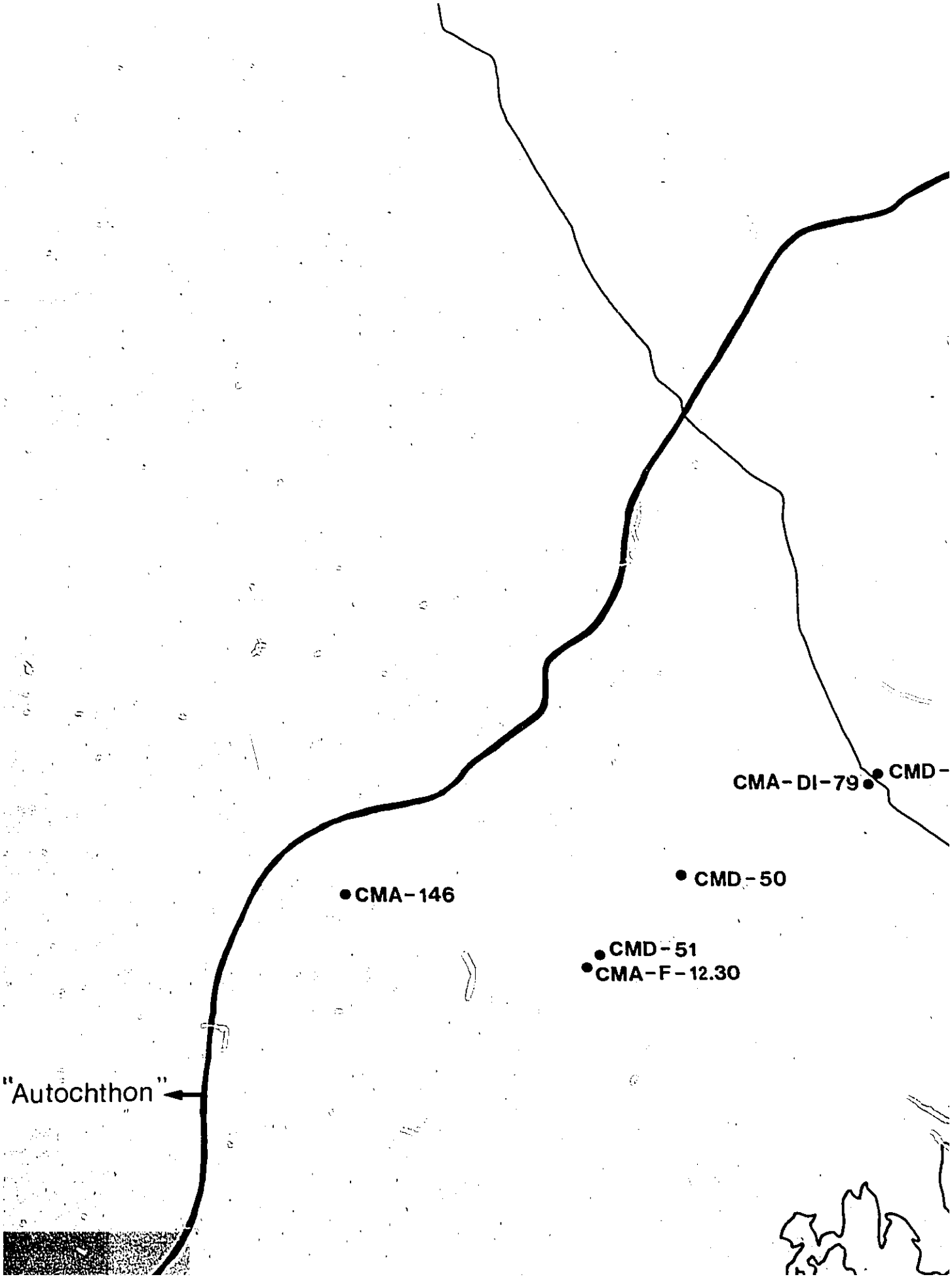
CMA-DI-79
CMD-
CMD-50
CMA-146
CMD-51
CMA-F-12.30
"Autochthon"

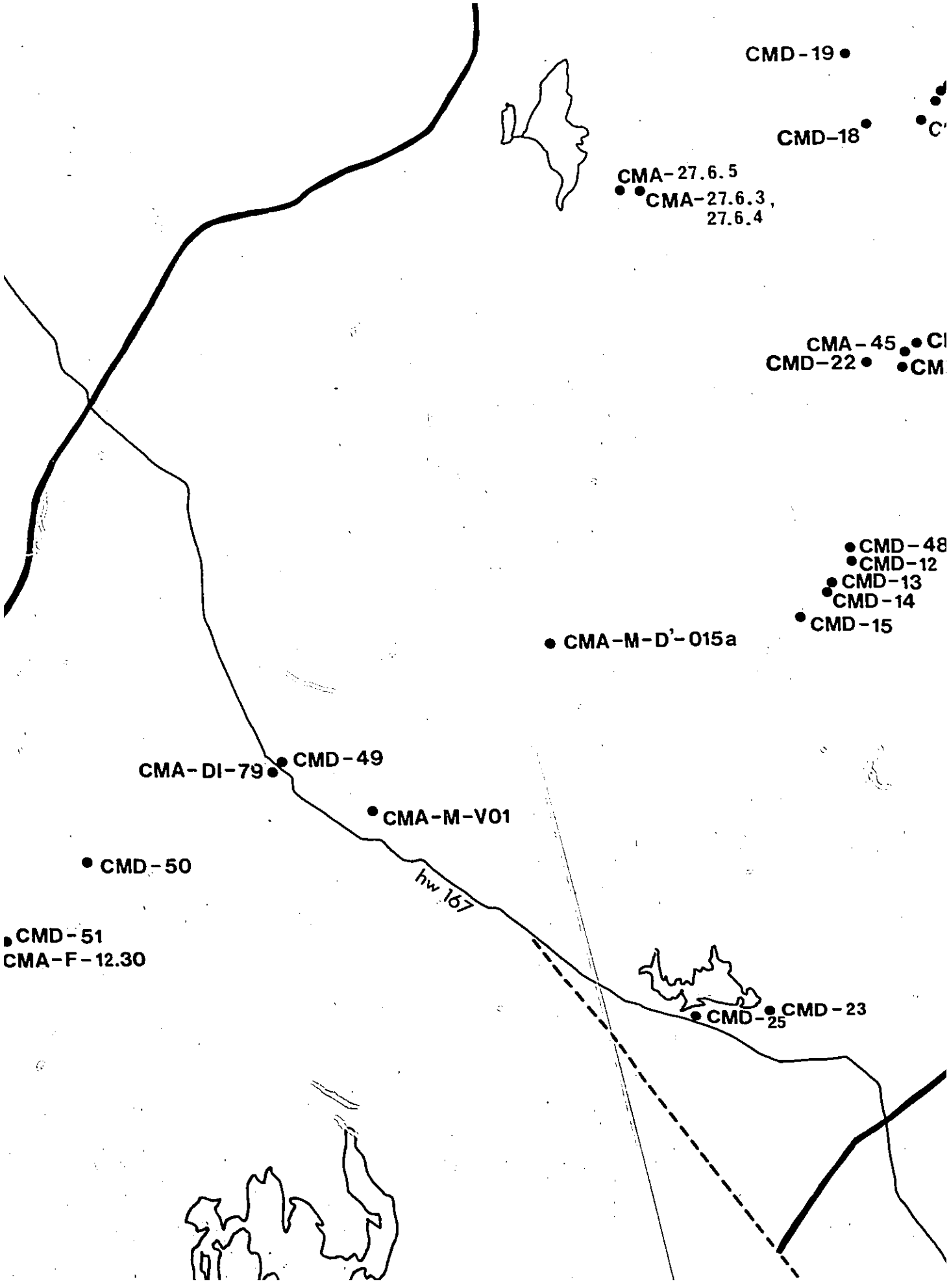
CMD-19
CMD-18
CMA-27.6.5
CMA-27.6.3,
27.6.4
CMA-45
CMD-22
CMD-48
CMD-12
CMD-13
CMD-14
CMD-15
CMA-M-D'-015a
CMA-DI-79
CMD-49
CMA-M-V01
CMD-50
hw 167
CMD-51
CMA-F-12.30
CMD-25
CMD-23

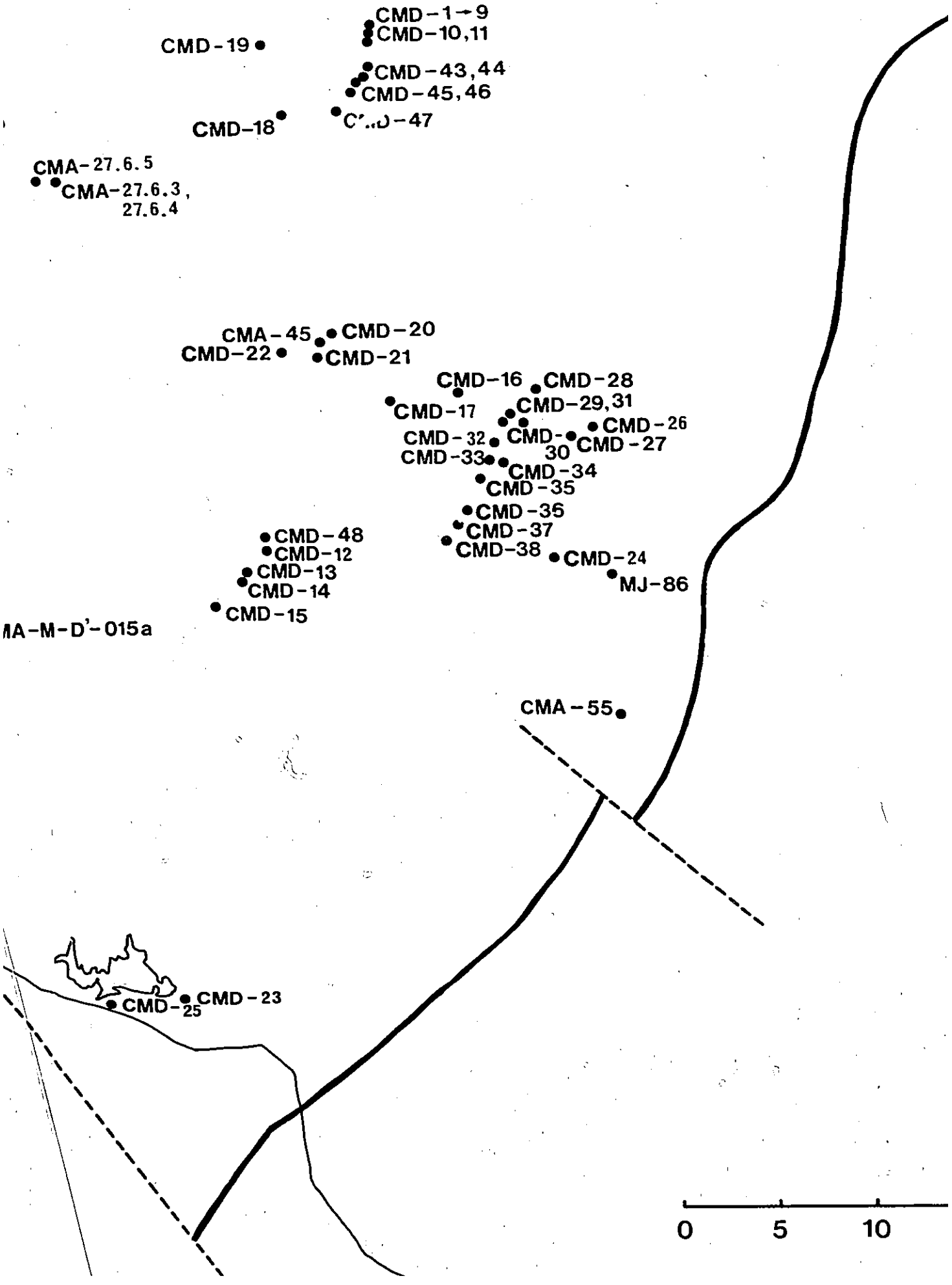
CMD-1→9
CMD-10,11
CMD-19
CMD-43,44
CMD-45,46
CMD-18
CMD-47
CMA-27.6.5
CMA-27.6.3,
27.6.4
CMA-45
CMD-20
CMD-22
CMD-21
CMD-16
CMD-28
CMD-17
CMD-29,31
CMD-26
CMD-32
CMD-30
CMD-27
CMD-33
CMD-34
CMD-35
CMD-36
CMD-37
CMD-48
CMD-38
CMD-12
CMD-24
CMD-13
MJ-86
CMD-14
CMD-15
MA-M-D'-015a
CMA-55
CMD-25
CMD-23
0
5
10

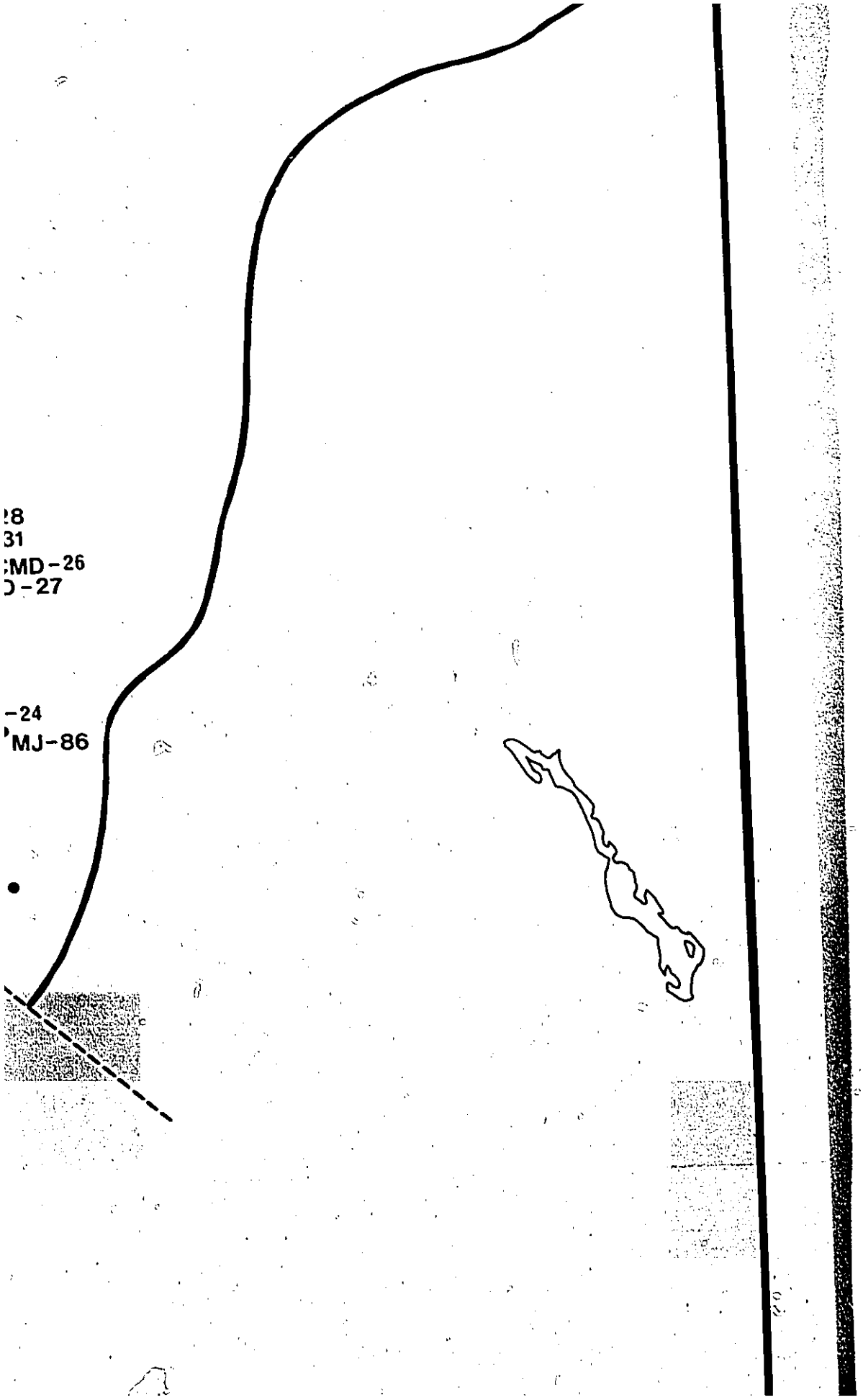
28
31
MD-26
D-27
-24
MJ-86

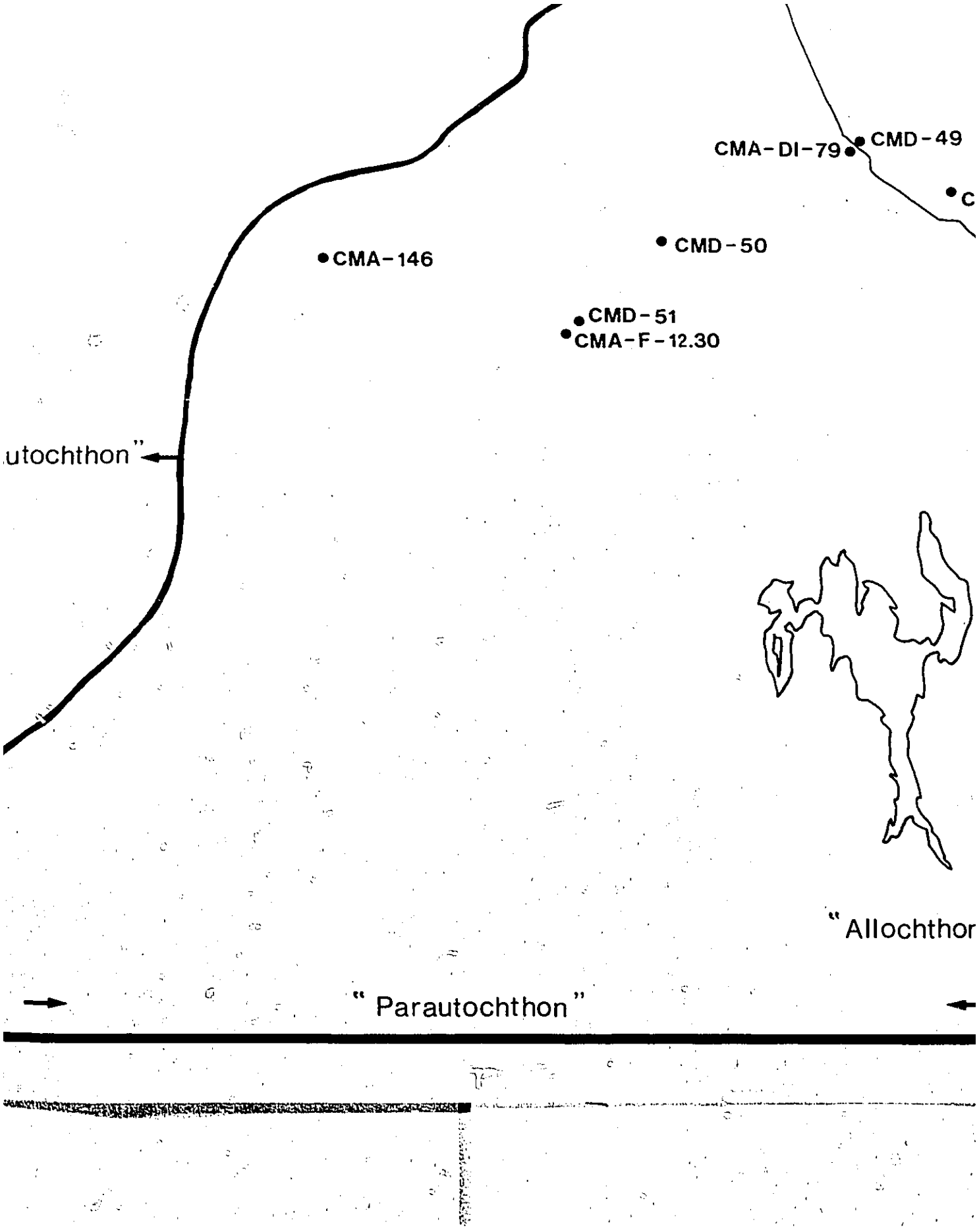
CMA-DI-79
CMD-49
C
CMD-50
CMA-146
CMD-51
CMA-F-12.30
utochthon"
"Allochthor
" Parautochthon"

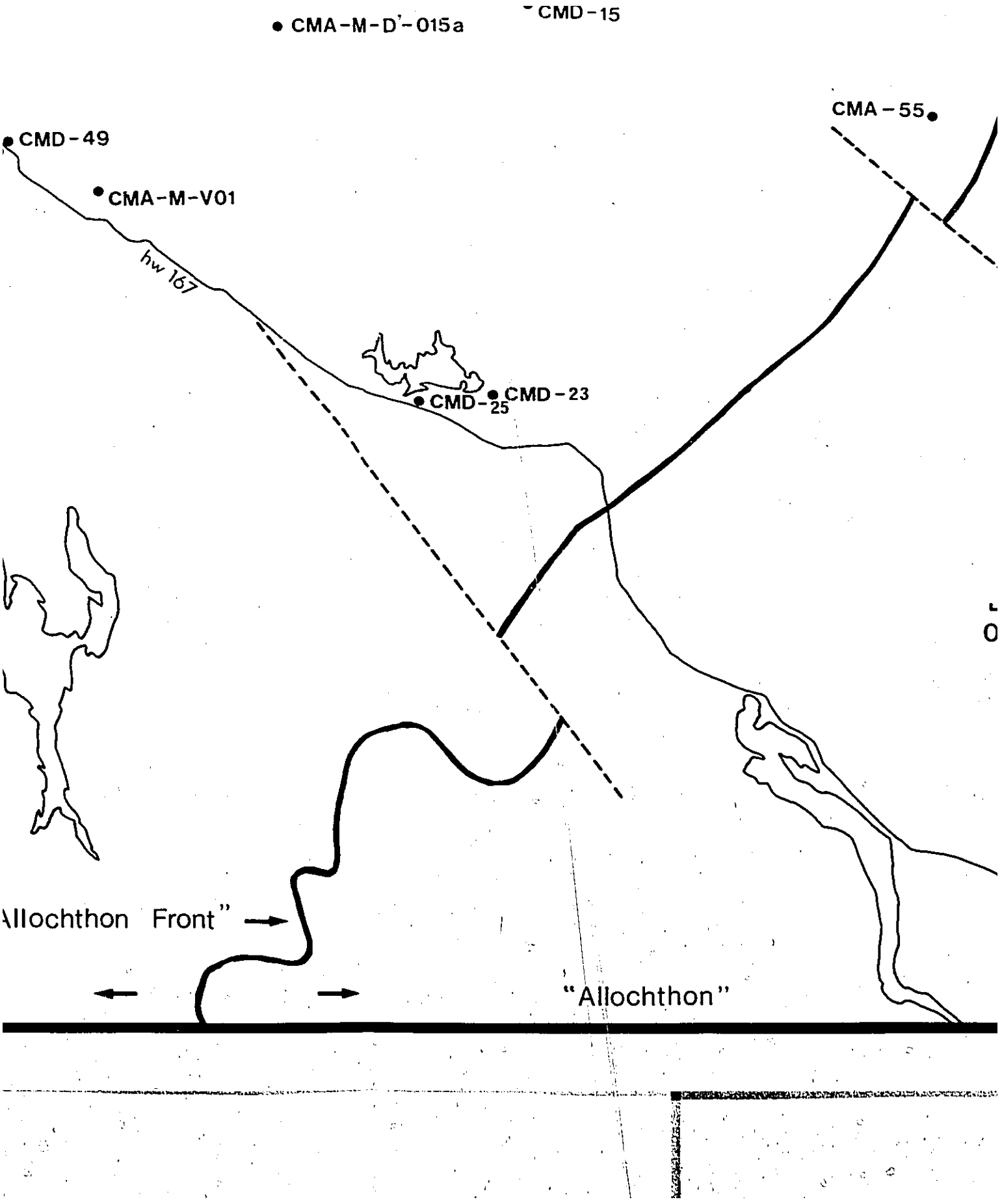
CMA-M-D'-015a
CMD-15
CMA-55
CMD-49
CMA-M-V01
hw 167
CMD-25
CMD-23
Allochthon Front"
"Allochthon"

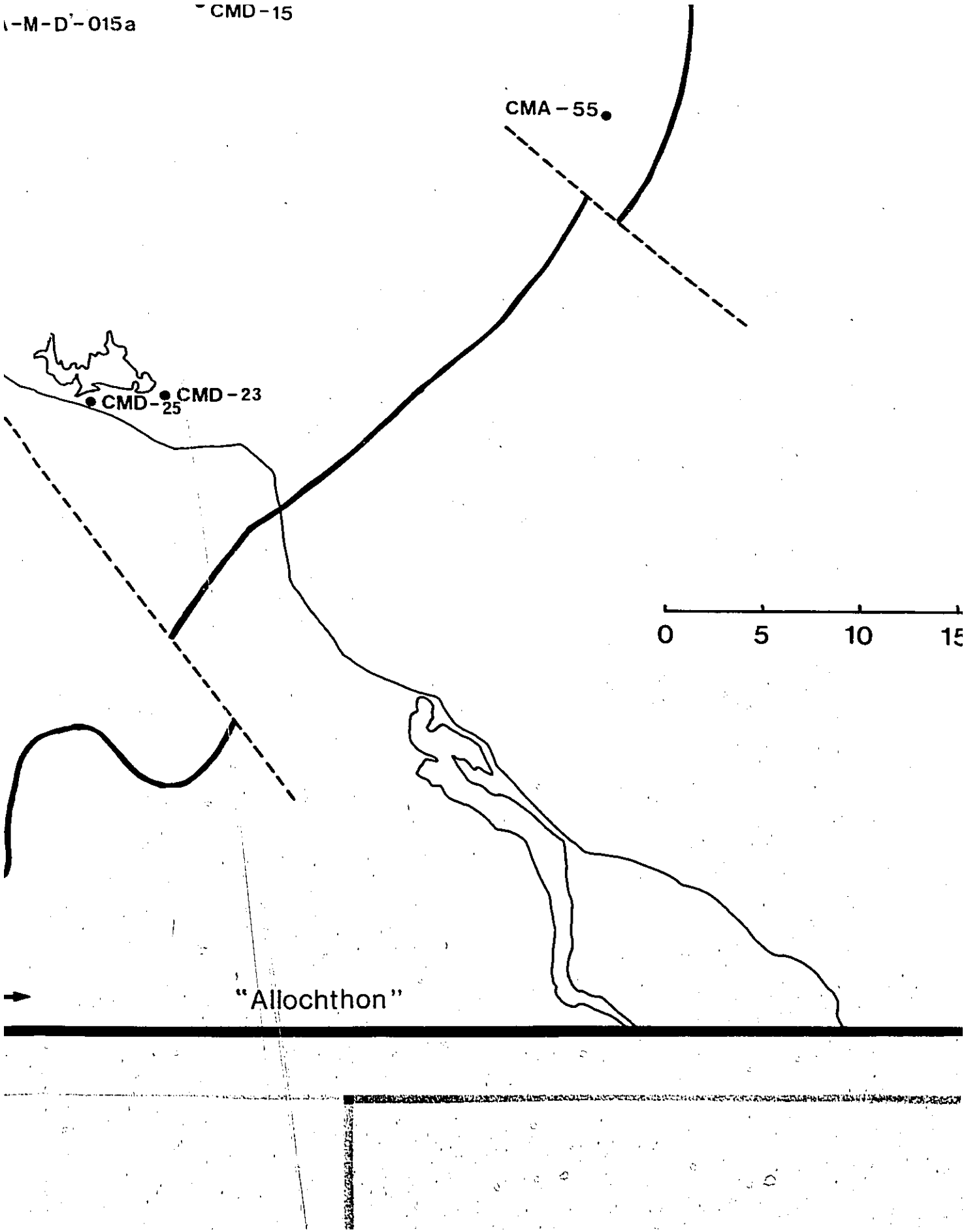
-M-D'-015a
CMD-15
CMA-55
CMD-25
CMD-23
0
5
10
15
"Allochthon"

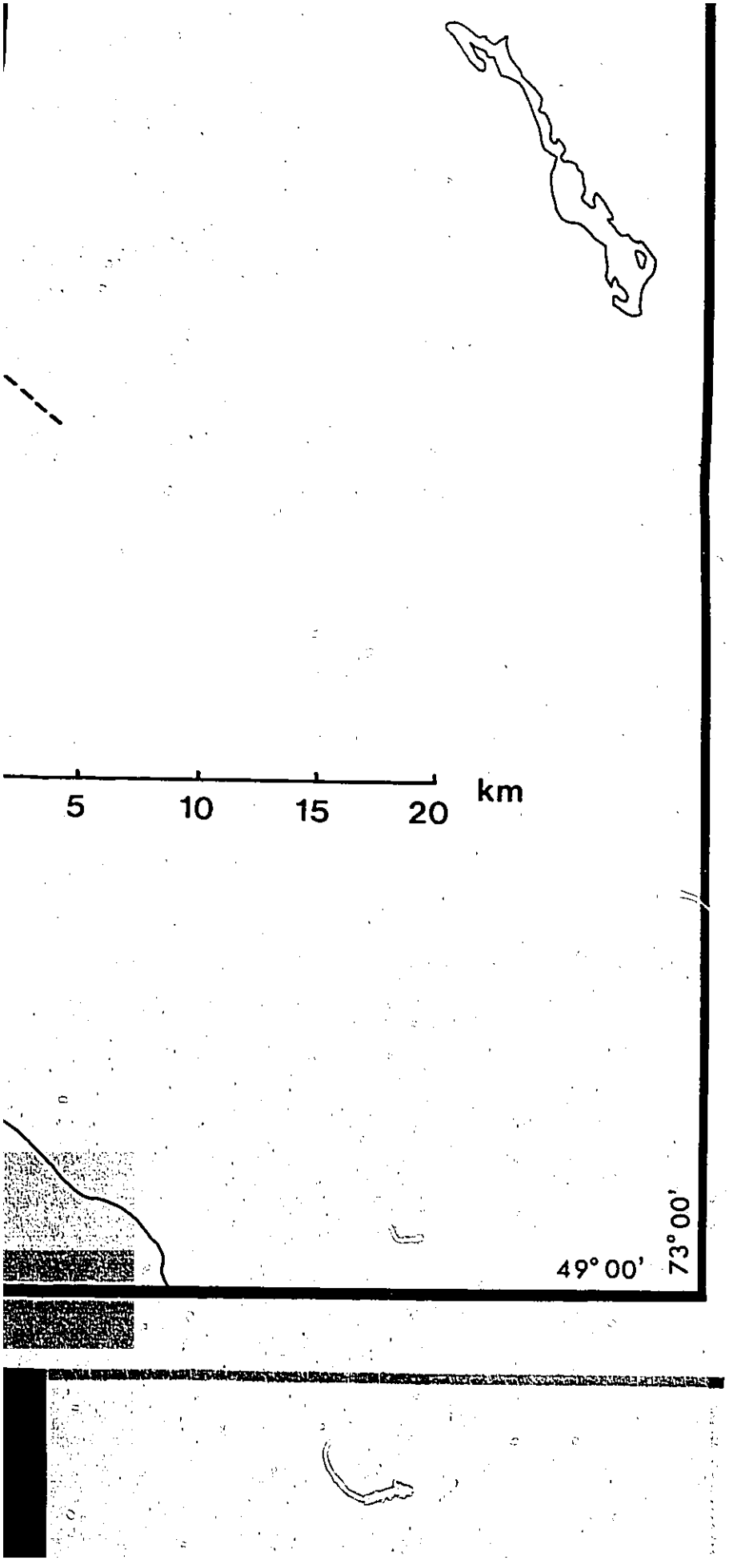
5
10
15
20
km
49° 00'
73° 00'

Figure 16

Distribution of mineral assemblages with respect to sample locations

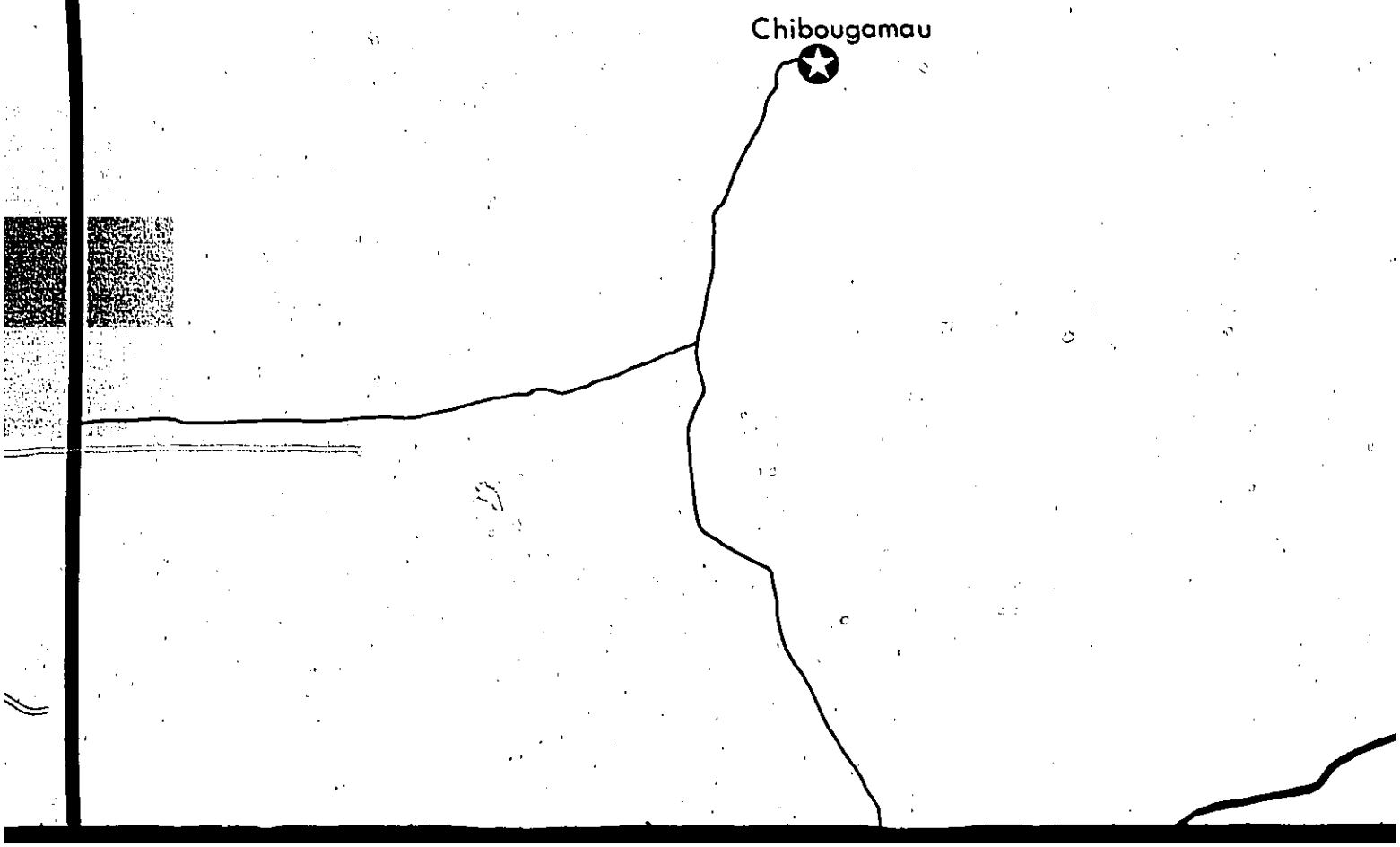

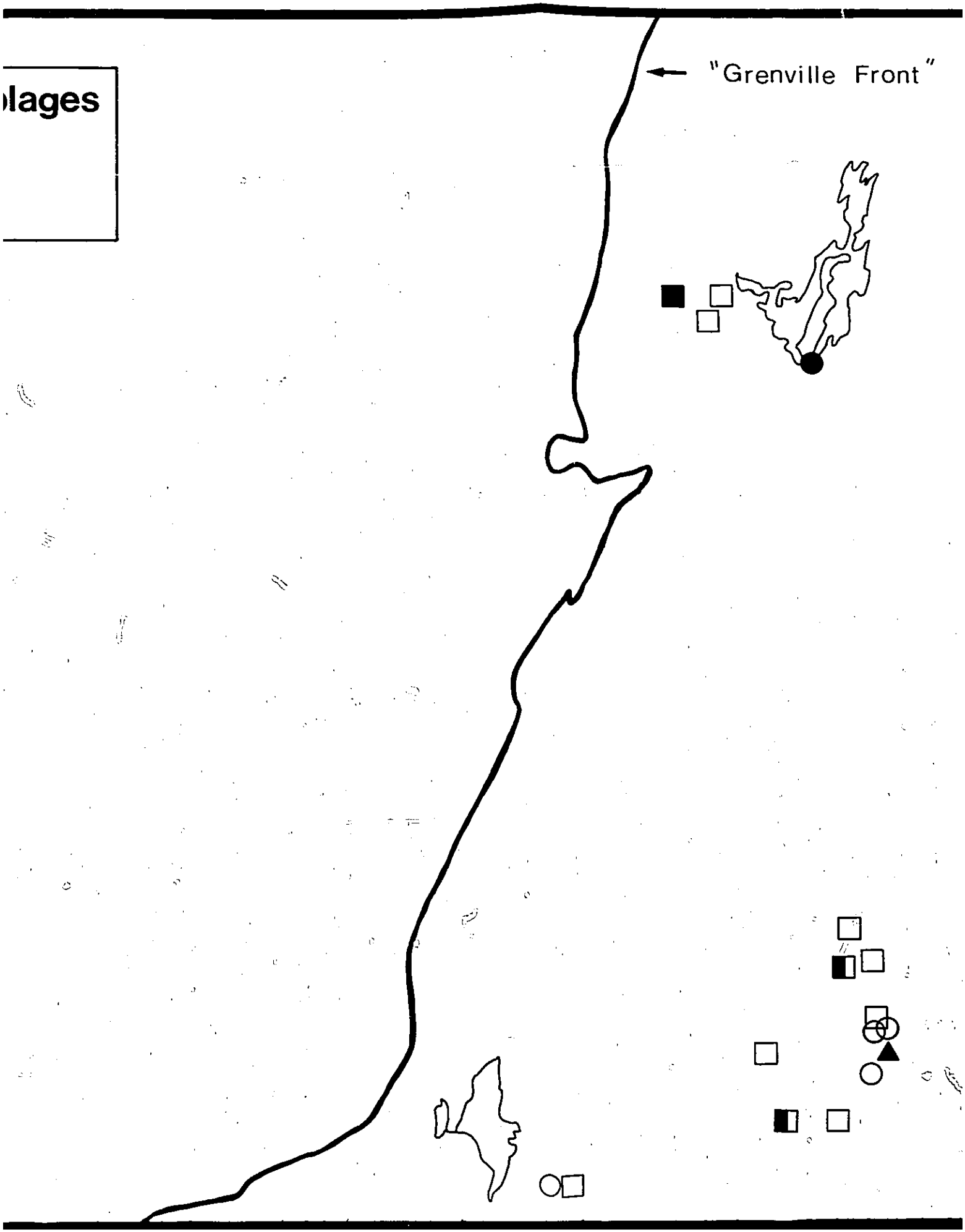
lages
"Grenville Front"

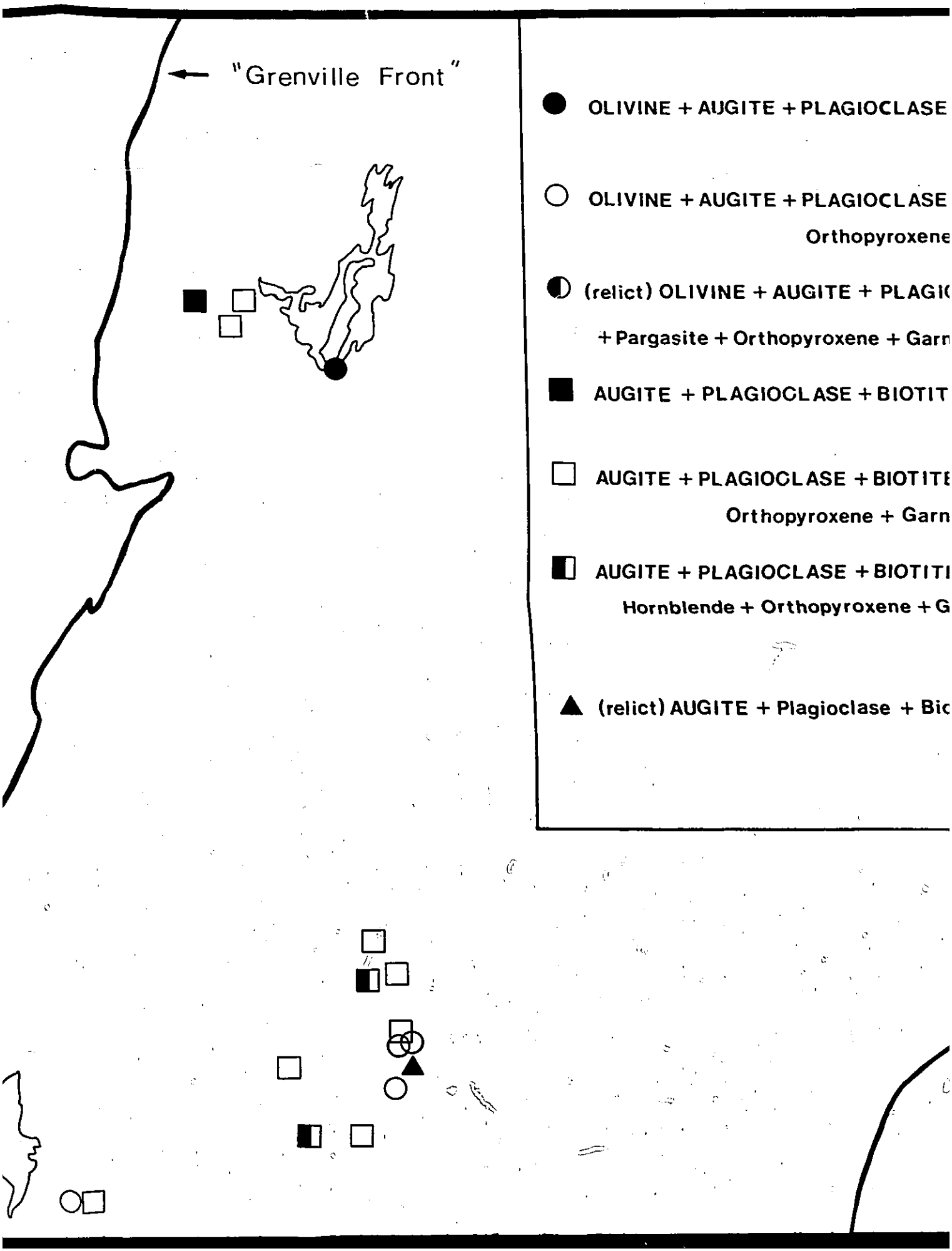
"Grenville Front"
OLIVINE + AUGITE + PLAGIOCLASE
OLIVINE + AUGITE + PLAGIOCLASE
Orthopyroxene
(relict) OLIVINE + AUGITE + PLAGI
+ Pargasite + Orthopyroxene + Garn
AUGITE + PLAGIOCLASE + BIOTIT
AUGITE + PLAGIOCLASE + BIOTITE
Orthopyroxene + Garn
AUGITE + PLAGIOCLASE + BIOTITI
Hornblende + Orthopyroxene + G
(relict) AUGITE + Plagioclase + Bic

50° 15'

● OLIVINE + AUGITE + PLAGIOCLASE + BIOTITE + Pargasite + Orthopyroxene

○ OLIVINE + AUGITE + PLAGIOCLASE + BIOTITE + Pargasite + Orthopyroxene + Garnet + Corundum

◐ (relict) OLIVINE + AUGITE + PLAGIOCIASE + BIOTITE + Biotite + Pargasite + Orthopyroxene + Garnet + Corundum + Spinel

■ AUGITE + PLAGIOCLASE + BIOTITE + Pargasite + Orthopyroxene

□ AUGITE + PLAGIOCLASE + BIOTITE + Pargasite + Orthopyroxene + Garnet + Corundum + Spinel

◧ AUGITE + PLAGIOCLASE + BIOTITE + Biotite + Pargasite + Hornblende + Orthopyroxene + Garnet + Diopside + Corundum + Spinel

▲ (relict) AUGITE + Plagioclase + Biotite + Hornblende + Garnet + Sphene + Calcite

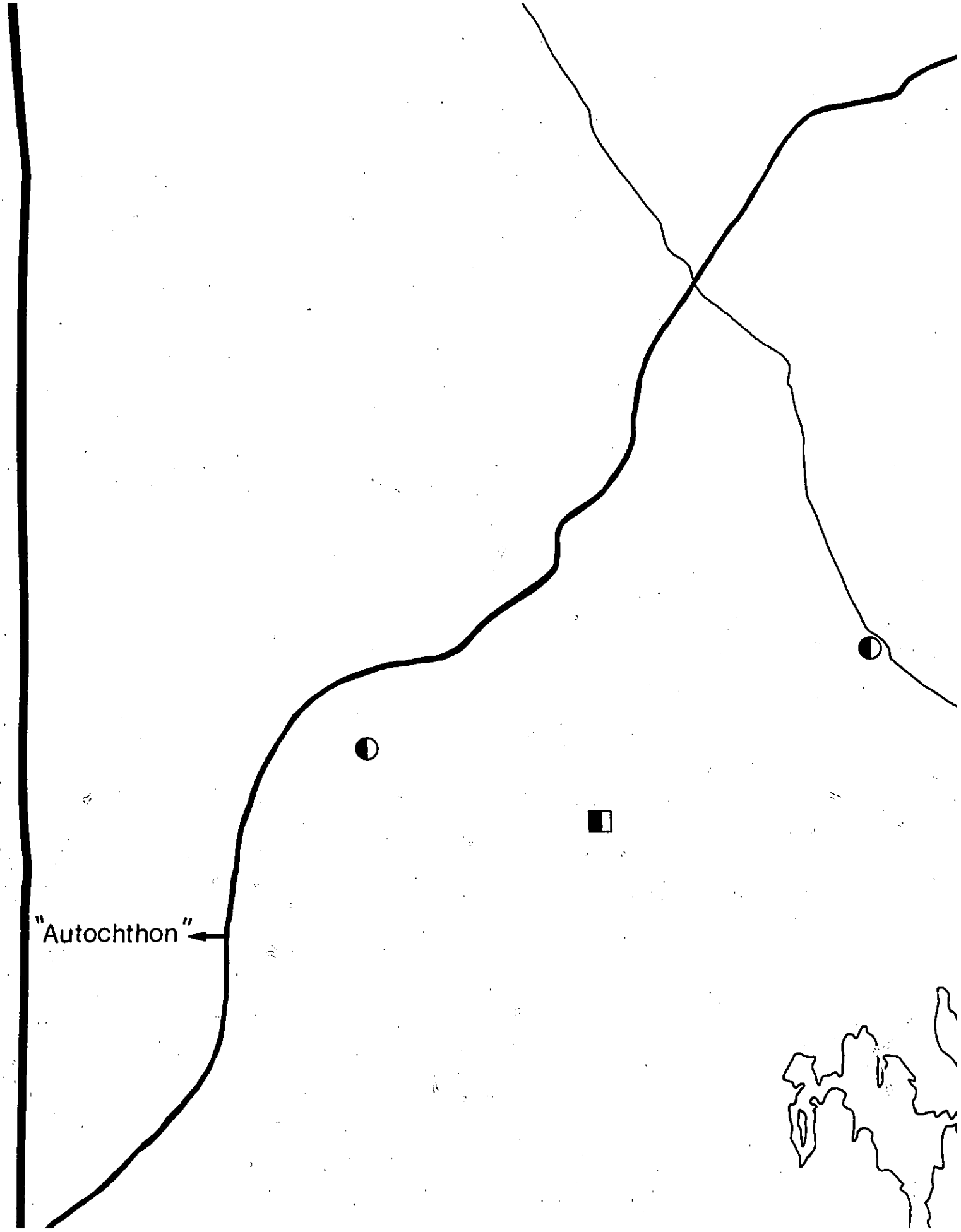
"Autochthon"

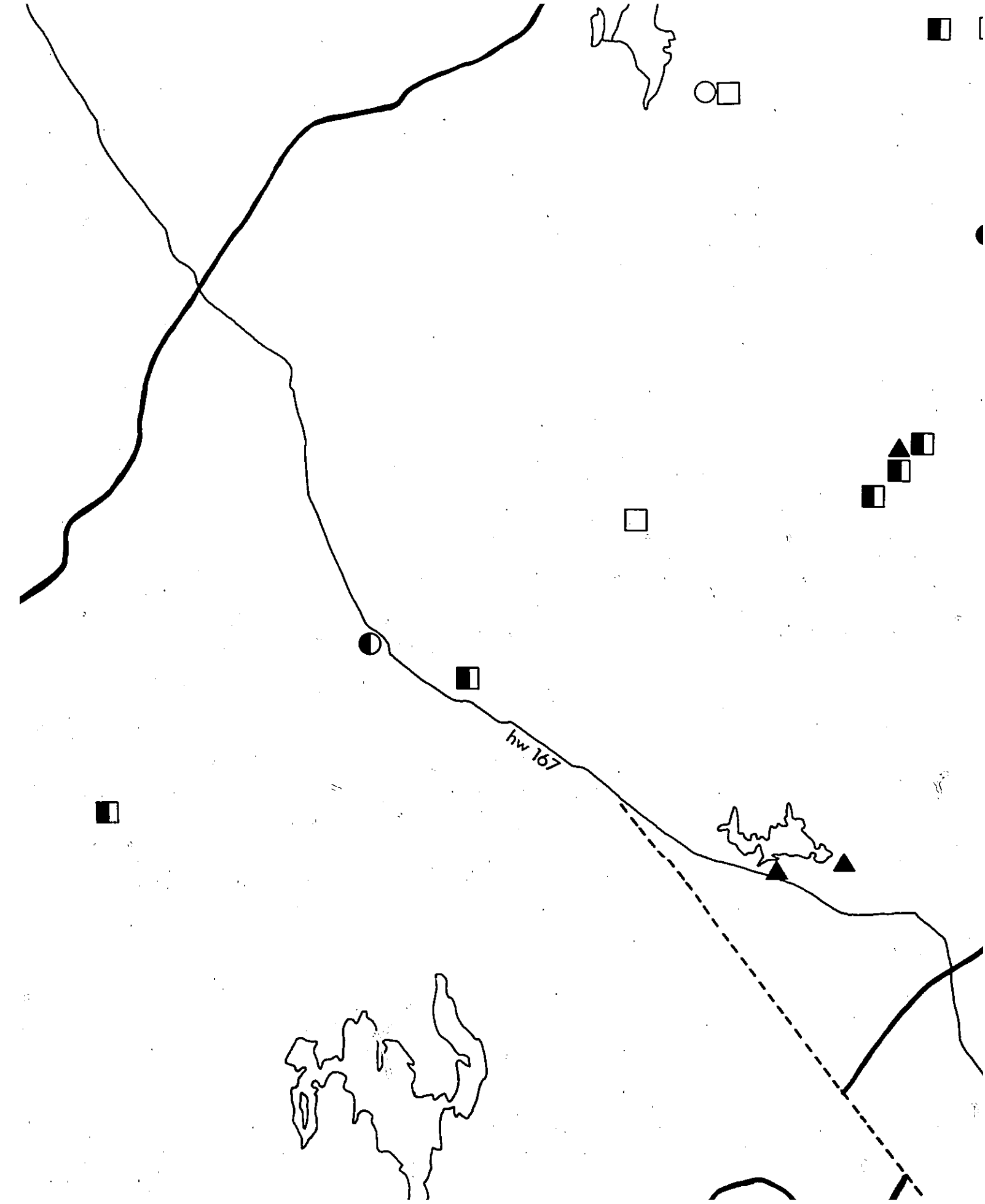
hw 167

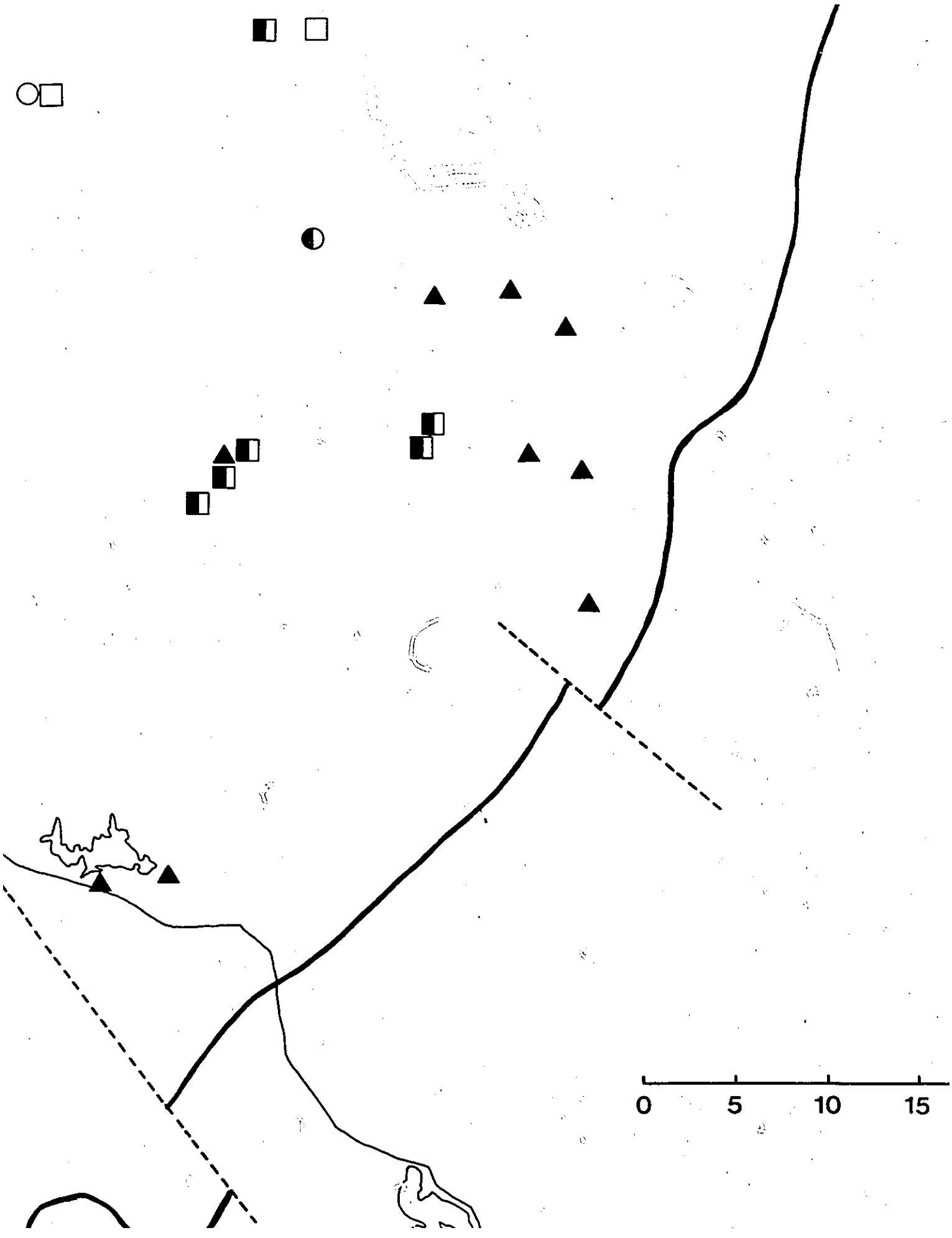
0
5
10
15

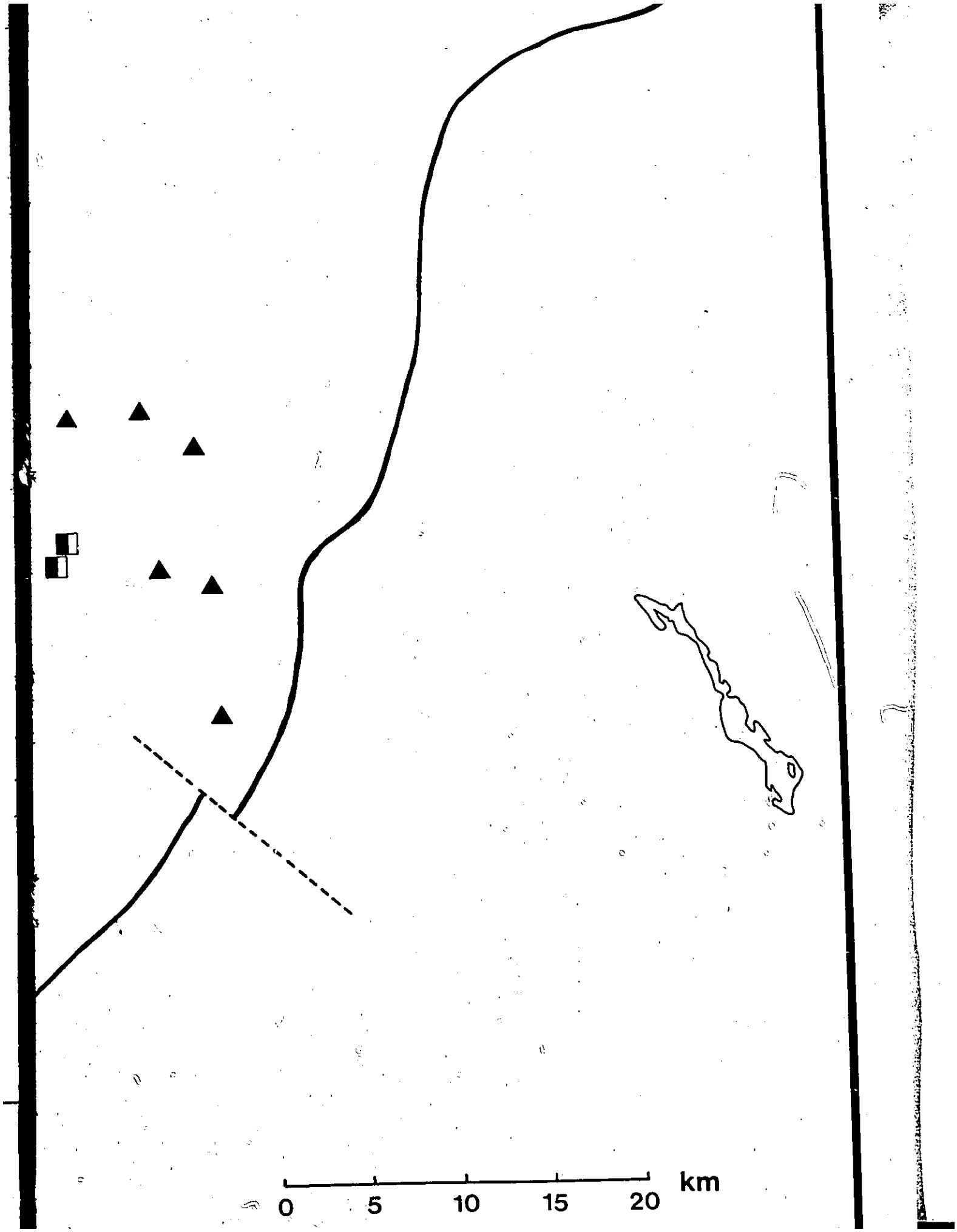
0
5
10
15
20
km

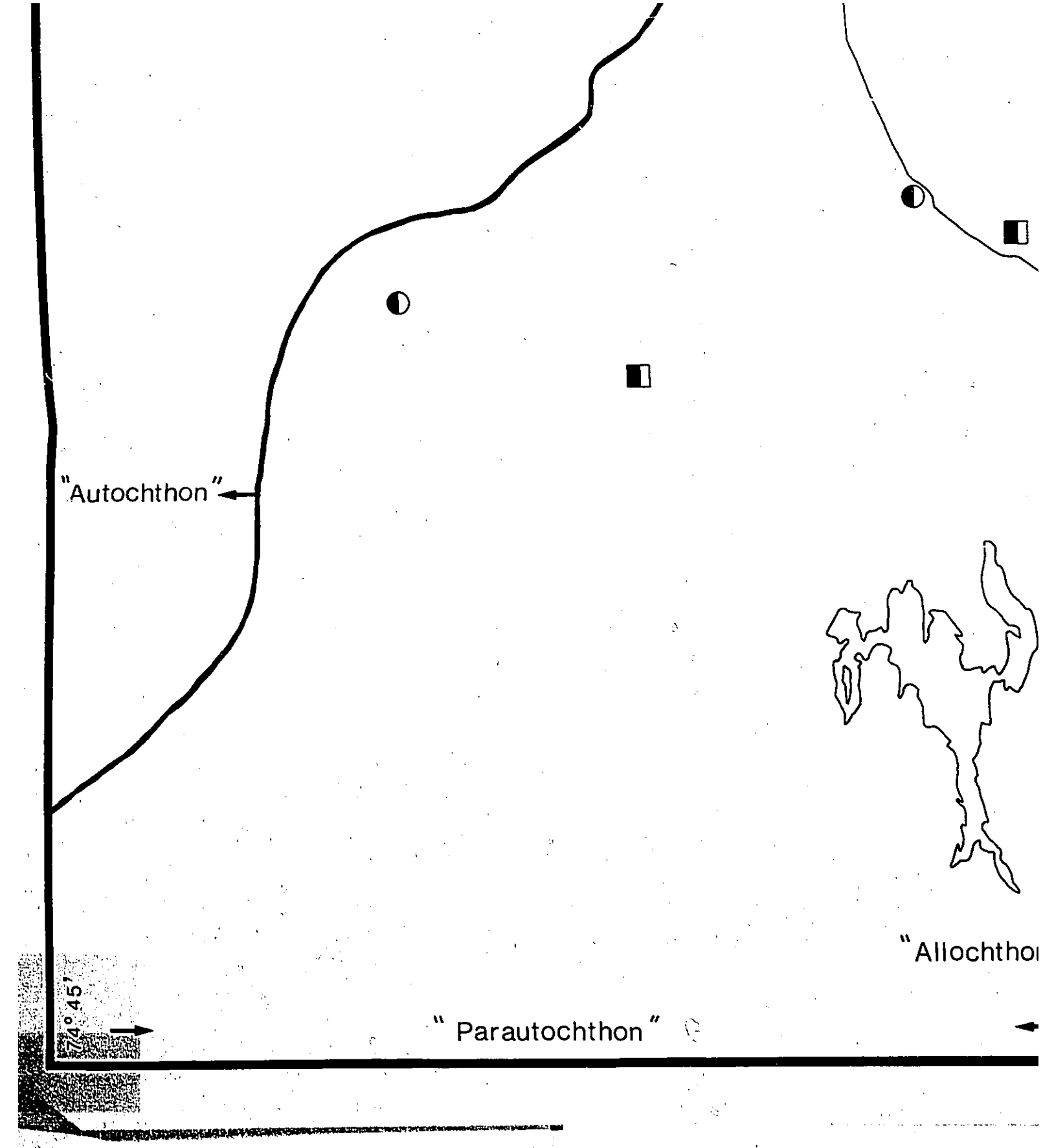
"Autochthon"
"Allochthon
74° 45'
" Parautochthon "

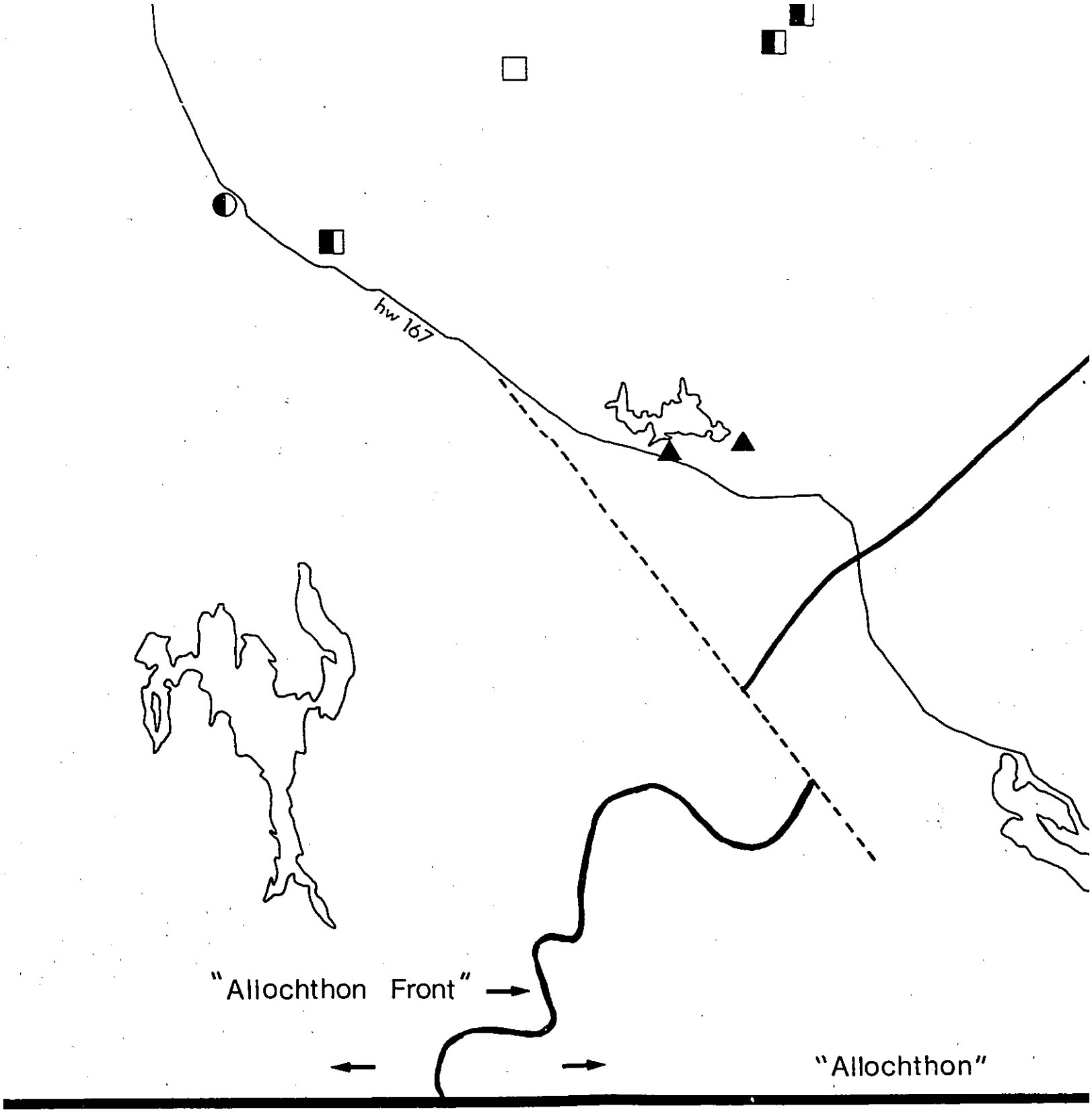
hw 167
"Allochthon Front"
"Allochthon"

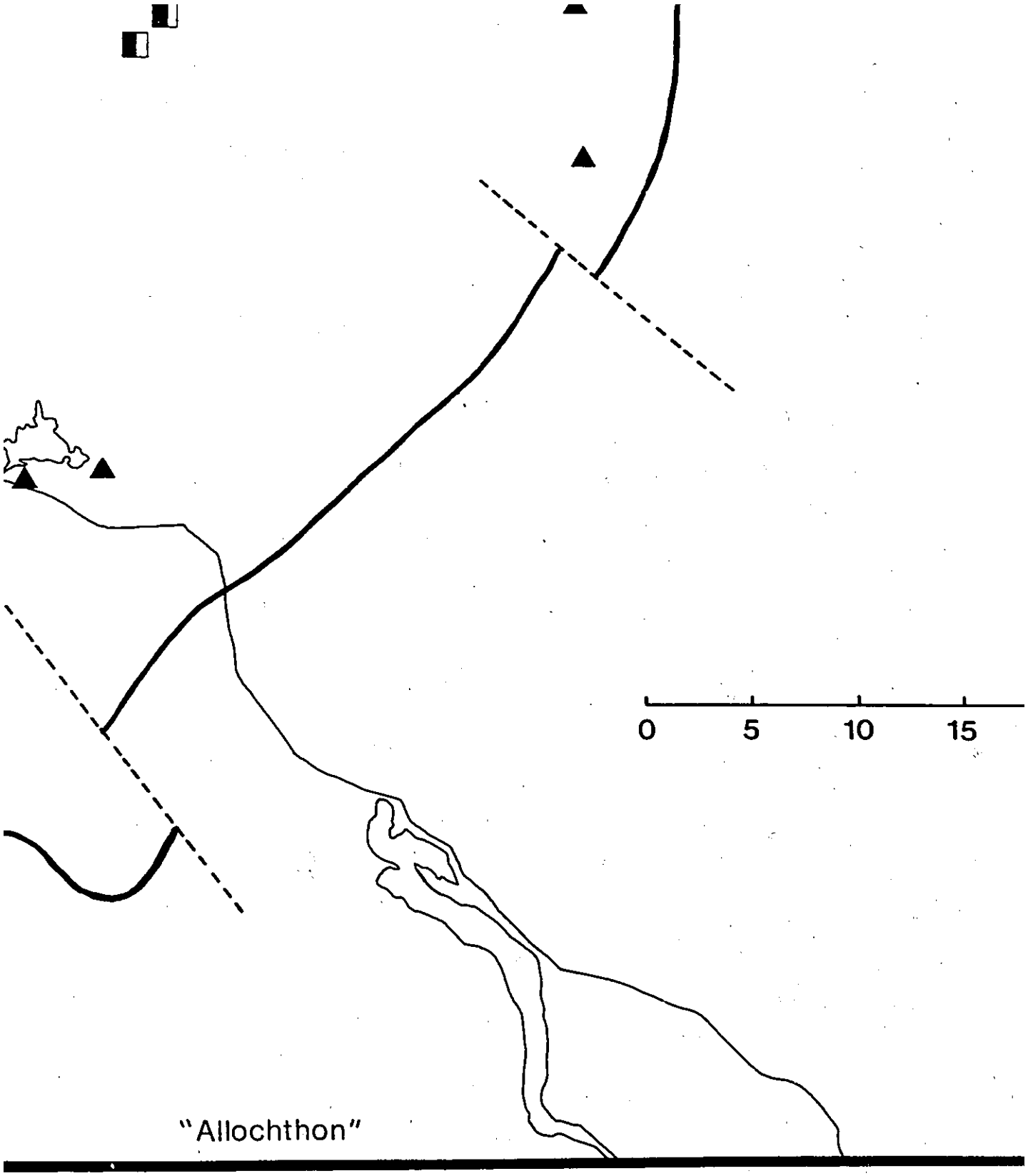
0
5
10
15
"Allochthon"

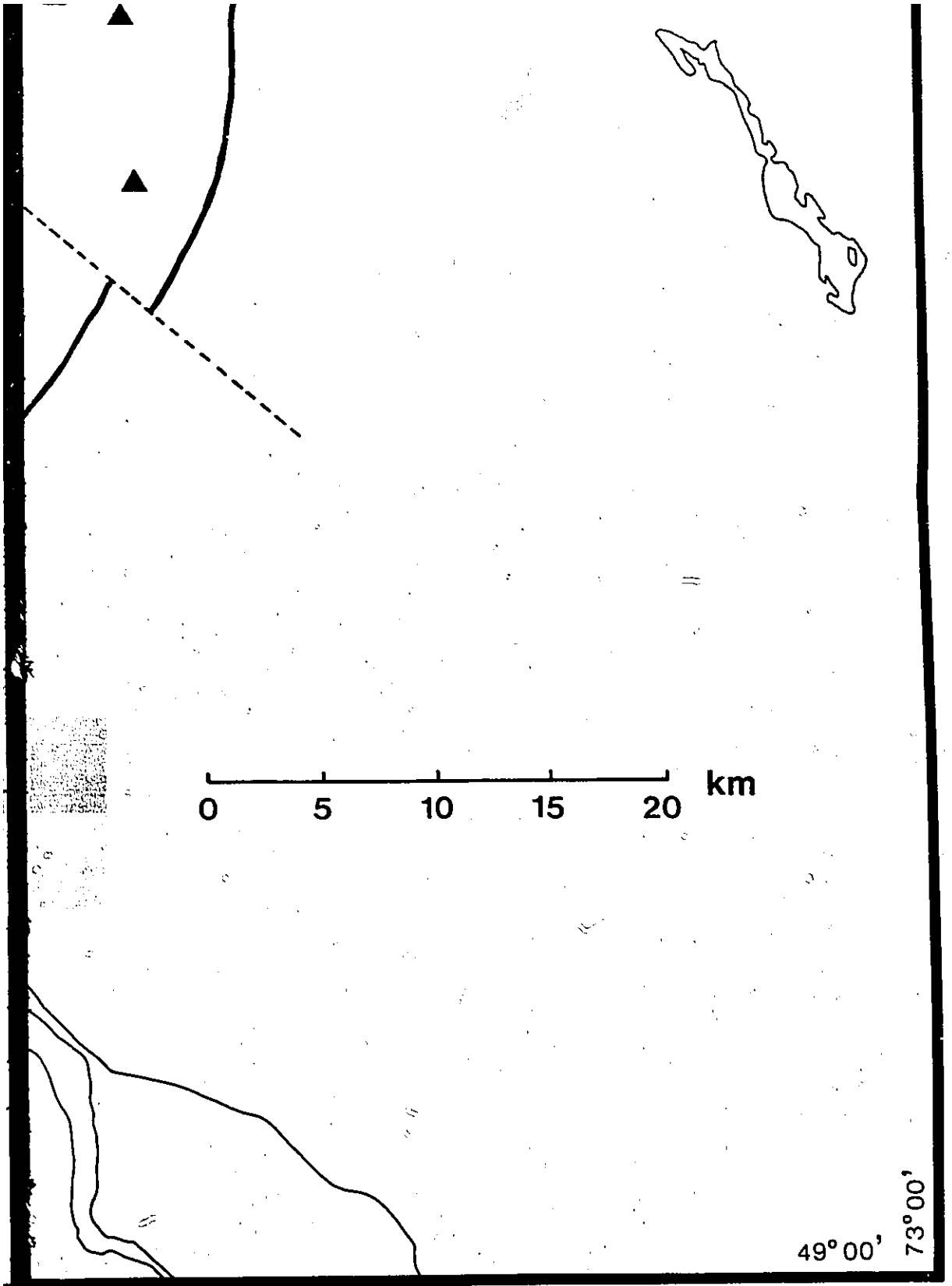
0
5
10
15
20
km
49° 00'
73° 00'

Figure 18

Distribution of corona types with respect to sample locations

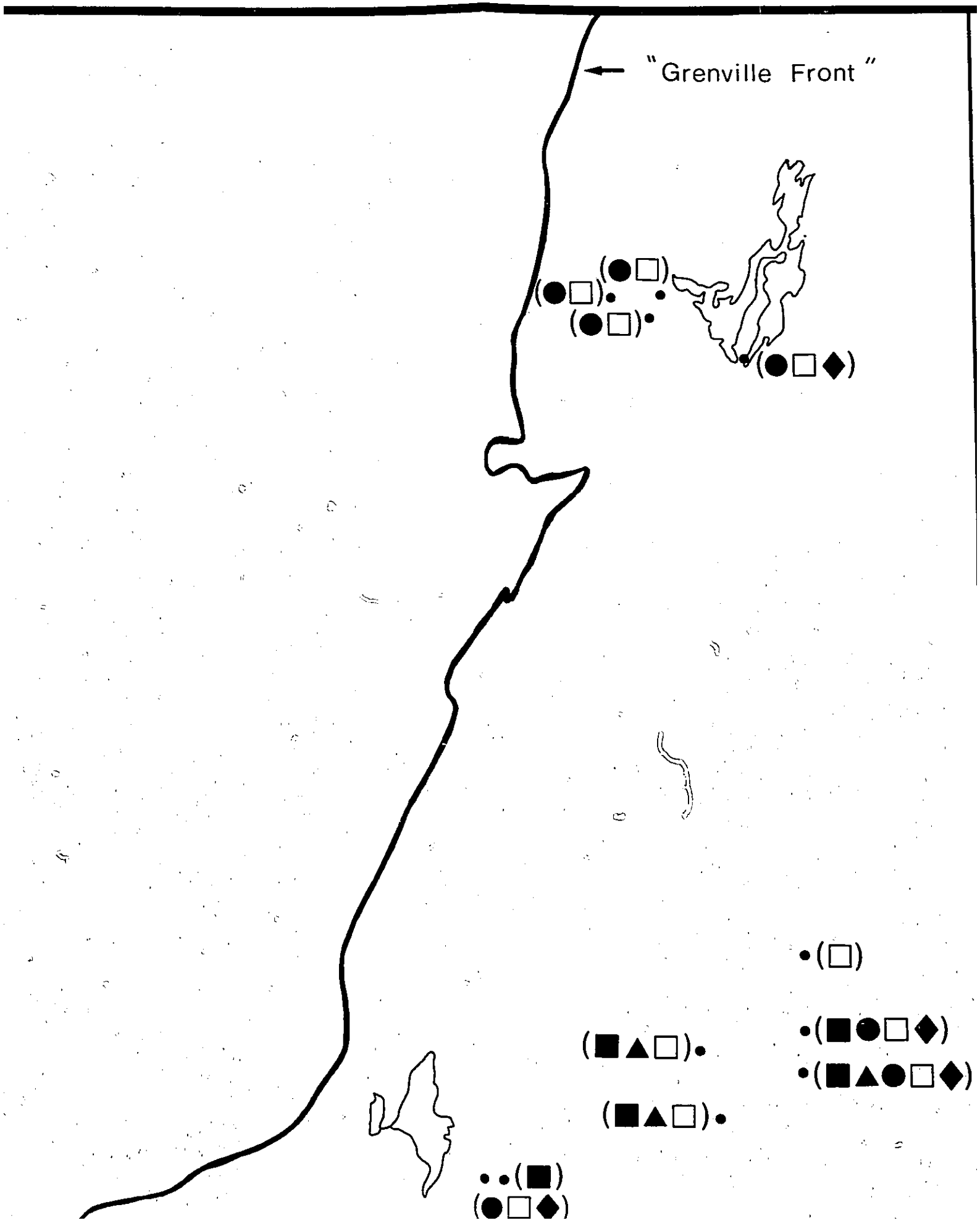
"Grenville Front"
(●□)
(●□)
(●□)
(●□◆)
•(□)
•(■●□◆)
•(■▲●□◆)
(■▲□)•
(■▲□)•
••(■)
(●□◆)

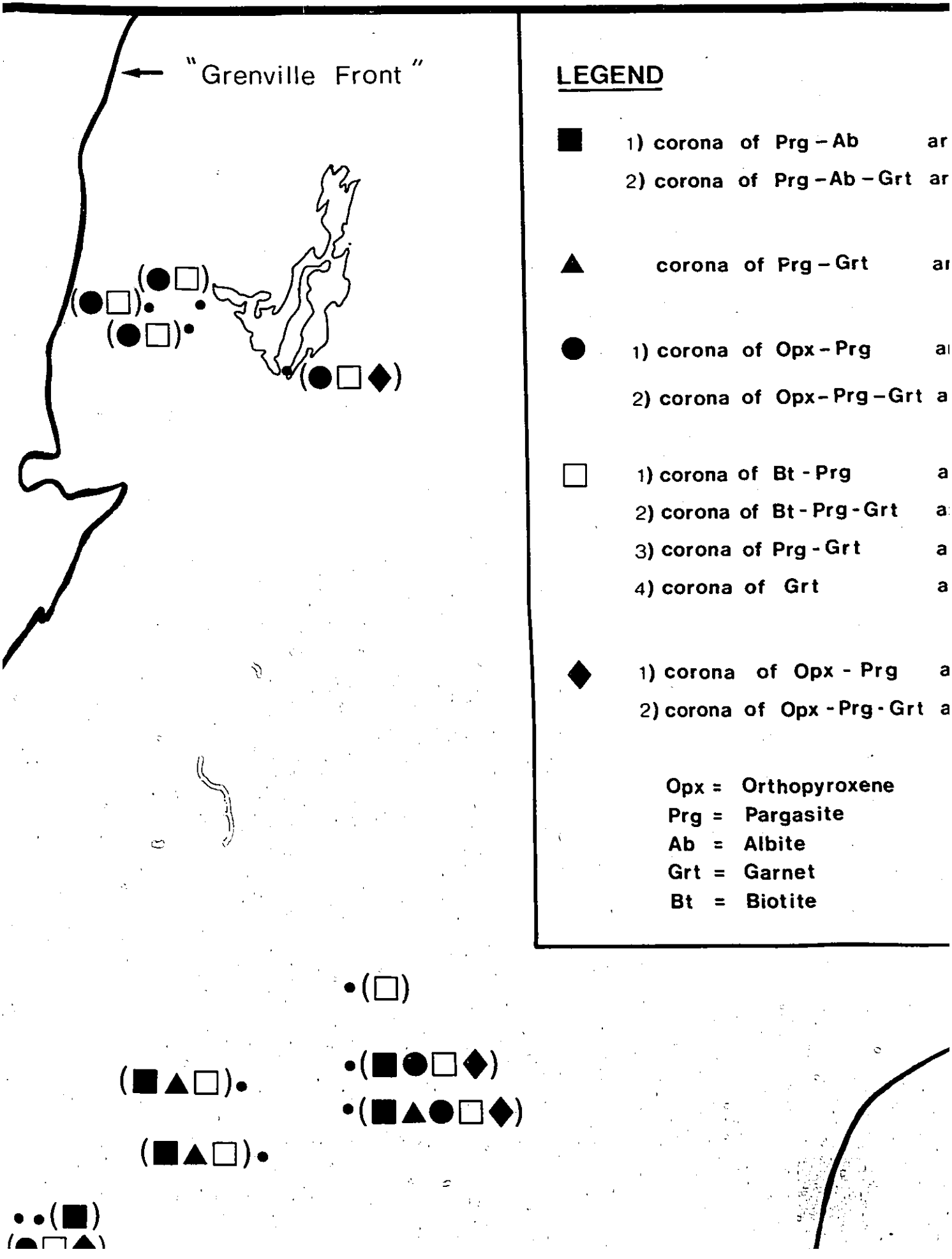
"Grenville Front"
LEGEND
■ 1) corona of Prg – Ab ar
2) corona of Prg – Ab – Grt ar
▲ corona of Prg – Grt ar
● 1) corona of Opx – Prg a
2) corona of Opx – Prg – Grt a
□ 1) corona of Bt - Prg a
2) corona of Bt - Prg - Grt a
3) corona of Prg - Grt a
4) corona of Grt a
◆ 1) corona of Opx - Prg a
2) corona of Opx - Prg - Grt a
Opx = Orthopyroxene
Prg = Pargasite
Ab = Albite
Grt = Garnet
Bt = Biotite

50° 15'

LEGEND

■ 1) corona of Prg – Ab around Augite

2) corona of Prg – Ab – Grt around Augite

▲ corona of Prg – Grt around Pyroxene aggregates

● 1) corona of Opx – Prg around Opx – Mag sympl.

2) corona of Opx – Prg – Grt around Opx – Mag sympl.

□ 1) corona of Bt - Prg around Mag - Ilm

2) corona of Bt - Prg - Grt around Mag - Ilm

3) corona of Prg - Grt around Mag - Ilm

4) corona of Grt around Mag - Ilm

◆ 1) corona of Opx - Prg around Olivine

2) corona of Opx - Prg - Grt around Olivine

Opx = Orthopyroxene
Prg = Pargasite
Ab = Albite
Grt = Garnet
Bt = Biotite

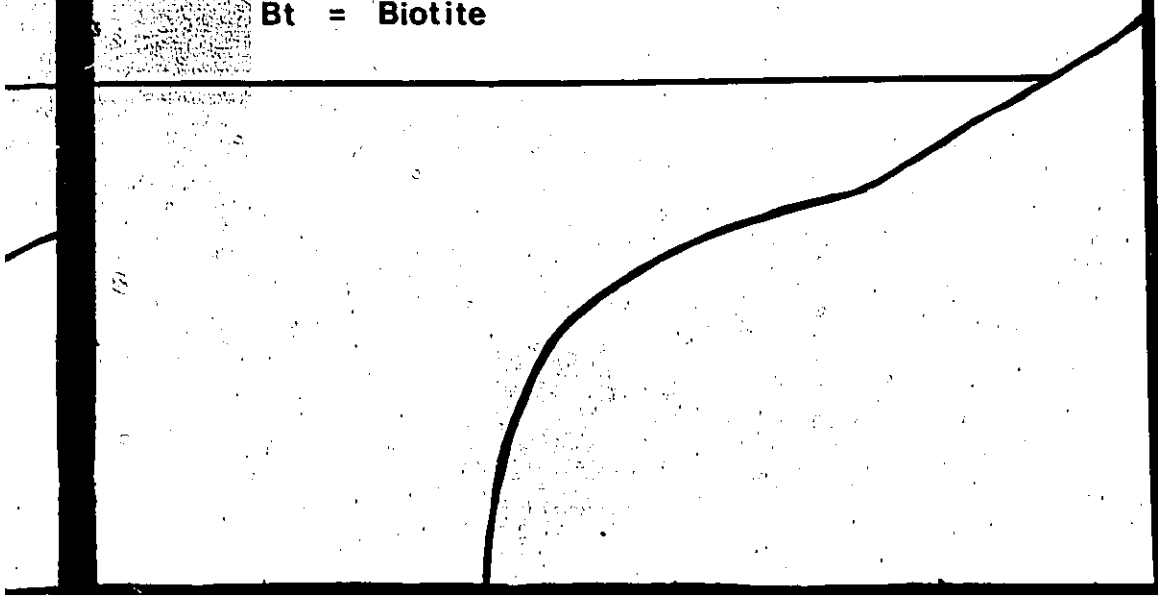

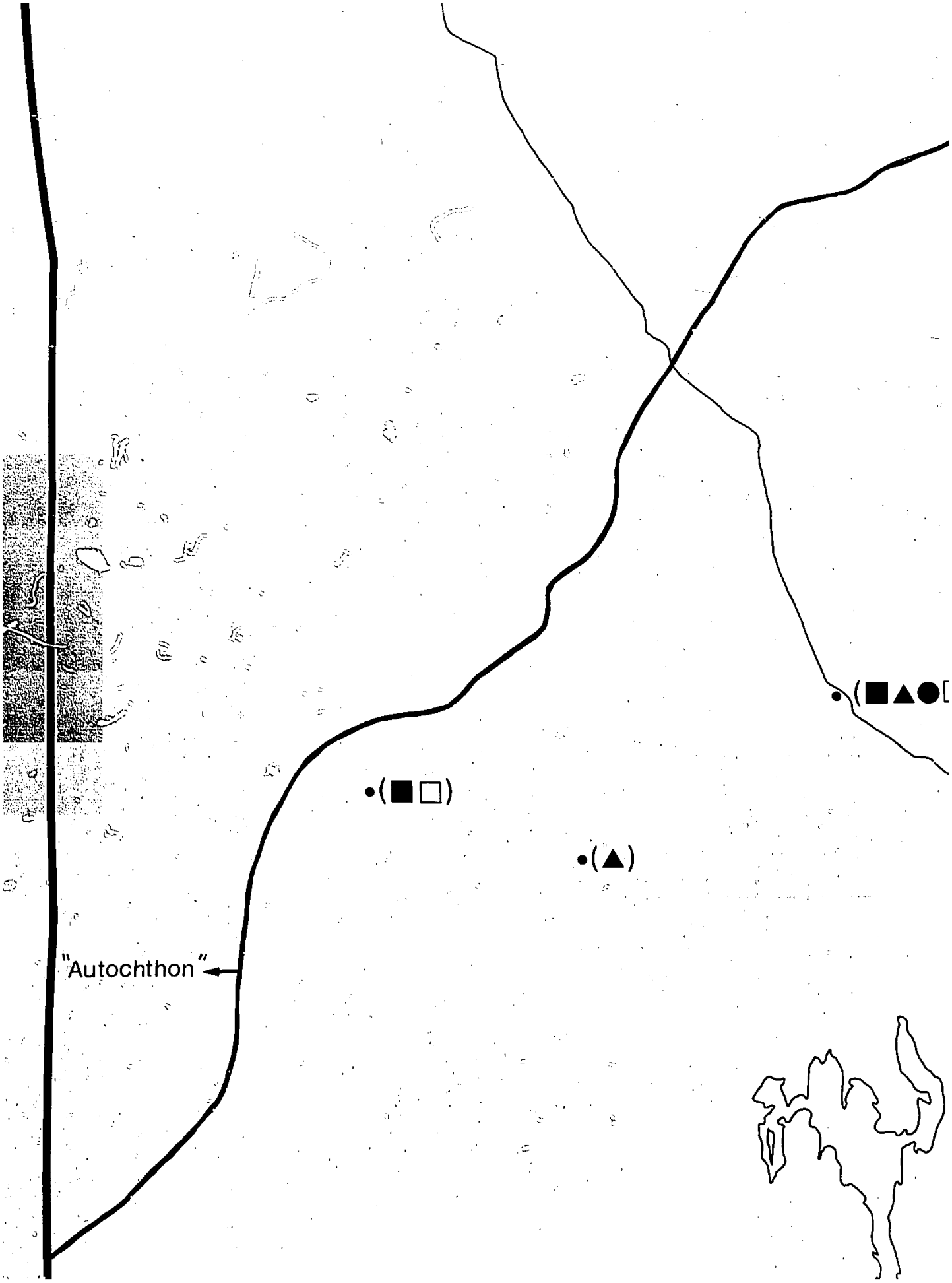
•(■▲●□
•(■□)
•(▲)
"Autochthon"

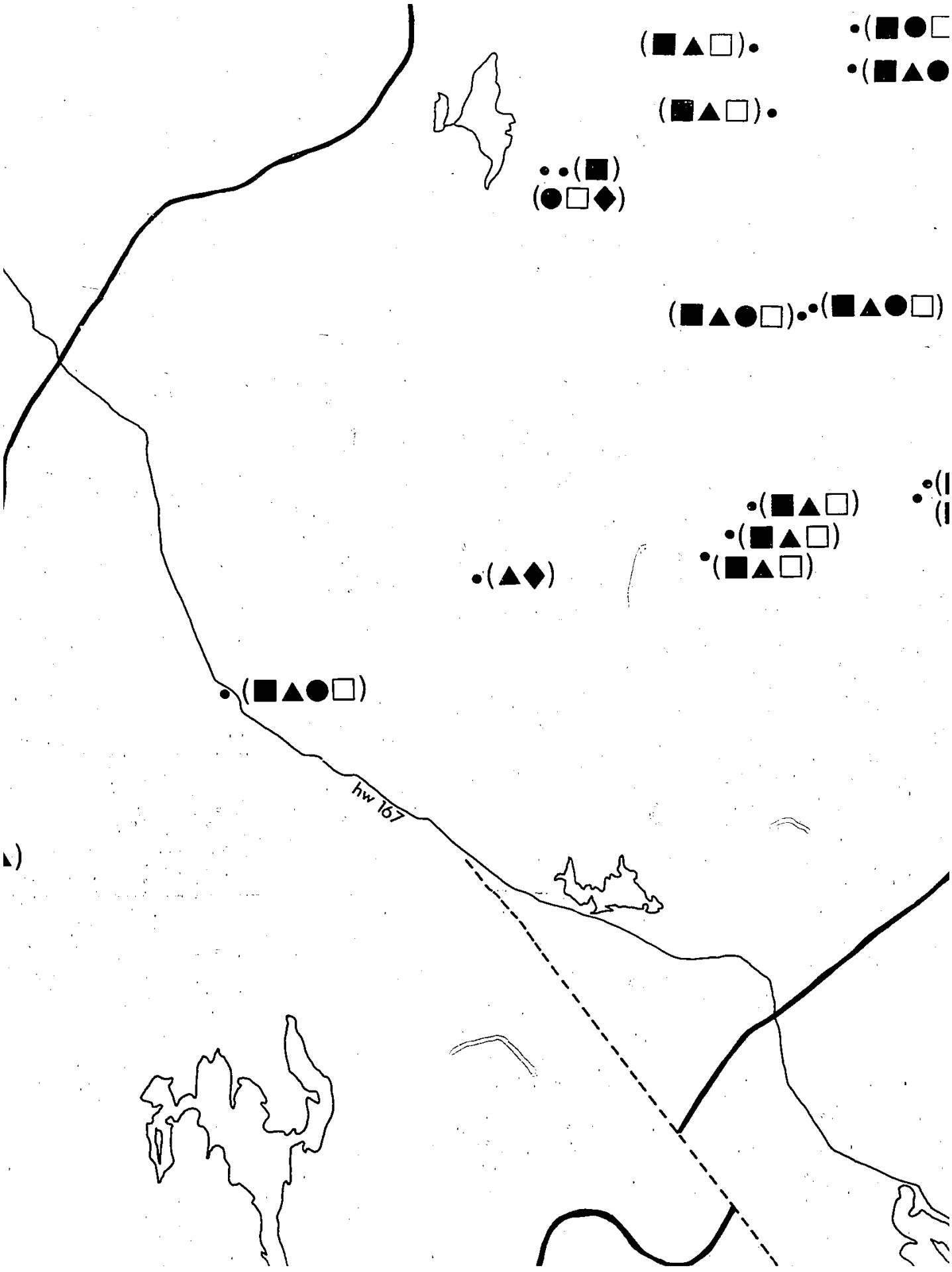
hw 167

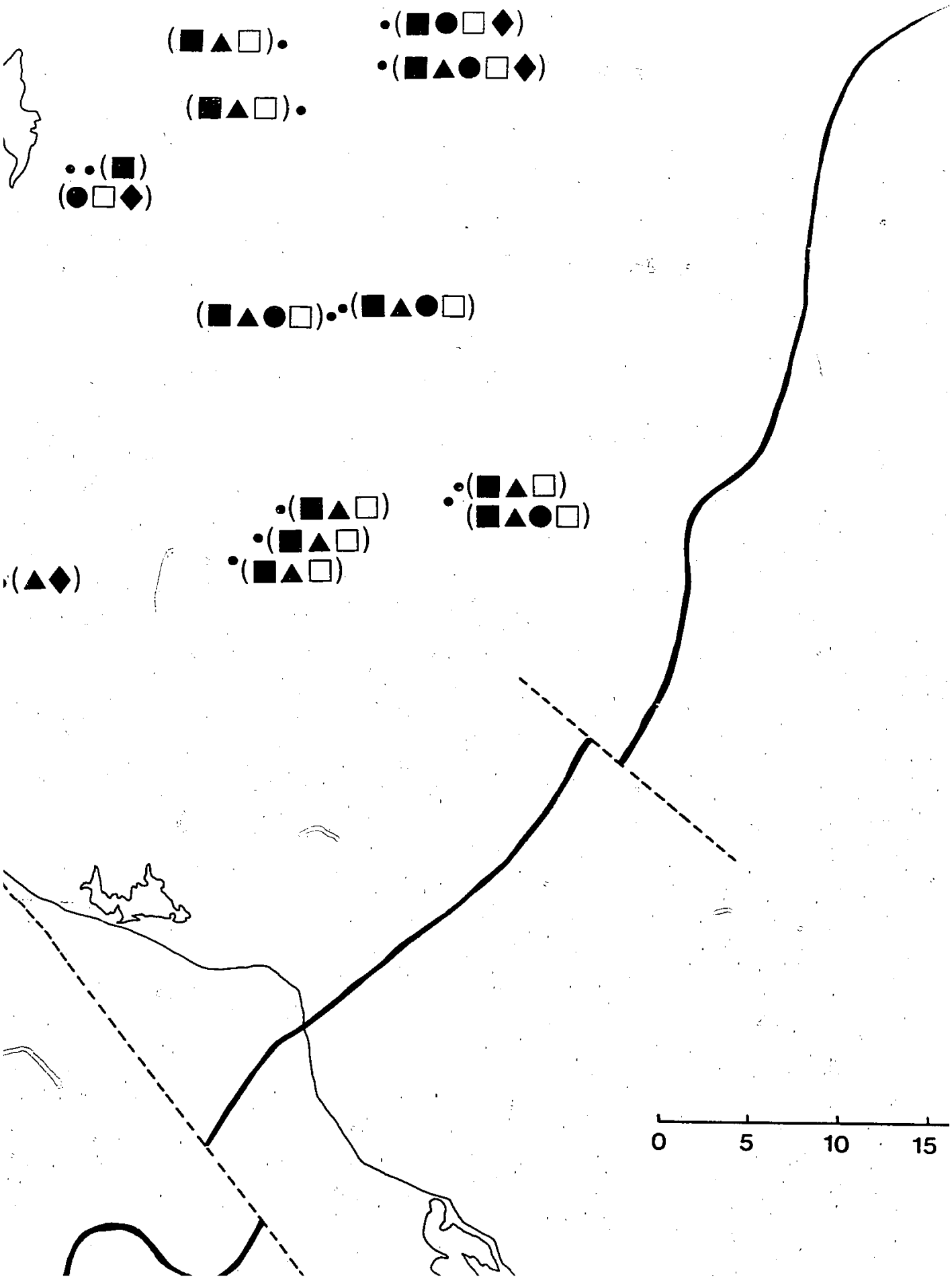
(■▲□)•
•(■●□◆)
•(■▲●□◆)
(■▲□)•
••(■)
(●□◆)
(■▲●□)••(■▲●□)
•(■▲□)
•(■▲□)
•(■▲□)
•(■▲□)
(■▲●□)
(▲◆)
0
5
10
15

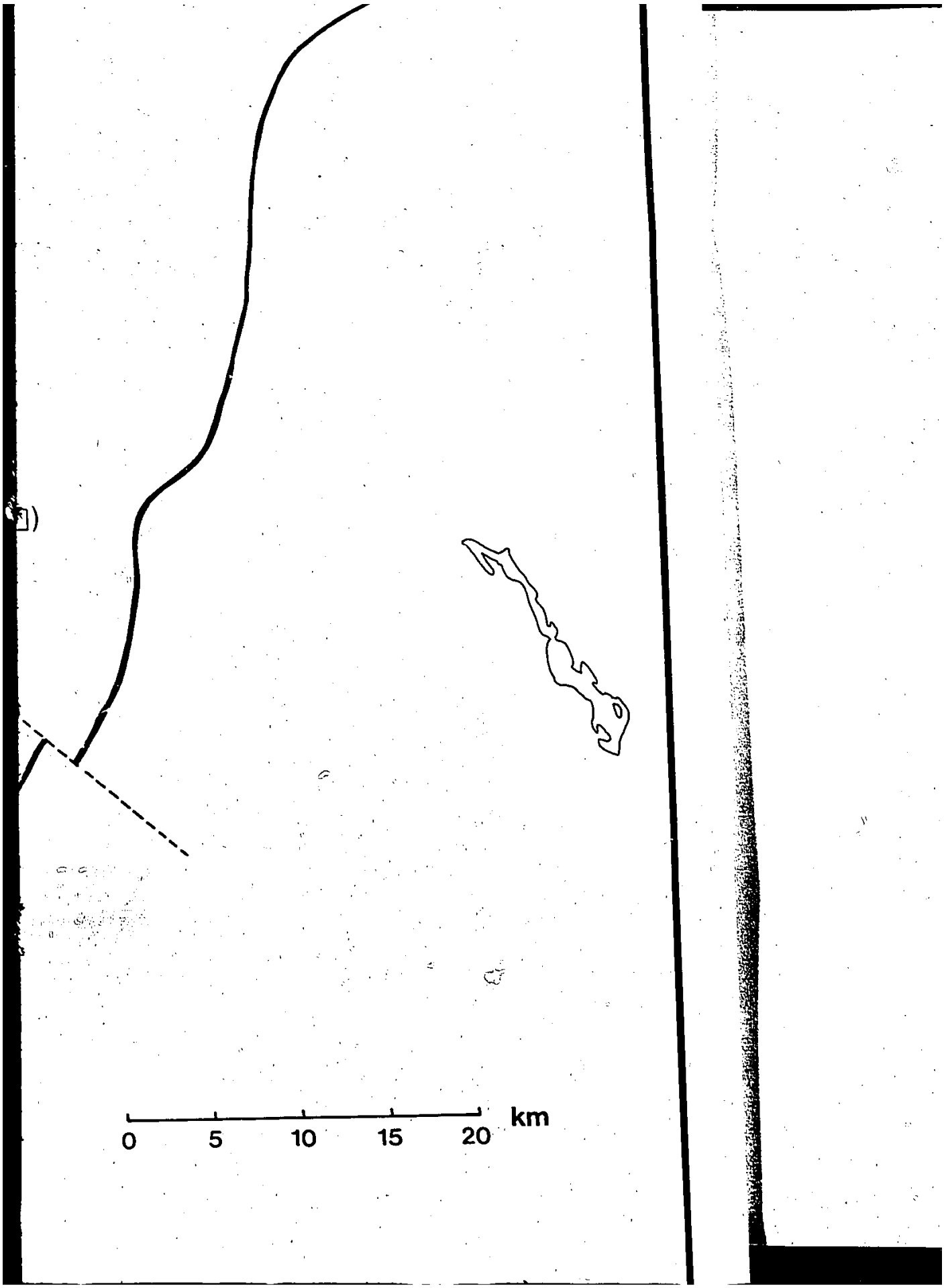
0
5
10
15
20
km

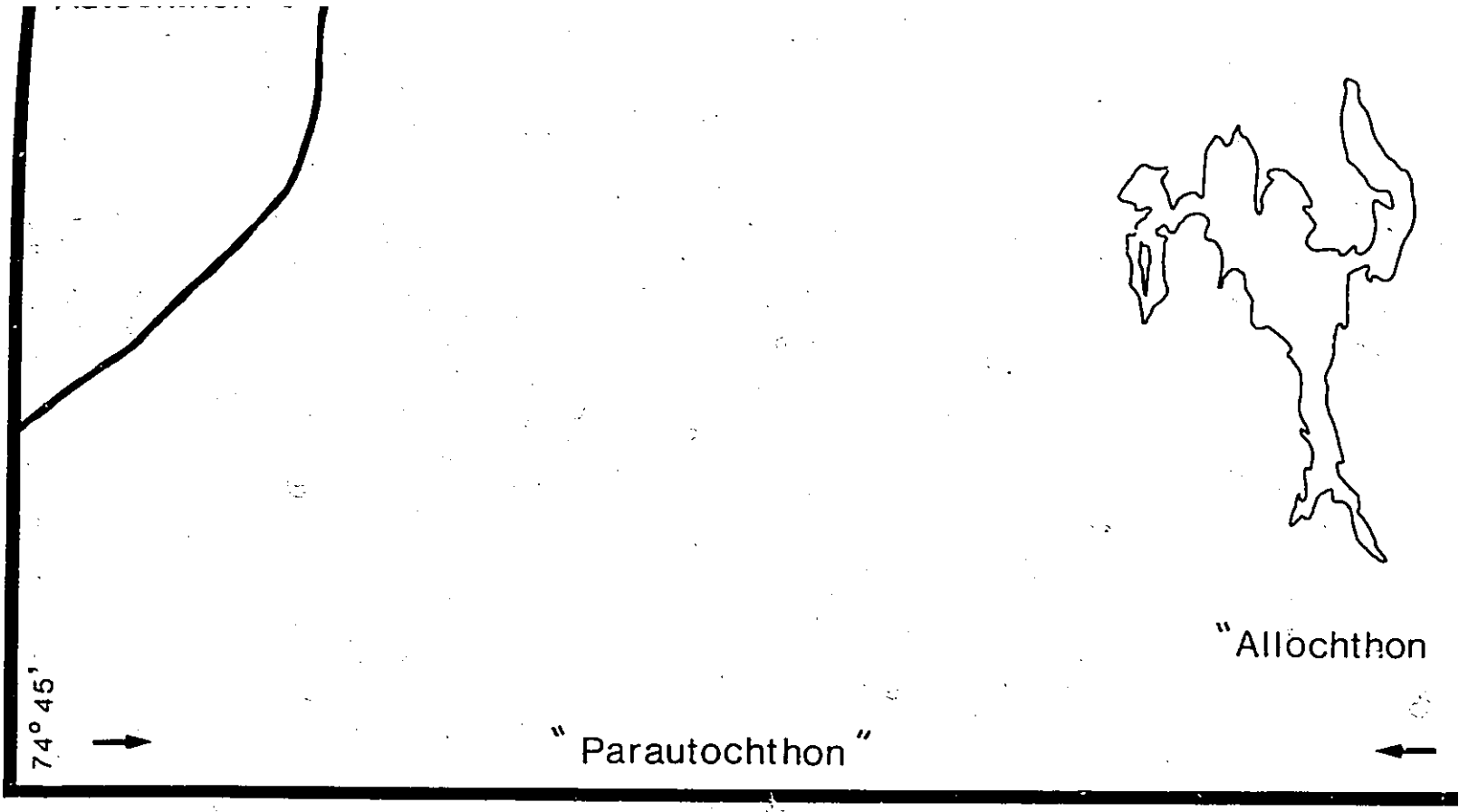
"Allochthon
74° 45'
" Parautochthon "

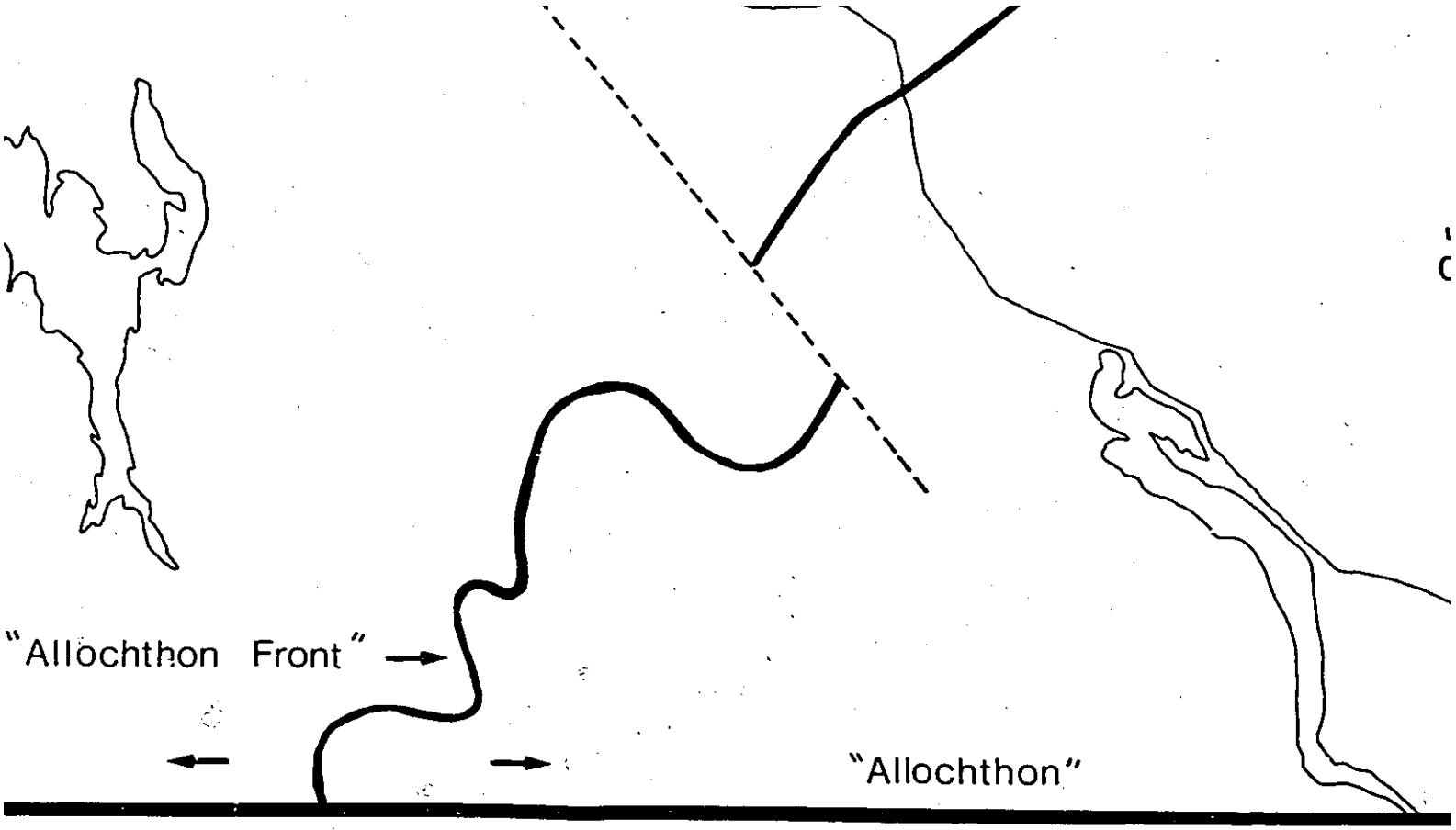
"Allochthon Front"
"Allochthon"

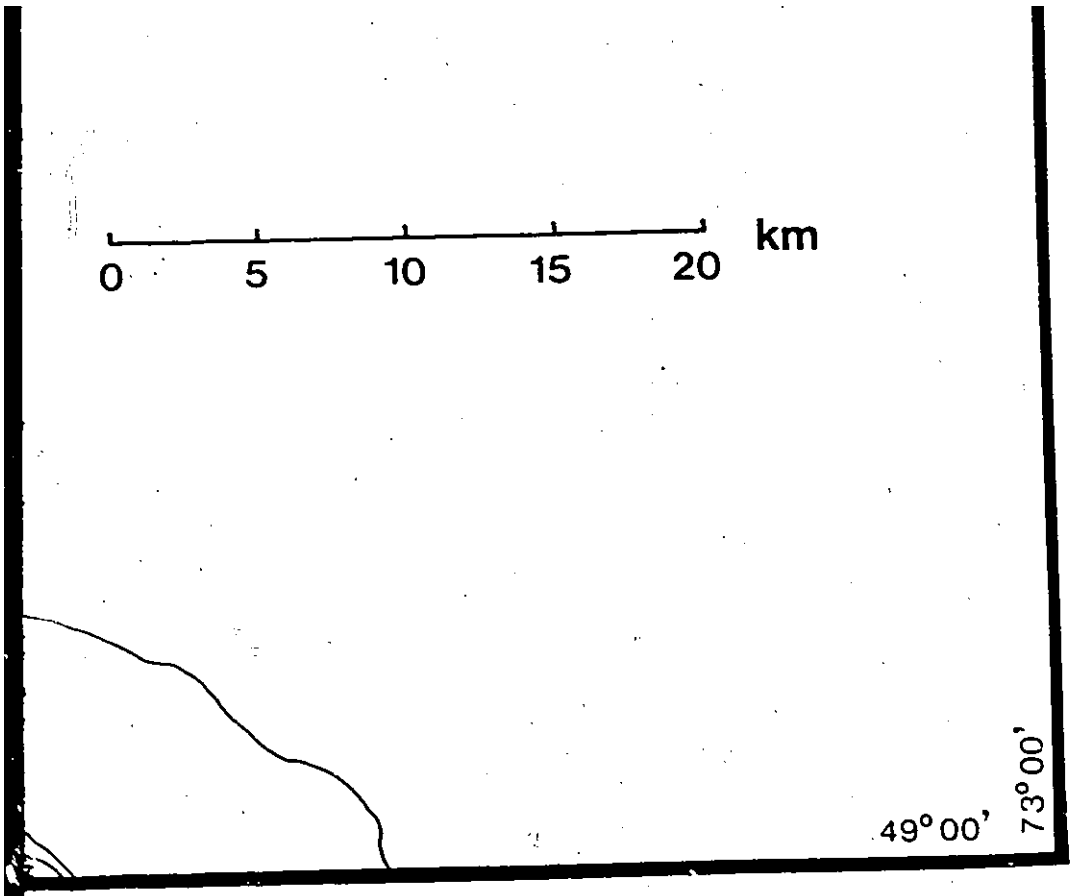
0
5
10
15
20
km
49° 00'
73° 00'

Figure 34

Distribution of geochemical groups with respect to sample locations

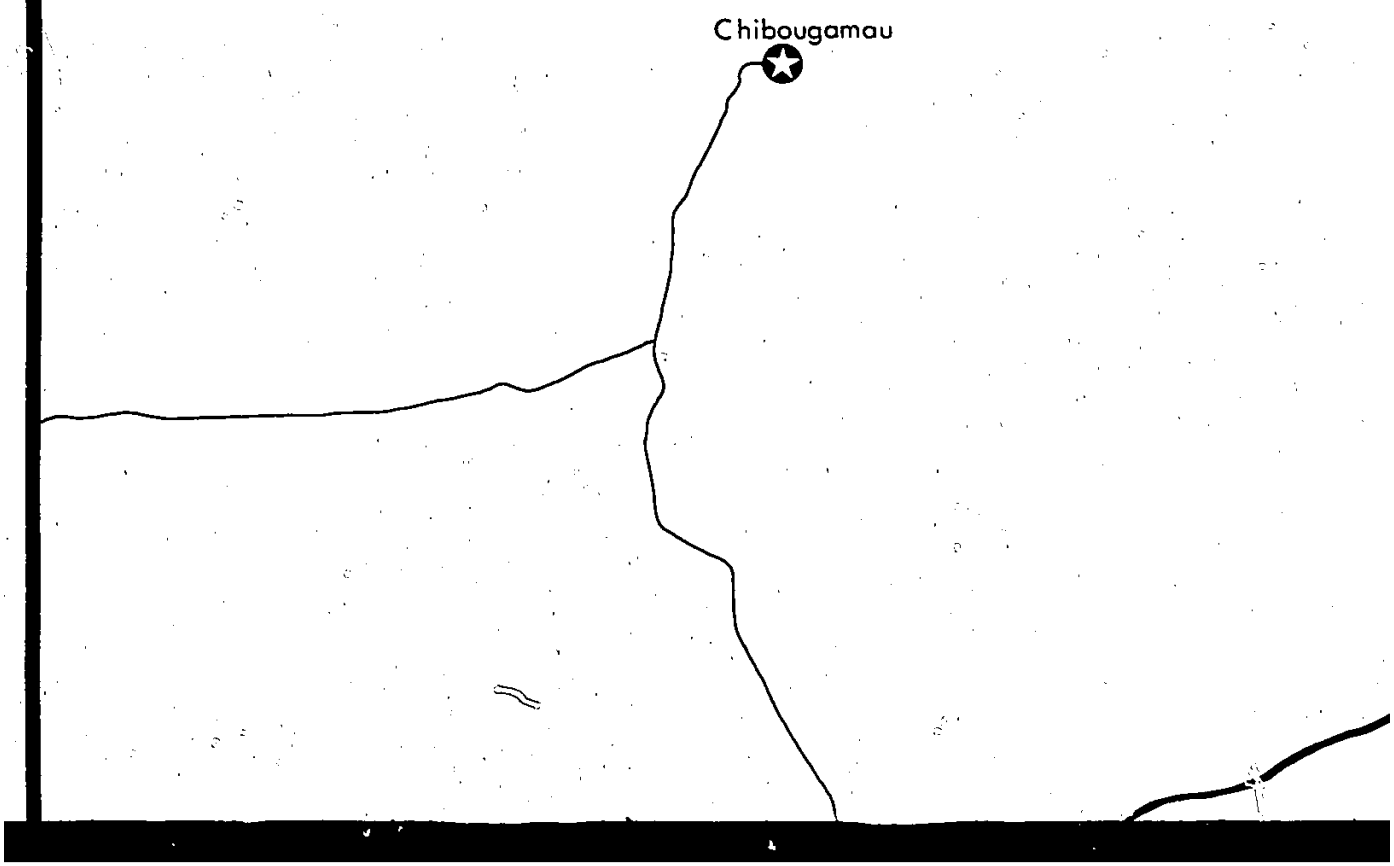

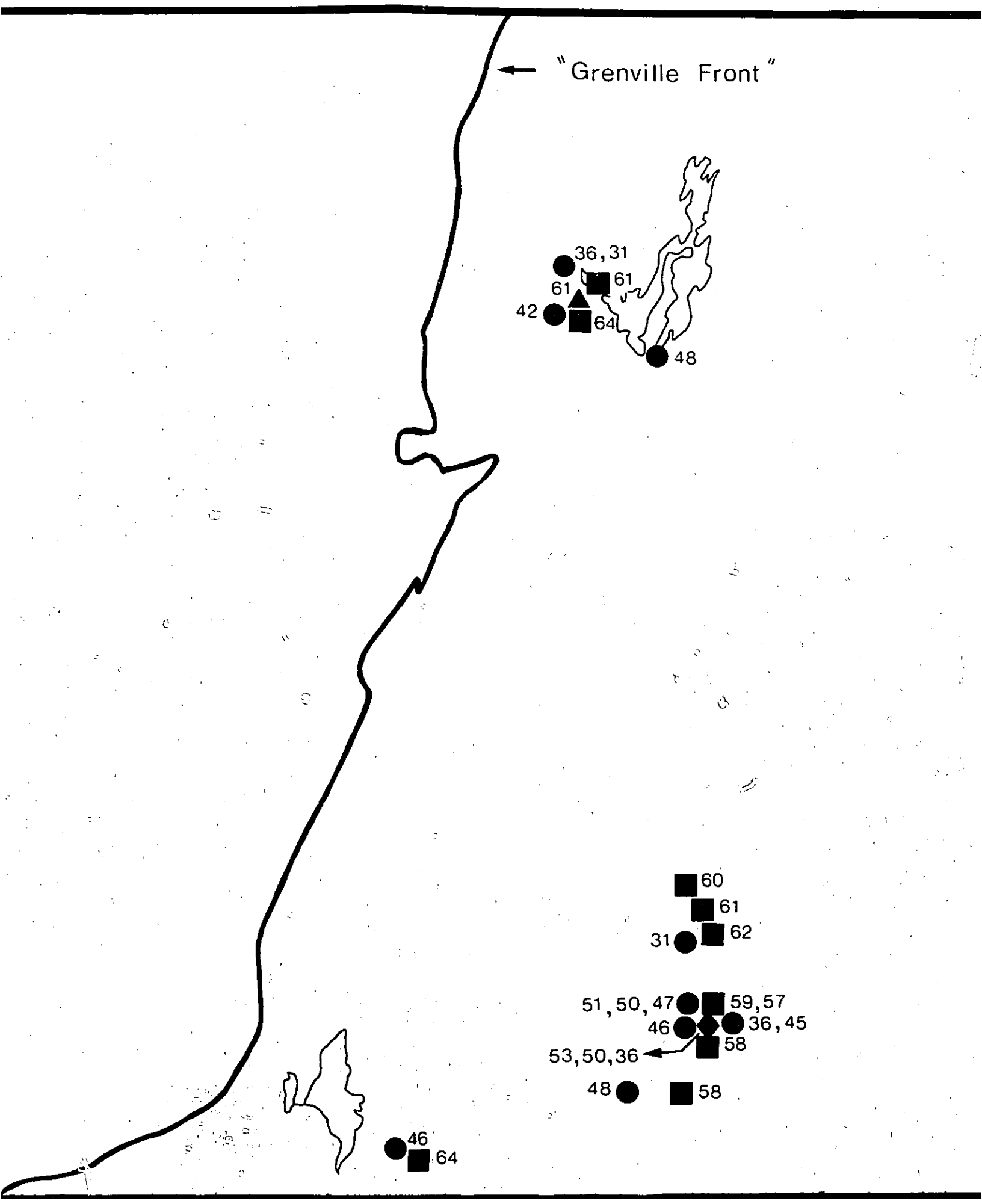
"Grenville Front"
36,31
61
61
42
64
48
60
61
31
62
51,50,47
59,57
46
36,45
58
53,50,36
48
58
46
64

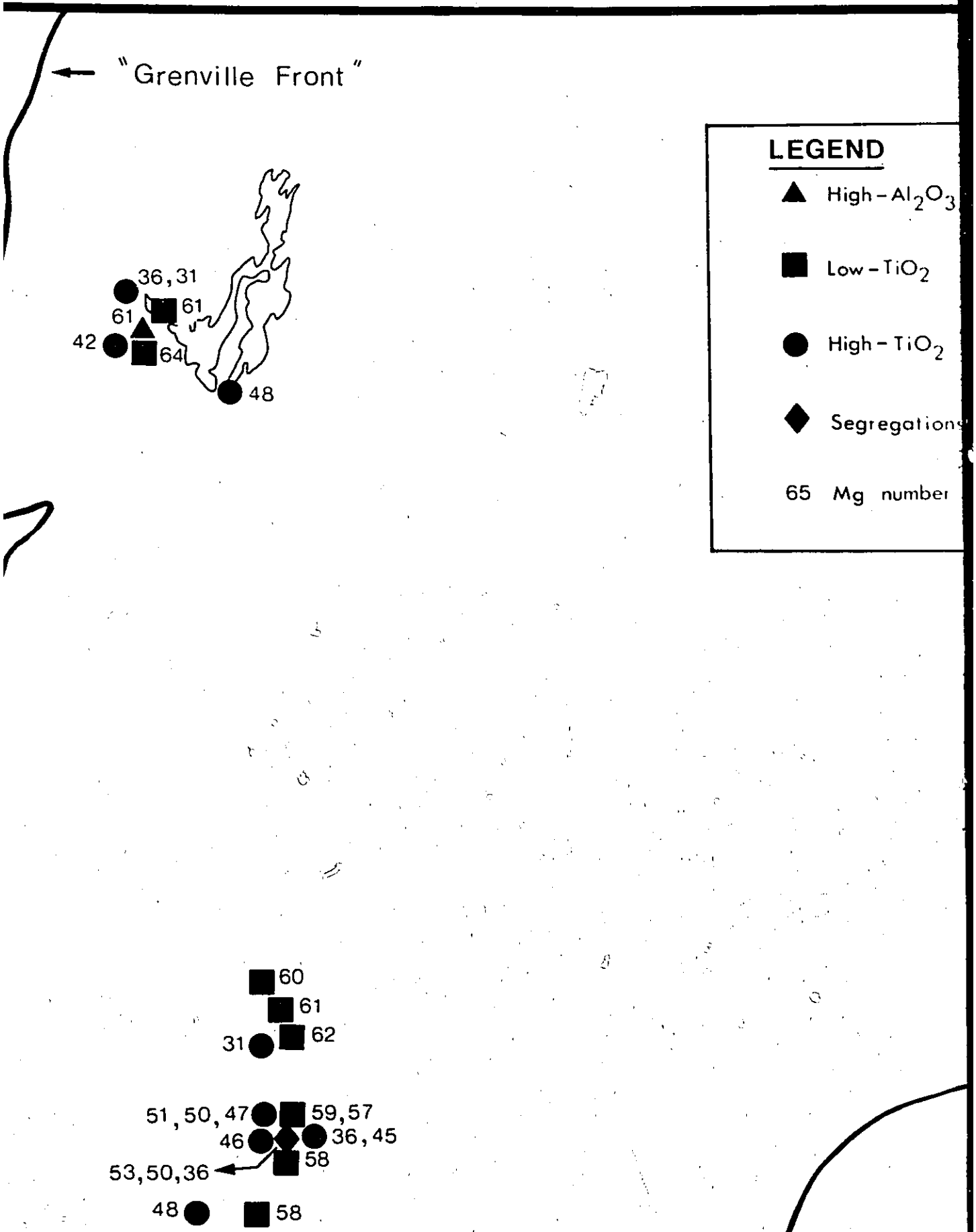
"Grenville Front"
LEGEND
High - Al_2O_3
Low - TiO_2
High - TiO_2
Segregations
65 Mg number
36,31
61
61
42
64
48
60
61
62
31
51,50,47
59,57
46
36,45
58
53,50,36
48
58

50° 15'

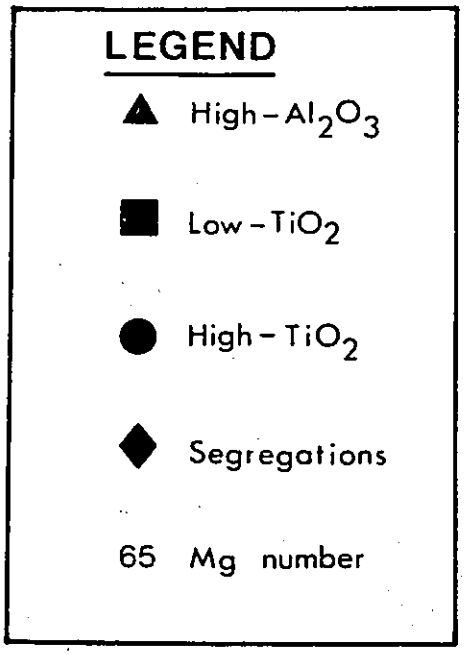
LEGEND
High – Al_2O_3
Low – TiO_2
High – TiO_2
Segregations
65 Mg number

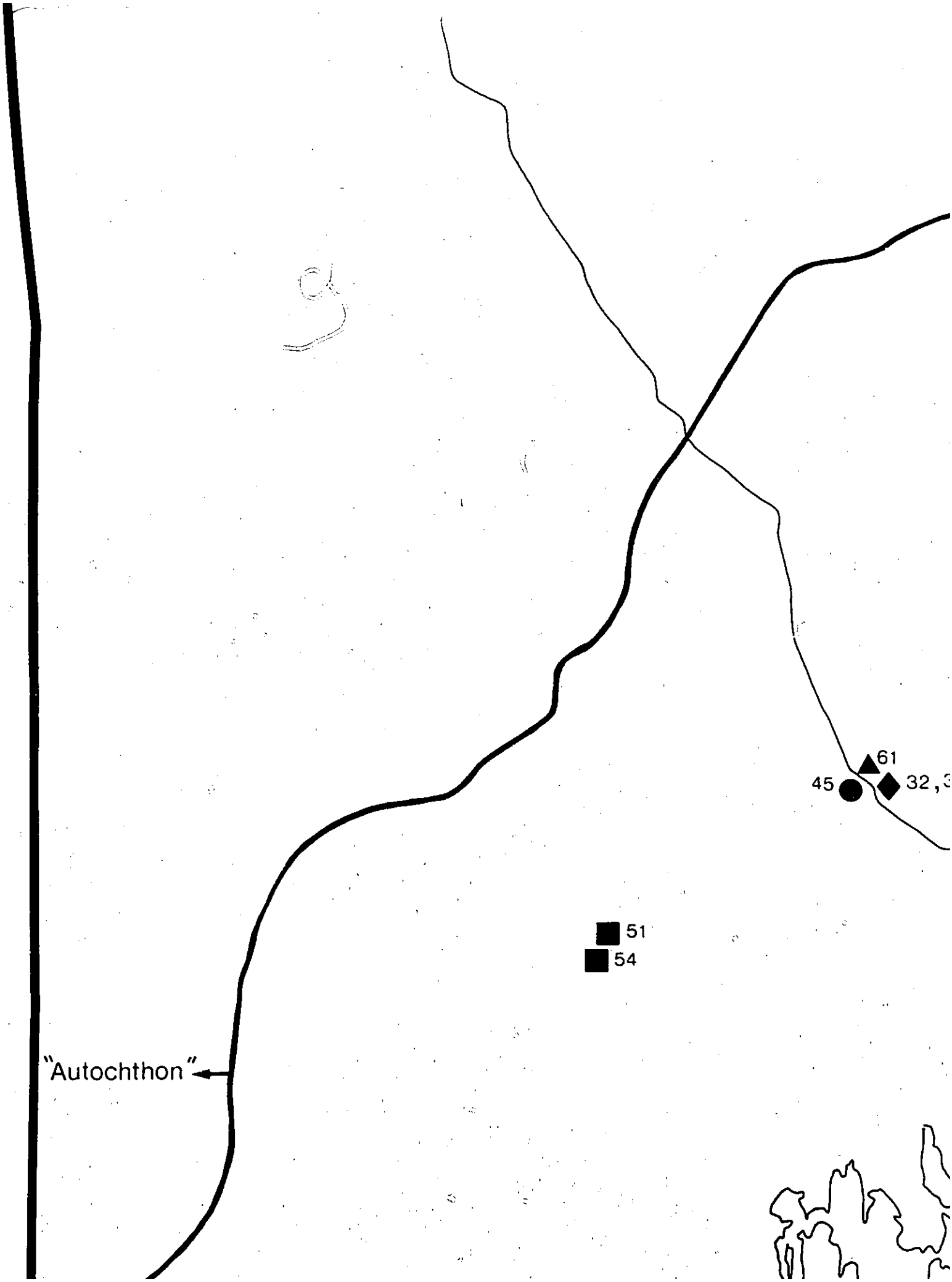
61
45
32,3
51
54
"Autochthon"

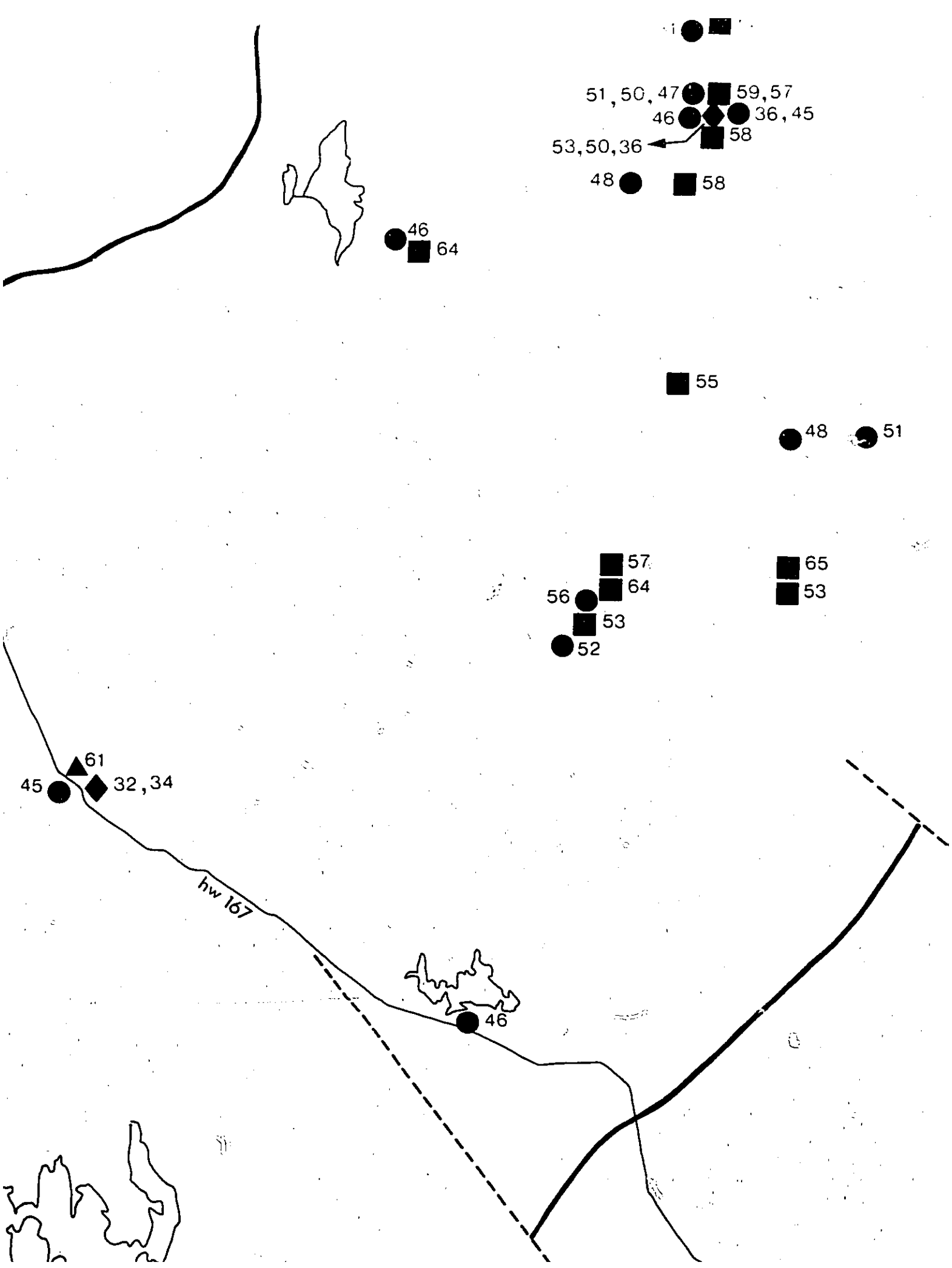
51, 50, 47
59, 57
46
36, 45
58
53, 50, 36
48
58
46
64
55
48
51
57
64
56
53
52
65
53
61
45
32, 34
hw 167
46

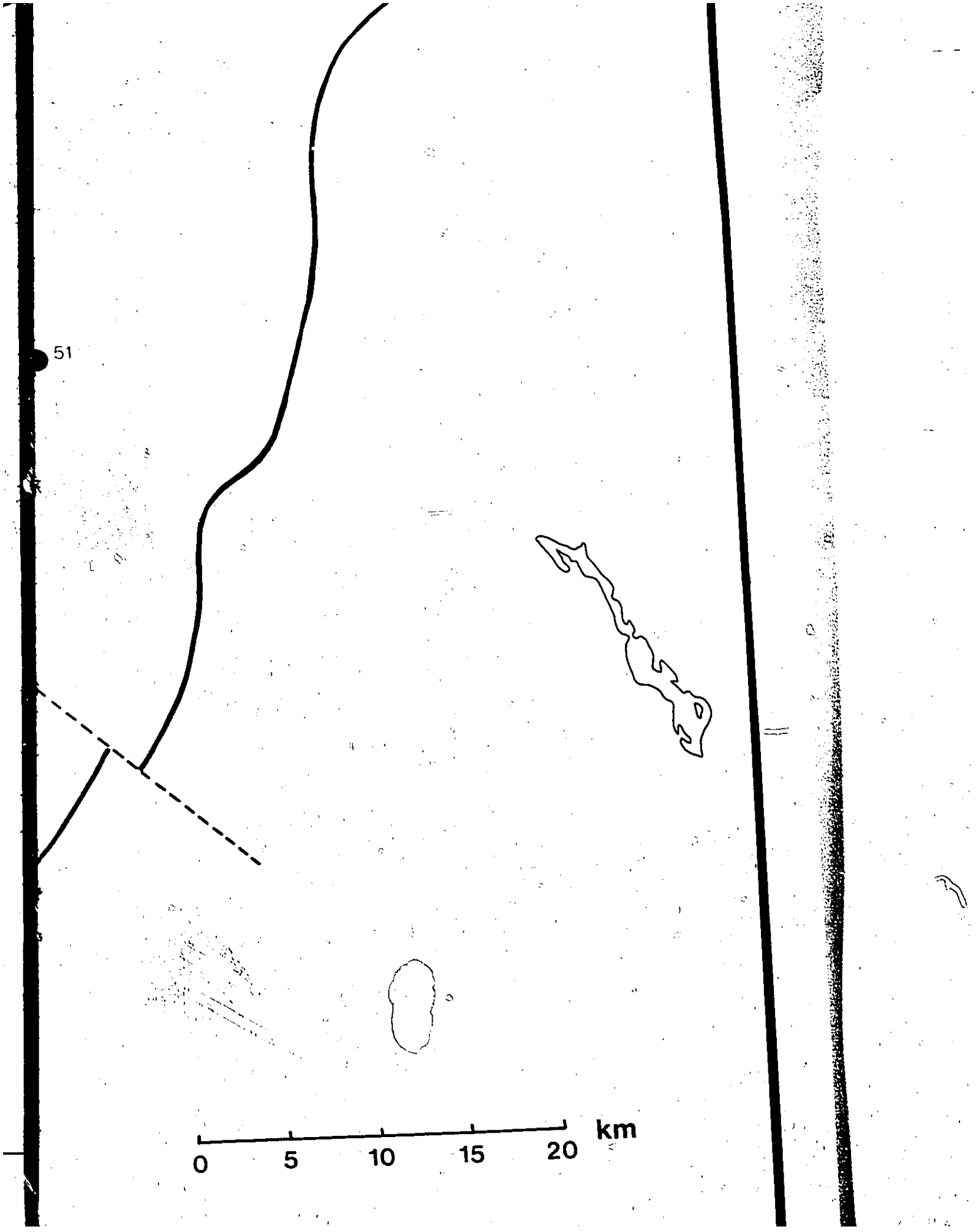
51
0
5
10
15
20
km

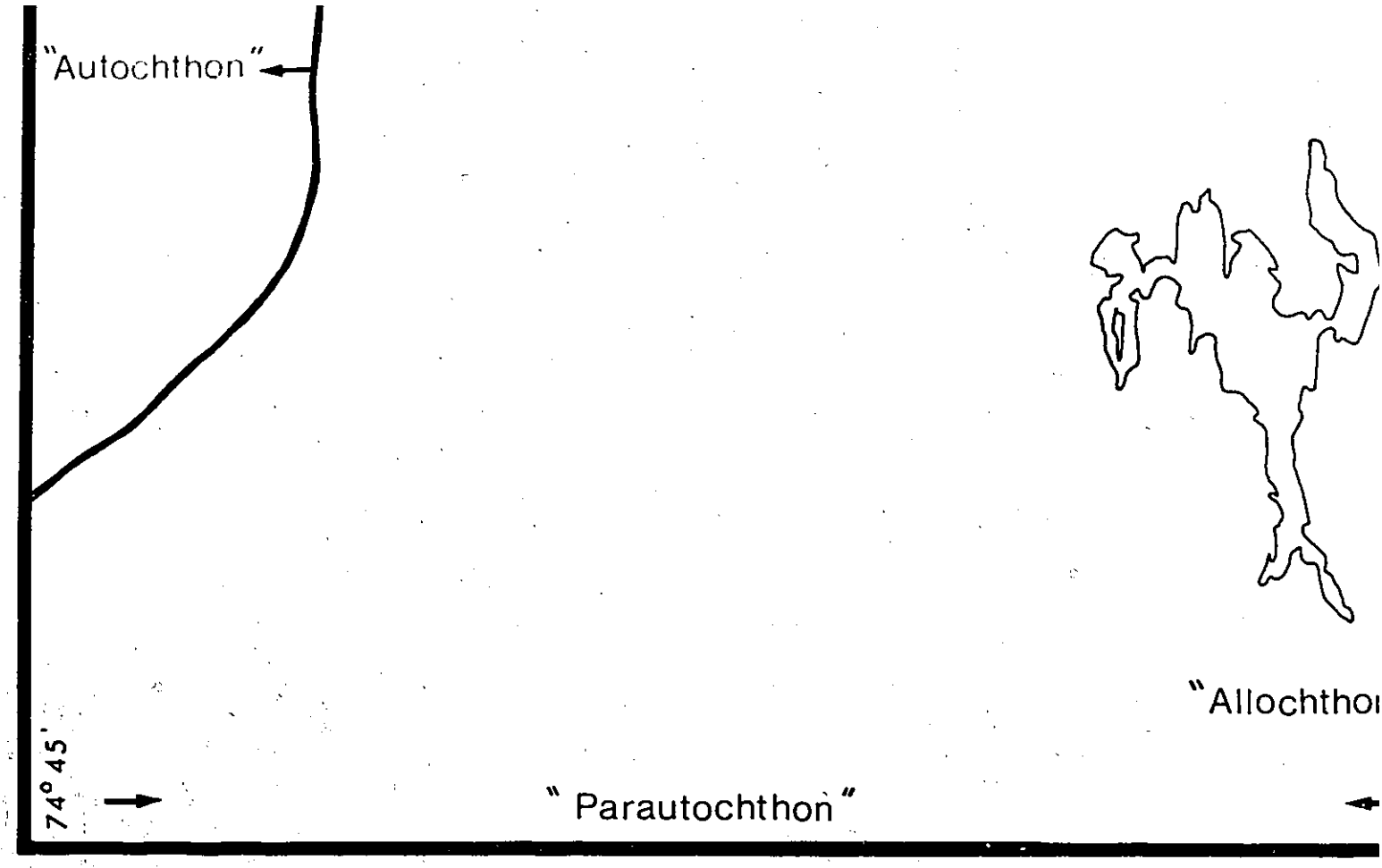
"Autochthon"
"Allochthon
74°45'
" Parautochthon"

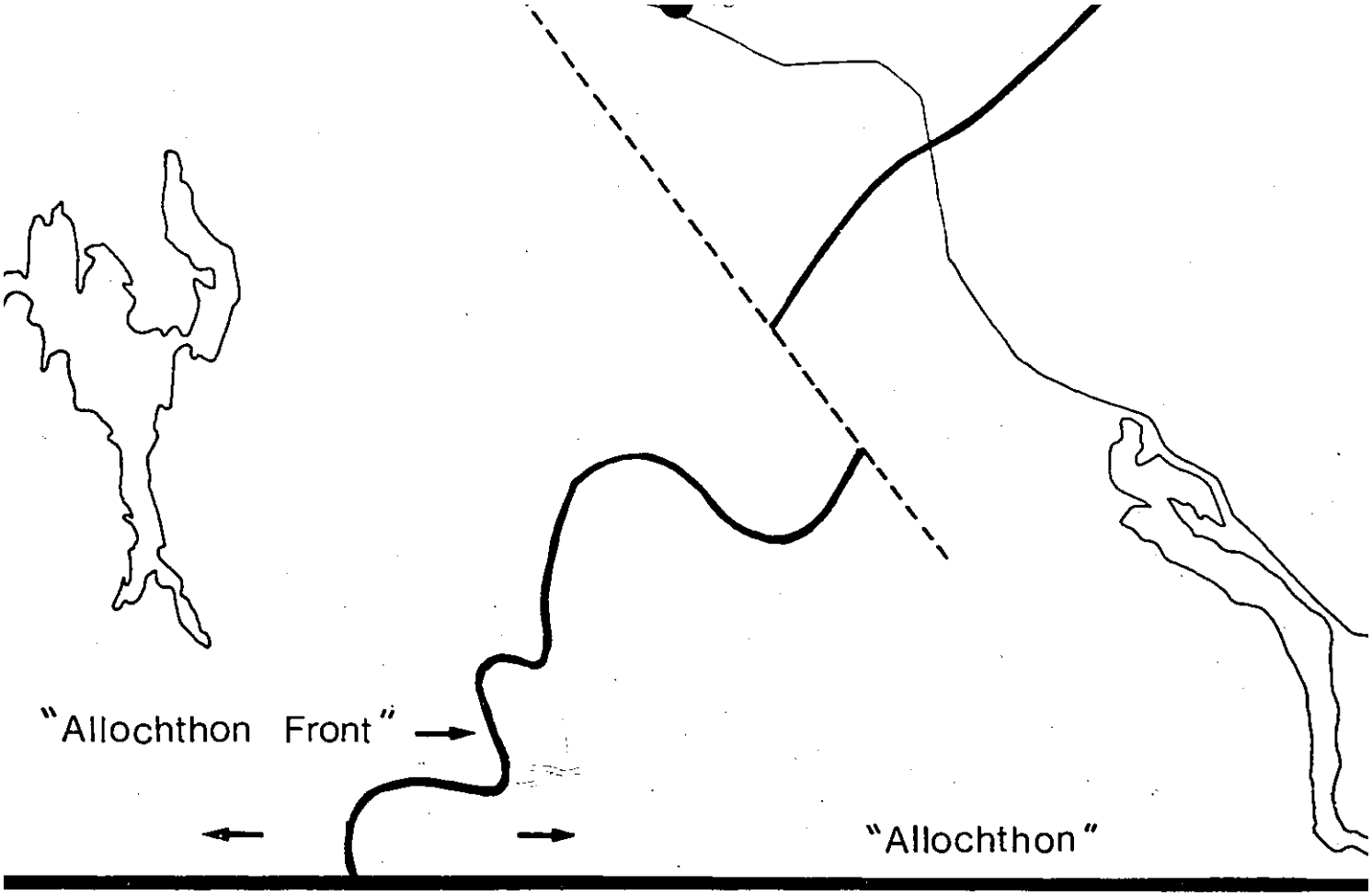
"Allochthon Front"
"Allochthon"

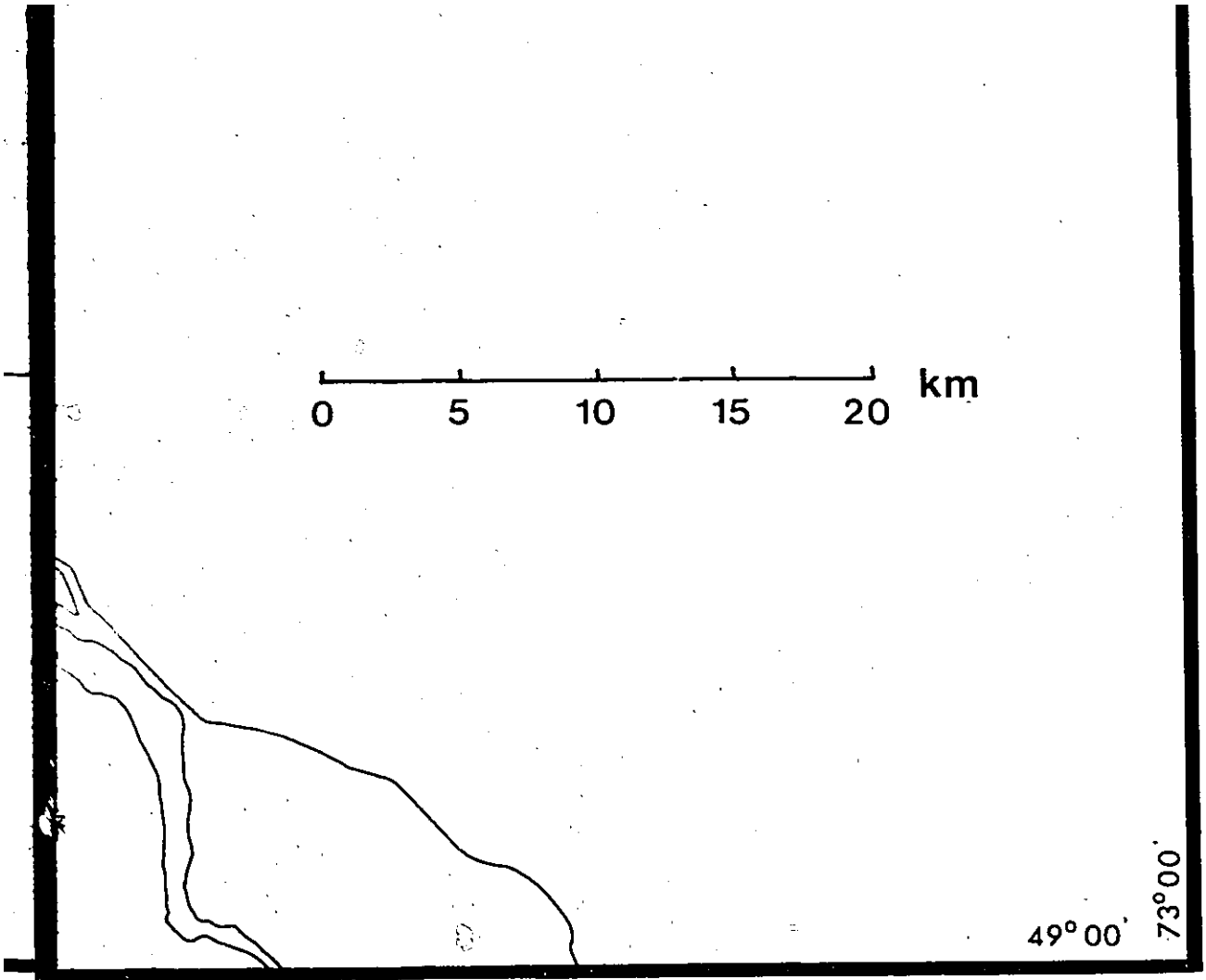
0
5
10
15
20
km
49° 00'
73° 00'